



**NITRIC OXIDE FORMATION ANALYSIS USING CHEMICAL
REACTOR MODELLING AND LASER INDUCED FLUORESCENCE
MEASUREMENTS ON INDUSTRIAL SWIRL FLAMES**

BY

SYED MASHRUK

A thesis submitted in partial fulfilment of the requirements for the degree of:

Doctor of Philosophy

in

Mechanical Engineering

**CARDIFF UNIVERSITY
SCHOOL OF ENGINEERING**

February 2020

To my dear wife

Xianyu

Summary

This thesis investigates nitric oxide formation in the combustion of fuel compositions representative of those produced by the power generator gas turbines. As power generation gas turbine manufacturers and operators strive for improvements in thermal efficiency while abiding by the emissions regulation put into place, more detailed understanding of formation of different emissions is required to accurately simulate combustion of increasingly volatile gaseous fuel supplies. Detailed modelling of an industrial scale high-pressure generic swirl burner has been carried out to predict the formation of oxides of nitrogen at exhaust. Three new models are proposed based on the models available in the literature and simulation results are compared against each other as well as with the experimental data. The predictions from the selected model at different conditions has been appraised against the experimental results using several chemical kinetics mechanisms from the literature to validate the proposed chemical reactor model.

Nitric oxide formation analysis is also carried out by taking in-flame non-intrusive laser induced fluorescence measurements for the first time on industrial swirl flames with a range of gaseous fuel. These experimental nitric oxide formation distributions are supported through the use of experimentally derived heat release intensities and numerical calculations. Changes in NO formations at different physical conditions with methane and methane-hydrogen fuel blends are discussed. Two calibration techniques are discussed and performed at the latter part of the thesis for quantification of the qualitative nitric oxide distribution data from this study in future. Data generated from this investigation provide opportunities for future validation work of chemical kinetics modelling and computational fluid dynamics analysis. In addition to that, results from this thesis will also inform gas turbine manufacturers on potential burner design modifications for better management of oxides of nitrogen emissions. Based on this work, future investigations may focus on quantitative nitric oxide formation analysis in alternative fuels like ammonia-methane-hydrogen blends.

Acknowledgements

I would like to start by thanking Prof. Richard Marsh for giving me this opportunity when I was on the verge of leaving the country and his continuous guidance, motivation and supervision for the last four years. I would also like to acknowledge Prof. Phil Bowen and Dr. Andrew Crayford for their thoughtful input and feedback throughout my PhD.

I am very grateful to Dr. Jon Runyon for all the late experimenting days and for all his teaching on laser operation with patience. I would also like to mention Dr. Dan Pugh for all the early morning lifts and continuous guidance since I came to Cardiff. To Dr. Tony Giles, Dr. Burak Gokepte and Mr. Steve Morries, I would like to express my heartiest gratitude for all the help on all those test days. Sincere appreciation to Mr. Jack Thomas and Mr. Terry Treherne for designing and building equipment to make this work a success. Many thanks to Gina Goddard-Bell for all the help to make my life easier at Cardiff.

My greatest gratitude also goes to the Flex-E-Plant Consortium for the funding of this work. I would like to thank Dr. Dave Abbott from Uniper Technologies and Dr. Suresh Sadasivuni from Siemens for valuable inputs on modelling of the swirl burner.

I will be forever grateful to my parents for all their teaching throughout my life, which made me the person I am. My father would have been the happiest person in the whole world if he were with us. I miss you dad every day since you left us and wish I could tell you about all the work I have done to make your dream come true.

For tolerating my behaviour, nonsense attitude and all the teaching since I came to UK eleven years back, I would like to thank my good friend and more than brother, Mahbub Sohel. There isn't enough space to mention all the people who helped me in reinforcing the believe that I can do it. To mention a few: Seif-Eddine Zitouni (for all the talks and fun we had), Mahmud Safat Khan (for all the good discussions since 2009).

Finally, I cannot describe the support and cooperation I had in words from my wonderful wife and life partner, Xianyu. This one is for you!

Nomenclature

β_{quench}	- Total Quenching
Γ	- Overlap Fraction
γ	- Cumulative Correction Factor
$2\gamma_A$	- Broadening Coefficient
δ	- Shift Coefficient
δ_D	- Diffusion (reaction) Thickness (mm)
δ_{flame}	- Flame Brush Thickness
δ_G	- Gradient Thickness
δ_t	- Reaction Zone Thickness
λ	- Thermal Conductivity
μ	- Dynamic Viscosity ($\text{kgm}^{-1}\text{s}^{-1}$)
μ_φ	- Mean Equivalence Ratio
ν	- Wavenumber (cm^{-1})
ρ	- Density (kgm^{-3})
σ	- Effective Rotational Cross Section (cm^2)
σ_φ	- Standard Deviation
Φ	- Equivalence Ratio
Φ_{FL}	- Fluorescence Yield
$\varphi(\nu)$	- Lineshape Function
Ω	- Solid Angle of Collection
A	- Total Fluorescence Rate (s^{-1})
A_{21}	- Spontaneous Emission Rate (s^{-1})
A_{noz}	- Burner Exit Nozzle Area (mm^2)
A_{tan}	- Tangential Inlet Area (mm^2)
$AvgInten_{NO}$	- Average NO PLIF Intensity
$AvgInten_{OH}$	- Average OH* chemiluminescence Intensity
B_{12}	- Einstein Coefficient ($\text{m}^3/\text{J}\cdot\text{s}^2$)
B_{21}	- Einstein Coefficient ($\text{m}^3/\text{J}\cdot\text{s}^2$)
C_F	- Calibration Factor
C_P	- Specific Heat Capacity at Constant Pressure
c	- Speed of Light (ms^{-1})
f_B	- Boltzmann Fraction
g_1	- Degeneracy of State 1
g_2	- Degeneracy of State 2
h	- Plank Constant
I_{IC}	- Intersystem Crossing Rate (s^{-1})

I_{LIF}	- LIF Intensity
I_v	- Spectral Irradiance ($W/cm^2 \cdot s^{-1}$)
L_{comb}	- Length of Quartz Confinement Tube (mm)
L_{turb}	- Turbulent Length Scale
Le	- Lewis Number
m	- Mass (g)
n	- Number of Moles
n_0	- Population Number Density
P_2	- Combustor Entry Pressure
P_{PD}	- Predissociation Rate (s^{-1})
Q'	- Volumetric Heat Release Rate (W/cm^3)
Q_{21}	- Rate of Quenching (s^{-1})
Q_{RET}	- Rate of Rotational Energy Transfer (s^{-1})
Q_{VET}	- Rate of Vibrational Energy Transfer (s^{-1})
Q_{tan}	- Tangential Flow Rate (s^{-1})
Q_{tot}	- Total Flow Rate (s^{-1})
r_{noz}	- Burner Exit Nozzle Radius (mm)
r_{tan}	- Effective Radius of the Tangential Inlet (mm)
R_{12}	- Rotational Temperature
Re	- Reynolds Number
s	- Unmixedness Parameter
S_F	- Fluorescence Signal
S_g	- Swirl Number
S_L	- Laminar Flame speed (ms^{-1})
S_T	- Turbulent Flame Speed (ms^{-1})
T_2	- Combustor Entry Temperature
T_u	- Unburned Temperature
u'	- Turbulent Velocity Fluctuation
W_{12}	- Absorption Rate (s^{-1})
W_{21}	- Stimulated Emission Rate (s^{-1})
X_{CH}	- CH Molar Concentration
X_{CH_2}	- CH ₂ Molar Concentration
X_{H_2O}	- H ₂ O Molar Concentration
X_{OH}	- OH Molar Concentration

Abbreviation List

AFT	-	Adiabatic Flame Temperature
BO	-	Blowoff
BPV	-	Backpressure Valve
CCC	-	Committee on Climate Change (UK)
CCD	-	Charge-Coupled Device
CCGT	-	Combined Cycle Gas Turbine
CCS	-	Carbon Capture and Storage
CFD	-	Computational Fluid Dynamics
CMF	-	Coriolis Mass Flowmeter
CRZ	-	Central Recirculation Zone
DUKES	-	Digest of United Kingdom Energy Statistics
EASEE	-	European Association for the Streamlining of Energy Exchange
ERZ	-	Edge Recirculation Zone
EU	-	European Union
FC	-	Fully Closed
FCV	-	Flow Control Valve
FO	-	Fully Open
FZ	-	Flame Zone
GA	-	Gas Analysis
GT	-	Gas Turbine
GTRC	-	Gas Turbine Research Center
HPCR	-	High Pressure Combustion Rig
HPSGB-2	-	High Pressure Generic Swirl Burner (Mk. II)
HPOC	-	High Pressure Optical Chamber
ICCD	-	Intensified Charge-Coupled Device
ID	-	inner Diameter
LBO	-	Lean Blowoff
LIF	-	Laser induced Fluorescence
LNG	-	Liquefied Natural Gas
MFC	-	Mass Flow Controller
MZ	-	Mixing Zone
NO _x	-	Oxides of Nitrogen
OD	-	Outer Diameter
PC	-	Partially Closed
PFZ	-	Post Flame Zone

PIV	-	Particle Imaging Velocimetry
PLIF	-	Planar Laser Induced Fluorescence
PVC	-	Precessing Vortex Core
P2G	-	Power-to-Gas
SNR	-	Signal to Noise Ratio
SO _x	-	Oxides of Sulphur
TBC	-	Thermal Barrier Coating
UK	-	United Kingdom
UKCS	-	United Kingdom Continental Shelf
UV	-	Ultraviolet
VSD	-	Variable Speed Drive

Contents Index

Summary	ii
Acknowledgements	iii
Nomenclature	iv
Abbreviation List	vi
List of Figures	xiv
List of Tables	xxii
Thesis Contribution	xxiv
1. Introduction.....	1
1.1. Natural Gas in the UK	2
1.1.1. LNG and Natural Gas - Hydrogen Blends	3
1.2. Source of Emissions	5
1.3. Impact of Fuel Quality Variation on NO _x Formation.....	8
1.4. Measurements of Emissions.....	9
1.5. Scope of Research	10
1.6. Aims and Objectives.....	11
1.7. Outline of this Thesis	12
2. LIF Theory and Literature Review.....	14
2.1. Formation and Reburn of Oxides of Nitrogen in Combustion.....	14
2.1.1. Thermal Mechanism	15
2.1.2. Prompt Mechanism	16
2.1.3. Fuel Mechanism	18
2.1.4. Minor Mechanisms	19
2.2. Chemiluminescence	21
2.3. Laser Induced Fluorescence (LIF) Spectroscopy	23
2.3.1. LIF Modelling: Quasi - Two - Level System	23
2.3.2. Absorption (W_{12}), Stimulated (W_{21}), and Spontaneous (A_{21}) Emission	24
2.3.3. Rotational and vibrational energy transfer (Q_{RET} and Q_{VET}).....	26
2.3.4. Quenching energy transfer (Q_{21})	27
2.3.5. LIF Equation: Two-Level Derivation.....	27
2.3.6. Broadening and Shifting of Spectral Lines.....	30

2.3.7.	Saturation and Population Recycling	36
2.3.8.	LIF Temperature Dependence	38
2.4.	Computational Simulation of NO-LIF	39
2.4.1.	Other NO-LIF Modelling Simulations.....	39
2.4.2.	LIFSim: Functionality.....	40
2.4.3.	LIFSim: LIF Model	41
2.5.	NO-LIF in the Literature	42
2.5.1.	A-X (0,0) Excitation Overview	43
2.5.2.	A-X (0,1) Excitation Overview	44
2.5.3.	A-X (0,2) Excitation Overview	45
2.5.4.	D-X (0,1) Excitation Overview	45
2.6.	Fundamentals of Flame Properties	46
2.6.1.	Laminar Burning Velocity.....	46
2.6.2.	Turbulent Burning Velocity	47
2.6.3.	Equivalence ratio (Φ):	49
2.6.4.	Adiabatic Flame Temperature (AFT)	49
2.6.5.	Swirl Characteristics.....	49
2.6.6.	Swirl Mechanism	51
2.7.	Summary.....	52
3.	Experimental Set-up, Methodologies and Data Processing.....	54
3.1.	Bunsen Type Burners.....	54
3.2.	High Pressure Combustion Rig (HPCR)	55
3.2.1.	High Pressure Optical Chamber (HPOC).....	56
3.2.2.	High Pressure Generic Swirl Burner (Mk. II)	56
3.2.3.	Fuel and Air Delivery System	59
3.3.	Selection of NO Excitation Wavelengths.....	60
3.4.	Laser System.....	63
3.5.	Detection System and Optical Setup	65
3.6.	Data Acquisition and Image Processing	68
3.6.1.	Data Acquisition.....	68
3.6.2.	Image Processing	69
3.7.	Emissions Gas Analysis	74

3.8.	Fuel Selection	76
3.8.1.	Fuel Matrix for Chemical Reactor Modelling	76
3.8.2.	Fuel Matrix for this Study	77
3.8.3.	Fuel Matrix for Future Work	77
3.9.	Numerical Calculations	79
3.9.1.	Chemical Kinetics Modelling	79
3.9.2.	Chemical Reactor Modelling	83
3.10.	Chemical Kinetics Modelling and Flame Thickness Calculations	86
3.10.1.	Flame Reaction Zone Thickness Calculations	89
3.11.	Summary	95
4.	Reactor Network Modelling Analyses	97
4.1.	Chemical Kinetics Model	97
4.2.	Reactor Network Models	100
4.2.1.	Models from Literature	100
4.2.2.	Proposed Models	102
4.3.	Comparison of Reactor Models	104
4.4.	Comparison of Mechanisms	111
4.4.1.	1.1 bara conditions	112
4.4.2.	2.2 bara conditions	117
4.4.3.	3.3 bara conditions	119
4.5.	Summary	122
5.	Planar NO-LIF in Unconfined Flames	124
5.1.	Bunsen burner NO-PLIF measurements	124
5.1.1.	Horizontal Orientation	124
5.1.2.	Vertical Orientation	126
5.2.	NO PLIF in HPGSB-2 without Quartz	138
5.2.1.	OH* Chemiluminescence Comparison	139
5.2.2.	NO PLIF Comparison	143
5.3.	CHEMKIN Simulation for NO prediction	153
5.3.1.	Benchmarking Modified Valera Model	154
5.3.2.	Comparison of Predictions with Measured NO Values	155
5.3.3.	Sensitivity Analyses	157

5.4.	Summary.....	171
6.	Planar NO-LIF in Confined Flame	173
6.1.	285.16 nm Excitation	173
6.1.1.	Base ($\Phi = 0.55 - 0.65$)	173
6.1.2.	Effects of Hydrogen Addition	184
6.1.3.	Effects of Confinement on Flame Shape and NO formation.....	196
6.2.	226.03 nm Excitation	211
6.2.1.	Non-preheated Conditions	211
6.2.2.	Pre-heated Conditions	216
6.2.3.	Effect of Pre-heating on NO Formation	218
6.3.	CHEMKIN Simulation for NO prediction	220
6.3.1.	Model Benchmarking	221
6.3.2.	Comparison Between Predicted and Measured NO	221
6.4.	Summary.....	228
7.	NO Calibration towards Quantitative Analysis.....	230
7.1.	Quenching and Calibration	231
7.2.	NO LIF in Bunsen flames.....	233
7.2.1.	NO PLIF Calibration at 285.16nm	234
7.2.2.	NO LIF Calibration at 226.03nm.....	239
7.3.	Summary.....	245
8.	Conclusions.....	246
8.2.	Chemical Reactor Modelling	246
8.3.	Qualitative NO Formation Analysis in Unconfined and Confined Flames	247
8.4.	NO Calibration towards Quantitative Analysis.....	249
	Recommendations for further Work	250
	References.....	251
	APPENDIX A - NO and O ₂ Excitation Spectra at the 'doubling range' of Dye Laser	274
	Appendix A.1 - NO Excitation Spectra - 1780 K.....	274
	Appendix A.2 - O ₂ Excitation Spectra - 1780 K	275
	Appendix A.3 - NO Excitation Spectra - 2210 K.....	276
	Appendix A.4 - O ₂ Excitation Spectra - 2210 K	277

Appendix A.5 - NO and O ₂ Excitation Spectra (285.1 - 285.2 nm) - 1780 K	278
Appendix A.6 - NO and O ₂ Excitation Spectra (285.1 - 285.2 nm) - 2210 K	279
APPENDIX B - MATLAB Routines	280
Appendix B.1 - MATLAB code for normalising shot-to-shot laser energy to the maximum laser energy	280
Appendix B.2 - MATLAB code for temporally averaging baseline images	281
Appendix B.3: MATLAB code for correcting online and offline images for baseline and normalised shot-to-shot laser energy variation	282
Appendix B.4: MATLAB code for time averaging NO-PLIF images at 285.16 nm excitation and laser sheet distribution correction	283
Appendix B.5: MATLAB code for time-averaging offline images	285
Appendix B.6: MATLAB code for time averaging offline corrected NO-LIF images at 226.03 nm excitation and laser beam distribution correction	287
Appendix B.7: MATLAB code for temporally averaging OH* chemiluminescence images	289
Appendix B.8: MATLAB code for Abel Conversion of time-averaged OH* chemiluminescence image	290
Appendix B.9: MATLAB code for calculating flame thickness from Abel Deconvoluted OH* chemiluminescence image	291
APPENDIX C - Geometry of Mixing Chamber, CRZ, ERZ and Flame Zone for CHEMKIN Reactor Models	293
Appendix C.1 - Geometry of Mixing Chamber	293
Appendix C.2: CFD Result used for CRZ, ERZ and Flame Zone Volume Calculation	294
APPENDIX D - Photographs of HPOC and Bunsen Burner Setup	295
APPENDIX E - Updated Chemical Kinetics Mechanisms with NO_x Formation Pathways and Required Inputs for the Models	296
Appendix E.1 - NO _x pathways for Aramco 1.3 Mechanism	296
Appendix E.2 - NO _x pathways for USII Mechanism	302
Appendix E.3 - NO _x pathways for NUIGalway Mechanism	315
Appendix E.4: Inputs required for the Rizk chemical reactor Network	320
Appendix E.5: Inputs required for the Valera chemical reactor network	321
Appendix E.6: Inputs required for the modified Rizk chemical reactor network	322

Appendix E.7: Inputs required for the modified Valera chemical reactor network	323
Appendix E.8: Inputs required for the simplified chemical reactor network	324
Appendix E.9: Inputs required for the unconfined HPGSB-2 chemical reactor network.....	325
Appendix E.10: Inputs required for the confined HPGSB-2 chemical reactor network.....	326

List of Figures

Figure 1-1: Changes in UK gas production and demand, 1998 - 2018. Reproduced from [19]	2
Figure 1-2: Major sources of UK gas supply and import dependency over the years. Reproduced from [28].	3
Figure 1-3: World energy demand in terms of end-use sector, region and fuel. Reproduced from [36].	5
Figure 1-4: Different GT pollutants with respect to equivalence ratio and power setting. Reproduced from [40].	7
Figure 1-5: Impact of fuel composition on NO _x emissions for four similar GTs. Reproduced from [21].	8
Figure 1-6: Typical variations in European Gas Specifications and Normal Compositions. Reproduced from [44].	9
Figure 2-1: Experimental and theoretical rates for $CH + N_2 \rightarrow NCN + H$. The black symbols denote experimental measurements and the coloured lines denote modelling results. Solid and dashed black lines indicate theoretical predictions. Adapted from Harding et al [74].	17
Figure 2-2: Typical chemiluminescence spectra of atmospheric natural gas-air flames at varying Φ . Reproduced from [103].	22
Figure 2-3: Simple Schematic of a Quasi-Two-Level System. Reproduced from [112].	24
Figure 2-4: Two-level LIF model and relevant energy transfer processes	28
Figure 2-5: Uncertainty in the energy level. Reproduced from [116].	31
Figure 2-6: Collisional Broadening	32
Figure 2-7: Voigt Profile. Reproduced from [112].	35
Figure 2-8: Population Recycling. Reproduced from [110].	37
Figure 2-9: Three-level LIF model in LIFSim. Reproduced from [129].	41
Figure 2-10: Recirculation in a swirling jet flow. Reproduced from [209].	52
Figure 3-1: (a) 25 mm Bunsen burner for qualitative NO-LIF; (b) 15 mm Bunsen burner for NO calibration experiment.	55
Figure 3-2: Photographs of HPOC during maintenance (left) and installed in the HPCR (right) with (a) laser beam/sheet entrance, (b) stainless steel casing, (c) air and fuel delivery lines, (d) fluorescence capture window, (e) flame observation window and (f) combustion exhaust.	56
Figure 3-3: Schematic of HPGSB-2 with open confinement (left) and convergent confinement (right), showing (a) pilot lance, (b) inlet plenum, (c) HPOC connecting flange, (d) mixing chamber, (e) burner exit nozzle and (f) quartz confinement. Dimensions in meters. Reproduced from [227].	57
Figure 3-4: Radial-tangential swirler geometries with $S_g = 0.8$. Tangential inlet width dimension in meters. Reproduced from [221].	58

Figure 3-5: Sectioned detail view of the HPSGB-2/HPOC assembly with (a) instrumentation and pilot lance, (b) inlet plenum, (c) mixing chamber, (d) radial-tangential swirler, (e) burner exit nozzle, (f) quartz window, (g) quartz burner confinement tube, and (h) HPOC casing.	59
Figure 3-6: NO and O ₂ excitation spectra. Chosen NO excitation wavelength highlighted.	61
Figure 3-7: Emission spectra for NO and O ₂ at 285.16 nm excitation.....	62
Figure 3-8: LIF characterization in NO doped CH ₄ /air flame at 285.16 nm. Arrow indicates the average laser energy for the experiments.	63
Figure 3-9: Schematic of experimental setup for qualitative NO-LIF and NO calibration measurement	66
Figure 3-10: LIF measurement system timing and image capture setup with HPOC	66
Figure 3-11: Data acquisition and processing overview.....	68
Figure 3-12: Gaussian fit for (a) laser sheet profile and (b) laser beam profile	71
Figure 3-13: Image processing for NO-PLIF at 285.16 nm excitation	72
Figure 3-14: Image processing for NO-LIF at 226.03 nm excitation.....	72
Figure 3-15: Gas analyser at GTRC	75
Figure 3-16: Dutton diagram with GS(M)R limits. Reproduced from [251]. Numbers (2,3 and 4) represent the positions of the proposed fuel blends in the gas interchangeability diagram.	78
Figure 3-17: Operational Algorithm of the CHEMKIN PREMIX program.....	80
Figure 3-18: Schematic representation of a PSR module	84
Figure 3-19: Modelled S _L of all experimental conditions as a function of AFT ..	87
Figure 3-20: Modelled S _L of all experimental conditions as a function of Φ	89
Figure 3-21: AFT plotted as a function of Φ for all experimental conditions, demonstrating the gentler slopes on the rich side due to the asymmetrical nature of the definition of Φ	89
Figure 3-22: Reaction zone thickness, δt , based on maximum CH and OH mole fraction location in one-dimensional flame model from CHEMKIN PREMIX code	91
Figure 3-23: Numerical and experimental flame thickness as a function of Φ ..	92
Figure 3-24: Numerical and experimental flame thickness as a function of AFT	92
Figure 3-25: Peak CH molar fraction locations from 1-D CHEMKIN calculations. Solid lines for HPOC conditions and dashed line for Bunsen burner conditions.	94
Figure 3-26: Peak OH molar fraction locations from 1-D CHEMKIN calculations. Solid lines for HPOC conditions and dashed line for Bunsen burner conditions.	94
Figure 4-1: Rizk model.....	101
Figure 4-2: Valera model	102
Figure 4-3: Modified Rizk model	103

Figure 4-4: Modified Valera model.....	103
Figure 4-5: Simplified model	104
Figure 4-6: Comparison of reactor models at 1.1 bara	106
Figure 4-7: Comparison of reactor models at 2.2 bara	109
Figure 4-8: Comparison of reactor models at 3.3 bara	110
Figure 4-9: Comparison of NO _x predictions at 1.1 bara	114
Figure 4-10: Comparison of NO _x predictions at 2.2 bara	118
Figure 4-11: Comparison of NO _x predictions at 3.3 bara	121
Figure 5-1: 25 mm Bunsen burner horizontal set-up, as installed (a) and with CH ₄ -air flame (b)	125
Figure 5-2: In-flame NO-LIF signal without NO seeding (ER = 0.88; 2.28 kW). Flow is from left to right.	125
Figure 5-3: Abel-transformed OH* chemiluminescence images (colormap normalised to maximum OH* intensity at each Φ) at varying Φ and fuel input thermal power	127
Figure 5-4: Abel-transformed OH* chemiluminescence images (colormap normalised to maximum OH* intensity relative to 2.47 kW thermal power at $\Phi = 1.28$) at varying ER and fuel input thermal power	128
Figure 5-5: CHEMKIN results showing (a) volumetric heat release rate and, (b) OH mole fraction as a function of 1-D spatial concentrations profiles for $\Phi = 1.28 - 1.4$	128
Figure 5-6: NO PLIF images (normalised to maximum intensity at each Φ) at varying Φ and fuel input thermal power.....	130
Figure 5-7: Relationship between Φ with average NO intensity and AFT	130
Figure 5-8: Relationship between average NO PLIF intensity with maximum CH mole fraction and volumetric heat release level	131
Figure 5-9: Maximum CH and CH ₂ mole fraction plotted as a function of Φ ...	132
Figure 5-10: Activation energy for CH ₄ plotted against Φ . Reproduced from [276].....	132
Figure 5-11: Average NO PLIF intensity plotted as a function of flame thickness	133
Figure 5-12: Abel - transformed OH* chemiluminescence and NO PLIF images side by side. Colormap normalised to maximum intensity at each Φ . Fuel input thermal power is shown in the respective images.....	134
Figure 5-13: Abel - transformed OH* chemiluminescence and NO PLIF images side by side. Colormap normalised to maximum intensity relative to (d) 2.47 kW thermal power at $\Phi = 1.28$. Fuel input thermal power is shown in the respective images.	135
Figure 5-14: Average OH intensity and maximum OH mole fraction plotted as a function of average NO intensity	137

Figure 5-15: Abel-transformed OH* chemiluminescence image at $\Phi = 0.55$ with CH ₄ /air flame. Reproduced from [221].	139
Figure 5-16: Abel-transformed OH* chemiluminescence images (colormap normalised to maximum OH* intensity at each Φ) at varying Φ . Flow direction from bottom to top. The black oval shape in (a) indicates the line from dot built up on quartz window.	140
Figure 5-17: Abel-transformed OH* chemiluminescence images (colormap normalised to maximum OH* intensity across range) at varying Φ	141
Figure 5-18: CHEMKIN results showing OH mole fraction as a function of 1-D spatial concentrations profiles for $\Phi = 0.81 - 1.1$	142
Figure 5-19: Maximum OH* intensity and maximum OH mole fraction as a function of Φ .	143
Figure 5-20: NO PLIF images (normalised to maximum intensity at each Φ) from lean to rich flames	144
Figure 5-21: Average NO PLIF intensity and AFT as a function of Φ	145
Figure 5-22: Average NO PLIF intensity and measured NO as a function of Φ .	146
Figure 5-23: Average NO PLIF intensity and volumetric heat release rate as a function of maximum CH mole fraction. Respective Φ is shown in increasing order.	146
Figure 5-24: Numerical and experimental flame thickness as a function of Φ . NO PLIF intensity is shown for every TPs in the graph.	147
Figure 5-25: Schematic showing the detailed premixed flame structure including the reaction zones. Reproduced from Law [194].	148
Figure 5-26: Measured NO and $(\delta G/\delta D)$ as a function of Φ .	149
Figure 5-27: Abel - transformed OH* chemiluminescence and NO PLIF images side by side. Colormap normalised to maximum intensity across the images.	150
Figure 5-28: Abel - transformed OH* chemiluminescence and NO PLIF images side by side. Colormap normalised to maximum intensity at each Φ .	151
Figure 5-29: Average NO PLIF intensity and maximum OH mole fraction from CHEMKIN as a function of average OH* chemiluminescence intensity. Φ is shown in the graph for each point in increasing order.	153
Figure 5-30: Model for open flame in HPOC	154
Figure 5-31: Experimentally measured and predicted NO as a function of Φ .	155
Figure 5-32: Computed normalized sensitivity coefficients of [OH] on net reaction rates at the flame zone reactor for (a) $\Phi = 0.94$, (b) $\Phi = 1.0$, (c) $\Phi = 1.1$. Units [-]	160
Figure 5-33: Quantitative reaction path diagram showing NO formation/consumption pathways predicted by GRI-Mech 3.0 mechanism at flame zone reactor for CH ₄ /air flames at (a) $\Phi = 0.94$, (b) $\Phi = 1.0$, and (c) $\Phi = 1.1$. Units [moles/cm ³ .s]	161

Figure 5-34: Quantitative reaction path diagram showing NO formation/consumption pathways at flame zone reactor predicted by Aramco 1.3 mechanism for CH ₄ /air flames at (a) $\Phi = 0.94$, (b) $\Phi = 1.0$, and (c) $\Phi = 1.1$. Units [moles/cm ³ .s].....	163
Figure 5-35: Quantitative reaction path diagram showing NO formation/consumption pathways predicted by SanDiego mechanism at flame zone reactor for CH ₄ /air flames at (a) $\Phi = 0.94$, (b) $\Phi = 1.0$, and (c) $\Phi = 1.1$. Units [moles/cm ³ .s].....	164
Figure 5-36: Quantitative reaction path diagram showing NO formation pathways predicted by M2 mechanism at post flame zone reactor (25 cm from burner exit) for CH ₄ /air flames at (a) $\Phi = 0.94$, (b) $\Phi = 1.0$, and (c) $\Phi = 1.1$. Units [moles/cm ³ .s].....	166
Figure 5-37: Computed normalized sensitivity coefficients of [NO] on net reaction rates at the flame zone reactor for (a) $\Phi = 0.94$, (b) $\Phi = 1.0$, (c) $\Phi = 1.1$. Units [-]	168
Figure 5-38: Variation of CH ₂ and OH mole fraction at the flame zone reactor as a function of Φ	169
Figure 5-39: Computed normalized sensitivity coefficients of [NO] on net reaction rates at the post flame zone reactor (25 cm from burner exit) for (a) $\Phi = 0.94$, (b) $\Phi = 1.0$, (c) $\Phi = 1.1$. Units [-].....	170
Figure 6-1: Abel-transformed OH* chemiluminescence images at varying Φ . Colormap normalised to maximum OH* intensity at each Φ and across column on the left side and right side, respectively. Flow direction is from bottom to top.....	175
Figure 6-2: CHEMKIN results showing (a) volumetric heat release rate and, (b) OH mole fraction as a function of 1-D spatial concentrations profiles for $\Phi = 0.55 - 0.65$	176
Figure 6-3: Maximum OH* intensity and maximum OH mole fraction as a function of Φ	176
Figure 6-4: NO PLIF images at varying Φ . Colormap normalised to maximum intensity at each Φ and across column on the left side and right side, respectively. Flow direction is from bottom to top.	177
Figure 6-5: Average NO PLIF intensity and AFT as a function of Φ	178
Figure 6-6: Average NO PLIF intensity and measured NO as a function of Φ ..	178
Figure 6-7: Average NO PLIF intensity and volumetric heat release rate as a function of maximum CH mole fraction. Respective Φ is shown in increasing order.	179
Figure 6-8: Numerical and experimental flame thickness as a function of Φ . NO PLIF intensity is shown for every TP in the graph.	180
Figure 6-9: Measured NO and $(\delta G/\delta D)$ as a function of Φ	181
Figure 6-10: Relative change in maximum OH and CH mole fraction location from CHEMKIN calculations as Φ changes.....	181

Figure 6-11: Abel - transformed OH* chemiluminescence and NO PLIF images side by side. Colormap normalised to maximum intensity at each Φ 182

Figure 6-12: Abel - transformed OH* chemiluminescence and NO PLIF images side by side. Colormap normalised to maximum intensity across the images. 183

Figure 6-13: Average NO PLIF intensity and maximum OH mole fraction from CHEMKIN as a function of average OH* chemiluminescence intensity. Φ is shown in the graph for each point in increasing order. 184

Figure 6-14: Effects on flame shapes with 15% H₂ additions. BASE fuel on left side and FARH₂ on right side. Colormap normalised to maximum intensity at each Φ . The black and red circles indicate the changes in flame attachment and CRZ envelope, respectively with H₂ addition. 187

Figure 6-15: Effects on flame shapes with 15% H₂ additions. BASE fuel on left side and FARH₂ on right side. Colormap normalised to maximum intensity across the images. 188

Figure 6-16: Influence of turbulence intensity and H₂ addition to CH₄ on the turbulence burning velocity. Reproduced from [297]. 188

Figure 6-17: Relative increase in S_L for CH₄ with H₂ addition (15% volumetric) 190

Figure 6-18: Relative increase in Q' for CH₄ with H₂ addition (15% volumetric) 190

Figure 6-19: Relative increase in maximum X_H, X_O and X_{OH} for CH₄ with H₂ addition (15% volumetric) 190

Figure 6-20: Maximum OH intensity and maximum OH mole fraction as a function of Φ 191

Figure 6-21: Effects on NO formations with 15% H₂ additions. BASE fuel on left side and FARH₂ on right side. Colormap normalised to maximum intensity at each Φ . Flow direction is from bottom to top. 192

Figure 6-22: Effects on NO formations with 15% H₂ additions. BASE fuel on left side and FARH₂ on right side. Colormap normalised to maximum intensity across the images. Flow direction is from bottom to top. 193

Figure 6-23: Effects of H₂ addition to the experimental NO and OH intensity with maximum OH mole fraction calculated from CHEMKIN 194

Figure 6-24: Comparison between BASE and FARH₂ in terms of AFT and ***AvgIntenNO***. 195

Figure 6-25: Comparison between BASE and FARH₂ in terms of ***δ flame*** and ***AvgIntenNO***. 195

Figure 6-26: Abel-transformed OH* chemiluminescence images (colormap normalised to maximum OH* intensity at each Φ) at varying Φ 197

Figure 6-27: Maximum OH* intensity and maximum OH mole fraction as a function of Φ 198

Figure 6-28: Abel-transformed OH* chemiluminescence images (colormap normalised to maximum OH* intensity across range) at varying Φ 199

Figure 6-29: Abel - transformed OH* chemiluminescence and NO PLIF images side by side. Colormap normalised to maximum intensity at each Φ	201
Figure 6-30: Abel - transformed OH* chemiluminescence and NO PLIF images side by side. Colormap normalised to maximum intensity across the images.	202
Figure 6-31: Average NO PLIF intensity and maximum OH mole fraction from CHEMKIN as a function of average OH* chemiluminescence intensity. Φ is shown in the graph for each point in increasing order.	203
Figure 6-32: Isothermal air flow PIV velocity vector maps with axial velocity contours for the unconfined HPGSB-2. Reproduced from [221].	205
Figure 6-33: Isothermal air flow PIV velocity vector maps with axial velocity contours for the confined HPGSB-2. Reproduced from [221].	205
Figure 6-34: Changes in flame shape and heat release locations between unconfined and confined flames. Colormap corrected to the maximum OH* intensity across column. Unconfined images in the left column and confined images in the right column.	207
Figure 6-35: Changes in NO formation and intensity between unconfined and confined flames. Colormap corrected to the maximum NO PLIF intensity across column. Unconfined images in the left column and confined images in the right column.	210
Figure 6-36: Maximum NO and OH* intensity as a function of Φ for confined and unconfined flames	211
Figure 6-37: NO LIF images excited by 226.03 nm wavelength from lean to rich flames. Colormap normalised to maximum intensity at each Φ . Flame direction is from bottom to top. Laser beam covering ≈ 12 mm from burner exit.	213
Figure 6-38: NO LIF images excited by 226.03 nm wavelength from lean to rich flames. Colormap normalised to maximum intensity across images. Flame direction is from bottom to top. Laser beam covering ≈ 12 mm from burner exit.	214
Figure 6-39: Comparison between NO LIF and PLIF data taken by 226.03 nm and 285.16 nm excitation wavelength, respectively.	215
Figure 6-40: <i>AvgIntenNO</i> and measured NO at exhaust as a function of Φ	216
Figure 6-41: NO LIF images at varying Φ . Colormap normalised to maximum intensity at each Φ and across column on the left side and right side, respectively. Flame direction is from bottom to top. Laser beam covering ≈ 12 mm from burner exit.	217
Figure 6-42: Effect of pre-heating on NO formation. Non-preheated conditions on the left side and preheated conditions on the right side. Colormap normalized to maximum intensity at each Φ	218
Figure 6-43: Effect of pre-heating on NO formation. Non-preheated conditions on the left side and preheated conditions on the right side. Colormap normalized to maximum intensity across images.	219
Figure 6-44: Effects of preheated premixed gases on NO formation	220

Figure 6-45: CHEMKIN model for flames with open confinement in HPOC	220
Figure 6-46: Experimentally measured and predicted NO as a function of Φ for preheated CH ₄ /air ($\Phi = 0.55 - 0.65$).....	224
Figure 6-47: Experimentally measured and predicted NO as a function of Φ for preheated CH ₄ /H ₂ /air ($\Phi = 0.55 - 0.65$).....	225
Figure 6-48: Experimentally measured and predicted NO as a function of Φ for preheated CH ₄ /air ($\Phi = 0.75 - 0.87$).....	226
Figure 6-49: Experimentally measured and predicted NO as a function of Φ for non-preheated CH ₄ /air ($\Phi = 0.81 - 1.1$).....	227
Figure 7-1: Location of the data points for the calibration curves in terms of (a) OH* chemiluminescence and (b) NO-LIF measurement.	235
Figure 7-2: Linear response of the quenching corrected LIF signal to increasing doping of NO in lean methane/air flame	236
Figure 7-3: Example of normalized temperature and composition dependent corrections to the NO LIF signal. Values are normalized by the correction term at 300K. Reproduced from [317].	237
Figure 7-4: Simple chemical reactor network model of the 15 mm Bunsen burner in CHEMKIN	238
Figure 7-5: Comparison of predicted NO with maximum heat loss with actual NO reading.....	238
Figure 7-6: Comparison of predicted NO with calibrated heat loss with actual NO reading	239
Figure 7-7: Corrected NO LIF images for calibration at 226.03 nm	240
Figure 7-8: Corrected NO LIF images for calibration at 226.03 nm. Colormaps normalised to maximum intensity across all images.	241
Figure 7-9: NO LIF calibration curve ($\lambda = 226.03$ nm) for 15 mm Bunsen burner with CH ₄ -air at atmospheric temperature and pressure	242
Figure A-0-1: NO Excitation Spectra at minimum AFT	274
Figure A-0-2: O ₂ Excitation Spectra at minimum AFT	275
Figure A-0-3: NO Excitation Spectra at maximum AFT.....	276
Figure A-0-4: O ₂ Excitation Spectra at maximum AFT	277
Figure A-0-5: NO and O ₂ excitation spectra (285.1 - 285.2 nm) at minimum AFT	278
Figure A-0-6: NO and O ₂ excitation spectra (285.1 - 285.2 nm) at maximum AFT	279
Figure C-0-1: HPGSB-2 Mixing Chamber	293
Figure C-0-2: CFD result used for CRZ, ERZ and flame zone volume calculation. Reproduced from [275].	294
Figure D-0-1: Photograph of HPCR setup with HPGSB-2	295
Figure D-0-2: Photograph of Bunsen burner setup.....	295

List of Tables

Table 1-1: GT pollutants and their effects with limitation strategy.....	6
Table 2-1: Typical values for natural line broadening	32
Table 3-1: Process specifications for Quantel TDL-90 [228].	61
Table 3-2: Specification of the laser system	64
Table 3-3: Specifications of the dyes used	65
Table 3-4: Fuel matrix for CHEMKIN model validation.....	76
Table 3-5: Fuel matrix for NO-LIF experiment	77
Table 3-6: Fuel matrix for future study.....	78
Table 3-7: Operating ranges for NO PLIF experiments.....	86
Table 4-1: Differences in predictions by the models compared to the experimental results.....	107
Table 4-2: Heat loss rates for different zones	111
Table 4-3: Differences in predictions by the mechanisms compared to the experimental results.....	115
Table 5-1: Flow conditions for 25mm Bunsen burner	126
Table 5-2: Flow conditions for HPOC swirl burner.....	138
Table 5-3: Heat loss rates for different zones	154
Table 5-4: Differences in predictions by the mechanisms compared to the experimental results (unconfined HPGSB-2)	156
Table 6-1: Flow conditions of Base fuel in HPGSB-2	174
Table 6-2: Flow conditions of FARH ₂ fuel in HPGSB-2.....	185
Table 6-3: Changes in flame angle (α) with fuel and equivalence ratio (Φ) ..	187
Table 6-4: Changes in flame angle (α) between unconfined and confined flames	208
Table 6-5: Flow conditions for non-preheated experiments at 226.03 nm	212
Table 6-6: Flow conditions for preheated experiments at 226.03 nm.....	216
Table 6-7: Heat loss rates for non-preheated conditions.....	221
Table 6-8: Differences in predictions by the mechanisms compared to the confined HPGSB-2 experimental results (Preheated CH ₄ /Air (Φ = 0.55 - 0.65))	222
Table 6-9: Differences in predictions by the mechanisms compared to the confined HPGSB-2 experimental results (Preheated CH ₄ /H ₂ /Air (Φ = 0.55 - 0.65)).....	222
Table 6-10: Differences in predictions by the mechanisms compared to the confined HPGSB-2 experimental results (Preheated CH ₄ /H ₂ /Air (Φ = 0.75 - 0.87)).....	222

Table 6-11: Differences in predictions by the mechanisms compared to the confined HPGSB-2 experimental results (Non-Preheated CH₄/Air ($\Phi = 0.81 - 1.1$)) 223

Table 7-1: NO LIF quenching and calibration parameters. Reproduced from [313] 232

Table 7-2: Premixed reactant flow rates, exhaust temperatures, and NO readings for NO dopant level of 0 - 1300 ppm 235

Table 7-3: Premixed reactant flow rates and exhaust temperatures for NO dopant level of 0 - 1000 ppm..... 242

Thesis Contribution

- Mashruk, S., Marsh, R., Runyon, J., Bowen, P.J., 2018. 'Methodology and comparison of quantitative NO-LIF imaging in a Bunsen burner with numerical simulation results' - 19th International Symposium on the Application of Laser and Imaging Techniques to Fluid Mechanics (ISBN 978-989-20-9117-8), pp 1509-1521.
- Mashruk, S., Marsh, R., Runyon, J., Bowen, P.J., 2018. 'Appraisal of quantitative NO-LIF imaging with a conical premixed flame and numerical simulations' - GT2018-77438. Poster presented at ASME TurboEXPO 2018, Oslo, Norway - Selected among top 5 posters at the conference.

1. Introduction

Energy is essential to the prosperity of human civilization. The demand for energy has been growing rapidly since the industrial revolution mainly due to the development of industry and the increase in population. The major source of energy comes from fossil fuels, and about 70% of the world's electricity production is from carbon-intensive fuels like coal, petroleum, natural gas, etc. [1], [2]. Gas turbines (GT) are globally used by the original equipment manufacturers (OEM) and operators for power generation to meet the increasing demand of energy, while operating with increased fuel flexibility to reduce the pressure on fossil fuel reserve as well as environmental impacts [3].

Gas turbines faces considerable challenges to meet the goal of pollutant-free combustion. The Earth's climate is warming, creating several potential threats to the natural environmental ecosystem. Natural greenhouse gases such as N_2O , O_3 , CO_2 , and CH_4 are responsible for the warming of Earth's atmosphere by absorbing and emitting infrared radiation. The concentrations of the latter two examples have increased significantly over the last 250 years [4], and are still rising. Concerns about the possibility of global ecological disasters have led to a number of important studies aimed at heightening public understanding and influencing national and international debate and policy [5]-[9].

As far back as 1972, Meadows et al [10] and recent studies [11]-[14], showed that during the twenty-first century, a very wide range of scenario assumptions always led to the conclusion that ecological disasters would lead to massive population reductions, unless an appropriate pollution limitation strategy was adopted by about the turn of century. In response to these warnings, various measures were taken to reduce emissions from gas turbines but still not nearly enough to compensate the damage already done.

1.1. Natural Gas in the UK

Natural gas has been the most important source of the UK power generation sector for the past three decades. The UK currently produces enough gas to meet almost half of its needs (44%) from the North Sea and the East Irish Sea, while 47% of the gas is imported from Europe and Norway via pipelines and remaining 9% comes to the UK by tankers in the form of liquefied natural gas (LNG) [15]. UK natural gas production peaked in 2000 [16], but since then it has been declining and from 2010 to 2011 faced its largest annual decline in over 40 years [17]. As a consequence, UK turn into a net importer of natural gas, as shown in Figure 1-1, which provides changes in UK gas production and demand between 1998 - 2018. UK's natural gas import dependency are predicted to increase up to 94% by 2050, with LNG being predicted to meet most of the demand even in scenarios where UK domestic shale gas production is exploited to its full potential [18] (refer to Figure 1-2).

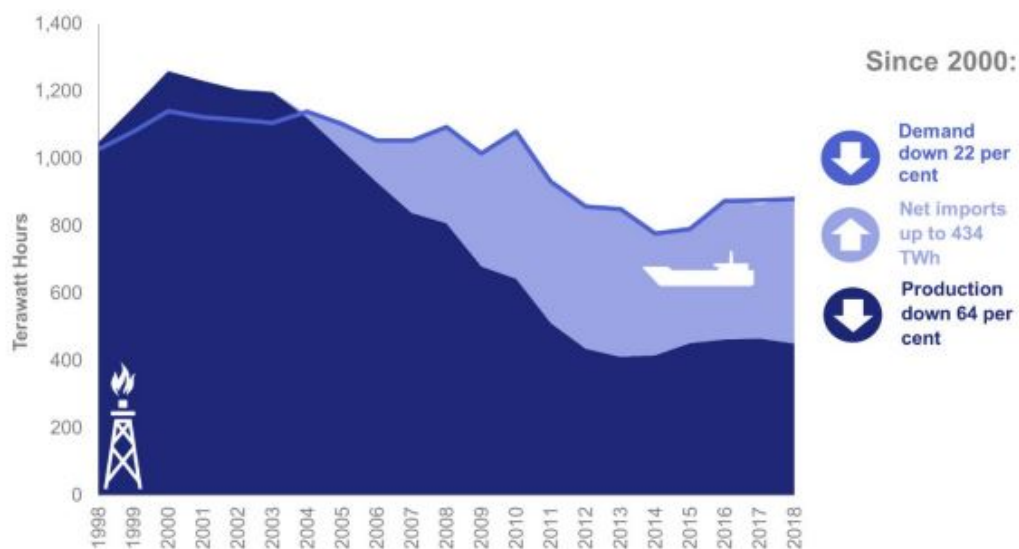


Figure 1-1: Changes in UK gas production and demand, 1998 - 2018. Reproduced from [19]

80% of the UK's 25 million homes are powered by gas currently, and around a quarter of the country's electricity is generated by gas-fired power stations [15]. Since, the first combined-cycle GT (CCGT) power station in the UK was opened in 1992, CCGT represented 46% of all power generated in the UK by 2008, compared with only 5.5% renewables [17]. Modern low emissions GTs are sensitive to variations in

natural gas composition. The focus on varying natural gas compositions is shown to be driven by an increase in the diversity of UK gas supply over the last decade due to substantial rise in LNG imports [17] and hydrogen is projected to play a more critical role in the future [20]. GT operators are already reporting several issues while operating with varying natural gas compositions [21], leading GT OEMs and researchers to increasingly address the issues with the wide variety of natural gas blends to be used in GT combustion [22]-[27].

1.1.1. LNG and Natural Gas - Hydrogen Blends

LNG has very different compositions and combustion properties than a typical natural gas. The UK has been importing LNG in regular basis since the opening of the LNG terminal at the Isle of Grain in 2015 [16], [17], [19], as shown in Figure 1-2. The potential sources of LNG into the UK have since expanded significantly, particularly with the construction of additional LNG export terminals worldwide and the opening of UK import terminals at Teesside, South Hook, and Dragon [19]. The share of LNG import in the UK has increased from 25% in 2009 to 35% in 2010 to 47% in 2011 but has declined in recent years due to the increased demand for LNG in Asia and increased coal usage [17], [19].

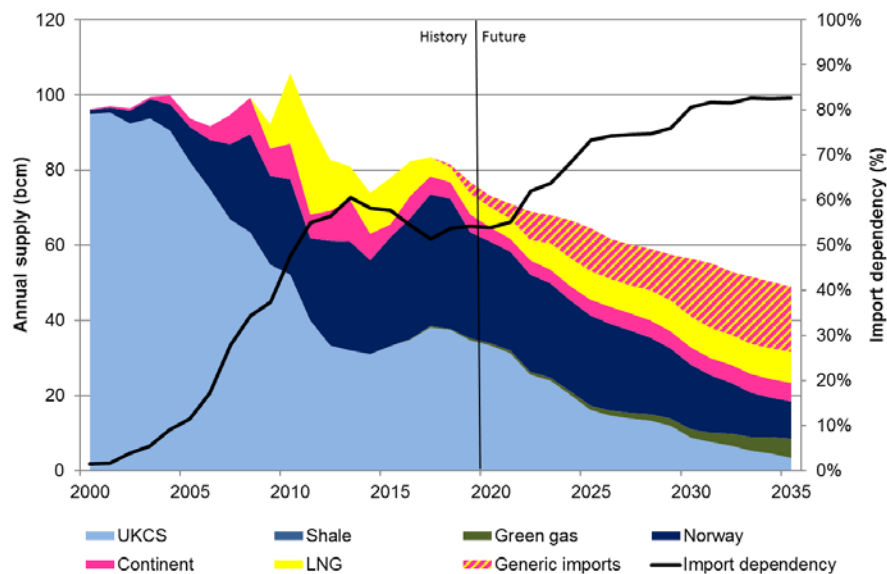


Figure 1-2: Major sources of UK gas supply and import dependency over the years. Reproduced from [28].

In addition to the 2008 United Kingdom Climate Change Act and 2011 UK Carbon Plan, the 2019 Net Zero Emissions law put into place the legal framework addressing climate change and greenhouse gas emissions in the UK, targeting to bring all greenhouse gas emissions to net zero by 2050 [29], [30]. These legislations will require renewable energy sources such as wind and solar power to contribute increasingly to electricity generation in the UK for the foreseeable future and technologies such as power-to-gas (P2G) being developed and implemented as a means of energy storage during times of peak renewable production coupled with reduced demand [31], [32]. P2G essentially converts the excess electricity into hydrogen (H_2) gas through an electrolysis process for storage in existing natural gas infrastructure [32]-[34]. GTs use the robust and flexible natural gas infrastructure to source fuel. With little to no modifications a blend of H_2 with natural gas can be transported within the existing infrastructure, which makes the entire system reusable without major expenditure. As a matter of fact, Netherlands has already injected up to 20% H_2 into their natural gas grid in a pilot project on the Island of Ameland some years ago [35]. However, further development effort is required to derive technical solutions with respect to the following challenges associated with high H_2 contents in the fuel:

- Autoignition: Higher autoignition risk due to lower ignition delay time;
- Flashback: Higher flashback risk due to higher flame speed or lower ignition delay time;
- Modified thermo-acoustic amplitude level and frequencies;
- Increased NO_x emissions;
- Higher pressure drop due to lower Wobbe Index (WI) (refer to Equation [3-5]);
- Reduced lifetime / need for more cooling of hot gas path components due to increased heat transfer.

1.2. Source of Emissions

World energy demand is set to grow over the next 20 years at broadly 1.4 percent per annum, leading to a total estimated of 18 billion toe by 2040, as shown in Figure 1-3 [36]. It should be noted that much of the growth is anticipated in the developing world.

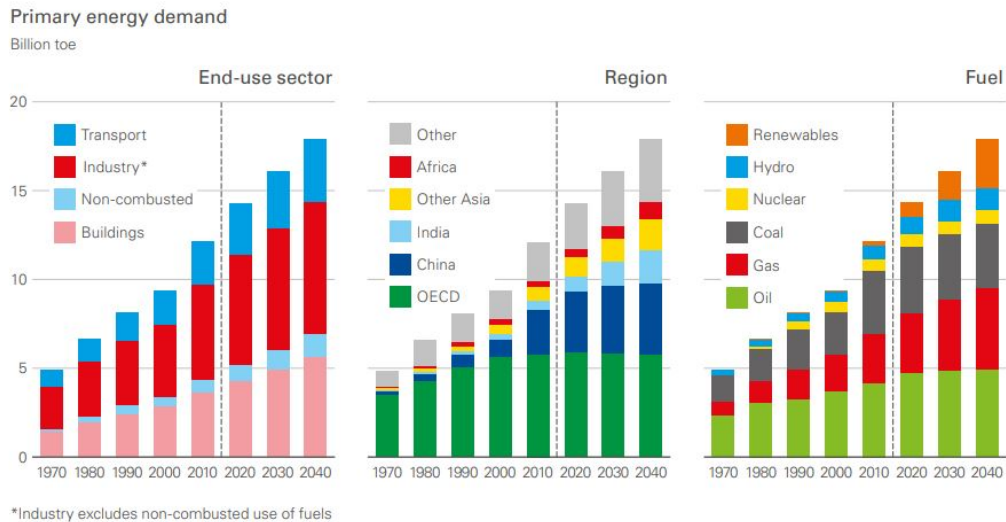


Figure 1-3: World energy demand in terms of end-use sector, region and fuel. Reproduced from [36].

Gas turbines emit quite a few pollutants to the atmosphere which includes Carbon Dioxide (CO_2), Oxides of Sulphur (SO_2), Carbon Monoxide (CO), Unburnt Hydrocarbons (UHC), Smoke Soot (C) and Oxides of Nitrogen (NO_x). Table 1-1 illustrates the effect and limitation strategy of these pollutants.

Carbon Dioxide is the consequence of complete and successful combustion of a fuel containing carbon. As such the limitation strategy is to improve thermal efficiency of the gas turbines, thus decreasing fuel use. Any sulphur present in the fuel may eventually result in oxides of sulphur. The level of sulphur permissible in fuel has already been progressively reduced over the years with some application and regions requiring sulphur content to be limited as low as 0.2% [37]. Smoke or soot is formed in local fuel-rich regions within the combustor. The tendency to produce soot increases markedly with pressure, making the high-pressure ratio gas turbines particularly susceptible to produce soot [38]. The design of the fuel injector and the mixing of air with the fuel have a very large impact on whether or not a particular combustor

produces substantial amount of soot as this design can exterminate the local fuel-rich regions within the combustor.

Table 1-1: GT pollutants and their effects with limitation strategy

POLLUTANT	EFFECT	LIMITATION STRATEGY
Carbon Dioxide (CO ₂)	Global warming	Increase system thermodynamic efficiency
Oxides of Sulphur (SO ₂)	Toxic, Corrosive	Removal of Sulphur from fuel
Carbon Monoxide (CO)	Toxic	Increase residence time and combustion temperature
Unburnt Hydrocarbons (UHC)	Toxic	Same as above
Smoke Soot (C)	Visible	Removal of local fuel rich zone
Oxides of Nitrogen (NO _x)	Toxic, Depletion of Ozone within Stratosphere	Reduction of residence time and combustion temperature
	Ozone increase at ground level	

Carbon monoxide and unburnt hydrocarbons are both the products of partial combustion and are formed in quantity in circumstances where the combustion zone temperature is low and/or the time available for combustion is insufficient. However, NO_x is the result of high combustion temperature which is high enough to dissociate molecular oxygen to atomic oxygen which in turn react with N₂ to produce NO and N. At lower temperature NO react with oxygen molecule to produce NO₂ [39].

For most stationary gas turbine applications, carbon monoxide and unburnt hydrocarbons are only a concern at low engine power. As engine power is increased, high pressures and temperatures reduce these partial products of combustion to acceptable levels. These pollutants are therefore usually only of consequence during the relatively short period associated with engine start-up and shutdown. Figure 1-4 illustrates the

production of different pollutants at different levels of engine power settings.

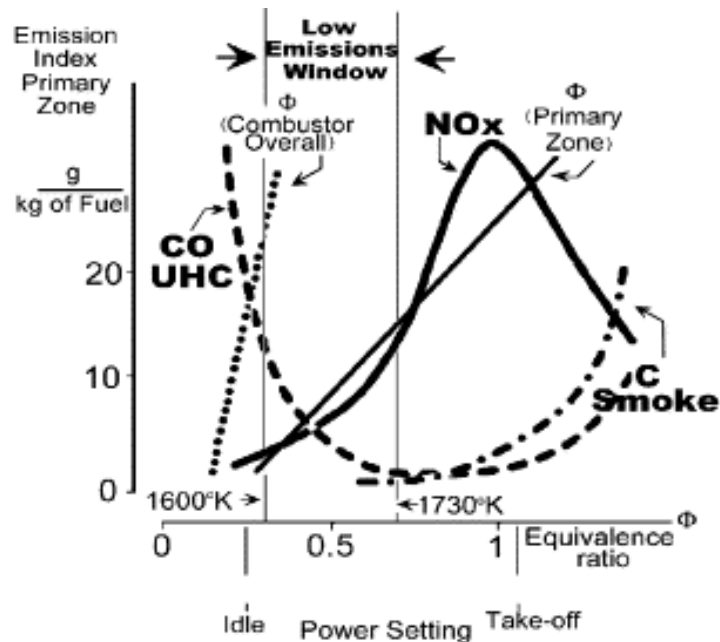


Figure 1-4: Different GT pollutants with respect to equivalence ratio and power setting. Reproduced from [40].

Oxides of nitrogen, however, increase with the engine power and are at the highest level when the machine is producing its design/rated power. New legislation has come into effect to reduce NO_x from 200 ppm to as low as 25 ppm and 9 ppm [38]. In addition to the legislation limiting NO_x , there is often requirement to use BACT (Best Available Control Technology) [41] or LAER (Lowest Available Emission Rate) [42]. These legislations pushed the combustor designers to move from conventional single stage combustor to three stage combustors where in the first stage we have low combustion temperatures because of the very large excess of fuel relative to the stoichiometric proportion. The design intention is that the second stage would rapidly mix the rich first stage exhaust with a fresh intake of air and fuel, and the third stage of the combustor would operate lean and with a low flame temperature [38].

1.3. Impact of Fuel Quality Variation on NO_x Formation

NO_x and CO emissions depend on factors including operating load, ambient conditions and fuel composition. NO_x tends to increase with increasing WI, as can be seen in Figure 1-5 which shows base-load NO_x emissions over a three month period for four GTs at E.ON [21]. These units are reported to be nominally identical, but differences in build, ageing and tuning result in different emission characteristics. It must be noted that this study was conducted in full-load scenarios.

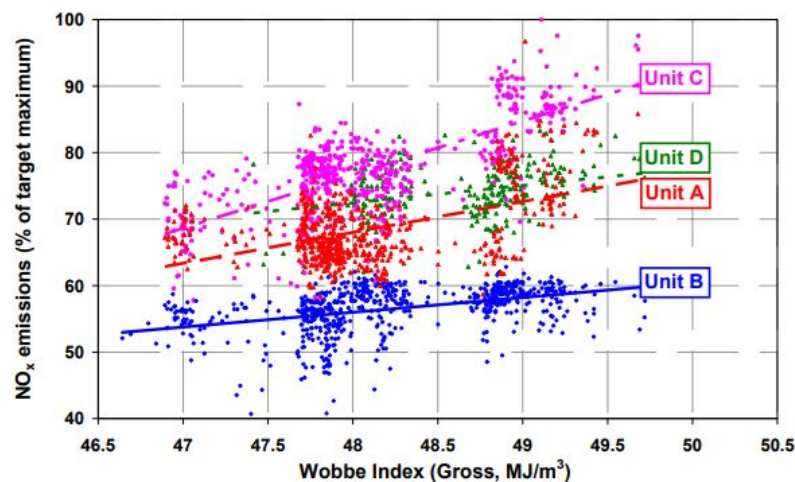


Figure 1-5: Impact of fuel composition on NO_x emissions for four similar GTs. Reproduced from [21].

An upward trend in NO_x is visible for units A and C, although there is significant scatter in the graph due to changes in atmospheric conditions. However, the trends for units B and D are not as significant as the others, showing a clear impact of fuel composition on NO_x emissions. Based on similar studies of GTs in the UK [43], estimates have been made of the increase in NO_x that would occur if GTs tuned on a gas with WI in the middle of the allowable range (refer to Figure 1-6) were supplied with gas at the top end of the acceptable range. For properly configured and tuned power generation GTs, increases of approximately 10% of target emissions were typical, with the range being 5 to 20% [21]. Thus a significant margin has to be allowed for fuel composition changes when tuning a GT, which is a balance between optimising emissions, dynamics and integrity. The additional margin needed to guarantee meeting emissions targets may compromise dynamics and load limitation.

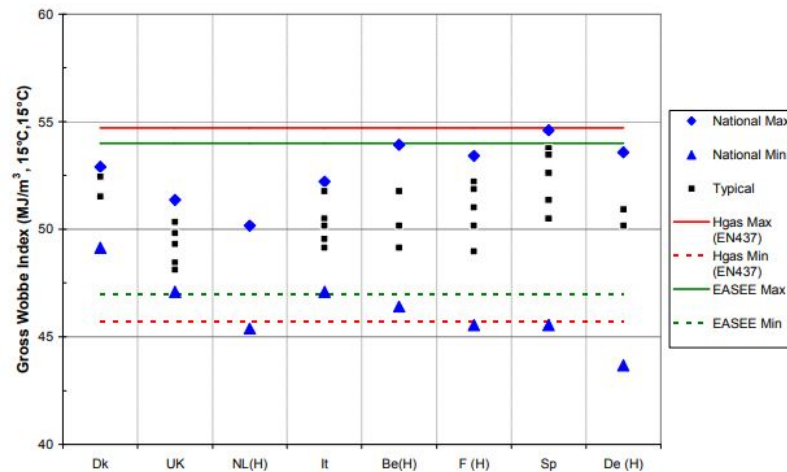


Figure 1-6: Typical variations in European Gas Specifications and Normal Compositions. Reproduced from [44].

1.4. Measurements of Emissions

Different types of gas analysers (chemiluminescence, FTIR, cascade etc. based) are used by research groups [45]-[47] to measure emissions at the exhaust but these instruments cannot measure emissions in the flames, which is vital to understand the formation of different species and thus limit the production of these species by proposing different strategies. Non-intrusive laser diagnostics techniques open the door to measure different species in the flame without affecting the flame shape and stability. This technique, incorporation with the gas analysers can provide effective solutions to reduce different types of emissions.

Since laser (Light Amplification by Stimulated Emission of Radiation) was first introduced by Theodore H. Maiman in 1960 [48], laser spectroscopy has developed into an effective tool over the years for fundamental research and applied diagnostics in nearly every major field of science and engineering. Laser-based diagnostic methods have contributed greatly to the development of practical combustion systems and fundamental combustion chemistry research [49], [50]. Laser has unique properties which enable selective and quantitative analyses of chemical (species concentration, reaction kinetics, etc.) and physical (temperature, flow-structure, gas velocity etc.) parameters with high temporal and spatial resolution. Compared to probe-based techniques [51], laser spectroscopy provides non-intrusive yet direct interrogation of

the combustion process without disturbing the flow-field. As a result, many laser-based optical methods are available currently for routine combustion diagnostics and studies are underway to optimize and refine their application range [49].

It is generally recognized that there is no single laser diagnostics strategy which is suited for all combustion conditions, and different strategies offer varying levels of accuracy, complexity and qualitative nature (single point, line or 2-D imaging) of obtainable data. Practical combustion systems constitute harsh, high-temperature and high-pressure environment with time-varying turbulent flow fields, multi-phase flows and generation of particulate matter. Therefore, for a given diagnostic method, practical combustion environments inherently offer unique challenges which complicate the application of the measurement method. The main spectroscopic method investigated in this study is laser induced fluorescence (LIF), which is a versatile and powerful tool for selective probing of chemical species and capable of providing single point, 1-D spectrally resolved, and 2-D spatially resolved information.

1.5. Scope of Research

GT power generation will continue to be a major contributor to the UK power generation system through 2050 and beyond, increasingly fuelled by H₂ enriched natural gas to meet peak demand, coupled with CCS applications. Environmental policies and regulations will keep GT operations in check within the restricted limits of various emissions, while maintaining high efficiency and reliability. Hence, this provides the motivation for this experimental and numerical combustion study.

EPSRC funded the £2M 'Flex-E-Plant' grant [52] to investigate four key issues: Plant Efficiency, Plant Flexibility, Fuel Flexibility, and Sustainability. These four intersecting themes have a considerable impact upon plant operation and design, combustion processes in general and the structural integrity of typical and advanced materials utilised in conventional power plants.

This study sets out to apply the advanced measurement techniques to measure NO emissions in an industry scaled swirl burner for the first

time from different fuel combinations to enable correlations to be proposed between different types of fuel, pollutant emissions and combustion stability using the combustion test rigs facilities available at Gas Turbine Research Centre (GTRC), Cardiff University. This particular research will set its focus on understanding and developing a novel laser diagnostics method to measure NO formation in the flame. In that pursuit, the LIF technique has been investigated in depth to measure NO, progressing towards future measurement of CO.

1.6. Aims and Objectives

The aim of this thesis was to aid GT OEMs and Utilities with NO_x emissions management during operation by developing a chemical reactor model of an industry-scale swirl burner for NO_x predictions and providing NO formation analysis by LIF measurements on industrial swirl flames.

To meet this aim, this study has the following primary objectives:

- Design, manufacture, and commission an experimental facility for detailed NO-LIF investigation.
- Develop a methodology for NO-LIF experiments at Cardiff University.
- Develop Chemical Reactor Network (CRN) models to simulate experimental conditions in industry scale swirl burners.
- Evaluation of the qualitative NO-LIF data with experimental heat release data and chemical kinetics calculations.
- Evaluate the effects of hydrogen addition in CH₄ flames in terms of flame stability and NO formation.
- Evaluate the effects of confinement on flame shapes, stability, and NO formation.
- Perform NO-LIF calibration experiments to quantify future NO-LIF measurements.

1.7. Outline of this Thesis

The structure of this thesis is summarised below chapter-by-chapter:

- Chapter 1 provides background and motivation of the work presented herein. Source of fuels for GT power generation sectors in the UK are described briefly, as well as the possible emissions from GT operations and the effect of fuel variation on NO_x emissions. Impact of laser in science and technology is also described here, mainly prioritising combustion laser diagnostics.
- Chapter 2 discusses all the possible NO formation mechanisms from the literature. It also includes elaborative discussions on theoretical background and physics associated with LIF technique. Finally, the dedicated webpage, LIFSim for NO spectroscopy and recent works in this field are briefly mentioned here.
- Chapter 3 provides details of experimental facilities and methodologies employed in this study, with a focus on non-intrusive combustion diagnostics. As the development of non-intrusive NO formation diagnostics in the flame for the first time in the UK has been a key outcome of this work. The detailed data processing methods are also described in this chapter.
- Chapter 4 has been dedicated specifically to model GTRC's High Pressure Optical Chamber (HPOC) in CHEMKIN environment to predict NO_x productions at the exhaust. Two chemical reactor models from literature are first discussed and evaluated by using seven different chemical mechanisms from literature and compared with the experimental data from a previous study at Cardiff University. By analysing these results, three new chemical reactor models are proposed and compared with each other. Finally, using the selected proposed model, NO_x productions are predicted and compared with experimental data at different temperature and pressure conditions.
- Chapter 5 explains and analyses the NO LIF measurements taken in open environments using two different burners. OH chemiluminescence measurements were taken as well to

understand the flame structure and heat release. These two different experimental datasets, together with chemical kinetics calculations are used to validate NO LIF measurements as experimental and flow conditions changes.

- After explaining and validating NO LIF measurements in open environments, Chapter 6 proceeds towards more conventional flow conditions for power generation GT operations. This chapter also analyse the effect of 15% H₂ addition on flame structure, heat release and NO formation. Furthermore, effects of confinement at the same flow conditions on flame shape and NO formation, in terms of change in centre recirculation zone (CRZ) shape and location are described here. Finally, comparisons are made between NO-LIF signals taken at two different NO excitation wavelengths, as well as between preheated and non-preheated flow conditions at 226.03 nm excitation wavelength.
- Chapter 7 details the NO calibration method by doping known amount of NO in a lean CH₄/air Bunsen burner flame and conducting LIF measurements above the flame, utilising two different excitation wavelengths above the flame. Hence, NO calibration curves are obtained for future quantitative NO analysis with alternative fuels.
- Chapter 8 concludes the thesis by stating the main outcomes of this study with recommendations for future work.
- Appendices are provided which detail the numerical coding scripts employed, photographs of key equipment, and modified chemical mechanisms utilised in this study.

2. LIF Theory and Literature Review

This Chapter outlines the background research performed as a foundation for the study presented in this thesis. NO_x formation pathways are described in detail at first to identify the source of NO_x in the flame chemistry. Basic theory behind LIF spectroscopy is discussed afterwards and functionality of a computational simulation code for just NO and O_2 spectroscopy is analysed. Finally, a historical breakdown on NO-LIF experiments are provided, with discussions about different NO excitation strategies.

2.1. Formation and Reburn of Oxides of Nitrogen in Combustion

Formation mechanisms of NO have been extensively studied for more than 50 years. Oxides of nitrogen present significant risk to both health and the environment. NO_x reacts with ammonia, moisture and other compounds to form small particles which if inhaled into sensitive lung tissues and those with asthma can aggravate lung diseases [53]. The formation of tropospheric ozone and acid rain through reaction in the atmosphere [54] raises environmental concerns over NO_x formation. NO_x formation and reburn reactions are counteracting, and their balance ultimately determines the final NO_x productions.

While approximately 10% of the atmospheric NO_x are produced naturally by lightning strikes, the vast majority is due to combustion sources [54]. Key reactions involved in these combustion processes are summarized here and mainly based on the published work of Miller and Bowman [55], [56] and textbooks of Glassman [57] and Warnatz [58]. These pathways can broadly be grouped into the following four primary mechanisms:

- Thermal Mechanism: This is the oldest NO_x sub-mechanism, controlled primarily by the elevated temperatures in the flame.
- Prompt(Fenimore) Mechanism: This pathway is regulated by interaction between nitrogen and hydrocarbon radicals.
- Fuel Mechanism: This sub-mechanism is similar to the prompt, limited to the fuels with nitrogen present and can be significant in relatively unclean fuel.

- Minor Mechanisms: Collection of several newly discovered NO_x mechanisms, these pathways can be of varying importance depending on conditions.

These mechanisms will be summarised in more detail in the following sections to discuss the important contributions to the understanding of each of these mechanisms.

2.1.1. Thermal Mechanism

This mechanism was first described by Yakov Borisovich Zel'dovich in 1947 [39]. Simple group of three reactions comprise the thermal NO formation mechanism:



Reaction [2-3] is the rate-limiting step in this mechanism with a relatively low reaction rate, owing to its high endothermicity and associated high activation energy of the nitrogen triple bond. Hence, high temperatures (above 1800K) are required in order to increase the reaction rate significantly [59]. Using a steady-state approximation of N-atom and assuming that the O-atom concentration may be calculated from equilibrium considerations, the maximum NO formation rate can be expressed as,

$$\frac{d[NO]}{dt} = 1.70 \times 10^{17} \cdot T^{1/2} \cdot e^{\left[-\frac{69750}{T(K)}\right]} [O_2]^{1/2}_{eq} \cdot [N_2]_{eq} \quad [2-4]$$

As can be seen from Equation [2-4], thermal NO is strongly dependent on temperature; it is generally the dominant source of NO production in high-temperature flames. In addition, it was seen that the thermal NO production in terms of mole fraction increases with pressure ($\sim\sqrt{p}$) [60].

Rates for reactions [2-1] to [2-3] are typically taken from a relatively limited data set, mainly with rates compiled by Baulch et al. [61]. However, there is some indication that these rates may be too high,

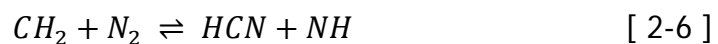
over-predicting rates of Thermal NO_x production and additional effort may be warranted to improve measurements of these rates [62].

2.1.2. Prompt Mechanism

The prompt mechanism is the most investigated and probably the most complex mechanism described in the literature due to the considerable coupling of the mechanism with the fuel oxidation. Fenimore [63], [64] identified the mechanism in the 1970's. NO forms rapidly in the flame zone of premixed flames in this mechanism, at much faster rate than the slow thermal mechanism.

2.1.2.1. Prompt NO Mechanism: HCN Mechanism

The formation of prompt NO is considered to be initiated through a rapid sequence of reactions resulting in fixation of nitrogen by hydrocarbon radicals. In 1970's and 1980's, many investigations proposed CH, CH₂, C₂, C₂H and C, among others as the potentially contributing species [55-59]. Ultimately, Blauwens et al [66] has shown that CH and CH₂ are the primary initiating species. Until 2000, the principle prompt reactions were considered to be:



Among these reactions, reaction [2-5] was considered to be the most important with reactions [2-6] to [2-8] considered to provide lesser contributions to prompt NO [68]. However, from early on it has been recognized that reaction [2-5] is spin forbidden [69], requiring that the reaction cross potential energy surfaces from a doublet to a quartet surface, a relatively slow process [67]. Instead, Moskaleva and Lin showed [70] that a better prompt initiating reaction, that conserves spin, is the reaction:



The resultant NCN then directly forms NO through the following paths [71]:



The products of NCN, particularly HCN, behave as previously understood and proceed to form NO in their own path [72], [73].

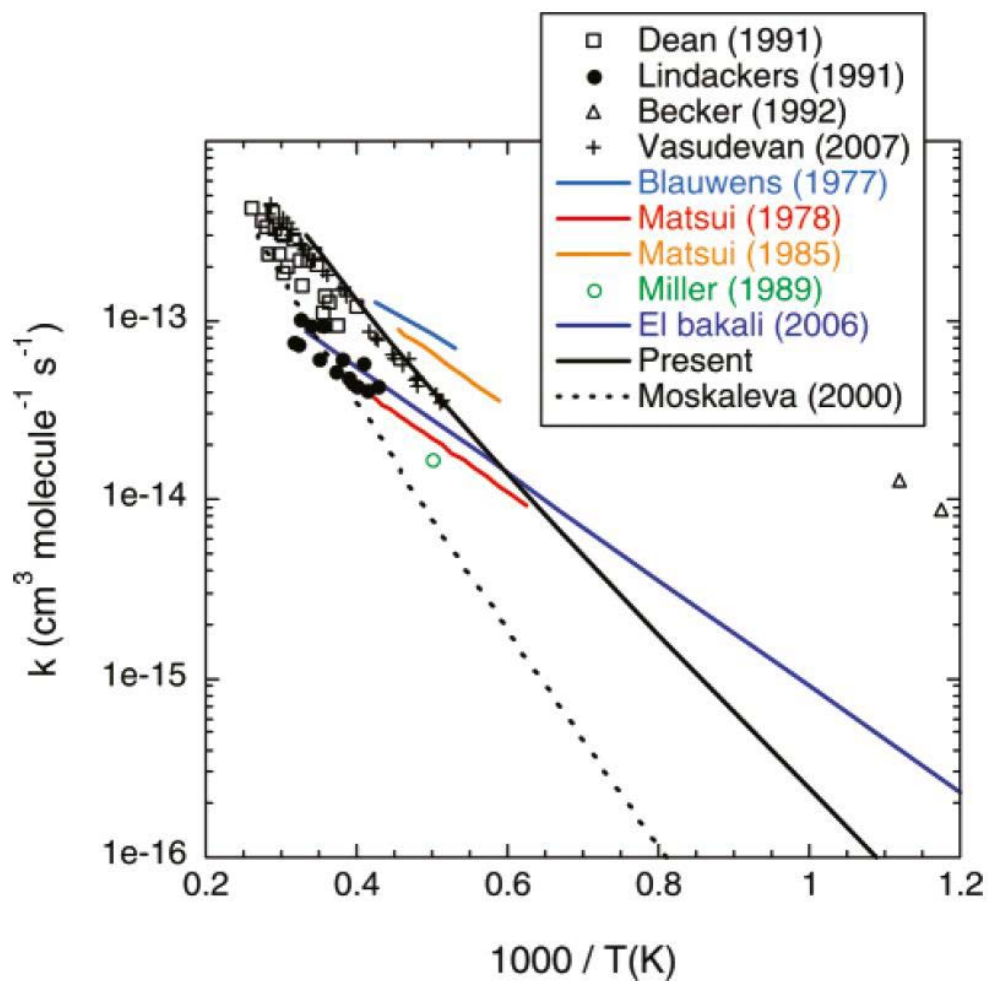


Figure 2-1: Experimental and theoretical rates for $\text{CH} + \text{N}_2 \rightarrow \text{NCN} + \text{H}$. The black symbols denote experimental measurements and the coloured lines denote modelling results. Solid and dashed black lines indicate theoretical predictions. Adapted from Harding et al [74].

Smith et al [75] demonstrated the presence of NCN in the low-pressure methane flames using LIF detection. Initially Moskaleva and Lin [70] predicted the rate constant for reaction [2-9] theoretically and it has

been continually improving ever since through experimental measurements [74], [76], [77] (refer to Figure 2-1).

2.1.2.2. Prompt NO Mechanism: N₂O Mechanism

NO can be produced during reaction sequences when N₂O is formed and removed in the combustion gases by a third body recombination reaction (M = collision partner),



NO formation by the N₂O mechanism increases as combustion goes leaner or as the burned gas temperature decreases. NO formation increases with increasing pressure due to the increase in the rate of third body collisions. However, the N₂O lifetime at combustion temperatures (>1500K) is less than 10ms, thus reaction [2-15] is not a significant production channel for NO, especially for most practical premixed flames at low pressures.

2.1.2.3. Prompt NO Mechanism: NNH Mechanism

NO can be produced during the formation and removal of NNH radicals. The key reactions involved in this process are as follows:



While the NNH mechanism can be a dominant source of NO production in low-pressure H₂/Air flames, its contribution is mostly negligible in high-pressure flames where the concentration of H radicals in the flame front is less.

2.1.3. Fuel Mechanism

A principle source of NO_x emission in fossil fuel combustion comes from nitrogen that is chemically bound in the fuel itself. This can be especially true for coal and ammonia combustion, where the coal may contain as much as 2% nitrogen by weight [65] and ammonia contains 82% nitrogen by weight. By the incorporation of nitrogen into the fuel molecule, the nitrogen - fixation reactions required for the prompt sub-

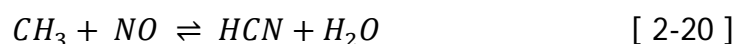
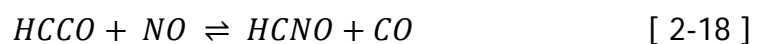
mechanism are effectively subverted, and the formation of NO through this fuel-bound nitrogen is considered largely independent of the initial fuel but rather more dependent on the combustion environment. The stable nitrogen-containing products formed as a result of the pyrolysis of the fuel are mainly HCN and NH₃, i.e. HCN is the principle pathway when the nitrogen is in an aromatic ring and NH₃ is the principle pathway when the nitrogen is in the form of an amine [63], [78]. Fuel-bound nitrogen is of significance mostly in combustion of coals or other heavy fuels. However, it should be noted that both pathways to fuel NO_x formation, either through HCN or NH₃, are members of the other NO_x mechanisms included in this analysis.

2.1.4. Minor Mechanisms

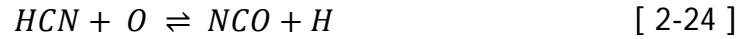
As the name suggests, these mechanisms may or may not have significant contributions to NO_x formation. Generally, these mechanisms can be significant, or even dominant, under certain combustion conditions and negligible at others. Four important minor mechanisms will be discussed in the following section.

2.1.4.1. NO - HCN Reburn

This mechanism was originally investigated as a NO_x reduction strategy through staged combustion, though it occurs naturally under many flame conditions. NO is recycled back to HCN through reactions with HC radicals to convert to either N₂ or back to NO. Determination of the specific HC radicals involved in the formation of HCN from NO has been studied by different groups [64], [71-74], and the following reactions have been identified as being the most important:



NO is more likely to be removed by the smaller radicals such as CH and C under radical rich conditions while HCCO and CH₃ can be more prominent under less radical rich conditions [82], [83]. As described in the Prompt sub-mechanism, HCN is controlled through O atom [84], and the conversion back to N₂ as follows:



2.1.4.2. Minor mechanisms: NO₂

The other primary component of NO_x, NO₂ has been observed to be present in significant quantities in the flame front [77-79]. The formation of NO₂ is driven by the presence of hydroperoxyl radical in the flame front through the following reaction:



The NO involved in the above equation is usually formed via other mechanisms in higher temperature regions of the flame and transported to the cooler regions of the flame with significant HO₂ concentrations. NO₂ is then rapidly converted back to NO through following pathways as it transits through the high temperature regions of the flame:



2.1.4.3. Minor mechanisms: N₂O

When the formation of Prompt NO is low due to low availability of CH under lean conditions and the thermal contribution is low due to lower flame temperatures, the N₂O mechanism become one of the remaining primary NO pathways [58], [65]. This mechanism is initiated by the formation of nitrous oxide (N₂O) through the third body reaction [2-32] and subsequent reaction to form NO in reaction [2-33].



Additionally, reaction [2-32] is enhanced at elevated pressure, and as a result, this mechanism can be significant at the lean premixed temperatures and pressures of gas turbine [88].

2.1.4.4. Minor mechanisms: NNH

Miller et al. [89] first proposed the role of NNH as a participant in the Thermal DeNO_x process for NO removal via non-catalytic reduction of NO by NH₃ [59], [82-85]. Though this mechanism is not a particular focus of this study, the Thermal DeNO_x process is an interesting application in which ammonia is injected under very specific temperature and oxygen conditions resulting in a self-sustaining reaction leading to the removal of NO through reaction with NH₂ radical as shown in reactions [2-34] and [2-35].



Later, Bozzelli and Dean [94] proposed an additional NO formation pathway through reaction of NNH with O atom (reaction [2-41]) as additional evidence for NO formation linked with NNH provided by Harrington et al. [95].



Additionally, another potential product of the $NNH + O$ reaction is N₂O. Combined with the N₂O mechanism above and the paired oxidation through amine radicals, the contribution of this mechanism can be significant under right conditions, particularly at temperatures below the Thermal mechanism limit. A more recent study of Klippenstein et al. [96] provides a detailed summary of the H/N/O reactions subset.

2.2. Chemiluminescence

Chemiluminescence is the most naturally emitted ultraviolet and visible radiation of flames, resulting from short lived electronically excited intermediate species such as OH*, CH*, C₂* and broadband CO₂*, formed during chemical process within a flame [97]. Since Broida and Gaydon

[98] required exposure times of up to 30 minutes to detect OH^* and CH^* radicals in 1950, the technique has developed significantly, with studies being carried out both experimentally and numerically by utilising advanced chemical kinetic models [99], [100]. Chemiluminescence measurements are not only limited to laboratory flames, with measurements conducted on industrial GT combustors from Siemens SGT-700/800 [101] and Alstom EV-10 [102]. Figure 2-2 shows aforementioned species in their respective electronically excited (A) states of OH^* (310 nm), CH^* (388, 431 nm), C_2^* (473 nm) and broadband CO_2^* , reproduced from [103].

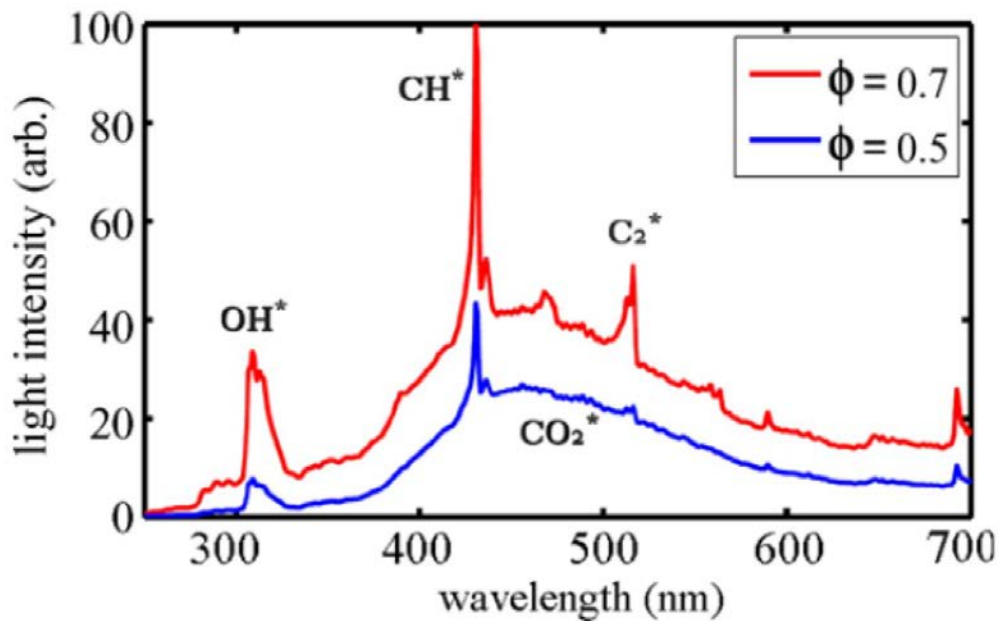


Figure 2-2: Typical chemiluminescence spectra of atmospheric natural gas-air flames at varying Φ . Reproduced from [103].

OH^* chemiluminescence emission measurements are of particular interest for this study as this measurement shows fundamental measure of heat release [104], [105], and flame structure [106], [107]. The OH^* chemiluminescence peak near 310 nm corresponds to the $A^2\Sigma \rightarrow X^2\Pi$ electronically excited to ground state energy level transition [103]. The dominant chemical production reactions for the formations of OH^* are $\text{H} + \text{O} + \text{M} \leftrightarrow \text{OH}^* + \text{M}$ [100] and $\text{CH} + \text{O}_2 \leftrightarrow \text{OH}^* + \text{CO}$ [103], [108]. OH^* radical destructs by spontaneous emission (refer to Section 2.3.2) of a photon or by returning to the ground state through collisional quenching. By

filtering out the broadband light emission, the intensity of emitted light from the spontaneous emission can be detected by the CCD camera.

2.3. Laser Induced Fluorescence (LIF) Spectroscopy

Not only combustion science but also many other scientific disciplines use Laser Induced Fluorescence (LIF) techniques for detection of chemical species. LIF technology is very effective in modern science as it is both quantum state and species selective, hence in theory permitting measurements of temperature, pressure, velocity, concentrations, reaction chemistry and density. In the field of combustion research, LIF has become probably the most popular method used for attempting measurement of minor species in flames and reacting flow. The basic LIF principle is to excite the targeted species to a higher level from ground level, then capturing the fluorescence signal when they return again to ground state. Planar Laser Induced Fluorescence (PLIF) imaging was developed to enable flow visualization and imaging of 2-D concentrations of chemical species and temperatures [43], [101-103].

2.3.1. LIF Modelling: Quasi - Two - Level System

Quasi - Two - Level dictates a two-step process where at first, the target molecules are excited to higher energy states by absorption of resonant photons of the laser and then eventually, excited molecules in the upper state relax back to the ground state by both radiative and non - radiative pathways to reach the steady - state and in the process, excess energy is released in terms of fluorescence signal. Non-radiative relaxation pathways can greatly reduce the LIF signal, and their magnitude and impact are of great importance when interpreting the signal quantitatively. Figure 2-3 illustrates a simple schematic of a quasi - two - level model for LIF [112], [113] of a typical diatomic molecule with electronic energy transitions between two levels.

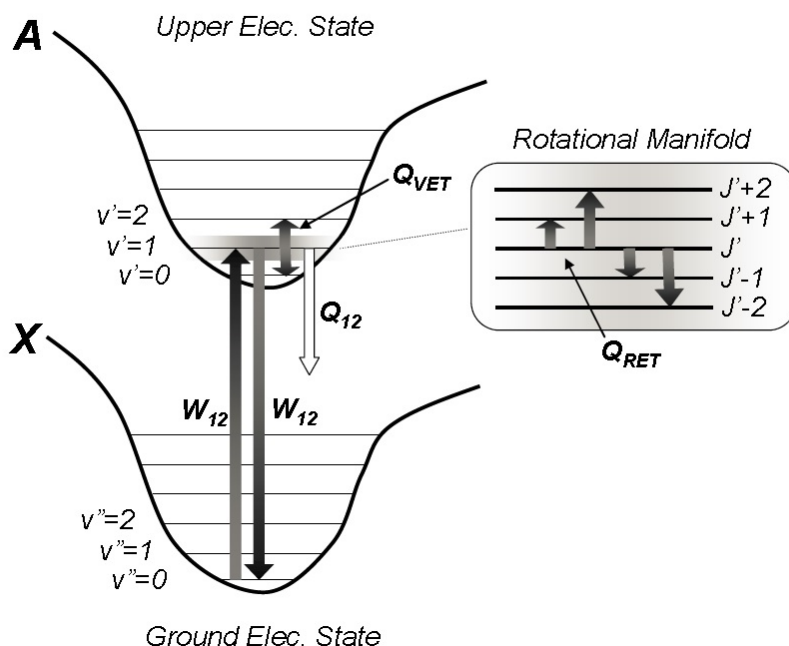


Figure 2-3: Simple Schematic of a Quasi-Two-Level System. Reproduced from [112]. In Figure 2-3, A state represents the 1st excited upper electronic state where X state is the ground electronic state. The parallel horizontal lines within the A and X states represent the vibrational levels and the rotational manifold attached to relevant $v' = 1$ vibrational state are magnified in the right inset. The narrow spectral width feature in modern lasers allows selective probing of the required individual rotational energy levels within the molecule. Once the molecule is excited to a specific rovibrational energy level to move to the upper electronic state, it can then move to other energy levels or return to the steady-state at the ground level via several energy transfer pathways. The relevant energy transfer mechanisms and dynamics of these mechanisms are discussed in detail in the following sections in this Chapter.

2.3.2. Absorption (W_{12}), Stimulated (W_{21}), and Spontaneous (A_{21}) Emission

These represent the excitation and de-excitation mechanisms directly coupled with the laser/molecule interaction. The laser excites the ground level population to an upper state through absorption of incident photons and stimulated emission by the laser induces a reverse, de-activation process simultaneously, causing the excited population in the

upper state to fall back to ground state. The absorption rate W_{12} (s^{-1}) is linearly dependent on the Einstein B_{12} coefficient ($m^3/J.s^2$):

$$W_{12} = \frac{B_{12}I_\nu}{c} \quad [2-37]$$

I_ν represents the laser irradiance per unit frequency interval (spectral irradiance in units of $W/cm^2.s^{-1}$) and c is the speed of light. Similarly, the stimulated emission rate $W_{21}(s^{-1})$ is given in terms of the Einstein B_{21} coefficient ($m^3/J.s^2$):

$$W_{21} = \frac{B_{21}I_\nu}{c} \quad [2-38]$$

Both absorption and stimulated emission are governed by Einstein B coefficients, which are related to each other as,

$$g_1B_{12} = g_2B_{21} \quad [2-39]$$

where g_1 and g_2 are the degeneracies of states 1 and 2, respectively. 'Degeneracy' here just means that there are more than one quantum states with the same sharply defined energy. In quantum mechanics, an energy level is said to be degenerate if it corresponds to two or more different measurable states of a quantum system. Conversely, two or more different states of a quantum mechanical system are said to be 'Degenerate' if they give the same value of energy upon measurement. For example, there can be a state where an electron is rotating one way around the nucleus and another state of the same energy where it rotates the opposite way. Incident laser irradiance, I_ν can also be described as a product of a normalized spectral irradiance, I_ν^0 and a dimensionless overlap fraction, Γ [114] (rate of actual photon absorption rate to the monochromatic limit) in systems, where transition and laser line shapes are spectrally broadened.

Spontaneous emission is very important for LIF signal production as this relative decay process constitutes the main mechanism for desired fluorescence signal. The molecule is spontaneously relaxed from an excited upper state to other states i in the lower electronic state by emitting fluorescence. The fluorescence rate is given by the Einstein A_{21}

coefficient (s^{-1}), and the total fluorescence rate A is the sum of the fluorescence rates over all individual transitions.

$$A = \sum_i A_{2i} \quad [2-40]$$

Einstein coefficients govern spontaneous and stimulated emission by:

$$\frac{A_{21}}{B_{21}} = 8\pi h\nu \quad [2-41]$$

where h is the Planck constant and ν is the wavenumber of the individual transition. In the physical sciences, the wavenumber is the spatial frequency of a wave. In multidimensional systems, the wavenumber is the magnitude of the wave vector. Multiplied by Planck's constant, it is the momentum of a wave.

2.3.3. Rotational and vibrational energy transfer (Q_{RET} and Q_{VET})

Collisions with other molecules enables molecules in specific rovibrational levels in the excited upper state to migrate to neighbouring rotational or vibrational states by internal energy transfer process. As Rotational energy transfer (RET) occurs around a vibrational level, RET is typically very fast and particularly important in LIF dynamics of short pulse nanosecond lasers. Thermal equilibrium gets perturbed as the laser excites population to upper electronic state from ground state. RET comes into action to re-establish the thermal equilibrium by refilling or depleting the relevant energy levels. The rate of RET, $Q_{RET}(s^{-1})$ induced by collisions with all other species j in the system is given by,

$$Q = \frac{P}{kT} \sum_j x_j v_j \sigma_{RET,j} \quad [2-42]$$

where x and v are the mole fraction of species j and relative velocity of the colliding particles ($v = \sqrt{8kT/\pi\mu}$ where μ is reduced mass, $\mu = m_1 m_2 / (m_1 + m_2)$), respectively. The parameter $\sigma(cm^2)$ is the effective rotational cross section for collisions with species j . Vibrational energy transfer (VET) is conceptually identical to RET and energy transfer occurs to neighbouring vibrational levels. VET is not of that much

importance for NO LIF as VET rates are much slower than other form of energy transfer mechanisms and the molecules will go to ground electronic state before VET can occur.

2.3.4. Quenching energy transfer (Q_{21})

Collisions with other molecules can cause molecules in the excited electronic state to relax down to a lower electronic energy state. The overall rate of quenching $Q_{21}(s^{-1})$ induced by collisions with all the other species j in the system is usually given in the same way as RET,

$$Q = \frac{P}{kT} \sum_j x_j v_j \sigma_{Q,j} \quad [2-43]$$

The term σ is the quenching cross sections upon collision with the species j . Quenching is the main difficulty to get proper LIF signal as it forces the excited molecules to return back to ground electronic state while RET and VET maintain the molecule in the upper electronic state with a possibility of good LIF signal. Equation [2-43] demonstrates that quenching is linearly dependent on pressure, indicating considerable impact on high pressure systems.

Other mechanisms like photoionization/photodissociation, predissociation, intersystem crossing can also have significant impact on the LIF signal alongside the above discussed mechanisms [50], [112], [113], [115]. Absorption of additional photons for molecules in the excited upper state causes the photodissociation or photoionization of the molecule. Predissociation occurs when molecules are excited into a rovibrational level of bonding state beyond the dissociation energy or onto a potential surface crossing to an anti-bonding state.

2.3.5. LIF Equation: Two-Level Derivation

The LIF equation is very important to understand and analyse LIF signals as it provides vital information about the key physics involved in the LIF process. Two-level model is analysed non-transiently to derive the LIF equation as the two-level model gives the easy understanding of excitation and de-excitation process involved in LIF. More accurate description of the actual physics and distribution of energy levels of real

diatomic molecules by quantum-mechanical density-matrix approach can be found in the literature e.g. [112], [116].

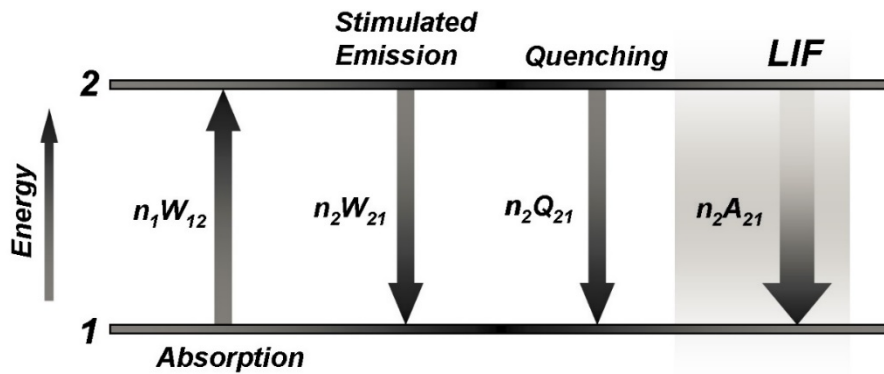


Figure 2-4: Two-level LIF model and relevant energy transfer processes

However, a two-level non-transient rate-analysis with simple mathematics is capable of describing most of the basic concepts. Theoretically, this type of approach is appropriate for atomic species and molecular systems in fully equilibrium or fully frozen rotational level manifolds. These models can be used as a first approximation in actual LIF experiments. Figure 2-4 shows the basic transitions involved in the two-level model. n_1 and n_2 represent the population number density of states 1 and 2, respectively with the total number of density, $n^0=n_1+n_2$.

In a non-transient approach, a constant laser intensity I_v^0 is assumed and therefore constant W_{12} (equation [2-37]) and W_{21} (equation [2-38]). Rate analysis can be performed to determine the rate of change of the population of molecules in level 2 as per equation [2-44].

$$\frac{dn_2}{dt} = \dot{n}_2 = n_1W_{12} - n_2(W_{21} + Q_{21} + A_{21}) \quad [2-44]$$

At steady state, $\dot{n}_2 \approx 0$ and the population density of state 2 can be represented as per equation [2-45].

$$n_{2,steady-state} = n_1 \frac{W_{12}}{(W_{21} + Q_{21} + A_{21})} \quad [2-45]$$

The steady state analysis above gives ideas of two limits of laser operation. When laser energies are higher than threshold of saturation, absorption and stimulated emission balance and the population of the two energy states are determined by the ratio of the degeneracies in a

two-level model. In this limit, the fluorescence signal is independent of laser intensity. The other limit of operation is known as 'weak excitation' where the laser intensity is well below saturation threshold, permitting the fluorescence signal to be linearly proportional to laser intensity. Usually, weak excitation is preferred since laser non-uniformities and attenuation effects pose practical problems in applying LIF in the saturated regime. When the stimulated emission from level 2 is much weaker than the sum of collisional and simultaneous decay process,

$$W_{21} = \frac{B_{21}I_v}{c} \ll A_{21} + Q_{21}. \quad [2-46]$$

Then $n_2 \ll n_1$, and $n_1^0 \approx n_1$. The population fraction in level 2 can be shown as,

$$n_2 = n_1^0 \frac{W_{12}}{A_{21} + Q_{21}}. \quad [2-47]$$

It can be verified experimentally that the fluorescence signal is proportional to the population of level 2, the rate of spontaneous emission A_{21} and the solid angle of collection Ω . The following expression indicates the fluorescence signal, S_F .

$$S_F = n_2 \times V \times A_{21} \times \frac{\Omega}{4\pi} (\text{photons/s}). \quad [2-48]$$

In practice, LIF intensity, I_{LIF} quantifies the fluorescence signal and according to equation [2-47], the population density of level 2 can be replaced by a function of the initial ground state population, n_1^0 . For more accurate modelling, we diverge from the strict concept of a two-level model and assume that the lower energy level has a manifold of rotational levels in thermal equilibrium. Boltzmann distribution can explain the population distribution of these lower energy levels [117] and the population of a specific rotational level can be written as $n_1^0 \times f_B$, where f_B represents the Boltzmann fraction of the individual energy level. In light of above discussions and by using equations [2-38], [2-47] and [2-48], the LIF intensity can be written as,

$$I_{LIF} = c \times I_v^0 \times n_1^0 \times f_B \times B_{21} \times V \times \Gamma \times \frac{\Omega}{4\pi} \times \frac{A_{21}}{A_{21} + Q_{21}} \quad [2-49]$$

where I_{ν}^0 is the spectral intensity of the probing laser, Γ is the dimensionless overlap function, V is the volume of excited molecules and c is the optical collection efficiency of the experimental set-up [114]. Equation [2-49] is known as the LIF equation and is the fundamental equation for interpretation of LIF signals in practical experimentation and non-transient computational simulations. Fluorescence yield (Φ) is the ratio of the spontaneous emission rate (LIF) to all excited state de-excitation rates and is represented by the term $\frac{A_{21}}{A_{21}+Q_{21}}$ in equation [2-49]. Fluorescence yield directly represents the fluorescence percentage of the excited population. Values of A_{21} for nitric oxide $A^2\Sigma^+$ ($v'=0$) state are $\sim 4.6 \times 10^6 \text{ s}^{-1}$, quenching rates (Q_{21}) values are on the order of $\sim 10^{10} \text{ s}^{-1}$, giving a fluorescence yield of the order of $\sim 10^{-4}$. For other molecules where predissociation and intersystem crossing are large, the fluorescence yield can be written as,

$$\Phi_{FL} = \frac{A_{21}}{A_{21} + Q_{21} + P_{PD} + I_{IC}} \quad [2-50]$$

where P_{PD} is the rate of predissociation and I_{IC} is the rate of intersystem crossing. Depending on the relative magnitudes of Q_{21} , P_{PD} and I_{IC} , one term can be dominant in the denominator of the fluorescence yield and significantly impact the dynamics of LIF.

2.3.6. Broadening and Shifting of Spectral Lines

This section reports the mechanisms for broadening and shifting in lineshape functions. These effects are particularly important in high pressure applications. Theoretically, dipole transition is defined by the energy difference between two quantum states but actual transitions are not monochromatic and exhibit a certain spectral width and shape. These lineshape features depend on pressure, temperature, concentration and range of collision partners involved, and therefore play an important role in the interpretation of optical spectra [112].

Lineshape functions $\varphi(\nu)$ reflect the relative variation in the spectral absorption coefficient with frequency and have been defined so that its integral over frequency is unity,

$$\int_{-\infty}^{+\infty} \varphi(\nu) d\nu = 1 \quad [2-51]$$

The width of the lineshape is due to spectral broadening caused by phenomena in the medium that perturb the transition's energy levels or the way in which individual atoms and molecules interact with light. Natural broadening, Doppler broadening and Collisional broadening are the three forms of broadening mechanisms that contribute to the observed line width.

Natural broadening: When the spectral width is caused by the molecule in the absence of interactions with other atoms, it is known as natural broadening. Heisenberg Uncertainty Principle governs this phenomenon which states that it is impossible to measure energy and time simultaneously.

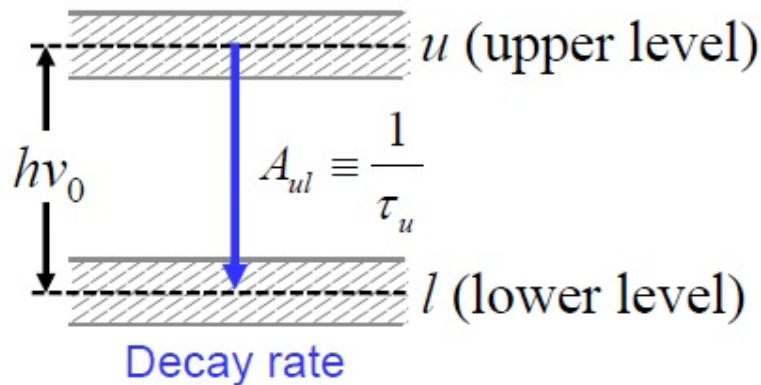


Figure 2-5: Uncertainty in the energy level. Reproduced from [116].

If we consider the energy levels in Figure 2-5, the uncertainty in the energy of \$u\$ to go to the lower level is limited by,

$$\Delta E_u \geq \frac{h}{2\pi\Delta t_u} \quad [2-52]$$

where \$\Delta t_u = \tau_u\$, is the uncertainty in time of occupation of \$u\$. The lifetimes of upper states, \$\tau_u\$ can be combined to give the total uncertainty of a transition. In units of frequency, this uncertainty is given by,

$$\Delta \nu_N = \Delta \nu_u + \Delta \nu_l = \frac{1}{2\pi} \left(\frac{1}{\tau_u} + \frac{1}{\tau_l} \right) = \frac{1}{2\pi\tau_u} \quad [2-53]$$

The resulting lineshape function can be mathematically modelled by 'Lorentzian Distribution'. Natural broadening is categorised as homogenous since the uncertainty principle applies to all atom in the same way. Natural broadening is typically much smaller than Doppler and Collisional broadening. Usually, in the case of NO, natural broadening is negligible for most conditions. Table 2-1 illustrates the typical values for natural line broadening.

Table 2-1: Typical values for natural line broadening

	τ_u	$\Delta\nu_N$	$\Delta\omega_N$
Electronic transitions	10^{-8} s	1.6×10^7 s ⁻¹	5×10^{-4} cm ⁻¹
Vib-rot transitions	10^{-2} s	16 s ⁻¹	5×10^{-10} cm ⁻¹

Collisional Broadening: This type of broadening is caused by the interactions of atoms and molecules in a gas. Energy level's lifetime is shortened due to perturbations that occur during the collision. This is also lifetime limited - time set by collision time interval. Let's consider the following collision between B molecule with A molecules in Figure 2-6.

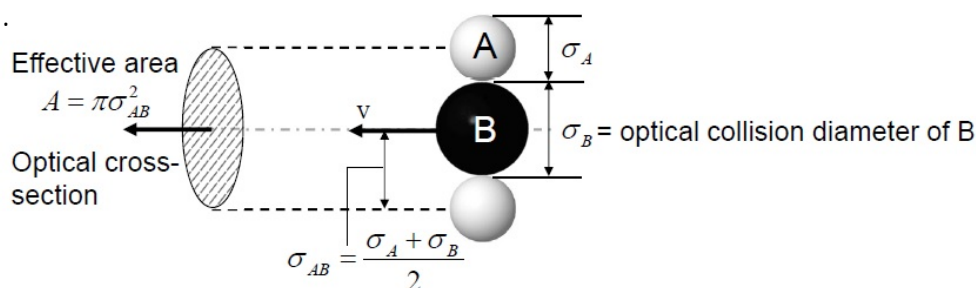


Figure 2-6: Collisional Broadening

The total collisional frequency of molecule B with all other collisional partners can be written as,

$$Z_B = P \sum_A X_A \cdot \pi \sigma_{AB}^2 \cdot \sqrt{\frac{8}{\pi \mu_{AB} kT}} \quad [2-54]$$

Where P is pressure, X_A is the mole fraction of species A, σ_{AB} is the optical collision diameter between species A and B, and μ_{AB} is the

reduced mass ($\mu_{AB} = m_A m_B / (m_A + m_B)$). By using equation [2-54] with $\frac{1}{\tau_u} = \frac{1}{\tau_l} = Z_B$, the spectral width of collisional broadening is given by,

$$\Delta v_c = \frac{1}{2\pi} \left(\frac{1}{\tau_{coll,upper}} + \frac{1}{\tau_{coll,lower}} \right) \cong \frac{Z_B}{\pi} \quad [2-55]$$

Molecular interactions are quite complex in the quantum level, which makes it difficult to derive analytical expressions for the collisional widths in practice. As an alternative, empirical expressions with adjustable parameters are utilised [118], [119]. Assuming that the interactions of different colliders A are independent, the collisional broadening is modelled as a product of the system pressure and sum of the mole fraction for each perturbing species A multiplied with its process-dependent collisional halfwidth $2\gamma_A$ as,

$$\Delta v_c = P \sum_A X_A 2\gamma_A \quad [2-56]$$

As a crude approximation, the broadening coefficient $2\gamma_A$ varies with temperature according to the following expression,

$$2\gamma(T) = c 2\gamma(T_0) \left(\frac{T_0}{T} \right)^n \quad [2-57]$$

T_0 denotes the reference temperature at 296K or 300K, n is the temperature coefficient with a typical value of 0.5 for hard sphere and c is an empirical scaling factor. Chang, Dirosa and Hanson determined the values for 2γ , c and n for the $A - X(0,0)$ transitions in shock tube experiments [110-112] while Vyrodov et al. [121] derived the values for collisional partners Ar, He, N₂, H₂O, O₂ and NO. Lorentzian function can be used to describe the lineshape due to collisional broadening:

$$\phi(v)_{coll} = \frac{1}{\pi} \frac{\Delta v_c / 2}{(v - v_0)^2 + (\Delta v_c / 2)^2} \quad [2-58]$$

Doppler Broadening: ‘Doppler Shift’ causes Doppler broadening which occurs when a molecule has a velocity component in the same direction as the propagation of the laser beam. The velocity is directly dependent on temperature as the thermal motion of the molecules causes it.

Mathematically, the Doppler lineshape can be represented by a Gaussian function as,

$$\phi(v)_D = \frac{2\sqrt{\ln 2}}{\sqrt{\pi} \Delta v_D} \exp \left[-\left(\frac{2\sqrt{\ln 2}}{\Delta v_D} (v - v_0) \right)^2 \right] \quad [2-59]$$

The Maxwellian velocity distribution function describes the random velocity distribution of molecules. The Maxwellian velocity distribution tells us what fraction of the molecules is in each velocity class, each with its own Doppler shift. By calculating the shift for each velocity component and averaging over the distribution, we can determine the FWHM of a Doppler-broadened line,

$$\Delta v_D(FWHM) = 2 \sqrt{\frac{2kT \ln 2}{mc^2}} v_0 \quad [2-60]$$

Where v_0 (cm^{-1}) is the center wavelength of the line, m the molecular mass, k the Boltzmann constant and c is the speed of light. Since the velocity of each individual molecule is different, Doppler broadening is also different for each molecule and is called inhomogeneous broadening with an inhomogeneous linewidth.

Voigt Profile: Sometimes Collisional broadening and Doppler broadening occurs simultaneously - resulting in the convolution of two lineshape profiles, one with a Gaussian and the other a Lorentzian function. In cases where neither effect is negligible, Voigt profiles [122] are used to combine the effects of the two profiles, and are generally used to describe absorption lineshapes for diatomic molecules including NO. For high-pressure applications the dominant effect which influences the lineshape width is pressure broadening. Collisional broadening leads to a decrease in the peak intensity of the absorption features as well as a blending effect of neighbouring transition lines. If we consider the following lineshapes with the convolution of Gaussian and Lorentzian with same area of unity as shown in Figure 2-7, at peak heights,

$$\phi(v_0)_{Dopp} = \frac{2\sqrt{\ln 2}}{\sqrt{\pi} \Delta v_D} = 0.94/\Delta v_D \quad [2-61]$$

$$\phi(\nu_0)_{Coll} = \frac{2}{\pi} \frac{1}{\Delta\nu_C} = 0.637/\Delta\nu_C \quad [2-62]$$

which demonstrates that the Gaussian is higher near peak while the Lorentzian is higher in the 'wings'. For $\frac{\Delta\nu_C}{\Delta\nu_D} = 1$,

$$\phi(\nu_0)_{Dopp} = 1.48\phi(\nu_0)_{Coll} \quad [2-63]$$

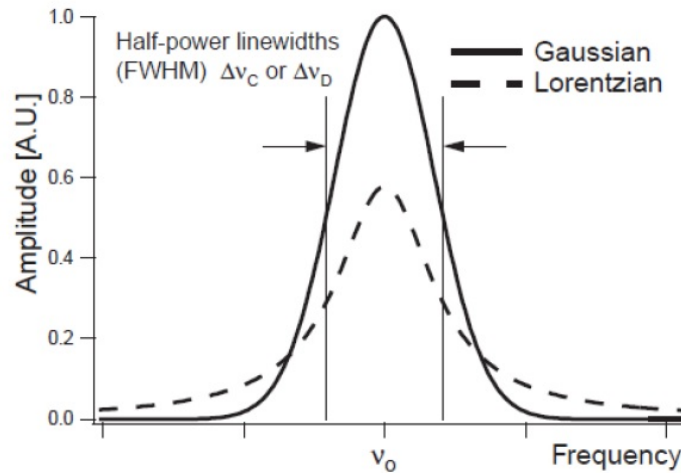


Figure 2-7: Voigt Profile. Reproduced from [112].

The physical argument employed in establishing the Voigt profile is that the effects of Doppler and collision broadening are decoupled. Thus, it is argued that every point on a collision-broadened lineshape is further broadened by Doppler effects.

Line Shifting Mechanisms: Variation in temperature and pressure also induce shifting of the position of the line centre. Interaction between two collision partners can have a perturbing effect on the intermolecular potential of the molecules. Changes in the potential energy surface lead to differences in the energy level spacing, resulting in a shift of the centre wavelength of the absorption lineshape which is known as pressure shifting or collisional shifting [122]. The empirical treatment of collisional shifting is analogous to that of collisional broadening and collisional shifting halfwidth can be described as,

$$\Delta\nu_S = P \sum_A X_A \delta_A \quad [2-64]$$

where P is pressure, X_A is mole fraction of species A and δ_A is the shift coefficient of species A with all other colliding species. The shift coefficient varies with temperature as,

$$\delta_A(T) = c\delta_A(T_0)(T_0/T)^M \quad [2-65]$$

where T_0 is the reference temperature, M is the temperature coefficient and c is an empirical scaling factor. Empirical parameters δ, c and M were measured in the literature [110-113] for nitric oxide for variety of colliders for the $A - X(0,0)$ transition.

2.3.7. Saturation and Population Recycling

Saturation: Saturation occurs in a simple two-level model when the induced emission is much larger than the collisional and spontaneous emissions,

$$W_{21} = \frac{B_{21}I_\nu}{c} \gg A_{21} + Q_{21} \quad [2-66]$$

where the fluorescence signal is independent of both the laser irradiance and the quenching rate [50], [123]. In the saturation regime, the rates of laser absorption and stimulated emission become so large that they dominate the state to state energy transfer into and out of the directly pumped levels. From the perspective of not affecting the fluorescence intensity, LIF in the saturation regime can potentially be less complicated with the added benefit of maximizing the fluorescence yield and therefore increasing detection sensitivity. However, complete saturation is required to realise the benefits mentioned above but complete saturation is difficult to achieve due to the specific wavelength region of absorption or the magnitude of the saturation intensity. Furthermore, the decrease of energy in the outer edges of the laser beam and the temporal deviation of pulse to pulse fluctuations introduce more complications. Due to all these reasons, though operating in the saturation regime has added benefits, application of LIF techniques in the linear regime using laser energy below the saturation is generally recommended. If the two-level diagram of Figure 2-4 is considered again, the following equation for saturation spectral irradiance can be derived,

$$I_v^{sat} = \frac{(A_{21} + Q_{21})c}{B_{12} + B_{21}} \quad [2-67]$$

where c is the speed of light. For most diatomic molecules, saturation spectral irradiance can be attained by the use of high-power pulsed lasers with typical pulse durations less than 10ns. In the case of NO, a 1mJ powered laser with a wavelength of 226.03nm and duration of 7ns pulse focused into a 1 mm diameter will start to show slight deviation from the linear regime. For actual molecules with multiple energy levels, more complex dynamics regarding saturation should be considered.

Population Recycling: Saturation effects can occur by both an overfilling of the upper excited state or by depleting the lower ground state and at the same time, population can either be removed or added to the laser couple states through rotational energy transfer (RET), which is on the same timescale as LIF. In the case of NO-LIF, the linear regime can be greatly extended at high pressure conditions as the rapid increase in the rotational energy transfer refills the depleted ground state while removing excess population in the upper excited state.

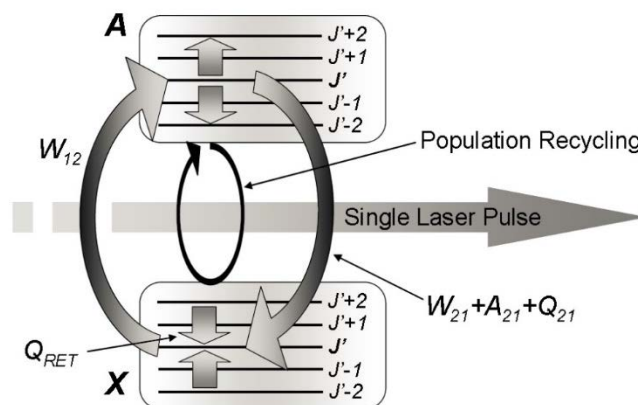


Figure 2-8: Population Recycling. Reproduced from [110].

This phenomenon is known as Population Recycling (refer to Figure 2-8) where fast energy transfer and fluorescence mechanism can allow excitation of the same molecule to occur multiple times with the same laser pulse. A de-excited population from the upper state is re-excited within the same laser pulse and is cycled back to the upper excited energy level. Knowledge of transient treatment with multiple energy

levels and accurate relevant RET rates are required to model population recycling and saturation effects in detail [124], [125].

2.3.8. LIF Temperature Dependence

As shown in equation [2-49], the temperature dependence of the LIF signal occurs as a result of the spectral overlap between the laser-spectral profile and the absorption spectrum of the molecule, the temperature variation of the laser-excited ground state population and the fluorescence yield. Two practical implications can arise from this temperature dependence. First, knowledge of the local temperature is required to correct for the signal variation while analysing using LIF quantitatively. Second, temperature can be detected in the probe volume by using the LIF signal. Several techniques have been developed previously implementing both one-line and two-line wavelength methods to isolate the temperature sensitivity of the signal for thermometry [126].

Two-line thermometry techniques offer the most versatility for the PLIF experimental effort and are dominantly used. Temperature is obtained by using the ratio of fluorescence signals obtained from excitation of two different ground states where the absorbing state populations are assumed to follow Boltzmann statistics and therefore a function of temperature. Rotational temperature for NO are typically obtained by selecting transitions that originate from different rotational states within the same vibrational level of the electronic ground state,

$$R_{12} = C_{12} \frac{I_{v1}^0 \times f_B(T) \times B_1 \times \Gamma_1(T) \times \phi_1(T)}{I_{v2}^0 \times f_B(T) \times B_2 \times \Gamma_2(T) \times \phi_2(T)} \quad [2-68]$$

where subscripts 1 and 2 refer to transition 1 and 2, respectively. C_{12} is the experimental constant for differences in optical efficiency. The main benefit of two-line thermometry is that by taking the ratio of fluorescence signals, the dependencies on the number density, mole fraction, overlap integral, partition function and collisional quenching may be minimized. In practice, the fluorescence ratio can be written as an explicit function of temperature as,

$$R_{12} = C_{12} \exp \left[-\frac{\Delta \varepsilon_{12}}{kT} \right] \quad [2-69]$$

where $\Delta \varepsilon_{12}$ is the energy difference (cm^{-1}) between the initial absorbing states. C_{12} can be calibrated from signal ratios using computational simulations or from a well characterized calibration source or region where temperature is accurately known. Temperature sensitivity is a parameter of major concern when using LIF for detection of temperature.

2.4. Computational Simulation of NO-LIF

There are some pre-requisites which must be satisfied and known to perform quantitative LIF measurements for a given molecule. First, an understanding of the absorption spectrum along with practical accessibility with a tunable laser is required. Second, the emission spectrum of the molecule should be well known. Third, the rate of radiative decay of the excited state should be known, due to the fact that fluorescence power is proportional to this rate. Fourth, an understanding of non-radiative pathways including quenching, photoionization and/or predissociation should be known.

2.4.1. Other NO-LIF Modelling Simulations

Several simulation programmes have been proposed over the years to simulate NO, each with a varying degree of complexity in the description of the LIF dynamics. Luque and Crosley [127] proposed LIFBASE which is the most general and widely distributed program with spectroscopy of several diatomics including OH, OD, NO, CH, CN, N_2 , SiH and CH. Though LIFBASE has a broad application base, spectroscopic details are incomplete for many of the molecules including NO as well as incomplete quenching model.

NO and OH spectroscopic models and fitting functions were implemented in a simulation program by Vyrodov and Heinze [121]. This model also lacked a detailed quenching model. Initial application of multi-line thermometry in high pressure flames was demonstrated by this model with successful temperature detection for flames under 20 bar.

DiRosa et al. [128] developed an advanced simulation program in FORTRAN for NO and O₂ which was widely used for pioneering work in NO-LIF. Details of spectroscopic parameters implemented in the modelling were similar to LIFSim [129], [130]. The ability to model O₂ simultaneously provided the ability to optimize excitation lines for UV NO-LIF in the presence of interference from O₂ LIF.

All these models consider steady-state LIF models with the population of laser-coupled ground state in equilibrium and rapid RET is assumed. This kind OF steady state model can satisfy most of the requirements of NO-LIF experiments. For transient modelling of NO excitation dynamics, a time-resolved simulation model has been implemented by Daily (University of Colorado) [124]. This model can clearly illustrate population recycling effects by showing the effects of fast RET and negligible VET.

2.4.2. LIFSim: Functionality

LIFSim enables computational simulations of excitation and emission process in LIF (NO and O₂) to assist in the quantitative analysis of species concentration in practical experiments. Functionalities of LIFSim are briefly described in this section.

Calculation of absorption spectra: Temperature, pressure, excitation wavelength range, spectral resolution, species concentration, laser parameters and the molecular spectroscopy parameters are required for calculation. The laser is tuned over a certain wavelength range and the absorption spectra are recorded.

Calculation of LIF excitation spectra: The laser is tuned over a certain wavelength range and the LIF signal is recorded at each spectral position. Parameters for calculation are temperature, pressure, excitation wavelength range and spectral resolution. The detection bandpass can be set arbitrarily.

Calculation of LIF fluorescence emission spectra: The laser is set to a fixed excitation wavelength and spectrally resolved LIF emission spectra are recorded. Parameters for calculation are temperature, pressure,

excitation wavelength, wavelength range and resolution for the fluorescence spectrum and simulated monochromatic function (slit function) with Gaussian and Lorentzian contribution.

Pressure and Temperature dependence of LIF signals: The LIF signal is calculated for a range of pressures and temperatures. Parameters for calculation are temperature range and resolution, pressure range and resolution and excitation wavelength. Calculations can be performed on a per molecule or per-volume basis.

Fit of simulated LIF excitation spectra to experimental data: Experimental LIF excitation can be fit using simulation by varying input parameters. The fitting is done via nonlinear-least-square-fitting (Levenberg-Marquadt) [131].

2.4.3. LIFSim: LIF Model

A simple non-transient three-level LIF model consists of lower ground level, upper excited level and a rotational manifold attached to the ground level is used for the calculation of LIF signals in LIFSim as illustrated in Figure 2-9.

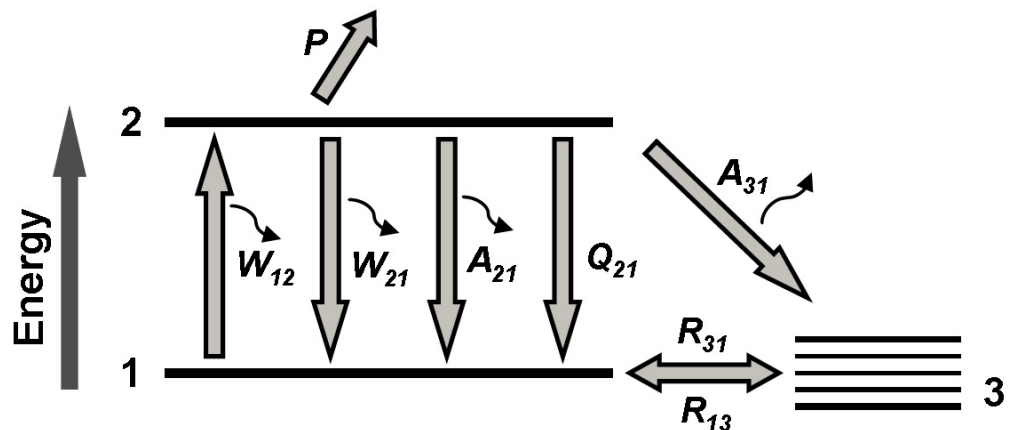


Figure 2-9: Three-level LIF model in LIFSim. Reproduced from [129].

The simplicity of the model enables rapid calculations of the LIF signals while the three-level concept is sufficient to capture most of the relevant physics required for analysis of experimental data. The model makes assumptions of an equilibrium population of the laser-coupled ground state (i.e. rapid ground state RET is assumed) and a single laser-

coupled upper state is used with no excited-state energy transfer. Fluorescence emission is calculated from a single upper state within the allowed branches to all possible rotational and vibrational levels of the electronic ground state, with quenching and predissociation (P) as the only non-radiative depopulation mechanism of the excited upper state. The steady-state rate equation approach in the linear regime for a three-level model collapses to a form identical to the LIF equation [2-49] which forms the backbone of the simulation calculations.

2.5. NO-LIF in the Literature

Extensive works has been done on NO-LIF for both laboratory and practical combustor applications. Grieser and Barnes [132] reported one of the first use of single point NO fluorescence measurements. Later, McKenzie and Gross [133] suggested the use of two-photon LIF of NO for single-point thermometry. Kychakoff et al. [134] reported the first 2-D imaging of NO fluorescence with seeded NO in CH₄/air flames. The first instantaneous 2-D PLIF temperature imaging was reported by Seitzman et al. [135], utilizing a one-line technique to measure the rotational temperature of NO seeded in fuel lean methane-air flames. Paul et al. [136] first reported two-line PLIF temperature imaging measurements.

Laser probing for NO measurements have mostly used the A-X system with transitions in the (0,0), (0,1) and the (0,2) bands at 226.03, 235 and 248 nm respectively and fluorescence signal detected at 232-252 nm ((0,1)+(0,2) detection), 217-232 nm ((0,0) detection) and 220-240 nm ((0,0)+(0,1) detection) respectively [129-132]. Additionally, some measurements have been taken in the D-X (0,1) band at 193 nm [141] but this band often experiences transmission problems in hot combustion environment. Lee et al. [142] evaluated all the strategies for quantitative NO measurements in high-pressure flames. To quantify NO concentrations in the flame from the LIF measurement, the temperature distribution in the flame needs to be accounted for as NO is highly temperature dependant. Comparison of NO LIF using A-X and D-X strategies are summarised in the following sections.

2.5.1. A-X (0,0) Excitation Overview

The A-X (0,0) transitions at 224 - 227 nm are the transitions most frequently used in the past. This has evolved into the standard technique for NO detection in flames and is the only technique sensitive to cold NO for flow field diagnostics [143], [144]. It has also been used extensively in high-pressure applications, such as small-scale laboratory flames, gasoline and diesel internal combustion engines. Laurendeau and co-workers have studied NO formations extensively in premixed, partially premixed and diffusion flames. They have reported quantitative single-point NO measurement in CH₄/air flames up to 15 bar [145], C₂H₆/air flames up to 15 bar [146]-[149], C₂H₄/air flames up to 12 bar [150], C₇H₁₆ spray flames up to 5 bar [151]-[153], and CO/H₂/CH₄/air flames up to 12 bar [154]. Most of the experiments were carried out using a frequency-doubled dye laser system tuned to the Q₂ (26.5) transition at 225.58 nm to minimize temperature dependence of the ground state population. O₂ LIF interference was quantified using spectroscopic measurements in the 1 - 12 bar range [114], [155], and subsequently influence of pressure on NO calibration was investigated [156]. Vyrodov and co-workers first reported NO measurements in high-pressure steady-state laminar flame burner up to 60 bar [157], and also the first to apply a multi-line fitting thermometry technique using a detailed spectral simulation model. They have also contributed to the database of collisional broadening coefficients of NO with N₂ and Ar as colliders in high-pressure environments [121]. DiRosa and co-workers have reported high-pressure NO-LIF spectroscopy in flames up to 10 bar [128], and presented a numerical simulation model for both NO and O₂ LIF. In addition, DiRosa et al. [118], [119] reported collisional broadening and shifting parameters for NO in high-pressure combustion environments. Schulz et al. [158], [159] reported NO LIF strategies, possible O₂ interferences and laser/signal attenuation by hot CO₂ and H₂O in detail using A-X (0,0) excitation up to 60 bar. Bockle et al. [160] reported the only NO-LIF study in atmospheric swirl flame using natural gas at $\Phi = 0.83$, utilizing R₁ (21.5) transition at 225.25 nm excitation. Sahu and Ravikrishna [161] recently conducted quantitative LIF and kinetic assessment of NO

formation in H₂/CO syngas-air counterflow diffusion flames, utilizing 226.03 nm excitation. NO formation in stagnation flames using the jet-wall experimental configuration, with C₁ - C₄ alkanes and alcohols was recently investigated utilizing 226.03 nm excitation by Watson et al. [162]-[164].

Alatas et al. [165] first performed practical NO-PLIF measurements in-cylinder. However, no details regarding specific excitation and detection bandpass was given. Braumer et al. [166] reported quantitative in-cylinder NO number density measurements in a spark-ignition engine fuelled with propane, utilizing R₁+Q₂₁ (21.5) transition at 225.25 nm. Dec and Canaan [137] performed semi-quantitative in-cylinder NO concentration measurements in a direct-injection diesel engine throughout the combustion cycle with pressures up to 65 bar. A frequency-doubled optical parametric oscillator (OPO) system was used to excite the P₁ (23.5), Q₁+P₂₁ (14.5), Q₂+R₁₂ (20.5) transition at 226.03 nm, proposed by Battles and Hanson [167] based on detailed spectroscopic investigations in flames up to 10 bar by DiRosa et al. [128]. 226.26 nm excitation in diesel spray flames in a modified single-cylinder engine was reported by Nakagawa et al. [168].

2.5.2. A-X (0,1) Excitation Overview

NO A-X (0,1) excitation in the 233-237 nm wavelength range reduces laser beam attenuation while providing sufficiently strong signals. This excitation have been reported in low pressure LIF measurements [169] and cavity ring-down investigations [170]. Jamette et al. [138] reported first application of NO A-X (0,1) LIF in high pressure combustion in a direct-injection spark-ignition gasoline engine, utilizing R₁+Q₂₁ (22.5), Q₁+P₂₁ (8.5), Q₂+R₁₂ (17.5) feature at 236.22 nm based on simulations of LIF excitation spectra of NO and O₂ in order to maximise the NO/O₂ LIF ratio. Chou et al. [171] showed application of A-X (0,1) excitation in an atmospheric NH₃/O₂ flame to avoid quasi-continuum NH₃ absorption near 226 nm.

2.5.3. A-X (0,2) Excitation Overview

This strategy was first introduced by Schulz et al. [172], has the benefit of enabling use of KrF excimer laser to excite the O₁₂ bandhead at 247.94 nm, which provides high-power accessibility with low populations in the $v' = 2$ vibrational level. Compared to A-X (0,0) and D-X (0,1) excitation, this strategy has less laser and signal attenuation by hot CO₂ and H₂O. In terms of interference, Schulz et al. concluded that at 247.94 nm, NO bandhead coincides with a local minimum in the O₂ B-X band. Furthermore, (0,2) excitation provides an important advantage by the possibility of blue-shifted detection of the (0,0) and (0,1) emission, thus eliminating the detection of CO₂ and polycyclic aromatic hydrocarbon (PAH) LIF. This strategy was also utilized for NO detection in sooting high-pressure ethylene/air flames [173], where strong PAH fluorescence was observed red-shifted to the excitation wavelength, but the blue-shifted NO detection minimized this interference. Schulz and co-workers applied this strategy for quantitative NO concentration imaging in a spark-ignition engine fuelled with propane [174], spark-ignition engine running under premixed [175] and non-premixed conditions [176], [177], and in direct-injected diesel engines fuelled with commercial diesel fuel [178], [179]. Andersen and co-workers have investigated qualitative NO-LIF distribution using NO A-X (0,2) strategy in a spark-ignition engine fuelled with iso-octane [180], [181], and quantitative 1-D measurements were shown in a spark-ignition engine fuelled with iso-octane and regular gasoline [182]. Recently, Akihama et al. [183] performed qualitative in-cylinder measurements using this strategy in a port-fuel injected spark-ignition engine fuelled with iso-octane at pressures up to 15 bar and, Bessler et al. [184] measured NO concentration in a direct-stratified-injection gasoline engine.

2.5.4. D-X (0,1) Excitation Overview

The D-X (0,1) strategy has a range of 192 - 195 nm and can be probed with the excitation of the R₁ (26.5) + Q₁ (32.5) at 193 nm radiation from an ArF excimer laser [185], [186] and has minimized interference from O₂ at 193.38 nm wavelength [187]. However, this transition suffers from

severe attenuation of the short-wavelength laser beam and signal in the high-pressure combustion environment, leading to complete signal loss at portions of the engine cycle, making quantitative NO measurements impossible. Previous attempts to quantify LIF signals [188]-[190] at this transition relied on unverified assumptions regarding the dependence of fluorescence quantum yield on pressure and temperature.

Andresen et al. [141] and Tanaka et al. [191] reported qualitative NO-LIF imaging using this transition in a spark-ignition gasoline engine with iso-octane. Meulen et al. performed NO imaging in a pre-chamber-injected diesel engine with n-C₇H₁₆ and diesel fuel [189], [192], and in a direct-injection diesel engine with maximum pressures of 75 bar [188], [190]. Arnold et al. [193] also carried out NO measurements in a direct-injection diesel engine fuelled with n-C₇H₁₆, utilizing this strategy.

2.6. Fundamentals of Flame Properties

There is a continuing demand for increased energy efficiency of gas turbines and reciprocating engines, with ever growing concerns related to the environment, energy and hazards. All these have, during the past few decades, stimulated a tremendous burst of interest and research activities in the field of combustion. The simultaneous occurrence of chemical reaction and transport of mass, momentum, and energy makes analyses of these problems extremely complex. Moreover, practical flames are nearly all turbulent because of the requirement to produce high volumetric rates of energy production for efficiency and compactness. This further complicates combustion research even if one addresses the problem at a fundamental level in which practical difficulties might be neglected. Fundamental flame properties that has been used in this study are discussed in this section.

2.6.1. Laminar Burning Velocity

The laminar burning velocity (also known as the laminar burning rate, or laminar flame speed) is a fundamental physiochemical property of a premixed combustible mixture, resulting from the collective effect of thermal and mass diffusion of the reactants and mixture exothermicity [194]. Due to the finite flame thickness, in a non-planar flame, the mass

rate of entrainment of unburned gas into the flame front, dm_u/dt is in general not the same as the rate of formation of the burned product, dm_b/dt . Hence Bradley et al. [195] suggested two definitions of laminar burning velocity from the literature. The first definition is based on the 'entrainment velocity' of unburnt mixture into the flame which was defined by Rallis and Garforth [196] as:

$$u_n = -\frac{1}{A\rho_u} \frac{dm_u}{dt} \quad [2-70]$$

where, A is the flame front area. The spatial velocity of the flame front, also known as the flame speed, S_n , is readily measurable by observing the flame's temporal development. However, flame speed is not a unique property of a combustible mixture but the sum of u_n and the gas expansion velocity, u_g , immediately adjacent to the flame front:

$$S_n = u_n + u_g \quad [2-71]$$

u_g is generally larger than u_n and is a function of the densities of burnt and unburned gas at any instant, as well as of the presence or absence of any constraining boundary.

The other definition of laminar burning velocity, u_{nr} was proposed by Bradley et al. [195], based on the appearance of burned products, has been computed for atmospheric methane-air mixtures as:

$$u_{nr} = \frac{1}{A\rho_u} \frac{dm_b}{dt} \quad [2-72]$$

This method of burning velocity is calculated from measurements of pressure rise in closed vessels, as in experiments in the literature [197]-[201]. Abdel-Gayed et al. [202] observed that under turbulent conditions, laminar burning velocity is analogous to the mass burning velocity, u_{tr} .

2.6.2. Turbulent Burning Velocity

Turbulent flames are found in practical devices over a wide spectrum of phenomena which depend on the intensity of the turbulence, the temperature and pressure of the reactants, the reactant fuel-air ratio and the fuel itself [203]. Dimensional analysis in these turbulent flames

revealed a range of premixed combustion modes: progressing from wrinkling laminar flamelets to well-stirred reactors. These modes corresponds to different regimes of combustions and require different approaches for understanding and modelling [204]. Classical premixed combustion diagrams [194], [205]-[207] assume that a reacting flow may be characterised in terms of two non-dimensional numbers:

1. The ratio of the turbulence integral length scale to the laminar flame thickness.
2. The ratio of the root-mean-square velocity fluctuation to the unstretched laminar burning velocity.

A turbulent flame has a propagation velocity that depends on the flow field parameters, as well as on the properties of the mixture and the initial condition. According to Turns [208], turbulent burning velocity, u_t is defined as the velocity at which unburned mixture enters the flame zone in a direction normal to the flame. In this definition, the flame surface is represented as some time-mean quantity, recognising that the instantaneous position of the high-temperature reaction zone may fluctuate widely. Experimentally, the value of u_t is usually measured from two-dimensional photographs of an essentially the three dimensional phenomenon. Traditionally, turbulent burning velocity has been related to the r.m.s. turbulent velocity and both of these quantities have been normalised by the laminar burning velocity.

Turbulent burning velocity (u_t) can be defined as the flame propagation due to the turbulence in the flame. u_t is considerably higher than u_l [194]. u_t is often described as per Equation [2-73]:

$$\frac{u_t}{u_l} = f(u', L_{turb}, \phi) \quad [2-73]$$

where u' is the turbulent velocity fluctuation and L_{turb} is the turbulent length scale. Turbulent flame speeds in GTs are about 10-20 m/s [24]. The enhance factor due to turbulence is also dependent on the fuel and stoichiometry. Lewis number, Le (thermal diffusivity/mass diffusivity) is often used to explain the impact of fuel by explaining the impact of thermal and molecular fuel diffusivity on the evolution of corrugated flamelets.

2.6.3. Equivalence ratio (Φ):

The equivalence ratio (Φ) of a system is defined as the ratio of the fuel-to-oxidiser ratio to the stoichiometric fuel-to-oxidiser ratio as per Equation [2-74]:

$$\phi = \frac{m_{fuel}/m_{ox}}{(m_{fuel}/m_{ox})_{st}} = \frac{n_{fuel}/n_{ox}}{(n_{fuel}/n_{ox})_{st}} \quad [2-74]$$

where, m represents the mass, n represents number of moles and suffix st stands for stoichiometric conditions. Stoichiometric condition is defined as when there is just enough oxidiser in the system to burn all the fuel content. When $\Phi = 1$, the combustion is stoichiometric, if $\Phi < 1$, the combustion is lean with excess air and if $\Phi > 1$, the combustion is said to be rich with incomplete combustion.

2.6.4. Adiabatic Flame Temperature (AFT)

The adiabatic flame temperature occurs when the combustion chamber is well insulated with no heat losses (adiabatic conditions). The peak AFT occurs at just over stoichiometry ($\Phi = 1.0$). As the flame goes lean ($\Phi < 1$) and percentage of combustion air increases, some of the heat generated is used to heat up the excess air, resulting drop in the flame temperature. By the same token, flame temperature also drops at the rich conditions ($\Phi > 1$), as some of the heat is used to heat up the excess fuel content.

2.6.5. Swirl Characteristics

GT swirl combustors rely on the interaction between a turbulent flow field and complex chemical reactions within the primary, intermediate, and dilution zones to generate the required turbine inlet temperature for the given load condition while reducing greenhouse gas (GHG) emissions, pressure loss, and instabilities. The design of the generic swirl burners utilized in this study is intended to replicate this flow-through, single can-type combustor operated in a fully premixed configuration. This geometry derives its flame stabilization mechanism mostly through the vortex breakdown structures resulting from the tangential velocity

imparted on the flow through the swirler in combination with the sudden expansion into the combustor primary zone.

The degree of swirl number, S , is a non-dimensional number that defines the axial flux of swirl momentum divided by the axial flux of axial momentum. S is defined as follows:

$$S = \frac{G_\theta}{G_x d/2} \quad [2-75]$$

$$G_\theta = \int_0^\infty (\rho u w + \rho u' w') r^2 dr \quad [2-76]$$

$$G_\theta = \int_0^\infty (\rho u^2 + \rho u'^2 + (p - p_\infty r^2)) dr \quad [2-77]$$

where u is the axial velocity (m/s), u' is the fluctuating axial velocity (m/s), w is the tangential velocity (m/s), ρ is the fluid density (kg/m³), and r is the radius (m).

However, the above equations require knowledge of all the velocity and pressure profiles for all conditions at different swirl numbers at each point of the flow regime. This lead to a very complex calculation. Syred and Beer [209] proposed that this expression could be simplified for constant density environments, i.e. isothermal conditions, to a simple function of geometry [210], [211].

$$S_{g,iso} = \frac{\pi r_e r_{eff}}{A_t} \quad [2-78]$$

where r_{eff} is the effective radius at the centre of the inlet pipe, r_e is the exit radius, and A_t is the total area of the tangential inlet. The geometrical swirl number, S_g , uses inlet conditions and ignores pressure variation effects across the flow for isothermal conditions. The density is assumed to be constant and the axial velocity can be obtained from the flow rate, Q , divided by the exit area, A_e . The angular velocity ω is taken as the inlet velocity multiplied by an effective radius r_{eff} . The geometrical swirl number is related to the inlet and outlet flow rates [210].

Under combustion conditions the geometrical swirl number is directly related to the inlet and outlet flow rates. The process is under constant pressure, so S changes according to the ratio of degrees of absolute temperature. The size of the exit volume and the axial velocity at the exit also increase with temperature [209], [210]. This causes a reduction in the ratio of angular momentum to axial momentum. Thus the geometrical swirl number is reduced as a consequence of the average inlet and outlet temperatures as follows:

$$S_{g,comb} = S_{g,iso} \left[\frac{T_{inlet}}{T_{outlet}} \right] \quad [2-79]$$

Another important dimensionless number is the Strouhal number [210] is useful for analysing oscillating unsteady flows:

$$S_r = \frac{fL}{U} \quad [2-80]$$

where f is the oscillation frequency (1/s), L is the characteristic length (m), and U is the mean flow velocity (m/s). Strouhal number, S_r represents a measure of the ratio of inertial forces due to the instability of the flow or the local acceleration to inertial forces due to changes in velocity from one point to another in the flow field. It represents the instability of the flow. Thus, it is a weak function of the Re number [210]. Thus, Swirl could be correlated to the frequency of the system using the following function:

$$S_r = \frac{fD_e^3}{Q} \quad [2-81]$$

where D_e is the exhaust diameter and Q is the flow rate.

2.6.6. Swirl Mechanism

Swirl is commonly used to: (i) stabilise high combustion intensity, (ii) limit the lengths of combustion through the production of higher rates of entrainment of ambient fluid, (iii) encourage fast mixing near the nozzle exit and on the boundaries of recirculation zones, and (iv) to improve flame stability as a result of the formation of the central recirculation zone. The recirculation zones heat the active chemical species distribution to the root of the flame, thus reducing the velocity

requirements for achieving flame stabilisation, which is only formed beyond a critical swirl number of 0.6. With sufficiently high Re (> 18000) and with swirl number greater than 0.6, large recirculation zones are produced, and high levels of turbulence are present in the system. The recirculation zones occur close to the exit nozzle as shown in Figure 2-10 [209], [210].

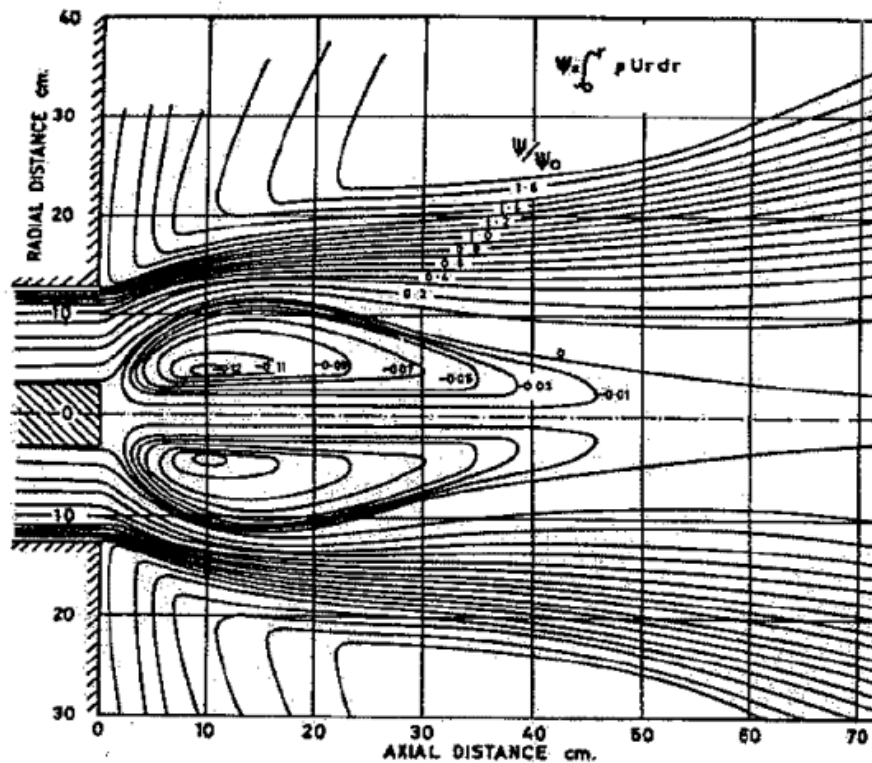


Figure 2-10: Recirculation in a swirling jet flow. Reproduced from [209].

2.7. Summary

In addition to the minor mechanisms, three most important NO formation mechanisms, namely thermal, prompt and fuel mechanisms were analysed. Knowledge about these NO formation pathways are vital to explain the NO-LIF investigations conducted in this study. To summarise in brief, thermal pathway become most important pathway at high temperature combustion, prompt mechanism depends on production of CH , CH_2 radicals, hence important at fuel-rich conditions, fuel mechanism is limited to the fuels with nitrogen present and can be significant in relatively unclean fuel. Among the minor mechanisms

discussed here, N_2O pathway has the sizable contributions at lean combustion.

The process of chemiluminescence measurement was described briefly, with more attention towards OH^* chemiluminescence. Further discussion on the development and use of this measurement in this study are provided in subsequent Chapters.

LIF spectroscopy was described as a quasi-two-level system, underlying the importance and dynamics of the relevant energy transfer mechanisms (W_{12} , W_{21} , A_{21} , Q_{RET} , Q_{VET} , Q_{21}). The derivation of LIF equation from non-transient two-level model was shown by considering population density, stimulated emission, quenching, fluorescence signal and Boltzmann distribution. Mechanisms for broadening and shifting of spectral lines were also discussed in terms of natural broadening, collisional broadening, Doppler broadening and voigt profile when collisional and Doppler broadening occurs simultaneously. The importance of laser energy saturation and population recycling was discussed and the impact of saturation on LIF signal linearity with laser energy was analysed. This section was concluded by examining LIF temperature dependence and giving an introduction on two-line thermometry technique for future work.

Historical developments on computational simulation codes for NO spectroscopy was discussed, showing LIFSim as the final outcome. The functionality of LIFSim was detailed in terms of absorption, excitation and emission spectra as well as pressure and temperature dependence of LIF signals. Finally, the non-transient three-level LIF model in the LIFSim was discussed briefly.

An overview of the past and ongoing works on NO-LIF measurements in laboratory and practical engine flames was given thereafter. Different strategies to excite NO molecules were discussed in terms of suitability of fuel compositions and experimental challenges. Finally, the Chapter was concluded by defining a few fundamental flame properties which has been used in the later part of this thesis.

3. Experimental Set-up, Methodologies and Data Processing

In this chapter, details regarding the experimental facility as well as a schematic of the computational framework for data acquisition and processing are discussed. The experimental work included in this thesis was performed at the Gas Turbine Research Centre (GTRC) at Cardiff University. Bunsen burners were used for qualitative analysis and calibration purposes. A high-pressure combustion diagnostics lab with optical accesses was assembled in the GTRC to facilitate laser diagnostics research in practical high-pressure combustion environments and served as the one of the primary locations for the experimental work presented in this thesis. The Bunsen burners were used to conduct the experiments in a steady, laminar flames at first, before transiting into more industry relevant turbulent flames in High Pressure Optical Chamber (HPOC) with three-way optical access, providing well-characterized flames in atmospheric pressure and wide range of equivalence ratios. Investigation of two laser excitation/detection strategies were enabled by additionally employing high-power lasers, optics, intensified cameras and data acquisition systems.

3.1. Bunsen Type Burners

A Bunsen burner is a device for combining a flammable gas with controlled amounts of air before ignition. It produces a hotter flame than would be possible using the ambient air and gas alone. Robert Bunsen, the German Chemist introduced it in 1855, from a design by Peter Desdega, who likely modified an earlier design by Michael Faraday [212].

For this study, two 25 mm and 15 mm Bunsen type burners (refer to Figure 3-1) were used for qualitative analysis and NO calibration by doping, respectively. Laminar, premixed methane/air flames with lean equivalence ratios ($\Phi = 0.68$ to $\Phi = 0.87$) and rich equivalence ratios ($\Phi = 1.28$ to $\Phi = 1.4$) were stabilized in 15 mm and 25 mm Bunsen burners, respectively, at atmospheric temperature and pressure. Dopant NO diluted in nitrogen (1% NO) was blended as a premixed reactant to yield

inlet NO concentrations up to 1300 ppm. Constant gas flows were provided by low-flow Coriolis mass-flow controllers (MFC). Air flows were controlled by a Bronkhorst M14V10I-RGD-22-K-S Coriolis MFC ($\pm 0.5\%$ accuracy and $\pm 0.05\%$ repeatability) and CH₄ and NO/N₂ flows were controlled by two separate M13V10I-RGD-22-K-S Coriolis MFCs ($\pm 0.5\%$ accuracy and $\pm 0.05\%$ repeatability). Both these MFCs use the Coriolis principle of operation [213], [214]. When viewed from a rotating frame of reference, the deflection of objects moving in a straight path can be described by Coriolis effect. The gasses and air flow through a tube which is vibrating and thus generating changes in amplitude, frequency or phase shift, depending on the mass flow through the tube. In contrast with the other flow meter principles which rely on the measurement of the volume, velocity or differential pressure, Coriolis MFC gives the fluid density as a secondary output, allowing precise mass flow rate measurement [215]. The MFCs were connected to a computer via RS232 port and controlled via FlowView application in the computer. All the MFCs were zero calibrated prior to use.

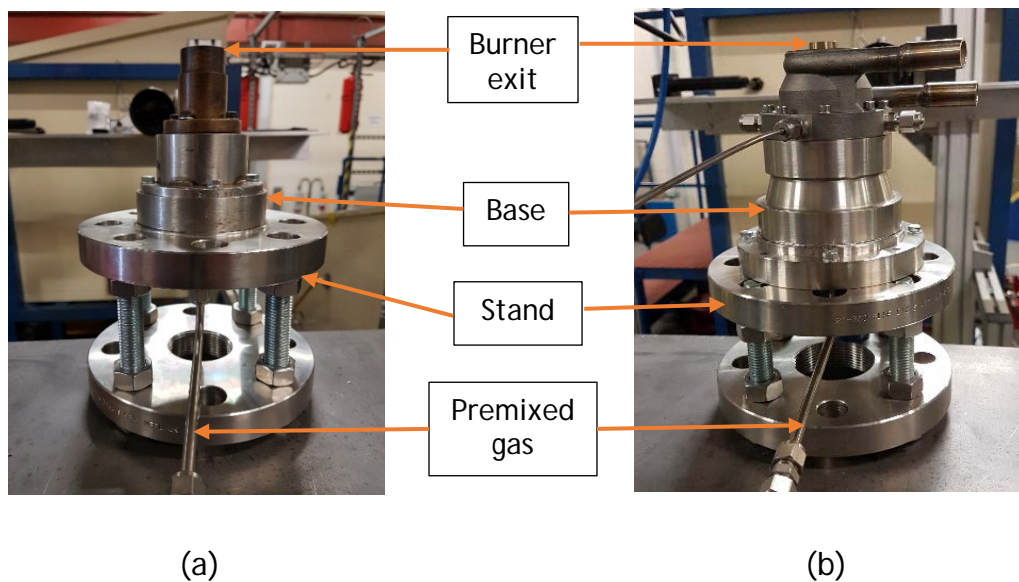


Figure 3-1: (a) 25 mm Bunsen burner for qualitative NO-LIF; (b) 15 mm Bunsen burner for NO calibration experiment.

3.2. High Pressure Combustion Rig (HPCR)

The HPCR is capable to operate at temperatures up to 900K and pressures up to 1.6 MPa with air mass flow rates up to 5kg/s. The detailed design and capabilities of the HPCR test facility can be found in

previous studies [216]-[220]. The critical components that make up the HPCR, namely the fuel and air delivery systems, the HPOC which provides the visual access for combustion diagnostics, the generic swirl burners and all the associated rig instrumentation for experimental condition monitoring are described in detail here [221]. A quick overview of these components is given in the following sections.

3.2.1. High Pressure Optical Chamber (HPOC)

In the current set-up, the HPOC has three operational windows to allow both axial and radial visual access to the burners and operational flames within it, as shown in Figure 3-2. Designed to allow the full pressure and temperature capabilities of HPCR, the HPOC is 0.716 m in length with an inside diameter (ID) of 0.315 m. A thermal barrier coating (TBC) has been installed along the entire ID of the HPOC to protect the stainless steel casing from excessive temperatures during the combustion experiments. External water-cooled copper coils wrapped around the HPOC OD near the exit flange takes care of the excessive heat during high thermal power experiments.

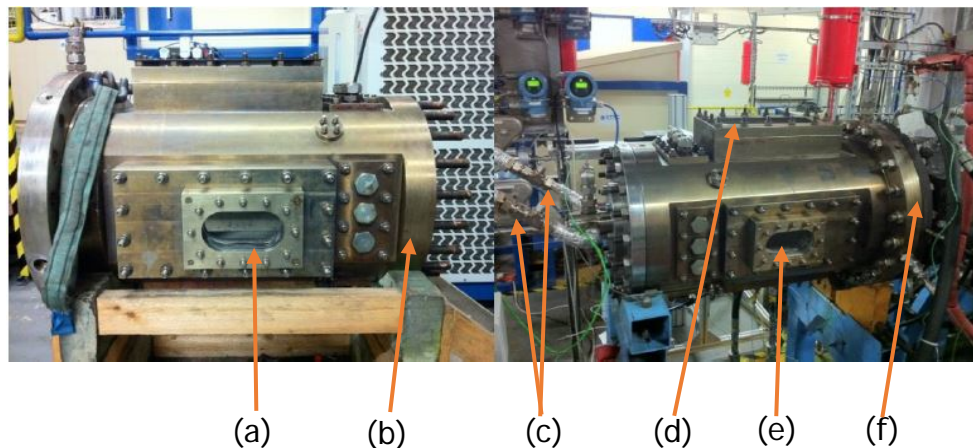


Figure 3-2: Photographs of HPOC during maintenance (left) and installed in the HPCR (right) with (a) laser beam/sheet entrance, (b) stainless steel casing, (c) air and fuel delivery lines, (d) fluorescence capture window, (e) flame observation window and (f) combustion exhaust.

3.2.2. High Pressure Generic Swirl Burner (Mk. II)

The HPGSB-2 differs from the 1st generation HPSGB [47], [222]-[226] in that the combustor expansion ratio has been reduced from 3.5 to 2.5, achieved by a reduction from 140 mm to 100 mm of the cylindrical quartz burner confinement tube ID while maintaining the burner exit

nozzle diameter of 40 mm, in order to simulate a GT combustion chamber and to establish flow structures that would normally be found in a confined swirl burner. The use of confinement also restricts ingress of surrounding oxygen into the flame while directing the reactants into the exhaust. Figure 3-3 shows the schematic of the HPGSB-2 with open and convergent confinement configurations. All the experiments in this study were conducted in the open confinement configuration. However, chemical reactor modelling in Chapter 4 was carried out in the convergent confinement configuration as the experimental data for modelling is taken from a previous study [221]. The HPGSB-2 provides optical access to the flame while achieving representative parameters of inlet pressure, temperature, and turbulence scales typical of a can-type industrial GT combustor.

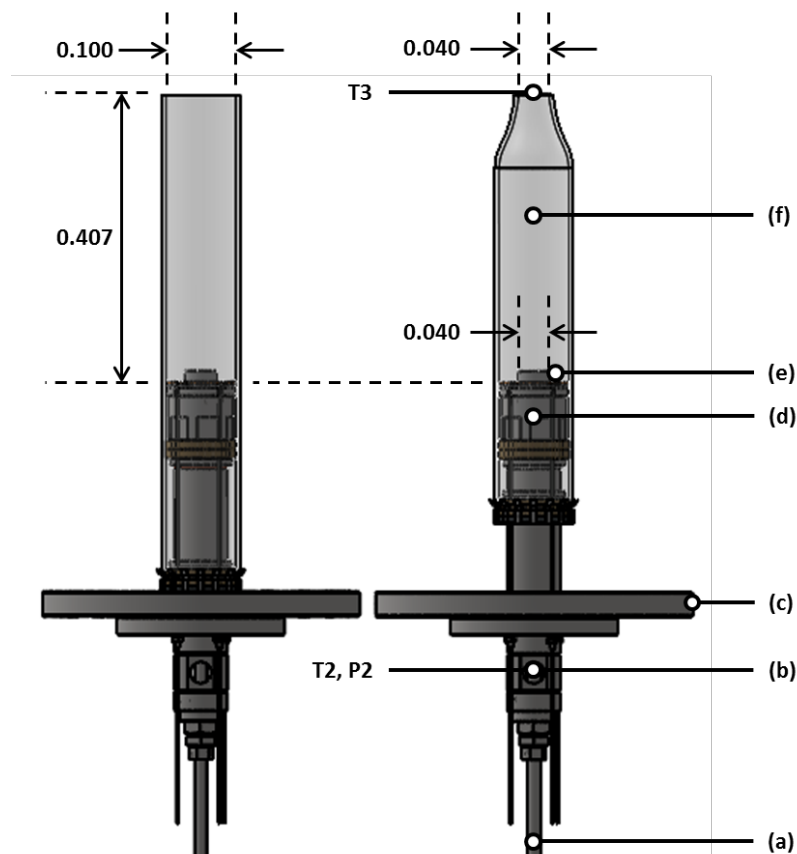


Figure 3-3: Schematic of HPGSB-2 with open confinement (left) and convergent confinement (right), showing (a) pilot lance, (b) inlet plenum, (c) HPOC connecting flange, (d) mixing chamber, (e) burner exit nozzle and (f) quartz confinement. Dimensions in meters. Reproduced from [227].

The HPGSB-2 is modular in its operation and geometry, both of which can be easily manipulated for parametric study of flow and flame

phenomena, including both piloted and non-piloted liquid and gaseous fuel operation, varying levels of fuel/air premixing, variable geometric swirl number combustor confinement length, and combustor outlet geometry. The radial-tangential swirler insert is modular on the HPGSB-2. The burner exit nozzle diameter is fixed at 40 mm for all swirler inserts while the width of the 9 radial-tangential swirl inlets varies between inserts. This yields a possible geometric swirl number (refer to Chapter 2.6.5) varying from $S_g = 0.5$ to $S_g = 2.0$. In this study, the burner was operated fully premixed, non-piloted, and with a geometric swirl number of $S_g = 0.8$, Figure 3-4.

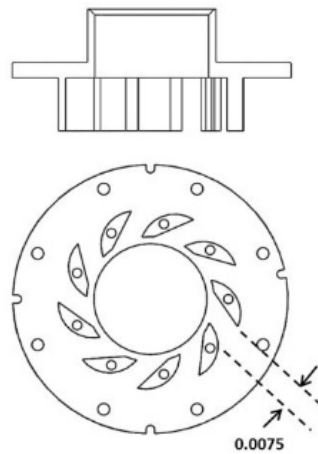


Figure 3-4: Radial-tangential swirler geometries with $S_g = 0.8$. Tangential inlet width dimension in meters. Reproduced from [221].

Figure 3-5 shows the sectioned detail view of the HPGSB-2/HPOC assembly. The fuel flow was split and blended as a jet in crossflow into two inlet air flows approximately 0.3 m before entering diametrically-opposed connections to the burner inlet plenum, while operating in fully premixed combustion. All reactants then travel along the flow path of the premixed chamber prior to entering the slot type radial-tangential swirler and then out from the exit nozzle into the quartz confinement tube where the swirl flame is stabilized. The quartz confinement tube is 5.5-6 mm thick and of length $L_{comb} = 407$ mm, which directs the exhaust into water-cooled exhaust piping towards the backpressure valve (BPV). All these flow paths yield a total premixing length of approximately 0.7 m and residence time over 20 ms at a flow velocity of 30 m/s [221]. The face of the swirler within the combustor is covered by a 3 mm thick

ceramic coating for thermal protection. The HPSGB-2 is fitted with an 18 mm outer diameter (OD) instrumentation and pilot lance inserted down the burner centreline. It contains seven 5 mm OD tubes, with one central tube intended for pilot fuel injection and the remaining six available for instrumentation. The open end of the lance protrudes 8.5 mm into the exit nozzle. Thus, if the exit nozzle was removed from the swirler, the open end of the lance would be in the same axial plane as the burner dump plane and ceramic burner face. This lance provides a bluff-body stabilization location within the burner exit nozzle while also allowing for temperature, static pressure, and dynamic pressure measurements to be made at this critical location.

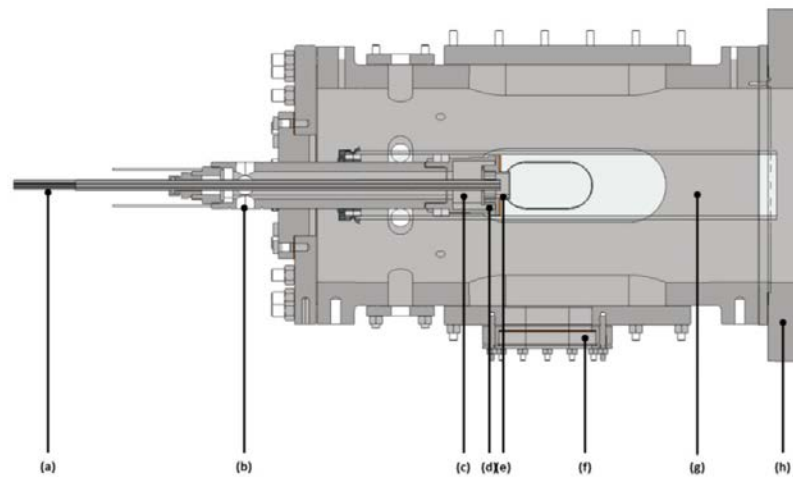


Figure 3-5: Sectioned detail view of the HPSGB-2/HPOC assembly with (a) instrumentation and pilot lance, (b) inlet plenum, (c) mixing chamber, (d) radial-tangential swirler, (e) burner exit nozzle, (f) quartz window, (g) quartz burner confinement tube, and (h) HPOC casing.

3.2.3. Fuel and Air Delivery System

The HPCR has been reconfigured for high repeatability and precise control over fuel and air flows through the use of dedicated flow control valves (FCV) and Coriolis mass flowmeters (CMF) on a total of 5 delivery lines. 2 of the 5 lines are used for air delivery, with the use of Emerson CMF025M mass flow meters capable of measurement up to 945 g/s (accuracy: $\pm 0.1\%$). Emerson CMF010M mass flow meter is used for the fuel delivery measurement up to 22.7 g/s (accuracy: $\pm 0.1\%$) in another 2 lines. The fuel and air mass flow rates are controlled in a remote location via a PLC system which is operated by inputting the desired FCV

position and monitoring the CMF output. For all experiments with the HPGSB-2, the air flow to the HPCR was provided by an Atlas Copco GA 45 variable speed drive (VSD) air compressor coupled with a Beko Drypoint DPRA960 air dryer to lower the combustion air dew point prior to metering and entering the burner. This VSD compressor can deliver up to 150 g/s air flow at 1.3 MPa. In fully premixed mode, the fuel is delivered from multi-cylinder packs stored in a remote onsite location and split after metering and introduced into the air stream prior to entering the burner.

3.3. Selection of NO Excitation Wavelengths

The four different transition strategies to excite NO has been discussed in detail in Chapter 2.5. The advantages and drawbacks of using each transition was also analysed from previous works done on NO-LIF. Considering those discussions and reviewing past studies [130], [139], [140], [142], 226.03 nm excitation wavelength was chosen at first for the experiments for this study, utilising A-X (0,0) transition. However, to achieve this wavelength from Quantel TDL-90 dye laser (refer to Section 3.4) the doubled dye beam has to be mixed with residual 1064 nm beam from the Nd:YAG laser. Due to the very sensitive controls of the 'mixing after doubling' unit, on average only about 0.1 mJ energy could be extracted from the UV beam at 226.03 nm, which is much lower than the prescribed energy (2-4 mJ) from previous studies [142], [161]. When the beam was converted to a sheet, through the use of sheet-optics, the energy density was even lower. The other excitation strategies were also investigated for suitability with TDL-90, in terms of laser energy. The A-X (0,1) and A-X (0,2) transitions at around 236 nm and 248 nm, respectively, also require 'mixing after doubling' strategy in TDL-90 dye laser, while minimum UV wavelength capability of the laser is 200 nm, making the D-X (0,1) strategy obsolete (refer to Chapter 2.5.4). Table 3-1 summarises the process specifications for Quantel TDL-90 dye laser.

Table 3-1: Process specifications for Quantel TDL-90 [228]

Wavelength Range (nm)	Process
200 - 217	Tripling
217 - 277	Mixing after doubling
277 - 360	Doubling
360 - 420	Mixing

As the TDL-90 dye laser was operated successfully at GTRC for previous studies [47], [223], [225] utilizing the 'doubling' process, investigations were conducted to find NO peaks at the 'doubling' range of wavelengths for TDL-90 (refer to Table 3-1). LIFSim [129], [130] web package was used to simulate NO and O₂ spectra for different flame temperatures at atmospheric pressure. The detailed NO and O₂ spectra in the 'doubling' range are given in Appendix A. Figure 3-6 shows NO and O₂ excitation spectra at region of interest for this study. There are quite a few wavelengths which has high NO excitation signal with very low O₂ interference. Among those wavelengths, 285.16 nm was chosen at Q2 (12.5) transition for this study as O₂ interference is negligible at this wavelength, yielding high signal-to-noise (SNR) ratio.

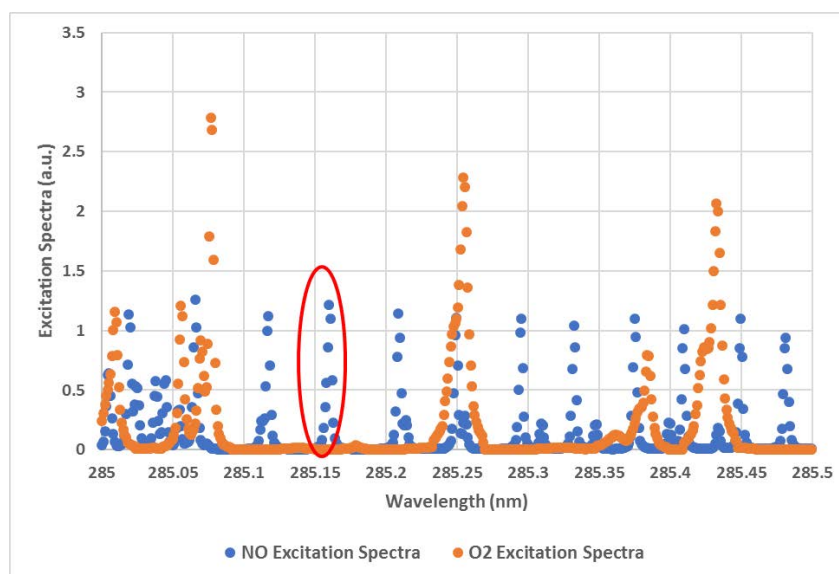


Figure 3-6: NO and O₂ excitation spectra. Chosen NO excitation wavelength highlighted.

NO filter from Dantec Dynamics (refer to section 3.5) was used to capture the NO fluorescence signal at 285.16 nm excitation wavelength. This filter has 40% transmissivity at 244 - 274 nm range. Figure 3-7 shows the emission spectra for NO and O₂ at 285.16 nm excitation for the range of the filter. Three peaks of NO signal are visible at (0,5) Q2 (12.5), (0,5) R12 (12.5) and (0,5) R2 (8.5) lines with relative signals of 72.7%, 15.2% and 12.1%, respectively. However, there are no O₂ interference in the filter's transmission region. As a consequence, offline signals to account for O₂ interference are unnecessary. No offline points were taken for NO-LIF experiments at 285.16 nm excitation. However, for the NO-LIF experiments conducted at 226.03 nm excitation, offline points were taken at 225.94 nm to account for O₂ interference. The choice of these wavelengths had been studied in the literature comprehensively [161]. The pump beam energy was maintained such that NO fluorescence signal is in the linear fluorescence regime, as discussed in Chapter 2.3.7. Figure 3-8 shows the variation of fluorescence intensity in a NO doped CH₄/air flame with laser beam energy, and thus, confirms the use of the linear LIF regime for the NO measurements at 285.16 nm excitation wavelength. The arrow indicates the average laser beam energy where the experiments were conducted for this study.

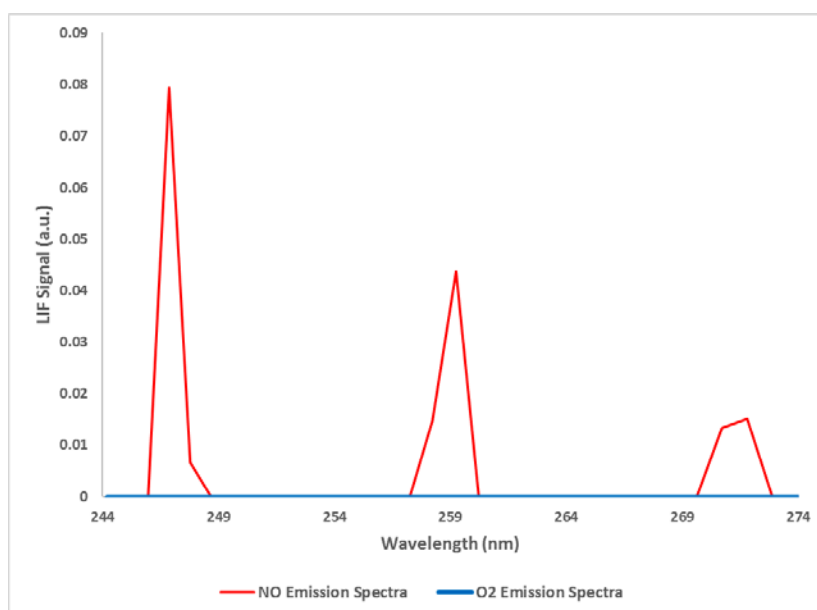


Figure 3-7: Emission spectra for NO and O₂ at 285.16 nm excitation

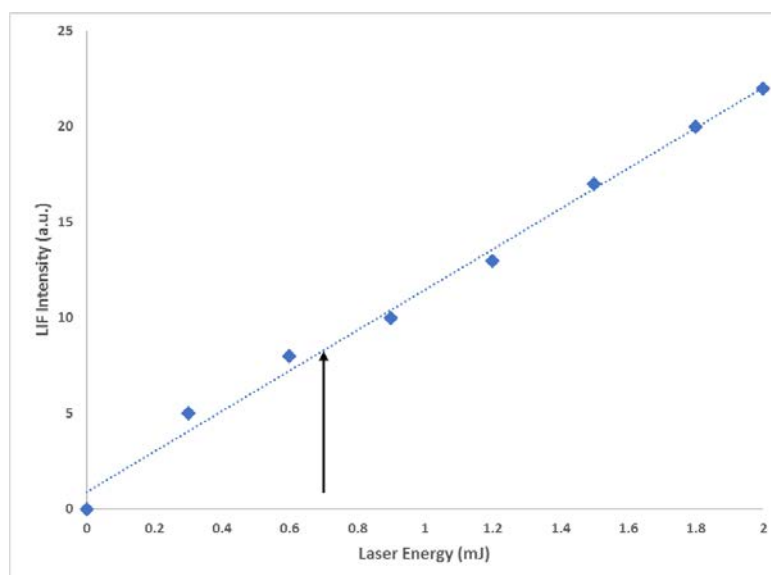


Figure 3-8: LIF characterization in NO doped CH₄/air flame at 285.16 nm. Arrow indicates the average laser energy for the experiments.

3.4. Laser System

In this study, light amplification by stimulated emission of radiation (LASER) is used as the primary source for perturbing specific energy states of target molecules. Short pulse laser used in this study enable short excitation (<10ns) and detection times (<1 μ s) to minimize interference of continuous signals such as chemiluminescence and ambient room light. Furthermore, short-pulse lasers are capable of generating intense concentration of laser energy over a very short duration, enabling two dimensional measurements to be made over extended volumes.

Lasers technology and understanding has greatly evolved over the last few decades and many different lasers are available commercially for practical use [229]-[231]. All lasers to date operate under the same principle of generating a population inversion between two energy states and then inducing fluorescence via stimulated emission of photons. Depending on the laser system, the pump-source can be a light source, electric discharge, or an alternative means of energy exchange. The primary laser system used in this study is a two state dye laser pumped by a neodymium-doped yttrium-aluminum-garnet (Nd:YAG) laser. Table 3-2 summarizes the specifications of the laser used in this study.

Experimental Set-up, Methodologies and Data Processing

Detailed descriptions can be found in textbooks of Siegman [229] and Demtroder [112].

Primary transitions used in the study are A-X(0,0) and (0,5) excitation of the NO molecule at 226.03 nm and 285.16 nm, respectively. These two transitions are generated by using three different dyes: combination of Rhodamine 590 (80%) and 610 (20%) for 226.03 nm and Pyrromethene 597 for 285.16 nm. General specifications on these dyes and applied concentrations are listed in Table 3-3. The output of the dye laser is then doubled using a doubling unit to the desired wavelength of 285.16 nm in the UV and the doubled output then mixed with the 1064 nm residual from the Nd:YAG laser using a mixing unit to the desired wavelength of 226.03 nm in the UV. The doubling and mixing unit consists of a nonlinear crystal (Potassium dihydrogen phosphate - KH_2PO_4 or KDP), compensator and a Pellin-Broka prism for isolation of the UV light.

Table 3-2: Specification of the laser system

	Nd: YAG Laser	Dye Laser
Manufacture and model	<i>Spectra Physics GCR 170-10</i>	<i>Quantel TDL-90-NBP2-UVM3</i>
Laser medium	<i>Nd^{3+} - doped Yttrium-aluminium-garnet ($\text{Y}_3\text{Al}_5\text{O}_{12}$) crystal</i>	<i>Fluorescent dye solution in organic solvent</i>
Pumping source	<i>Flash lamp</i>	<i>Nd:YAG</i>
Repetition rate	<i>10 Hz</i>	-
Laser transition	<i>$\text{Nd}^{3+} \ ^4F_{3/2} \rightarrow \ ^4I_{11/2}$</i>	<i>Dye $S_1 \rightarrow S_0$</i>
Laser wavelength	<i>1064 nm, frequency doubled to 532 nm</i>	<i>570 - 580 nm, frequency doubled to 285.16 nm and mixing to 1064 nm after doubling to 226.03.03 nm</i>
Pulse energy	<i>450 mJ/pulse @ 532 nm</i>	<i>0.7~ 1.2 mJ/pulse @ 285.16 nm 0.07~ 0.14 mJ/pulse @ 226.03 nm</i>
Pulse length	<i>7-10 ns</i>	<i>7-10ns</i>

Table 3-3: Specifications of the dyes used

	Rhodamine 590	Rhodamine 610	Pyrrromethene 597
Transition in study	$NO A^2 \Sigma-X^2 \Pi (0,0)$	$NO A^2 \Sigma-X^2 \Pi (0,0)$	$NO A^2 \Sigma-X^2 \Pi (0,5)$
Chemical Comp.	$C_{28}H_{31}ClN_2O_3$	$C_{28}H_{31}N_2O_3.Cl$	$C_{30}H_{49}N_2BF_2$
Solvent	<i>Ethanol</i>	<i>Ethanol</i>	<i>Ethanol</i>
Max emission (nm)	566	580	582
Concentration used (g/L)	Oscillator - 0.05 Amplifier - 0.02	Oscillator - 0.07 Amplifier - 0.02	Oscillator - 0.15 Amplifier - 0.04

Modern dye lasers usually use multi-stage amplification (typically two), employing two cells which sequentially amplify the final output. The first cell is coupled with a prism or a diffraction grating for simultaneous amplification and selective tuning of a specific wavelength. It is often referred to as the preamplifier. The following cells act purely to boost the narrowband beam through stimulated amplification. Laser alignment and power optimization was carried out using a Gentec SOLO power meter. One drawback of a dye laser system is that organic dyes lose their strength over time and require changing.

3.5. Detection System and Optical Setup

Two main experimental setups were used in this study: 2-D LIF-imaging and PLIF-imaging in the Bunsen burners and the HPOC. Schematics for PLIF imaging configurations in Bunsen burner and HPOC are shown in Figure 3-9 and 3-10, respectively. For LIF imaging, the sheet optics were taken off from the setup, keeping everything else same as the PLIF-imaging setup. And for the chemiluminescence measurements, laser system was not used.

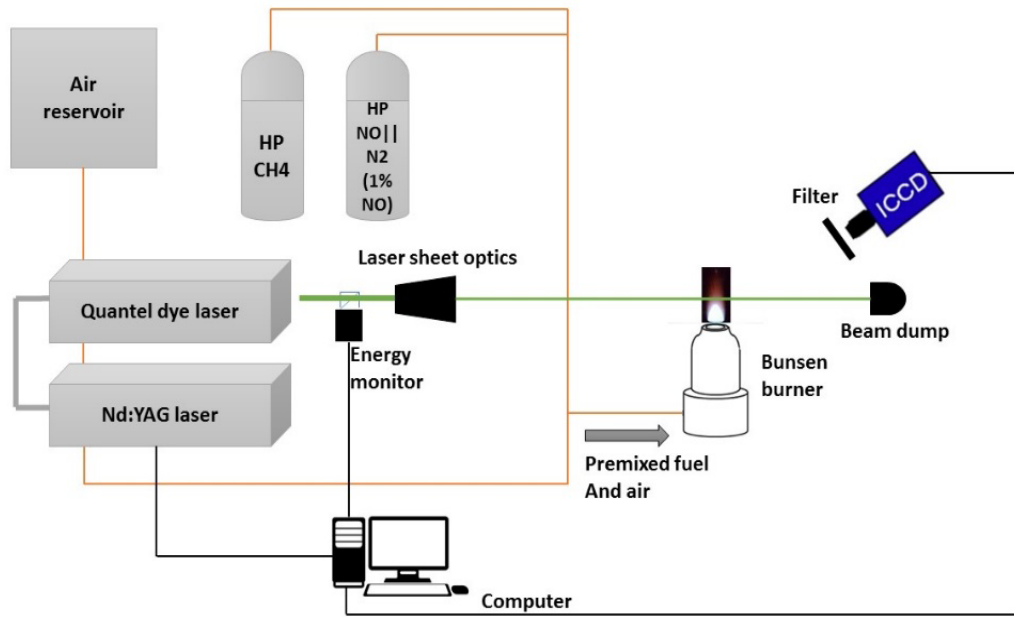


Figure 3-9: Schematic of experimental setup for qualitative NO-LIF and NO calibration measurement

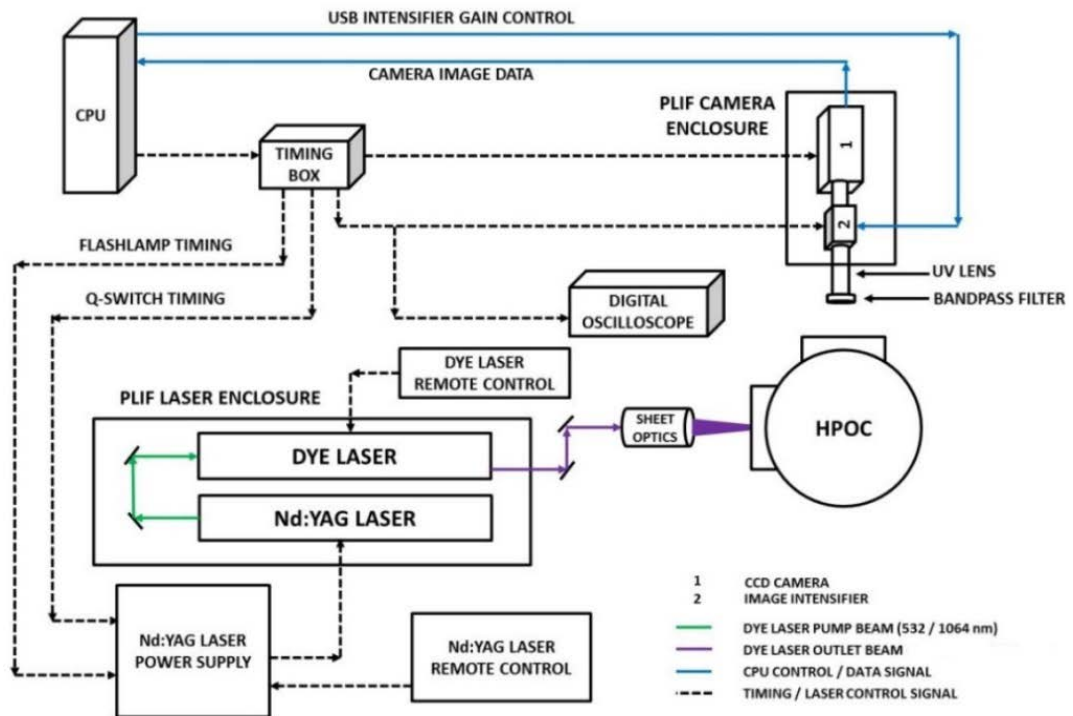


Figure 3-10: LIF measurement system timing and image capture setup with HPOC

The dye laser output beam was directed through a set of sheet-forming optics to provide a laser sheet approximately 25 mm in width and 2-3 mm thick. A 30R/70T UV plate beam splitter was placed between the dye laser output beam and the sheet-forming optics to reflect 30% of the beam to a Gentec QE12LP-S-MB energy detector to monitor and record shot-to-shot energy variation. The laser sheet entered the flame volume through a side window of the HPOC with the capture camera focused through the top window of the HPOC, 90° relative to the laser sheet and axial fluid flow. The laser sheet elevation was fixed in the same plane as the burner exit nozzle centreline. Both for the chemiluminescence and LIF measurements, the resulting signal was captured through the use of a CCD camera (Dantec HiSense Mk II, 1.3 megapixel resolution) coupled with an image intensifier (Hamamatsu C9546-C03L), 78 mm focal length UV lens (Pentax C91698, f/3.8), and narrow bandpass filter set. A 248 nm bandpass filter with FWHM of 40 nm from Dantec Dynamics, combined with a UG-5 bandpass filter from Edmund Optics (combined transmissivity of 40%) were used for 285.16 nm NO excitation and a custom-made high transmission 254 nm bandpass filter with FWHM of 10 nm from Asahi-Spectra, combined with the UG-5 bandpass filter from Edmund Optics (combined transmissivity of 68%) were used for 226.03 nm NO excitation. The UG-5 bandpass filter was used to suppress the noise from visible light wavelengths. Each image is 1024 x 1344 pixels in the axial (y) and radial (r) directions, respectively, with a resolution of 13.6 pixels/mm (0.0054 mm²/pix) yielding a field of view of approximately 75 mm x 100 mm. This results in the ability to image from the burner exit nozzle to 75 mm downstream and from the burner exit nozzle centreline to 50 mm in either radial direction. Thus, in all proceeding images, r=0 mm represents the burner exit nozzle centreline and y = 0 mm represents the edge of the burner exit nozzle.

The Nd:YAG laser produced pulse energies of 450 mJ/pulse at 532 nm to pump the dye laser at a repetition rate of 10 Hz. The shot-to-shot stability of the Nd:YAG laser energy was 1.5%. The dye laser produced pulse energies of 0.07-0.14 mJ/pulse at 226.03 nm and 0.7-1.2 mJ/pulse at 285.16 nm but lost further energy when the beam was deflected to

the energy monitor. Spectrosil® 2000 material was used for the quartz windows, which allows above 90% transmissivity in the desired wavelengths [232].

3.6. Data Acquisition and Image Processing

The system used for data acquisition and processing is discussed in this section. The experimental setup for data acquisition involves synchronization of laser pulses with the camera exposure and intensifier, readout of the camera system, simultaneous monitoring of the laser energy and implementation of proprietary acquisition routines. Additional computational routines and data file were accessed via Dynamic Studio and Matlab routines. An overview of the data acquisition and processing involved in this study are shown in Figure 3-11.

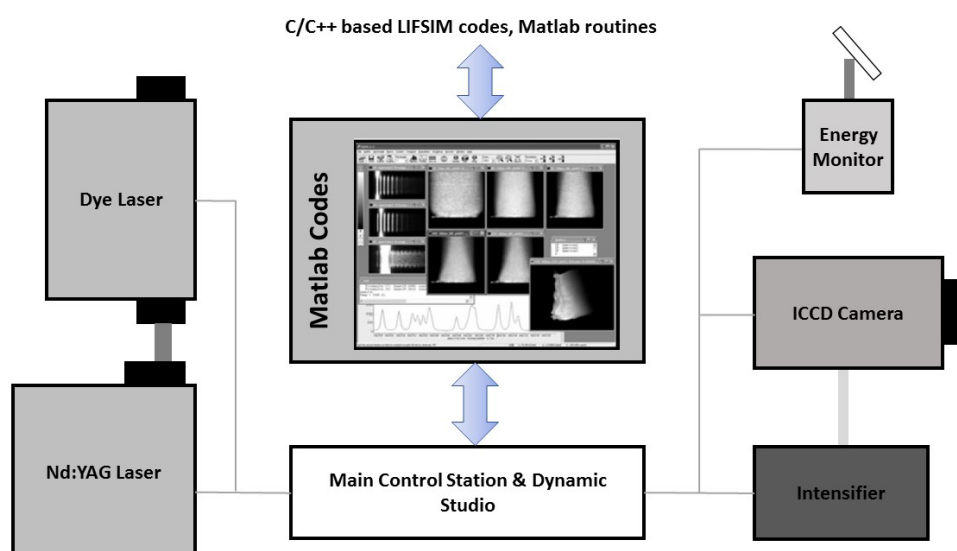


Figure 3-11: Data acquisition and processing overview.

3.6.1. Data Acquisition

DynamicStudio is a CCD image acquisition and processing program developed by Dantec Systems. The synchronization of the camera shutter, image intensifier gate, Nd:YAG flashlamp, and Nd:YAG Q-switch is controlled by DynamicStudio software and a Berkeley Nucleonics BNC 575-8C pulse generator to ensure that signal capture was appropriately timed with the dye laser excitation light pulse. Image intensifier gate was opened for 100 ns for LIF measurements and at 400 μ s for OH chemiluminescence measurements. Image intensifier gain was kept

constant at 999 for all LIF measurements and at 800 for all chemiluminescence measurements. The acquisition period of the ICCD was synchronized with the fluorescence event by providing an appropriate delay with respect to the start of trigger to the Q-switch of the Nd:YAG laser. A parametric study on the effects of the gate timing (t_{gate}) on measured intensity values was conducted and presented in a previous study [221]. The LIF system at the GTRC can be fully operated from a remote data capture and timing control computer system outside of the experimental area.

NO LIF has interference from O₂ LIF, as discussed earlier in Section 3.3. So offline signals had to be taken to measure these interferences and subtract them out from the main signal. For 285.16 nm NO excitation, no offline data was taken (refer to Figure 3-7), and for 226.03 nm NO excitation, offline data was taken at 225.94 nm. As the spectral intensity of the CCD camera changes over the experimental campaign, baseline signals were also taken at every point by turning the laser off. 500 images were taken for every online points while 200 images were taken for every offline points, baseline signals and chemiluminescence measurements.

3.6.2. Image Processing

From the literature discussed in Chapter 2.2 indicates that there are not only multiple approaches to the measurement of OH* chemiluminescence, but also numerous methods utilized for the processing and presentation of chemiluminescence measurements, with the reporting of time-averaged intensity values [106], [233] common along with both background correction and the use of a variety of deconvolution algorithms, including the Abel transformation [101], [234], [235]. The general method applied here involves noise filtering using a 3x3 pixel median filter, background removal, temporal averaging, and the use of an Abel inversion for deconvolution of the OH* CL signals. While images are captured via DynamicStudio software, image processing for OH* chemiluminescence was conducted using MATLAB codes from a

previous study at Cardiff University [221], which can be found in Appendix B.8 and B.9.

Whereas chemiluminescence is a line-of-sight integrated imaging technique, the benefit of LIF measurements is that the light intensity that is captured by each CCD pixel is the result of a response to an excitation light source and therefore yields a real-time representation of the excited species concentration at the location of the line-of-sight laser light or light sheet. Therefore, no deconvolution methods need to be utilized. The most often utilized method of LIF image processing and analysis applied here, are described below, involves baseline correction, laser energy correction, correction for laser sheet intensity distribution, offline noise correction from O₂ LIF and finally for quantitative NO-LIF, convert the LIF intensity values to NO concentration using NO calibration data from Chapter 7. While images are captured using DynamicStudio software, all image processing is conducted using MATLAB codes, which can be found in Appendix B.1 - B.6.

Baseline removal from each instantaneous image was conducted at first for both online and offline images, prior to be corrected by normalized laser energy pulses (refer to Figure 3-13(a),(b) and Figure 3-14(a),(b)). As mentioned before, laser pulse energies were recorded for respective images and normalized by the maximum pulse of the test campaign to ensure comparative data across all the experimental points. Baseline images (refer to Figure 3-13(b) and Figure 3-14(b)) were captured at the field of view without the laser firing, but with a flame present in the burner. Corrected offline images then averaged and subtracted from each corrected online image, as illustrated in Figure 3-14(c), (d). Finally, time averaged offline image was subtracted from each online image and then time averaged (refer to Figure 3-14(c), (d)).

LIF images were also corrected for variation in the laser intensity distribution along the planar light sheet (for PLIF images) and UV beam (for 1D LIF images). This was required because the laser light intensity across the light sheet and UV beam does not follow a top-hat distribution and are instead more Gaussian, with higher intensities towards the middle and lower intensity towards the edge. As LIF intensity is a

function of the input laser energy (refer to Equation [2-49]), it is therefore necessary to correct the measured intensity values for this energy distribution. This was accomplished first by measuring the laser sheet profile and UV beam profile, fitting a Gaussian distribution to the measured intensity distribution, and then systematically correcting the measured intensity values using the distribution. The Gaussian fit was utilized because it provides a statistically symmetric representation of averaged sheet intensity with a significant fluctuating component due to the shot-to-shot variation in the dye laser energy (25%) which also influences the laser sheet profile shape. The normalized profiles were calculated using the average of 500 images. Gaussian fits for laser sheet (R-square = 0.9931) and beam profile (R-square = 0.773) are illustrated in Figure 3-12 (a) and (b), respectively. After implementing laser intensity distribution correction, images were also corrected for the temperature dependence of the NO-LIF signal by using calculated adiabatic flame temperature (AFT) for each condition.

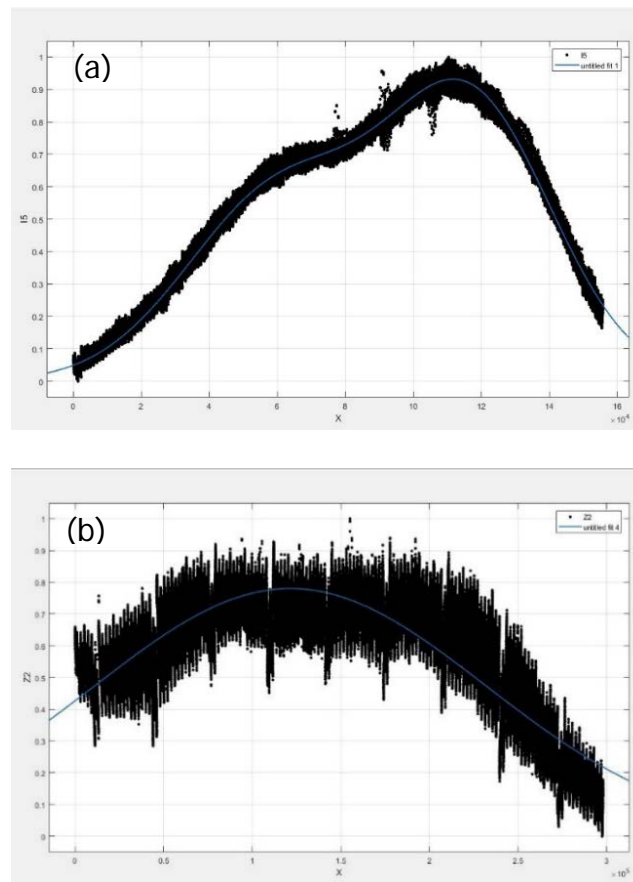


Figure 3-12: Gaussian fit for (a) laser sheet profile and (b) laser beam profile

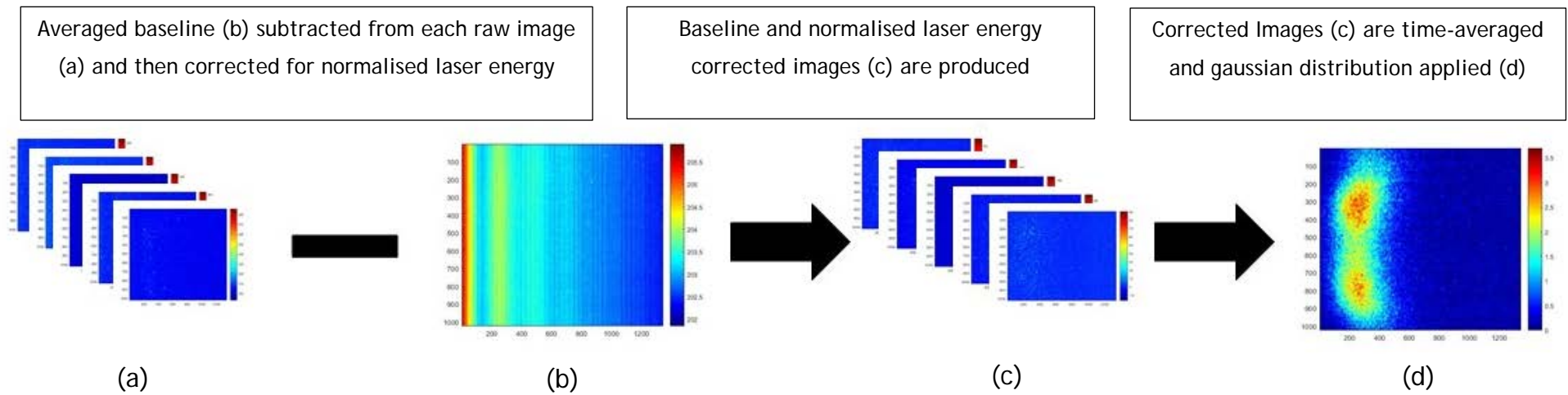


Figure 3-13: Image processing for NO-PLIF at 285.16 nm excitation

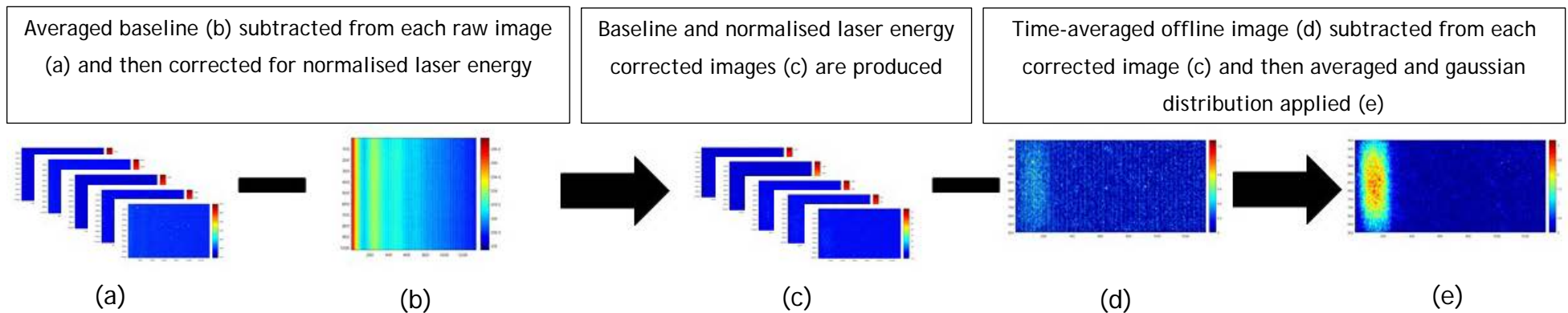


Figure 3-14: Image processing for NO-LIF at 226.03 nm excitation

Hot combustion products like CO₂ and H₂O have long been ignored as potential absorbers in laser-based combustion diagnostics work. However, at wavelengths shorter than 250 nm for CO₂ and shorter than 230 nm for H₂O their influence becomes important and increases towards shorter wavelengths [159]. This causes attenuation of the laser as well as the fluorescence light. The transmission depends not only on the wavelength, but also on the path length and therefore on flame geometry and experimental configuration. This produces nearly opposite effects: with (0,0) excitation and red-shifted detection, strong laser attenuation but weak signal attenuation occurs; with (0,5) excitation and blue-shifted detection, laser attenuation is weak, but signal attenuation is stronger.

Therefore, the images need to be corrected for attenuation of the excitation laser light and the fluorescence signal, which is dominated by absorption from hot CO₂ with a small contribution from hot H₂O; note that absorption contributions from NO and O₂ are negligible in the flames studied here. Attenuation of the laser light and fluorescence signal need to be corrected on a pixel-by-pixel basis using Beer-Lambert's Law and absorption coefficients known from shock tube measurements [158] and simple consideration of the geometry. These corrections require knowledge of the local temperature distribution because the CO₂ and H₂O absorptions are temperature dependent and the CO₂ and H₂O number densities can be obtained using an assumption of thermal equilibrium in the post-flame gas. However, local temperature distribution could not be extracted for this study due to testing time allocation and complexity of the laser requirements. As a consequence, this correction could be implemented in the future.

Finally, to convert the NO data from qualitative to quantitative, calibration experiments were done by seeding varying amount of NO in the flame and capture the corresponding images. This process is described in detail in Chapter 7. The calibration factor (C_F) was obtained from this experiment and used to convert the qualitative data to NO concentration. The NO concentration in ppm relative to the calibration flame temperature can be expressed as,

$$N_{ppm,RT} = C_F \cdot S_F \quad [3-1]$$

where S_F is the digital fluorescence signal. The [NO] in absolute ppm can then be expressed as,

$$N_{ppm,abs} = \left(\frac{T}{T_c}\right) \cdot \left(\frac{\gamma_c}{\gamma}\right) \cdot \left(\frac{I_0}{I_{0,c}}\right) \cdot N_{ppm,RT} \quad [3-2]$$

where, T is the local flame temperature, γ is the cumulative correction factor for effects of collisional quenching, Boltzmann fraction distribution and laser line/absorption line overlap fraction and I_0 is the laser irradiance. The subscript 'C' refers to the quantities in the calibration flame. The cumulative correction factor can be obtained using the LIFSIM tool [129], where temperature, pressure, major species concentrations, excitation wavelengths etc. are provided as input. A similar approach has been widely implemented by Laurendeau and group [236]-[241]. As previously mentioned, temperature distributions were not obtained for this study. Conversion of qualitative data to quantitative data could potentially be undertaken as future work.

3.7. Emissions Gas Analysis

Exhaust gas sampling and gas analysis (GA) was conducted via an industry standard system from Signal Gas Analysers Ltd, which has been used in multiple experimental combustion campaigns with the HPSGB [47], [222], [223], [225], [226], [242] and HPGSB-2 [243]-[245]. Figure 3-15 displays an image of the gas analyser, clearly showing the analysis units, alarm sensors and calibration gas supply. At the end of the open-ended cylindrical quartz confinement, an equal area (7 holes) exhaust sample probe was placed at the immediate exit and for the Bunsen burner setup, sample prob was placed above the flame. The exhaust gas sample line, filter and distribution manifolds were maintained at 433 K, while a heated pump was used to deliver sample into the analyser setup. Total NO_x concentrations were measured hot and wet (NO_x meas) by using a heated vacuum chemiluminescence analyser (Signal Instruments 4000VM) to avoid any losses associated with dropout in condensed exhaust H_2O , with data corrected to the equivalent dry conditions (NO_x dry) using a calculated equilibrium water molar fraction, $X_{\text{H}_2\text{O}}$, and then normalized

(NO_x dry, 15% O₂) to a reference value of 15% O₂ (O_{2,ref}) concentration per Equations [3-3] and [3-4], respectively. Exhaust O₂ measurements (O_{2,meas}) used in Equation [3-4] were made using a paramagnetic analyser (Signal Instruments 9000MGA). This was calibrated in the range 0-22.52% vol O₂.

$$NO_{x,dry} = \frac{NO_{x,meas}}{(1 - X_{H_2O})} \quad [3-3]$$

$$NO_{x,dry, 15\% O_2} = NO_{x,dry} * \left(\frac{20.9 - O_{2,ref}}{20.9 - O_{2,meas}} \right) \quad [3-4]$$

Individual NO and NO₂ measurements were also taken as well as total NO_x measurement, calibrated for 0-37.1 ppmV NO and 0-1.9 ppmV NO₂. For NO calibration experiments detailed in Chapter 7, the gas analyser was calibrated for 1000 ppmV NO. Both measurements were taken hot/wet and corrected similarly as described above.

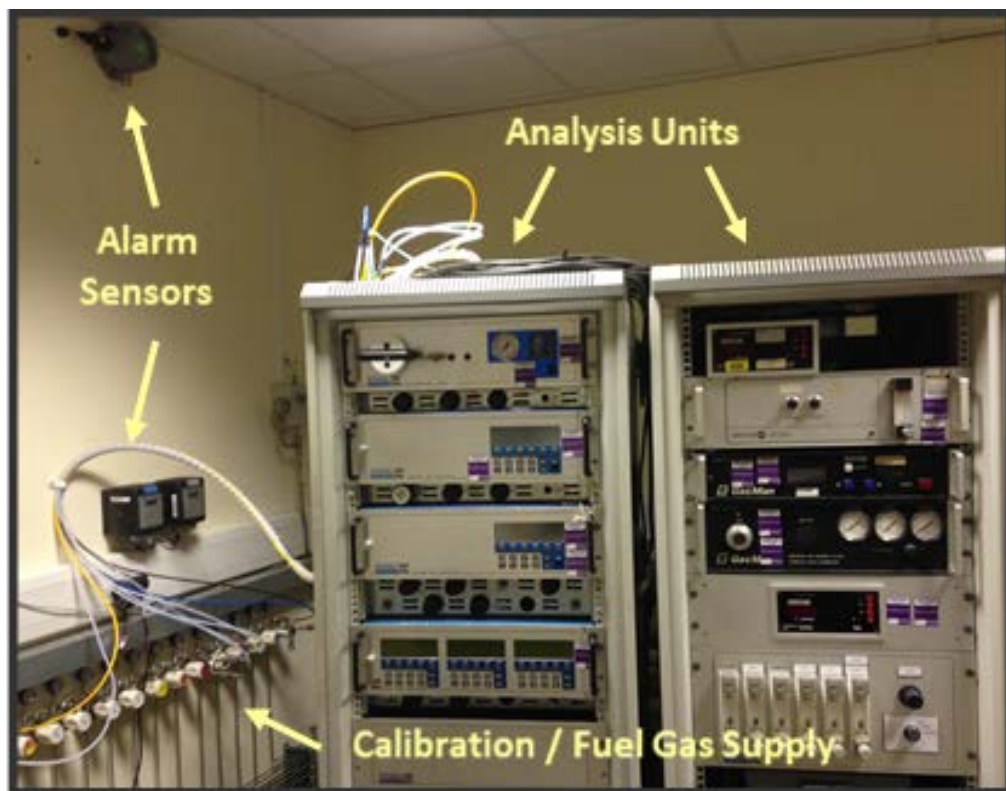


Figure 3-15: Gas analyser at GTRC

3.8. Fuel Selection

This Section reports three different fuel blend selections for chemical reactor modelling, experimental work to validate NO-LIF experiments and for future work with NO-LIF.

3.8.1. Fuel Matrix for Chemical Reactor Modelling

This fuel matrix was taken from a previous study [221], for which NO_x values were available at the exhaust, measured using the gas analyser mentioned earlier in Section 3.7. All these experiments were carried out at the same experimental set-up discussed earlier in Section 3.2. Methods for different chemical reactor modelling for the HPGSB-2 burner are described in detail in Chapter 4. NO_x predictions from the model are compared and analysed with the measured values in Chapter 4, 5 and 6. These fuel blends were chosen to maintain similar WI (refer to Equation [3-5]) while changing the molar H:C ratio. The fuel blends utilised were also selected to be industrially relevant, focusing on small changes in natural gas composition that may influence GT manufacturers and operators currently and in the near future. Table 3-4 displays the fuel blends used for validating chemical reactor model.

$$WI = \frac{\text{Calorific Value (volumetric)}}{\sqrt{\text{relative density}}} \quad [3-5]$$

Table 3-4: Fuel matrix for CHEMKIN model validation

Fuel Designation	Fuel Blend Components (mol%)					WI (MJ/m ³)	Molar H:C Ratio
	CH ₄	C ₂ H ₆	C ₃ H ₈	H ₂	N ₂		
BASE	100	0	0	0	0	50.72	4.000
MIDNG	90	6	4	0	0	52.91	3.754
FARNG	85	15	0	0	0	53.09	3.739
EMIX1	85	0	12.61	0	2.39	53.09	3.589
FARH ₂	85	0	0	15	0	48.86	4.353

3.8.2. Fuel Matrix for this Study

CH₄ is the primary constituent of natural gas, which is widely used to produce electricity by industrial GTs. Among fossil fuels, CH₄ will be exploited more and more in the near future due to its relative abundance and 'cleanliness'. Among other hydrocarbons and fossil fuels, CH₄ releases least amount of carbon and produces more heat and light energy by mass. As such, this comes with no surprise that CH₄ is also the most commonly used fuel in laboratory experiments [145], [169], [225], [236].

According to the study by Altfeld and Pinchbeck [246], future and upgraded industrial GTs are forecasted to run with 15% H₂ by volume fuel blends, prompting P2G applications having H₂ fractions in CH₄ to be fixed at 15% vol. However, current limit for H₂ fraction in the UK natural gas grid is limited to only 0.1% vol [247]. Thus, the fuel blend with H₂ was kept to 15% vol for this study, as 15% volumetric limit is acknowledged to be sufficient for future potential application in power generation as well as P2G applications. Fuel blends for NO-LIF experiments are shown in Table 3-5.

Table 3-5: Fuel matrix for NO-LIF experiment

Fuel Designation	Fuel Blend Components (mol%)					WI (MJ/m ³)	Molar H:C Ratio
	CH ₄	C ₂ H ₆	C ₃ H ₈	H ₂	N ₂		
BASE	100	0	0	0	0	50.72	4.000
FARH ₂	85	0	0	15	0	48.86	4.353

3.8.3. Fuel Matrix for Future Work

Industrial low emission GTs are sensitive to the variations in natural gas compositions. The increasing dependence on natural gas imports in the UK has led to increased gas composition variation within the distribution system. As discussed in Chapter 1.3, several studies [44], [248]–[250] has been done on the impact of natural gas composition variations on the operation of GTs for power generation. Figure 1-5 illustrated the impact on NO_x emission due to the natural gas composition variation. These

Experimental Set-up, Methodologies and Data Processing

changes can result in forced reductions in power generation. Studies from the industry [21], [44], [248] also concluded that rapid changes in compositions resulted in emergency shutdowns due to control issues, resulting in adverse impact on revenues and component life. These issues warrant further investigation on NO_x formation with typical changes in natural gas supply. In that pursuit, fuel blends in Table 3-6 are proposed to investigate the issues with natural gas variations and its impact on NO_x formation. The molar percentage of CH_4 is kept constant to 80%, while the percentages of the other fuel components is altered to keep the WI in the borderline of the acceptable range in the gas interchangeability diagram (refer to Figure 3-16).

Table 3-6: Fuel matrix for future study

Fuel Designation	Fuel Blend Components (mol%)										WI (MJ/m ³)
	CH ₄	C ₂ H ₆	C ₃ H ₈	C ₄ H ₁₀	C ₅ H ₁₂	C ₆ H ₁₄	C ₇ H ₁₆	H ₂	N ₂	CO ₂	
EMIX2	80	9	2	1.5	1	0	0	3.5	3	0	51.71
EMIX3	80	8	3	3	0	0	0	0	0	6	49.39
EMIX4	80	7.75	2.5	2.45	0.95	0.2	0.15	0	6	0	50.99

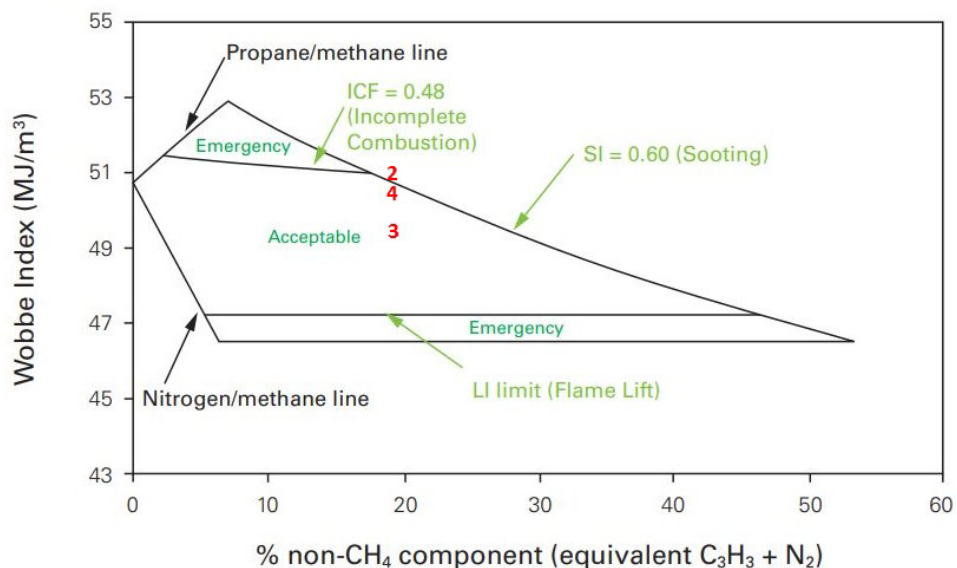


Figure 3-16: Dutton diagram with GS(M)R limits. Reproduced from [251]. Numbers (2,3 and 4) represent the positions of the proposed fuel blends in the gas interchangeability diagram.

3.9. Numerical Calculations

Numerical investigations in terms of chemical kinetics modelling were carried out in this study to provide fundamental support to observed changes in flame shape, stability, and emissions during the experimental measurements.

Chemical reactor modelling was also performed to model the HPGSB-2 in CHEMKIN-PRO [252] platform to predict NO_x emissions with various fuel combinations at atmospheric as well as elevated conditions.

3.9.1. Chemical Kinetics Modelling

The various theoretical flame properties described in Chapter 2.6 require the calculation of several flame parameters; the laminar flame speed, AFT and flame thickness. In order to do so a chemical kinetic modelling software was used. The CHEMKIN-PRO software package, developed by Sandia National laboratories, was chosen. This software facilitates the formulation, interpretation and solution of different problems involving elementary gas-phase chemical kinetics into simulations of fluid dynamics. The software offers modelling and simulation of freely propagating, adiabatic, one dimensional planar flame to obtain the laminar burning velocity. This permits comparison between experimental and computational simulation of flame speeds for the fuel and air blends investigated in this study. This software is heavily relied on in analogous fields of research, examples of which can be found in [45], [245], [253], [254], as well as in optimization of various combustion and chemical processing systems. The operational algorithm of the CHEMKIN PREMIX code is represented in a flow-chart format in Figure 3-17.

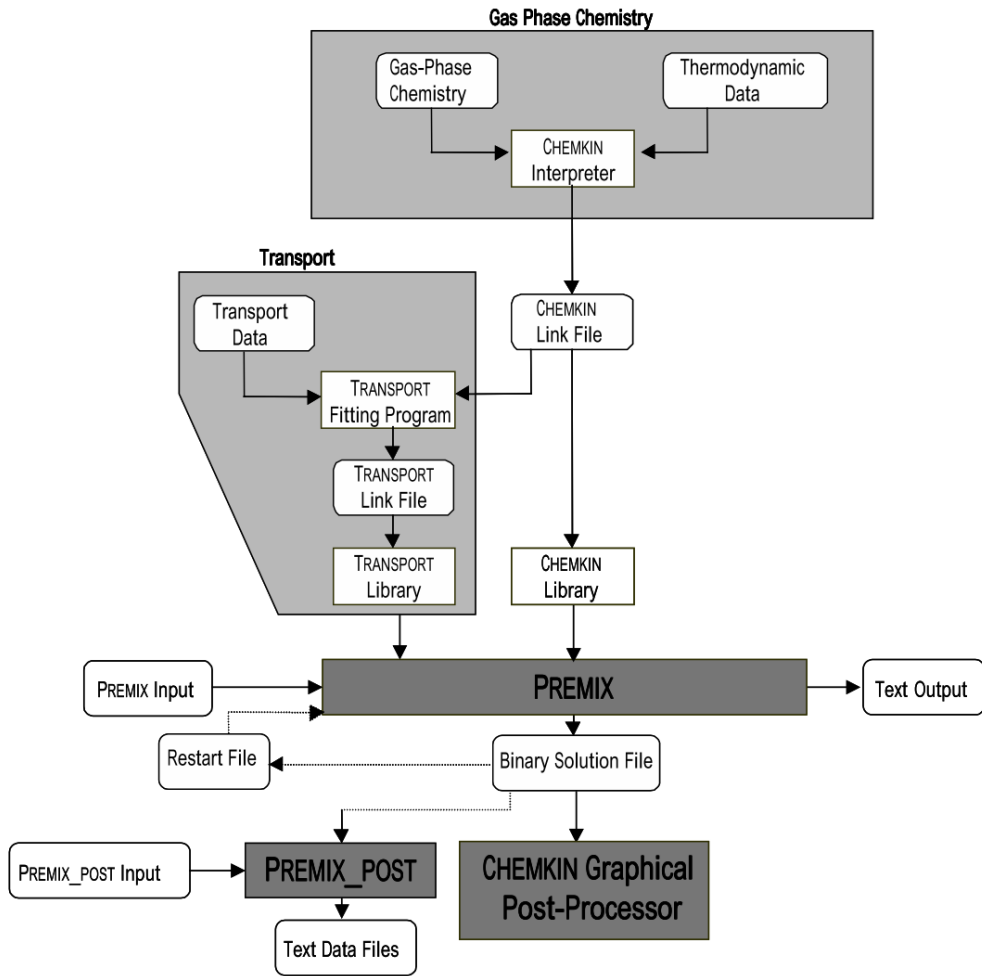


Figure 3-17: Operational Algorithm of the CHEMKIN PREMIX program

To stimulate a premixed freely-propagating, adiabatic, one-dimensional planar flame the PREMIX program of the CHEMKIN-PRO software is used. The PREMIX program models spatial profiles of temperature and chemical species throughout a steady-state laminar flame front. For the purpose of this work a simulation domain of length 10cm is considered, with a total maximum number of a 1000 grid points allowed to resolve the computational domain.

The equations governing steady, isobaric, one-dimensional flame propagation modelling are summarised below [252], [255]:

$$\dot{M} = \rho u A \quad [3-6]$$

$$\dot{M} \frac{dT}{dx} - \frac{1}{C_p} \frac{d}{dx} \left(\lambda A \frac{dT}{dx} \right) + \frac{A}{C_p} \sum_{k=1}^K \rho Y_k V_k C_{pk} \frac{dT}{dx} + \frac{A}{C_p} \sum_{k=1}^K \dot{\omega}_k h_k W_k = 0 \quad [3-7]$$

$$\dot{M} \frac{dY_k}{dx} + \frac{d}{dx} (\rho A Y_k V_k) - A \dot{\omega}_k W_k = 0 \quad (k = 1, \dots, K) \quad [3-8]$$

$$\rho = \frac{p \bar{W}}{RT} \quad [3-9]$$

Equations [3-6], [3-7], [3-8] and [3-9] shows equation of continuity, energy, species and state, respectively. In the above equations, the mass flow rate (\dot{M}) is introduced in the continuity equation, with ρ and u the density and velocity of the fluid mixture, respectively. The cross-sectional area of the stream encompassing the flame is represented by A , which by default is taken to equal unity and to be constant. The flame configuration is adiabatic, whereby definition there is no heat loss. In this case, temperatures are computed from the energy equation, which also introduces the spatial co-ordinate of the flame and thermodynamic properties including; the constant-pressure heat capacity (C_p), thermal conductivity (λ) and the specific enthalpy (h). Other properties including mass fraction (Y_k) and diffusion velocity (V_k) are defined in relation to specific chemical species ($k=1, \dots, K$). The molecular weight is defined for individual components and the mixture average (\bar{W}). The net chemical production rate of each species ($\dot{\omega}_k$), results from competition among all the chemical reaction involving that species. Each reaction is assumed to follow the law of mass action and the forward rate co-efficients are obtained from the ensuing Arrhenius form [252]:

$$k_f = A T^B \exp\left(\frac{-E_a}{RT}\right) \quad [3-10]$$

where, (A) is the pre-exponential and B the temperature factors with respect to each chemical reaction, (R) the universal gas constant and (E_a) the activation energy.

Other than the chemical reaction rates, the transport properties for example diffusion co-efficients are also of concern. Two models are available when evaluating transport properties, one based on mixing-average formulas and the other using a multi-component diffusion model. The multi-component model was used to evaluate transport properties for the purpose of this work, as it is the most accurate approach but often more computationally intensive. A brief description is provided below, with full details available in the CHEMKIN transport manual [256].

A system of equations involving species mole fractions, binary diffusion co-efficients and molecular and thermodynamic properties of the species are computed to evaluate the multi-component diffusion coefficient, thermal conductivities and thermal diffusion co-efficients. The method by Dixon-Lewis [257] is followed by the program. The diffusion velocity (\mathbf{V}_k), is assumed to be composed of two parts:

$$V_k = \mathcal{V}_k + \mathcal{W}_k \quad [3-11]$$

where (\mathcal{V}_k) is the ordinary diffusion velocity and (\mathcal{W}_k) the thermal diffusion velocity. The ordinary velocity diffusion term is defined as:

$$\mathcal{V}_k = \frac{1}{X_k \bar{W}} \sum_{j \neq k}^K W_j D_{k,j} \mathbf{d}_j \quad [3-12]$$

where (X_k), is the mole fraction, (\bar{W}), the mean molecular weight of the mixture, (W_j), is the molar mass of species j , and ($D_{k,j}$) is the binary diffusion co-efficient of species k into j . The term \mathbf{d}_j is defined as:

$$\mathbf{d}_j = \nabla X_k + (X_k - Y_k) \frac{1}{p} \nabla p \quad [3-13]$$

The thermal diffusion velocity (\mathcal{W}_k) is defined as:

$$\mathcal{W}_k = - \frac{D_k^T}{\rho Y_k} \frac{1}{T} \nabla T \quad [3-14]$$

where (D_k^T), is the thermal diffusion co-efficient for species k .

All the experimental conditions in this study were simulated in CHEMKIN-PRO [252] environment using two separate modules. Equilibrium program [258] was used to calculate AFT and the PREMIX program [259] was

utilised to calculate laminar flame speed (S_L) and molar concentrations of CH (X_{CH}), CH₂ (X_{CH_2}), OH (X_{OH}) and H₂O (X_{H_2O}). Solutions in this program were based on an adaptive grid of 1000 points, with mixture-averaged transport properties and trace series approximation. GRI-Mech 3.0 mechanism [260] was utilised for these calculations as this mechanism is optimised for use with CH₄ and natural gas compositions. Furthermore, Halter et al. [261] reported good agreements between GRI-Mech 3.0 mechanism and experimental CH₄-H₂ laminar flame measurements at pressure up to 5.5 bara and H₂ mole fraction up to 0.2. Hence, GRI-Mech 3.0 mechanism was used for CH₄-H₂ blend in this study, as H₂ was kept to 15% volumetrically.

3.9.2. Chemical Reactor Modelling

HPGSB-2 was modelled in CHEMKIN-PRO environment to predict NO_x emission at exhaust. Few modelling approaches were considered for this investigation with seven different chemical kinetics mechanisms which are detailed in Chapter 4. The main two types of chemical reactors are detailed herein:

Perfectly Stirred Reactor (PSR): A PSR is also commonly referred to as a continuously stirred tank reactor (CSTR) in chemical engineering literature. This is a zero-dimensional ideal reactor in which perfect mixing occurs. In the PSR, combustion takes place uniformly in the control volume without any spatial or temporal variation of parameters. Residence time in the PSR is the dominant parameter, which defines the available time the reactants have in reactor. A PSR may be used in the regions in combustor where the turbulence intensity or mixing degree is high due to circulation, i.e. mixing, flame, central recirculation, and edge recirculation zones.

In addition to fast mixing, the modelling of PSRs requires several assumptions. First, mass transport to the reactor walls is assumed to be infinitely fast. Therefore, the relative importance of surface reactions to gas-phase reactions is determined only by the surface-to-volume ratios of each material and the relative reaction rates (rather than by transport constraints). Second, the flow through the reactor must be characterized

by a nominal residence time, which can be deduced from the flow rate and the reactor volume.

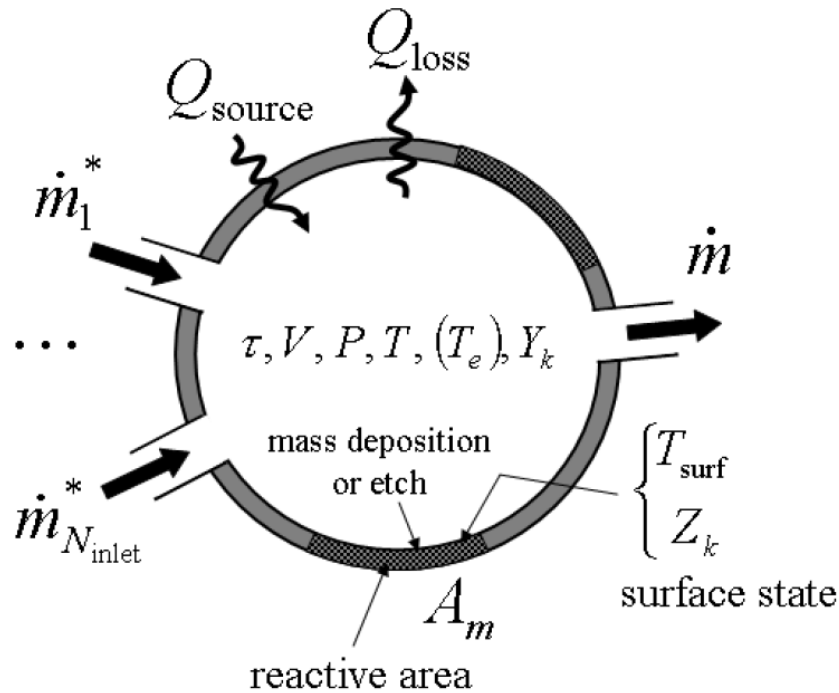


Figure 3-18: Schematic representation of a PSR module

Figure 3-18 illustrates the conceptual representation of a generic reactor chamber. A steady flow of reactants is introduced through the inlet with a given species composition and temperature. For transient systems, there may be no flow, such that the system is closed with respect to mass transfer other than surface losses or gains. In some cases, the sum of the mass flow rates into the reactor, $\sum \dot{m}_i^*$, may not be equal to the mass flow rate out of the reactor, \dot{m} , due to deposition on or etching of surface materials. For open systems, the reactor pressure is specified, so that the conservation equations determine the volume outflow. Although Figure 3-18 depicts a single surface in the reactor, an actual reactor may contain many different material surfaces, such as reactor walls, silicon wafer, substrate holder, etc. Each of these materials may have a different set of reaction kinetics associated with it. For this reason, the system has the capability of defining multiple surface materials that represent different fractions of the total surface area, with corresponding surface chemistry mechanisms. In addition to modelling a single well mixed reactor, CHEMKIN-PRO allows the user to build a

reactor “cluster” composed of many reactor modules connected in series, with the possibility of “recycling” streams feeding back to upstream reactors or being directed forward to downstream reactors. Further details on PSR reactors can be found here [256].

Plug Flow Reactor (PFR): PFR has no temporal variation like PSR but is a one-dimensional reactor, which means the flow properties are changing in the axial direction while they remain uniform in radial direction. However, no mixing takes place in the axial direction. Regions of the combustor where flow is one-dimensional, and turbulence is low, i.e. post-flame zone can be modelled by a PFR.

Tubular flow reactors have long been used throughout the chemical process industries. The tube flow configuration is a natural choice for processes that are carried out in a continuous fashion. For this reason, such reactors are usually operated at steady state. Traditional applications have included both homogeneous reactions (carried out in an empty tube) and fluid-solid heterogeneous reactions in packed beds. More recently, tubular reactors have been used extensively to deposit thin solid films via chemical vapor deposition (CVD). While this is technically a batch process with regard to the solid deposit, the reactor still operates essentially at steady state for extended periods of time. The PFR models describe the steady-state, tube flow reactor that can be used for process design, optimization, and control.

Because the general equations for chemically reacting flow involve transport phenomena in addition to kinetics and thermodynamics, rigorous reactor models are by necessity multidimensional. However, there are often practical as well as mathematical reasons for considering idealized models of reduced dimensionality. In the case of tube flow, the accepted ideal is the plug-flow reactor, in which it is assumed that there is no mixing in the axial (flow) direction but perfect mixing in the direction(s) transverse to this. It can be shown [262] that the absence of axial mixing allows the achievable reactant conversion to be maximized. Likewise, the lack of transverse gradients implies that mass-transfer limitations are absent, once again enhancing the reactor performance.

Along with these practical advantages, the plug flow reactor is computationally efficient since it is modelled using first-order ordinary differential equations (ODE's), and no transport properties are needed. Further details on PFR reactors can be found here [256].

3.10. Chemical Kinetics Modelling and Flame Thickness Calculations

Table 3-7 provides the full range of experimental conditions evaluated in this study. Note that all values are calculated based on the full premixed reactant flows, in particular the Reynolds number, which accounts for changes in premixed dynamic viscosity using Equation [3-15],

$$Re = \frac{\bar{u}D_{noz}\rho_{premix}}{\mu_{premix}} \quad [3-15]$$

where \bar{u} is the mean burner exit nozzle velocity, D_{noz} is the nozzle diameter, ρ_{premix} is the total premixed reactant density and μ_{premix} is the total premixed dynamic viscosity calculated through use of the Colorado State University online transport properties calculator [263].

Two different burners with CH₄ were used to conduct the open flame NO-PLIF combustion experiments presented in this Chapter. The 25mm Bunsen burner for $\Phi = 1.28 - 1.4$ and HPGSB-2 without confinement for $\Phi = 0.81 - 1.1$.

Table 3-7: Operating ranges for NO PLIF experiments

Fuel	Φ	T ₂ (±5 K)	P _{therm} (kW)	Burner	\bar{u} (m/s)	Re (x10 ³)	AFT (K)	S _L (m/s)	NO excitation wavelength (nm)
CH ₄	1.28 - 1.4	298	2.5-2.7	Bunsen	0.5 - 0.5	0.85 - 0.86	1970 - 2059	0.14 - 0.25	285.16
CH ₄	0.81 - 1.1	298	26	HPGSB - 2 (Quartz off)	6 - 8	16.5 - 21.8	2013 - 2205	0.28 - 0.38	285.16
CH ₄	0.81 - 1.1	298	26	HPGSB - 2	6 - 8	16.5 - 21.8	2013 - 2205	0.28 - 0.38	285.16
CH ₄	0.55 - 0.65	573	42	HPGSB - 2	31 - 35	27.6 - 31.3	1788 - 1962	0.50 - 0.68	285.16
CH ₄ /H ₂	0.55 - 0.65	573	42	HPGSB - 2	30 - 35	26.6 - 31.1	1793 - 1966	0.45 - 0.75	285.16
CH ₄	0.81 - 1.1	298	42	HPGSB - 2	10 - 13	26.7 - 35.6	2013 - 2205	0.28 - 0.38	226.03
CH ₄	0.75 - 0.85	573	42	HPGSB - 2	24 - 27	65.4 - 73.6	2115 - 2244	0.89 - 1.07	226.03

Chemical kinetics modelling of the experimental conditions was conducted using two separate modules within CHEMKIN-PRO [252]. First, the equilibrium program was used to model AFT. Second, the PREMIX program was used to model S_L , which is based upon modelling of 1-D adiabatic planar freely propagating flame. Moreover, equilibrium exhaust H_2O concentrations, X_{H_2O} , for use in the correction of wet exhaust gas emissions measurements (Equations [3-3]), and OH (X_{OH}) and CH (X_{CH}) radical 1-D profiles to identify the heat release and reaction zones, respectively. Solutions in this model are based on an adaptive grid of 1000 points, with mixture-averaged transport properties and trace series approximation. Both the equilibrium and the PREMIX [259] models employed the GRI-Mech 3.0 reaction mechanism [260] which is optimized for use with methane and natural gas compositions and comprises 53 chemical species and 325 reactions. This mechanism has also been shown to have good agreement with experimental CH_4 - H_2 laminar flame speed measurements at pressures up to 5.5 bara and mole fractions up to 0.2 [261]. Thus, GRI-Mech 3.0 has also been used in the evaluation of H_2 flames in this study, as the volume fraction is limited to 15% and the experiments were atmospheric pressure conditions.

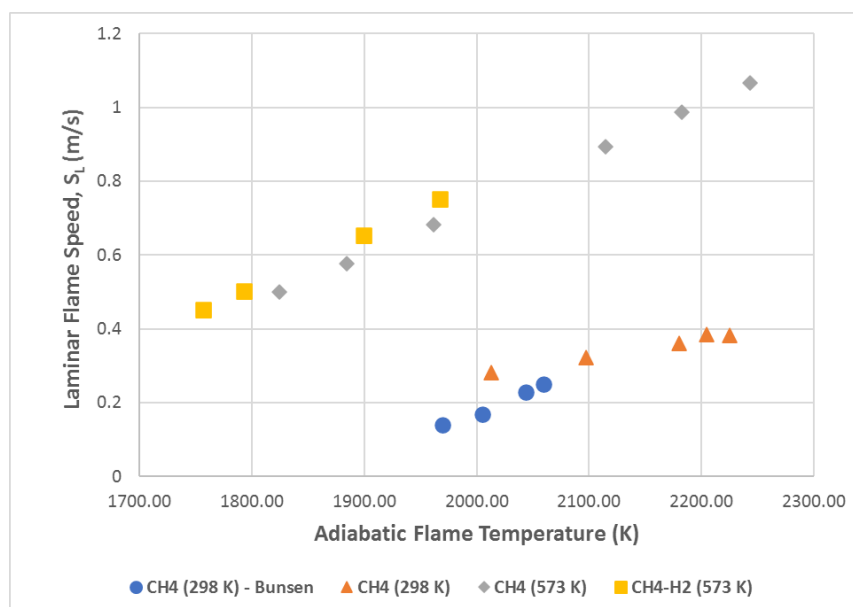


Figure 3-19: Modelled S_L of all experimental conditions as a function of AFT

The influence of AFT, Φ , and fuel composition on S_L and burner operability was evaluated for all experimental conditions, with kinetic modelling results presented in Figure 3-19 and 3-20. Modelled laminar flame speed, S_L is plotted as a function of AFT and Φ in Figure 3-19 and 3-20, respectively. As expected, an increase in AFT increases S_L , thus reactivity, of all fuels, with quasi-linear relationships for lean conditions ($\Phi < 1$) at fixed pressure conditions. However, as seen in Figure 3-20, at the rich conditions considered here, S_L decreases as Φ increases. Differences in S_L can be seen in the same Φ but different entry temperature (T_2). Higher T_2 results in higher S_L in the same fuel at same Φ . Addition of H_2 in the fuel increases S_L further compared to the CH_4 flames (without H_2).

The characteristic rich shifting of the maximum adiabatic flame temperature from the stoichiometric value for mixtures of hydrocarbon and air is caused by product dissociation and hence reduced amount of heat release. Since the extent of dissociation is greater on the lean side as a result of the stoichiometry of dissociated products, AFT peaks on the rich side [264]. Figure 3-21 plots AFT as a function of Φ for all the fuel conditions considered here. It must be noted that AFT peaks here at stoichiometry as there was no conditions considered here between stoichiometry and $\Phi = 1.1$, where AFT usually peaks as seen in literature [264]. As expected, higher T_2 corresponds to higher AFT, irrespective of Φ . A gentler slope of the curve is seen on the rich side as compared to those on the lean side, as shown in Figure 3-21. This asymmetry is caused by the asymmetrical nature of the definition of Φ in that Φ spans between 0 and 1 for lean mixtures but is spread out from 1 to ∞ for rich mixtures.

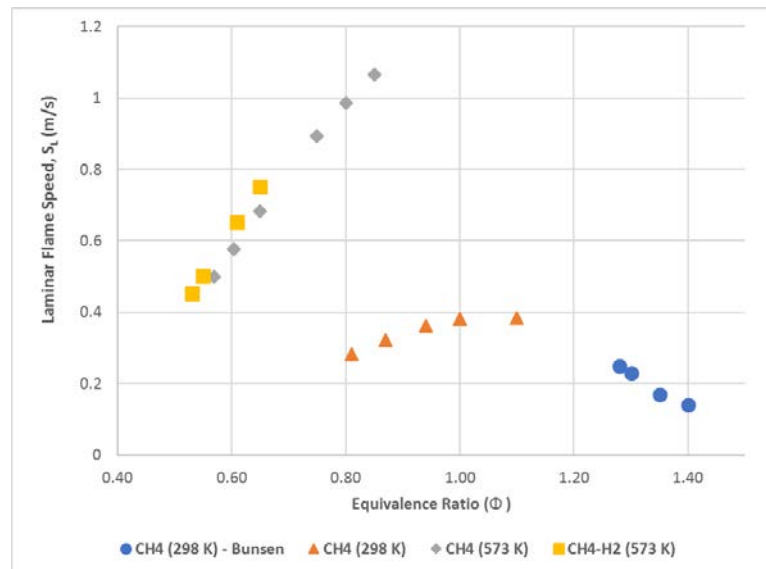


Figure 3-20: Modelled S_L of all experimental conditions as a function of Φ

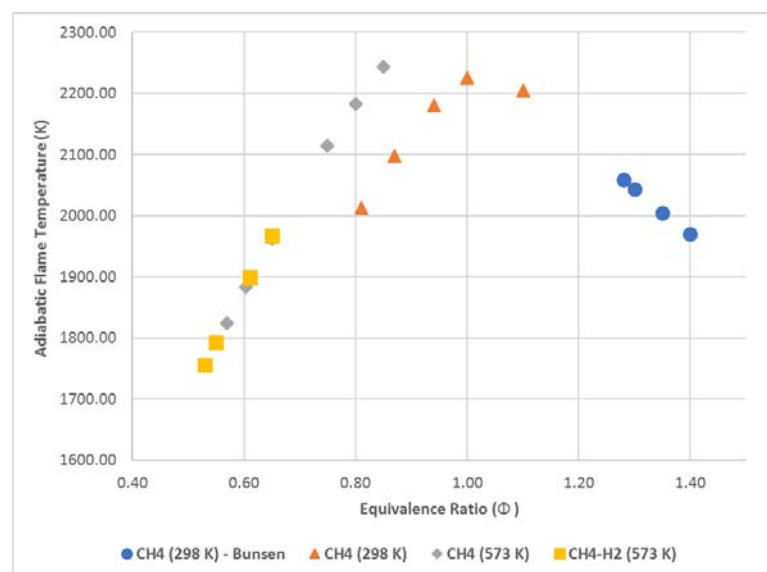


Figure 3-21: AFT plotted as a function of Φ for all experimental conditions, demonstrating the gentler slopes on the rich side due to the asymmetrical nature of the definition of Φ

3.10.1. Flame Reaction Zone Thickness Calculations

Utilizing non-intrusive measurements and numerical chemical kinetic modelling, a series of evaluations of the influence of fuel composition on fundamental characteristics such as the localized heat release and reaction zone thickness has been conducted. The methods of calculating

flame and reaction zone thickness calculations both numerically and experimentally is described in this section.

3.10.1.1. Numerical Methods

Two definitions of laminar flame thickness have been proposed in literature [194]. The first commonly referred to as the diffusion (reaction) thickness δ_D , is given by

$$\delta_D = \frac{\lambda}{\rho_u C_p S_L} \quad [3-16]$$

Where λ is the thermal conductivity, ρ_u is the mixture unburned density, C_p is the mixture heat capacity at constant pressure and S_L is the laminar flame speed. λ , ρ_u and C_p was obtained through use of the Colorado State University online transport properties calculator [263] and S_L was obtained from chemical kinetics simulation as described earlier.

However, due to the ambiguous definition of these properties (i.e. the temperature at which the λ/C_p ratio is assessed), Jomaas et al. [265] recommended the following equation, termed the gradient thickness (δ_G) for different unburned temperatures (T_u),

$$\delta_G = \frac{AFT - T_u}{\left(\frac{dT}{dx}\right)_{max}} \quad [3-17]$$

This expression relies on the extraction of the gradient of the temperature profile from the PREMIX CHEMKIN [259] calculations. From a previous study at Cardiff University, Runyon [221] proposed a new definition for reaction zone thickness (δ_t) as the one dimensional axial distance between the preheat zone (represented by peak CH molar concentration) and the reaction zone (represented by peak OH molar concentration).

Figure 3-22 represents the modeled conditions for CH₄-air flame in TP 4 of Table 5-1.

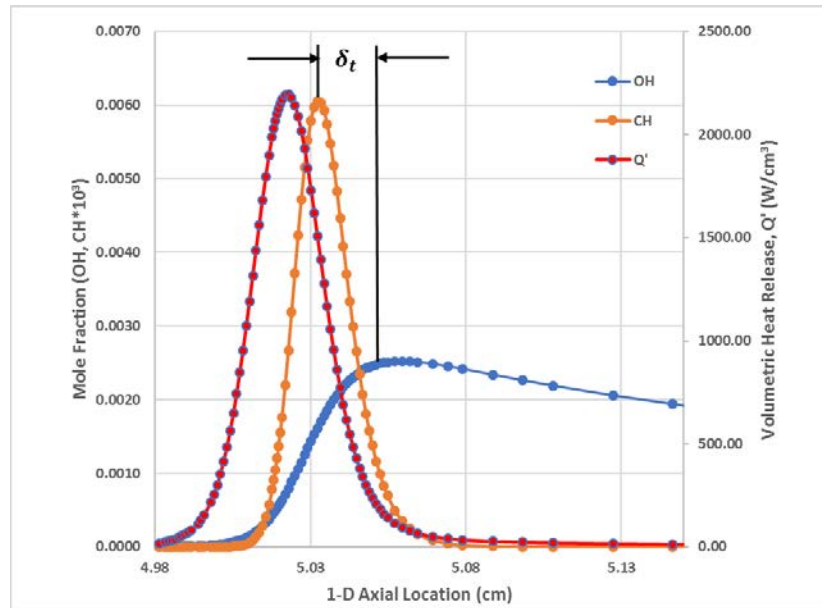


Figure 3-22: Reaction zone thickness, δ_t , based on maximum CH and OH mole fraction location in one-dimensional flame model from CHEMKIN PREMIX code

3.10.1.2. Flame Thickness Measurements from Non-intrusive Method

A bespoke image processing technique for the extraction of key flame features was developed for use with the temporally averaged images in a previous study at Cardiff University [221]. This technique binarizes the OH* chemiluminescence image by identifying the location of the maximum OH chemiluminescence intensity in each row of the image and then locating the maximum gradient of OH* chemiluminescence intensity on either side of that maximum location. This yields a flame brush thickness, δ_{flame} , for each row which is then averaged over all rows where the maximum OH chemiluminescence intensity level is at least 50% of the overall image maximum OH chemiluminescence intensity. This code development and functionality is described in detail here [221]. The modified MATLAB code is given in Appendix B.9.

3.10.1.3. Numerical and Experimental Measurements Comparison

Flame thickness calculated from above numerical methods and experimentally for the conditions in Table 3-7 are discussed and compared in this section. Figure 3-23 plots flame thickness as a function of Φ . It must be noted that flame thickness calculated from numerical methods (δ_D, δ_G and δ_t) are plotted in the primary axis and experimentally measured flame brush thickness (δ_{flame}) is plotted on the secondary axis.

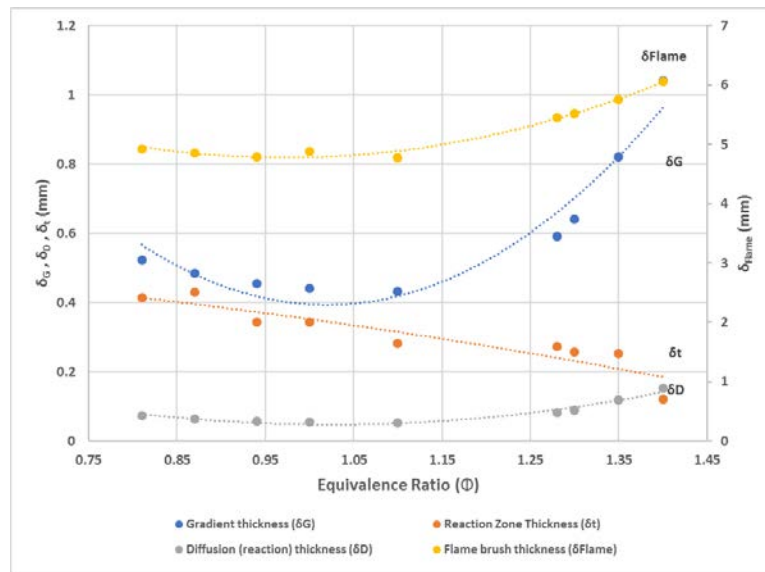


Figure 3-23: Numerical and experimental flame thickness as a function of Φ

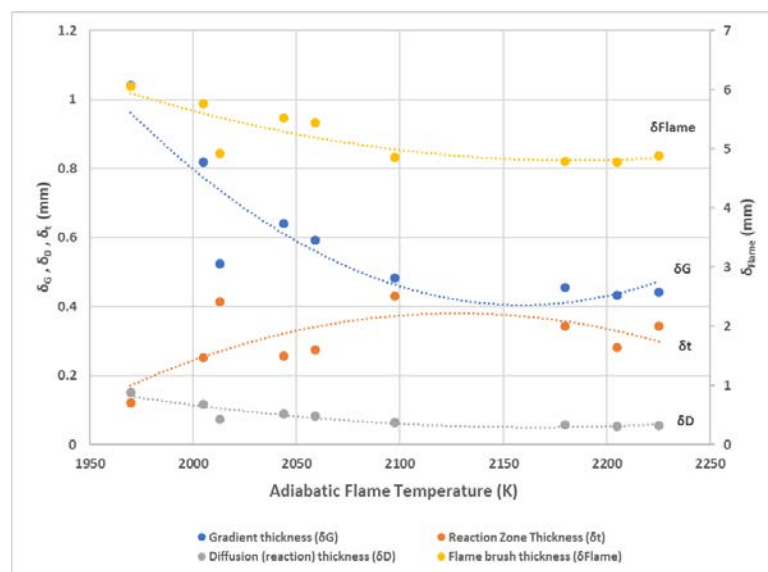


Figure 3-24: Numerical and experimental flame thickness as a function of AFT

Gradient thickness decreases with Φ for the lean conditions and then increases as the flame gets richer. This is due to the trend of AFT with Φ as shown in Figure 3-21. It is unsurprising that the gradient thickness trend is analogous to the inverse of the AFT trend, due to the method of calculation of gradient thickness. The relationship between gradient thickness and AFT is even clearer in Figure 3-24 where flame thickness is plotted against AFT. Gradient flame thickness decreases until about 2150K and then increases with AFT. The slope of the polynomial fit is much more prominent at $\text{AFT} < 2150\text{K}$ and $\Phi > 1.05$.

The diffusion (reaction) thickness follows similar trend as gradient thickness. This is due to the fact that $\lambda/(C_p S_L)$ ratio increases for the lean side ($\Phi < 1$) and decreases at the rich flames ($\Phi > 1$). However, as per Law [194], diffusion (reaction) thickness is about 10 times smaller than gradient thickness.

The flame brush thickness (δ_{flame}), calculated using the processed image of OH chemiluminescence measurement, follows the same trend as the gradient and diffusion (reaction) thickness. However, as CH chemiluminescence measurement was not considered to measure δ_{flame} , the results are about 10 times higher than gradient thickness.

Reaction zone thickness (δ_t) follows the same trend as others for the lean conditions but is opposite to the trend for rich flames. δ_t decreases as Φ increases on the rich side. Figure 3-25 and Figure 3-26 shows the peak CH and OH molar fraction locations, respectively from 1-D CHEMKIN calculations. OH peak locations are very close to each other as Φ changes, moving slightly to the left as Φ increases from 0.81 to 1.1 and then moving slowly to the right as flame gets richer. However, the changes in CH peak locations are more noticeable, moving to left as fuel goes towards stoichiometry from lean conditions and then moves to the right as the stoichiometry gets richer. As the OH peak locations do not change as much as CH peak locations in the rich conditions, opposing trend can be seen in rich flame thickness.

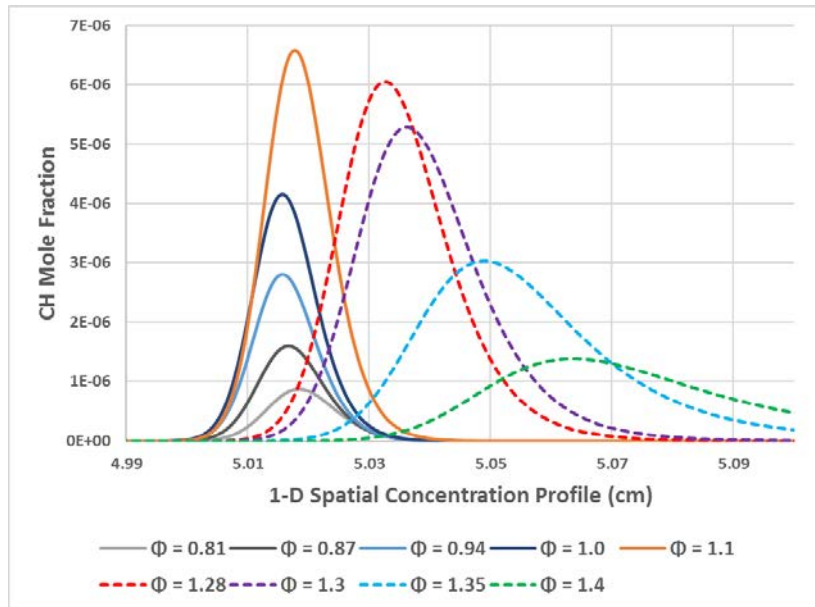


Figure 3-25: Peak CH molar fraction locations from 1-D CHEMKIN calculations. Solid lines for HPOC conditions and dashed line for Bunsen burner conditions.

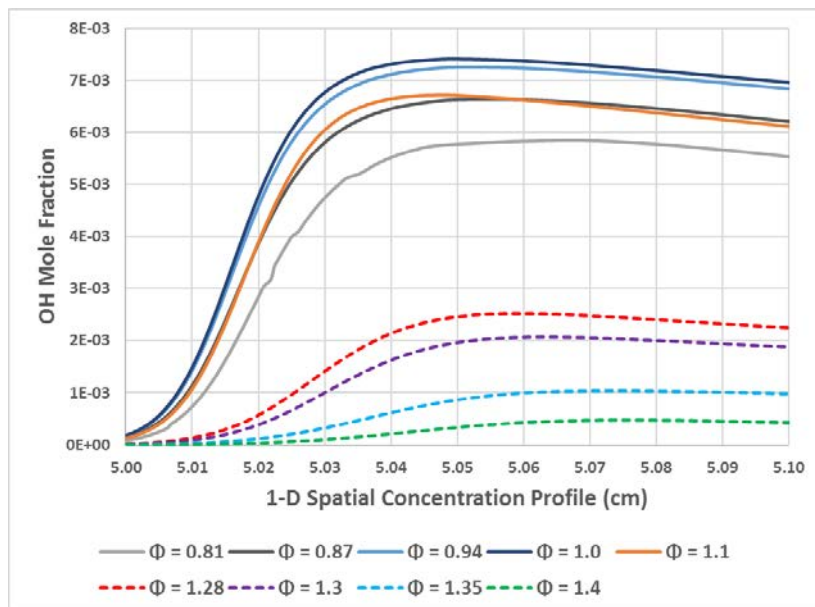


Figure 3-26: Peak OH molar fraction locations from 1-D CHEMKIN calculations. Solid lines for HPOC conditions and dashed line for Bunsen burner conditions.

3.11. Summary

The Chapter started with discussing the operation for both the Bunsen burners, in terms of operability, gas mixing system and mass flow controllers. HPCR test facility at GTRC was described briefly with the HPOC set-up, before introducing the high-pressure generic swirl burner - 2 (HPGSB-2) where main experiments for this study were carried out - fully premixed, non-piloted, and with a geometric swirl number of 0.8. The Section was concluded by detailing the five lines fuel and air delivery system in the HPCR.

Difficulties with the laser system to attain substantial laser beam energy at 226.03 nm UV output was considered hereafter. NO and O₂ excitation and emission spectra was investigated in the 'doubling' range of the dye laser to attain required laser beam energy level. By considering sustainable NO excitation and minimum O₂ interference, 285.16 nm was chosen as the primary NO excitation wavelength for this study.

The laser system at GTRC was discussed next by specifying the operations of the Nd:YAG pump laser and the dye laser. The fundamental $\lambda=1064$ nm was doubled by passing through SHG optics, to pump the dye laser at $\lambda=532$ nm. Pyromethene 597 dye was used to get the desired UV output of 285.16 nm by utilising a doubling unit, while 80/20 combination of Rh 590 and 610 dyes were used to get UV output of 226.03 nm by utilising 'mixing after doubling' technique.

Experimental setups were discussed for both the Bunsen burners and HPOC experiments by examining the schematics for both the burners. Data acquisition system from the experiments and the procedures for image processing were discussed in detail with aids of step-by-step figures for both 226.03 and 285.16 nm NO excitation experiments.

The operation of the exhaust gas analyser which was used to measure NO_x and O₂ concentrations for the experiments in this study was examined as well. Next, the reasonings behind three different fuel selections for chemical reactor modelling, NO-LIF experiments for this study and potential future work were explained.

Experimental Set-up, Methodologies and Data Processing

The Chapter was concluded by describing the theories behind numerical calculations by Chemkin-PRO. Flame thickness were calculated using four different methods. Gradient (δ_G), diffusion (δ_D) and flame brush thickness (δ_{flame}) decreased with Φ for the lean conditions and then increased as the flame got richer. Reaction zone thickness (δ_t) followed the same trend as others for the lean conditions but opposed the trend for rich flames.

4. Reactor Network Modelling Analyses

In this chapter, a physics-based model of the combustion chamber is developed for predicting NO_x emissions. The objective of the model is to predict the emissions of current and future industrial gas turbine engines across different conditions. The approach taken is to capture the physical relationships among operating conditions, combustor design parameters, and pollutant emissions. The model is developed using only high-level combustor design parameters and ideal reactors in CHEMKIN® environment. Seven different mechanisms were used in the final model to quantify and analyse the difference between the predictions and experimental data.

The goal of this chapter is to develop an emissions prediction procedure for use in the conceptual design phase. The approach is to use simplified physics-based models to bridge the gap between the empirical and high-fidelity approaches. Different models that were considered, and NO_x predictions from the selected model with different mechanisms are analysed and compared with experimental results in detail in this chapter.

4.1. Chemical Kinetics Model

Seven different fuel-oxidant reaction chemical kinetics mechanisms were selected to examine the dependence of NO_x emissions predictions on the fuel-oxidant mechanism. These mechanisms were selected based on their applicability with different hydrocarbons and H₂ fuel blends.

The first mechanism is GRI-MECH 3.0, which is used as a baseline case, because it is widely used in many combustion simulation environments. The second mechanism is Aramco 1.3, which is a newly developed chemical kinetic mechanism of C1-C4 based hydrocarbon and oxygenated fuels over a wide range of experimental conditions. C1-C3 mechanism from the CRECK Modelling Group is used as the third mechanism for comparison. To examine the performance of NO_x predictions with a relative low-cost mechanism, the University of California San Diego Mechanism is also employed as the fourth mechanism. The fifth mechanism is USC Mech Version 2 is treated as an extended version of

GRI-Mech 3.0 to enhance its ability to predict propane flames. Ranzi-Paolo mechanism from University of Illinois is used as the sixth mechanism for this comparative study. Pentane Isomers mechanism from NUI Galway is employed as the final mechanism, which gives extended number of species and reactions.

GRI-Mech 3.0

GRI-Mech 3.0 [260] is the most widely used and validated mechanism for modelling natural gas combustion. It includes the reactions for hydrogen, carbon monoxide, methane, ethylene and propane combustion. However, the scope of the propane chemistry is minimized. It is competent for modelling fuel combustion, which includes propane as a minor constituent. Thus, this mechanism can be treated as a 'perfect' C1 mechanism, but a 'pseudo' C1-C3 mechanism. This mechanism includes NO formation and reburn chemistry for predicting NO_x emissions. The GRI-Mech 3.0 contains 325 reactions and 56 species, and all the reactions and the corresponding thermochemical data as well as transport coefficients can be found on its website.

Aramco 1.3

The development of Aramco 1.3 [266] was approached in a hierarchical fashion 'from the bottom up', starting with a C1 sub-mechanism and grown by the inclusion of larger carbon species such as ethane, ethylene, acetylene, higher C3-C4 and oxygenated species. It is a detailed chemical kinetic mechanism that has been developed to describe the oxidation of small hydrocarbon and oxygenated hydrocarbon species. The mechanism has 253 species and 1542 reactions. NO_x pathways were added as a part of this study and listed in Appendix E.1.

CRECK

The CRECK mechanism [267] is a general and detailed chemical kinetic model that has been developed and tested to investigate the interaction between NO and hydrocarbons during the oxidation of a hydrocarbon at low temperatures. The model describes the influence of NO and was validated through comparison with several different experimental data

sets for various temperatures, stoichiometries and hydrocarbon fuels. It has 115 species and 2141 chemical reactions.

University of California San Diego Mechanism (SanDiego)

SanDiego mechanism (2014 Version) [268] is another widely used mechanism for hydrogen, carbon monoxide and C1-C3 hydrocarbons combustion. The philosophy of the development of this mechanism is to minimize the required species and reactions for describing the calibration target. Thus, the computational cost and uncertainty are limited. 50 species and 247 reactions are included in this mechanism.

USC Mech Version 2 (USII)

USC Mech Version 2 [269] is a recent mechanism for modelling high temperature oxidation of hydrogen, carbon monoxide and C1-C4 hydrocarbons. The C1 and C2 reactions are based on GRI-Mech 1.2, 3.0 and an ethylene and acetylene reaction model. It also includes reactions for benzene and toluene oxidation. Therefore, this reaction includes 111 species and 784 reactions, which is relatively complex. This mechanism does not include NO_x reactions. NO_x pathways were added to this mechanism and given in Appendix E.2.

Ranzi-Paolo Mechanism

The Ranzi-Paolo Mechanism [270] includes hydrocarbons up to C7 and aromatic species (benzene and toluene). The mechanism includes the chemistry of NO_x and PAH formation. The reaction mechanism was synergistically improved using pathway analysis and measured benzene profiles and then used to characterize the effects of partial premixing and strain rate on the flame structure and the production of NO_x and soot precursors. This mechanism consists of about 170 species and 5000 reactions.

NUI Galway Mechanism

The NUI Galway Mechanism [271] includes three pentane isomers: *n*-pentane, *iso*-pentane and *neo*-pentane. This mechanism was chosen on

the basis of future heavy hydrocarbons experiments at GTRC. NO_x pathways were added to this mechanism and included in Appendix E.3.

4.2. Reactor Network Models

The emissions predictions approach is a modelling process consisting of two main elements: (1) object-oriented one-dimensional (1-D) flow model to provide a simple, common procedure for modelling different types of combustors, (2) chemical reactor network (CRN) model representative of the combustor flow field. In that pursuit, two chemical reactor models from literature is considered first, followed by three new proposed models based on the models from literature.

4.2.1. Models from Literature

Two models from previous studies, namely Rizk model and Valeria model are considered here. Though Rizk model is based on liquid fuel, it is considered here to alter the model for gaseous fuel.

Rizk Model

The first model that was considered was based on the work of Rizk et al. [272] because it has several attractive features. The flame zone model accounts for fuel atomization and incompletely vaporized fuel droplets, and unmixedness was modelled by dividing the flame zone into five Perfectly Stirred Reactor (PSR) with different equivalence ratios, determined by the 'unmixedness' parameter, s [273].

$$s = \frac{\sigma_{\varphi}}{\mu_{\varphi}} \quad [4-1]$$

Where σ_{φ} is the standard deviation and μ_{φ} is the mean equivalence ratio. Fuel and air flows among five groups in the flame zone were distributed using normal distribution. Each group in the flame zone (FZ) had a stoichiometric reactor, followed by a normal reactor and a mixer which was used for the air flow. All the flows were calculated based on the geometric consideration of the chamber and distributed among the five groups using normal distribution.

Residence time in stoichiometric reactor is strongly dependent on air inlet pressure (P_2) and temperature (T_2):

$$\tau_{st} = B \cdot \varphi_{in}^{-0.3} \cdot \exp(A \cdot \varphi_{in}^{7.2}) \quad [4-2]$$

Where,

$$A = 0.244 - 0.000277 \cdot P_2 \quad [4-3]$$

$$B = 0.245 \cdot \left(\frac{T_2}{1000}\right)^8 \cdot \exp(0.135 \times 10^8 \cdot T_2^{-2.35}) \quad [4-4]$$

For T_3 greater than 811K, the expression for the parameter B is given by,

$$B = 0.00089 \cdot T_2 - 0.394 \quad [4-5]$$

The units of P_2 and T_2 are in kPa and K respectively.

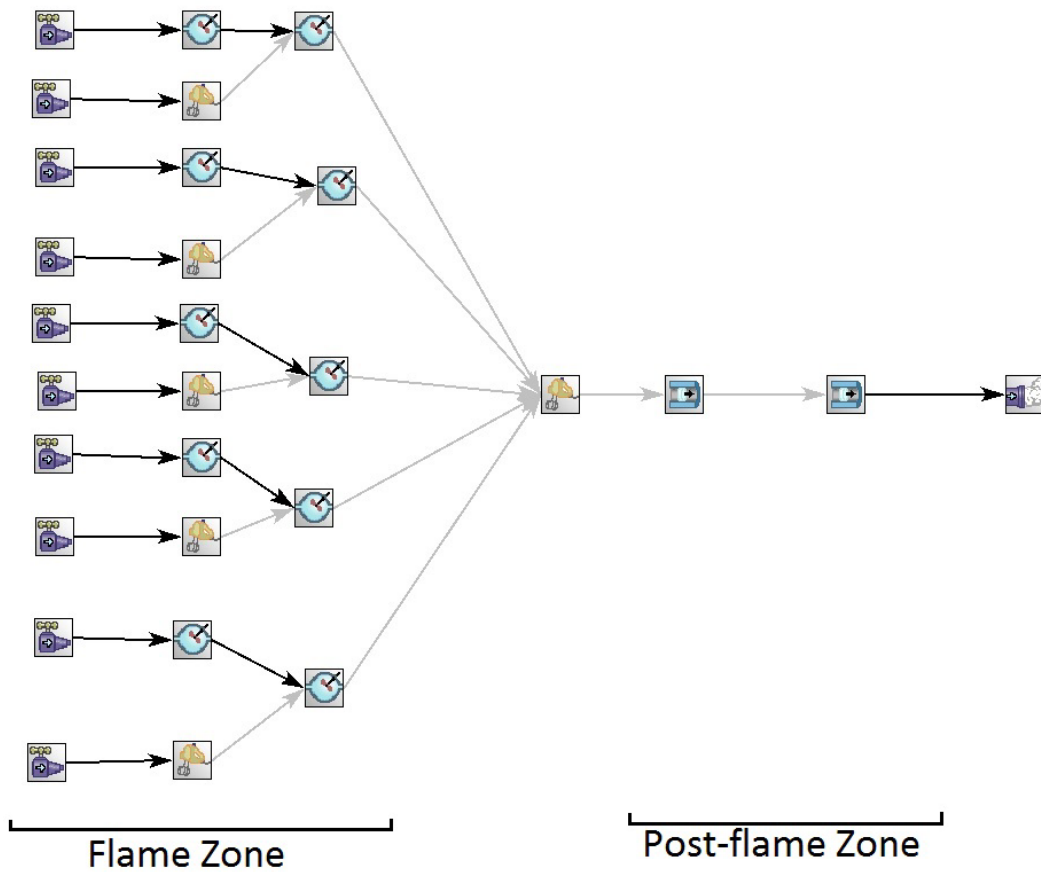


Figure 4-1: Rizk model

Post-flame zone (PFZ) was modelled by two Plug Flow Reactors (PFR). 1st PFR was used to model the cylindrical post-flame zone and the 2nd PFR was used to model the convergent end zone. Figure 4-1 and Appendix E.4 represents the chemical reactor network and required inputs for the model respectively.

Valera Model

The Valera model, Figure 4-2, was used in a different project to model the HPSGB at GTRC [274]. This model takes into account of the recirculation zone of the swirl flame. Three PSRs were used to model the mixing zone, flame zone and recirculation zone (RZ). In the model, 80% of the flow goes into the post-flame zone and 20% goes into the recirculation zone from the flame zone. Similarly, 80% of the flow goes into the flame zone and 20% goes into the mixing zone from the central recirculation zone. Recirculation was approximated to 20% from previous experimental results obtained using the same device [210]. Post-flame zone was modelled as discussed before for the previous models. Appendix E.5 shows the inputs required for the Valera reactor model.

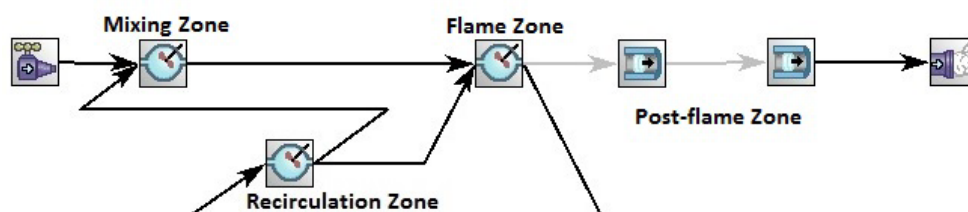


Figure 4-2: Valera model

4.2.2. Proposed Models

Three new models are proposed in this Section which are mainly based on the models from previous studies. The operations and build-ups of these new models are discussed herein.

Modified Rizk Model

This model, Figure 4-3, is necessarily a variation of the Rizk model, where only one group was used to model the flame zone, instead of using five groups via normal distribution, thus reducing the effects of unmixedness parameter and droplet atomization. Post-flame zone was

kept exactly like the Rizk model. Appendix E.6 shows the inputs required for this reactor model.

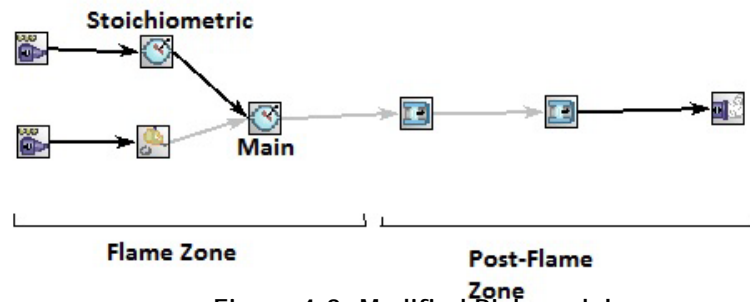


Figure 4-3: Modified Rizk model

Modified Valera Model

This model is a variation of the Valera model to further improve the emissions prediction, by implementing CFD results from a parallel study [275] (refer to Appendix C.2) to predict the volume of the central recirculation zone (CRZ) and edge recirculation zone (ERZ). A mixer was used between the mixing zone and flame zone reactors, as it seemed impractical that the flow from CRZ and ERZ will go into the mixing zone. According to the CFD prediction, recirculation from CRZ was set to 70% into the flame zone reactor and from the flame zone, the flow was split three ways: 75%, 20% and 5% into post-flame zone, CRZ and ERZ respectively. Volume for the mixing zone PSR was calculated from the geometry shown in Appendix C.1. Figure 4-4 and Appendix E.7 represents the chemical reactor network and required inputs for the model respectively. It must be noted that additional inputs (heat loss rate and residence time) are required for this model to make it more robust and improve the emissions predictions.

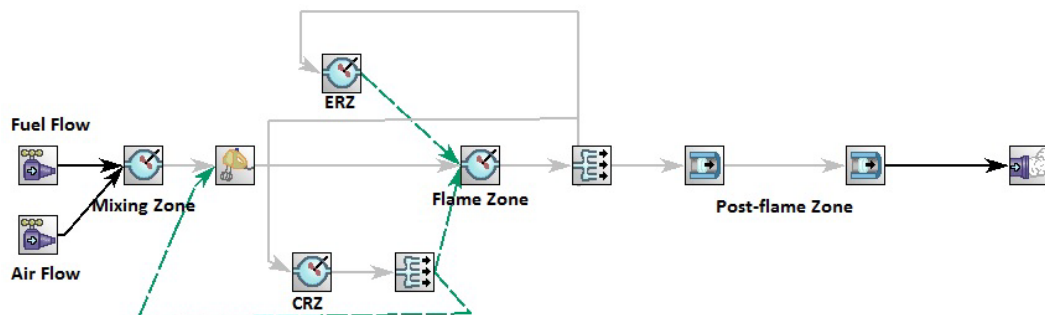


Figure 4-4: Modified Valera model

Simplified Model

This model, Figure 4-5 is the simplest and low cost among all of them, with a PSR used for mixing zone (MZ) and another PSR for flame zone, while keeping post-flame zone same. Mixing zone was modelled using the geometric configuration of the HPGSB - 2, prior to entering the combustion chamber. Appendix C.1 shows the mixing chamber which was used to model the PSR for mixing zone. Appendix E.8 shows the inputs required for the third reactor model.



Figure 4-5: Simplified model

4.3. Comparison of Reactor Models

NO_x predictions from the five reactor models are compared with experimental data in this section. GRI-MECH 3.0 mechanism was used to run the models for this comparison. All the five fuel mixes (Base, EMIX1, FARNG, MIDNG, FARH2) described in Chapter 3.8.1 at three different pressure ratios (1.1, 2.2 and 3.3 bara) are used in the models for predictions comparisons. All the NO_x values are corrected to the equivalent dry conditions and then normalized to a reference value of 15% O₂ concentrations as per Equations [3-3] and [3-4]. NO_x values in ppm are plotted against the AFT in Figure 4-6, Figure 4-7 and Figure 4-8. Table 4-1 shows the percentages differences in decimal by the models compared to the experimentally derived data.

Figure 4-6 plots the models' predictions and experimental data at 1.1 bara pressure ratio. The Rizk model overpredicts the NO_x values by a factor of ~ five on average for all the fuel blends as the model takes into consideration of the unmixedness of fuel and air. This model also divides the flame zone into five sections using normal distribution. In reality though, the combustion chamber is fully premixed. For the modified Rizk model, where only one zone was used to model the flame zone, still with the unmixedness parameter in the flame zone, NO_x predictions comes

down considerably in Base, EMIX1, FARNG and MIDNG fuels but overpredicts emissions for FARH₂ blend by a factor of ~ 3.5 due to the presence of H₂ in the fuel mix. The simplified model was the low cost among all the models and underpredicts NO_x across all fuel mixes at 1.1 bara. The Valera and the modified Valera models, where recirculation was taken into consideration, predict NO_x closest to the experimental value.

Figure 4-7 illustrates the models' predictions and experimental data at 2.2 bara pressure ratio. Once again, the Rizk model overpredicts NO_x values by a long margin (by a factor of ~ 4) but predictions from the modified Rizk model is lot closer to the experimental values compared to the 1.1 bara predictions at low AFTs but overpredicts at higher AFTs. The simplified model underpredicts NO_x value across all fuel blends as before. The modified Valera model gives the best predictions (within ~ 10%) across all fuel blends at 2.2 bara, while the Valera model overpredicts NO_x values by around 55% for all fuel blends.

Figure 4-8 depicts the models' predictions and experimental data at 3.3 bara pressure ratio. The Rizk and the modified Rizk model overpredict considerably compared to the experimental data and the overprediction increases as the AFT increases. The recirculation model from Valera give better predictions at 3.3 bara with the modified Valera model's prediction are closest to the experimental values.

It can be concluded from the above discussions and the figures that the recirculation models are the better predictors of the NO_x values. In particular, the modified Valera model gives very close prediction at higher pressures. The simplified model underpredicts across all the fuel blends and pressure conditions. But the simplicity and low time consumption of the model makes it a potential model to be considered for further development in the future. The Rizk and modified Rizk models are not suitable for the combustion chamber under scrutiny, mainly due to the unmixedness parameter included in those models, and the chamber being fully premixed.

Reactor Network Modelling Analyses

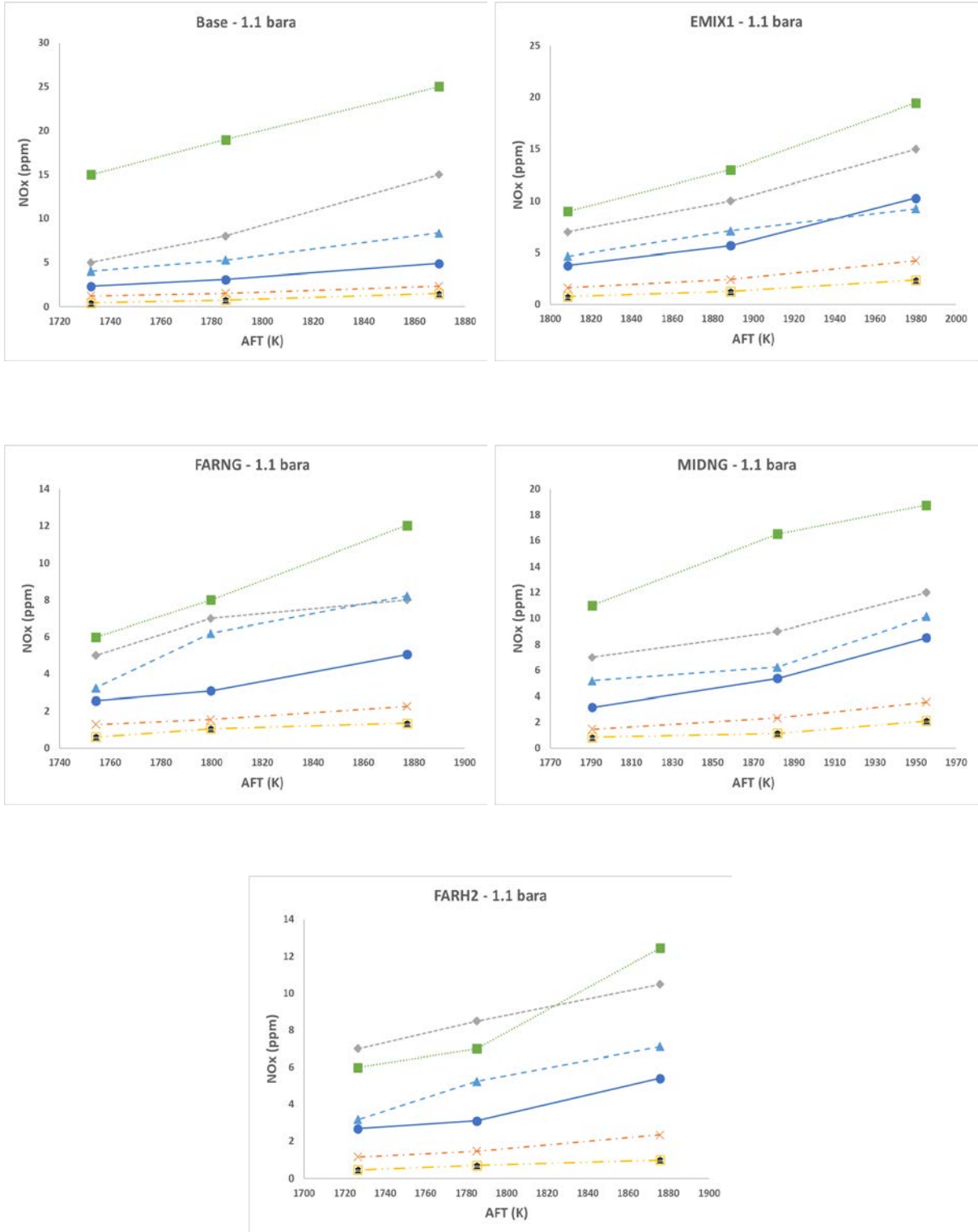
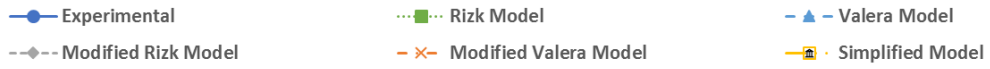


Figure 4-6: Comparison of reactor models at 1.1 bara

Table 4-1: Differences in predictions by the models compared to the experimental results

Test Point	Eq. Ratio (Φ)	PR	AFT (K)	Percentage (%) Change – in decimal				
				Rizk Model	Valera Model	Mod. Rizk Model	Mod. Valera Model	Simplified Model
BASE-CQ-8-8	0.6	1.1	1869.7	4.14	0.72	2.09	-0.52	-0.69
BASE-CQ-8-9	0.55	1.1	1785.5	5.15	0.70	1.59	-0.50	-0.76
BASE-CQ-8-11	0.5	1.1	1732.4	5.47	0.73	1.16	-0.46	-0.81
BASE-CQ-8-12	0.6	2.2	1873.7	4.02	0.76	1.86	-0.07	-0.37
BASE-CQ-8-13	0.55	2.2	1782.6	4.28	0.91	1.80	-0.11	-0.69
BASE-CQ-8-14	0.531	2.2	1749.3	3.32	0.54	0.44	-0.14	-0.70
BASE-CQ-8-17	0.6	3.3	1875.9	3.82	0.79	2.21	0.21	-0.40
BASE-CQ-8-18	0.55	3.3	1794.2	4.73	1.30	1.23	0.11	-0.52
BASE-CQ-8-19	0.533	3.3	1753.5	3.96	0.36	1.02	-0.01	-0.63
EMIX1-CQ-8-1	0.65	1.1	1980	0.89	-0.10	0.46	-0.59	-0.77
EMIX1-CQ-8-2	0.6	1.1	1888.7	1.29	0.25	0.76	-0.57	-0.78
EMIX1-CQ-8-3	0.55	1.1	1808.4	1.38	0.23	0.85	-0.58	-0.80
EMIX1-CQ-8-5	0.653	2.2	1981.5	1.54	0.41	0.55	-0.08	-0.64
EMIX1-CQ-8-6	0.6	2.2	1899.4	2.49	0.43	0.53	-0.13	-0.65
EMIX1-CQ-8-7	0.55	2.2	1813.1	3.71	0.66	1.02	-0.20	-0.75
EMIX1-CQ-8-9	0.65	3.3	1973.1	1.53	0.47	0.57	0.27	-0.44
EMIX1-CQ-8-10	0.6	3.3	1888	2.66	0.53	1.54	0.20	-0.49
EMIX1-CQ-8-11	0.55	3.3	1793	4.60	1.10	3.13	0.15	-0.38
EMIX1-CQ-8-12	0.525	3.3	1748.2	5.18	0.63	2.47	0.15	-0.62
FARNG-CQ-8-1	0.6	1.1	1877.1	1.38	0.62	0.58	-0.55	-0.73
FARNG-CQ-8-2	0.55	1.1	1799.7	1.59	1.01	1.27	-0.50	-0.66
FARNG-CQ-8-3	0.527	1.1	1754.2	1.34	0.27	0.95	-0.50	-0.77
FARNG-CQ-8-5	0.6	2.2	1889	4.18	0.56	2.44	-0.05	-0.52
FARNG-CQ-8-6	0.55	2.2	1794.5	4.17	0.65	1.30	-0.04	-0.47
FARNG-CQ-8-7	0.532	2.2	1763.2	2.73	0.06	0.36	-0.06	-0.77

Reactor Network Modelling Analyses

FARNG-CQ-8-9	0.6	3.3	1876.2	2.95	0.56	1.51	0.21	-0.51
FARNG-CQ-8-11	0.55	3.3	1792.7	3.90	0.99	2.17	0.12	-0.46
FARNG-CQ-8-13	0.531	3.3	1758.9	3.58	1.03	2.33	0.37	-0.53
MIDNG-CQ-8-1	0.642	1.1	1955.33	1.20	0.19	0.41	-0.58	-0.75
MIDNG-CQ-8-2	0.6	1.1	1881.84	2.07	0.16	0.68	-0.57	-0.79
MIDNG-CQ-8-3	0.55	1.1	1790.65	2.49	0.65	1.22	-0.54	-0.73
MIDNG-CQ-8-5	0.646	2.2	1962.09	1.86	0.39	0.65	-0.11	-0.51
MIDNG-CQ-8-6	0.6	2.2	1881.95	2.04	0.40	1.24	-0.11	-0.50
MIDNG-CQ-8-7	0.55	2.2	1791.18	1.69	0.63	2.23	-0.15	-0.66
MIDNG-CQ-8-8	0.53	2.2	1756.71	1.26	0.52	1.90	-0.16	-0.68
MIDNG-CQ-8-10	0.65	3.3	1966.96	0.82	0.59	0.30	0.32	-0.37
MIDNG-CQ-8-11	0.6	3.3	1874.55	2.35	0.92	1.23	0.24	-0.42
MIDNG-CQ-8-12	0.55	3.3	1790.82	2.41	1.42	1.79	0.16	-0.44
MIDNG-CQ-8-13	0.529	3.3	1753.93	2.04	0.81	1.66	0.13	-0.62
FARH2-CQ-8-1	0.6	1.1	1875.7	1.30	0.31	0.94	-0.57	-0.82
FARH2-CQ-8-2	0.55	1.1	1785.2	1.25	0.68	1.73	-0.53	-0.78
FARH2-CQ-8-3	0.5	1.1	1726.5	1.23	0.18	1.60	-0.57	-0.83
FARH2-CQ-8-6	0.6	2.2	1874.9	4.00	0.41	1.74	-0.15	-0.65
FARH2-CQ-8-7	0.55	2.2	1792.6	3.07	0.65	1.44	-0.15	-0.73
FARH2-CQ-8-8	0.5	2.2	1732.8	3.14	0.61	0.88	-0.17	-0.94
FARH2-CQ-8-10	0.6	3.3	1872.8	3.78	0.56	1.79	0.31	-0.35
FARH2-CQ-8-11	0.55	3.3	1785.6	3.74	0.81	3.01	0.30	-0.36
FARH2-CQ-8-12	0.5	3.3	1705.6	3.00	0.78	1.86	0.27	-0.86

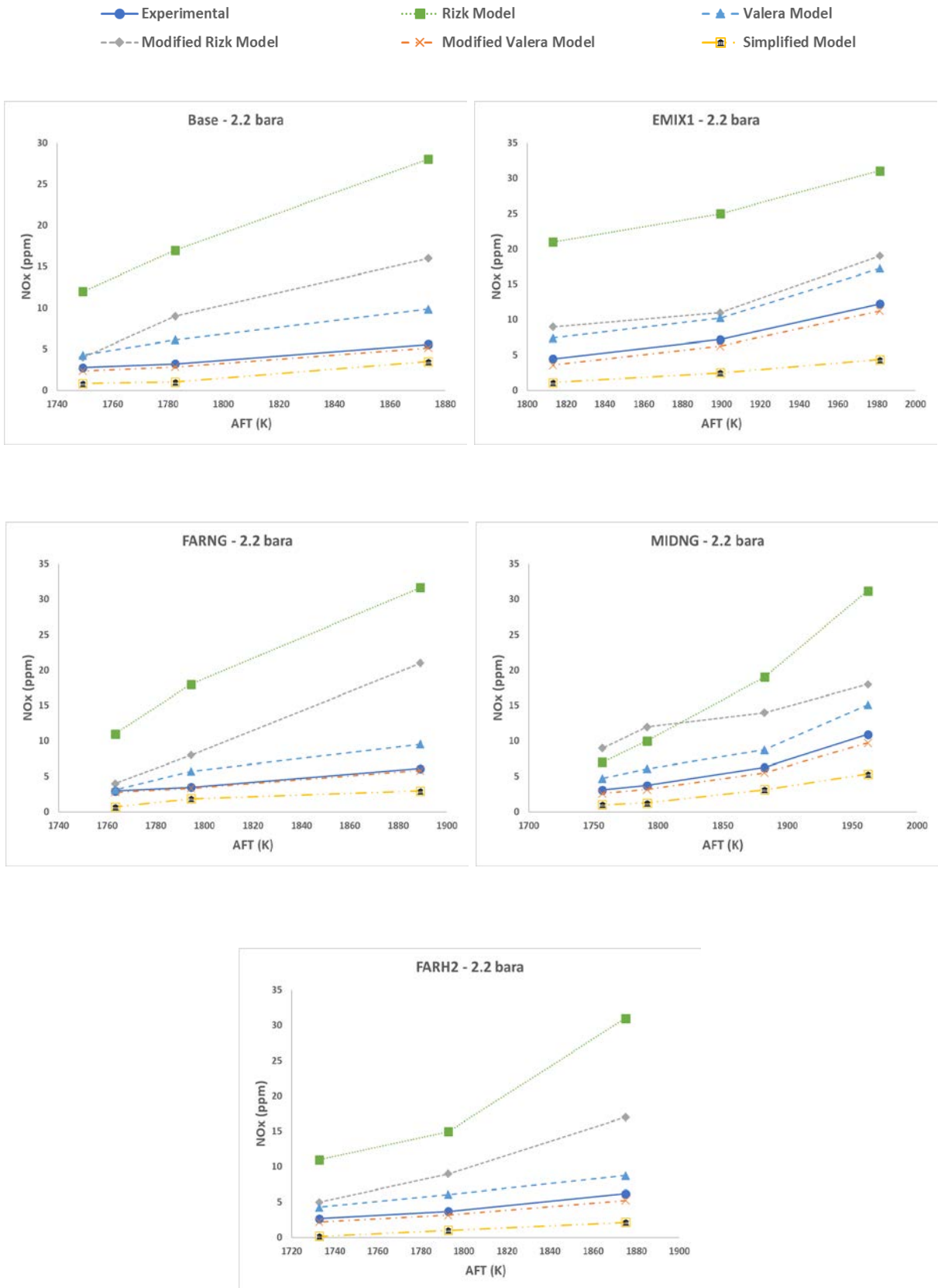


Figure 4-7: Comparison of reactor models at 2.2 bara

Reactor Network Modelling Analyses

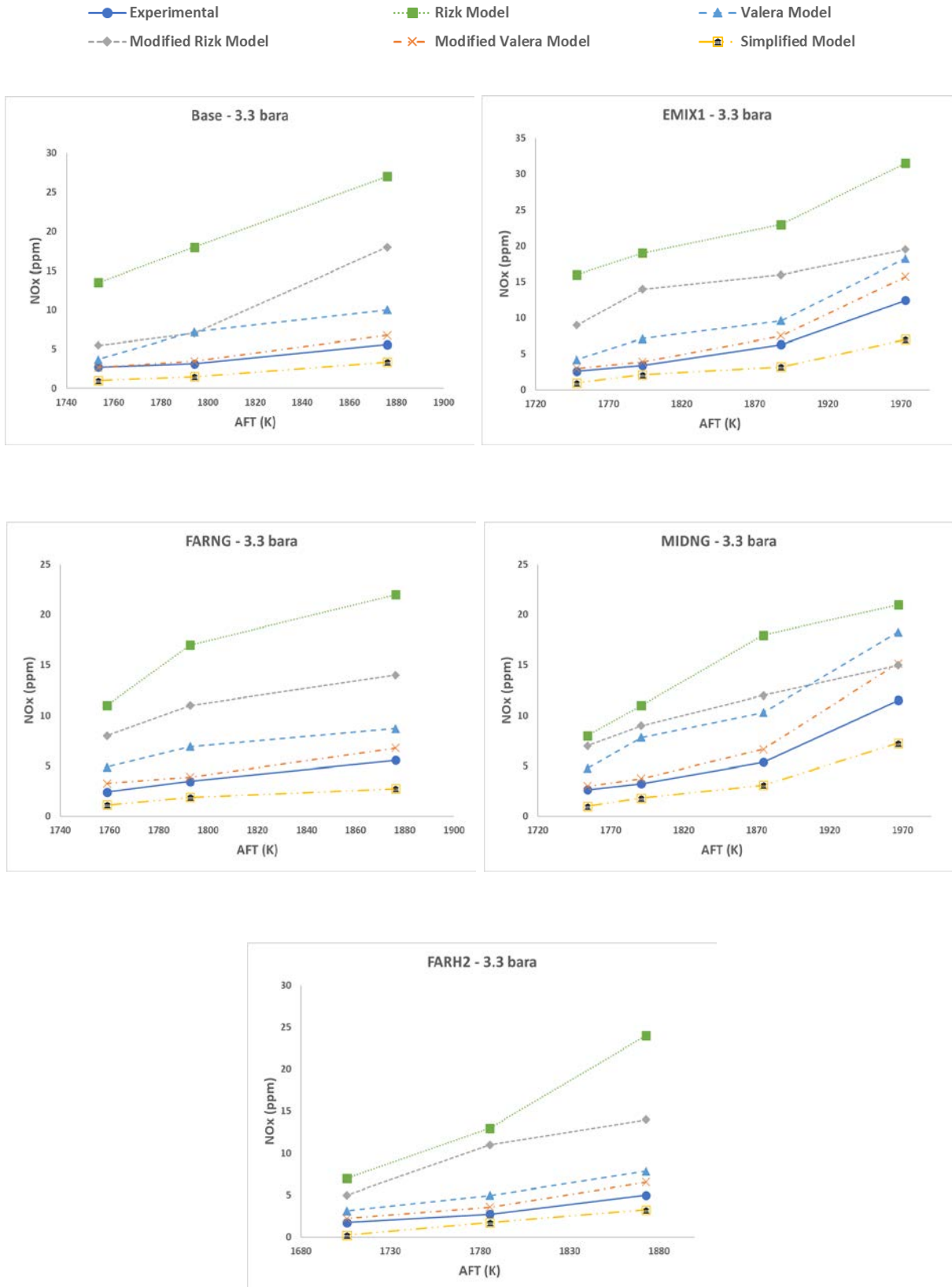


Figure 4-8: Comparison of reactor models at 3.3 bara

4.4. Comparison of Mechanisms

The modified Valera model is used to compare the seven mechanisms mentioned in Section 4.1 (GRI-Mech 3.0, Aramco 1.3, CRECK, SanDiego, USII, Ranzi-Paolo, NUIGalway) with the fuel blends mentioned in Chapter 3.8.1 (Base, EMIX1, FARNG, MIDNG, FARH₂) for this study. This section will analyse NO_x predictions from all these mechanisms in the five different fuel blends (preheated to 573K) at three different pressure conditions (1.1, 2.2 and 3.3 bara). As discussed in Chapter 2.1, NO_x formations are dependent on pressure conditions. Hence, pressure is selected as an independent variable for NO_x predictions comparison in this study. The experimental results are then compared to model predictions. All the NO_x values are corrected to the equivalent dry conditions and then normalized to a reference value of 15% O₂ concentrations as per Equations [3-3] and [3-4].

Table 4-2: Heat loss rates for different zones

Zone	Heat loss rate (J/sec)
Mixing	100
Flame	6850
CRZ	1370
ERZ	342

As discussed in Chapter 2.1, NO_x formation by any pathways are dependent on flame temperature. Hence, the importance of the heat loss rate to the surroundings through the quartz confinement is paramount as this could reduce the flame temperature significantly. However, it was not possible to quantify the heat loss rates in the experiments. As a consequence, heat loss rates were set to match the experimental NO_x emissions at one condition and presumed to be constant for all the other simulations. Heat loss rate for all four PSRs (Premixed, Flame, CRZ and ERZ) in the model were set according to Table 4-2 to match the experimental NO_x value of Base (100% CH₄) at 3.3 bara, $\Phi = 0.5$ using GRI-Mech 3.0. For the purpose of the following

analysis, these values were assumed to be constant for all other investigated conditions with different mechanisms.

NO_x predictions from all the mechanisms are compared and analysed against the experimental concentrations in the following sub-sections. Table 4-3 shows the percentages differences in decimal by the mechanisms compared to the experimentally derived data.

4.4.1. 1.1 bara conditions

Figure 4-9 plots NO_x predictions and experimental results against AFT for all the fuel blends at 1.1 bara. The following results can be seen from Figure 4-9:

- NO_x predictions from each mechanism shows upward trends with increasing AFT due to increasing thermal NO production. GRI-Mech 3.0 underpredicts NO_x for all the fuel blends at 1.1 bara by about 50-55%. Aramco 1.3 predictions were very close to the experimental values at 1.1 bara across all fuel blends. It underpredicts Base and FARH2 NO_x concentrations by 8-22%, while predictions for all the other higher hydrocarbon blends are very close to the experimental NO_x values. This agrees with the fact that Aramco 1.3 mechanism was based on higher hydrocarbons. CRECK underpredicts NO_x values for Base by a factor eight (87%). However, NO_x values for all the other fuel blends are underpredicted by about 20-30%. SanDiego, being a low-cost mechanism, predicts the NO_x concentrations quite well across the fuel blends (underpredicts by 9% for FARNG and about 15-20% for all the other blends). USII, by far gives the best NO_x predictions among all the other mechanisms at 1.1 bara. NO_x values for every point at 1.1 bara with USII are within 4-8% of the experimental results. The Ranzi-Paolo mechanism gives good predictions for FARH2 and MIDNG blends among other blends, overpredicting NO_x values by 10-20% and 20-30% respectively. It underpredicts NO_x value for Base by nearly 80%, while overpredicts EMIX1 and FARNG NO_x concentrations by 20-30% and 40-60% respectively. The final mechanism, NUIGalway exhibits lowest NO_x values predictions

amongst all the other mechanisms across all the fuel blends except Base at 1.1 bara.

- Changing the fuel blend from Base to EMIX1, for equivalence ratios of 0.6 and 0.55, experimental NO_x values increases by about 17% and 22%, respectively. Aramco 1.3, SanDiego, USII and NUIGalway mechanisms predict similar increase in NO_x concentrations. The predicted increase for GRI-Mech 3.0 and CRECK mechanisms for both these cases are approximately by factors of one and seven, respectively. The Ranzi-Paolo mechanism shows increase by factors of 1.45 and 8.89 for equivalence ratios of 0.6 and 0.55, respectively.
- The predicted increase from Base to FARH2 fuel blend by the CRECK mechanism by factors of six for equivalence ratio of 0.65. This is much higher than experimental increase by factor of one. However, NO_x predictions by CRECK mechanism is much closer to the experimental concentrations for FARH2 blend than it is for Base fuel blend. The percentage increase predicted by Aramco 1.3, SanDiego, USII and NUIGalway mechanisms agree closely to the experimental increase of 12%.
- The experimental increase of NO_x concentrations from Base to MIDNG and FARNG are approximately 10% and 4%, respectively for equivalence ratio of 0.6. The percentage increase predictions from Aramco 1.3, SanDiego, USII and NUIGalway mechanisms matches quite closely to the experimental increase from Base to MIDNG.

Reactor Network Modelling Analyses

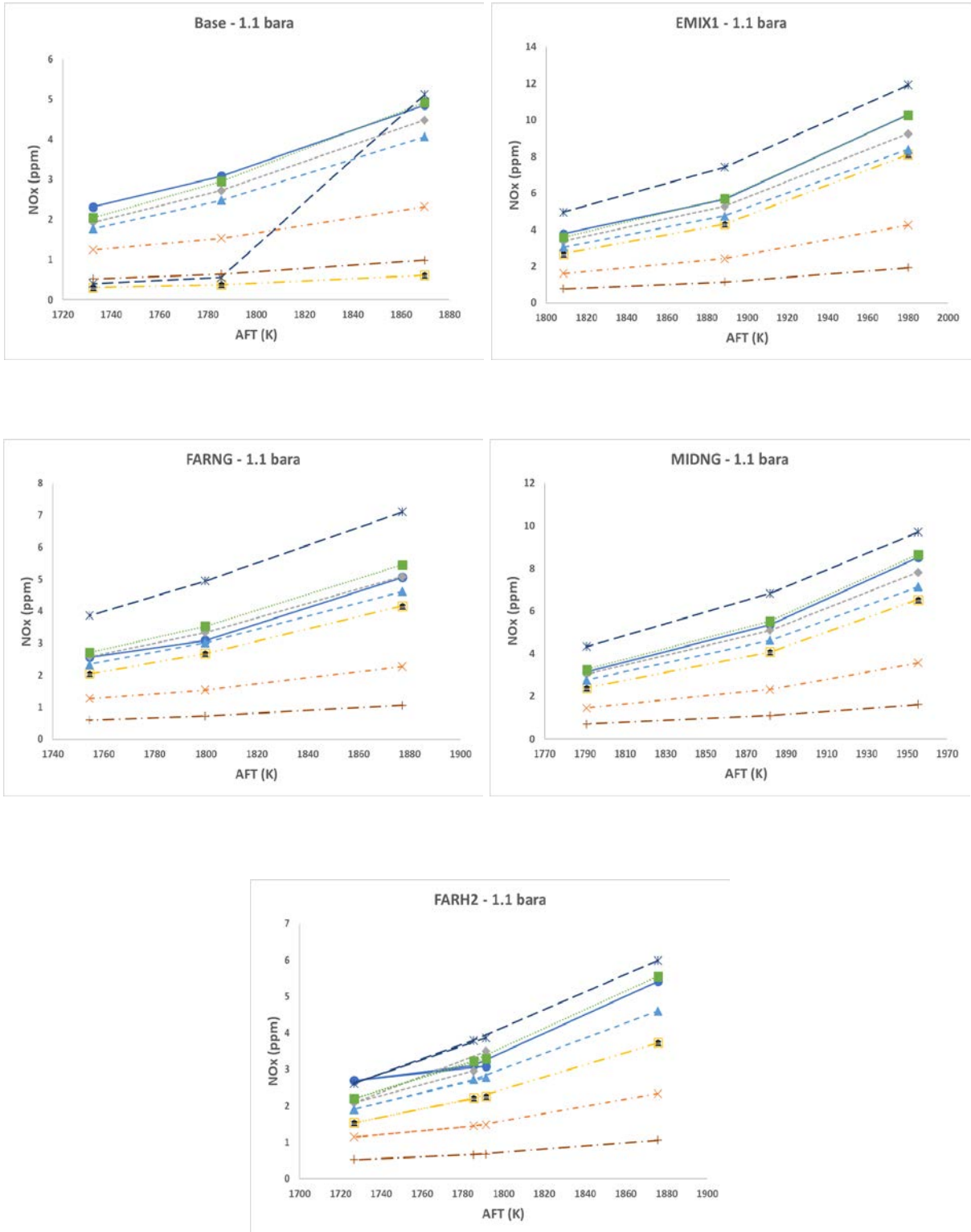


Figure 4-9: Comparison of NO_x predictions at 1.1 bara

Table 4-3: Differences in predictions by the mechanisms compared to the experimental results

Test Point	Eq. Ratio (Φ)	PR	AFT (K)	Percentage (%) Change – in decimal						
				GRI-MECH 3.0	Aramco 1.3	CRECK	SanDiego	USII	Ranzi-Paolo	NUIGalway
BASE-CQ-8-8	0.6	1.1	1869.7	-0.52	-0.08	-0.87	-0.16	0.01	0.05	-0.80
BASE-CQ-8-9	0.55	1.1	1785.5	-0.50	-0.12	-0.88	-0.20	-0.04	-0.82	-0.79
BASE-CQ-8-11	0.5	1.1	1732.4	-0.46	-0.17	-0.87	-0.23	-0.12	-0.83	-0.78
BASE-CQ-8-12	0.6	2.2	1873.7	-0.07	0.08	0.26	0.74	0.80	-0.60	-0.65
BASE-CQ-8-13	0.55	2.2	1782.6	-0.11	0.82	-0.78	0.67	0.75	-0.70	-0.69
BASE-CQ-8-14	0.531	2.2	1749.3	-0.14	0.65	-0.80	0.51	0.69	-0.74	-0.71
BASE-CQ-8-17	0.6	3.3	1875.9	0.21	0.67	-0.56	0.99	1.10	-0.45	-0.52
BASE-CQ-8-18	0.55	3.3	1794.2	0.11	1.40	0.42	0.99	1.09	-0.59	-0.59
BASE-CQ-8-19	0.533	3.3	1753.5	-0.01	-0.53	-0.73	0.81	0.93	0.14	-0.65
EMIX1-CQ-8-1	0.65	1.1	1980	-0.59	-0.10	-0.21	-0.18	0.00	0.16	-0.81
EMIX1-CQ-8-2	0.6	1.1	1888.7	-0.57	-0.07	-0.24	-0.16	0.01	0.31	-0.80
EMIX1-CQ-8-3	0.55	1.1	1808.4	-0.58	-0.11	-0.29	-0.20	-0.05	0.31	-0.80
EMIX1-CQ-8-5	0.653	2.2	1981.5	-0.08	0.95	-0.60	0.70	0.91	0.76	0.85
EMIX1-CQ-8-6	0.6	2.2	1899.4	-0.13	0.85	-0.73	0.62	0.77	-0.61	-0.66
EMIX1-CQ-8-7	0.55	2.2	1813.1	-0.20	0.69	-0.80	0.50	0.65	0.54	0.58
EMIX1-CQ-8-9	0.65	3.3	1973.1	0.27	1.54	-0.31	1.20	1.45	1.67	-0.36
EMIX1-CQ-8-10	0.6	3.3	1888	0.20	1.54	-0.54	1.18	1.32	-0.43	1.32
EMIX1-CQ-8-11	0.55	3.3	1793	0.15	1.44	-0.68	1.14	1.27	-0.60	-0.60
EMIX1-CQ-8-12	0.525	3.3	1748.2	0.15	1.40	0.66	1.14	1.33	-0.64	-0.62
FARNG-CQ-8-1	0.6	1.1	1877.1	-0.55	0.01	-0.18	-0.09	0.08	0.40	-0.79
FARNG-CQ-8-2	0.55	1.1	1799.7	-0.50	0.08	-0.13	-0.02	0.14	0.60	-0.76
FARNG-CQ-8-3	0.527	1.1	1754.2	-0.50	0.01	-0.20	-0.09	0.06	0.51	-0.77
FARNG-CQ-8-5	0.6	2.2	1889	-0.05	1.07	0.68	0.83	0.95	-0.59	0.89
FARNG-CQ-8-6	0.55	2.2	1794.5	-0.04	1.05	0.50	0.83	0.99	-0.68	0.84
FARNG-CQ-8-7	0.532	2.2	1763.2	-0.06	0.99	-0.79	0.79	0.98	-0.71	0.79

Reactor Network Modelling Analyses

FARNG-CQ-8-9	0.6	3.3	1876.2	0.21	1.60	-0.56	1.27	1.30	1.04	1.33
FARNG-CQ-8-11	0.55	3.3	1792.7	0.12	1.42	-0.70	1.14	1.19	-0.62	-0.62
FARNG-CQ-8-13	0.531	3.3	1758.9	0.37	1.88	-0.67	1.58	1.68	-0.59	-0.57
MIDNG-CQ-8-1	0.642	1.1	1955.33	-0.58	-0.08	-0.23	-0.16	0.02	0.14	-0.81
MIDNG-CQ-8-2	0.6	1.1	1881.84	-0.57	-0.05	-0.24	-0.14	0.03	0.27	-0.80
MIDNG-CQ-8-3	0.55	1.1	1790.65	-0.54	-0.03	-0.24	-0.12	0.04	0.38	-0.78
MIDNG-CQ-8-5	0.646	2.2	1962.09	-0.11	0.91	-0.63	0.67	0.85	0.61	-0.61
MIDNG-CQ-8-6	0.6	2.2	1881.95	-0.11	0.91	-0.73	0.68	0.82	-0.61	-0.66
MIDNG-CQ-8-7	0.55	2.2	1791.18	-0.15	0.78	-0.79	0.59	0.75	-0.71	-0.71
MIDNG-CQ-8-8	0.53	2.2	1756.71	-0.16	0.74	-0.80	0.57	0.76	-0.74	-0.71
MIDNG-CQ-8-10	0.65	3.3	1966.96	0.32	1.62	-0.28	1.27	1.48	1.57	1.46
MIDNG-CQ-8-11	0.6	3.3	1874.55	0.24	1.63	-0.54	1.28	1.36	-0.42	1.18
MIDNG-CQ-8-12	0.55	3.3	1790.82	0.16	1.46	-0.68	1.18	1.26	-0.59	-0.59
MIDNG-CQ-8-13	0.529	3.3	1753.93	0.13	1.37	-0.71	1.13	1.26	-0.64	-0.62
FARH2-CQ-8-1	0.6	1.1	1875.7	-0.57	-1.00	-0.31	-0.15	0.03	0.11	-0.80
FARH2-CQ-8-2	0.55	1.1	1785.2	-0.53	-0.05	-0.29	-0.12	0.04	0.22	-0.79
FARH2-CQ-8-3	0.5	1.1	1726.5	-0.57	-0.22	-0.43	-0.29	-0.18	-0.03	-0.80
FARH2-CQ-8-5	0.55	1.1	1791.4	-0.52	0.13	-0.27	-0.10	0.07	0.25	-0.78
FARH2-CQ-8-6	0.6	2.2	1874.9	-0.15	0.80	-0.73	0.59	0.73	-0.62	-0.67
FARH2-CQ-8-7	0.55	2.2	1792.6	-0.15	0.77	-0.79	0.59	0.74	-0.70	0.73
FARH2-CQ-8-8	0.5	2.2	1732.8	-0.17	0.69	-0.81	0.54	0.74	0.29	0.65
FARH2-CQ-8-10	0.6	3.3	1872.8	0.31	0.05	-0.48	1.35	1.47	0.88	-0.44
FARH2-CQ-8-11	0.55	3.3	1785.6	0.30	1.74	-0.62	1.41	1.52	-0.52	-0.53
FARH2-CQ-8-12	0.5	3.3	1705.6	0.27	1.53	0.59	1.35	1.57	-0.63	-0.59

4.4.2. 2.2 bara conditions

This sub-section will analyse NO_x concentration predictions from seven mechanisms with experimental values. As shown in Figure 4-10, the fifth model with the various mechanisms provides the following results at 2.2 bara:

- The GRI-Mech 3.0 mechanism predicts NO_x concentrations very closely to the experimental values across all the fuel blends at 2.2 bara. Overall, this mechanism underpredicts the experimental concentrations only by 5-10% for all the fuel blends except FARH2, which is underpredicted by 15%.
- All the C1-C4 hydrocarbons mechanisms, namely, Aramco 1.3, SanDiego and USII depict similar upward trend for NO_x concentrations as the AFT increases for all the fuel blends. Their predicted NO_x values are in very close range to each other (within +/- 5-8%) for all the fuel blends except for Base at the highest AFT, where the Aramco 1.3 mechanism NO_x deviate from the other two mechanisms by 18%, getting very closer to the experimental NO_x concentration of 5.59 ppm at 0.6 equivalence ratio. However, all these mechanisms overpredict the NO_x concentrations by a factor of two.
- For FARNG fuel blend, the CRECK mechanism underpredicts NO_x concentration by 80% at equivalence ratio of 0.5. However, as the AFT increases, the mechanism exhibits overprediction tendency for FARNG blend by 50% and 59% for equivalence ratios of 0.55 and 0.6, respectively. For all the other fuel blends, this mechanism consistently exhibits lowest NO_x concentrations compared to the other mechanisms.

Reactor Network Modelling Analyses

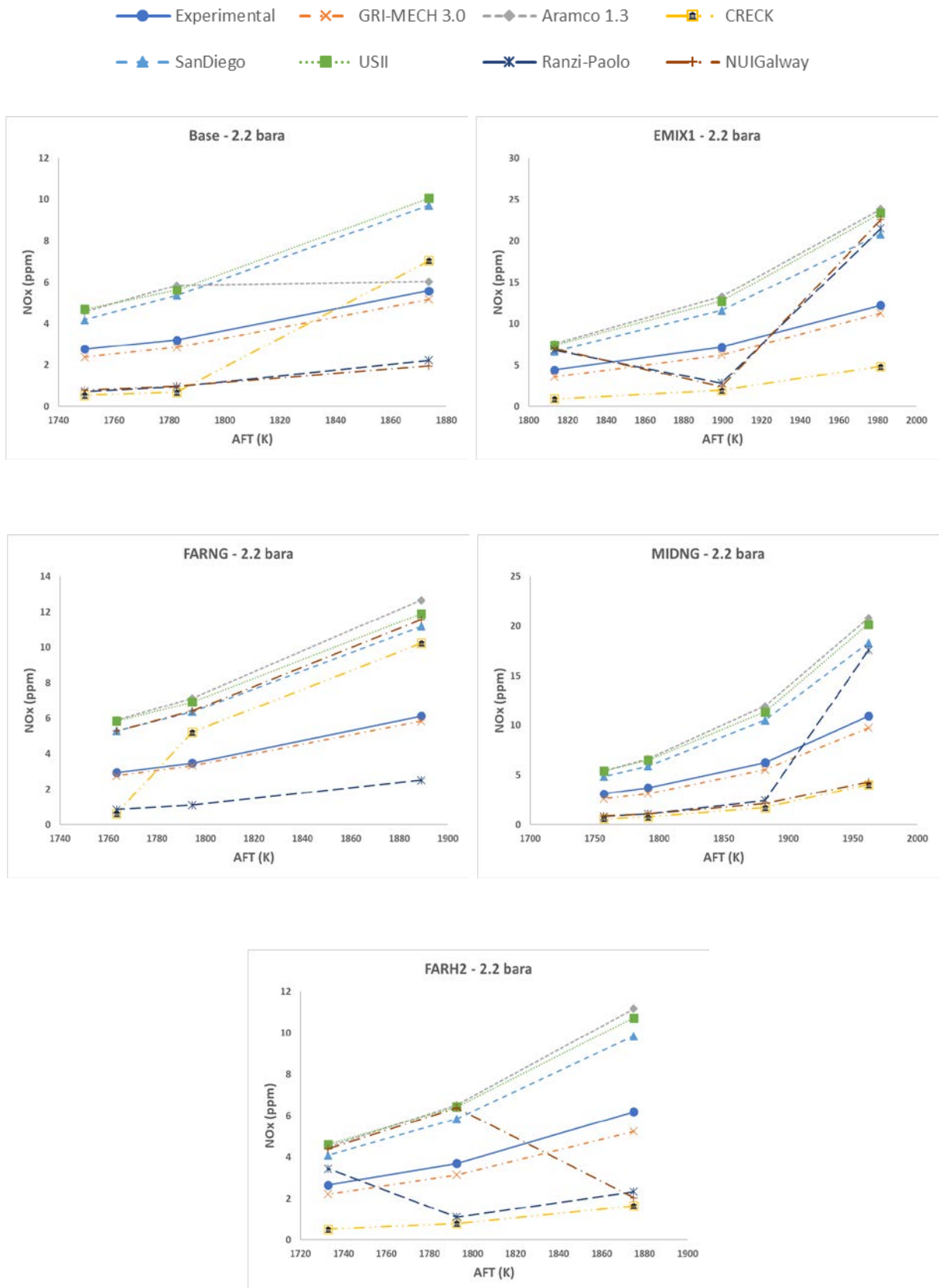


Figure 4-10: Comparison of NO_x predictions at 2.2 bara

- The higher hydrocarbons (more than C4) mechanisms, Ranzi-Paolo and NUIGalway exhibits similar predictions for EMIX1 fuel blend, overpredicting NO_x concentrations by about 80% and 55% for equivalence ratios of 0.65 and 0.55, while underpredicting by 62% for 0.6 equivalence ratio. These two mechanisms also underpredict NO_x values for Base and MIDNG fuel blends by factor of three. The Ranzi-Paolo mechanism underpredicts NO_x values by factor of about three for FARNG blend, while the NUIGalway mechanism overpredicts by factor of two. Interestingly, these two mechanisms show opposite trends for FARH2 fuel blend. As the AFT changes from 1733K to 1793K, Ranzi-Paolo mechanism NO_x prediction decreases while NUIGalway shows increased prediction. However, when AFT increases from 1793K to 1875K, both the mechanisms show opposite predictions.

4.4.3. 3.3 bara conditions

Figure 4-11 illustrates NO_x predictions against increasing AFT for all the fuel blends at 3.3 bara and 573K inlet conditions. The results are compared against each other and the experimental data here:

- For the Base fuel blend at 3.3 bara, the GRI-Mech 3.0, USII, SanDiego and NUIGalway mechanisms predict similar trends for NO_x concentrations as the increasing experimental values with AFT. The GRI-Mech 3.0 predictions are closest to the experimental values among other mechanisms. The SanDiego and USII mechanisms overpredict by a factor of two, while the NUIGalway mechanism underpredicts by factor of about two-three. The CRECK mechanism predictions are similar to the predictions by NUIGalway mechanism at 0.6 and 0.5 equivalence ratios. Same can be said for the Ranzi-Paolo mechanism at equivalence ratios of 0.6 and 0.55.
- Changing the fuel from Base to EMIX1 blend sees the percentage increase of experimental NO_x values by 12% and 7% for the equivalence ratios of 0.6 and 0.55, respectively. Similar

percentage increase is predicted by the GRI-Mech 3.0 and Ranzi-Paolo mechanisms. The GRI-Mech 3.0, Aramco 1.3, SanDiego, USII and CRECK mechanisms shows similar increasing NO_x prediction trend with increasing AFT as the experimental concentrations. The GRI-Mech 3.0 predictions agree closely to the experimental values. The Aramco 1.3, USII and SanDiego mechanisms overpredict NO_x values by factors of overall between two and three.

- NO_x predictions from the GRI-Mech 3.0, SanDiego, USII and NUIGalway mechanisms follows the same trend as experimental results for FARH2 fuel blend. The GRI-Mech 3.0 mechanism predicts NO_x concentrations very closely to the experimental values, overpredicting by 27-30% overall. The SanDiego and USII mechanisms overpredict NO_x concentrations by a factor two to three. Compared to Base fuel blend, NO_x concentrations goes down by 10-12% for FARH2 blend.

- Changing fuel from Base to FARNG and MIDNG, experimental NO_x concentration goes down very slightly (between 1-5%) for equivalence ratios of 0.6 and 0.5 but goes up by 3-8% for 0.55 equivalence ratio. The Aramco 1.3, SanDiego, USII, GRI-Mech 3.0 and CRECK mechanisms predict similar trend as experimental NO_x results. C1-C4 mechanisms, namely Aramco 1.3, SanDiego and USII predictions for both FARNG and MIDNG fuel blends are within 2-5% of each other. The GRI-Mech 3.0 predictions are again the closest to the experimental data for these two fuel blends.

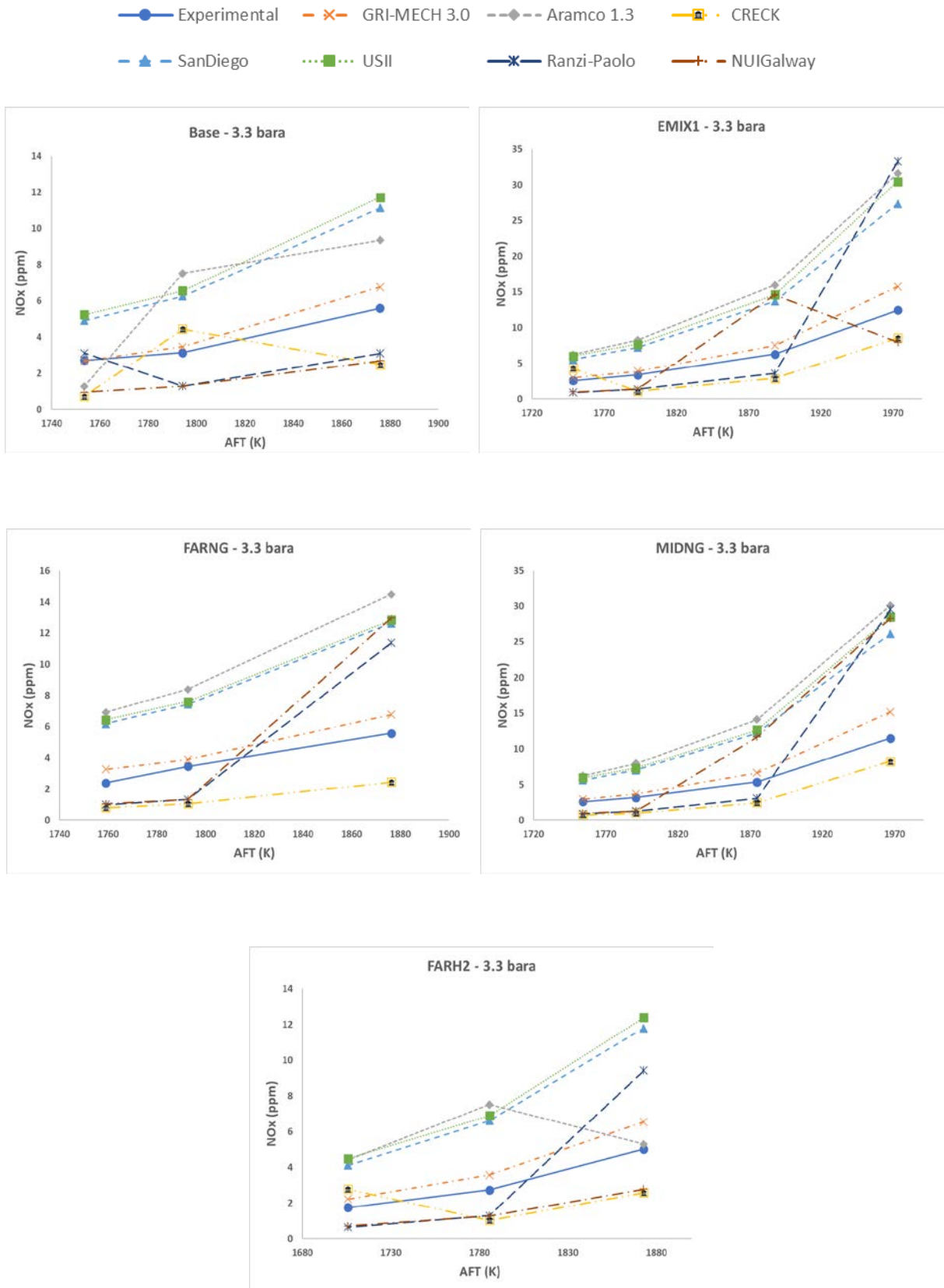


Figure 4-11: Comparison of NO_x predictions at 3.3 bara

4.5. Summary

Various mechanisms and reactor network models are compared to analyse the prediction results with experimental data. Modelling of the HPGSB-2 with the recirculation models provide simple and quick information on the overall behaviour of fuel oxidation and pollutant formation. At the same time, chemical reactor modelling provides many challenges. In particular, accuracies in the kinetic rate constants for both fuel oxidation and pollutant formation must be further improved. The choice and selection of reactor network arrangement may also be significantly enhanced with the aid of more complex computational fluid dynamic models if the combustor to be modelled is not truly perfectly stirred reactor. Nevertheless, chemical reactor modelling provides great insight to the various NO_x formation pathways. Valuable information on the behavioural trends of the various fuels tested can also be obtained. The following summarizes the results from this chapter:

- The chemical reactor models with 'unmixedness' parameter overpredict NO_x concentrations by a significant margin across all the fuel blends and at all conditions. Even after converging the flame zone into a single zone from five zones overpredicts compared to experimental data. The simplest model (third model) follows the same trends as the experimental data but underpredicts NO_x concentrations.
- Results from the recirculation models are much closer to the experimental data. Specially, the modified Valera model where data from CFD analysis are included to enhance the prediction capability, gives close results to experimental data.
- The C1-C4 mechanisms (Aramco 1.3, SanDiego and USII) gives good predictions across all fuel blends at 1.1 bara. At 1.1 bara, all the mechanisms predict similar increasing trend for NO_x as the experimental results. However, as the pressure increases, deviation from the experimental trend is seen for some

mechanisms, specially the high hydrocarbon mechanisms (Ranzi-Paolo and NUIGalway).

- The GRI-Mech 3.0 mechanism gives overall good predictions at 2.2 and 3.3 bara, with the C1-C4 mechanisms giving overall higher predictions and high hydrocarbon mechanisms underpredicting NO_x concentrations compared to the experimental data.

5. Planar NO-LIF in Unconfined Flames

The objective of this Chapter is to probe NO-PLIF measurements and compare how the PLIF measurements compare with the NO formation theories. Intrusive techniques for NO concentration measurements, such as probed or extractive gas sampling, are not well suited to measurements in regions of flames with fine structures such as flame front. Rather, in-situ laser diagnostics offer robust techniques for measuring certain species through LIF with minimal disturbance to the flame. This Chapter discusses NO PLIF measurements to the flame front regions of the 25 mm Bunsen burner and HPGSB-2 burner without confinement. Between these two burner configurations, NO formations in lean and rich conditions are considered. This allows for the consideration of both thermal and non-thermal contributions. Additionally, the non-intrusive nature of this technique allows for a better measurement of the relatively rapid formation of NO in the flame front as a distinct contribution from the thermal mechanism. Chemical kinetics modelling is performed to calculate AFT, laminar flame speed, flame thickness, OH and CH production. These results are used to validate NO formation and heat release within the PLIF images and OH* chemiluminescence images, respectively. Finally, NO formation is predicted and compared with the measured values at the exhaust using the modified Valera model with some changes to accommodate open flame HPOC configuration.

5.1. Bunsen burner NO-PLIF measurements

A 25mm Bunsen burner was used in horizontal and vertical orientations to take NO-PLIF measurements qualitatively. This burner was described in Chapter 3.1. The results from these experiments will be analyzed in this section. It must be noted that no gas analyzer was used for the experiments at 25mm Bunsen burner as the goal here was to commission the NO-PLIF set-up at GTRC.

5.1.1. Horizontal Orientation

Qualitative NO PLIF measurements were first made with a 25 mm diameter Bunsen burner placed horizontally in the Gas Turbine Research

Centre's High Pressure Optical Chamber (HPOC) (refer to Chapter 3.2.1) as shown in Figure 5-1. The flame was asymmetric in this orientation and buoyancy effects were apparent in the flame. However, good evidence of NO production in the flame can be seen in Figure 5-2. The laser sheet was traversed along the flame, cutting the flame in the center line of nozzle and NO fluorescence was averaged over 500 shots for this image. As expected, there is limited NO production in the central cold zone, with NO mainly produced in the surrounding hot flame zone due to thermal and prompt NO.



Figure 5-1: 25 mm Bunsen burner horizontal set-up, as installed (a) and with CH₄-air flame (b)

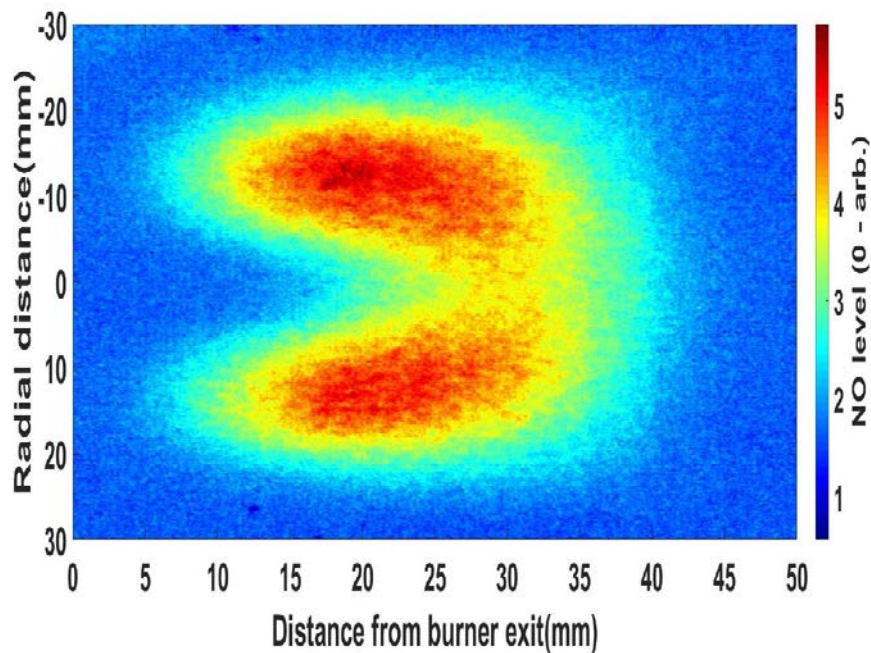


Figure 5-2: In-flame NO-LIF signal without NO seeding (ER - 0.88; 2.28 kW). Flow is from left to right.

5.1.2. Vertical Orientation

The burner was then installed vertically outside the HPOC and operated between equivalence ratios of 1.4 and 1.28 with CH₄/air flame. These rich conditions were chosen as theoretically they produce more NO, hence strong LIF signal. This change in equivalence ratio from $\Phi = 1.4$ to $\Phi = 1.28$ was achieved by decreasing air flow at constant air flow. Thus, as equivalence ratio is decreased, the flame burning velocity increases and gas velocity decreases. Table 5-1 shows the details of flow conditions for this investigation. Heat release level and NO formation at each test point were measured experimentally by OH* chemiluminescence and NO-PLIF, respectively. These results will be discussed in detail in this section. Table 5-1 shows the flow conditions with laminar flame speed values from simulation for this investigation.

Table 5-1: Flow conditions for 25mm Bunsen burner

Test point	CH ₄ mass flow (g/s)	Air mass flow (g/s)	T ₂ (K)	Equivalence ratio (Φ)	AFT (K)	CH ₄ speed (m/s)	Air speed (m/s)	Total flow speed (m/s)	Laminar Flame speed (m/s)
1	0.0538	0.66	298	1.40	1970	0.065	0.441	0.506	0.135
2	0.0519	0.66	298	1.35	2005	0.062	0.441	0.503	0.175
3	0.05	0.66	298	1.30	2044	0.060	0.441	0.501	0.229
4	0.0493	0.66	298	1.28	2059	0.059	0.441	0.5	0.252

5.1.2.1. OH* Chemiluminescence Comparison

Experimental evaluation has been made for CH₄/air flames at 25mm Bunsen burner in fuel rich conditions. Flame stabilization and overall heat release are evaluated based on Abel-transformed OH* chemiluminescence measurements in Figure 5-3 and Figure 5-4. Figure 5-3 and Figure 5-4 shows the Abel-transformed OH* chemiluminescence measurements at varying thermal power and equivalence ratios, indicating the conical flame shape expected in a Bunsen burner such as this. The images were normalized by their respective maximum intensity

value in Figure 5-3 and by the highest measured intensity value across the range in Figure 5-4.

As the flame stabilizes closer to the nozzle and heat release intensity increases between 10 - 20 mm from burner exit as evident by the OH* chemiluminescence in Figure 5-3. There are clear increases in heat release intensity as Φ decreases, which correlates with the maximum OH mole fractions calculated from CHEMKIN simulations in Figure 5-5. The relative increase in O₂ concentration had a significant effect on flame position, causing OH* emission to increase, allowing the flame to attach in the shear zone, correlating with laminar flame velocity presented in Table 5-1. Heat release level is stronger near the nozzle exit for $\Phi = 1.4$, as the equivalence ratio decreases, heat release level gets stronger and form an inverse U shape at $\Phi = 1.28$. This corresponds to the balance between turbulent flame speed and gas speed. As the turbulent flame velocity increases and gas velocity decreases at $\Phi = 1.28$, the flame stabilizes closer to the burner nozzle.

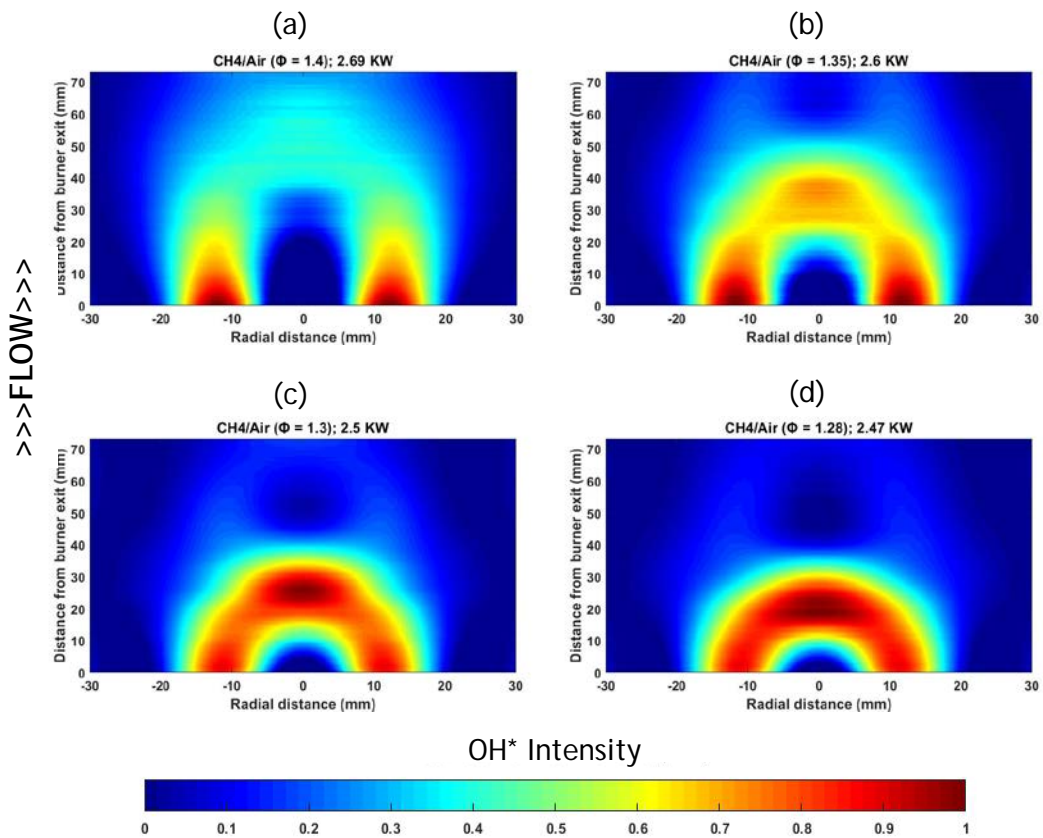


Figure 5-3: Abel-transformed OH* chemiluminescence images (colormap normalised to maximum OH* intensity at each Φ) at varying Φ and fuel input thermal power

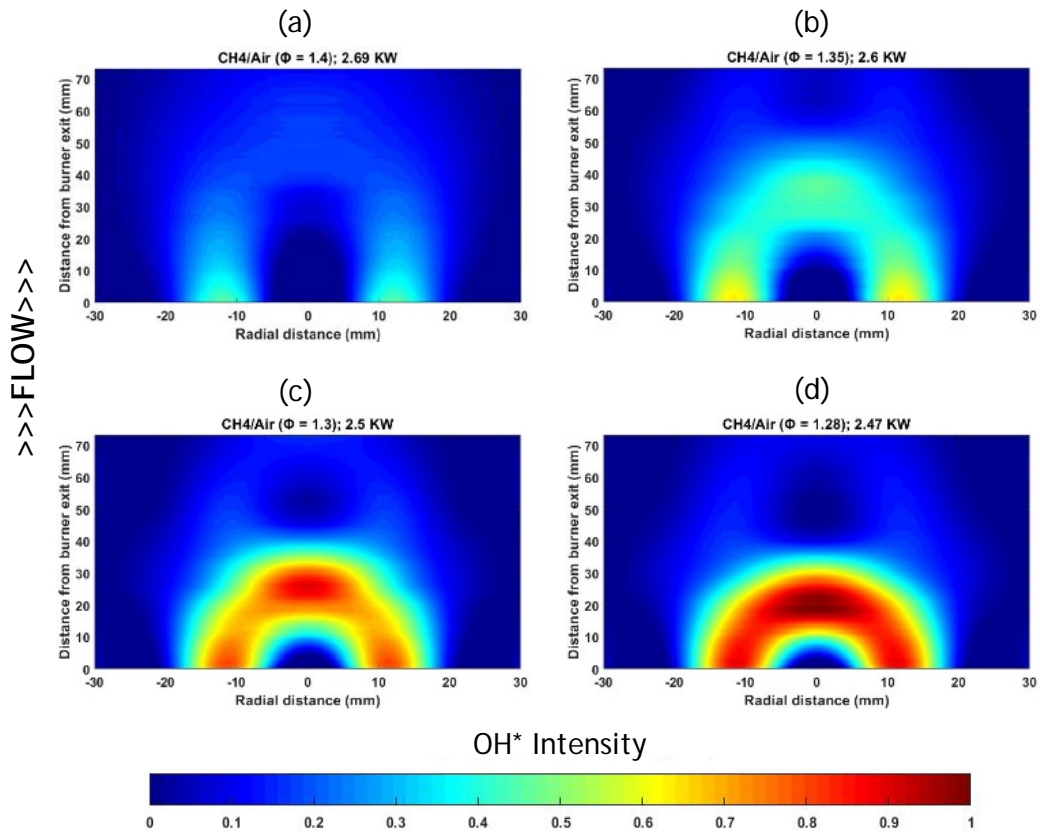


Figure 5-4: Abel-transformed OH* chemiluminescence images (colormap normalised to maximum OH* intensity relative to 2.47 kW thermal power at $\Phi = 1.28$) at varying ER and fuel input thermal power

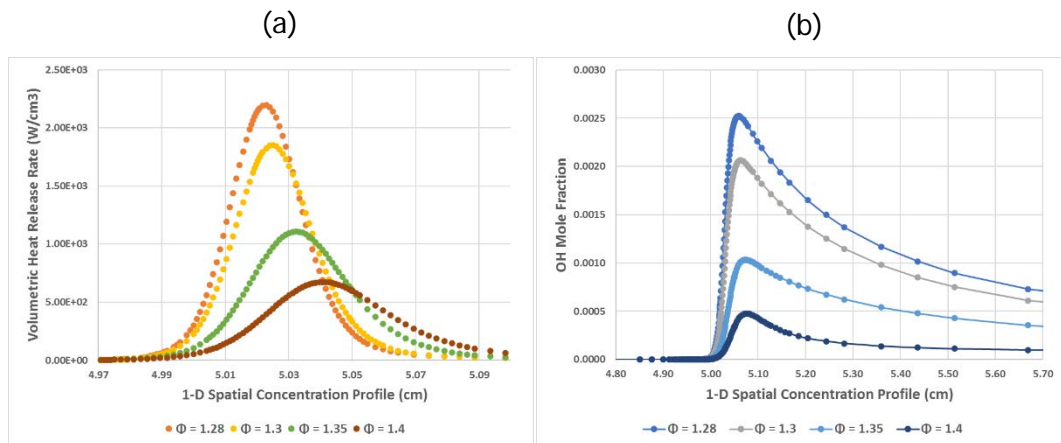


Figure 5-5: CHEMKIN results showing (a) volumetric heat release rate and, (b) OH mole fraction as a function of 1-D spatial concentrations profiles for $\Phi = 1.28 - 1.4$

The relative OH* chemiluminescence intensity from Figure 5-4 shows the increase in intensity as the fuel flow decreases. This is further validated from the CHEMKIN numerical simulation in Figure 5-5, volumetric heat release rate (a) and OH mole fraction (b) increases with relative

increased level of O₂. The location of maximum volumetric heat release rate and OH mole fraction moves further away as Φ increases, which is also evident from the experimental data in Figure 5-3 and Figure 5-4.

The structure of the heat release zones influences the thermoacoustic stability of the flame as the local speed of sound is influenced and the exhaust gas composition, in particular NO_x emissions in which temperature and residence time in areas of highest heat release are of critical considerations.

5.1.2.2. NO PLIF Comparison

The NO PLIF results for the flow conditions in Table 5-1 are presented in Figure 5-6. Each image presented has been normalized against its own image maximum and then fit to the same false colormap to illustrate the location of NO formation clearly. NO formation across the range seems quite similar, with increasing NO formation in the center of the burner as Φ decreases. All the images show strong LIF signal at the center of the flames at the either sides of the centerline. NO LIF signal fades away from the center of the flame due to reduced heat release level.

Figure 5-7 shows the relationship between Φ with average NO PLIF intensity and AFT. Average NO PLIF intensity ($AvgInten_{NO}$) is calculated by summing all the pixel values (I_{NO}) in the image and dividing by the product of number of rows and columns, as per Equation [5-1].

$$AvgInten_{NO} = \frac{\sum_{i=1}^{m} \sum_{j=1}^{n} I_{NO_{i,j}}}{m \times n} \quad [5-1]$$

$AvgInten_{NO}$ increases with AFT and decreases with rich Φ . This agrees with the Zel'dovich Mechanism described in Chapter 2.1.1. As Φ increases, availability of O₂ decreases, which restricts the rate-limiting step in the NO formation process in Equation [2-1]. The rate-limiting step requires the breaking of the tight N₂ bond and as such is favoured to form in high-temperature gases. As a rough guideline, thermal NO formation is usually considered to be unimportant at temperatures below 1800K (refer to Chapter 2.1.1). So, it comes with no surprise that $AvgInten_{NO}$ is lowest at AFT = 1970K.

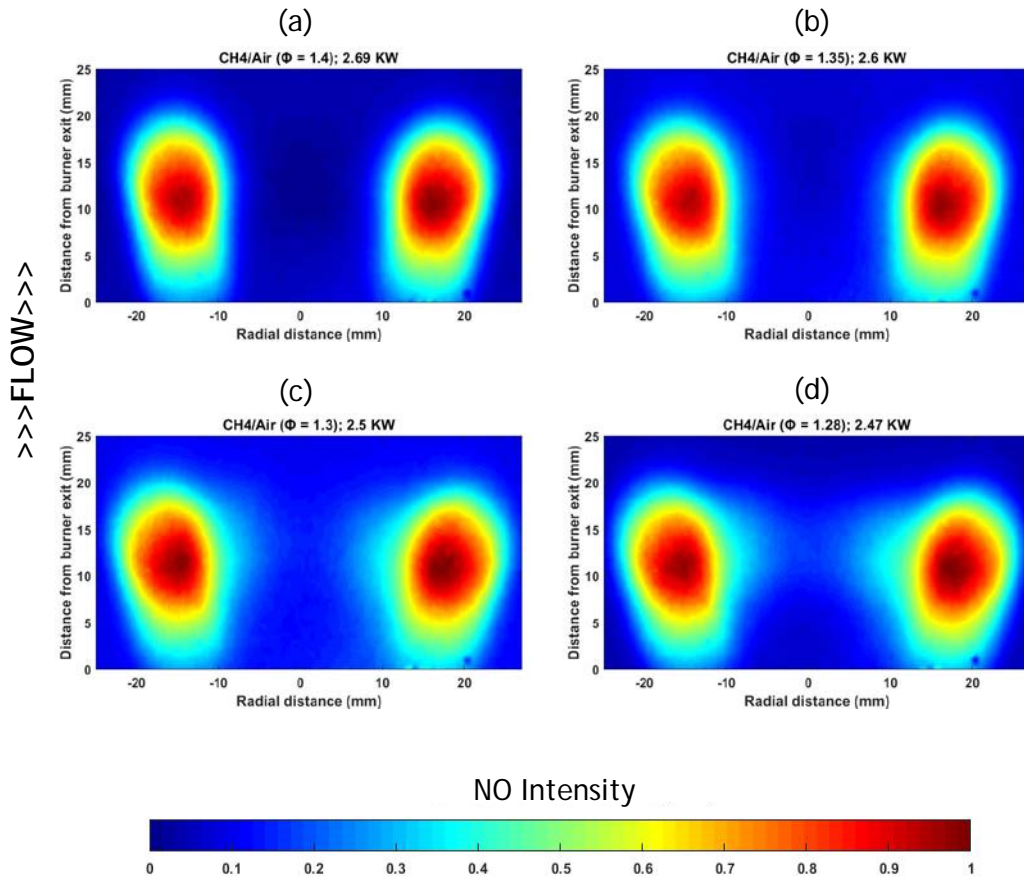


Figure 5-6: NO PLIF images (normalised to maximum intensity at each Φ) at varying Φ and fuel input thermal power

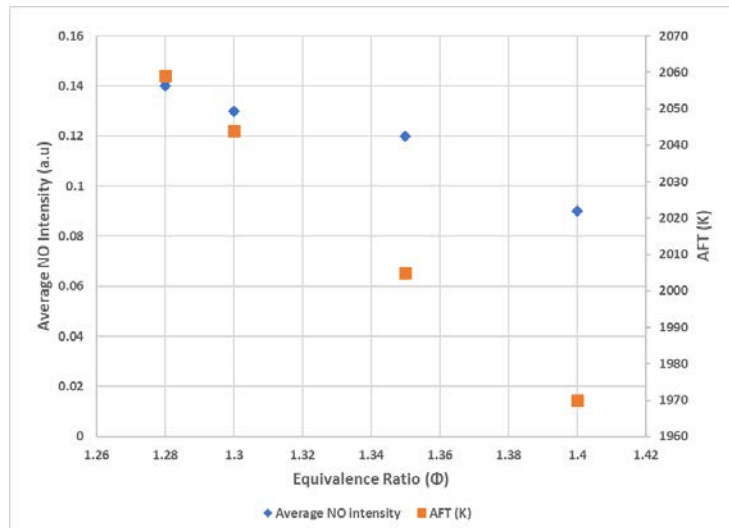


Figure 5-7: Relationship between Φ with average NO intensity and AFT

The prompt NO mechanism was proposed when it was observed that there is substantial NO formation in the upstream, colder part of premixed hydrocarbon flames, where the O atom concentration is relatively low, and the Zel'dovich mechanism cannot fully explain the NO production. It was also observed that the flame front NO formation tends to increase as the unburned mixture becomes fuel rich. This mechanism was described in detail in Chapter 2.1.2. Figure 5-8 plots $AvgInten_{NO}$ against maximum CH mole fraction and volumetric heat release rate derived from CHEMKIN calculations. As expected, $AvgInten_{NO}$ values increase with both maximum CH mole fraction and volumetric heat release level.

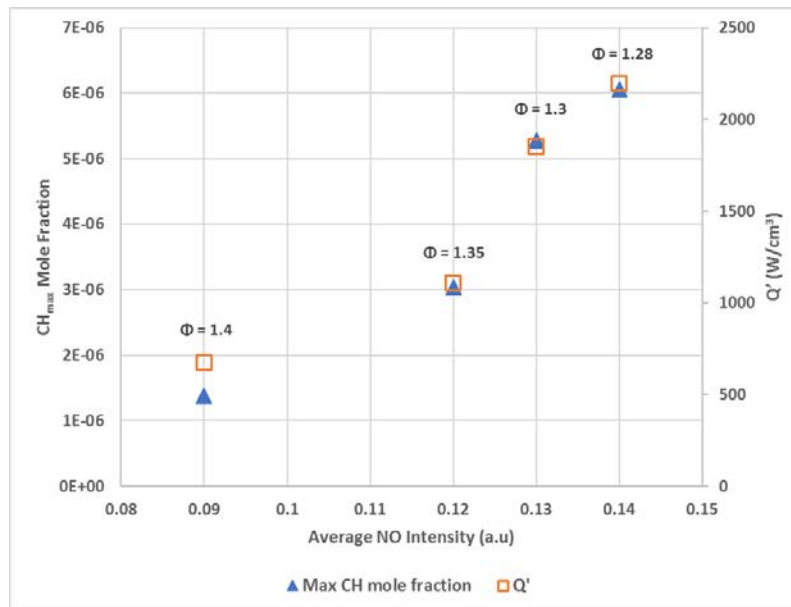


Figure 5-8: Relationship between average NO PLIF intensity with maximum CH mole fraction and volumetric heat release level

It should be noted that maximum CH mole fraction values are decreasing with increasing Φ in Figure 5-8. To examine this further, both maximum CH and CH₂ mole fractions are plotted against Φ in Figure 5-9. Figure 3-21 shows that AFT decreases with increasing Φ . However, activation energy (E_a) increases with Φ beyond stoichiometry. Figure 5-10 shows the relationship between Φ and E_a , this data is taken from a parallel study at Cardiff University [276]. This justifies the decreasing CH and CH₂ molar fraction trend with increasing Φ , even though there is more

fuel in the mixture, low AFT restricts CH and CH₂ production, due to higher temperature needed to reach the required E_a. In the preheated mixture cases, the temperature will be high enough to achieve the required activation energy.

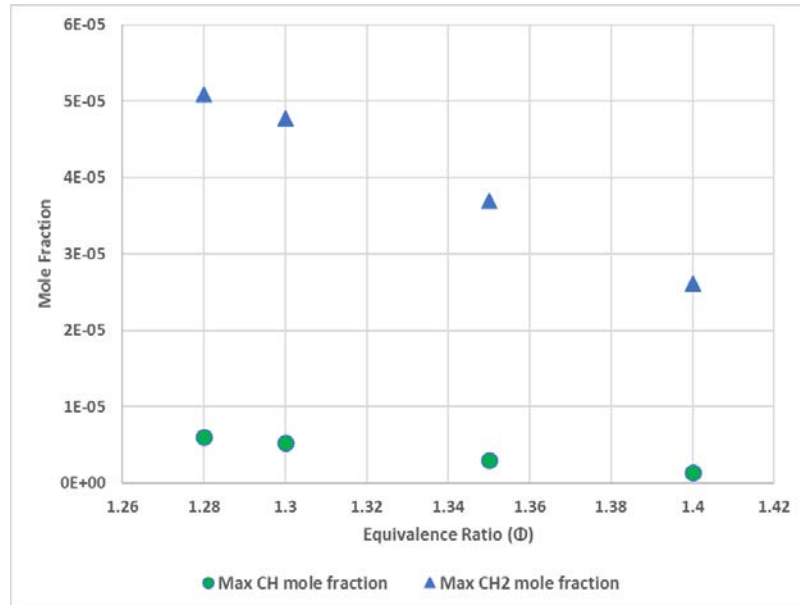


Figure 5-9: Maximum CH and CH₂ mole fraction plotted as a function of Φ

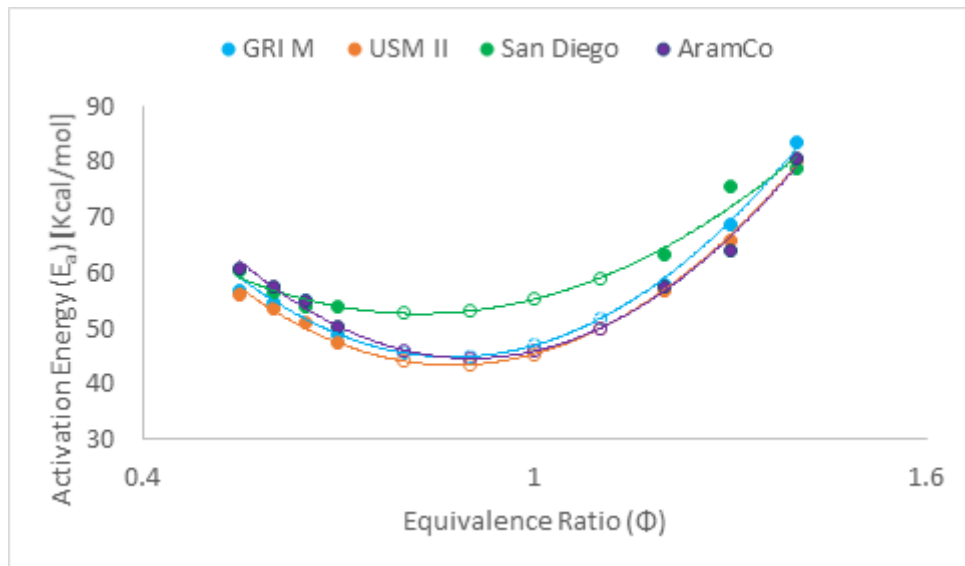


Figure 5-10: Activation energy for CH₄ plotted against Φ . Reproduced from [276].

$AvgInten_{NO}$ is plotted against flame thickness in Figure 5-11. It must be noted that flame thickness calculated from numerical methods (δ_D, δ_G and δ_t) are plotted in the primary axis and experimentally

measured flame brush thickness (δ_{flame}) is plotted on the secondary axis. δ_D , δ_G and δ_{flame} decreases quasi-linearly with increasing $AvgInten_{NO}$ but δ_t increases proportionally with increasing $AvgInten_{NO}$. The reasons behind this trend was analysed earlier in Chapter 3.10.1.3.

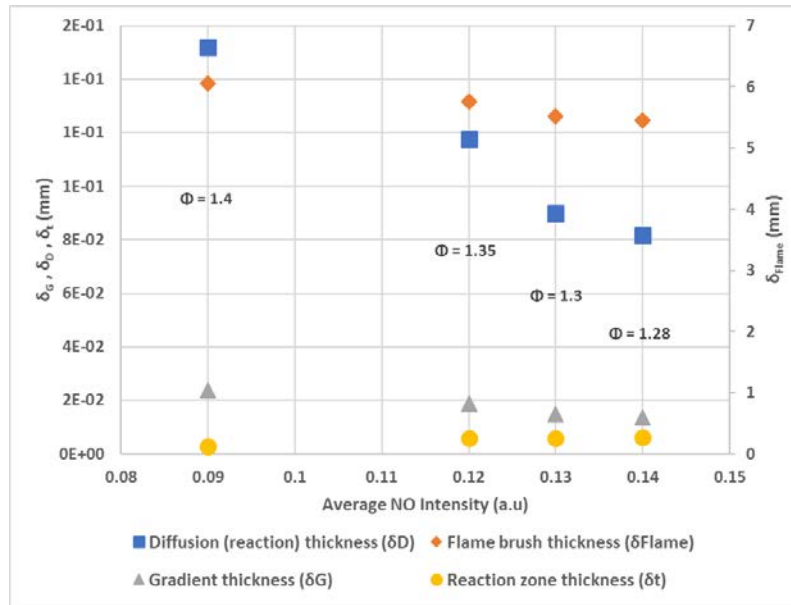


Figure 5-11: Average NO PLIF intensity plotted as a function of flame thickness

Figure 5-12 and 5-13 shows the OH^* chemiluminescence and NO PLIF images side by side for respective conditions with colormap normalized to maximum Φ and to maximum intensity relative to 2.47 kW fuel input thermal power at $\Phi = 1.28$, respectively. Laser sheet path is indicated on the first images (refer to Figure 5-12 (a) and Figure 5-13 (a)) of each figure. Both horizontal and vertical axes limits are identical for OH^* chemiluminescence and NO PLIF images to compare the relationship between NO formation and heat release.

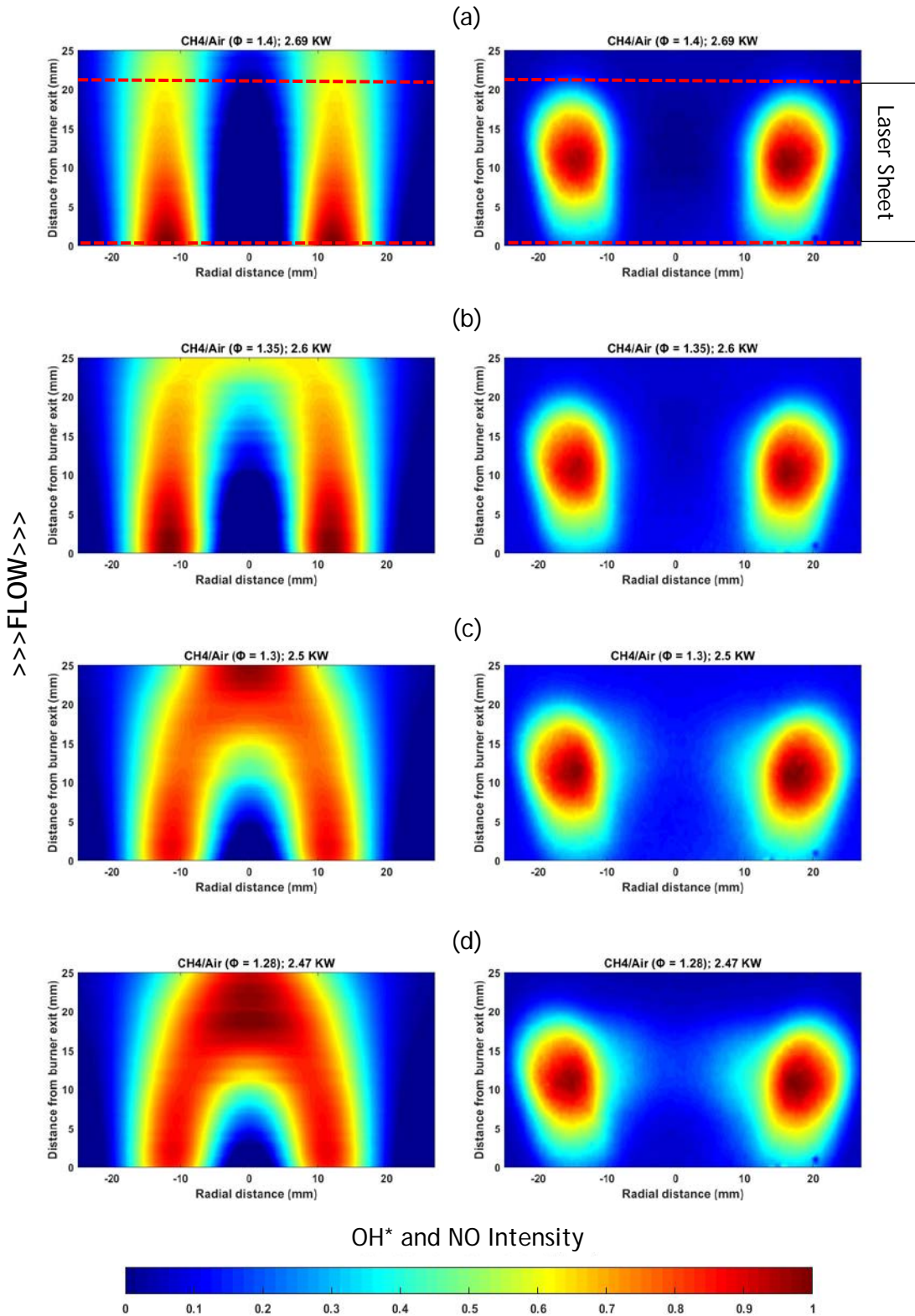


Figure 5-12: Abel - transformed OH* chemiluminescence and NO PLIF images side by side. Colormap normalised to maximum intensity at each Φ . Fuel input thermal power is shown in the respective images.

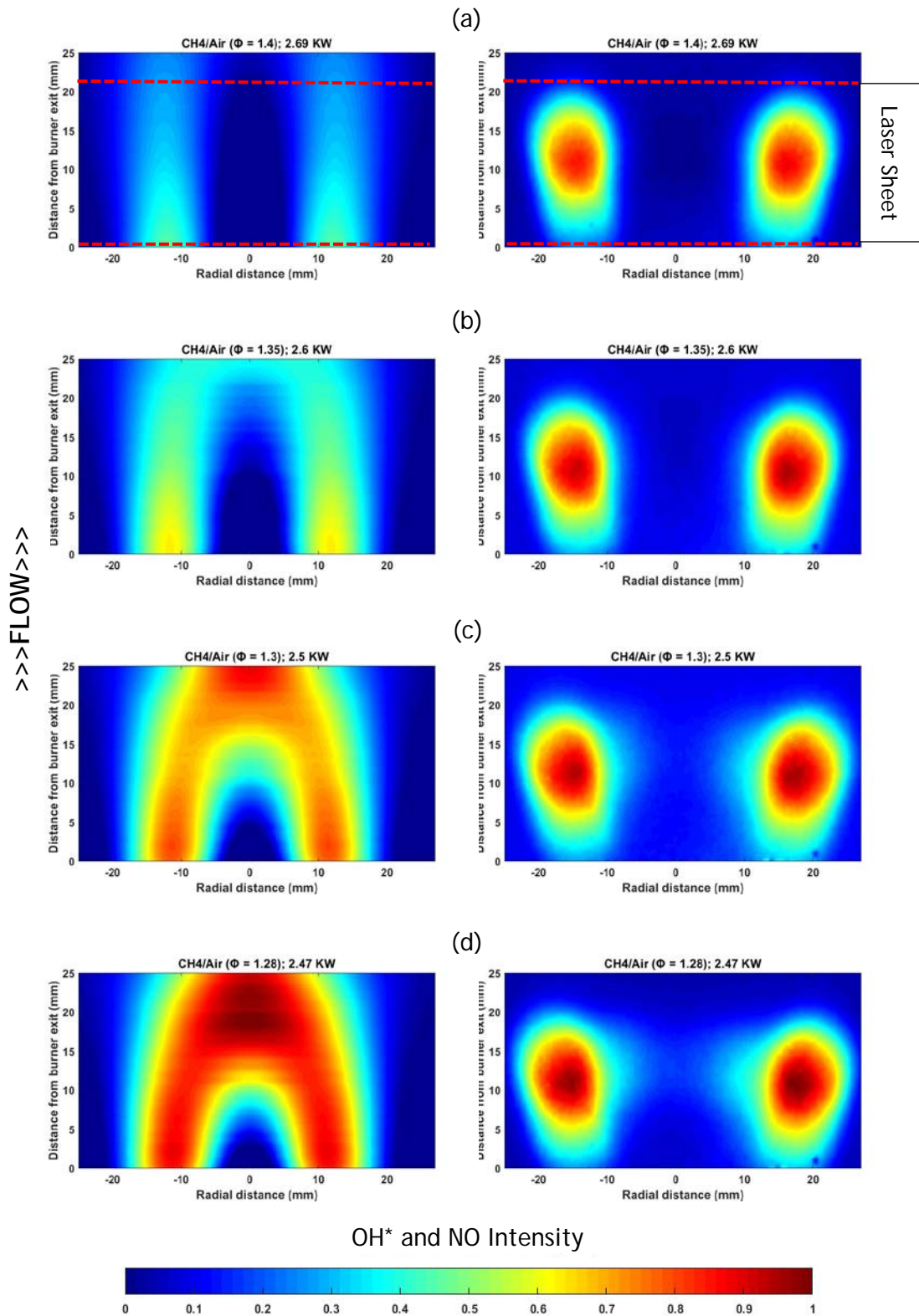


Figure 5-13: Abel - transformed OH^* chemiluminescence and NO PLIF images side by side. Colormap normalised to maximum intensity relative to (d) 2.47 kW thermal power at $\Phi = 1.28$. Fuel input thermal power is shown in the respective images.

When analyzing the images in Figure 5-12 and Figure 5-13, It can be seen that there is no NO formation on the top part of the images (between 20 - 25 mm from burner exit), even though heat releases is evident from OH* chemiluminescence images. This is due to the fact that laser sheet path does not cover the top 5 mm of the images, so NO was not excited at this area, hence lack of NO formation in the images.

As mentioned earlier, air flow was kept constant with fuel flow decreasing as Φ decreased from 1.4 to 1.28. This is evident from the OH* chemiluminescence images, as the flame stabilizes closer to the nozzle exit, with increasing heat release level as Φ decreases. NO formation intensity also shows upwards trends with increasing heat release level, specially between $\Phi = 1.3$ and 1.28, clear NO formation can be seen in the middle, near the surrounding area of burner center.

In Figure 5-13, where colormaps for both OH* chemiluminescence and NO PLIF are normalized to the maximum intensity at $\Phi = 1.28$, clear differences in heat release level are evident as the fuel flow decreases. Increase in NO PLIF intensity level can be observed as heat release level escalates. However, the gradient between the NO PLIF images is much smaller than the gradient between the heat release level as Φ decreases. This corresponds to the decreasing AFT as Φ increases in the rich flames as shown in Figure 3-21. AFT values in TP 1 - 4 (refer to Table 5-1) are within 90 K of each other, with little increase with decreasing Φ . Thus, thermal NO production does not vary significantly between those points. Prompt NO formations depends on the availability of CH, CH₂ and CH₃ radicals, generated at various activation energies. As shown in Figure 5-9, CH and CH₂ mole fractions are declining with increasing Φ . Potentially, this behavior is due to the global activation energy (refer to Figure 5-10) increasing coupled with a declining AFT. Note that the total activation energy calculated assumes a one-step global reaction [194]. However due to the difficulty of precisely experimentally measuring such quantities, it was deemed satisfactory for this work to try and relate this theoretical activation energy to CH radical production. Consequently, differences in NO formations are not as evident as heat release level in these non-preheated rich conditions.

Figure 5-14 plots average OH chemiluminescence intensity (on primary axis) and maximum OH mole fraction (on secondary axis) against average NO PLIF intensity. Average OH chemiluminescence intensity ($AvgInten_{OH}$) is calculated by summing all the pixel values (I_{OH}) in the image and dividing by the product of number of rows and columns, as per Equation [5-2].

$$AvgInten_{OH} = \frac{\sum_{i=1}^m \sum_{j=1}^n I_{OH_{i,j}}}{m \times n} \quad [5-2]$$

$AvgInten_{NO}$ increases quasi-linearly with increasing $AvgInten_{OH}$ and maximum OH mole fraction. Between $\Phi = 1.4$ and $\Phi = 1.35$, $AvgInten_{NO}$ increases most, even though $AvgInten_{OH}$ and maximum OH mole fraction increases slightly. Thereafter, the increase in NO intensity is almost linear with OH intensity and mole fraction. This may be explained from OH chemiluminescence images in Figure 5-13 (a) and (b), where flame was stabilized beyond laser sheet path for $\Phi = 1.4$ but flame was stabilized inside the laser sheet path for $\Phi = 1.35$ and thereafter.

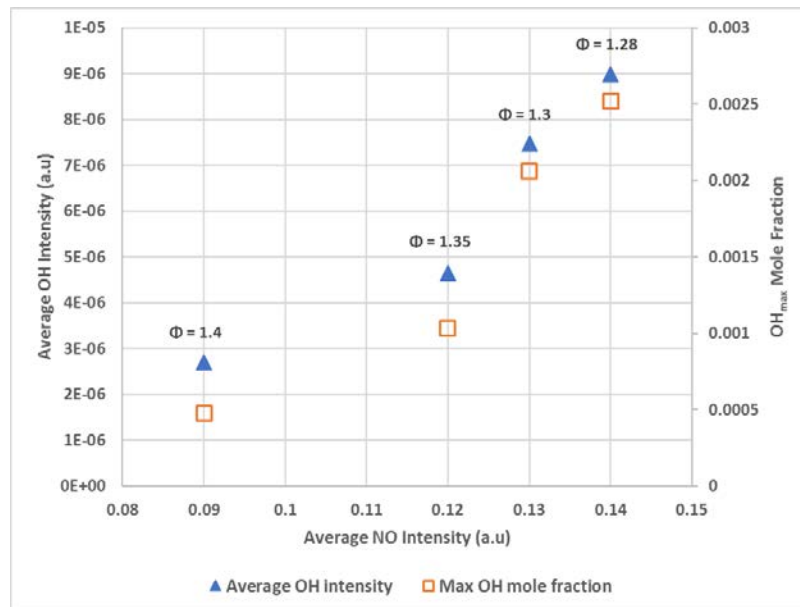


Figure 5-14: Average OH intensity and maximum OH mole fraction plotted as a function of average NO intensity

5.2. NO PLIF in HPGSB-2 without Quartz

The 2nd generation HPGSB-2 was commissioned in 2015 and many experimental combustion studies has been undertaken at the GTRC with this burner since then (refer to Chapter 3.2.2). This burner was used for all the experiments described and analyzed in this section and the following chapters. For the NO formation investigation in this section the quartz was taken off, allowing for open flame investigation in the swirl burner, only confined by the HPOC. Heat release levels will be analyzed in terms of OH* chemiluminescence intensity and NO formation in the flame in terms of PLIF data. These two sets of data will be compared side by side to correlate thermal NO production with heat release level. Table 5-2 presents the flow conditions for this investigation. Five test points considered for this section, covering from lean conditions ($\Phi = 0.81$) to rich flames ($\Phi = 1.1$). Fuel flows were kept constant, while changing air flows, thus keeping constant thermal power, to attain required equivalence ratios for all the experiments in HPGSB-2. All the test points in this section was conducted in atmospheric conditions (298K and 1.1 bara), with a constant thermal power of 26 kW. The gas analyser (refer to Chapter 3.7) was used for the test conditions in Table 5-2.

Table 5-2: Flow conditions for HPOC swirl burner

Test point	CH ₄ mass flow (g/s)	Air mass flow (g/s)	Entry Temperature, T ₂ (K)	Equivalence ratio (Φ)	AFT (K)	CH ₄ speed (m/s)	Air speed (m/s)	Total flow speed (m/s)	Laminar Flame speed (m/s)
5	0.52	11.2	298	0.81	2013	0.62	7.36	7.98	0.2821
6	0.52	10.2	298	0.87	2097	0.62	6.85	7.47	0.3226
7	0.52	9.5	298	0.94	2180	0.62	6.34	6.96	0.3610
8	0.52	8.9	298	1.0	2225	0.62	5.96	6.58	0.3817
9	0.52	8.2	298	1.1	2205	0.62	5.42	6.04	0.3840

5.2.1. OH* Chemiluminescence Comparison

OH* chemiluminescence images represent the flame stabilization and indicates the heat release levels and locations in the flame. Comparison is made in the CH₄/air flames as the flame goes from lean to rich conditions. The Abel-transformed OH* chemiluminescence results for CH₄/air flames with varying Φ conditions are presented in Figure 5-16. Each image presented has been normalized against its own image maximum and then fit to the same false colormap. There seems to be a line 40mm from the burner exit in all the Abel-transformed images in Figure 5-16, this is due to the fact that there was a dot built up on the HPOC window. When the images were Abel-transformed, the dot transformed to a line. The window was replaced for all the subsequent experiments. All the flames are observed to stabilize along the outward expanding shear layer between the CRZ and ERZ, yielding conical, V-shaped flames which expand radially outward from 10mm either side of the burner exit nozzle centerline ($r = \pm 10\text{mm}$).

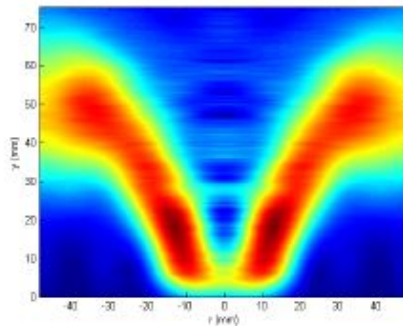


Figure 5-15: Abel-transformed OH* chemiluminescence image at $\Phi = 0.55$ with CH₄/air flame. Reproduced from [221].

Figure 5-15 shows an Abel-transformed OH* chemiluminescence image for CH₄/air flame at $\Phi = 0.55$ from a previous study at Cardiff University [221]. Instantly we can see significant differences in the flame shape compared with the richer flames in Figure 5-16. Near the lean blow off (LBO) limit, as shown in Figure 5-15, flame stabilizes near the center of the nozzle exit, but as the flame gets richer, it seems to stabilize further away from the center of the nozzle exit.

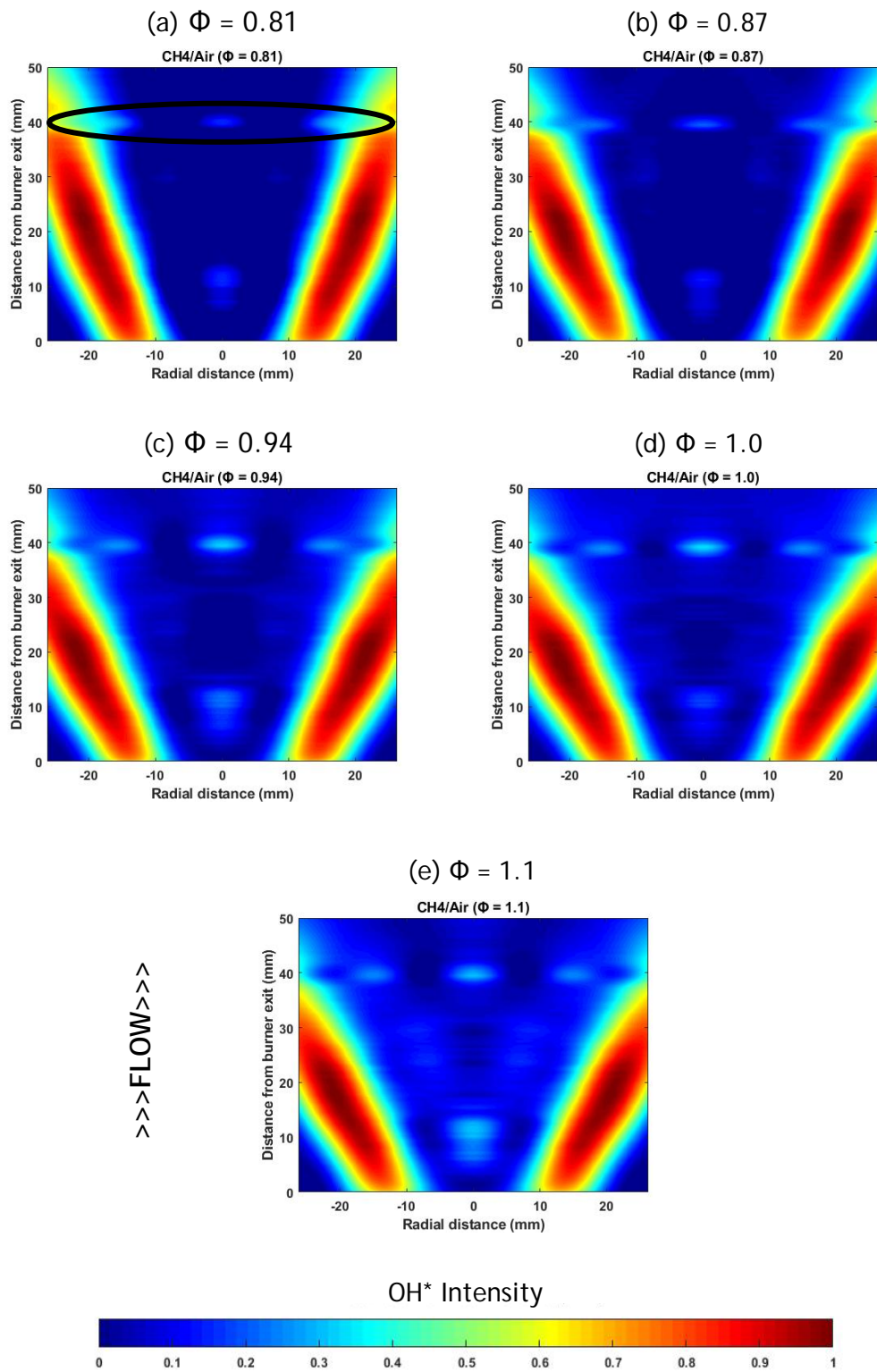


Figure 5-16: Abel-transformed OH* chemiluminescence images (colormap normalised to maximum OH* intensity at each Φ) at varying Φ . Flow direction from bottom to top. The black oval shape in (a) indicates the line from dot built up on quartz window.

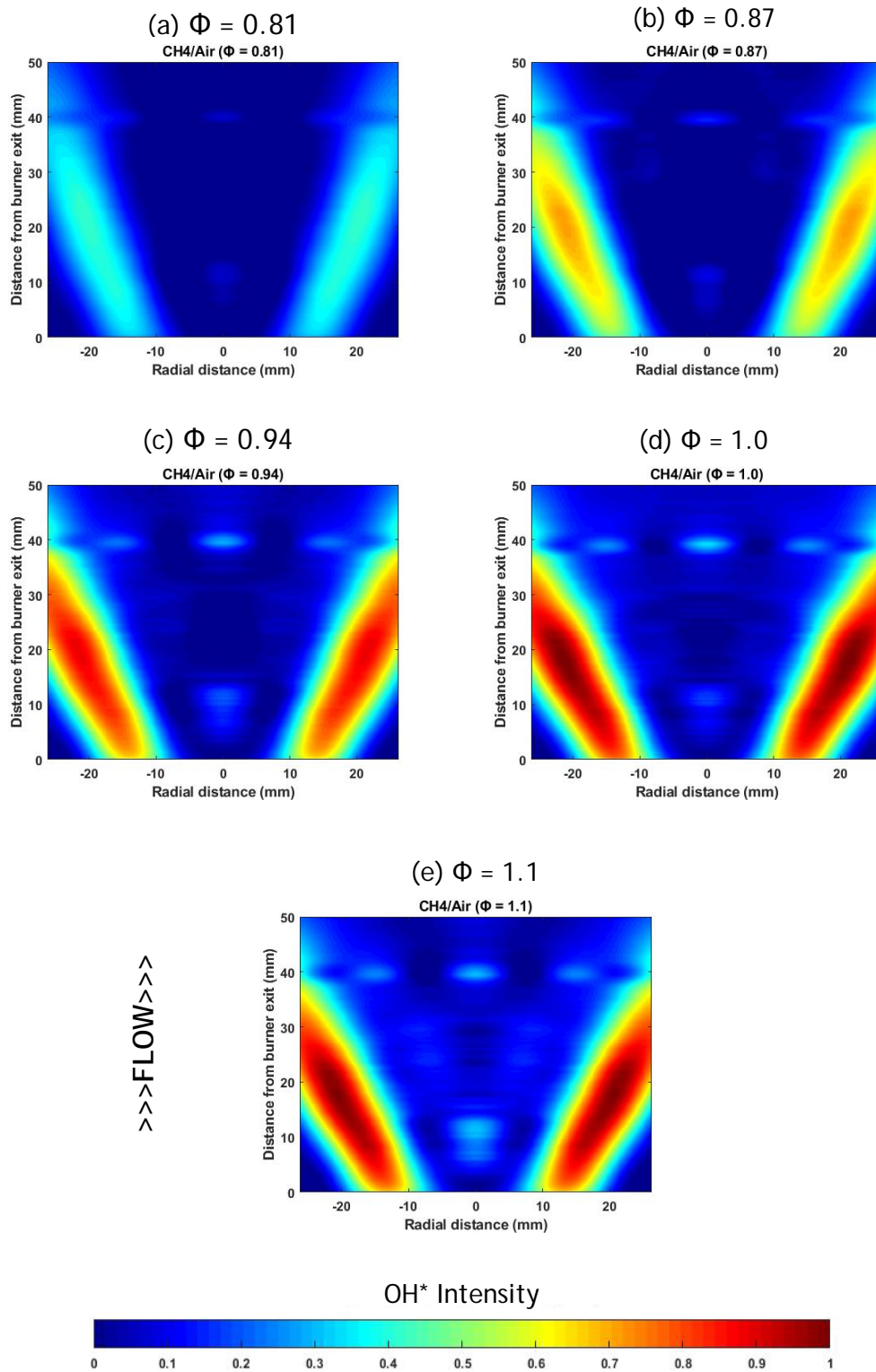


Figure 5-17: Abel-transformed OH* chemiluminescence images (colormap normalised to maximum OH* intensity across range) at varying Φ

From Figure 5-16, the flame reaction zone retracts axially upstream and radially outward as Φ increases. As the Φ increases and air flow decreases, the flame gets wider, as the CRZ gets stronger due to more relative fuel content in the flow. This is clearly evident in the images in Figure 5-16, the intensity of the images in the centerline gets stronger as air flow decreases. The flames also get shorter with decreasing air flow. With decreasing gas flow velocity and increasing burning velocity, the flame stabilizes closer to the burner nozzle exit.

Figure 5-17 represents Abel-transformed OH^* chemiluminescence images, colormap corrected to maximum OH^* intensity across the range. Changes in heat release intensity are quite evident as Φ changes from 0.81 to 0.94, minimal differences in intensity thereafter up to $\Phi = 1.1$. This agrees with Figure 5-18, where OH mole fraction calculated from CHEMKIN is plotted against 1-D spatial concentration profile. Calculated maximum OH mole fraction and maximum OH^* chemiluminescence intensity follow the same trend as shown in Figure 5-19, when plotted against Φ . Both increases until stoichiometry, then drops as the gas mixture gets rich.

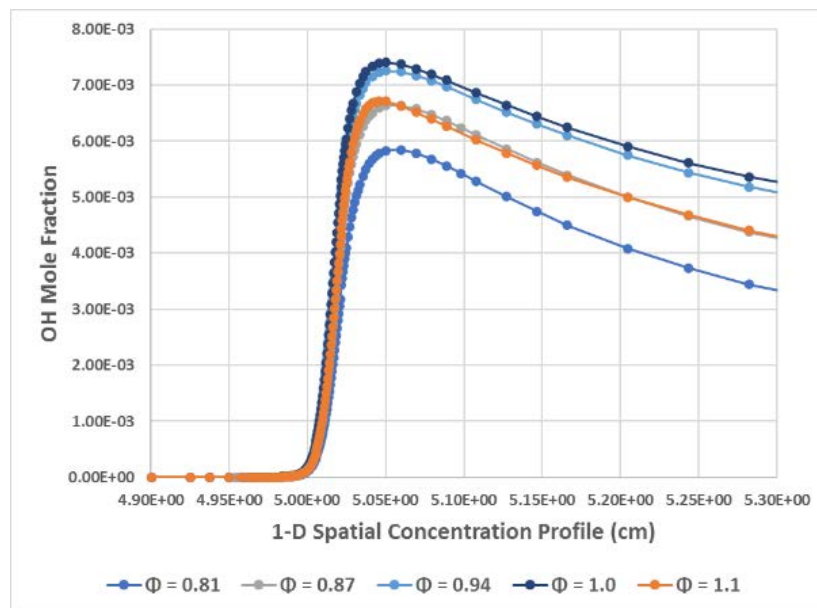


Figure 5-18: CHEMKIN results showing OH mole fraction as a function of 1-D spatial concentrations profiles for $\Phi = 0.81 - 1.1$

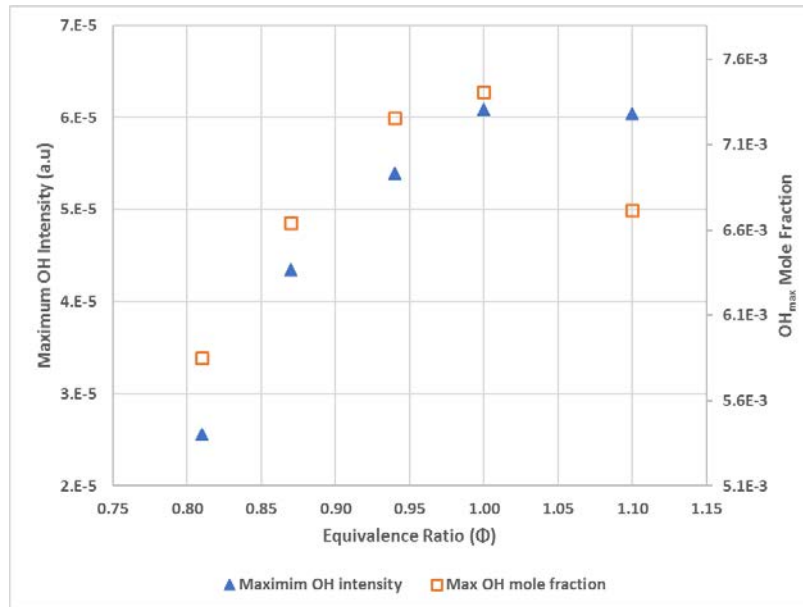


Figure 5-19: Maximum OH* intensity and maximum OH mole fraction as a function of Φ

5.2.2. NO PLIF Comparison

Qualitative NO PLIF results in HPOC without confinement are discussed and analyzed here. From combustion theory, NO formation gets stronger as premixed gas moves towards stoichiometry and then gets weaker in rich conditions due to the balance in availability of excess O₂ and flame temperature [38]. This is evident from Figure 5-20, where NO PLIF images at $\Phi = 0.81 - 1.1$ are presented. Each image is normalized to its maximum intensity pixel value to clearly identify NO formation at each point. NO PLIF intensity increases as Φ increases up to 0.94 and declines thereafter as flame gets richer. Interestingly, NO formations are visible in the center of every images in Figure 5-20, which is quite opposite to the NO-PLIF images in the Bunsen burner (refer to Figure 5-6), where barely any NO formations were seen at the burner centerline. In swirling flames, hot combustion gases are recycled at the centerline of the burner, creating CRZ, which helps stabilizing the flame [210]. This is the reason behind NO formation at the centerline near the burner exit as seen in Figure 5-20.

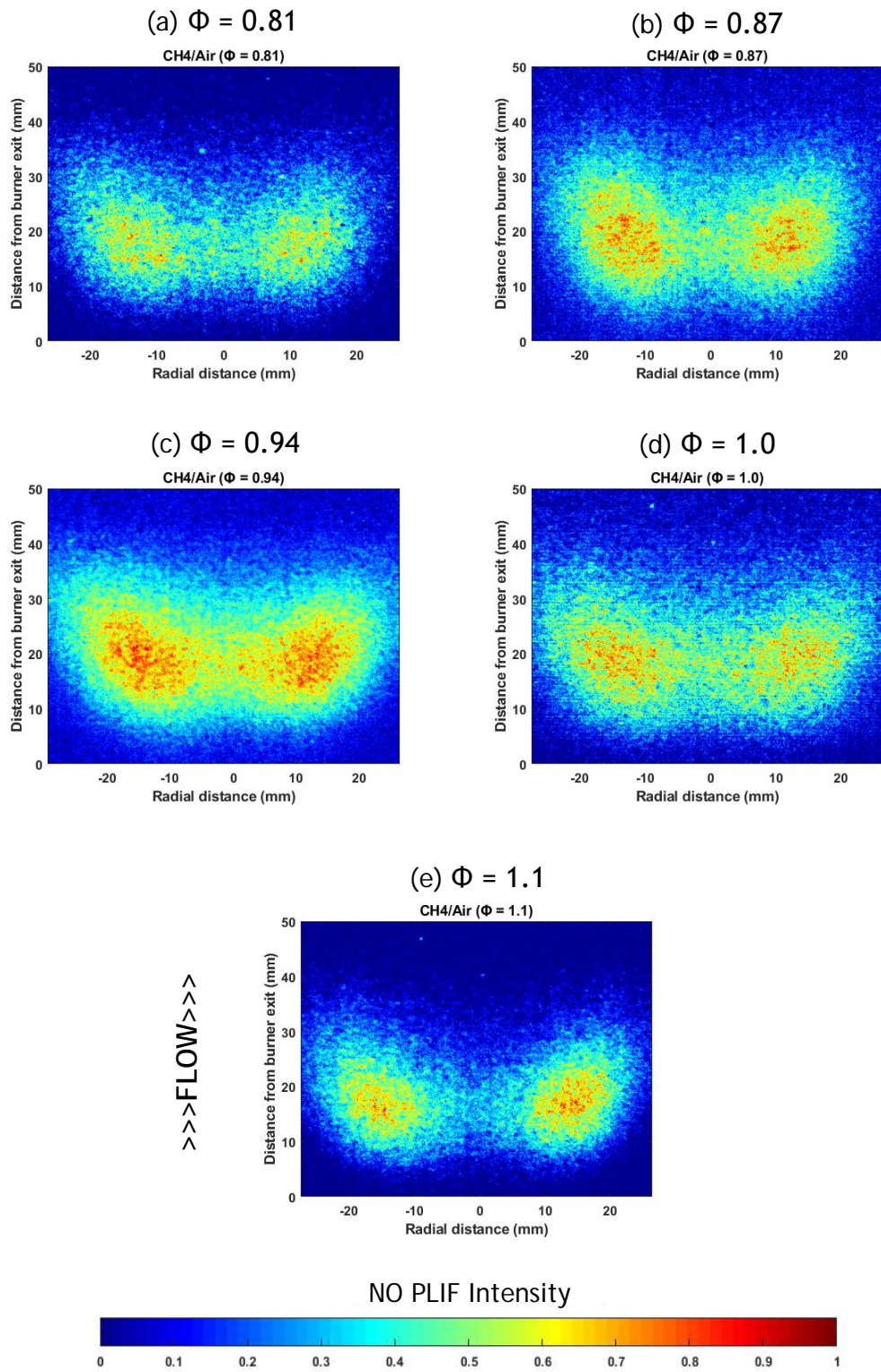


Figure 5-20: NO PLIF images (normalised to maximum intensity at each Φ) from lean to rich flames

$AvgInten_{NO}$ and AFT are plotted as a function of Φ in Figure 5-21. $AvgInten_{NO}$ value peaks at $\Phi = 0.94$ while AFT peaks at $\Phi = 1.0$ and then both the values decline as flame gets richer. This can be explained as a balance between flame temperature and O_2 availability. Abundance O_2 is available in any lean conditions for the rate-limiting step (refer to Equation [2-1]) in the Zel'dovich mechanism to initiate. However, thermal NO formation rate is highly dependent on temperature as described in Equation [2-4]. In the experimental conditions considered here, TP7 ($\Phi = 0.94$) has abundance O_2 and highest AFT among the lean conditions. As a result, $AvgInten_{NO}$ peaks at $\Phi = 0.94$ for lean conditions and this is also confirmed by Figure 5-22, where NO measured by gas analyser and $AvgInten_{NO}$ is plotted as a function of Φ . As premixed gas moves to stoichiometry, there is no excess O_2 but highest AFT for the test points in this Section. As a result, thermal NO production drops at stoichiometry and drops even further at $\Phi = 1.1$, where both O_2 concentration and AFT declines. However, prompt NO becomes important in the downstream at stoichiometry and rich flames, where CH radicals become more available due to increasing hydrocarbon presence in the unburned gas.

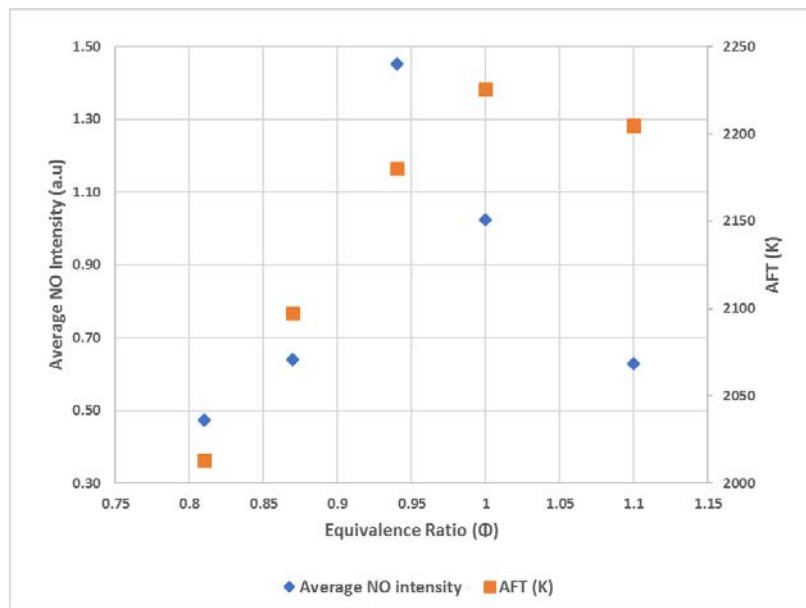


Figure 5-21: Average NO PLIF intensity and AFT as a function of Φ

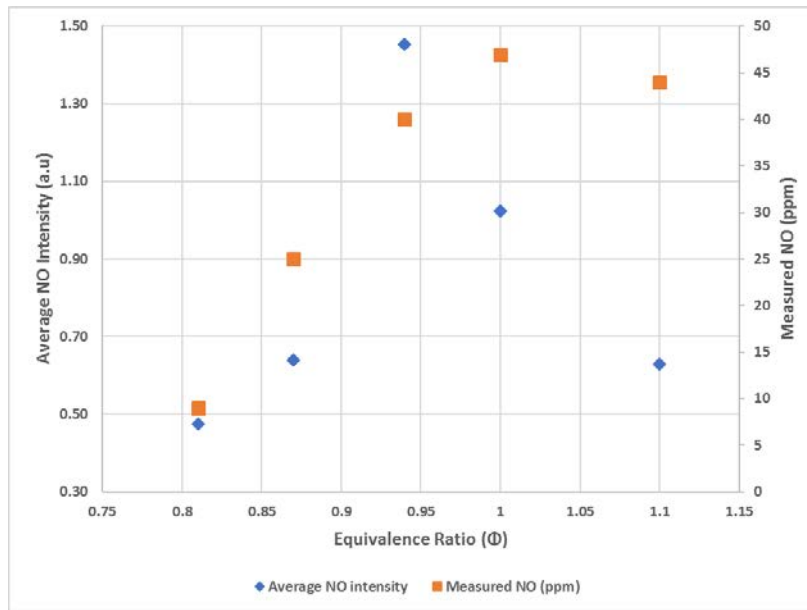


Figure 5-22: Average NO PLIF intensity and measured NO as a function of Φ

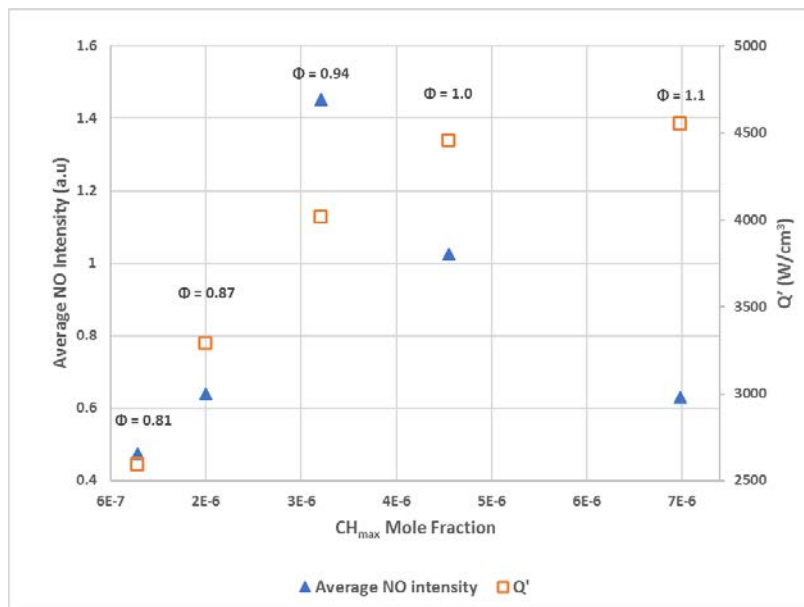


Figure 5-23: Average NO PLIF intensity and volumetric heat release rate as a function of maximum CH mole fraction. Respective Φ is shown in increasing order.

Maximum CH mole fraction and volumetric heat release level calculated by CHEMKIN increases with Φ , as can be seen in Figure 5-23. Presence of CH radicals are expected to get stronger as fuel gets richer, simply due to more hydrocarbons present in the unburned mixture. NO PLIF measurements were taken at the flame zone in this study, where mainly thermal NO forms. Prompt NO formation mainly occurs in hot combustion gas in the downstream, as described by Fenimore et al. [64]. This is the reason why in Figure 5-22, $AvgInten_{NO}$ peaks at $\Phi = 0.94$, whereas NO measured by gas analyser peaks at stoichiometry. Gas analyser measure the total NO produced in the flame but NO PLIF measurement looks mainly at thermal NO formation at the flame front. Prompt NO mechanism is of great importance in the pre-heated and pressurized conditions as the reaction rates of Equation [2-5] and [2-6] are dependent on pressure and temperature and increase exponentially with temperature. So, it can be safely assumed that prompt NO pathways are not as vital as thermal NO pathways for the flow conditions of this study.

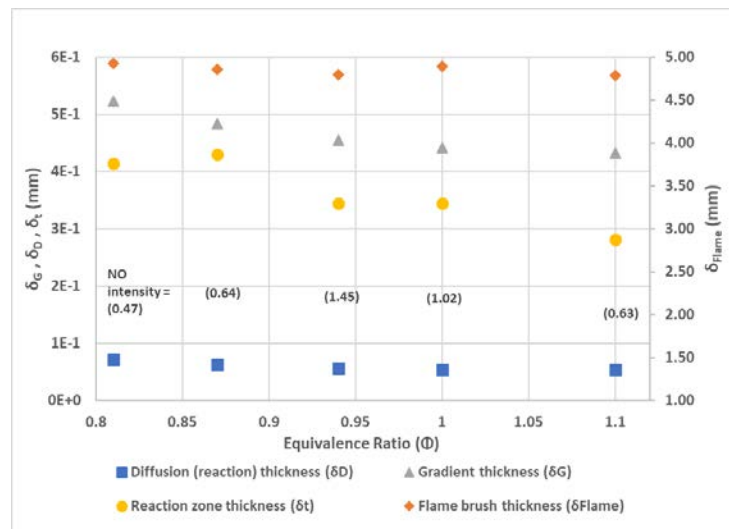


Figure 5-24: Numerical and experimental flame thickness as a function of Φ . NO PLIF intensity is shown for every TPs in the graph.

Figure 5-24 plots flame thickness as a function of Φ . It must be noted that flame thickness calculated from numerical methods (δ_D , δ_G and δ_t) are plotted on the primary axis and experimentally measured flame brush thickness (δ_{flame}) is plotted on the secondary axis. $AvgInten_{NO}$

also shown in the graph as Φ changes. δ_G and δ_t values show decreasing trend with increasing Φ . As per the Equation [3-17] to calculate δ_G , numerator of the equation is a sole function of AFT as inlet temperature is fixed to 298 K and denominator value increases with Φ . So, it is logical that δ_G is showing decreasing trend with Φ . δ_t behaviour with Φ was explained in detail in section 3.10.1.3. Up to $\Phi = 0.94$, all the methods to calculate flame thickness shows decreasing trend but $AvgInten_{NO}$ values show opposite trend. Detailed premixed flame structure from Law [194] is reproduced in Figure 5-25, clearly indicating δ_G and δ_D , with Y_u being the concentration of the fresh mixture and $Y_b = 0$ indicating its complete combustion upon crossing the flame. δ_G covers both the preheat and reaction region, while δ_D indicates the reaction region. As Φ increases, both δ_G and δ_D decreases but the (δ_G/δ_D) ratio increases, which is indicative to the total NO formation. Figure 5-25 shows very good agreement in the trend between measured NO values and (δ_G/δ_D) ratio with increasing Φ .

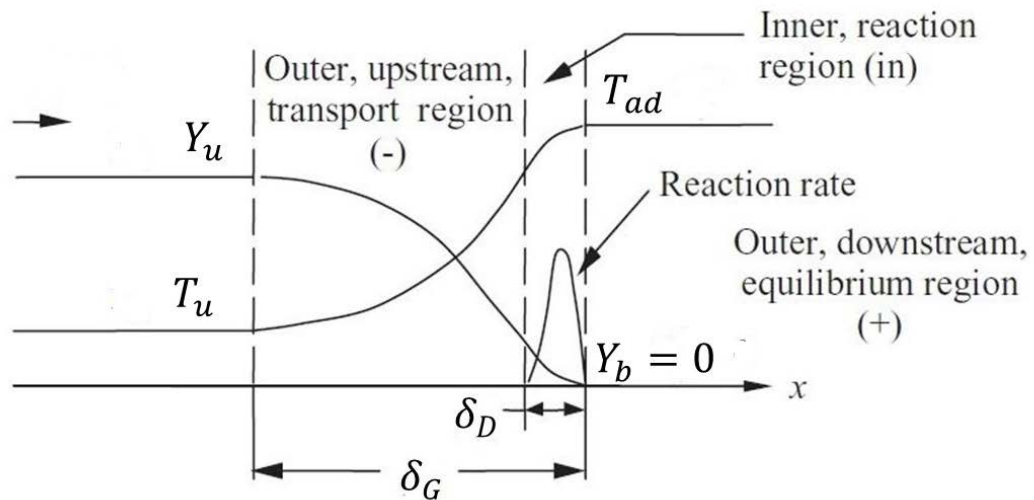


Figure 5-25: Schematic showing the detailed premixed flame structure including the reaction zones. Reproduced from Law [194].

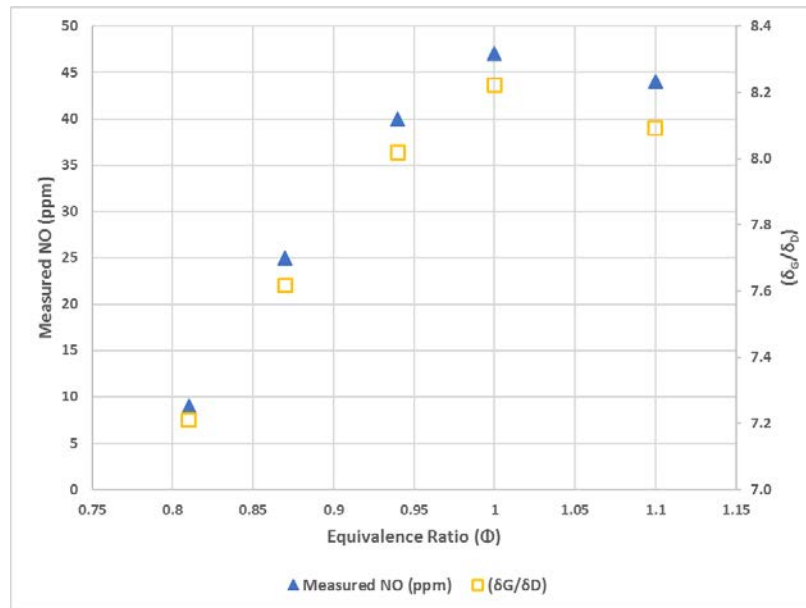


Figure 5-26: Measured NO and (δ_G/δ_D) as a function of Φ

Figure 5-27 and Figure 5-28 shows the OH* chemiluminescence and NO PLIF images side by side for respective conditions in HPOC with colormap normalized to maximum Φ and to maximum intensity across the images, respectively. Laser sheet path is indicated on the first images (refer to Figure 5-27 (a) and Figure 5-28 (a)) of each figure. Both horizontal and vertical axes are kept to same limits for OH* chemiluminescence and NO PLIF images to compare the relationship between NO formation and heat release better. Flows are from bottom to top in these images. NO formations shown only in the path of laser sheet, as NO cannot be excited without laser energy for the PLIF images, whereas OH* chemiluminescence images shows the heat release in whole flame as laser energy is not required for chemiluminescence measurements.

Planar NO-LIF in Unconfined Flames

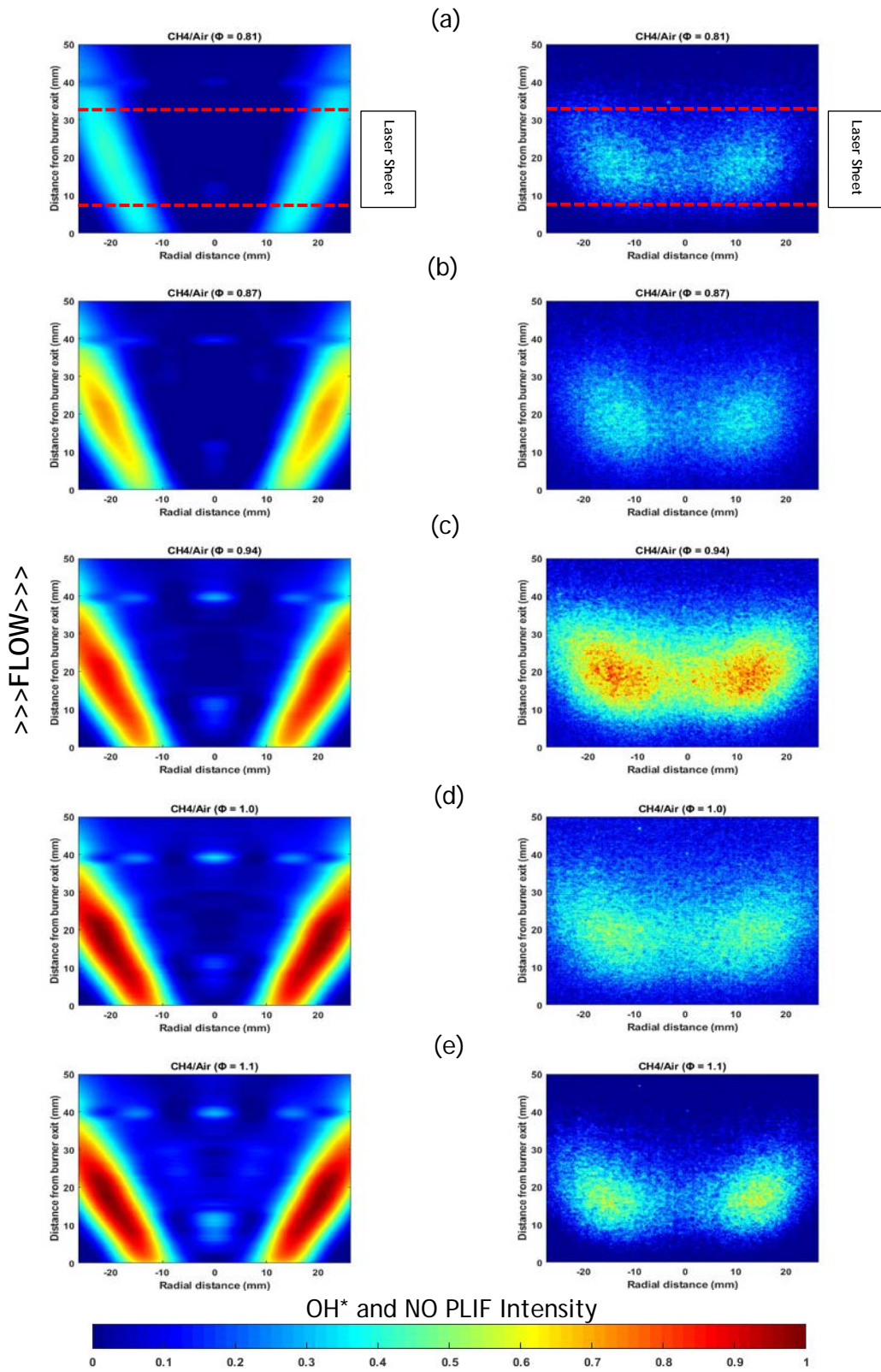


Figure 5-27: Abel - transformed OH^* chemiluminescence and NO PLIF images side by side. Colormap normalised to maximum intensity across the images.

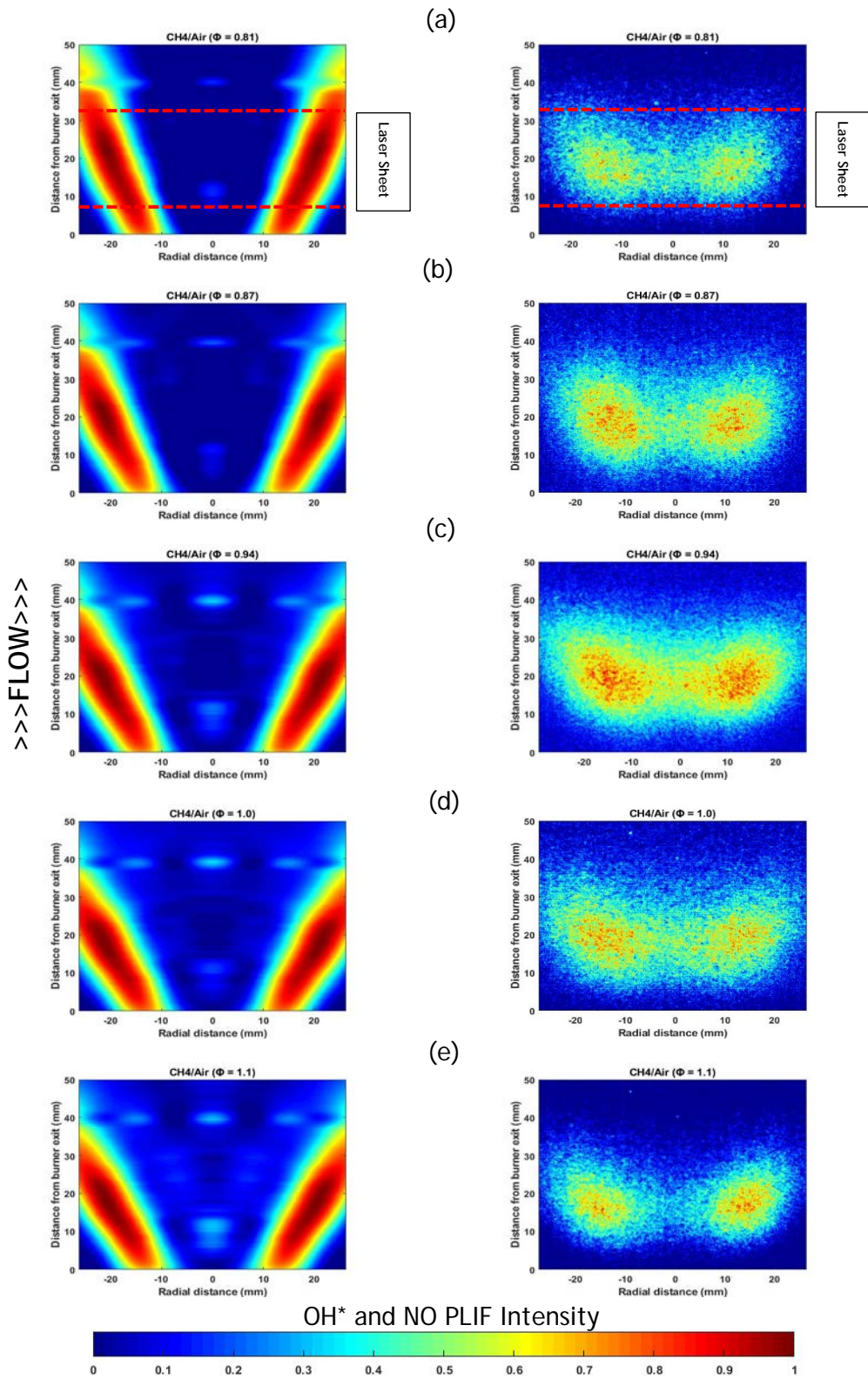


Figure 5-28: Abel - transformed OH^* chemiluminescence and NO PLIF images side by side. Colormap normalised to maximum intensity at each Φ .

From Figure 5-27 NO PLIF images, there are differences in the intensity level between the left and the right side of each images. The area of NO formation and intensity level in the left side is higher than right side. As discussed in Chapter 3.6.2, when laser sheet passes the flame from left to right side, laser energy gets attenuated by UV from major product species like CO₂ and H₂O. So, as the laser sheet goes from left to right, CO₂ and H₂O absorb laser energy in the flame. As a result, variations in PLIF images can be seen at the either side of the burner exit. Attenuation of laser light and the fluorescence signal can be corrected on a pixel-by-pixel basis using Beer-Lambert's Law [277] and absorption coefficients known from shock tube measurements [158] and simple consideration of geometry. Local flame temperature distribution is needed for this correction because the CO₂ and H₂O absorption coefficients are temperature dependent and the CO₂ and H₂O number densities can be obtained using an assumption of thermal equilibrium in the post-flame gas.

In Figure 5-28, where colormaps for both OH* chemiluminescence and NO PLIF images are normalised to the maximum intensity across images, clear differences in heat release level are apparent as the air flow decreases. NO PLIF intensity increases with increasing heat release level up to $\Phi = 0.94$, then NO PLIF intensity declines as Φ moves towards stoichiometry and beyond (refer to Figure 5-28 (d) and (e)), even with apparent increasing heat release levels from respective OH* chemiluminescence images. As discussed earlier, this is related to the trade-off between availability of excess O₂ and flame temperature.

Figure 5-29 depicts the relationships between $AvgInten_{NO}$, $AvgInten_{OH}$, maximum OH mole fraction from CHEMKIN calculations and Φ . $AvgInten_{OH}$ increases with increasing Φ while maximum OH mole fraction peaks at stoichiometry and then decreases at $\Phi = 1.1$ as expected. The apparent opposite trend in $AvgInten_{OH}$ from stoichiometry to rich condition can be attributed to the fact that OH* chemiluminescence image for $\Phi = 1.1$ was taken in a different day than the other points. $AvgInten_{NO}$ values rise with increasing $AvgInten_{OH}$ and maximum OH mole fraction values up to $\Phi = 0.94$, then

$AvgInten_{NO}$ values declines as there are no more excess O_2 in the mixture.

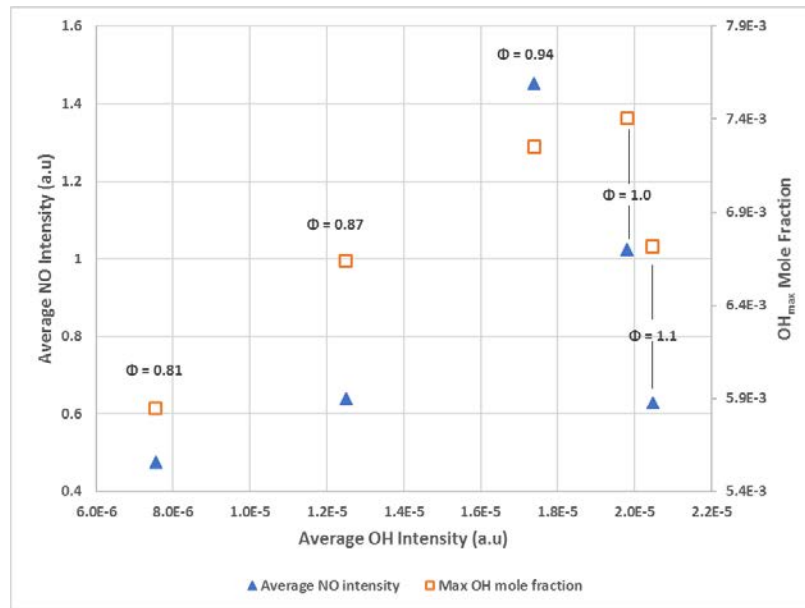


Figure 5-29: Average NO PLIF intensity and maximum OH mole fraction from CHEMKIN as a function of average OH^* chemiluminescence intensity. Φ is shown in the graph for each point in increasing order.

5.3. CHEMKIN Simulation for NO prediction

It is of utmost importance of this study to have a verified model of HPGSB-2 combustion rig. In that pursuit, the modified Valera model, described in Chapter 4.2 is used to predict NO emissions and compare the predictions with measured data by gas analyser at the exhaust of HPOC. The model was modified to match the geometrical changes of the open flame in HPOC. One PFR was used to model the post-flame zone, changing from two PFRs in the original model. the second PFR was used in the original model to simulate the converge geometry of the quartz at the end. As the quartz was taken off to investigate open flame at HPOC, second PFR was no longer necessary. ERZ was also taken off as the flame was unconfined (refer to Chapter 6.1.3). Recirculation from CRZ was kept to 70% into the flame zone reactor and from the flame zone, the flow was split two ways: 80% and 20% into post-flame zone and CRZ respectively. Figure 5-30 and Appendix E.9 represents the chemical reactor network and required inputs for the model respectively.

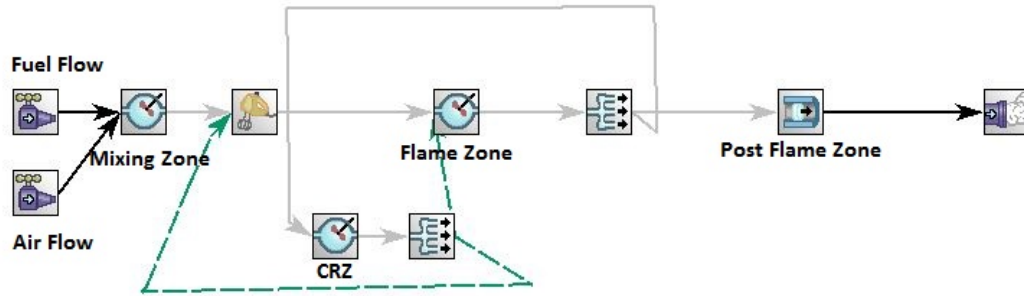


Figure 5-30: Model for open flame in HPOC

5.3.1. Benchmarking Modified Valera Model

Modified Valera model has been re-benchmarked due to the open flame conditions in the HPOC and changes in the flow conditions mentioned in Table 5-2. Heat loss rate for all four PSRs (Premixed, Flame, CRZ and ERZ) in the model were set according to Table 5-3 to match the experimental NO value of TP 8 at 1.1 bara, $\Phi = 1.0$ using GRI-Mech 3.0. For the purpose of the following analysis, these values were assumed to be constant for all other investigated conditions with different mechanisms.

Table 5-3: Heat loss rates for different zones

Zone	Heat loss rate (J/sec)
Mixing	0
Flame	7953
CRZ	1590

The volume of the mixing, flame zone, CRZ and ERZ kept similar to the modified Valera’s model. NO predictions from all the mechanisms are compared and analysed against the experimental concentrations in the following sub-sections.

5.3.2. Comparison of Predictions with Measured NO Values

This model is used to compare the seven mechanisms mentioned in Chapter 4.1 (GRI-Mech 3.0, Aramco 1.3, CRECK, SanDiego, USII, Ranzi-Paolo, NUIGalway) with the flow conditions mentioned in Table 5-2. Figure 5-31 compares the changes in measured and predicted NO as Φ changes. Table 5-4 shows the percentages differences in decimal by the mechanisms compared to the experimentally derived data at the unconfined HPGSB-2. NO predictions from each mechanism shows upward trends up to stoichiometry, as thermal NO formation increases with increasing AFT and then all the mechanisms predict low NO at $\Phi = 1.1$, as seen in measured NO.

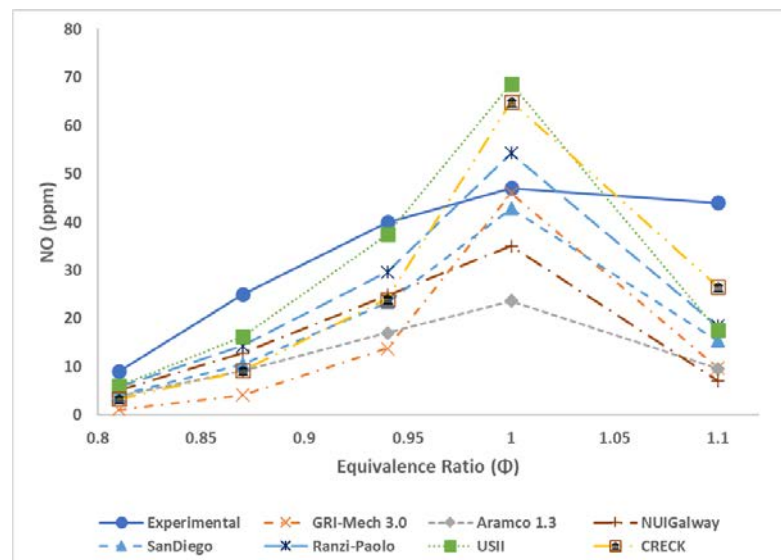


Figure 5-31: Experimentally measured and predicted NO as a function of Φ

Following points can be made by analysing the graph carefully:

- GRI-Mech 3.0 mechanism underpredicts NO production at exhaust for all the flow conditions, underpredicting NO formation in a decreasing order (88%, 83% and 65% as Φ increases up to 0.94 and then underpredicts NO values by nearly 78% for $\Phi = 1.1$).
- Aramco 1.3 and NUIGalway mechanisms predictions trends closely matches to the experimental trend than the other mechanisms, as can be seen in Figure 5-31. On average, Aramco 1.3 underpredicts NO production by 60%, while NUIGalway predictions are closer to the measured values (48% underprediction on average).

Table 5-4: Differences in predictions by the mechanisms compared to the experimental results (unconfined HPGSB-2)

Eq. Ratio (Φ)	PR	AFT (K)	Percentage (%) Change - in decimal						
			GRI- Mech 3.0	Aramco 1.3	NUIGalw ay	SanDiego	Ranzi- Paolo	USII	CRECK
0.81	1.1	2013	-0.88	-0.55	-0.43	-0.55	-0.37	-0.34	-0.63
0.87	1.1	2097	-0.54	-0.63	-0.49	-0.58	-0.43	-0.35	-0.63
0.94	1.1	2180	0.54	-0.57	-0.38	-0.42	-0.26	-0.06	-0.40
1	1.1	2225	4.11	-0.50	-0.26	-0.09	0.16	0.46	0.38
1.1	1.1	2205	0.08	-0.78	-0.84	-0.65	-0.58	-0.60	-0.40

- Ranzi-Paolo, USII and CRECK mechanisms overpredict NO formation by factor of around one and a half. USII mechanism predictions are closest to the actual values for the lean conditions, specially underpredicting NO production just by 6% at $\Phi = 0.94$.
- SanDiego mechanism predicts NO production most accurately at stoichiometry and its predictions at lean conditions are very similar to CRECK mechanism predictions. Every mechanism underpredict NO values at the only rich condition ($\Phi = 1.1$) considered here.

Overall, the model predicts the trends with increasing Φ successfully with all the mechanisms considered here. The predictions can be improved substantially with volumetric inputs for the PSRs from CFD in the open flame conditions.

5.3.3. Sensitivity Analyses

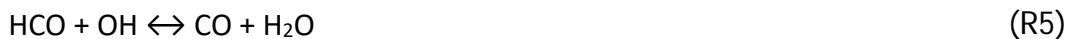
Numerical simulation results provided theoretical details of the important species obtained from the combustion process of the conditions considered in this study in a swirl burner type combustion system. Results show some discrepancies between the kinetic mechanisms, a known fact among different mechanisms that is under research. Interestingly, the temperatures predictions are considerably homogeneous between the mechanisms. However, temperature predictions from GRI-Mech 3.0 [260] are consistently lower than the other mechanisms, which translate into similar trend for OH mole fraction predictions in the flame zone and post flame zone reactors. NO predictions do not coincide between reaction mechanisms as well, and perhaps the highest discrepancies among other species of interest. This is a consequence of variation in sensitivity of a few reactions which are analysed later in this Section.

From Figure 5-31, the predictions from the mechanisms starts to deviate from the experimentally obtained NO emissions at $\Phi = 0.94$ by more than 30% and deviation is maximum at the stoichiometry and rich conditions considered in this study. USII mechanism overpredicts NO emissions by

some margin at stoichiometry while Aramco 1.3 and SanDiego underpredicts NO emissions for all conditions with a smaller margin for SanDiego. GRI-Mech 3.0 matches the experimental result at stoichiometry but underpredicts NO emissions for all the other conditions. Bearing this in mind, sensitivity analyses of the species of interest have been carried out with mechanisms GRI-Mech 3.0, Aamco 1.3 and SanDiego at $\Phi = 0.94 - 1.1$.

5.3.3.1. [OH] Sensitivity Analysis

The OH radicals are found at large concentrations in the reaction zones of hydrogen based fuels as they play an important role to oxidise the fuel and reduce the ignition delay time [58]. The net reaction rate sensitivity analyses of [OH] in the flames considered here have been carried out, to identify the key reactions involved in the production and consumption of OH radical in the reaction zone, Figure 5-32. The key elementary reactions influencing [OH] identified from the analyses are as follows:



The chain branching reaction $\text{H} + \text{O}_2 \leftrightarrow \text{O} + \text{OH}$ (R1) is one of the most important elementary reactions in combustion that provides the necessary OH radicals in any hydrogen based flame. The H_2/O_2 dissociation/recombination reaction $\text{H} + \text{OH} + \text{M} \leftrightarrow \text{H}_2\text{O} + \text{M}$ (R2) found to play important role on laminar flame speed but no effect on ignition delay time [278]. Carbon monoxide is a major intermediate species and its oxidation to CO_2 through the reaction $\text{OH} + \text{CO} \leftrightarrow \text{H} + \text{CO}_2$ (R3) is responsible for a significant fraction of the exothermicity accompanying

hydrocarbon oxidation [279]. Nearly all carbon atoms in the hydrocarbon fuels are converted to CO through formaldehyde (CH₂O) and/or formyl radicals (HCO) [57], [280]. HCO converts to CO during the high-temperature combustion of hydrocarbons through the reactions $\text{HCO} + \text{M} \leftrightarrow \text{H} + \text{CO} + \text{M}$ (R4) and $\text{HCO} + \text{OH} \leftrightarrow \text{CO} + \text{H}_2\text{O}$ (R5). The reaction $\text{OH} + \text{HO}_2 \leftrightarrow \text{O}_2 + \text{H}_2\text{O}$ (R6) is an efficient removal mechanism for HO_x radicals (OH and HO₂) and produce oxygen molecule and water in the process. The elementary reaction $\text{H} + \text{O}_2 + \text{H}_2\text{O} \leftrightarrow \text{HO}_2 + \text{H}_2\text{O}$ (R7) is exclusively present in M1 and plays an important role in [OH] consumption in the mechanism. Since R7 does not feature in the other mechanisms, it has been excluded from comparative sensitivity analyses between the mechanisms.

Figure 5-32 compares normalized sensitivity coefficients computed utilizing mechanisms M1 - M3 at $\Phi = 0.94 - 1.1$. Reactions R1 and R2 perform key roles in the net OH radical concentration for all three conditions considered here with all three mechanisms. However, R1 displays positive sensitivity whereas R2 shows negative sensitivity for [OH], indicating both the reactions occurring at forward direction. Interestingly, M1 shows highest sensitivity for R1 and least sensitivity for R2 among other mechanisms. Sensitivity from M3 and M4 for these two reactions are quite consistent with each other. The discrepancies in the sensitivity coefficients among the mechanisms can be attributed to the different rate constant (k) values for these reactions. k values for M3 and M4 are very close to each other. Sensitivity coefficients for these two reactions increases as flame moves towards rich condition, more than double at $\Phi = 1.1$, compared to $\Phi = 0.94$. From this observation, it can be inferred that hydrogen atom plays more crucial role at R1, as availability of O₂ is reducing at richer conditions. Reaction R2 is dependent on R1, as R1 produces OH radicals and R2 consumes OH radicals.

Planar NO-LIF in Unconfined Flames

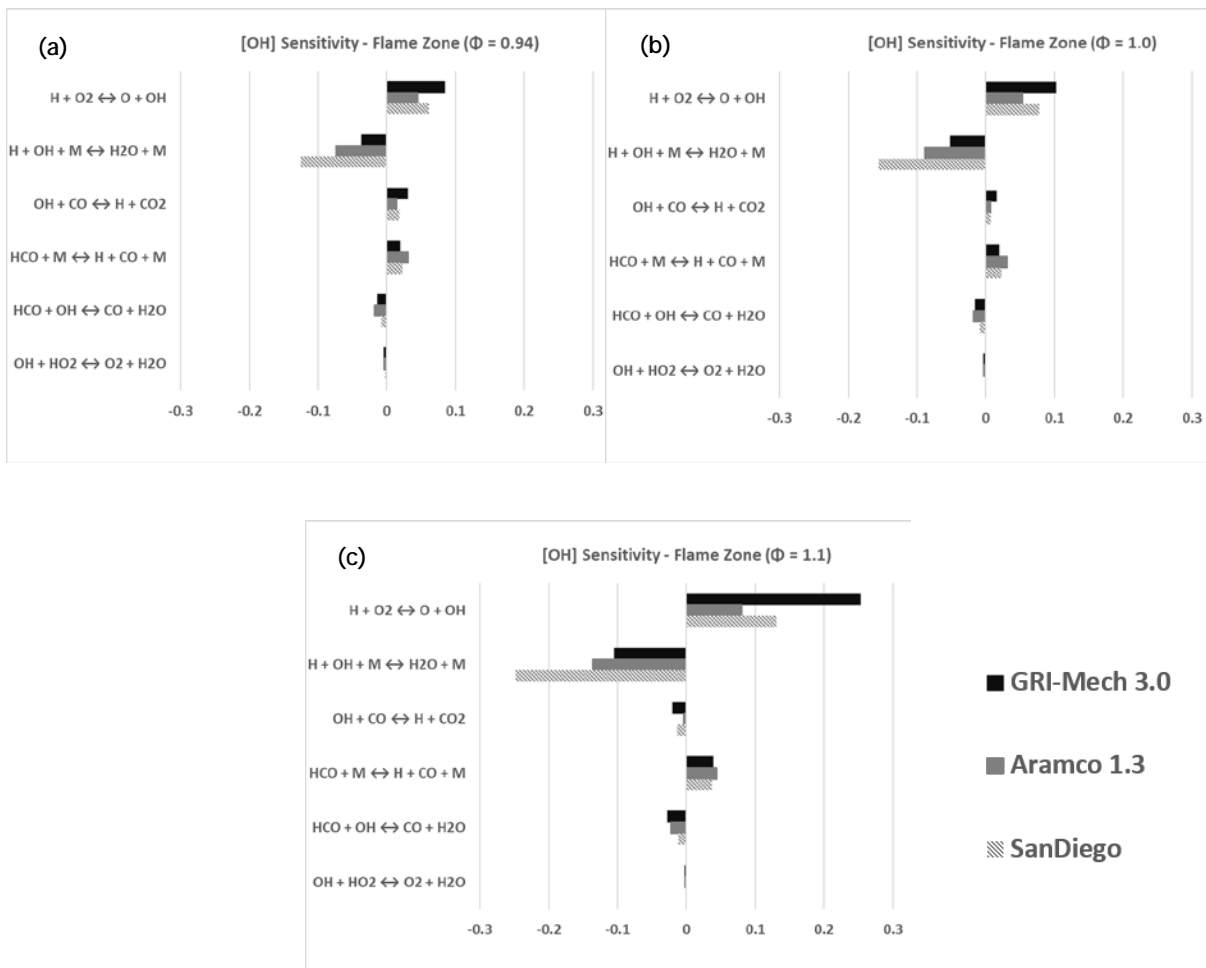


Figure 5-32: Computed normalized sensitivity coefficients of [OH] on net reaction rates at the flame zone reactor for (a) $\Phi = 0.94$, (b) $\Phi = 1.0$, (c) $\Phi = 1.1$. Units [-]

Reaction R3 shows positive sensitivity at the lean condition and stoichiometry but displays negative sensitivity at the rich condition for all three mechanisms. It must be noted that positive sensitivity for R3 is reduced at stoichiometry compared to the lean condition. This trend in sensitivity for R3 can be attributed to the production of CO_2 and CO. CO_2 production is highest at the lean condition, lower at stoichiometry and lowest at the rich condition, where CO production takes over due to reduction in excess O_2 . Hence, R3 operates backwards for the lean condition and stoichiometry, producing OH radicals but the reaction operates at forward direction at $\Phi = 1.1$ by consuming OH radicals. Formyl radical reactions R4 and R5 have positive and negative sensitivity, respectively for all the conditions and mechanisms. Sensitivity coefficients for R4 and R5 almost similar for $\Phi = 0.94$ and 1.0 but almost doubles for $\Phi = 1.1$. This can be attributed to the highest

HCO formation at rich condition due to the increased hydrocarbon content. Reaction R6 has negligible effect on overall OH production for all the conditions.

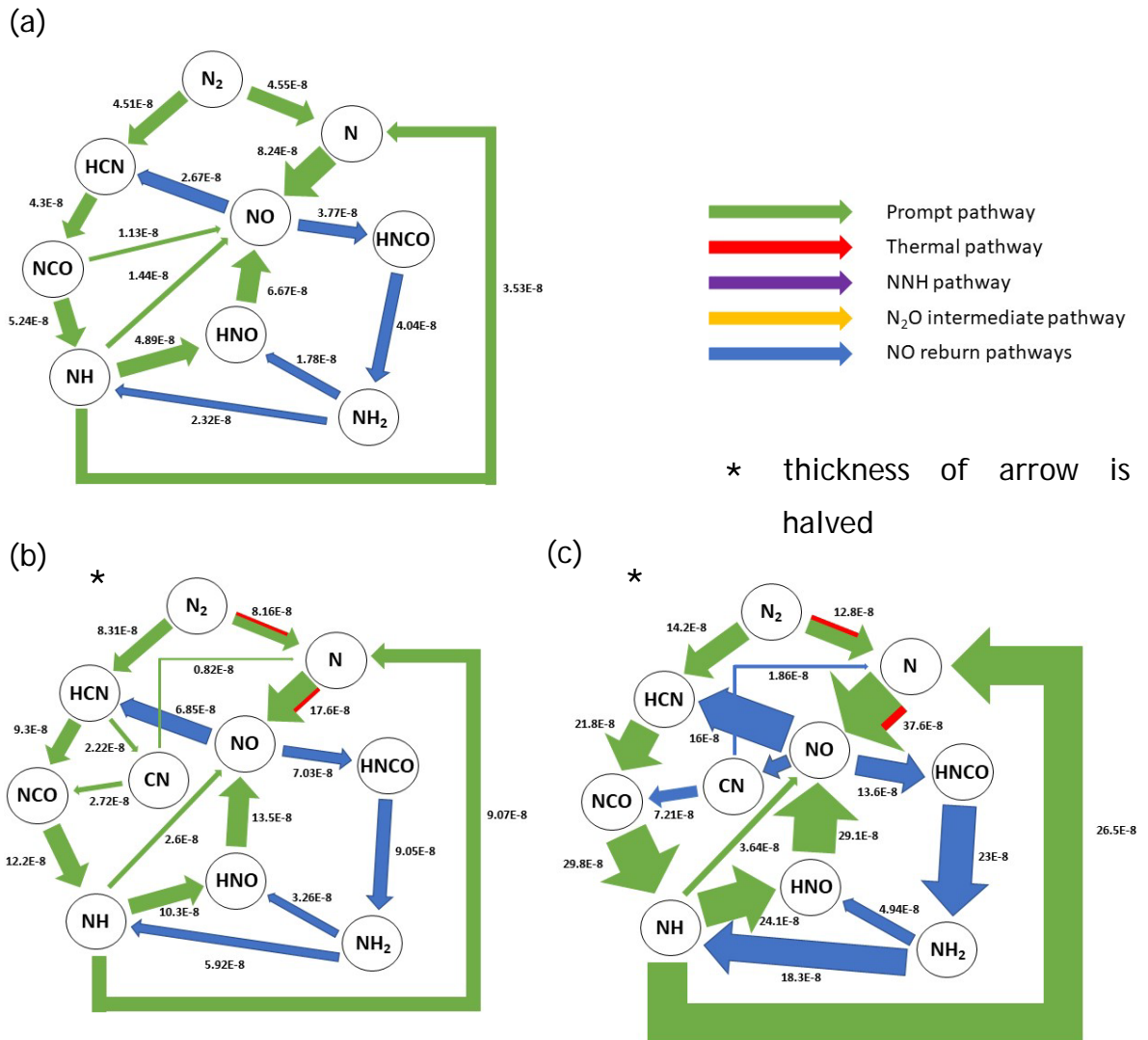


Figure 5-33: Quantitative reaction path diagram showing NO formation/consumption pathways predicted by GRI-Mech 3.0 mechanism at flame zone reactor for CH₄/air flames at (a) $\Phi = 0.94$, (b) $\Phi = 1.0$, and (c) $\Phi = 1.1$. Units [moles/cm³.s]

5.3.3.2. [NO] Sensitivity Analysis

[NO] Sensitivity analyses is carried out in this Section with the aids of NO formation pathways and absolute rate of production (ROP) for NO to identify and analyse various paths of NO formation and consumption for premixed CH₄/air flames in industry scale swirl burner at lean to rich conditions. Figure 5-33, Figure 5-34 and Figure 5-35 show NO formation

pathways at the flame zone reactor predicted by GRI-Mech 3.0, Aramco 1.3 and SanDiego mechanisms, respectively at the flame zone reactor for $\Phi = 0.94 - 1.1$.

GRI-Mech 3.0 mechanism predicts NO formation (Figure 5-33) mainly by prompt mechanism at the flame zone reactor and NO production increases as Φ increases, due to increasing availability of hydrocarbon radicals. Molecular N_2 converts to atomic nitrogen and HCN by reacting with CH radical at the lean condition. However, as the Φ increases, flame temperature increases, resulting in introduction of thermal pathway to convert N_2 to N, in addition to the prompt pathway. Nitrogen atom converts to NO by reacting with OH and O_2 , while some of the NO converts back to N through the reactions $C + NO \leftrightarrow CO + N$ and $CH + NO \leftrightarrow N + HCO$. HCN converts to NCO by reacting with atomic oxygen, and NCO subsequently reacts with atomic hydrogen to produce NH radical. Interestingly, some of the NCO react with O and OH radicals to produce NO at the lean condition but these reactions have very minimal effect at the higher Φ considered here due to reduction in the production of the radicals. NH converts to NO following two different pathways: small amount directly converting to NO by reacting with O radical and mainly through $NH \Rightarrow HNO \Rightarrow NO$ route. Substantial amount of NH convert to atomic nitrogen through the reactions $NH + H \leftrightarrow N + H_2$ and $NH + OH \leftrightarrow N + H_2O$, which in turn produce further NO.

NO is recycled back to HCN through reactions with HC radicals and produce O and OH radicals in the process. NO also reacts with CH_2 radicals to produce HNCO and H, and these two products react with each other to produce NH_2 radical and CO. NH_2 radicals react with H and OH radicals to produce NH, and with atomic oxygen to convert to HNO. Some of the NO molecules convert to CN at the rich condition by reacting with C.

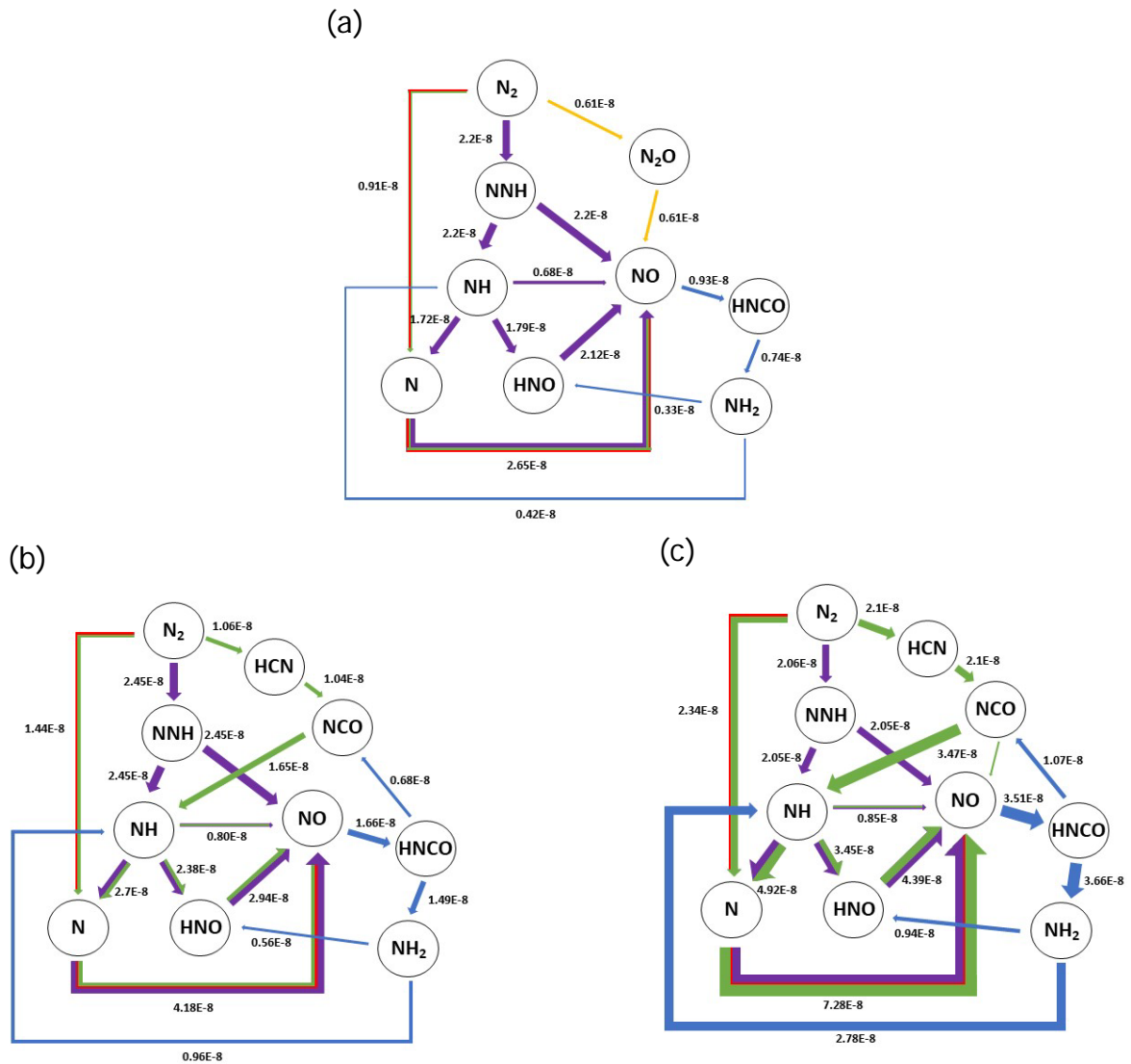


Figure 5-34: Quantitative reaction path diagram showing NO formation/consumption pathways at flame zone reactor predicted by Aramco 1.3 mechanism for CH_4/air flames at (a) $\Phi = 0.94$, (b) $\Phi = 1.0$, and (c) $\Phi = 1.1$. Units [$\text{moles}/\text{cm}^3 \cdot \text{s}$]

Figure 5-34 illustrates NO formation pathways at the flame zone reactor predicted by Aramco 1.3 mechanism at (a) $\Phi = 0.94$, (b) $\Phi = 1.0$ and (c) $\Phi = 1.1$. Interestingly, despite employing the same nitrogen chemistry as M1 mechanism, there are significant differences in the pathway predictions between these two mechanisms. Aramco 1.3 predicts NO formation mainly through NNH pathway at the lean condition and prompt pathway becomes more important with increasing Φ due to increase in hydrocarbon radical's availability. Molecular N_2 converts to NNH through the reactions $\text{N}_2 + \text{H} \leftrightarrow \text{NNH}$ and $\text{N}_2 + \text{H} + \text{M} \leftrightarrow \text{NNH} + \text{M}$, and some of the NNH converts back to N_2 through the reaction $\text{NNH} + \text{H} \leftrightarrow \text{H}_2 + \text{N}_2$.

Planar NO-LIF in Unconfined Flames

The latter reaction becomes more prominent at the rich condition, resulting in decrease in NNH production from N_2 . NNH converts to NH and NO by reacting with O radicals.

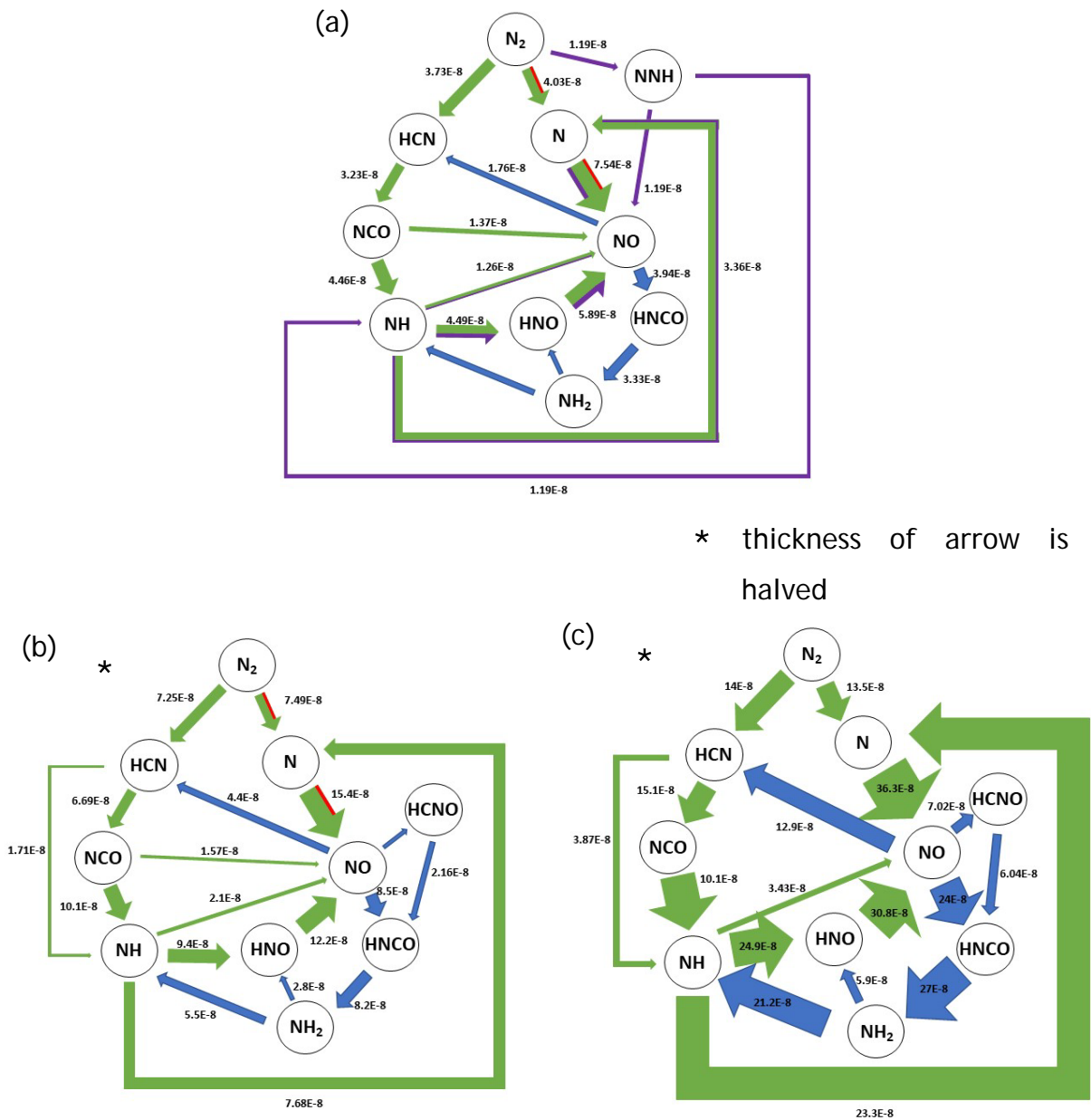


Figure 5-35: Quantitative reaction path diagram showing NO formation/consumption pathways predicted by SanDiego mechanism at flame zone reactor for CH_4 /air flames at (a) $\Phi = 0.94$, (b) $\Phi = 1.0$, and (c) $\Phi = 1.1$. Units [$\text{moles}/\text{cm}^3 \cdot \text{s}$]

N_2O intermediate pathway also contributes to NO production (Figure 5-34 (a)) through the reactions $N_2O + H \leftrightarrow NH + NO$ and $N_2O + O \leftrightarrow 2NO$ at $\Phi = 0.94$. However, this pathway does not contribute at higher equivalence ratios due to decrease in O radicals' production and available third body,

as N_2 converts to N_2O through the third body reaction $N_2 + O(+M) \leftrightarrow N_2O(+M)$.

NO pathways at the flame zone reactor predicted by SanDiego mechanism are shown in Figure 5-35 for (a) $\Phi = 0.94$, (b) $\Phi = 1.0$ and (c) $\Phi = 1.1$. Interestingly, predictions from SanDiego mechanism includes both prompt and NNH pathways at $\Phi = 0.94$, with a small contribution from thermal pathway. However, NNH pathway becomes negligible, compared to the more prominent prompt pathway at higher Φ conditions. This behaviour can be attributed to the balance between NNH and N_2 conversions and increased availability of HC radicals. The reaction $N + NO \leftrightarrow N_2 + O$ operates in the forward direction at the rich condition from M3 mechanism prediction, due to increase in NO production and decreased O radical availability, resulting in negligible contribution from thermal pathway, Figure 5-35 (c).

From the simulation results, NO production in the post flame zone reactor is almost doubled for $\Phi = 0.94$ and 1.0 by the Aramco 1.3 mechanism prediction, whereas the increase in NO production in the PFZ reactor is minimal by the GRI-Mech 3.0 mechanism prediction and small increase from the prediction by the SanDiego mechanism. Hence, NO formation pathways in the post flame zone reactor is analysed in Figure 5-36 for (a) $\Phi = 0.94$, (b) $\Phi = 1.0$ and (c) $\Phi = 1.1$. It must be noted that Figure 5-36 displays NO formation pathways 25 cm from the burner exit.

Thermal pathway is the most prominent NO formation mechanism in the post flame zone reactor, as can be seen in Figure 5-36 due to increased temperature in the zone and O radical availability. NO formation decreases significantly at the rich condition due to reduction in O and OH radical production. NNH and N_2O intermediate pathways are also predicted to have small contributions towards NO production at the post flame zone. Interestingly, prompt pathway does not play any role in the post flame zone NO formation. This can be attributed to HC radicals already being burnt out in the flame zone.

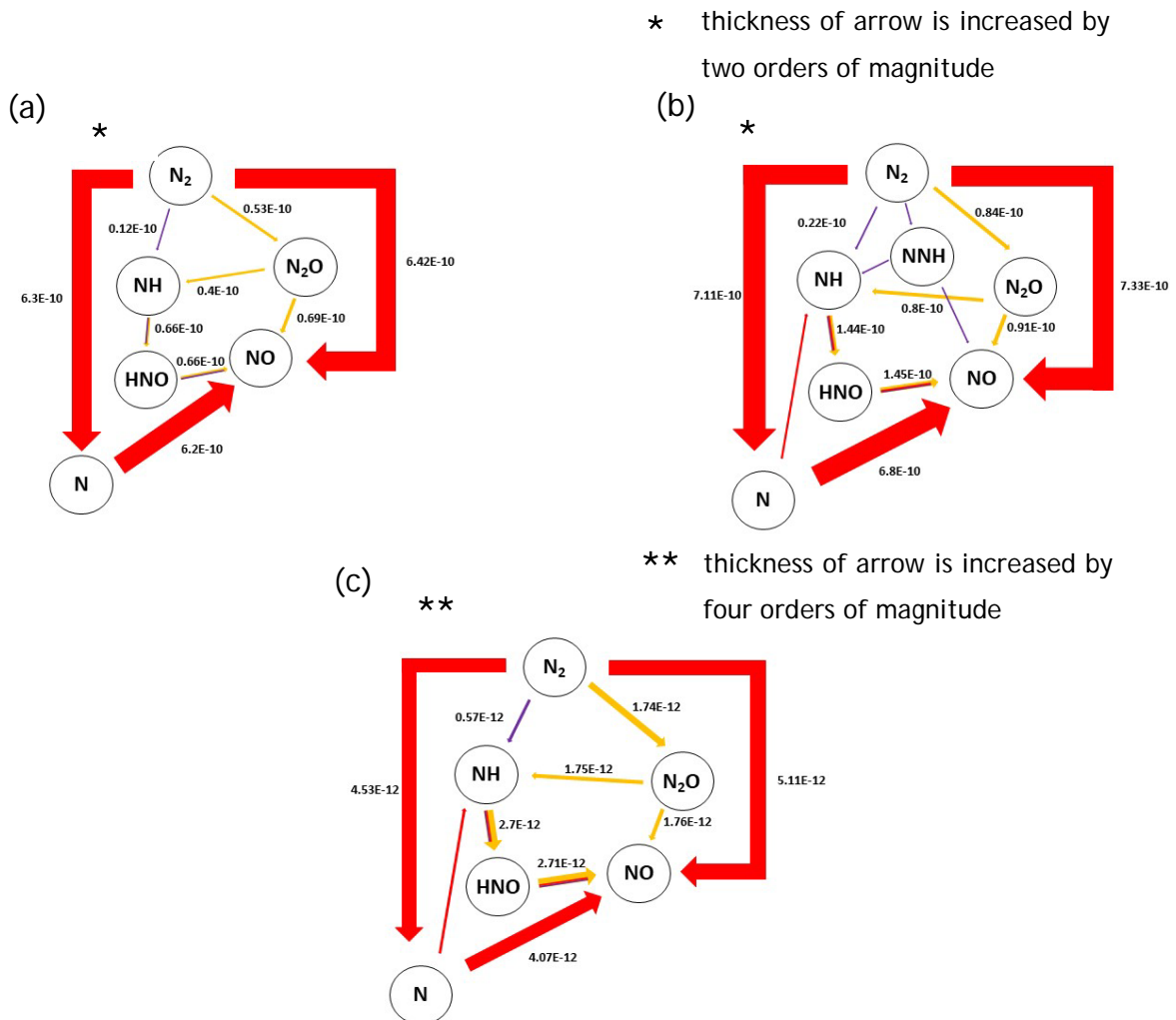
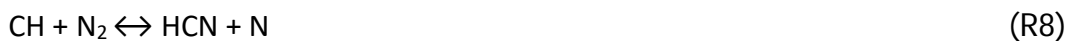


Figure 5-36: Quantitative reaction path diagram showing NO formation pathways predicted by M2 mechanism at post flame zone reactor (25 cm from burner exit) for CH₄/air flames at (a) $\Phi = 0.94$, (b) $\Phi = 1.0$, and (c) $\Phi = 1.1$. Units [moles/cm³.s]

Important reactions affecting NO production are identified next by conducting [NO] sensitivity analyses at the flame zone, predicted by M1, M2 and M3 mechanisms in the CH₄/air flame at $\Phi = 0.94 - 1.1$. From the NO formation analyses earlier, the key elementary reactions influencing the NO formation are as follows:





The reaction $\text{CH} + \text{N}_2 \leftrightarrow \text{HCN} + \text{N}$ (R8) is the most important initiating reaction of the prompt pathway NO formation implemented in all the three mechanisms considered here. The next two reactions $\text{CH} + \text{O}_2 \leftrightarrow \text{O} + \text{HCO}$ (R9) and $\text{CH} + \text{H}_2\text{O} \leftrightarrow \text{H} + \text{CH}_2\text{O}$ (R10) prevent molecular N_2 to convert to atomic N through prompt pathway by CH radical reacting otherwise. The reaction $\text{O} + \text{CH}_3 \leftrightarrow \text{H} + \text{CH}_2\text{O}$ (R11) avert CH_3 radicals to convert to the important CH radicals, hence reducing NO production from the prompt pathway. The reaction $\text{NNH} + \text{O} \leftrightarrow \text{NH} + \text{NO}$ (R12) is the key chain termination reaction for NO formation through NNH pathway. The reaction $\text{CH}_2 + \text{OH} \leftrightarrow \text{CH} + \text{H}_2\text{O}$ (R13) converts CH_2 radicals to CH radicals, thus improving NO formation through prompt pathway. The next reaction $\text{N} + \text{NO} \leftrightarrow \text{N}_2 + \text{O}$ (R14) is the well-known key step for NO production in the thermal pathway. The next three reactions $\text{NH} + \text{NO} \leftrightarrow \text{N}_2\text{O} + \text{H}$ (R15), $\text{N}_2\text{O} + \text{H} \leftrightarrow \text{N}_2 + \text{OH}$ (R16) and $\text{N}_2 + \text{O}(+\text{M}) \leftrightarrow \text{N}_2\text{O}(+\text{M})$ (R17) are representing the N_2O intermediate pathway. The recombination reaction $\text{H} + \text{O}_2(+\text{M}) \leftrightarrow \text{HO}_2(+\text{M})$ (R18) consumes molecular oxygen and thus restricts the process of NO formation. Reactions R17 and R18 along with R2 only feature in post flame zone [NO] sensitivity analyses.

Figure 5-37 shows the normalised sensitivity coefficients of NO production at the flame zone reactor for GRI-Mech 3.0, Aramco 1.3 and SanDiego mechanisms at (a) $\Phi = 0.94$, (b) $\Phi = 1.0$ and (c) $\Phi = 1.1$. Reaction R8 displays highest positive sensitivity for GRI-Mech 3.0 and SanDiego mechanisms. Sensitivity for R8 increases with increasing Φ due to increasing fuel content in the mixture. Conversely, reactions R9, R10 and R11 have high negative sensitivity coefficients as these reactions

restrict HC radicals to react with molecular nitrogen. Impact of R9 reaction on [NO] decreases with increasing Φ due to reduction in O_2 availability, while sensitivity of reaction R10 increases as Φ rises due to increasing production of H_2O . Interestingly, sensitivity for reaction R11 stays nearly constant for all three conditions by SanDiego but increases for Aramco 1.3 mechanism and decreases for GRI-Mech 3.0 mechanism as Φ increases. The differences in this behaviour can be attributed to the pre-exponential factor (A) values for this reaction. The A values for reaction R11 are given as $5.060E+13$, $5.540E+13$ and $8.430E+13$ for GRI-Mech 3.0, Aramco 1.3 and SanDiego mechanisms, respectively.

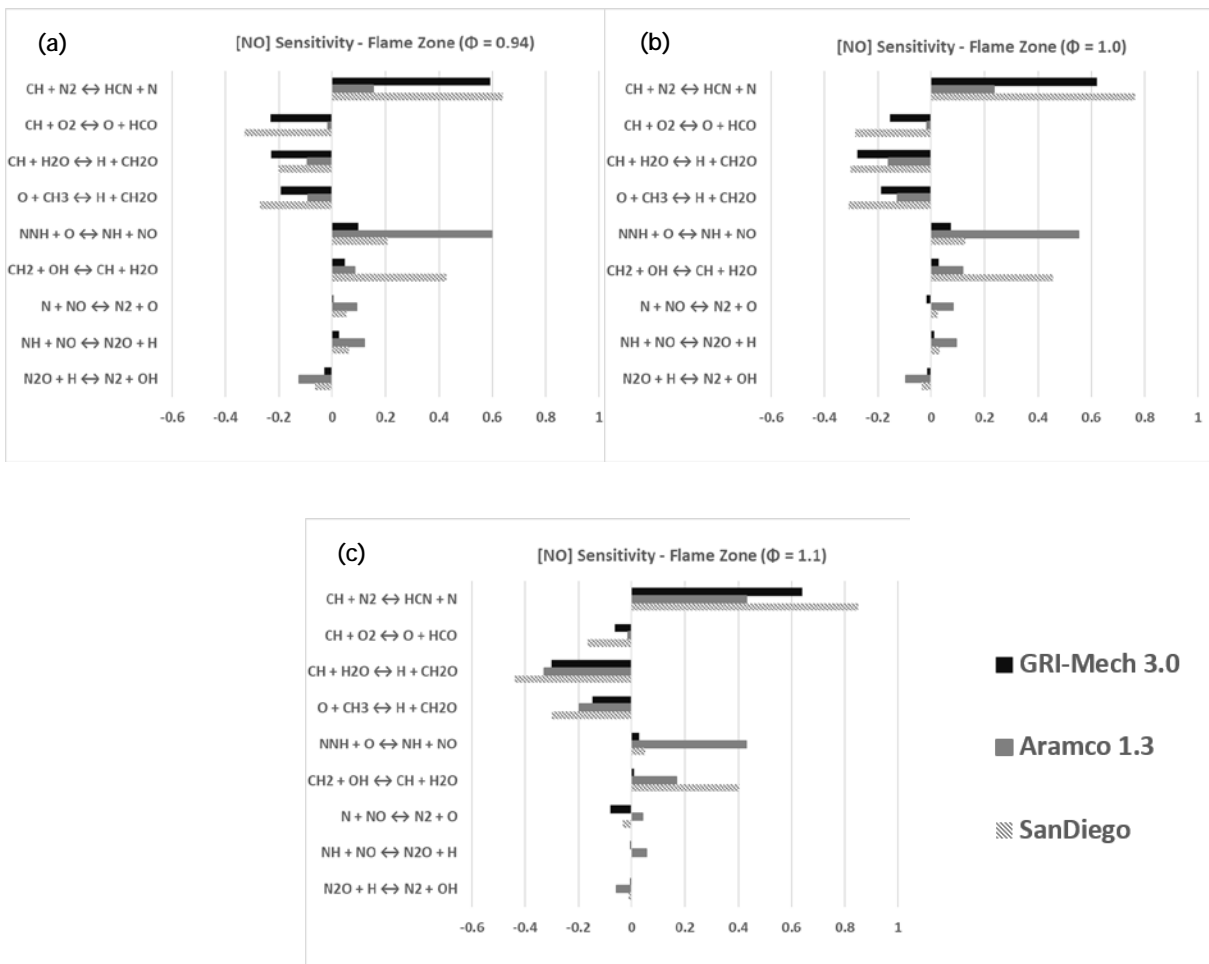


Figure 5-37: Computed normalized sensitivity coefficients of [NO] on net reaction rates at the flame zone reactor for (a) $\Phi = 0.94$, (b) $\Phi = 1.0$, (c) $\Phi = 1.1$. Units [-]

The contributions from NNH pathway (reaction R12) has the highest impact on Aramco 1.3 mechanism as it was seen earlier in NO formation

pathway analysis. Sensitivity coefficients for reaction R12 decreases with increasing Φ , as O radical production reduces. Reaction R13 is a key reaction to produce CH radicals which in turn initiate NO formation through prompt pathway. Like reaction R11, reaction R13 displays discrepancies in terms of trend in sensitivity coefficients values for the three mechanisms compared here. Sensitivity coefficients value for reaction R13 has decreasing and increasing trend for GRI-Mech 3.0 and Aramco 1.3 mechanisms, respectively, while the value increases for SanDiego mechanism at first and then decreases as Φ increases. However, this reaction has the same A value of $1.130E+07$ for all three mechanisms. This behaviour can be attributed to the differences in CH₂ and OH species productions predicted by the three mechanisms, Figure 5-38.

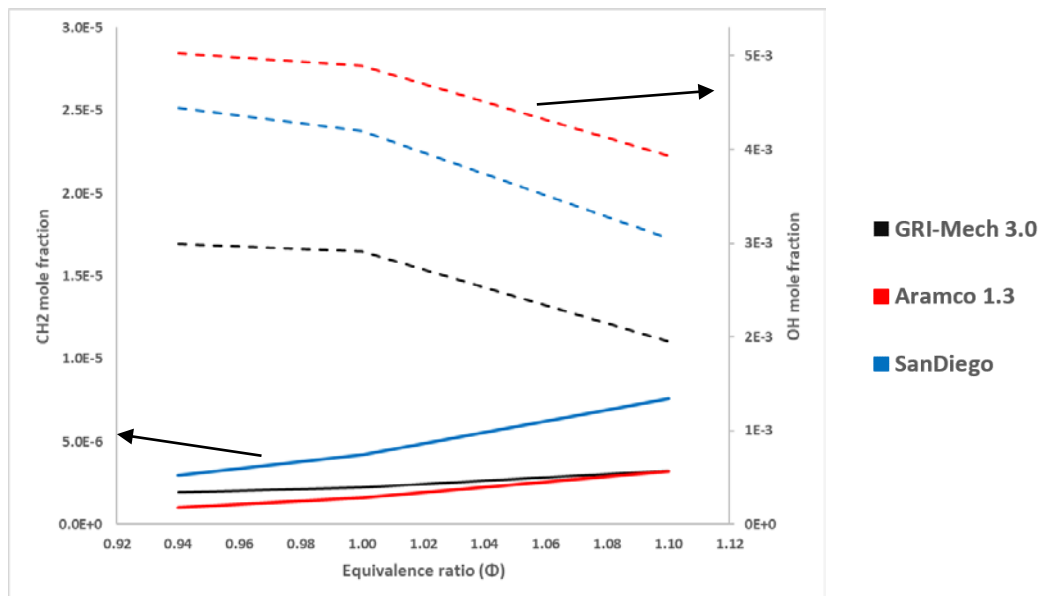


Figure 5-38: Variation of CH₂ and OH mole fraction at the flame zone reactor as a function of Φ .

NO formation through thermal pathway (R14) and N₂O intermediate pathway (R15 and R16) have very small impact compared to prompt and NNH pathways for all three mechanisms under investigation in the flame zone reactor. Aramco 1.3 has the highest sensitivity coefficients value for reactions R14, R15 and R16. Sensitivity for reaction R14 decreases as Φ increases due to decrease in O radical production. Moreover, at higher

Planar NO-LIF in Unconfined Flames

Φ , mechanisms GRI-Mech 1.3 and SanDiego predict the reaction R14 to operate in the opposite direction to facilitate NO consumption.

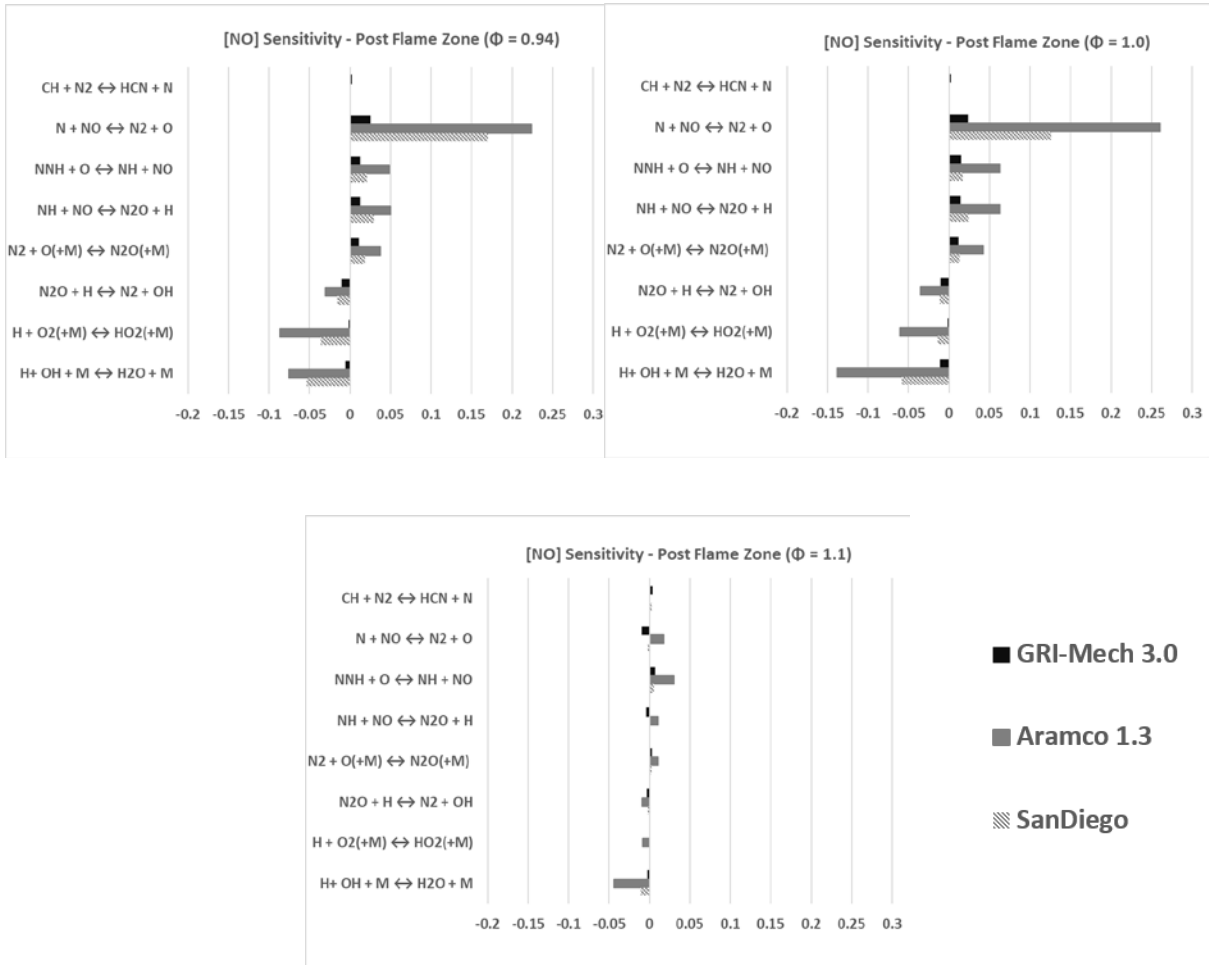


Figure 5-39: Computed normalized sensitivity coefficients of [NO] on net reaction rates at the post flame zone reactor (25 cm from burner exit) for (a) $\Phi = 0.94$, (b) $\Phi = 1.0$, (c) $\Phi = 1.1$. Units [-]

Next, [NO] sensitivity analysis at the post flame zone reactor are carried out to identify the key reactions and NO formation pathways. Figure 5-39 compares the normalised sensitivity coefficients at 25 cm from the burner exit in the post flame zone reactor by the mechanisms at (a) $\Phi = 0.94$, (b) $\Phi = 1.0$ and (c) $\Phi = 1.1$. Contrary to the flame zone, prompt pathway (reaction R8) has very minimal contributions towards NO production at the post flame zone. Thermal pathway (reaction R14) followed by NNH pathway (reaction R12) and N_2O intermediate pathway (reactions R15-R17) become the main contributors of NO formation at $\Phi = 0.94$ and 1.0. However, at the rich condition, NO production reduces

drastically due to reduction in oxygen and temperature. Reactions R2 and R18 display negative sensitivities for all three conditions and by all three mechanisms as they consume OH radical and molecular oxygen which are crucial for NO formation.

5.4. Summary

The objective of this chapter was to validate NO PLIF measurements by examining the formation of NO through the flame front of CH₄/air flames in Bunsen burner and HPOC in unconfined configuration and comparing the results with theoretical calculations from CHEMKIN. This was achieved through a qualitative NO PLIF experimental campaign, incorporating careful control of the experimental boundary conditions and CHEMKIN analysis. The Following observations can be made from this chapter:

- For the 25 mm Bunsen burner, the flame stabilized closer to the nozzle and heat release intensity increases between 10 - 20 mm from burner exit as Φ decreased, resulting in higher NO formation. $AvgInten_{NO}$ increases with AFT and decreases with rich Φ as per Zel'dovich mechanism. Decreasing trend of maximum CH and CH₂ mole fraction calculated from CHEMKIN with increasing Φ was correlated with decreasing AFT and increasing activation energy requirements.
- For the open flame at HPOC, the flame reaction zone retracted axially downstream and radially outward as Φ increased. As Φ increased and air flow decreased, the flame got wider, as the CRZ got stronger due to more relative fuel content in the flow. With decreasing gas flow velocity and increasing turbulent flame velocity, the flame stabilized closer to the burner nozzle exit. PLIF images indicated NO formation got stronger as premixed gas moved towards stoichiometry and then got weaker in rich conditions. Prompt NO pathways found responsible for differences in peaks for $AvgInten_{NO}(\Phi = 0.94)$ and measured NO ($\Phi = 1.0$) by gas analyser. Laser energy attenuation by UV absorption from CO₂

and H₂O was identified as the reason behind the asymmetry in the NO PLIF images.

- Simple changes were made to the modified Valera model to model the open flame at HPOC. All seven mechanisms considered here exhibited same trend with increasing Φ as the measured NO trend, which again validated the model at atmospheric conditions. It can be concluded from the results, the model prediction may improve if the recirculation values and volume values for flame zone, CRZ and ERZ is derived from CFD for open flame conditions.
- Chemical reactor modelling of the unconfined HPGSB - 2 was undertaken to locate the source of NO formation observed in the experimental data. Discrepancies were found between the chemical kinetic mechanisms' predictions on NO formation pathways. Quantitative reaction path diagrams showed the prompt pathway to be the dominant source of NO formation at the flame zone with very low contribution from thermal pathway at the stoichiometry and rich conditions. However, significant contributions from the NNH pathway at the flame zone were predicted by Aramco 1.3 mechanism with increasing contributions from prompt pathway as Φ increases. SanDiego mechanism predicted NO formation mainly from prompt pathway with small contributions from NNH pathway at $\Phi = 0.94$, and thermal pathway contributed by a small margin at the lean and stoichiometry condition. Sensitivity analyses at the post flame zone indicated NO formation contributions mainly from thermal pathway due to high temperature, followed by the NNH and N₂O intermediate pathways.

6. Planar NO-LIF in Confined Flame

In the previous chapter, NO formation in the open flames were discussed and analysed through non-intrusive LIF and chemiluminescence measurements. In this chapter, NO formation is investigated in confined flames using two different excitation wavelengths (285.16 and 226.03 nm) as discussed in Chapter 3.3, and compared with comparative data from CHEMKIN calculations. 285.16 nm NO excitation wavelength is used to analyse NO formation at typical gas turbine running conditions in the industry. Effects of adding H₂ in CH₄ flames on flame shapes and NO formation are also considered here. Results from these different excitation wavelengths are compared and verified against the measured data by gas analyser. Effect of confinement on the flame shape and NO formation are also discussed here. Finally, all the investigated conditions are simulated using the modified Valeria model (refer to Chapter 4.2.2) with some changes to accommodate open confinement HPOC configuration. NO predictions from the mechanisms detailed in Chapter 4.1 are compared with the measured values at exhaust.

6.1. 285.16 nm Excitation

285.16 nm excitation wavelength was used to conduct qualitative NO-PLIF measurements in the HPOC, using HPGSB-2 with CH₄ and CH₄/H₂ fuels at various Φ and experimental data is validated by comparing with the data from numerical analysis in CHEMKIN platform, using GRI-Mech 3.0 mechanism [260]. Numerical analysis in CHEMKIN was completed using the same methodology described in Chapter 3.10.

6.1.1. Base ($\Phi = 0.55 - 0.65$)

NO PLIF investigations were conducted for Base fuel at a range of Φ in the operating region of power generation [3], [281]. This lean range of Φ was chosen for low AFT and corresponding effects on emissions and combustion stability. Many previous investigations were conducted by researchers to understand the flame shape, stability and exhaust emissions in these ranges of Φ [282]-[288]. To the author's knowledge, investigations were done herein for the first time to understand the changes in NO formations as Φ varies in an industry scale swirl burner

with gaseous fuels by conducting NO PLIF experiments. The purpose of this investigation was to monitor the changes in NO formation and correlate this with flame shape, heat release intensity and also evaluate the relationships between these characteristics, which are vital for safe operation in these ranges. OH* chemiluminescence data were taken at each point to understand the flame shape and correlate NO formation with heat release. Table 6-1 displays the flow conditions for this investigation.

Table 6-1: Flow conditions of Base fuel in HPGSB-2

Test point	CH ₄ mass flow (g/s)	Air mass flow (g/s)	Entry Temperature, T ₂ (K)	Equivalence ratio (Φ)	AFT (K)	CH ₄ speed (m/s)	Air speed (m/s)	Total flow speed (m/s)	Laminar Flame speed (m/s)
10	0.835	26.11	573	0.55	1788	1.93	33.47	35.4	0.499
11	0.835	23.93	573	0.6	1878	1.93	30.68	32.61	0.577
12	0.835	22.09	573	0.65	1962	1.93	28.32	30.25	0.682

6.1.1.1. OH* Chemiluminescence Comparison

Changes in heat release intensity and flame stabilization locations as Φ varies at Base fuel are presented in terms of Abel-transformed OH* chemiluminescence images in Figure 6-1. Colormaps are normalized to the maximum intensity at each image and across the column for left-side and right-side images, respectively in Figure 6-1. Left-side images show the locations of heat release and flame stabilization points, whereas right-side images display the changes in heat release level as Φ varies.

From Figure 6-1, the heat release zone gets shorter and stabilizes closer to the burner exit as Φ increases. This corresponds to the flow conditions illustrated in Table 6-1, where total flow speed decreases but S_L increases with increasing Φ . And as the turbulent flame speed is intricately related to S_L for CH₄, turbulent flame speed matches the flow speed closer to the burner exit at $\Phi = 0.65$, creating a CRZ closer to the burner exit, compared to the leaner conditions. But as the flow gets leaner, flow speed increases, forcing to form CRZ further away from the burner exit, hence flame stabilizes further away.

When the Abel-transformed OH^* chemiluminescence images are normalized to the maximum intensity across the images (refer to Figure 6-1 right-side images), an observable increase in heat release is evident as Φ increases. Heat release intensity and flame temperature increase can be attributed to the increased fuel contents in the unburned mixture. This is further validated from CHEMKIN simulation results shown in Figure 6-2, where (a) volumetric heat release and (b) maximum OH mole fraction is plotted as a function of 1-D spatial concentration profile. Maximum OH mole fraction and volumetric heat release rate increases with Φ as it is apparent in Figure 6-1. This is further validated in Figure 6-3, where maximum OH^* intensity and maximum OH mole fraction calculated from CHEMKIN at each point are plotted as a function of Φ . Both increases as Φ increases as expected.

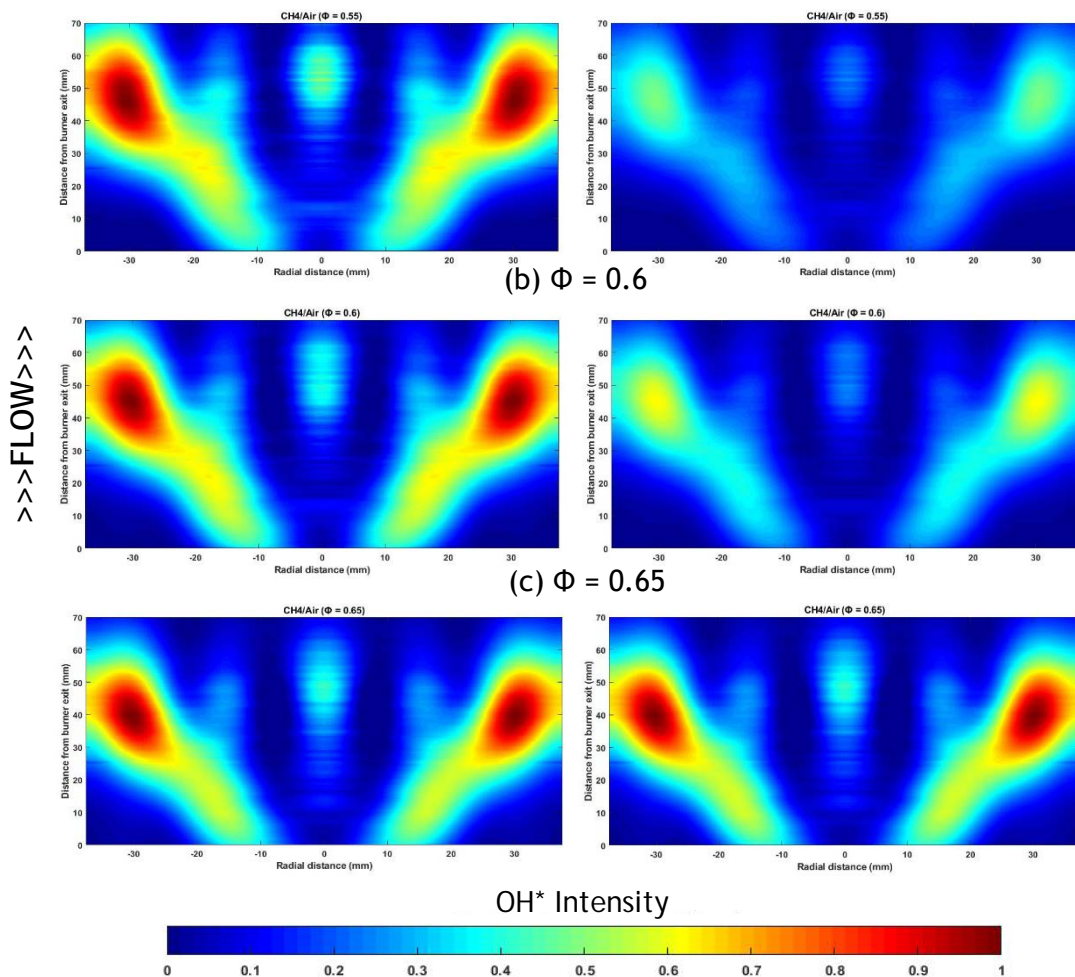
(a) $\Phi = 0.55$ 

Figure 6-1: Abel-transformed OH^* chemiluminescence images at varying Φ . Colormap normalised to maximum OH^* intensity at each Φ and across column on the left side and right side, respectively. Flow direction is from bottom to top.

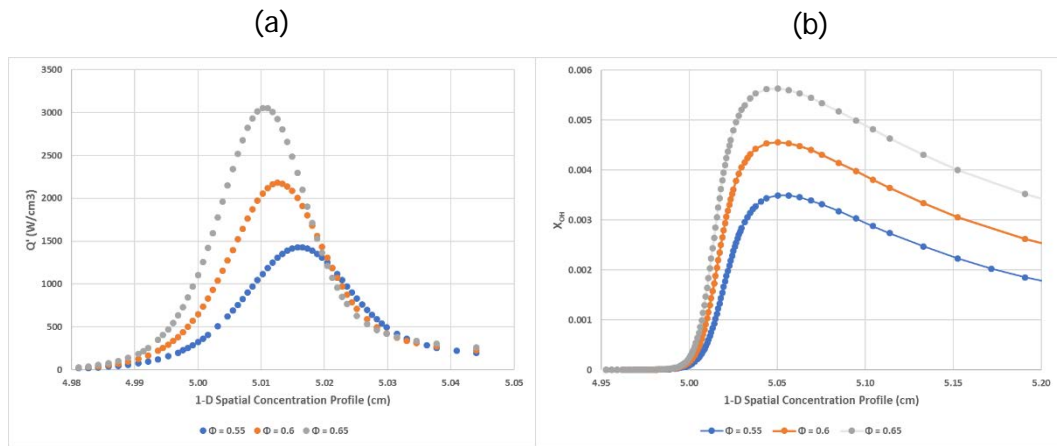


Figure 6-2: CHEMKIN results showing (a) volumetric heat release rate and, (b) OH mole fraction as a function of 1-D spatial concentrations profiles for $\Phi = 0.55 - 0.65$

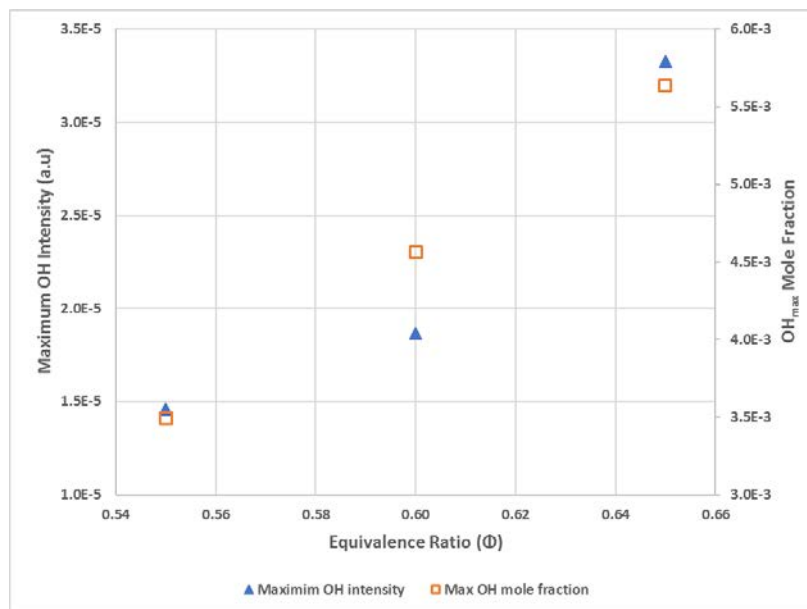


Figure 6-3: Maximum OH* intensity and maximum OH mole fraction as a function of Φ

6.1.1.2. NO PLIF Comparison

Qualitative NO PLIF experiments were conducted at the flow conditions described in Table 6-1 to analyse the changes in intensities and locations of NO formation as Φ varies. As Φ increases, flame temperature increases, contributing increased NO formation in the flame from Zel'dovich pathway (refer to Chapter 2.1.1). This is evident from the experimental results presented in Figure 6-4, where colormaps are normalized to the maximum intensity at each image and across the column for left-side and right-side images, respectively. Left-side images show the locations of NO formations near the burner exit, whereas right-

side images display the changes in NO formation intensity level as Φ varies. This increased trend in NO formation is further validated in Figure 6-5, where $AvgInten_{NO}$ and AFT are plotted as a function of Φ . With increasing Φ , availability of excess O_2 in the flame decreases but still enough to burn the increasing fuel contents completely, resulting in increased flame temperature, contributing to increasing NO intensity trend.

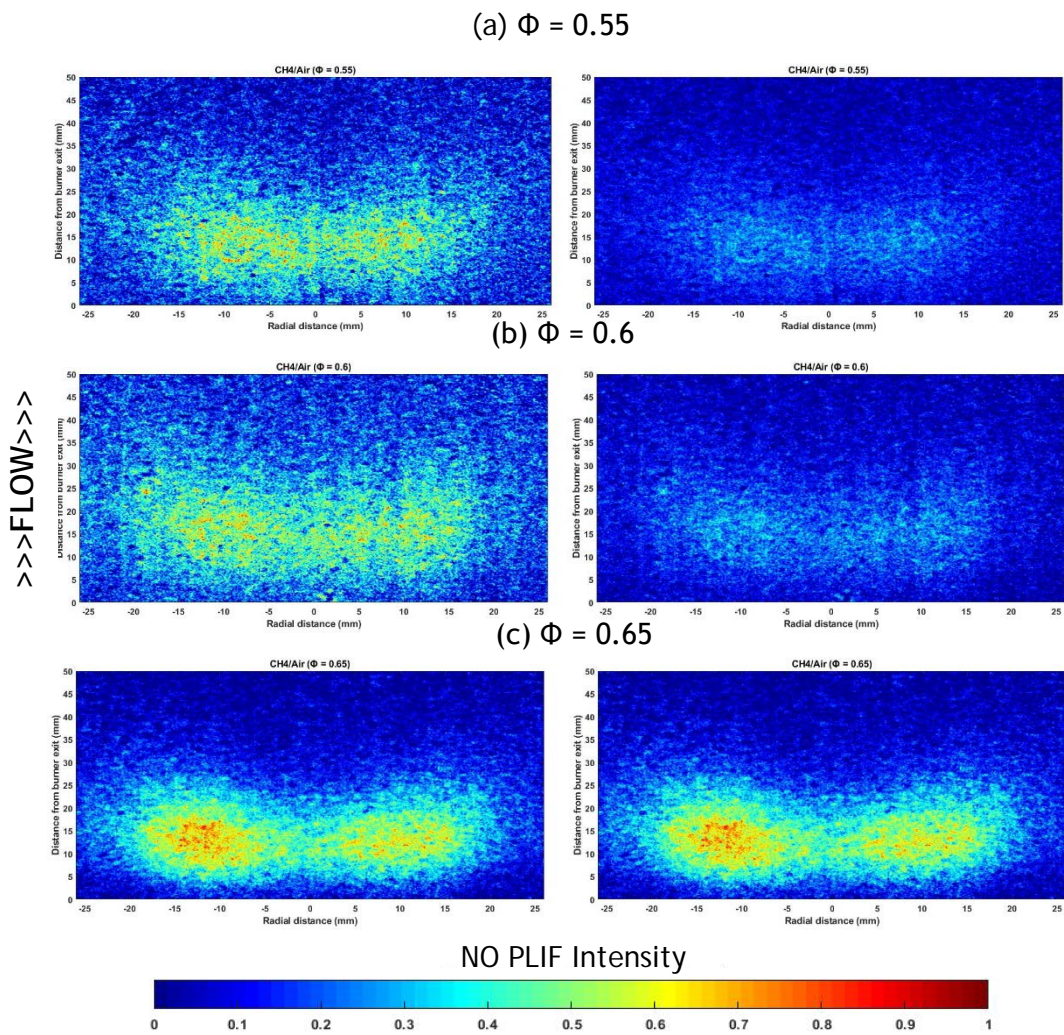


Figure 6-4: NO PLIF images at varying Φ . Colormap normalised to maximum intensity at each Φ and across column on the left side and right side, respectively. Flow direction is from bottom to top.

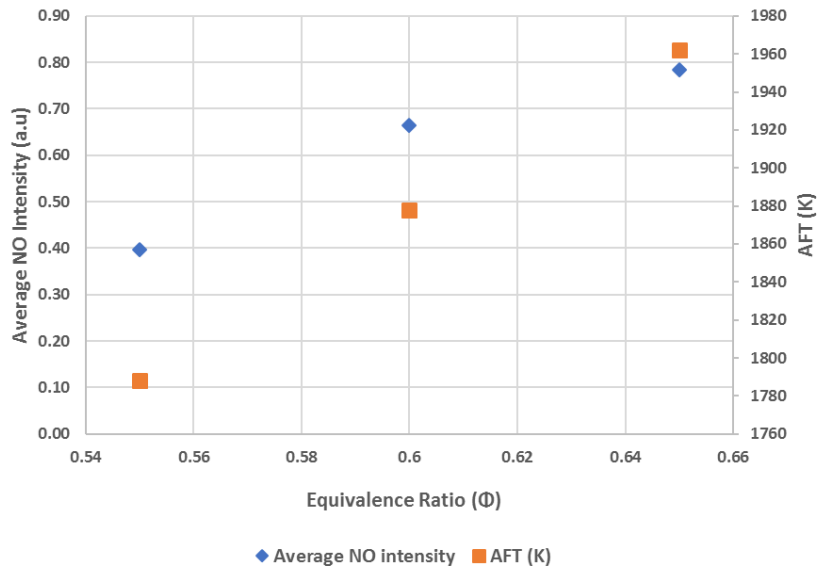


Figure 6-5: Average NO PLIF intensity and AFT as a function of Φ

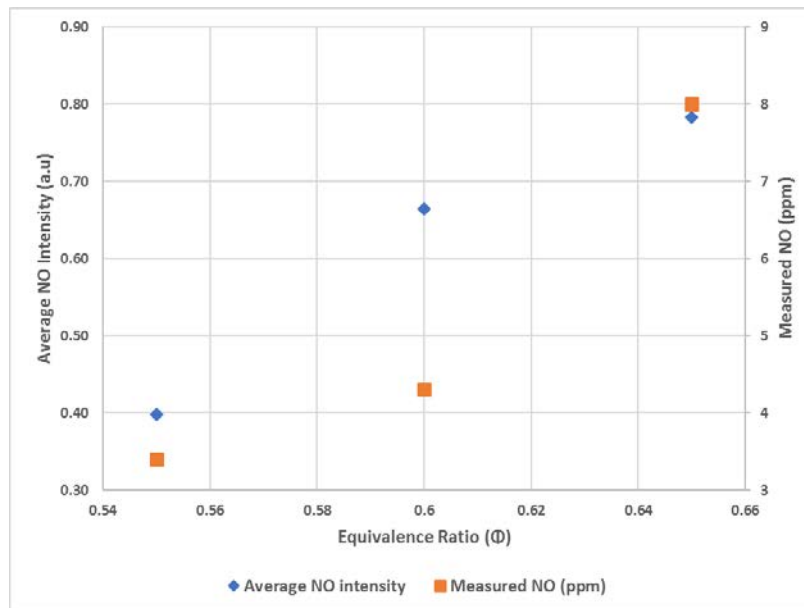


Figure 6-6: Average NO PLIF intensity and measured NO as a function of Φ

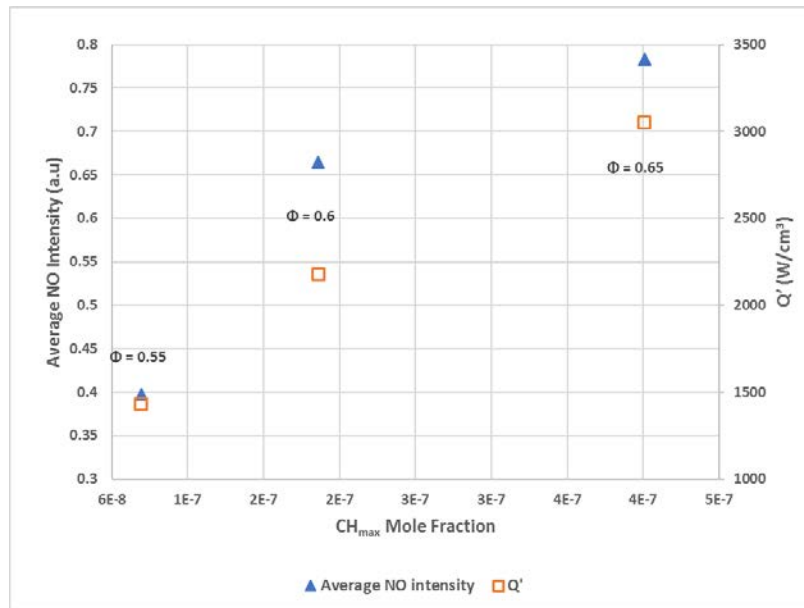


Figure 6-7: Average NO PLIF intensity and volumetric heat release rate as a function of maximum CH mole fraction. Respective Φ is shown in increasing order.

NO was measured at exhaust by the gas analyser at each point and is plotted with $AvgInten_{NO}$ against Φ in Figure 6-6. Both measured NO at exhaust and $AvgInten_{NO}$ from NO PLIF data show the same increasing trend as Φ increases. It must be noted that measured NO at exhaust accounts for both thermal and prompt NO. As NO PLIF measurements were taken at burner exit, it can be safely assumed that NO formations captured were mainly from thermal pathway. As measured NO by gas analyser follows the same trend as $AvgInten_{NO}$ from NO PLIF experiments, it can be concluded that NO formed from prompt pathway downstream follows the same increasing trend as Φ increases. This conclusion agrees with Figure 6-7, where $AvgInten_{NO}$ and Q' are plotted against maximum CH mole fraction calculated from CHEMKIN for each points under investigation. Respective Φ for each point is also shown on the graph. Maximum CH mole fraction increases with Φ , contributing to increasing NO formations downstream from prompt pathway. Volumetric heat release calculated from CHEMKIN also increases as Φ increases. This behaviour is consistent with the experimental data from OH* chemiluminescence and NO PLIF.

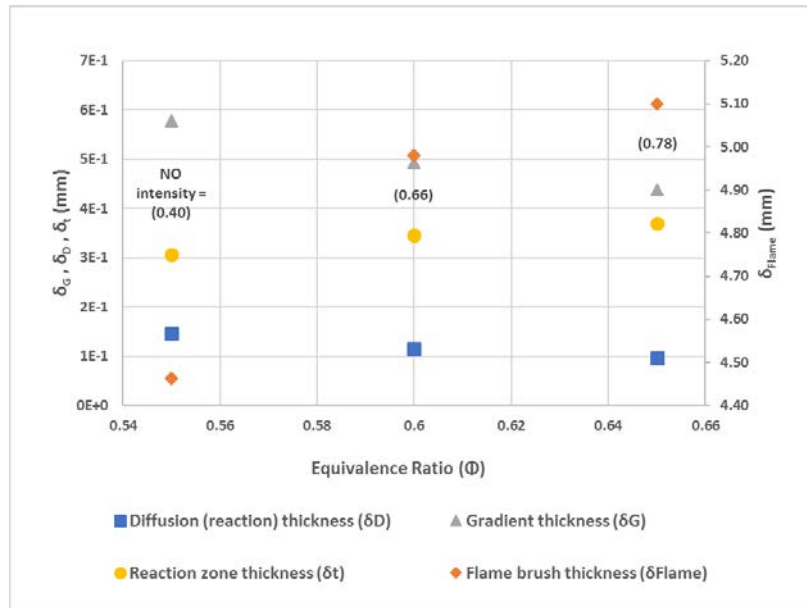


Figure 6-8: Numerical and experimental flame thickness as a function of Φ . NO PLIF intensity is shown for every TP in the graph.

Figure 6-8 plots flame thickness as a function of Φ . Flame thickness is calculated in four different ways both numerically and experimentally as mentioned earlier in Chapter 3.10.1.2. It must be noted that flame thickness calculated from numerical methods (δ_D , δ_G and δ_t) are plotted on the primary axis and experimentally measured flame brush thickness (δ_{flame}) is plotted on the secondary axis. $AvgInten_{NO}$ also shown in the graph as Φ changes. δ_t and δ_{flame} show the same increasing trend as $AvgInten_{NO}$ with increasing Φ . As mentioned earlier in Chapter 3.10.1.1, δ_t is the difference between maximum OH and CH mole fraction location calculated from CHEMKIN at each point. Location of the maximum CH mole fraction shifts to the right quicker than the maximum OH mole fraction as Φ increases (refer to Figure 6-10), resulting in larger δ_t with increasing Φ . δ_{flame} is calculated from the experimental flame shape from OH* chemiluminescence images (refer to Chapter 3.10.1.2), which contributes to the linearity between δ_{flame} and NO formation. δ_D and δ_G represent the flame reaction thickness and whole flame thickness including preheat zone, respectively. They both show decreasing trend with increasing Φ but rate of decrease for δ_D is slower than δ_G as Φ increases, resulting in relatively larger flame reaction thickness. This relatively larger flame reaction thickness allows more reactions to take

place as residence time increases, hence $AvgInten_{NO}$ value increases. Figure 6-9 shows very good agreement in the trend between measured NO values and (δ_G/δ_D) ratio with increasing Φ . (δ_G/δ_D) ratio represents the relative change in flame thickness as Φ varies.

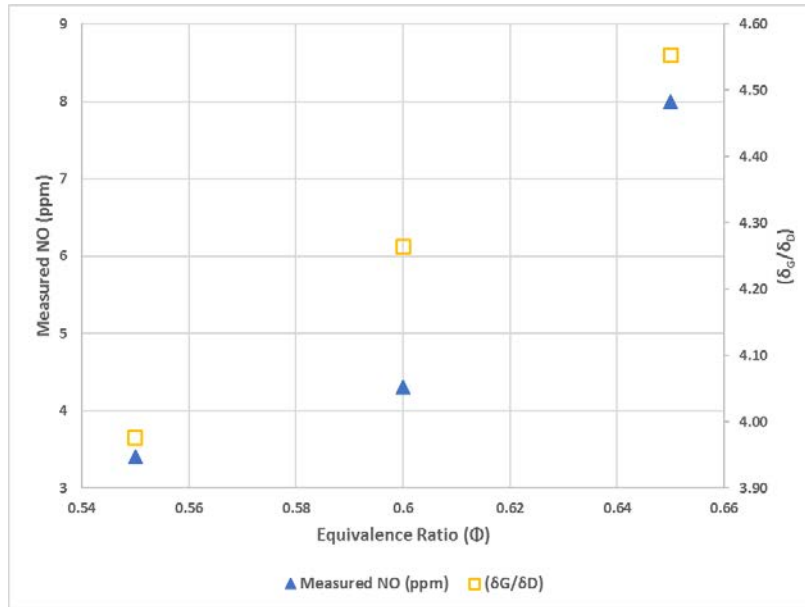


Figure 6-9: Measured NO and (δ_G/δ_D) as a function of Φ

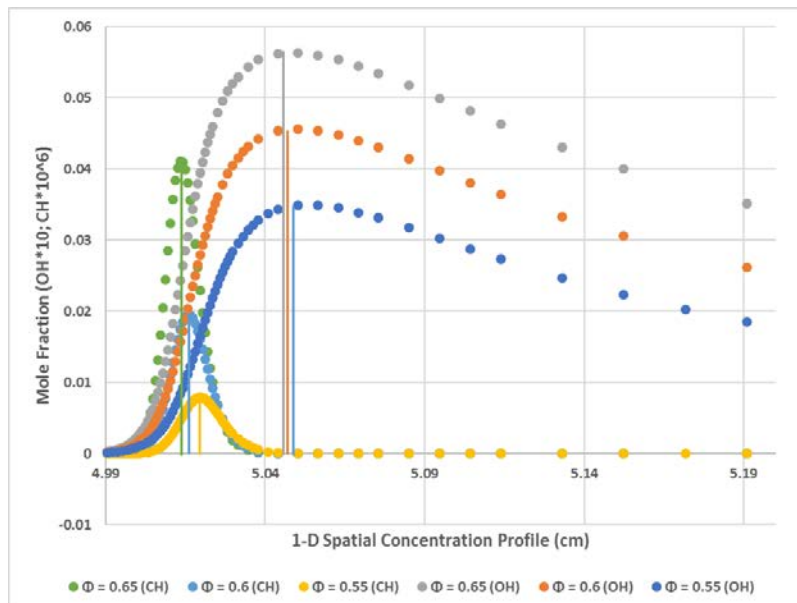


Figure 6-10: Relative change in maximum OH and CH mole fraction location from CHEMKIN calculations as Φ changes

Planar NO-LIF in Confined Flame

Figure 6-11 and Figure 6-12 shows the OH* chemiluminescence and NO PLIF images side by side for the flow conditions mentioned in Table 6-1 with colormap normalized to maximum Φ and to maximum intensity across the images, respectively. The laser sheet path is indicated by the red dashed line on the first images (refer to Figure 6-11 (a) and Figure 6-12 (a)) of each figure. Both horizontal and vertical axes are kept to the same limits for OH* chemiluminescence and NO PLIF images to compare the relationship between NO formation and heat release more effectively. Flows are from bottom to top in these images. NO formations shown only in the path of laser sheet, as NO cannot be excited without laser energy for the PLIF images, whereas OH* chemiluminescence images shows the heat release in whole flame as laser energy is not required for chemiluminescence measurements.

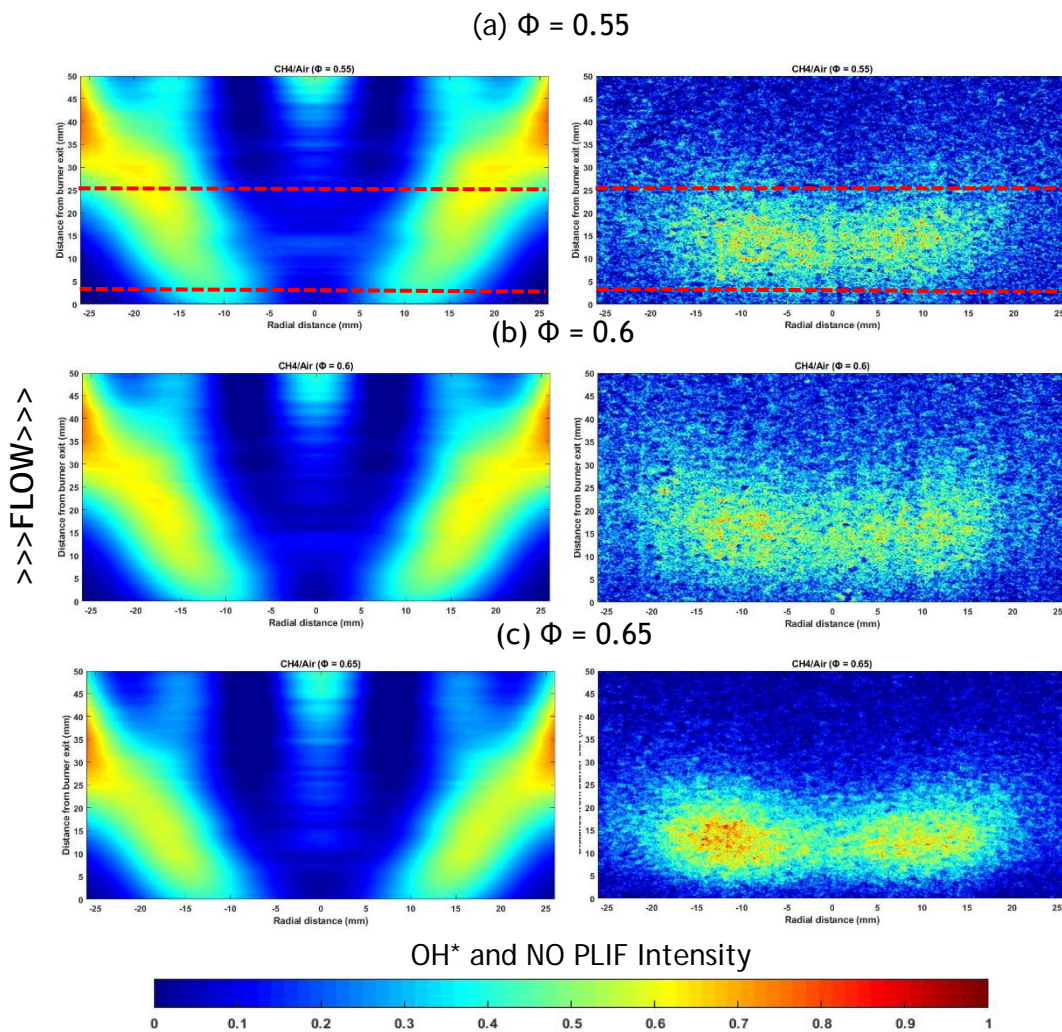


Figure 6-11: Abel - transformed OH* chemiluminescence and NO PLIF images side by side. Colormap normalised to maximum intensity at each Φ .

From Figure 6-11, the flame is lifted from burner exit as Φ decreases. As mentioned earlier, NO PLIF measurements were taken at the burner exit. These two effects, combined with increase in flame thickness, flame temperature result in increasing NO formation at the burner exit with increasing Φ . Figure 6-12 demonstrates the increase in heat release level intensity and consequent increase in NO formation intensity as Φ increases.

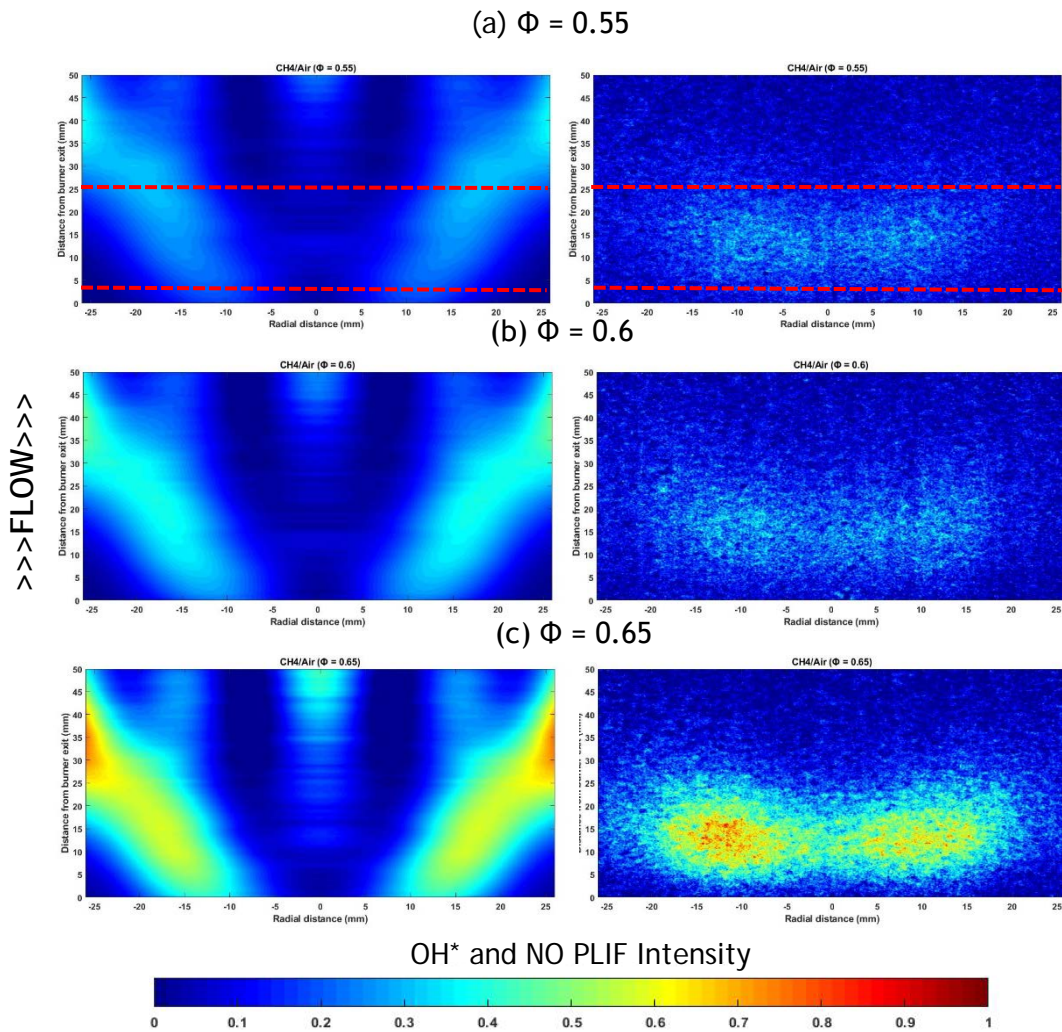


Figure 6-12: Abel - transformed OH* chemiluminescence and NO PLIF images side by side. Colormap normalised to maximum intensity across the images.

Relationships between $AvgInten_{NO}$, $AvgInten_{OH}$, maximum OH mole fraction from CHEMKIN calculations and Φ are shown in Figure 6-13 for the flow conditions under investigation here. $AvgInten_{NO}$ shows linear increasing trend with increasing $AvgInten_{OH}$ and maximum OH mole fraction as expected.

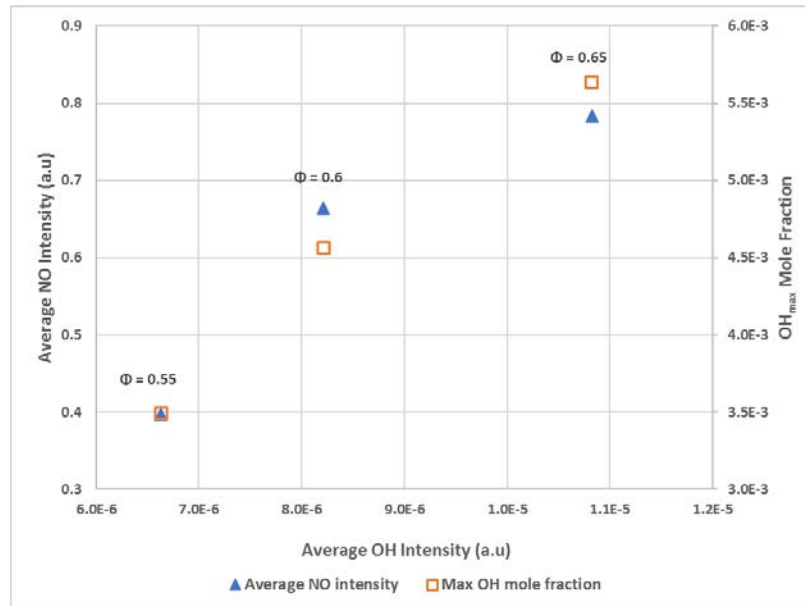


Figure 6-13: Average NO PLIF intensity and maximum OH mole fraction from CHEMKIN as a function of average OH* chemiluminescence intensity. Φ is shown in the graph for each point in increasing order.

6.1.2. Effects of Hydrogen Addition

A variety of low carbon intensity hydrogen production methods are currently being explored to enable the use of hydrogen as an energy vector within existing natural gas infrastructure [32], [289]–[292]. Extensive studies regarding the changes in combustion characteristics witnessed upon H_2 addition to CH_4 /air flames measured using various laboratory apparatus have been conducted, summarised in [293]–[296]. The changes in the locations and intensities of NO formation at the burner exit with H_2 addition has not been investigated so far to the author's best knowledge. Consequently, NO PLIF experiments were conducted in preheated $FARH_2$ fuels (85% CH_4 /15% H_2) at atmospheric pressure. OH* chemiluminescence data were taken at each point to understand the flame shape and correlate NO formation with heat

release level. Table 6-2 displays the flow conditions for this investigation.

Table 6-2: Flow conditions of FARH₂ fuel in HPGSB-2

Test point	CH ₄ mass flow (g/s)	H ₂ mass flow (g/s)	Air mass flow (g/s)	Entry Temperature, T ₂ (K)	Equivalence ratio (Φ)	AFT (K)	Total flow speed (m/s)	Laminar Flame speed (m/s)
13	0.806	0.018	26.32	573	0.55	1793	37.12	0.502
14	0.811	0.018	24.06	573	0.6	1882	34.23	0.653
15	0.801	0.018	22.17	573	0.65	1966	32.84	0.752

6.1.2.1. Changes in Flame Stabilization & Heat Release Levels

To isolate the influence of hydrogen addition on premixed CH₄ flame stabilization mechanisms, experiments were conducted at the same Φ with a fixed HPGSB-2 burner geometry and nominally similar flow and turbulence conditions (refer to Table 3-7). Substantial changes in flame shapes and stabilization locations are observed from the Abel-transformed OH* chemiluminescence images in Figure 6-14 and Figure 6-15, when 15% H₂ was added with CH₄. Figure 6-14 and Figure 6-15 show the OH* chemiluminescence images for BASE and FARH₂ fuels side by side at the same Φ . Images are normalised to maximum intensity at each Φ for Figure 6-14 to illustrate the changes in flame shapes and stabilization points with H₂ addition, whereas at Figure 6-15, colormap is normalised to the maximum intensity across images to display the changes in heat release level as Φ changes and H₂ added to CH₄.

From Figure 6-14, both BASE and FARH₂ flames are observed to stabilize along the outward expanding shear layer between the CRZ and ERZ, yielding conical, V-shaped flames which expand radially outward from the burner exit centreline ($r = 0$ mm). However, the influence of hydrogen addition is immediately apparent, as the flames are observed to transition upstream towards the burner exit nozzle at each Φ , compacting the heat release zones. In addition to that, CRZ appears to envelop larger area with H₂ addition. This is the result of the compounding effect of the thermo-diffusive behaviour of CH₄-H₂ blends

with increased turbulence and chemical reactivity as the hydrogen encourages chain-branching reactions, thus the heat release proceeds on a reduced chemical time scale while the flow time scale has been held nominally constant. According to Runyon et al. [223], turbulent burning velocity influences the flame structure and stabilization under elevated conditions, and this will be further influenced by the fuel compositions in the reacting swirl flow. To that end, a study by Kido et al. [297] investigated turbulent flame velocity of CH₄-H₂ fuel blend, which is of significant interest to understand the flame shapes and stabilization points of FARH₂ blends. Results from this study are given in Figure 6-16, where turbulent flame velocity is plotted as a function of increased turbulence intensity at $\Phi = 0.8$ and atmospheric conditions. It can be observed that turbulent flame velocity increases with increasing turbulent intensity, although it is not apparent if the trend is nonmonotonic or saturates. What is perhaps most interesting in this data is the influence of H₂ addition assuming a fixed turbulence intensity. With the addition of H₂, the turbulent burning velocity increases compared to pure CH₄ at an assumed constant turbulence intensity. While this data was captured at atmospheric temperature and pressure conditions, it is indicative of a difference in behaviour between these two fuels which, in other fundamental measures such as S_L and AFT, have been observed to increase reactivity.

As a comparison between the varying fuel compositions and the distribution of heat release areas and flame shape, Table 6-3 displays the changes in flame angle (α) with change in fuel composition and equivalence ratio. The derived flame angle for CH₄/air flame at $\Phi = 0.65$ is shown in Figure 6-14 (c) for reference. This provides a quantitative measure of the mean heat release distribution within the field of view and highlights the influence of variable fuel composition, pressure, and turbulence on observed flame stabilisation locations. Further information on this methodology can be found in the work by Han and Hochgreb [298]. With addition of hydrogen, flame angle decreases due to high diffusivity of H₂. Interestingly, flame angle also decreases with increasing Φ . This can be attributed to methane's thermo-diffusive

response under lean conditions as with increasing Φ , Re decreases for the conditions considered here.

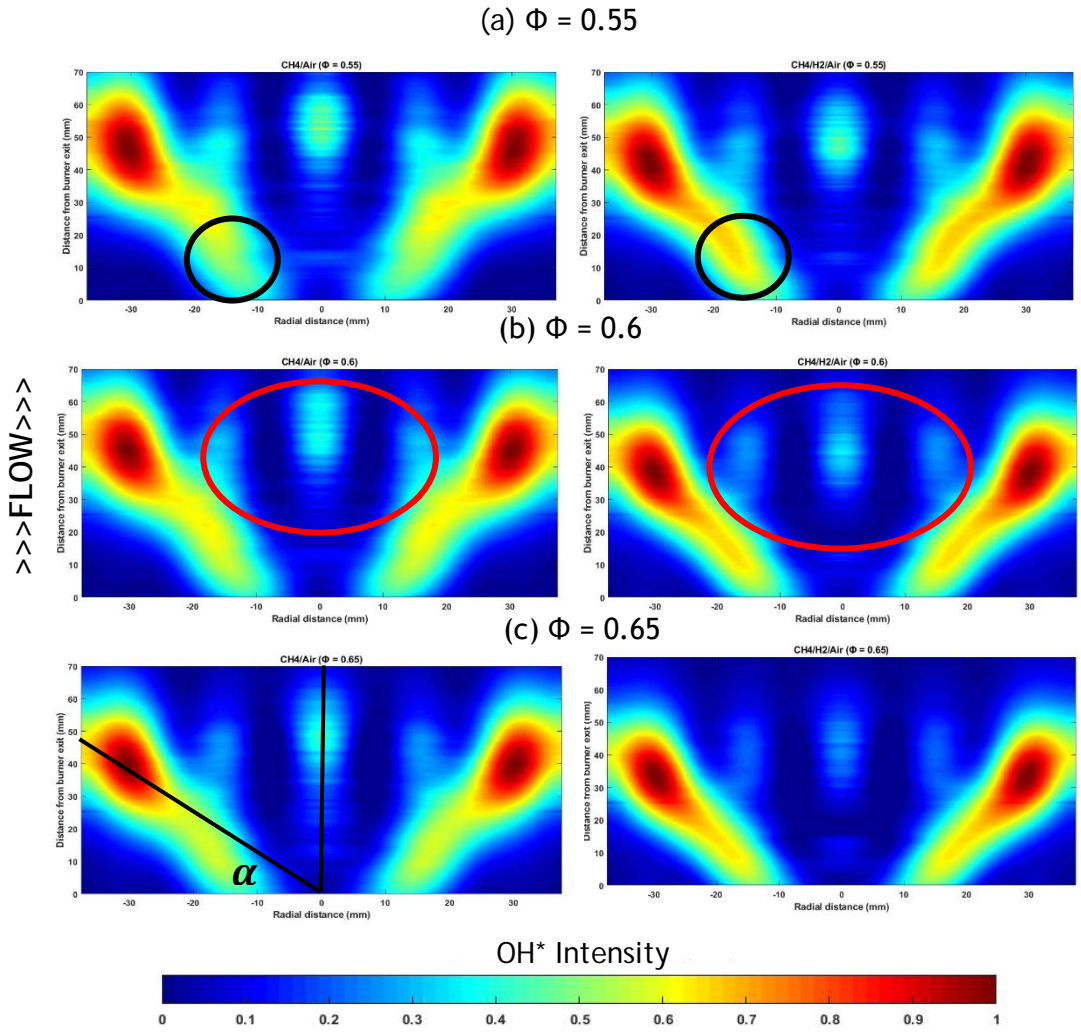


Figure 6-14: Effects on flame shapes with 15% H₂ additions. BASE fuel on left side and FARH₂ on right side. Colormap normalised to maximum intensity at each Φ . The black and red circles indicate the changes in flame attachment and CRZ envelope, respectively with H₂ addition.

Table 6-3: Changes in flame angle (α) with fuel and equivalence ratio (Φ)

Equivalence Ratio (Φ)	Flame angle (α)	
	CH ₄ -air	CH ₄ -H ₂ -air
0.55	56.47°	53.92°
0.6	55.95°	51.77°
0.65	52.18°	48.41°

Planar NO-LIF in Confined Flame

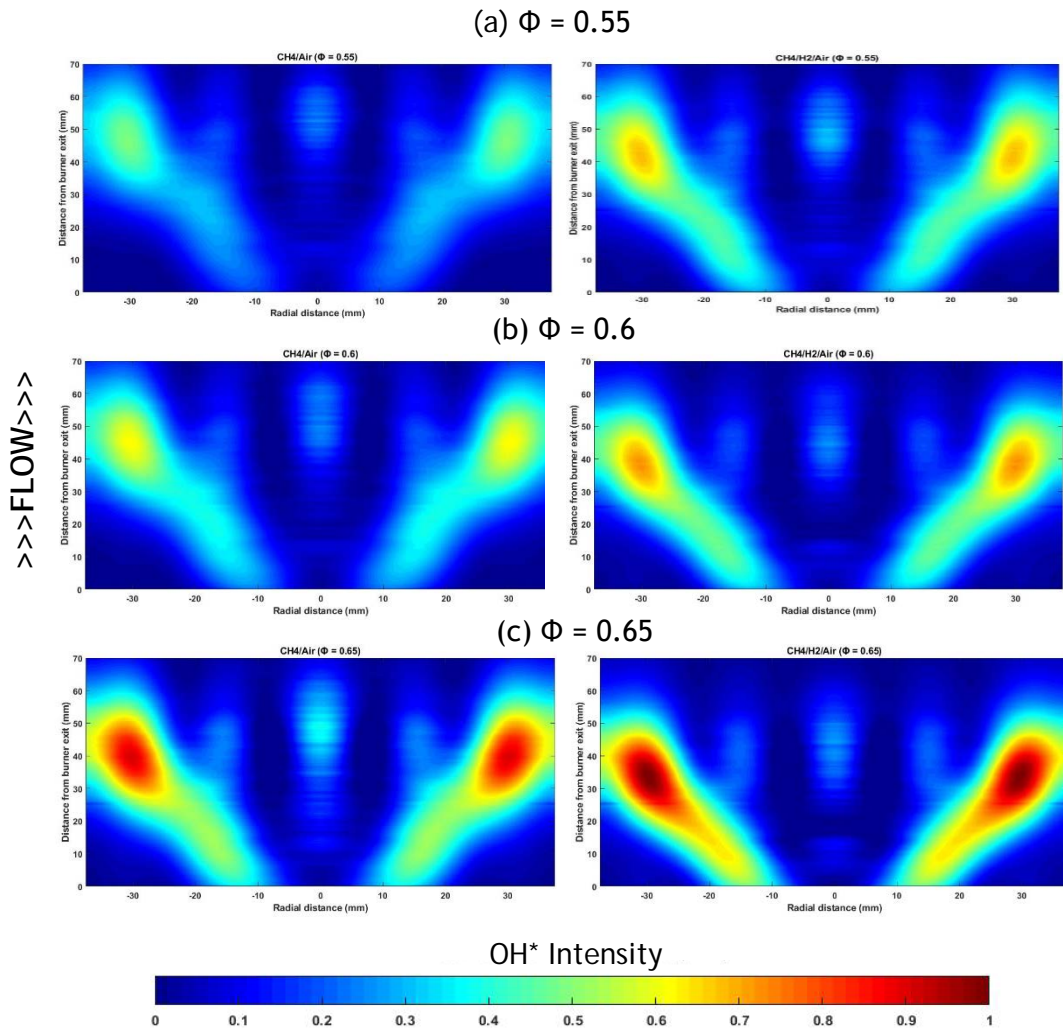


Figure 6-15: Effects on flame shapes with 15% H₂ additions. BASE fuel on left side and FARH₂ on right side. Colormap normalised to maximum intensity across the images.

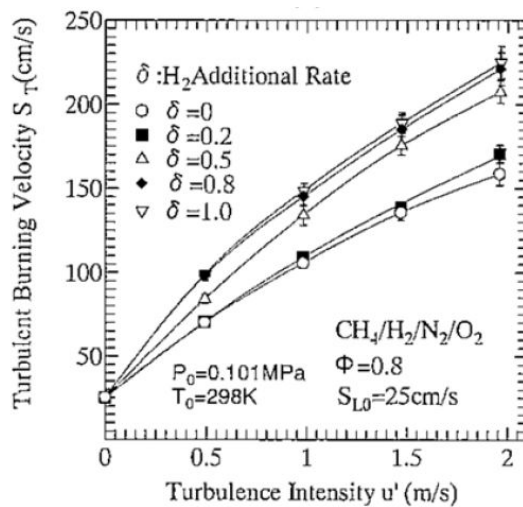


Figure 6-16: Influence of turbulence intensity and H₂ addition to CH₄ on the turbulence burning velocity. Reproduced from [297].

A relatively small amount of H₂ is seen to augment the burning intensity of CH₄. Relative increase in S_L, Q' and maximum mole fraction of H, O and OH radicals were calculated from CHEMKIN simulations using GRI-Mech 3.0 mechanism [260] and plotted against Φ in Figure 6-17, Figure 6-18 and Figure 6-19, respectively. As shown in Figure 6-18, the burning intensity of CH₄ is significantly enhanced, consequence of the facilitated diffusion and reactivity of H₂. This enhanced heat release augments as Φ decreases, with a relative increase in volumetric heat release rate of \approx 12% at $\Phi = 0.55$, analogous to relative increases witnessed in S_L (refer to Figure 6-17). Recently, Nilsson et al. [299] experimentally and numerically studied the chemical kinetic effects of H₂ enrichment (up to 50% volumetric) on the S_L of natural gas blends containing various amount of higher hydrocarbons. Their modelling indicates that H₂ addition to CH₄ affects the overall oxidation mechanism to a greater extent than for C₂₊ alkanes. The production of important active radicals (H*, O*, OH*) is sharply increased, resulting in enhanced reactivity, and by extension faster S_L. Of particular significance with respect to the topic of this study, Nilsson et al. [299] concluded that at lean conditions, the combustion enhancement can be attributed to the increased concentration of H* radical. In order to give better perception of the differences witnessed, Figure 6-19 plots the increase in H*, O* and OH* radical concentrations for the CH₄/H₂ experiments conducted. When no other fuel is present, CH₄ oxidation is initiated by its reaction with O₂ and by thermal dissociation. In the CH₄/H₂ blends, H₂ reacts first, leading to the formation of radicals (H, O, OH) which enhances the oxidation mechanics of CH₄, leading to increased burning intensity and reactivity, reflected in augmented flame speeds [300].

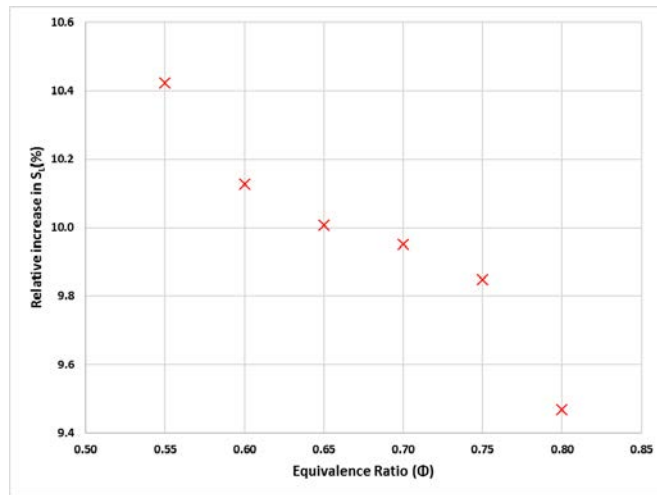


Figure 6-17: Relative increase in S_L for CH_4 with H_2 addition (15% volumetric)

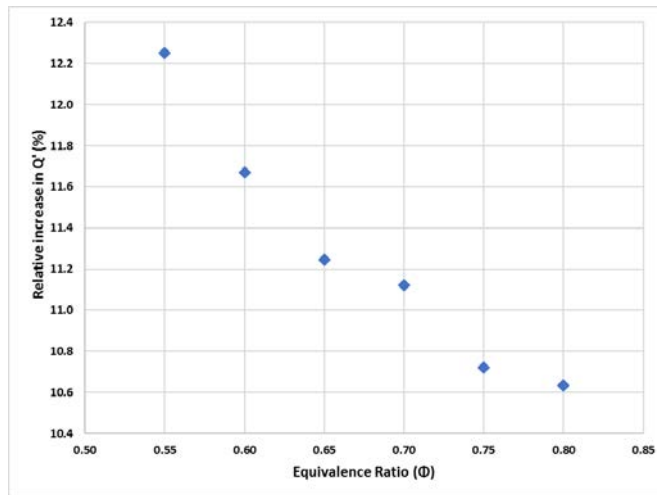


Figure 6-18: Relative increase in Q' for CH_4 with H_2 addition (15% volumetric)

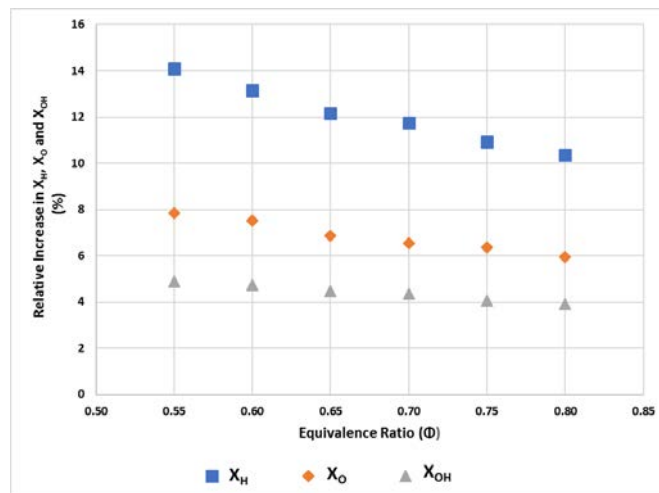


Figure 6-19: Relative increase in maximum X_H , X_O and X_{OH} for CH_4 with H_2 addition (15% volumetric)

Increases in heat release levels as H₂ was added with CH₄ for the same Φ are shown in Figure 6-15. In each FARH₂ case, the flame stabilizes closer to the burner exit and displays more heat release level compared to the 100% CH₄ flames. This is further confirmed by Figure 6-20, where maximum OH intensity from experiment and maximum OH mole fraction calculated from CHEMKIN for both BASE and FARH₂ fuels are plotted against Φ . As expected, FARH₂ displays higher OH intensity and OH mole fractions than BASE fuel at respective Φ due to the higher reactivity of H₂. The area of highest heat release increases for every FARH₂ flames, compared to the respective BASE flames. The structure of the heat release zones will influence NO_x emissions in which temperature and residence time play key formation roles.

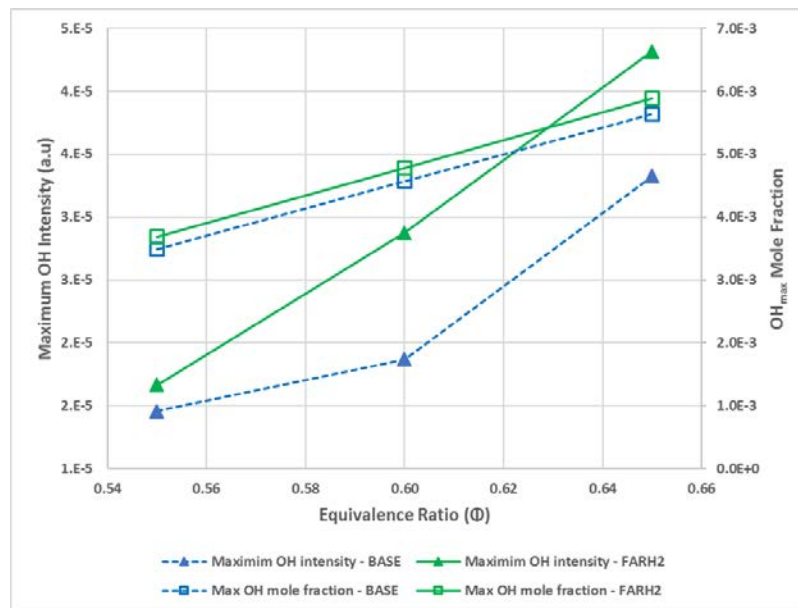


Figure 6-20: Maximum OH intensity and maximum OH mole fraction as a function of Φ

6.1.2.2. Changes in NO Formations

Changes in NO formations as H₂ is added to CH₄, evident from NO PLIF experiment results are discussed and analysed here. As mentioned before, NO PLIF data were taken at the burner exit for every point considered here. Clear changes in NO formations can be seen from the NO PLIF images in Figure 6-21 and Figure 6-22, when 15% H₂ was added with CH₄. Figure 6-21 and Figure 6-22 show the NO PLIF images for BASE

and FARH₂ fuels side by side at same Φ . Images are normalised to maximum intensity at each Φ for Figure 6-21 to illustrate the changes in NO formation with H₂ addition, whereas at Figure 6-22, colormap is normalised to the maximum intensity across images to display the changes in NO intensity level as Φ changes and H₂ added to CH₄.

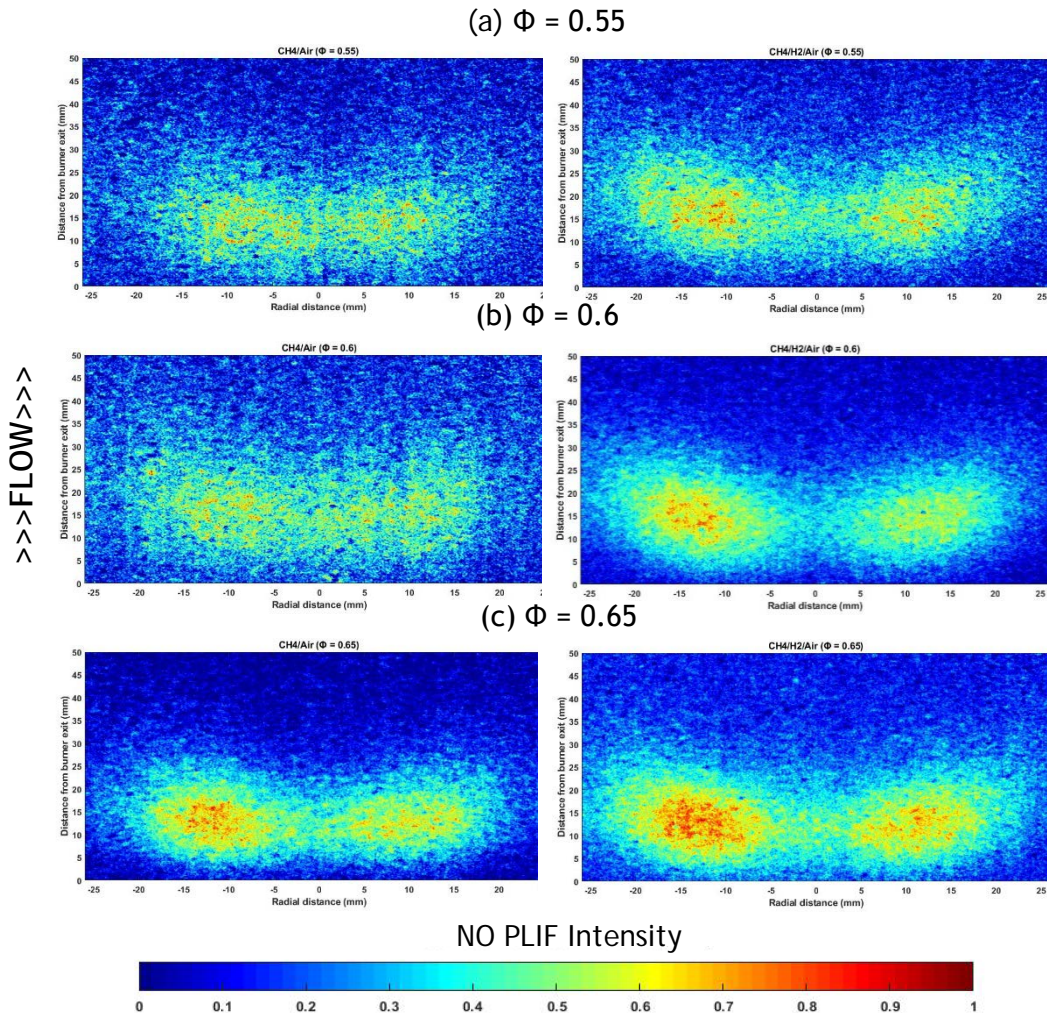


Figure 6-21: Effects on NO formations with 15% H₂ additions. BASE fuel on left side and FARH₂ on right side. Colormap normalised to maximum intensity at each Φ . Flow direction is from bottom to top.

Clear differences in captured NO formation can be seen from Figure 6-21, when H₂ is added to CH₄. As the production of OH* radical intensifies in FARH₂ fuels (refer to Figure 6-15), which can be attributed to higher flame temperature, hence production of thermal NO increases. Figure 6-19 shows the relative increase of radicals (H*, O* and OH*) when H₂ is added to CH₄ and thus increase the reaction rate through the reactions (1) $H + O_2 \leftrightarrow O + OH$, (2) $O + H_2 \leftrightarrow H + OH$, and (3) $OH + H_2 \leftrightarrow$

H + H₂O [301]. Figure 6-22 shows the increase in NO intensity for the same Φ , as H₂ is added to CH₄. The formation of NO has a direct correlation to the OH availability as shown in Figure 6-23, where experimentally obtained $AvgInten_{NO}$ and $AvgInten_{OH}$ is plotted against maximum OH mole fraction calculated from CHEMKIN. Respective Φ for each point is also shown on the graph. Substantial increases in $AvgInten_{NO}$ and $AvgInten_{OH}$ can be observed for FARH₂ fuel compared to BASE fuel as expected.

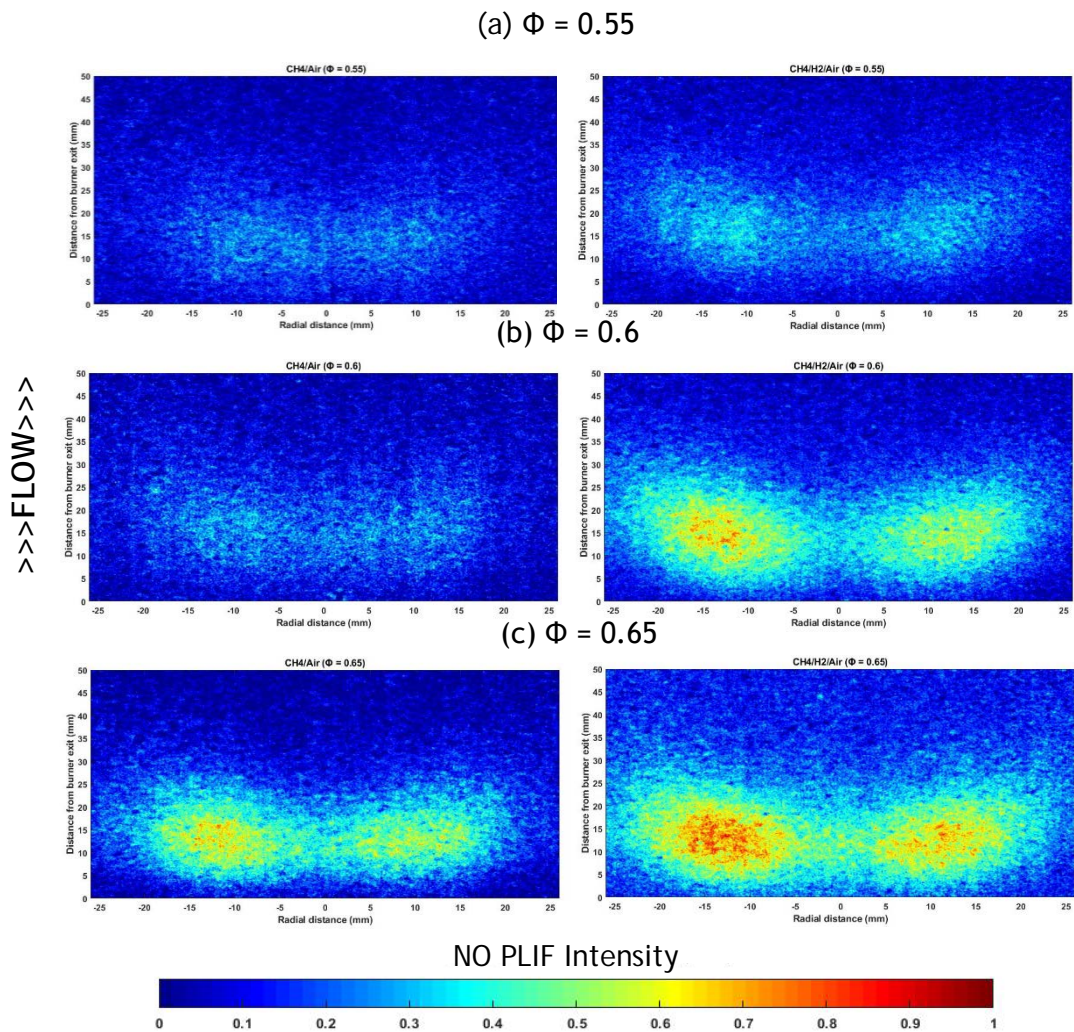


Figure 6-22: Effects on NO formations with 15% H₂ additions. BASE fuel on left side and FARH₂ on right side. Colormap normalised to maximum intensity across the images. Flow direction is from bottom to top.

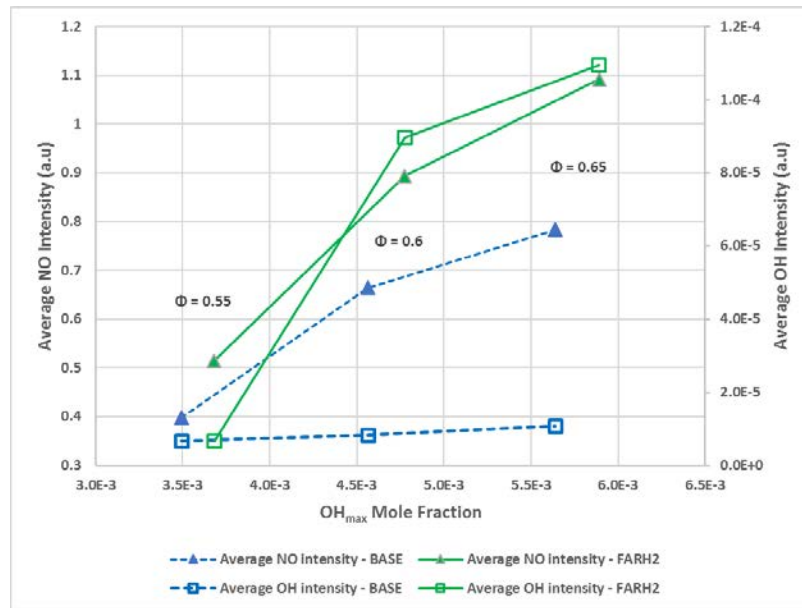


Figure 6-23: Effects of H₂ addition to the experimental NO and OH intensity with maximum OH mole fraction calculated from CHEMKIN

$AvgInten_{NO}$ and AFT are plotted as a function of Φ in Figure 6-24, whereas Figure 6-25 shows the effect of H₂ addition on flame brush thickness. Experimentally derived δ_{flame} from OH* chemiluminescence images for FARH₂ fuel show a similar trend as the one displayed by the BASE fuel; albeit with minimally thinner flame thicknesses. Theoretically, the reaction zone thickness decreases with flame brush thickness, resulting in shorter residence time. However, this loss of residence time is compensated by the much higher mass diffusivity exhibited by H₂ with respect to CH₄ [194]. Furthermore, since the activation energy of H₂ is much lower than that of CH₄ ($E_a = 25$ [302] and 45 [303] kJ/mol, respectively), lower temperatures are needed to trigger the combustion phenomena. This enhanced reactivity, leads to greater burning intensity, a by-product of the augmented production of radical concentrations (in particular H, OH, O), which promote the oxidation mechanisms of CH₄; consequently, partially explaining the increased measured thermal NO.

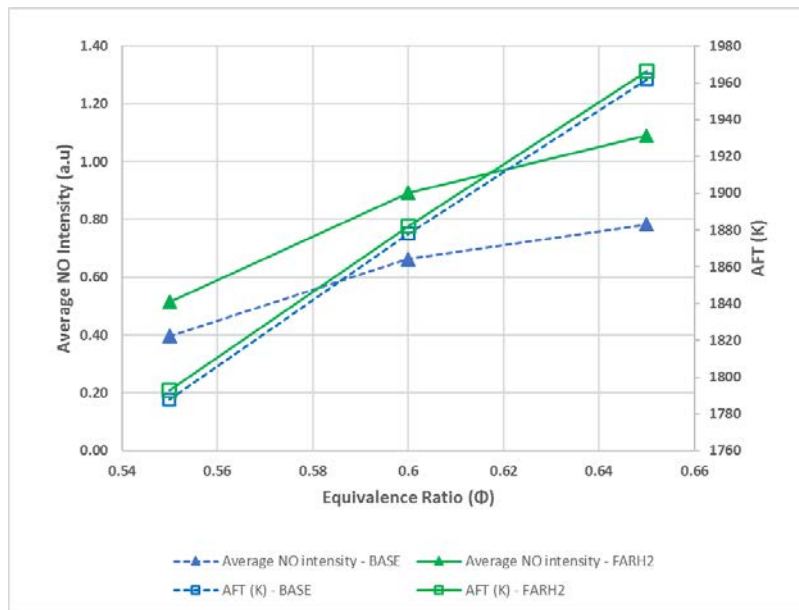


Figure 6-24: Comparison between BASE and FARH₂ in terms of AFT and $AvgInten_{NO}$.

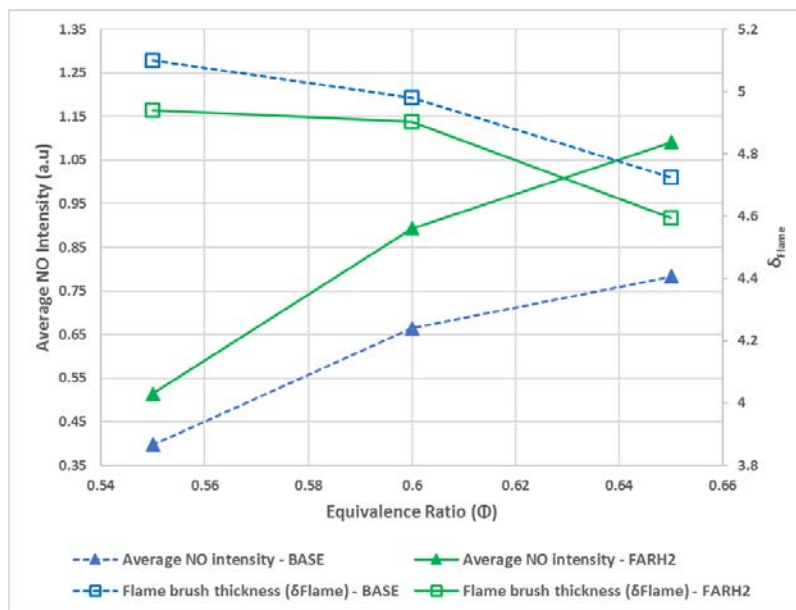


Figure 6-25: Comparison between BASE and FARH₂ in terms of δ_{flame} and $AvgInten_{NO}$.

6.1.3. Effects of Confinement on Flame Shape and NO formation

Flow conditions for this investigation were presented in Table 5-2. These conditions were investigated again using the HPGSB-2 with quartz confinement fitted, making it a confined flame investigation. OH* chemiluminescence and NO PLIF data were taken at each condition to correlate thermal NO formation with heat release level. Fuel flows were kept constant as before, while changing air flows, thus keeping thermal power constant, to attain required equivalence ratios (0.8 - 1.1) for this investigation. All the test points in this section were conducted in atmospheric conditions (298K and 1.1 bara), with a constant thermal power of 26 kW and emissions data were taken at the exhaust by using industry standard system from Signal Gas Analyser Ltd (refer to Chapter 3.7). At the end of this section, OH* chemiluminescence and NO PLIF images between open and confined environments are compared and analysed.

6.1.3.1. OH* Chemiluminescence Comparison

The Abel-transformed OH* chemiluminescence (refer to Chapter 3.6.2) results for CH₄/air flames with varying Φ conditions are presented in Figure 6-26. Each image presented has been normalized against its own image maximum and then fit to the same false colormap to better understand the heat release locations and flame stabilization at each point. Overall, the flame retracts axially upstream and radially inward as Φ increases. The area of heat release increases with increasing S_L , especially in the lean conditions, causing the flames to stabilize nearer to the burner exit with increasing Φ .

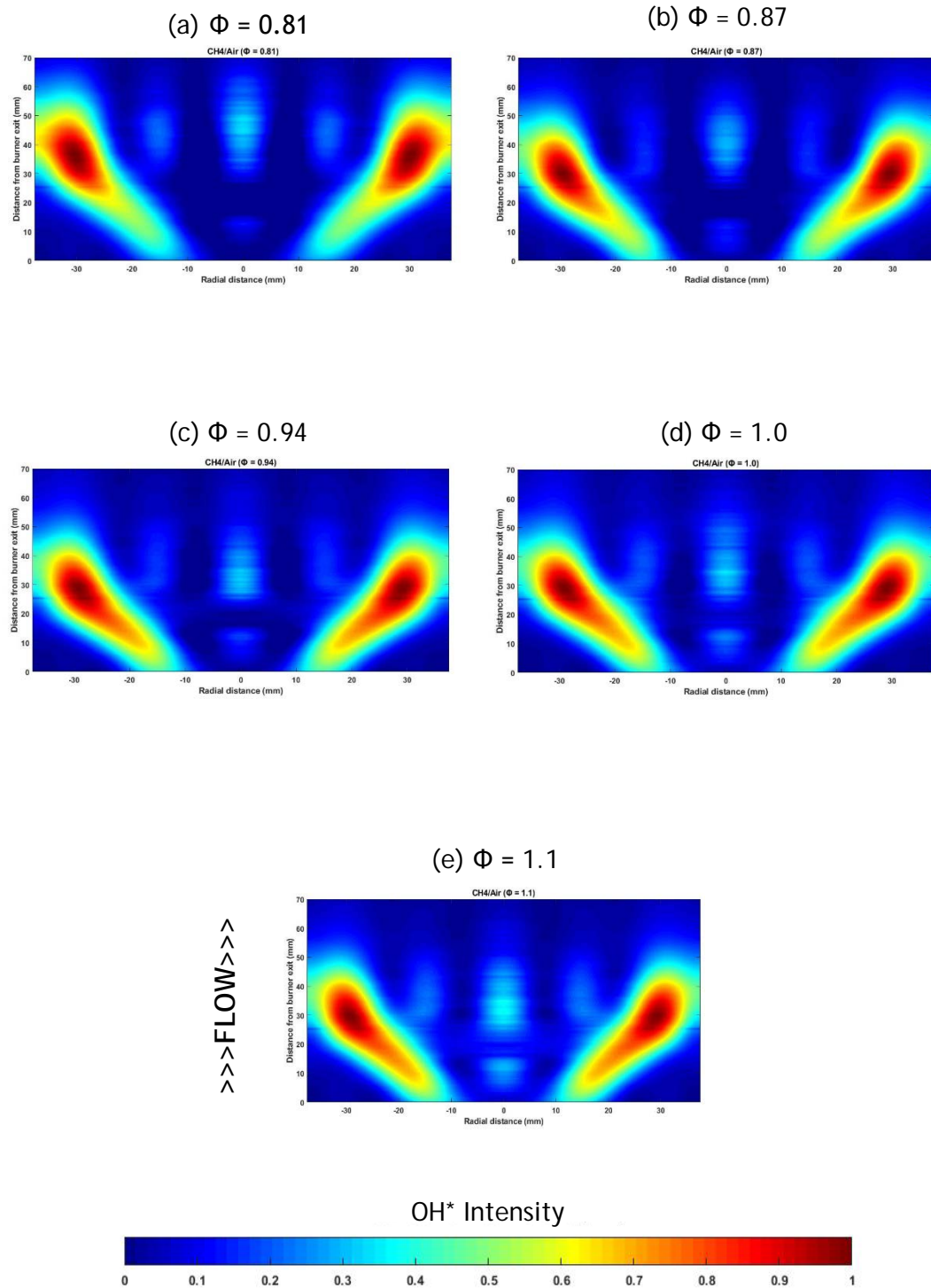


Figure 6-26: Abel-transformed OH* chemiluminescence images (colormap normalised to maximum OH* intensity at each Φ) at varying Φ

Figure 6-28 represents Abel-transformed OH* chemiluminescence images, colormap corrected to maximum OH* intensity across range. Heat release intensity increases as Φ changes from 0.81 to stoichiometry, and then decreases at $\Phi = 1.1$. This agrees with Figure 5-18, where OH mole fraction calculated from CHEMKIN is plotted against 1-D spatial concentration profile. Calculated maximum OH mole fraction and maximum OH* chemiluminescence intensity follow the same trend as shown in Figure 6-27, when plotted against Φ . Both increases until stoichiometry, then drops as the gas mixture gets rich. These heat release behaviors also agree with the correlation between Φ and AFT, shown in Figure 3-21.

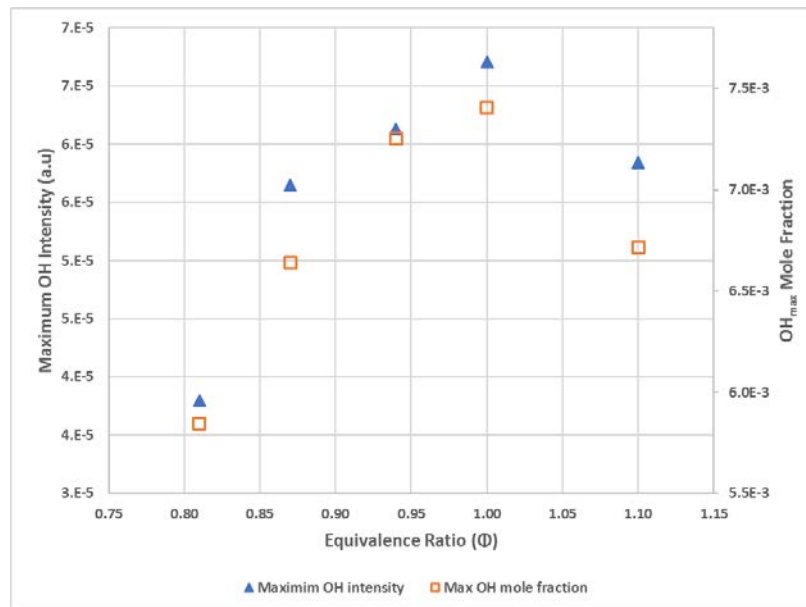


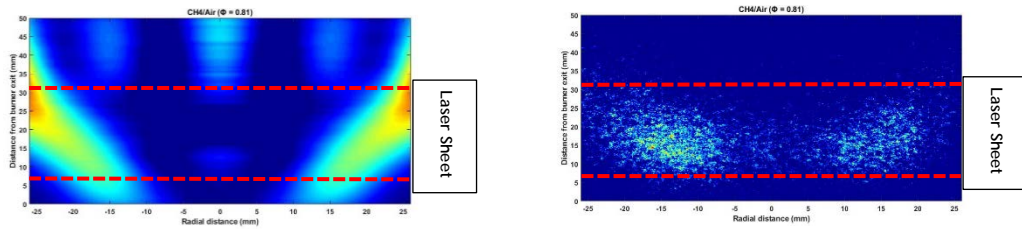
Figure 6-27: Maximum OH* intensity and maximum OH mole fraction as a function of Φ

6.1.3.2. NO PLIF Comparison

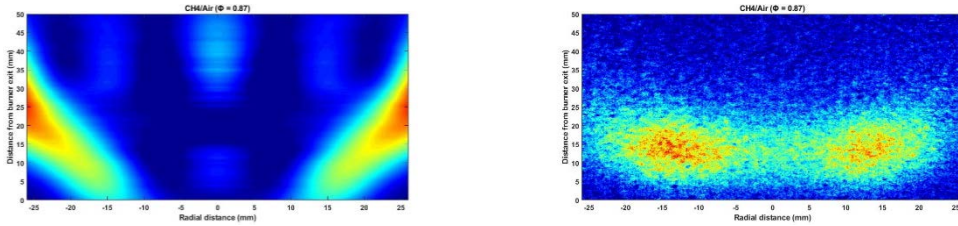
Figure 6-29 and Figure 6-30 shows the OH* chemiluminescence and NO PLIF images side by side for respective conditions in HPOC with colormap normalized to maximum Φ and to maximum intensity across the images, respectively. Laser sheet path is indicated on the first images (refer to Figure 6-29 (a) and Figure 6-30 (a)) of each figure. Both horizontal and vertical axes are kept to same limits for OH* chemiluminescence and NO PLIF images to compare the relationship between NO formation and heat release better. Flows are from bottom to top in these images. NO formations shown only in the path of laser sheet, as NO cannot be excited without laser energy for the PLIF images, whereas OH* chemiluminescence images shows the heat release in whole flame as laser energy is not required for chemiluminescence measurements.

Similar trends can be seen here as the flames in the unconfined flames, described in detail in Chapter 5.2.2. In Figure 6-30, where colormaps for both OH* chemiluminescence and NO PLIF images are normalised to the maximum intensity across images, clear differences in heat release level are apparent as the air flow decreases. NO PLIF intensity increases with increasing heat release level up to $\Phi = 0.94$, then NO PLIF intensity declines as Φ moves towards stoichiometry and beyond (refer to Figure 6-30 (d) and (e)), even with apparent increasing heat release levels from respective OH* chemiluminescence images. As discussed earlier, this is related to the trade-off between availability of excess O₂ and flame temperature. Flame temperature has the maximum value just after stoichiometry due to product dissociation. Since the extent of dissociation is greater on the lean side as a result of the stoichiometry of dissociated products, peaking occurs on the rich side. However, for the conditions considered here, availability of excess O₂ ends at $\Phi = 0.94$. From the Zel'dovich pathway described in Chapter 2.1.1, both the availability of excess O₂ and high flame temperatures are pre-requisites for thermal NO formation. Hence, NO PLIF intensity peaks at $\Phi = 0.94$, whereas OH* chemiluminescence intensity has maximum value at stoichiometry.

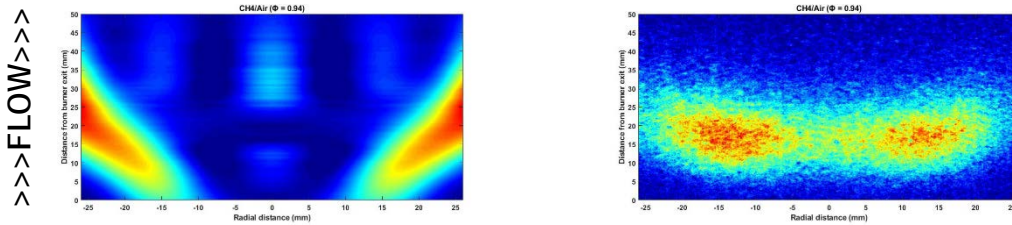
(a) $\Phi = 0.81$



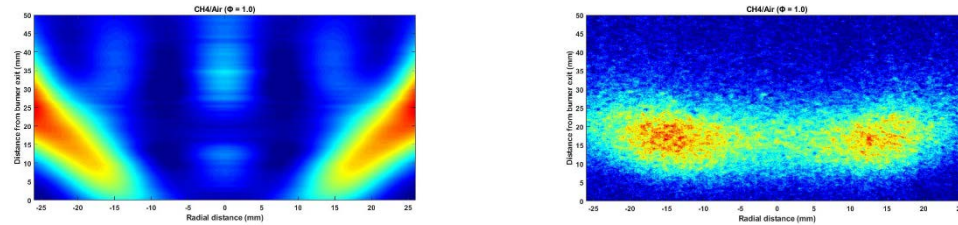
(b) $\Phi = 0.87$



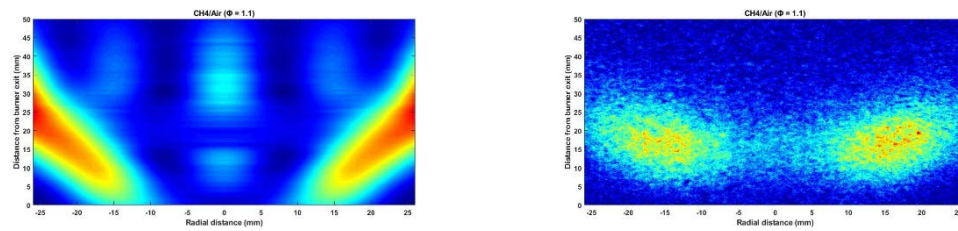
(c) $\Phi = 0.94$



(d) $\Phi = 1.0$



(e) $\Phi = 1.1$



OH* and NO PLIF Intensity

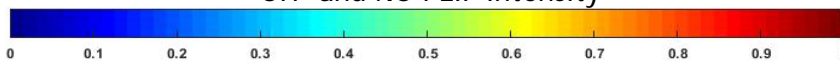
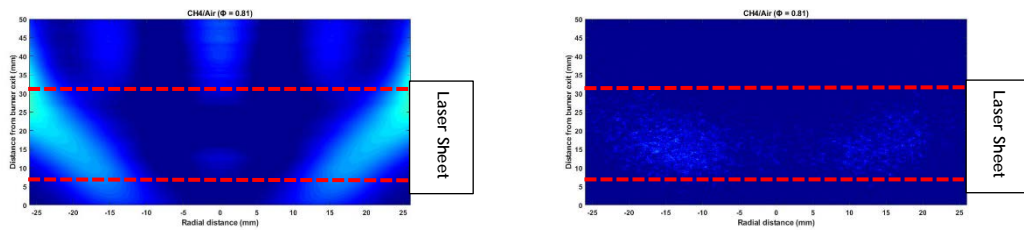
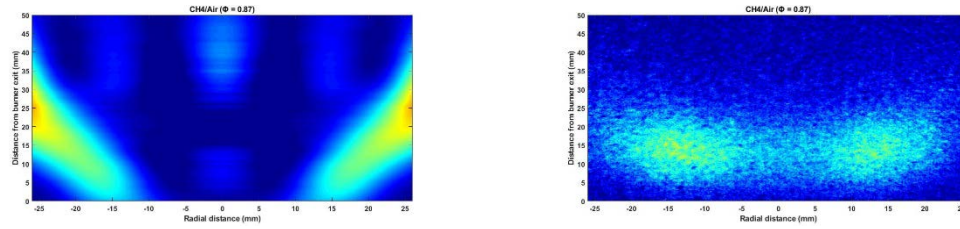


Figure 6-29: Abel - transformed OH* chemiluminescence and NO PLIF images side by side. Colormap normalised to maximum intensity at each Φ .

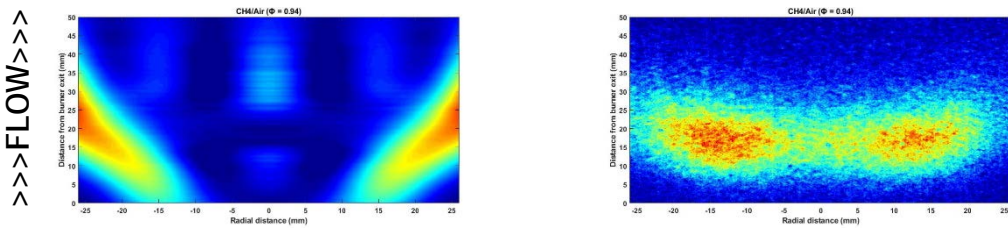
(a) $\Phi = 0.81$



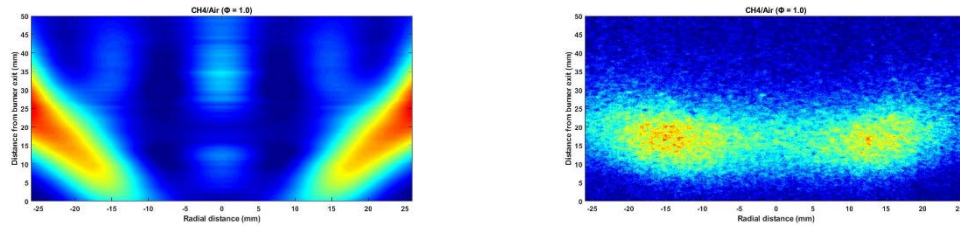
(b) $\Phi = 0.87$



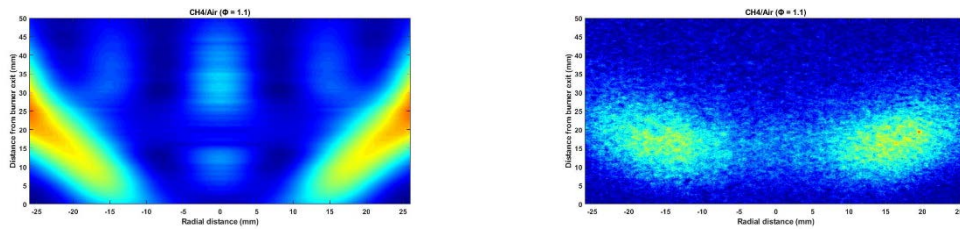
(c) $\Phi = 0.94$



(d) $\Phi = 1.0$



(e) $\Phi = 1.1$



OH* and NO PLIF Intensity



Figure 6-30: Abel - transformed OH* chemiluminescence and NO PLIF images side by side. Colormap normalised to maximum intensity across the images.

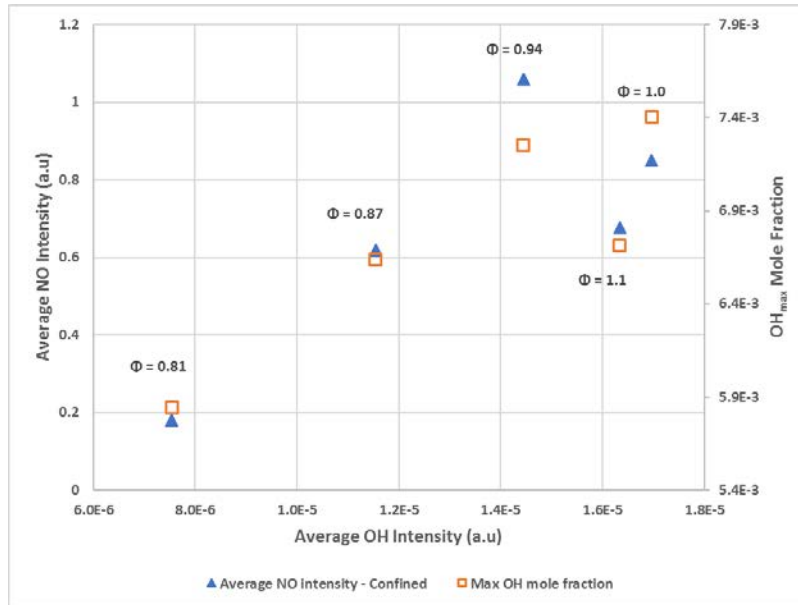


Figure 6-31: Average NO PLIF intensity and maximum OH mole fraction from CHEMKIN as a function of average OH* chemiluminescence intensity. Φ is shown in the graph for each point in increasing order.

$AvgInten_{NO}$ and maximum OH mole fraction from CHEMKIN calculations are plotted against $AvgInten_{OH}$ in Figure 6-31, where Φ is also shown for respective points. $AvgInten_{OH}$ and maximum OH mole fraction increases up to stoichiometry and falls at $\Phi = 1.1$, thus validating OH* chemiluminescence experiments. However, as mentioned earlier, $AvgInten_{NO}$ values rise with increasing $AvgInten_{OH}$ and maximum OH mole fraction values up to $\Phi = 0.94$, then $AvgInten_{NO}$ values declines as there are no more excess O_2 in the mixture. Compared to Figure 5-29, where similar properties were compared for unconfined flames, opposite trend seen in $AvgInten_{OH}$ from stoichiometry to rich condition are not replicated here as all the confined points were taken on the same day.

6.1.3.3. Comparison between Unconfined and Confined Flames

In this section, flame shape and NO formation are compared in terms of OH* chemiluminescence and NO PLIF data, respectively between unconfined and confined flames. The shape of CRZ changes between the unconfined and confined flame, thus changing the flame shape significantly. The CRZ recirculates heat and active chemical species to the root of the flame, allowing flame stabilisation and flame establishment to occur in regions of relative low velocity where flow and turbulent flame velocity can be matched, aided by the recirculation of heat and active chemical species [209], [304].

According to the findings by Syred and Dahmen [305], Syred and Beer [209], Gupta et al. [304], the size and shape of the CRZ and ERZ can be dramatically altered as the swirl burner flow expands into a combustion vessel. It can also induce weak regions of forward axial flow on the central axis inside the CRZ [209], [306]. Confinement ratio, defined as diameter of confinement vessel (D_0) / exhaust diameter of swirl burner (D_e), is the dominant factor, the smaller this ratio the larger is the effect [210]. This ratio is much smaller in the confined cases investigated here, than the unconfined points. As discussed by Gupta et al. [304], the CRZ formed by an unconfined swirl burner arises because of the sudden expansion and associated entrainment effects on the edge of the swirling flow. This causes decay in swirl velocity profile, which in turn generates strong radial and axial pressure gradients, creating the CRZ. This process is affected in the presence of confinement, altering the size and shape of the CRZ, whilst also causing an ERZ to form as the flow sticks to the external wall.

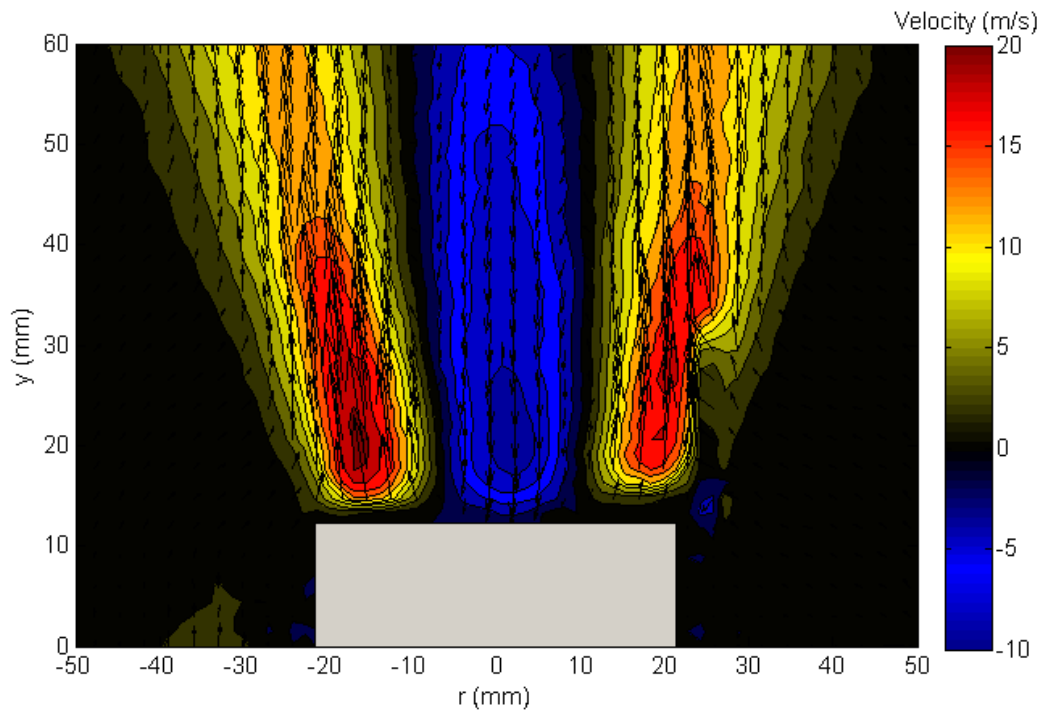


Figure 6-32: Isothermal air flow PIV velocity vector maps with axial velocity contours for the unconfined HPGSB-2. Reproduced from [221].

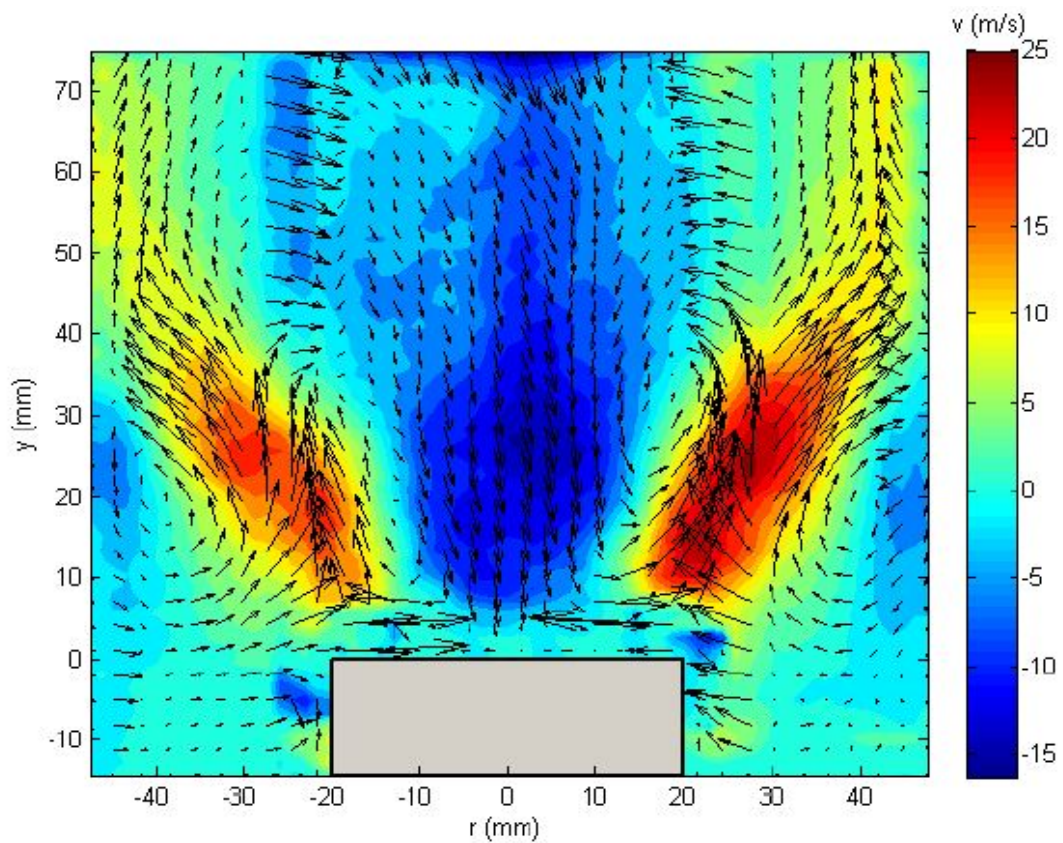


Figure 6-33: Isothermal air flow PIV velocity vector maps with axial velocity contours for the confined HPGSB-2. Reproduced from [221].

Particle imaging velocimetry (PIV) measurements were taken in HPGSB -2 for isothermal conditions with and without confinement in a previous study [221] at Cardiff University. The resultant velocity vector maps for unconfined and confined conditions (equivalent to $\Phi = 0.55$) are presented in Figure 6-32 and 6-33, respectively. Each vector map is then overlaid with coloured contours of mean axial velocity. Significant changes in CRZ shape is evident between confined and unconfined flames from the figures. In unconfined flame, CRZ shaped into a rectangular form due to the sudden expansion on the edge of the swirling flow, causing decay in swirl velocity profile. However, the presence of confinement significantly alters the shape of CRZ as flame stays attached to the confinement due to Coanda effect [307]. From Figure 6-33, a number of coherent flow structures are visible, including a CRZ along the burner central axis (with upstream flow velocities up to -17 m/s) and two radially symmetric ERZs near the flow expansion from the burner exit nozzle at $r = \pm 40$ mm, $y = 25$ mm. A vortex breakdown structure along the central axis is also can be seen. Separating these two coherent structures, an outward-expanding shear layer of zero axial velocity is also present, and it is this highly turbulent, low velocity area where the swirl flame stabilizes, as discussed earlier.

Differences in flame structures between unconfined and confined flames at same Φ can be seen in Figure 6-34, where OH^* chemiluminescence images are illustrated side by side for unconfined and confined flames, unconfined images on the left side and confined images on the right side. Colormaps for both unconfined and confined images are corrected to their respective maximum intensity at stoichiometry. As expected, in both cases heat release level increases from lean mixture to stoichiometry and then decreases at the rich side. Flame also expands radially outwards for both the cases as Φ increases. Flame attaches closer to the nozzle exit as Φ increases up to stoichiometry and then lifts slightly at $\Phi = 1.1$. As the fuel flow kept constant for this investigation, total flow velocity decreases with increasing Φ and as shown in Figure 3-20, SL increases linearly as Φ increases up to stoichiometry and nearly stays same at $\Phi = 1.1$. As turbulent flame velocity is intricately linked

with SL, up to stoichiometry, total flow velocity decreases and turbulent flame velocity increases as the CRZ stabilizes the flame closer to the burner exit while the flame lifts by little at $\Phi = 1.1$.

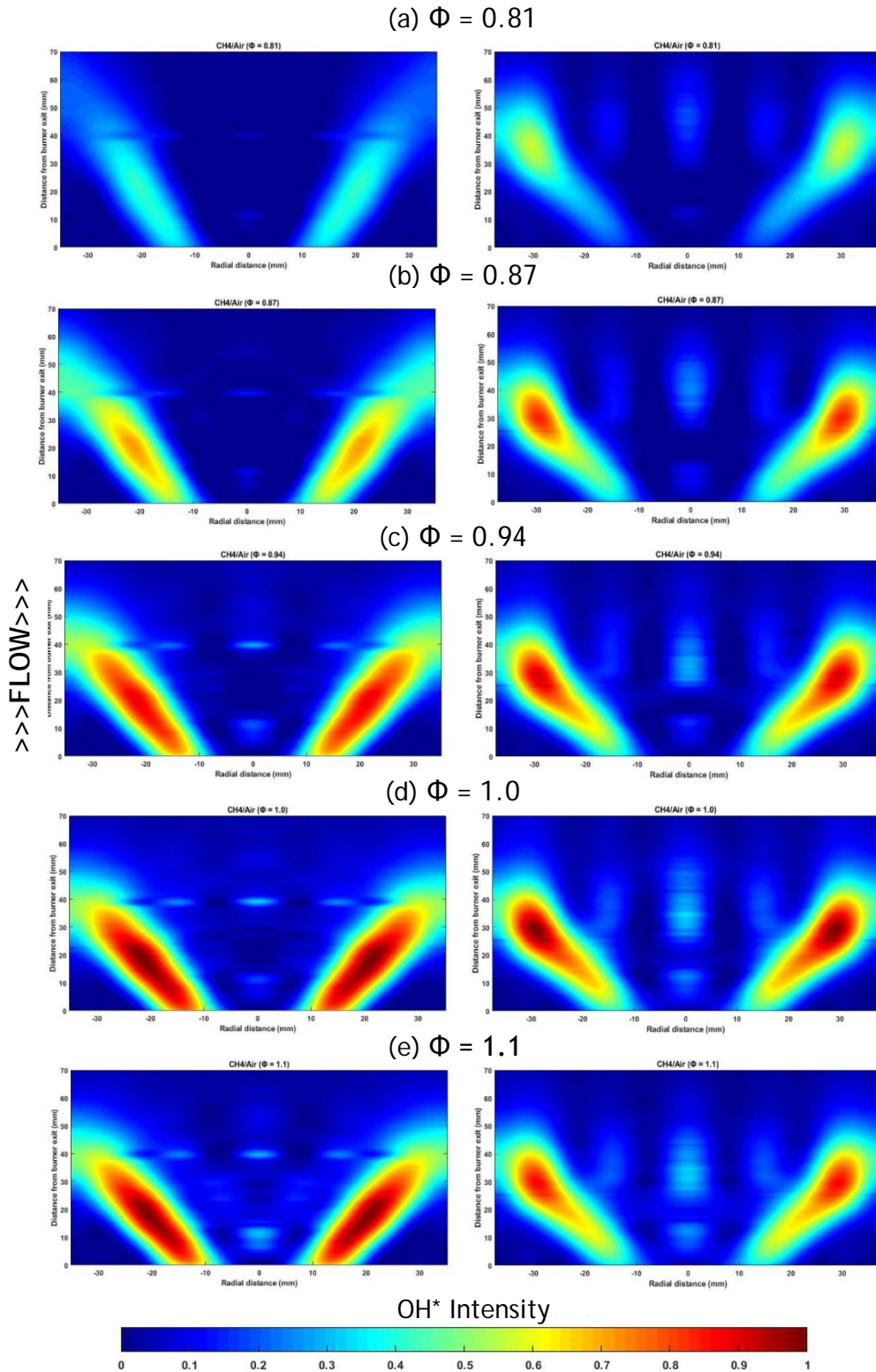


Figure 6-34: Changes in flame shape and heat release locations between unconfined and confined flames. Colormap corrected to the maximum OH* intensity across column. Unconfined images in the left column and confined images in the right column.

The changes in CRZ shapes between unconfined and confined flames are also evident from Figure 6-34. The isothermal PIV images correlates to the flame shapes extracted experimentally. CRZ shapes similar to the Figure 6-33 can be depicted from the confined convex flame shapes, whereas the flame shapes at unconfined images correlates to the rectangular shaped CRZ shown in Figure 6-32. It can also be concluded that size of CRZ increases as flow velocity decreases and turbulent flame velocity increases.

Table 6-4: Changes in flame angle (α) between unconfined and confined flames

Equivalence Ratio (Φ)	Flame angle (α)	
	Unconfined	Confined
0.81	47.03°	50.23°
0.87	44.35°	45.05°
0.94	42.45°	44.50°
1.0	39.96°	43.73°
1.1	40.66°	45.53°

Table 6-4 displays the changes in flame angle (α) between the unconfined and confined flames at the conditions considered here. The methodology of deriving these flame angles was detailed earlier in Section 6.1.2. Confined conditions display higher α for the same Φ . This can be attributed to the Coanda effect and lower confined ratio for the confined conditions as discussed earlier. Interestingly, flame angle decreases with increasing Φ until stoichiometry but increases for the rich condition considered here. This can be attributed to the drop in flame speed at the rich condition, Chapter 3.10.

Figure 6-35 illustrates the changes in NO formations between unconfined and confined flames. Colormaps are normalized to the maximum NO intensity across columns to show the changes in intensity as Φ changes. NO formation is stretched in the confined flames as the CRZ is ball shaped, compared to the rectangular shaped CRZ in unconfined flames. Location of NO formation is closer to the nozzle exit for confined flames as flames are attached closer to the nozzle exit as can be seen from Figure 6-34. NO PLIF intensities in the confined flames stronger visually than the confined flames due to higher momentum of the flow (refer to Figure 6-32 and Figure 6-33), apart for $\Phi = 0.81$. This is also confirmed from Figure 6-36, where maximum NO (primary vertical axis) and OH* intensity (secondary vertical axis) for confined and unconfined flames are plotted against Φ . For the purpose of comparison between confined and unconfined flames, maximum NO and OH* intensity values for unconfined flames are corrected for the absence of confinement. This increase in intensities can also be attributed to the shape of CRZ, as it can be seen from Figure 6-32 and 6-33, that both the area and maximum velocities of confined CRZ is greater than unconfined CRZ. Due to the increased presence of hot combustion gases in the confined CRZ, more thermal NO forms, resulting in higher maximum NO intensity. The low NO PLIF intensity in the lean ($\Phi = 0.81$) confined flame may be the result of laser wavelength shifting during the experiment, a common problem of dye lasers [308]. Clear correlation can be seen between heat release intensity and NO formation from Figure 6-36, as Φ increases, with the exception at stoichiometry due to the balance between availability of excess O₂ and flame temperature (refer to Chapter 5.2.2).

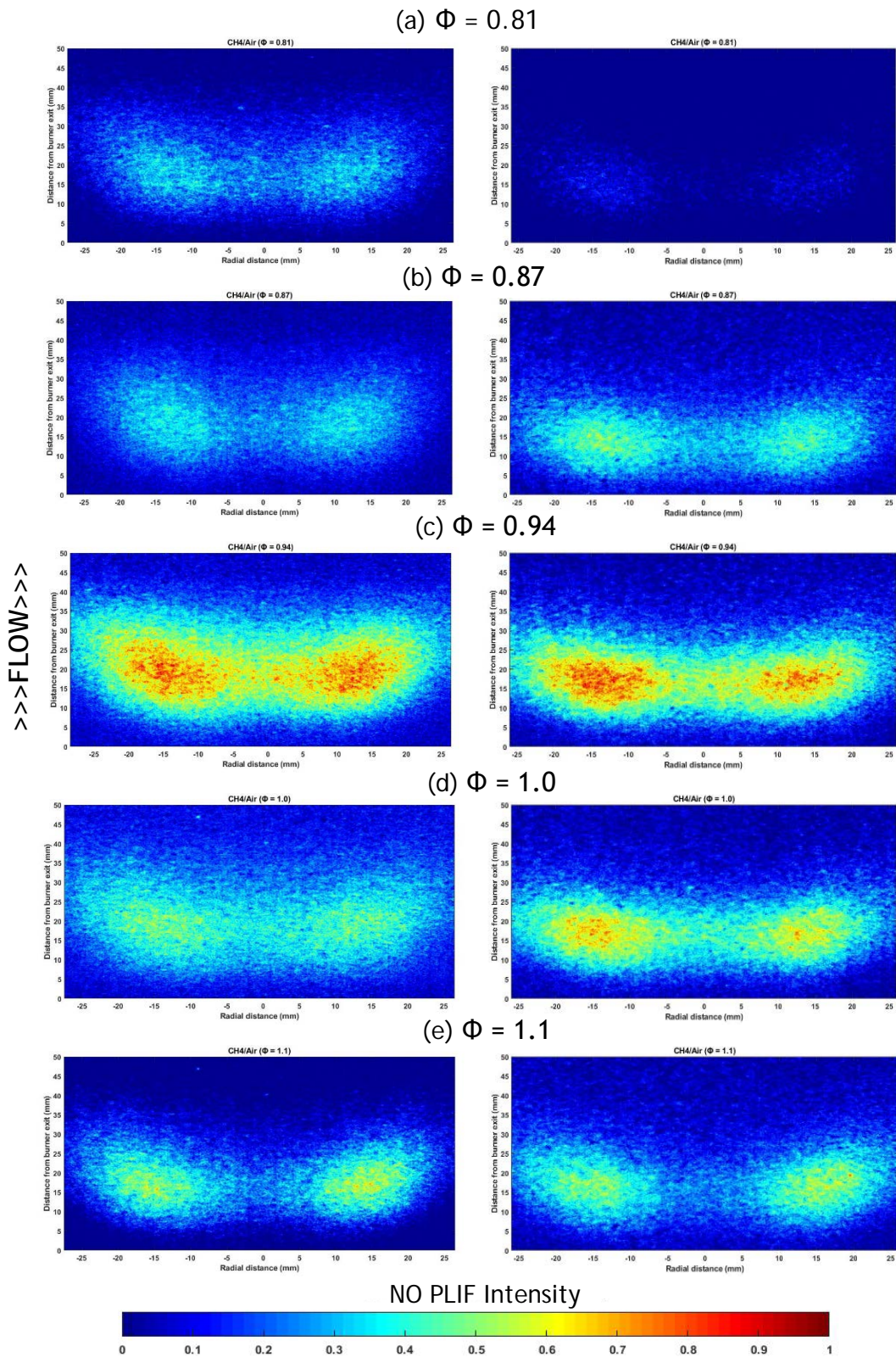


Figure 6-35: Changes in NO formation and intensity between unconfined and confined flames. Colormap corrected to the maximum NO PLIF intensity across column. Unconfined images in the left column and confined images in the right column.

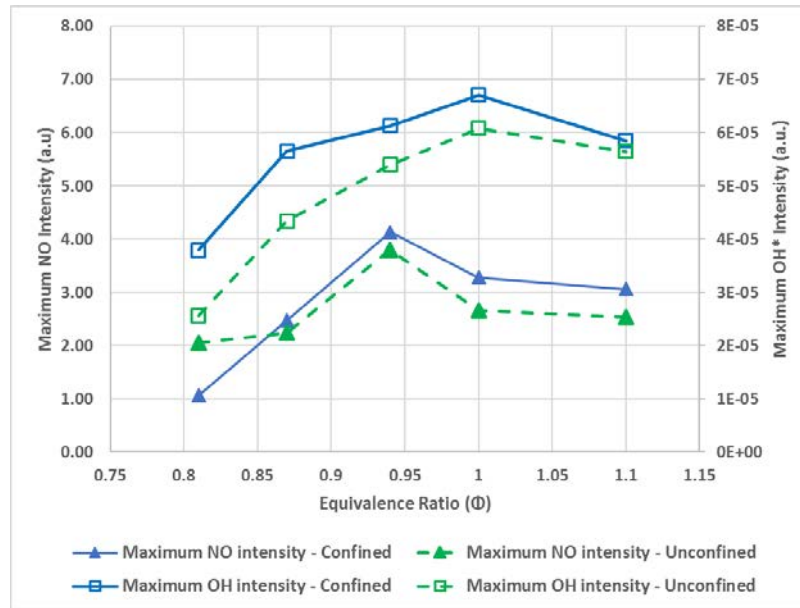


Figure 6-36: Maximum NO and OH* intensity as a function of Φ for confined and unconfined flames

6.2. 226.03 nm Excitation

226.03 nm excitation wavelength has been widely used for qualitative and quantitative NO LIF analysis (refer to Chapter 2.5.1). A few points were taken at this wavelength for this investigation due to the functional instabilities of the laser systems. Sheet optics were taken off from the laser systems and laser beam was used instead of laser sheet due to the energy deficiency at 226.03 nm. Five points were investigated at atmospheric temperature and pressure conditions and three points were investigated at preheated temperature and atmospheric pressure. All the experiments investigated in this section were conducted in the HPGSB-2 burner with open confinement at GTRC and NO LIF images were taken at burner exit. The findings from 226.03 nm will be compared and analysed with the data from 285.16 nm at same Φ and fuel types in this section.

6.2.1. Non-preheated Conditions

In this section, experimental points at atmospheric temperature and pressure conditions are analysed, discussed and compared with the similar points at 285.16 nm wavelength excitation. In that pursuit, equivalence ratios were kept similar to the flow conditions described in

Chapter 5.2. Gas Analyzer measurements were taken at these points to compare with NO LIF intensity measured at burner exit. Flow conditions for this investigation are presented in Table 6-5.

Table 6-5: Flow conditions for non-preheated experiments at 226.03 nm

Test point	CH ₄ mass flow (g/s)	Air mass flow (g/s)	Entry Temperature, T ₂ (K)	Equivalence ratio (Φ)	AFT (K)	CH ₄ speed (m/s)	Air speed (m/s)	Total flow speed (m/s)	Laminar Flame speed (m/s)
16	0.835	17.729	298	0.81	2013	1.00	11.82	12.82	0.2821
17	0.835	16.506	298	0.87	2097	1.00	11.01	12.01	0.3226.03
18	0.835	15.277	298	0.94	2180	1.00	10.19	11.19	0.3610
19	0.835	14.361	298	1.0	2225	1.00	9.57	10.57	0.3817
20	0.835	13.055	298	1.1	2205	1.00	8.70	9.70	0.3840

NO LIF images for this investigation are illustrated in Figure 6-37 and Figure 6-38. Colormaps are normalised to the maximum intensity at each Φ to display changes in NO formation in Figure 6-37 and to the maximum intensity across images in Figure 6-38 to illustrate the change in NO intensities as the flame becomes richer. It must be noted that NO LIF images here only covers ≈ 12 mm downstream, compared to ≈ 25 mm from the burner exit for NO PLIF images as diameter of the laser beam is much smaller than laser sheet width.

NO LIF images show similar trends with increasing Φ , as was shown by NO PLIF images excited by 285.16 nm wavelength, reaffirming the choice of the alternate excitation wavelength to accommodate stable laser energy requirements in the laser systems at GTRC. From Figure 6-37, NO formation at the burner exit is lowest at $\Phi = 0.81$, NO formation gets stronger as flame gets richer up to $\Phi = 0.94$ and then falls as flame goes through stoichiometry to rich condition ($\Phi = 1.1$). This trend was explained using Zel'dovich mechanism and balance between the availability of excess O₂ and flame temperature earlier in Chapter 5.2.2. Figure 6-38 illustrates the changes in NO LIF intensity as Φ changes, stark differences can be seen in the intensity as the flame gets richer.

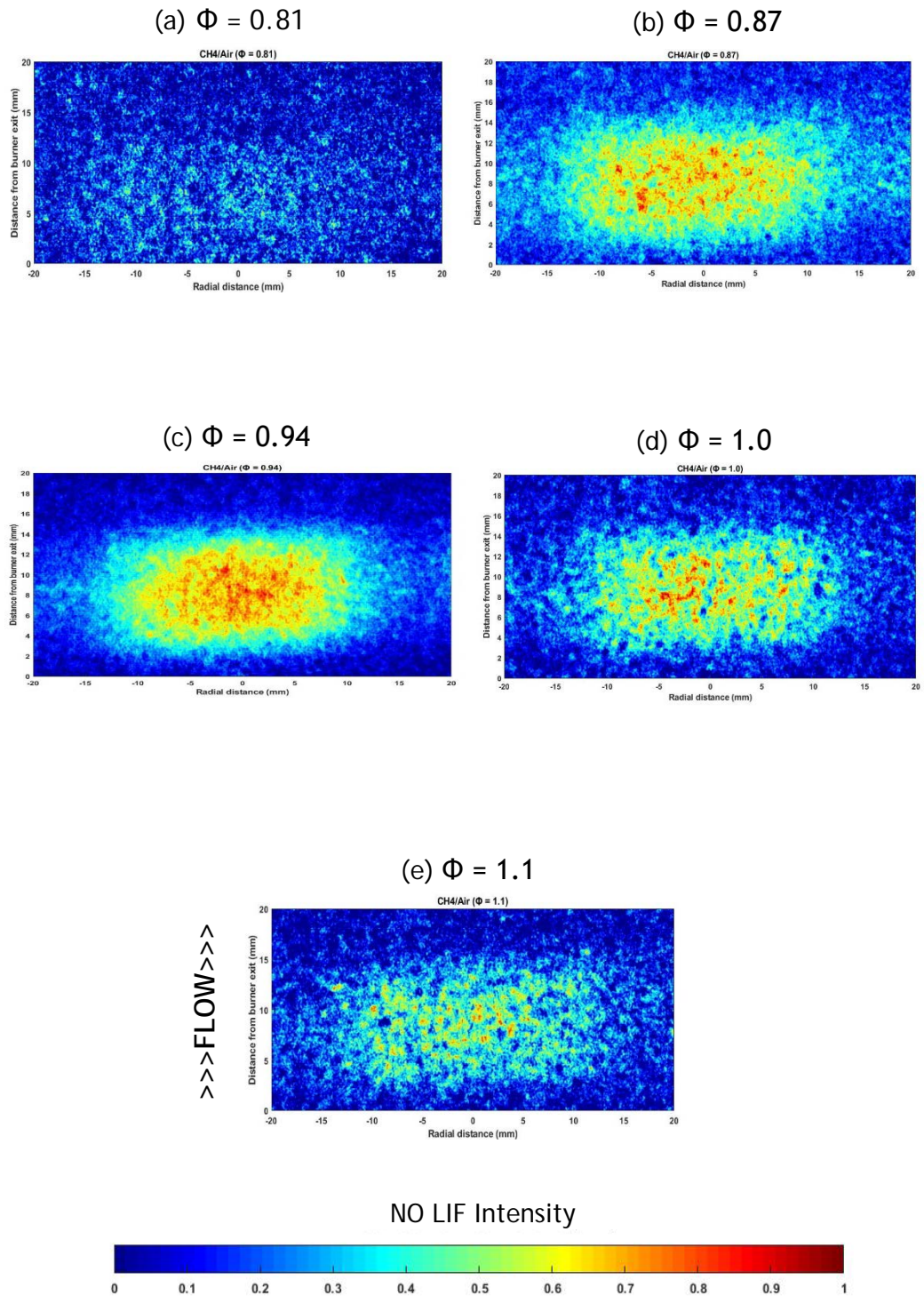


Figure 6-37: NO LIF images excited by 226.03 nm wavelength from lean to rich flames. Colormap normalised to maximum intensity at each Φ . Flame direction is from bottom to top. Laser beam covering ≈ 12 mm from burner exit.

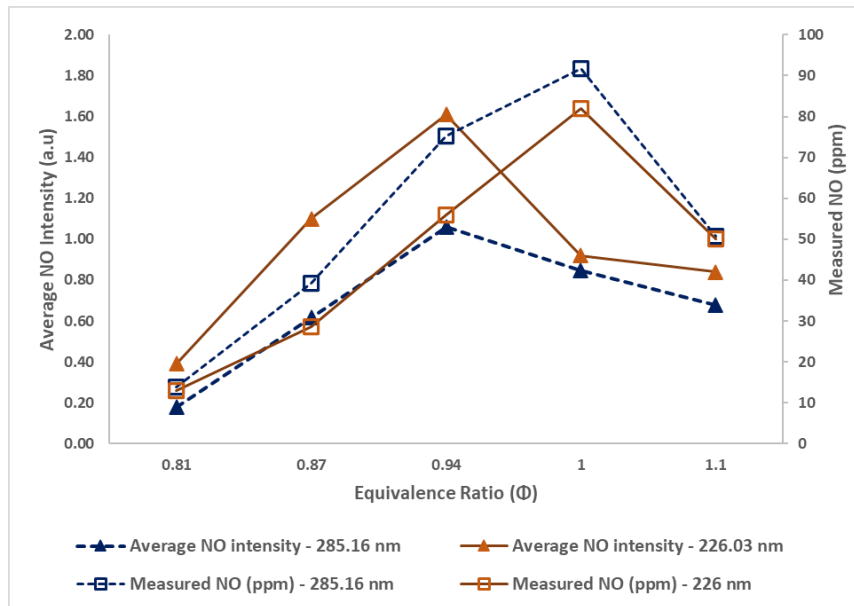


Figure 6-39: Comparison between NO LIF and PLIF data taken by 226.03 nm and 285.16 nm excitation wavelength, respectively.

Comparative analysis between data collected by 226.03 nm and 285.16 nm excitation wavelength are shown in Figure 6-39, where $AvgInten_{NO}$ and NO measured by gas analyser are plotted as a function of Φ . It must be noted that even though the experiments for NO LIF and PLIF have same Φ , they differ in thermal power (42 and 26 kW, respectively), hence NO measured at exhaust by the gas analyser differs in the graph. From Figure 6-39, NO LIF intensity at 226.03 nm is much higher than when excited by 285.16 nm, even though the laser energy was much lower at 226.03 nm and according to gas analyser measurements, less NO was produced at 42 kW conditions where 226.03 nm measurements were taken. Reasons for this higher intensity at 226.03 nm wavelength excitation was described in detail in Chapter 3.3. At stoichiometry, both NO LIF and PLIF intensity drops but NO measured at the exhaust peaks at stoichiometry. This can be attributed to the NO formation pathways. Both NO LIF and PLIF measurements were taken at burner exit, hence only captured thermal NO as prompt NO usually forms downstream in the post-flame zone, whereas NO measured at exhaust were formed from both thermal and prompt pathways. Thermal NO production declines at stoichiometry due to unavailability of excess O_2 .

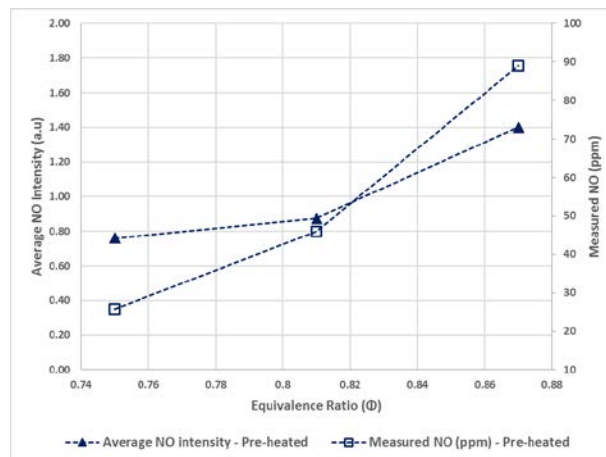
6.2.2. Pre-heated Conditions

Three experimental points were taken at 226.03 nm wavelength excitation for this investigation. Premixed gases were preheated to 573K to compare and analyse the difference in NO formation compared to non-pre-heated conditions. Flow conditions for this investigation are given in Table 6-6. The gas analyser (refer to Chapter 3.7) was used to capture NO emissions at exhaust.

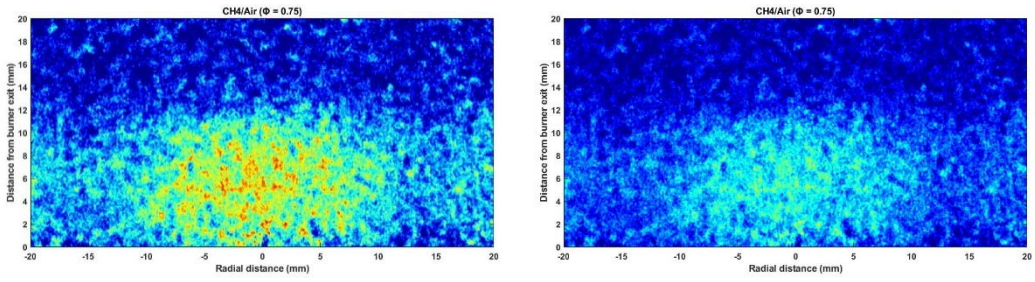
Table 6-6: Flow conditions for preheated experiments at 226.03 nm

Test point	CH ₄ mass flow (g/s)	Air mass flow (g/s)	Entry Temperature, T ₂ (K)	Equivalence ratio (Φ)	AFT (K)	CH ₄ speed (m/s)	Air speed (m/s)	Total flow speed (m/s)	Laminar Flame speed (m/s)
21	0.835	19.148	573	0.75	2115	1.93	24.55	26.48	0.8676
22	0.835	17.729	573	0.81	2183	1.93	22.73	24.66	0.9586
23	0.835	16.506	573	0.87	2244	1.93	21.16	23.09	1.0635

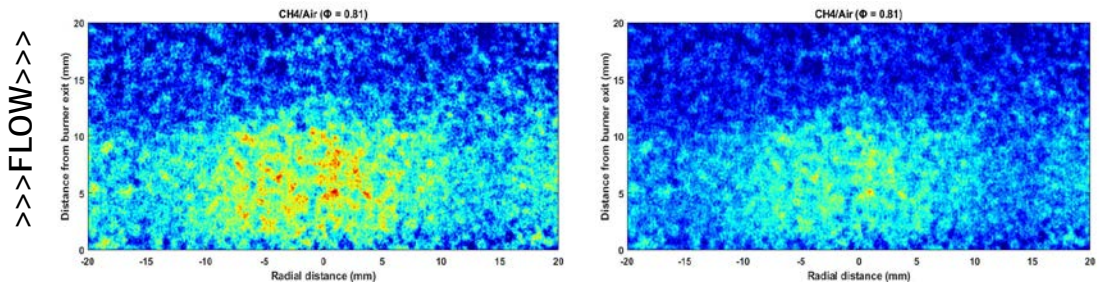
The experimental results are presented in Figure 6-41, where colormaps are normalized to the maximum intensity at each image and across the column for left-side and right-side images, respectively. Left-side images show the locations of NO formations near the burner exit, whereas right-side images display the changes in NO formation intensity level as Φ varies. Thermal NO formation increases as Φ increases in lean conditions due to increase in flame temperature. This is also evident in Figure 6-40, where $AvgInten_{NO}$ and NO measured at exhaust are plotted against Φ .

Figure 6-40: $AvgInten_{NO}$ and measured NO at exhaust as a function of Φ

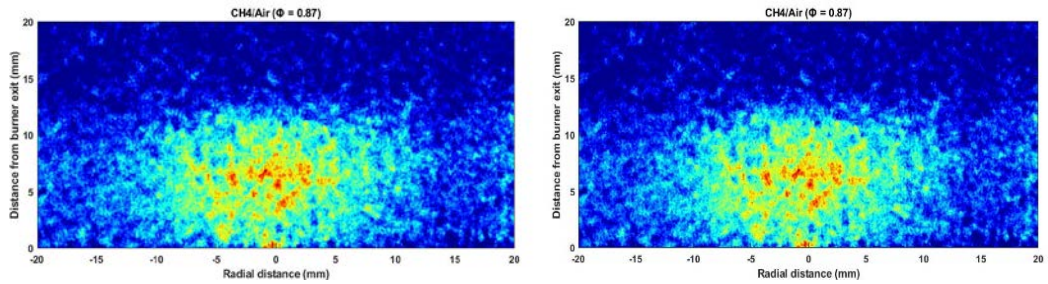
(a) $\Phi = 0.75$



(b) $\Phi = 0.81$



(c) $\Phi = 0.87$



NO LIF Intensity

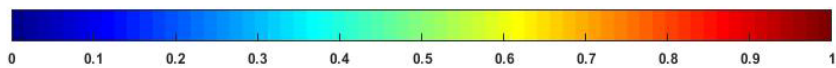


Figure 6-41: NO LIF images at varying Φ . Colormap normalised to maximum intensity at each Φ and across column on the left side and right side, respectively. Flame direction is from bottom to top. Laser beam covering ≈ 12 mm from burner exit.

6.2.3. Effect of Pre-heating on NO Formation

As described in Chapter 2.1.1, temperature plays an important role in NO formation in thermal pathway. In fact, according to [309], thermal NO_x production rate doubles for every 90 K temperature increase beyond 2200 K. Two experimental points at $\Phi = 0.81$ and 0.87 are considered here to analyse the changes in NO formations between non-preheated and preheated conditions at atmospheric pressure. Figure 6-42 and Figure 6-43 depict NO formations and changes in intensity, respectively as the entry temperature for premixed gases changes. Colormaps are normalised to maximum intensity at each point and across the images in Figure 6-42 and Figure 6-43, respectively. Non-preheated NO-LIF data are shown in left side and preheated images in right side. Laser beam pathways are also shown in each image of Figure 6-42 by dashed red line. The shift of laser beam downstream by ≈ 2 mm is clearly visible in the non-preheated flame at $\Phi = 0.87$.

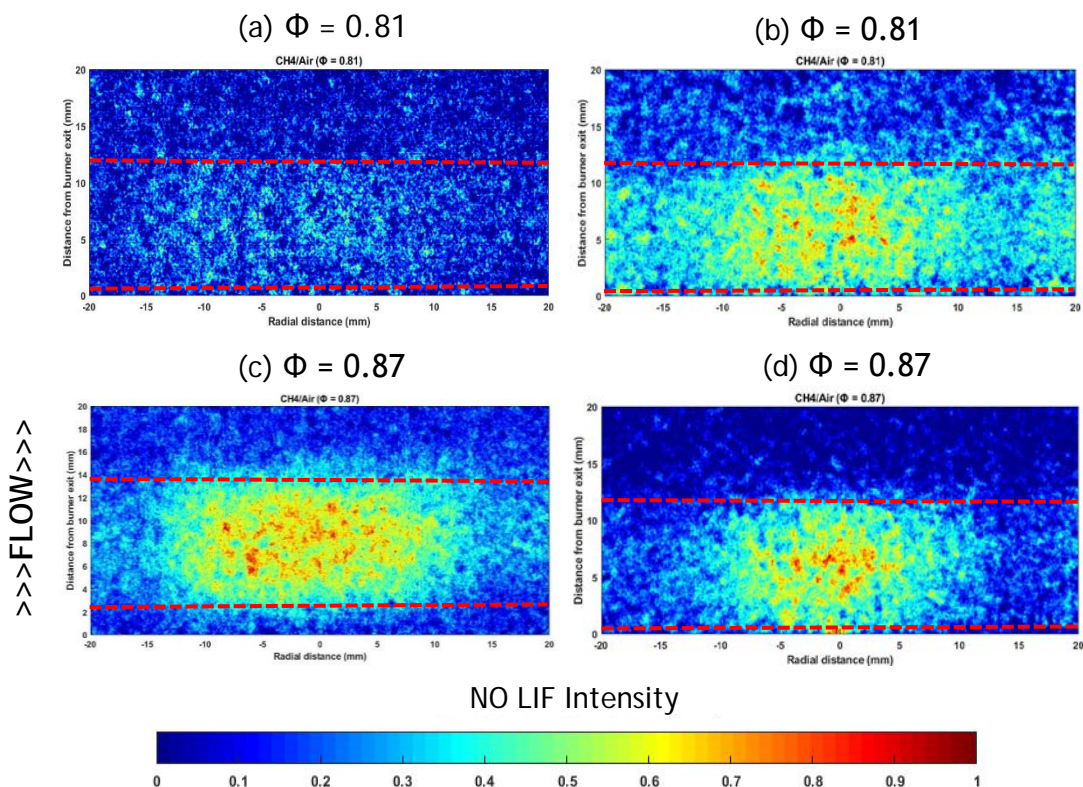


Figure 6-42: Effect of pre-heating on NO formation. Non-preheated conditions on the left side and preheated conditions on the right side. Colormap normalized to maximum intensity at each Φ .

Clear difference in NO formation and intensities between non-preheated and preheated gases are visible for $\Phi = 0.81$ in Figure 6-42 (a), (b) and Figure 6-43 (a), (b). $AvgInten_{NO}$ increases by a factor of more than two as can be seen in Figure 6-44, where $AvgInten_{NO}$ and NO measured at exhaust by the gas analyser are plotted against Φ . However, the difference in $AvgInten_{NO}$ for $\Phi = 0.87$ is not as high as expected, even though the difference in measured NO at exhaust is higher in $\Phi = 0.87$ than $\Phi = 0.81$. The shift of the laser beam downstream at non-preheated flame by a small margin can be attributed to the lower increase in $AvgInten_{NO}$ as the flame expands radially outwards, making a conical V shape. Further investigations with quantitative analysis are necessary here, while making sure the laser beam path remains constant.

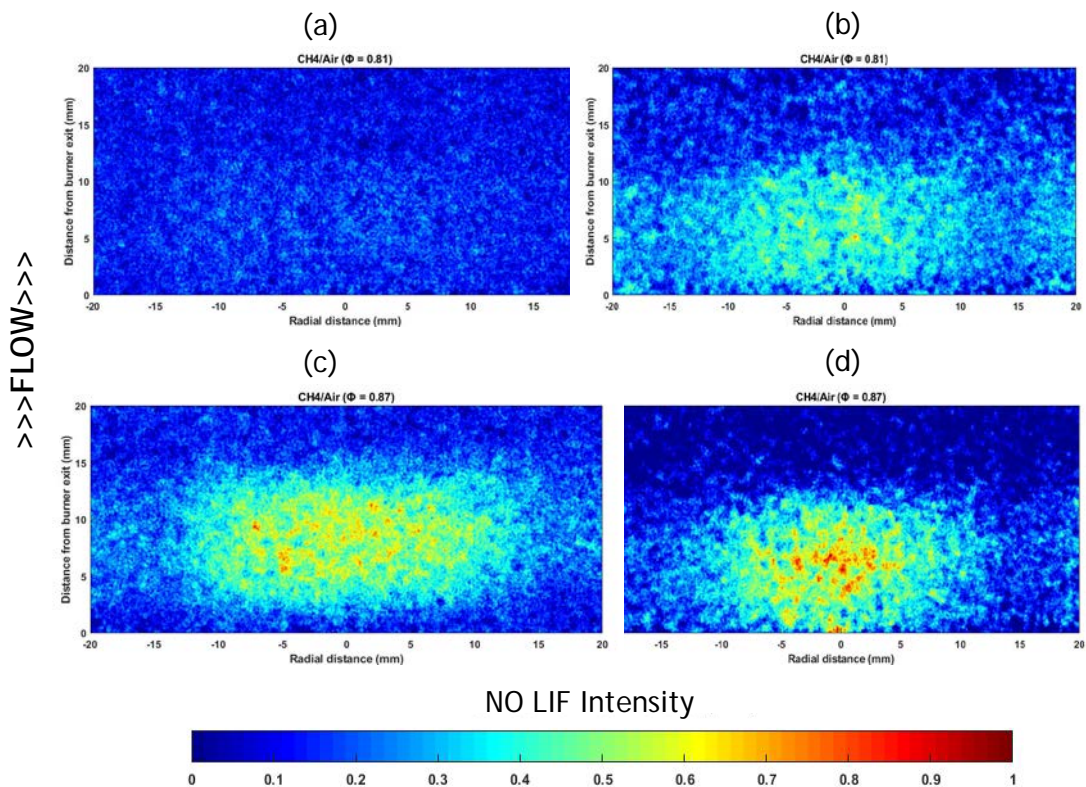


Figure 6-43: Effect of pre-heating on NO formation. Non-preheated conditions on the left side and preheated conditions on the right side. Colormap normalized to maximum intensity across images.

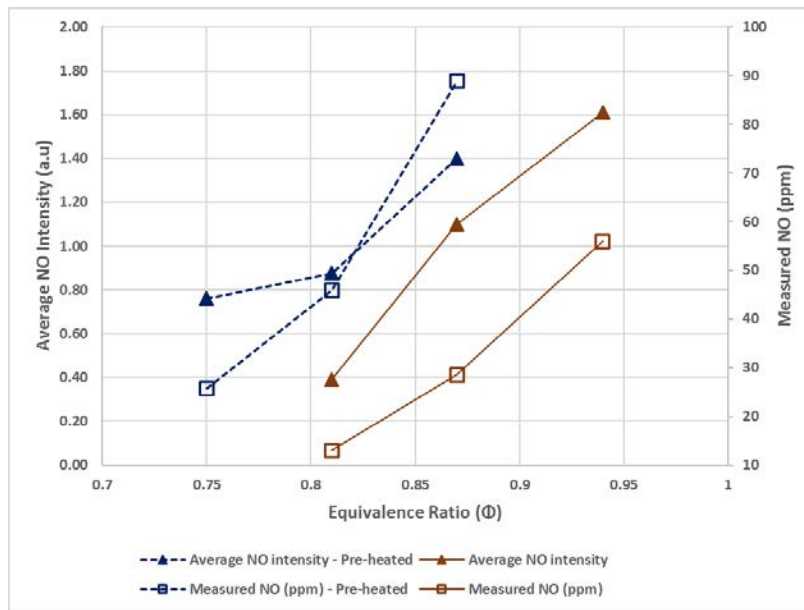


Figure 6-44: Effects of preheated premixed gases on NO formation

6.3. CHEMKIN Simulation for NO prediction

All the experimental points discussed and analysed in this Chapter are simulated using the modified Valera model described in Chapter 4.2 to predict NO emissions and compare with the measured NO by the gas analyser at the exhaust of HPOC. A slight change to the model is made by reducing the number of PFRs to model the post-flame zone from two to one as open confinement was used for the investigations in this Chapter. Recirculation from the CRZ was kept to 70% into the flame zone reactor and from the flame zone, the flow was split three ways: 75%, 20% and 5% into post-flame zone, CRZ and ERZ respectively as before. The modified model and the inputs required for the model are represented in Figure 6-45 and Appendix E.10.

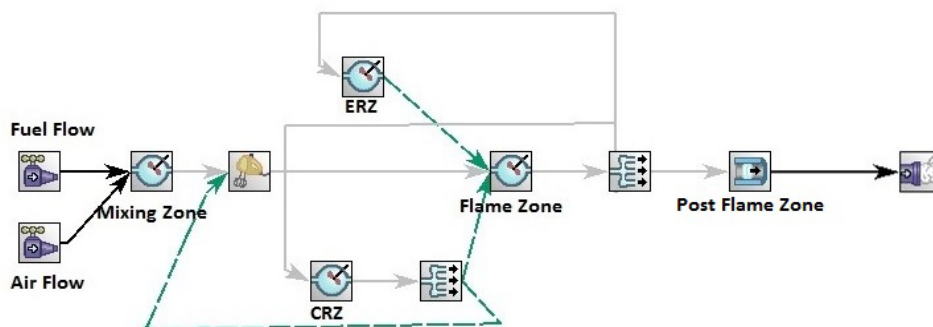


Figure 6-45: CHEMKIN model for flames with open confinement in HPOC

6.3.1. Model Benchmarking

For the preheated experimental points investigated here, heat loss rate kept to the same values as illustrated in Table 4-2. For the non-preheated points, heat loss rates are modified according to Table 6-7, to match NO emissions at $\Phi = 0.81$ (refer to TP 16 at Table 6-5) using GRI-Mech 3.0 mechanism [260] and assumed constant for all the other non-preheated experimental conditions investigated here. The volume of the mixing, flame zone, CRZ and ERZ kept similar to the modified Valera's model.

Table 6-7: Heat loss rates for non-preheated conditions

Zone	Heat loss rate (J/sec)
Mixing	0
Flame	8400
CRZ	1600
ERZ	400

6.3.2. Comparison Between Predicted and Measured NO

The model is used to simulate the flow conditions depicted in Table 6-1, Table 6-2, Table 6-5 and Table 6-6 with the seven mechanisms described in Chapter 4.1. The NO predictions from all these mechanisms for the respective experimental points are analysed and compared with measured NO at exhaust using the gas analyser.

6.3.2.1. CH₄/Air ($\Phi = 0.55 - 0.65$) - Preheated

Predicted and measured NO for the flow conditions in Table 6-1 are shown as a function of Φ in Figure 6-46. The following results can be seen from Figure 6-46 and Table 6-8:

- All mechanisms except SanDiego and CRECK follows the same increasing trend as the measured NO with increasing Φ . NO predictions from SanDiego mechanism rises with Φ at first and then falls, while CRECK mechanism predicts lower NO formation at $\Phi = 0.6$ then increases by a factor of ≈ 2 .

Table 6-8: Differences in predictions by the mechanisms compared to the confined HPGSB-2 experimental results (Preheated CH₄/Air ($\Phi = 0.55 - 0.65$))

Φ	PR	AFT(K)	Percentage (%) Change - in decimal						
			GRI-Mech 3.0	Aramco 1.3	NUIGalway	SanDiego	Ranzi-Paolo	USII	CRECK
0.55	1.1	1788	-0.18	0.82	-0.61	0.65	-0.63	0.99	0.59
0.6	1.1	1878	0.00	1.20	-0.54	0.99	1.49	1.42	-0.72
0.65	1.1	1962	-0.07	1.04	-0.59	-0.89	1.13	1.30	-0.72

Table 6-9: Differences in predictions by the mechanisms compared to the confined HPGSB-2 experimental results (Preheated CH₄/H₂/Air ($\Phi = 0.55 - 0.65$))

Φ	PR	AFT(K)	Percentage (%) Change - in decimal						
			GRI-Mech 3.0	Aramco 1.3	NUIGalway	SanDiego	Ranzi-Paolo	USII	CRECK
0.55	1.1	1793	-0.30	0.54	-0.69	0.38	0.94	0.66	0.13
0.6	1.1	1882	0.00	1.21	-0.56	0.98	1.56	1.41	0.61
0.65	1.1	1966	-0.06	1.07	-0.60	0.86	1.21	1.30	0.53

Table 6-10: Differences in predictions by the mechanisms compared to the confined HPGSB-2 experimental results (Preheated CH₄/H₂/Air ($\Phi = 0.75 - 0.87$))

Φ	PR	AFT(K)	Percentage (%) Change - in decimal						
			GRI-Mech 3.0	Aramco 1.3	NUIGalway	SanDiego	Ranzi-Paolo	USII	CRECK
0.75	1.1	2115	0.12	1.28	-0.48	1.18	1.31	1.89	0.16
0.81	1.1	2183	0.11	1.24	-0.43	1.11	1.27	1.85	0.14
0.87	1.1	2243	0.10	1.07	-0.37	1.01	1.26	1.74	0.75

Table 6-11: Differences in predictions by the mechanisms compared to the confined HPGSB-2 experimental results (Non-Preheated CH₄/Air ($\Phi = 0.81 - 1.1$))

Φ	PR	AFT(K)	Percentage (%) Change - in decimal						
			GRI-Mech 3.0	Aramco 1.3	NUIGalway	SanDiego	Ranzi-Paolo	USII	CRECK
0.81	1.1	2013	0.02	-0.38	-0.82	-0.81	-0.72	0.65	-0.06
0.87	1.1	2097	0.25	-0.44	-0.84	0.15	0.30	0.81	0.07
0.94	1.1	2180	0.52	-0.51	-0.85	0.17	-0.66	0.86	0.26
1	1.1	2225	1.04	-0.25	-0.88	0.33	-0.65	1.01	0.75
1.1	1.1	2205	-0.88	-0.92	-0.95	-0.97	-0.77	-0.93	-0.94

- Predictions from GRI-Mech 3.0 mechanism follows measured NO values near perfectly for the test points investigated here. USII and Aramco 1.3 mechanisms overpredict NO productions for each Φ , while the rate of overprediction increases with increasing Φ .
- NUIGalway mechanism underpredicts NO values by an overall 55 - 60%. Ranzi-Paolo mechanism underpredicts NO productions by 63% at $\Phi = 0.55$ but overpredicts by a factor of two for $\Phi = 0.6$ and 0.65.

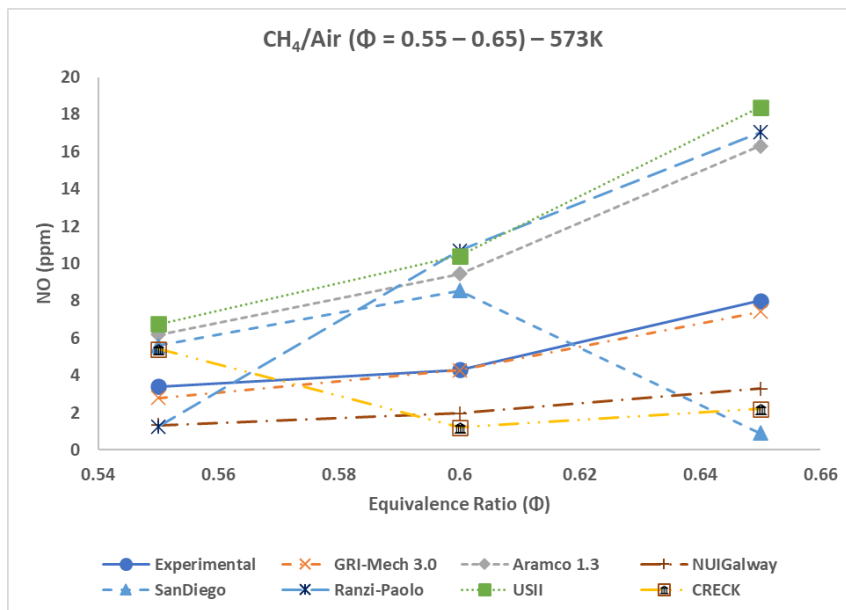


Figure 6-46: Experimentally measured and predicted NO as a function of Φ for preheated CH₄/air ($\Phi = 0.55 - 0.65$)

6.3.2.2. CH₄/H₂/Air ($\Phi = 0.55 - 0.65$) - Preheated

Figure 6-47 represents NO values from the gas analyser measurements and CHEMKIN model predictions as a function of Φ for the flow conditions in Table 6-2. Table 6-9 shows the percentages differences in decimal by the mechanisms compared to the experimentally derived data. Following conclusions can be made by comparing the predictions with the measured data:

- The proportional relationship between NO formation and Φ are predicted correctly by every mechanism for this fuel blend. GRI-Mech 3.0 mechanism predictions are again closely matched

by experimental results, underpredicting NO values at $\Phi = 0.55$ by 30% but near perfect predictions at $\Phi = 0.6$ and 0.65 .

- All the other mechanisms except NUIGalway overpredict NO formations for every point considered here, which again laments the importance of the heat loss assumptions in the PSRs in the model.
- NUIGalway mechanism predictions show lowest NO formation values among other mechanisms yet again, warranting needs for further improvements of the mechanism.

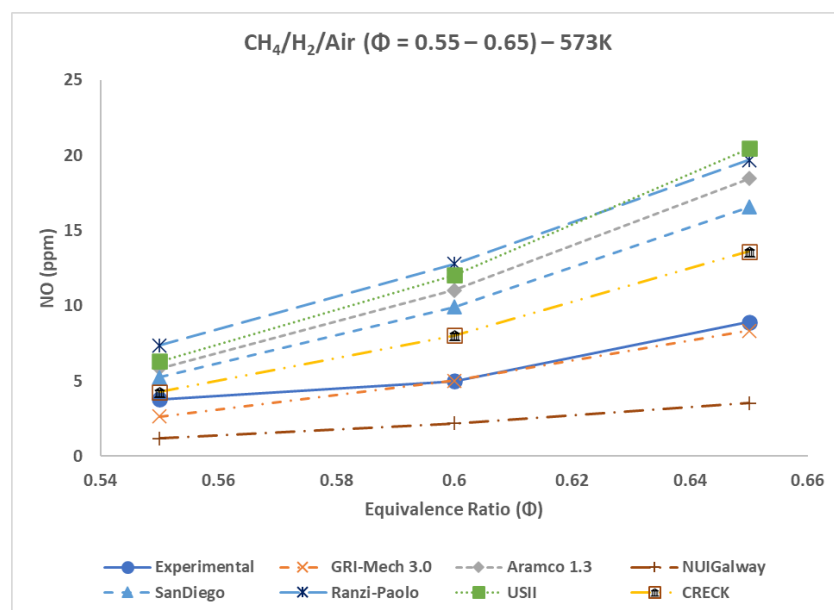


Figure 6-47: Experimentally measured and predicted NO as a function of Φ for preheated $\text{CH}_4/\text{H}_2/\text{air}$ ($\Phi = 0.55 - 0.65$)

6.3.2.3. CH_4/Air ($\Phi = 0.75 - 0.87$) - Preheated

Figure 6-48 compares NO predictions with measured NO values for the flow conditions showed in Table 6-6. Table 6-10 shows the percentages differences in decimal by the mechanisms compared to the experimentally derived data. The predictions are analysed here:

- Predictions from all the mechanisms considered here follow the same expected trend as the measured NO by the gas analyser. GRI-Mech 3.0 again predicts NO production better than all the other mechanisms, making the mechanism

favourable for preheated CH_4 and CH_4/H_2 flames. The CRECK mechanism also gave good prediction for $\Phi = 0.75$ and 0.81 but overpredicting by 60% at $\Phi = 0.87$.

- NO overprediction was shown by all the other mechanisms except NUIGalway. USII mechanism predicts the highest NO for all the Φ and predictions by Ranzi-Paolo, SanDiego and Aramco 1.3 mechanisms are very similar, overpredicting by a factor of around two.

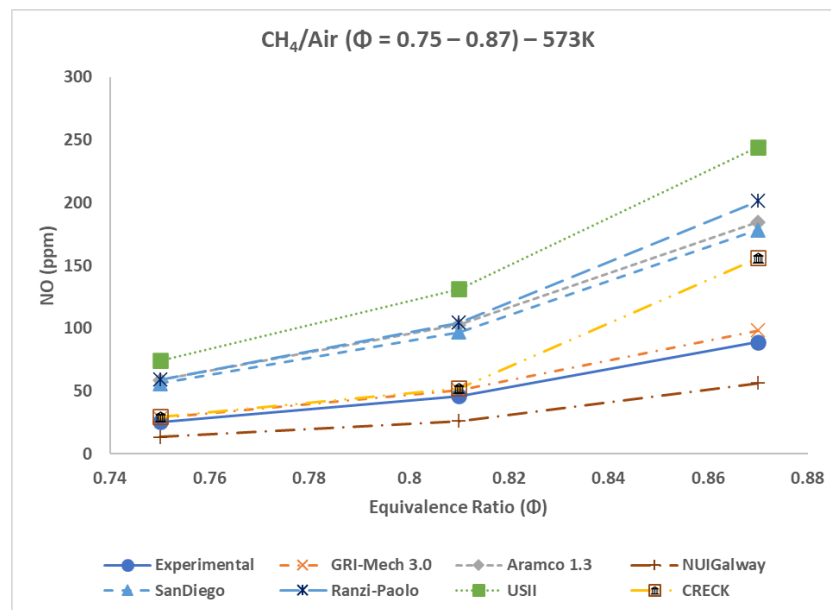


Figure 6-48: Experimentally measured and predicted NO as a function of Φ for preheated CH_4/air ($\Phi = 0.75 - 0.87$)

6.3.2.4. CH_4/Air ($\Phi = 0.81 - 1.1$) - non-preheated

Figure 6-49 compares the changes in measured and predicted NO for the flow conditions in Table 6-5 as Φ changes. Table 6-11 shows the percentages differences in decimal by the mechanisms compared to the experimentally derived data. NO predictions from each mechanism except Ranzi-Paolo demonstrate upward trends up to stoichiometry, as thermal NO formation increases with increasing flame temperature and then all the mechanisms predict low NO at $\Phi = 1.1$, as seen in measured NO.

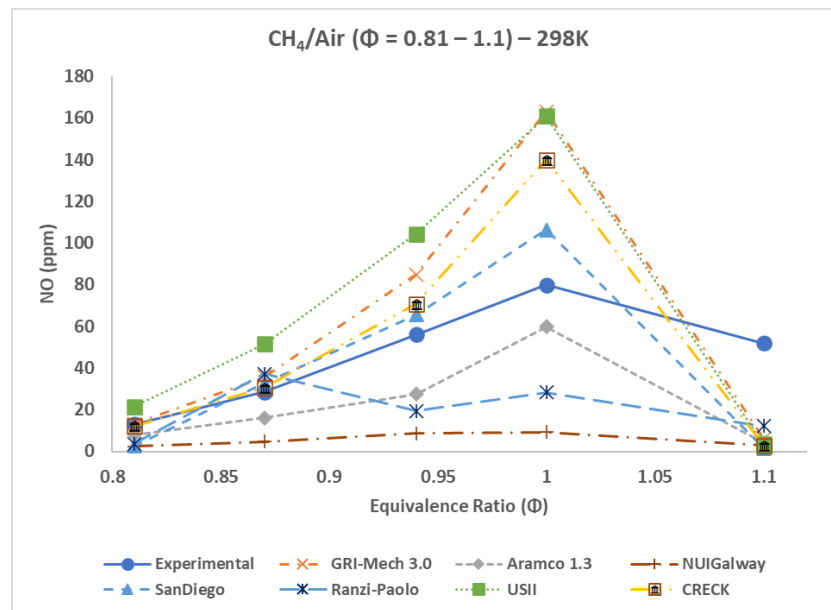


Figure 6-49: Experimentally measured and predicted NO as a function of Φ for non-preheated CH₄/air ($\Phi = 0.81 - 1.1$)

Following points can be made by analysing the graph carefully:

- Other than Ranzi-Paolo mechanism predictions, every other mechanism predict NO formation as expected from lean to rich flames. SanDiego mechanism predictions are closest to the measured NO at exhaust until stoichiometry. As was seen for the flames in HPOC without confinement in Chapter 5.3.2, NO formations are underpredicted at $\Phi = 1.1$ by all the mechanisms in HPOC with open confinement. Possible explanation for this phenomenon could be high lance tip temperature at $\Phi = 1.1$, as this point was taken at the end and lance tip was already heated up from the previous experiments, which could affect the flame temperature. Further investigations are needed to understand the NO predictions at rich conditions.
- At $\Phi = 0.87$, NO predictions from all the mechanisms are very close to the measured value but the predictions drift further away from the measured values as the flame moves towards stoichiometry. Aramco 1.3 and NUIGalway mechanisms underpredict NO formation for all the points investigated here.

6.4. Summary

This Chapter built up on the qualitative NO-PLIF findings in the unconfined flames. NO formation investigation was carried out using the selected excitation wavelengths for BASE and FARH₂ fuels in HPGSB-2. The experimental results were validated using theoretical calculations from CHEMKIN and heat release intensities from the flames. The Chapter summarised with the following observations:

- NO formation analysis was performed for BASE fuel in the operating region ($\Phi = 0.55-0.65$) of industrial GTs. Comparisons were made between NO PLIF results, heat release intensities and CHEMKIN simulation results. The flame stretched radially, contributing to larger CRZ envelope and stabilized closer to the burner exit as Φ increased. As a consequence, NO formation was stretching out radially with more NO formations due to increased heat release intensity, with increasing Φ .
- Effects of 15% volumetric H₂ addition on the flame shapes and NO formation with nominally similar flows and turbulent conditions was analysed afterwards. Addition of H₂ augmented the burning intensity of CH₄, consequently higher volumetric heat release results from CHEMKIN calculations. Flame stabilized closer to the burner exit as a result, compared to the BASE fuel at same Φ . Due to the above changes in the flame shape and heat release intensity, NO formation intensity increased with radial stretch for FARH₂ fuel.
- Confinement shown to have significant effects on CRZ area in the flame and consequently NO formation. Formation of NO was stretched in the confined flames as the CRZ was ball shaped, compared to the rectangular shaped CRZ in the unconfined flames. Heat release intensity increased for the confined flames due to higher momentum of flow as shown in the PIV images, resulting in higher NO formation.

- NO LIF images were taken utilising 226.03 nm excitation wavelength at the same equivalence ratios as 285.15 nm excitation wavelength. Hence, $AvgInten_{NO}$ values from both the excitation wavelengths were compared, both following the same trend, thus validating the choice of 285.15 nm excitation wavelength.
- Finally, all the test points considered in this Chapter were simulated to predict NO production at exhaust, using slightly changed modified Valera model to accommodate for open confinement in place of convergent confinement. The predictions from the model were analysed and compared with the measured NO values at exhaust by the gas analyser.

7. NO Calibration towards Quantitative Analysis

Precise concentration measurement of NO in premixed flames is one of the crucial parts of NO formation investigation as it quantifies NO concentration, which is vital for validating CFD and chemical kinetics models and for locating areas of above-average NO production. In this pursuit, a LIF technique is applied to measure NO concentration within the flame. The unique excitation properties of laser light allow selective and quantitative probing of many chemical species with high temporal and spatial resolution in combustion environments [50], [310]. As discussed earlier in Chapter 2, NO formation mechanisms have already been extensively studied and well documented in literature [56], [58] as well as UV LIF of NO, including single point, 1-D line imaging and 2-D planar imaging for understanding NO formation in laboratory flames and practical combustion systems [142], [155], [161], [172].

For LIF diagnostics, calibrating semiquantitative data by using a known concentration of the molecule under study is advantageous as all effects of detection efficiency (e.g. filter transmission) and collisional quenching are accounted for. However, a source of hot NO must be provided for calibration when NO is excited from the second vibrational level [311]. NO calibration technique by doping NO in lean Bunsen flame and excited by 285.16 and 226.03nm wavelength is described and analyzed in detail in this Chapter. This Chapter aims to describe NO calibration method in unconfined Bunsen burner flame with varying NO doping level up to 1300 ppm and addresses the difficulties encountered along the way.

Doping NO in the premixed reactants calibration requires consideration of the interaction between dopant and flame chemistry. Several experiments have investigated the interactions between NO and different flame types [150], [174], [312]. According to Cattolica et al. [312], linear correlation between NO LIF signal and NO concentration remained valid, even after converting 40% NO in flame while doping very high level of NO (4000-8000 ppm) in lean hydrogen/air flames. Reisel and Laurendeau [150] predicted 5% NO concentration reductions in ethene/air lean flames ($\Phi = 0.9$) in simulation calculations. Flame

development and temperatures can also be affected if NO dopant levels are too high Schulz et al. [174] reported that, in a spark-ignition engine fueled with propane/air, only 10% NO was converted in a lean flame ($\Phi = 0.9$) compared to 40% reduction of NO in fuel-rich conditions ($\Phi = 1.25$) at dopant levels of 1000 ppm. In the same experiment no changes in engine performance were found at NO dopant levels of up to 1500 ppm.

7.1. Quenching and Calibration

Correlation of the NO LIF signal to a local NO concentration requires consideration for a number of factors. When operating in the linear fluorescence regime, the fluorescent signal can be shown to be linearly responsive to the number density of the probed species, however species temperature and collisional quenching effects must be considered carefully. Equation [7-1] describes the relationship between measured LIF signal and NO number density.

$$S_{NO} \sim C_{opt} \tau_{\lambda} B_{12} I_L f_b \Gamma \phi n_{NO}^{\circ} \quad [7-1]$$

Where S_{NO} is the LIF signal, C_{opt} is the collection and calibration constant, τ_{λ} is the transmissivity of the collection optics, B_{12} is the Einstein coefficient for absorption, I_L is the laser irradiance, f_b is the Boltzmann population fraction in the ground state, Γ is the laser line overlap integral, ϕ is the fluorescent yield, and n_{NO}° is the NO number density.

The optical collection constant and transmissivity, C_{opt} and τ_{λ} , can be grouped into a single term that is determined empirically and will be discussed shortly. The absorption coefficient, B_{12} is a constant for a given species and transition. The laser irradiance, I_L is monitored for shot-to-shot fluctuations and therefore this value is determined experimentally. The Boltzmann fraction, f_b in the ground state is temperature dependent but can be calculated using Boltzmann statistics. The overlap integral, Γ is primarily influenced through the spectral width of the laser, which remains nearly constant. The fluorescent yield, ϕ is temperature and composition dependent. Estimates for the quenching rate can be made following the work of Settersten [313]. Finally, the number density, n_{NO}° can be relative to the

NO Calibration towards Quantitative Analysis

concentration through the ideal gas law to be temperature and pressure dependent.

Table 7-1: NO LIF quenching and calibration parameters. Reproduced from [313]

Term	Units	Function	Constants			
			C ₁	C ₂	C ₃	C ₄
B_{12}	m ² /(J.s)		2.38x10 ⁹			
f_b	-	$c_1e^{c_2/T} + c_3e^{-c_4/T}$	-0.2822	-1799	0.2183	408.4
A_{21}	1/s		5.72x10 ⁶			
σ_k						
NO	Å	$c_1e^{c_2/T} + c_3e^{-c_4/T}$	37.3	11.7	60	0.011
H ₂ O	Å	$c_1(300/T)e^{c_2/T} + c_3e^{-c_4/T}$	121.2	0.676	100	0.010
CO ₂	Å	$c_1e^{c_2/T} + c_3e^{-c_4/T}$	38.0	173	46	0.0022
O ₂	Å	$c_1e^{c_2/T} + c_3e^{-c_4/T}$	22.0	59.1	4.3	0.00195
CO	Å	$c_1e^{c_2/T} + c_3e^{-c_4/T}$	4.23	128	17.5	0.00198
N ₂	Å	$c_1e^{c_2/T} + c_3e^{-c_4/T}$	1.88	-2130	84	0.0121

Table 7-1 illustrates the quenching and calibration terms of interest. The total quenching rate can be estimated through the mole fraction weighted sum of the collisional quenching for each species. Equation [7-2] shows the relation for individual quenching rates from bath gas species k .

$$Q_k = \sigma_k \left(\frac{N}{V}\right) \sqrt{\frac{8k_B T}{\pi \mu_k}} \quad [7-2]$$

$$\mu_k = \frac{M_k M_{NO}}{M_k + M_{NO}} \quad [7-3]$$

The relation for the total quenching rate for all major bath gas quenching species is shown in equation [7-4].

$$Q_{21} = \sum X_k Q_k \quad [7-4]$$

This relation allows for the correction of the NO LIF signal due to variations in the temperature and species composition through the flame. The quenching rate is introduced into equation [7-1] through the fluorescent yield via equation [7-5].

$$\phi = \frac{A_{21}}{A_{21} + Q_{21}} \quad [7-5]$$

The next step is to determine the calibration factor for optics and transmissivity, C_{opt} . The standard procedure for doing this calibration process is to seed known concentrations of NO into the unburned gas mixture of lean flames. The resultant change in NO LIF signal with doped NO concentration is linear, with the slope of the fit equal to the NO LIF signal response per ppm concentration. This calibration procedure has been utilized by several different studies [314]-[316], with the primary assumption rooted in the need for only minor consumption of NO through the flame front, which is a reasonable approximation under lean conditions [139]. Details of steps taken to achieve the NO calibration curve for 285.16 and 226.03 nm excitation wavelength is described in the following sections.

7.2. NO LIF in Bunsen flames

As discussed in Chapter 3.1, NO LIF in a 15 mm Bunsen burner flame is examined in this section. After applying the correction scheme for background, dark current, O₂ LIF, shot-to-shot fluctuations in total energy and energy distribution, pixel linearity, and spatial calibration, images such as those in Figure 7-7 are produced. Following certain qualitative trends can be observed:

- Specifying the exit velocity as a constant factor of the laminar burning velocity gives an acceptable performance of stabilizing and controlling the height of the flame, allowing the flame to stay within frame under considerably different exit velocities.

NO Calibration towards Quantitative Analysis

- Absorption of the excitation beam through the flame results in the slight attenuation of the fluorescence signal when comparing the left- and right-hand sides of the image.
- NO LIF fluorescence increases from lean to rich.
- The flame front is a relatively straight region once sufficiently far from the base of the flame or from the tip of the flame.
- The region of interest, the area within the first 25 to 35 mm normal to the flame front, is the targeted region for observing the NO doped in the flame.
- NO LIF fluorescence in the region of interest for lean flames shows a relatively slow increase in signal normal to the flame, whereas the stoichiometric flames show a more rapid rise, while the rich flames show the highest gradient in NO LIF signal.

7.2.1. NO PLIF Calibration at 285.16nm

For the NO calibration experiment at 285.16nm, a 15 mm diameter Bunsen burner (refer to Chapter 3.1) was used, and lean methane/air flame was stabilized on the burner nozzle by maintaining approximately equal burning and flow velocities as the NO dopant level changes from 0 - 1300 ppm. Table 7-2 shows the experimental mass flow rates at different dopant level of NO. Temperature and NO concentration were recorded in the post-flame zone (25 mm above the burner exit) with a K-type thermocouple and a Signal Instruments 4000VM NO_x analyzer (refer to Chapter 3.7). Measurements taken by the NO_x analyzer were hot/wet and not corrected for exhaust oxygen concentration. As seen in Table 7-2, up to 25.5% of the doped NO was lost in the flame at 400 ppm seeding. With the NO seeding at 1300 ppm, the NO loss in the flame was the lowest observed in the dataset at 9.2%. While some NO loss through the flame was expected, additional losses can be attributed to atmospheric diffusion as the burner was operated unconfined. The burner was operated leaner as the NO seeding levels were being reduced to stabilize the flame. Figure 7-1 illustrates the location of the data point taken at 1300 ppm seeding for the calibration curve in terms of (a) OH* chemiluminescence measurements and (b) NO LIF measurements.

Table 7-2: Premixed reactant flow rates, exhaust temperatures, and NO readings for NO dopant level of 0 - 1300 ppm

Seeded NO (ppm)	CH ₄ mass flow (g/s)	Air mass flow(g/s)	Equivalence ratio (Φ)	NO-N ₂ mass flow (g/s)	Temperature (K)	NO reading (ppm)	NO lost in flame (%)
1300	0.0079	0.15	0.91	0.0237	1059	1180	9.23%
1000	0.0079	0.15	0.91	0.0177	1062	836	16.4%
800	0.0079	0.15	0.91	0.0138	1067	653	18.4%
700	0.0078	0.15	0.89	0.0120	1033	588	16.0%
600	0.0078	0.15	0.89	0.0101	1051	507	15.5%
500	0.0069	0.15	0.79	0.0083	1013	404	19.2%
400	0.0065	0.15	0.75	0.0065	1025	298	25.5%
300	0.0063	0.16	0.68	0.0051	999	231	23.0%
200	0.0063	0.16	0.68	0.0034	979	166	17.0%
100	0.0063	0.16	0.68	0.0017	1015	81	19.0%
0	0.0063	0.16	0.68	0	1004	11	-

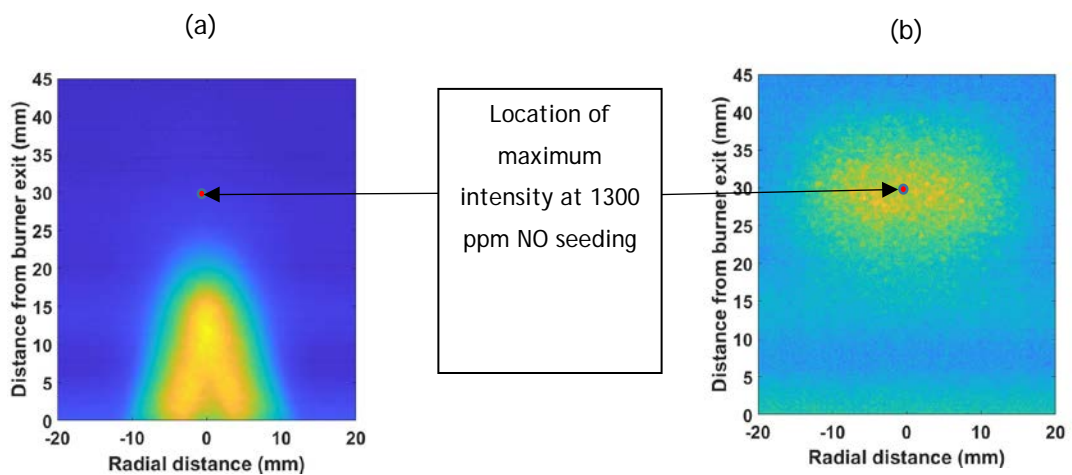


Figure 7-1: Location of the data points for the calibration curves in terms of (a) OH* chemiluminescence and (b) NO-LIF measurement.

NO Calibration towards Quantitative Analysis

A calibration constant was determined for methane-air flame as shown in Figure 7-2, seeding ten doped concentrations of NO into lean premixed stream from a 1% NO in N₂ gas standard. The LIF fluorescence at 25 mm normal to the nozzle exit then corrected for all the temperature and compositionally dependent factors, including collisional quenching using the relation in equation [7-4], the Boltzmann fraction f_b , and correction of number density to mole fraction. These terms were collectively named β_{quench} for convenience. The remaining constant terms in equation [7-1] were then grouped into the calibration term.

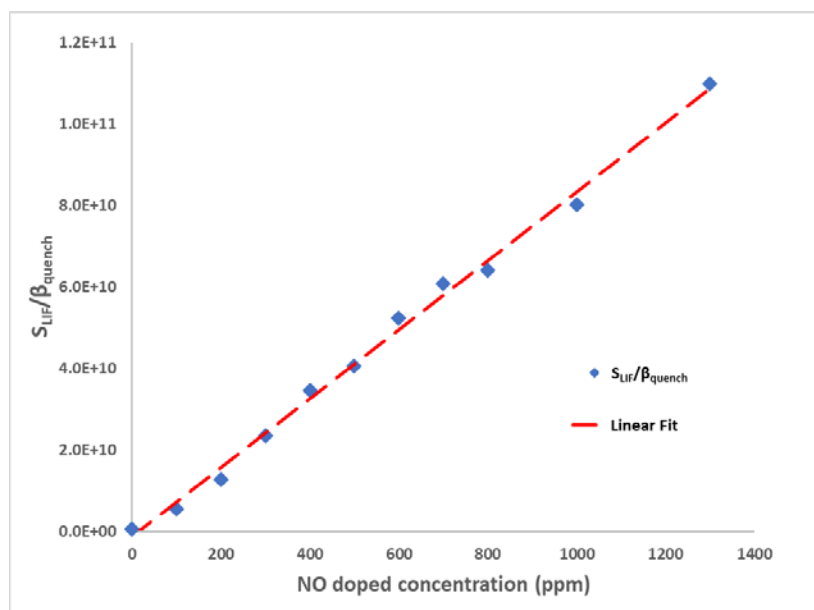


Figure 7-2: Linear response of the quenching corrected LIF signal to increasing doping of NO in lean methane/air flame

The final step is to apply corrections for all the temperature and compositionally dependent quenching rates to the flame. Figure 7-3 shows an example of the temperature dependence of the LIF correction terms, normalized by the correction at 300K. The dark blue line indicates the Boltzmann fraction up to 2200K as calculated using the relation in Table 7-1. A peak in population fraction can be seen around 800K, with a nearly linear decay with increasing temperature. Meanwhile, the lighter blue curve shows the correction due to collisional quenching. For this figure, the composition is based on the equilibrium combustion products of stoichiometric methane. The dashed red line

indicates the total quenching β_{quench} , including the Boltzmann fraction, quenching rate, and conversion from number density to mole fraction, defined as:

$$\beta_{quench} = f_b \frac{A_{21}}{A_{21} + Q_{21}} \frac{1}{T} \quad [7-6]$$

Finally, the LIF signal can be correlated to the molar concentration of NO as:

$$S_{NO} = C_{cal} \beta_{quench} (T, X_k) X_{NO} \quad [7-7]$$

which accounts for variations in the collisional quenching, Boltzmann population fraction, local temperature and composition, and ICCD sensor response to LIF emission. This correction can then be applied to all the NO LIF profiles measured.

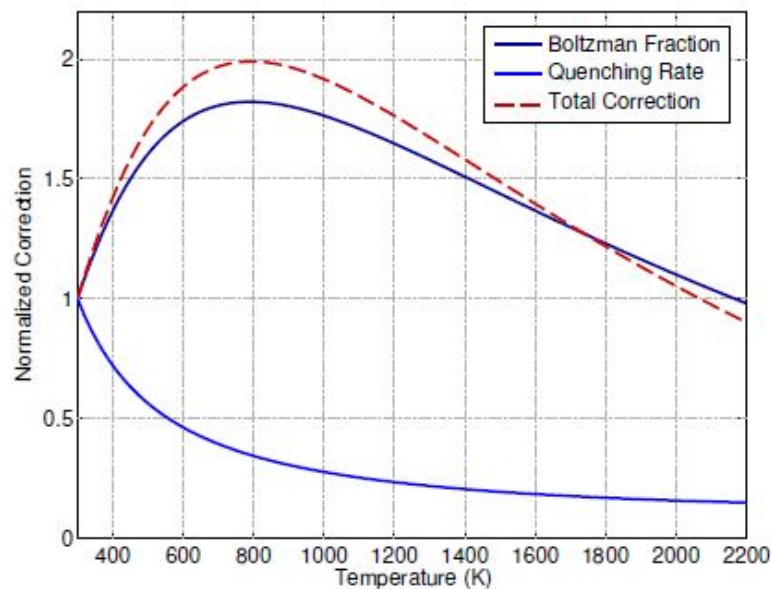


Figure 7-3: Example of normalized temperature and composition dependent corrections to the NO LIF signal. Values are normalized by the correction term at 300K. Reproduced from [317].

7.2.1.1. Numerical Simulation

As can be seen in Table 7-2, NO measured by the gas analyzer was always below the actual seeded NO level. Chemical reactor modelling is utilized here to correlate NO concentration level with heat loss to the surrounding.

NO Calibration towards Quantitative Analysis

The 15 mm Bunsen burner was modelled in CHEMKIN environment as per Figure 7-4, Perfectly Stirred Reactors (PSR) were used to model the mixing zone and flame zone and a Plug Flow Reactor (PFR) was used to model the post-flame zone. Two different studies were conducted using GRI-MECH 3.0 mechanism [260] with this model to predict the NO in post-flame zone.



Figure 7-4: Simple chemical reactor network model of the 15 mm Bunsen burner in CHEMKIN

In the first study (refer to Figure 7-5), the burner was simulated using the maximum heat loss at each condition. As mentioned before, all the NO measurements were taken at 25 mm above the burner exit, however, as NO seeding was reduced from 1300 ppm to 100 ppm, the flame height was reduced as the flame could only be stabilized with the reduced NO flow by reducing the fuel flow. Thus, more heat loss is expected at the reference height as the NO seeding was reduced. Thus, the model predicts lower NO reading at high seeding levels as at these points, the reference height was not sufficient for maximum heat loss to occur. Similarly, as NO seeding concentrations decreased, the model better predicts the measurements.

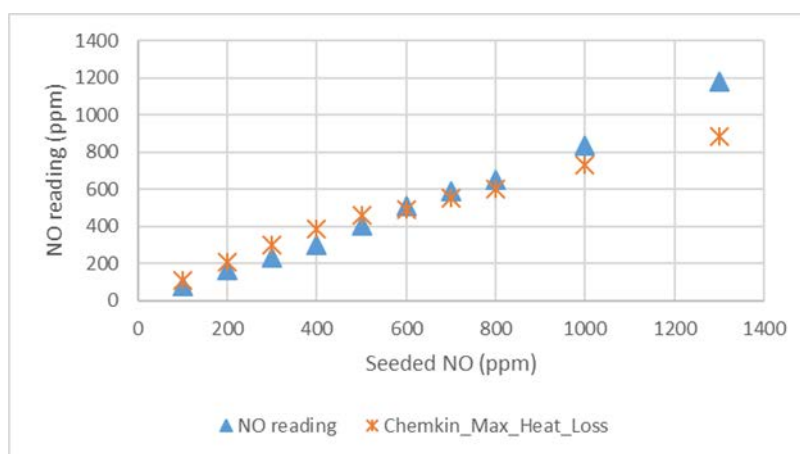


Figure 7-5: Comparison of predicted NO with maximum heat loss with actual NO reading.

At 600 ppm, the model predicts the NO reading correctly. However, below 600 ppm, the simulation slightly overpredicts the actual reading. As the flame was getting leaner due to the reduction of fuel with decreased NO seeding, the flame stabilized nearer the burner exit. Thus, the areas of maximum heat release zone were compacted, forming thermal NO in the flame, causing the model to slightly over-predict than the gas analyzer reading.

For the second study (refer to Figure 7-6), the modelled heat loss was modified for the 1300 ppm case to match the actual NO reading and the heat loss was then modified as a function of adiabatic flame temperature for the subsequent points. Good agreements were found between the actual and predicted reading in this study.

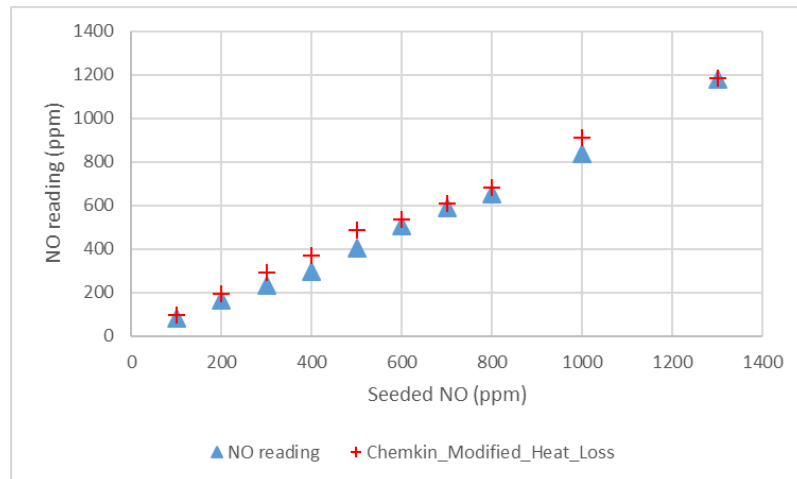


Figure 7-6: Comparison of predicted NO with calibrated heat loss with actual NO reading

7.2.2. NO LIF Calibration at 226.03nm

For this calibration work, laser beam at 226.03nm wavelength was pointed 30 mm normal to the burner nozzle. The laser sheet was not used for this calibration experiment. The same 15 mm Bunsen burner as before was used to conduct this calibration. Temperature was recorded in the post-flame zone with a K-type thermocouple, but NO_x analyzer was not used to measure the NO concentration. This experiment was conducted in lean operation conditions ($\Phi = 0.79$ to 0.9) for the reasons discussed earlier in Section 7.2.1. The burner was operated leaner as the

NO Calibration towards Quantitative Analysis

NO doping levels were being reduced to stabilize the flame. Figure 7-7 shows the corrected NO LIF images from 0ppm to 1000ppm NO seeding levels.

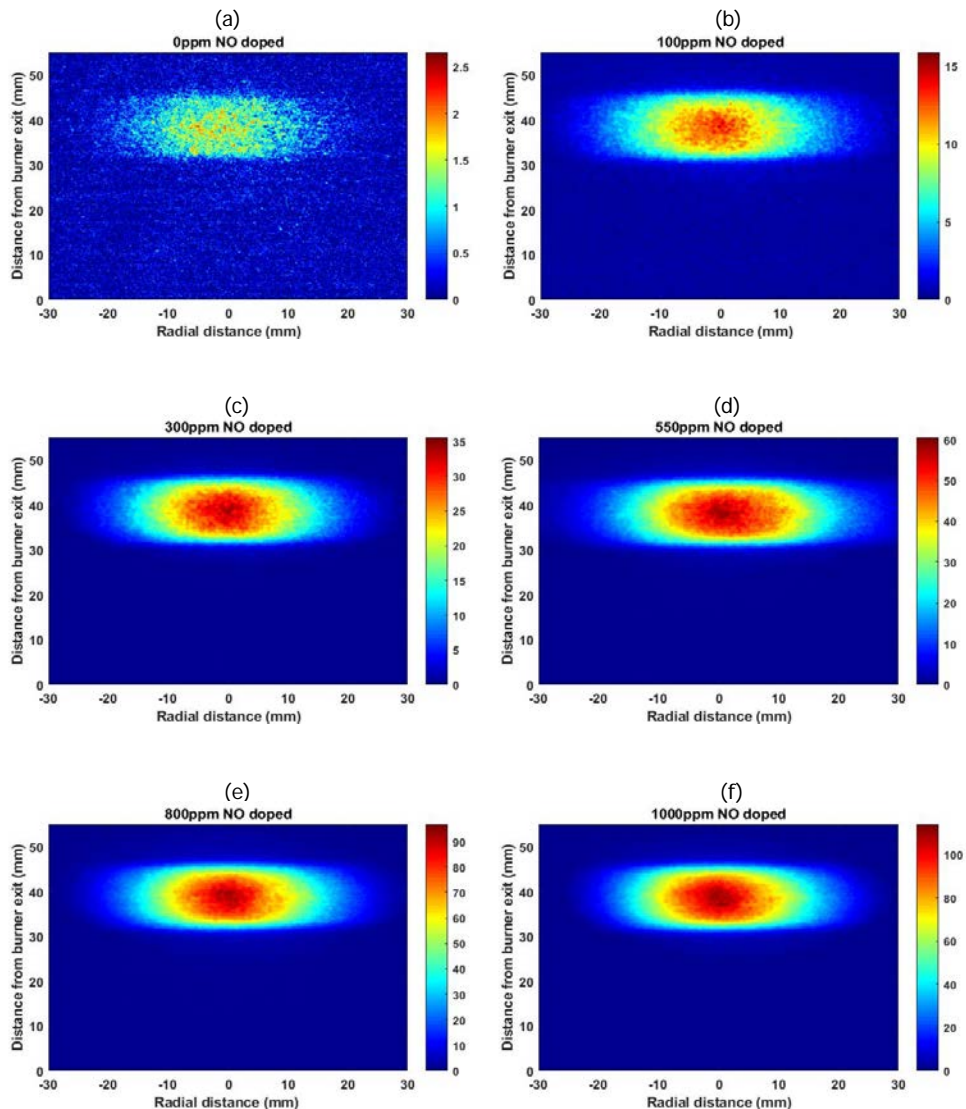


Figure 7-7: Corrected NO LIF images for calibration at 226.03 nm

It is clear from the NO LIF images in Figure 7-7 that the resolution of the images improves with increasing NO doping level. This is because pixel intensities have more contrast with increasing NO level at the beam path compared to the background. It also must be noted that each image shown in Figure 7-7 has different scale on their right. As expected, NO LIF intensity goes up as NO doping increases. Figure 7-8 illustrates the NO-LIF images with colormaps normalized to maximum intensity across all images. Increase in LIF intensity is visible with increasing NO doping

level, as expected. Table 7-3 shows the premixed reactant flow rates and exhaust temperatures for NO dopant level of 0 - 1000 ppm.

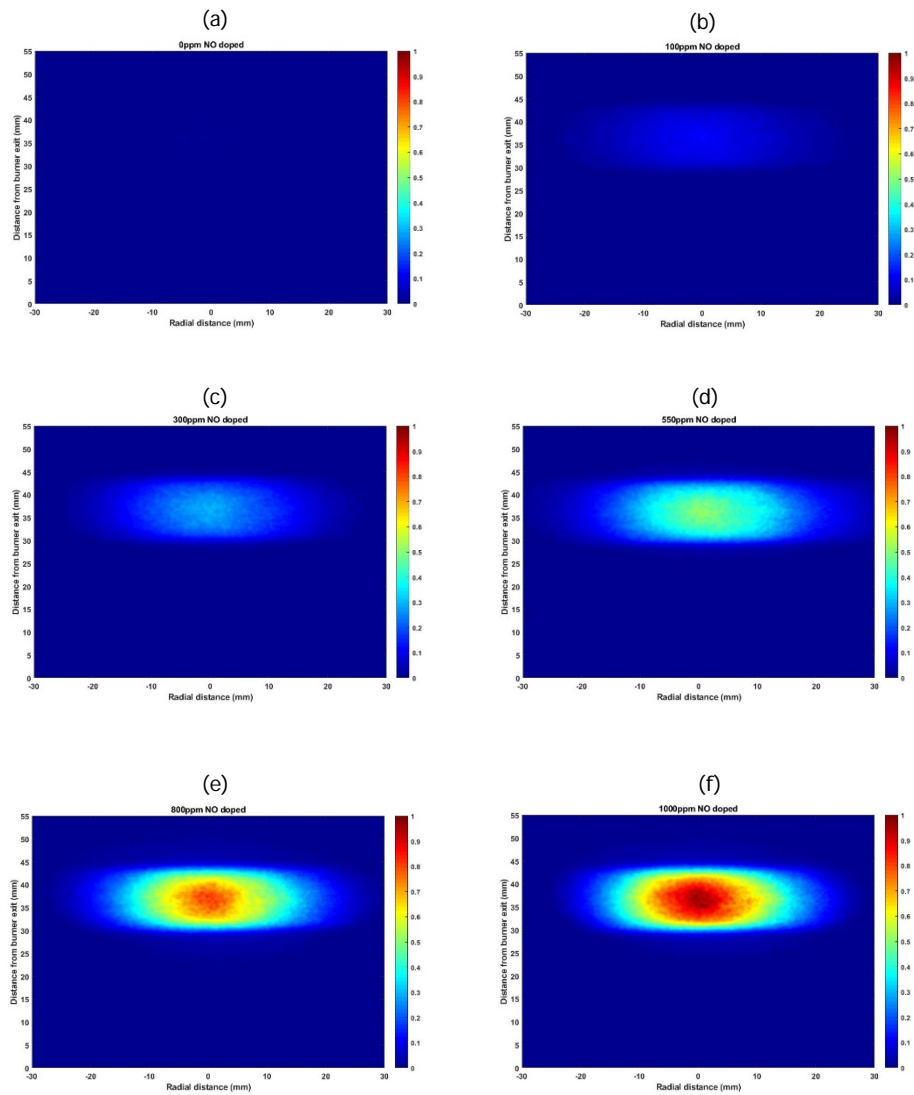


Figure 7-8: Corrected NO LIF images for calibration at 226.03 nm. Colormaps normalised to maximum intensity across all images.

NO Calibration towards Quantitative Analysis

Table 7-3: Premixed reactant flow rates and exhaust temperatures for NO dopant level of 0 - 1000 ppm

Seeded NO (ppm)	CH ₄ mass flow (g/s)	Air mass flow(g/s)	Equivalence ratio (Φ)	NO-N ₂ mass flow (g/s)	Temperature (K)
1000	0.0061	0.117	0.9	0.0138	945
800	0.0061	0.121	0.87	0.0111	899
550	0.0061	0.124	0.85	0.0076	898
300	0.0059	0.124	0.82	0.004	918
100	0.0059	0.128	0.79	0.0014	908
0	0.0059	0.128	0.79	0	923

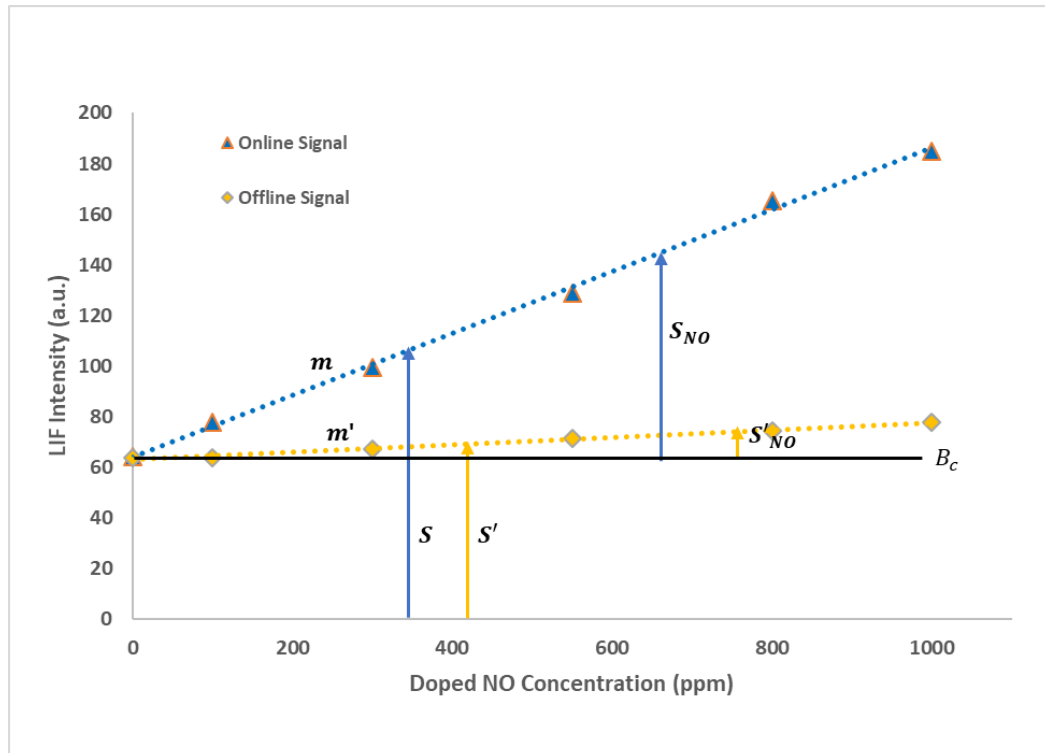


Figure 7-9: NO LIF calibration curve ($\lambda = 226.03$ nm) for 15 mm Bunsen burner with CH₄-air at atmospheric temperature and pressure

Thomsen et al. [155] proposed a calibration technique to transfer calibration data from atmospheric conditions to high pressure conditions. This technique assumes that the broadband interferences from O₂, CO₂ and H₂O are relatively constant in value over a range of excitation wavelengths.

Figure 7-9 represents the calibration curves obtained by varying the amount of NO doped into a reference flame. As both the curves meet at the y axis at 0 ppm seeding, the same background signals (B_c) occurs at both excitation wavelengths. Then, the online (S) and offline (S') LIF intensities at any point in the doping curve can be written as,

$$S = B_c + S_{NO} \quad [7-8]$$

$$S' = B_c + S_{NO}' \quad [7-9]$$

Similarly, the slopes of the two calibration curves m and m' ,

$$S_{NO} = m[NO] \quad [7-10]$$

$$S_{NO}' = m'[NO] \quad [7-11]$$

where [NO] is the total NO concentration, doped plus undoped, in the flame. A factor g can be derived such that,

$$g = \frac{S_{NO}'}{S_{NO}} = \frac{m'}{m} \quad [7-12]$$

From Equation [7-8] and [7-9] , the LIF signal for the undoped condition in generic flames can be derived as,

$$S_{NO_u} = S_u - S'_u + S_{NO_u}' \quad [7-13]$$

where S_u and S'_u are signal of online and offline in undoped condition respectively. Now, using the definition of g ,

$$S_{NO_u} = S_u - S'_u + gS_{NO_u} \quad [7-14]$$

Finally, solving for S_{NO_u} and B_c in terms of g ,

$$S_{NO_u} = \frac{(S_u - S'_u)}{(1 - g)} \quad [7-15]$$

$$B_c = \frac{(S'_u - gS_u)}{(1 - g)} \quad [7-16]$$

NO Calibration towards Quantitative Analysis

According to Ravikrishna et al. [318], the NO concentration in ppm relative to the calibration flame temperature can be expressed as,

$$N_{ppm,RT} = C_b S_{NO_u} \quad [7-17]$$

where C_b is the gradient of the calibration curve. The [NO] in absolute ppm can then be expressed as,

$$N_{ppm,abs} = \left(\frac{T}{T_C}\right) \left(\frac{\gamma_C}{\gamma}\right) \left(\frac{P_C}{P}\right) \left(\frac{I_0}{I_{0,C}}\right) N_{ppm,RT} \quad [7-18]$$

where T is the local flame temperature, P is the local flame pressure, γ is the cumulative correction factor for the effects of collisional quenching, Boltzmann fraction distribution and laser line/absorption line overlap fraction and I_0 is the laser irradiance. The subscript 'C' refers to the quantities in the calibration flame. The cumulative correction factor is obtained using LIFSim tool [129], where temperature, pressure, major species concentrations, excitation wavelengths amongst others are provided as input.

As discussed earlier in Chapter 3.6.2, all the raw images are corrected for any non-uniform energy distribution of the laser sheet by using an averaged LIF image of the burner seeded with NO. The images are then corrected for attenuation of the excitation laser light and fluorescence signal, which is dominated by absorption from hot CO₂ with a small contribution from hot H₂O. Attenuation of the laser light and fluorescence signal are corrected on a pixel-by-pixel basis using Beer-Lambert's Law [277] and absorption coefficients known from shock tube measurements [159] and simple consideration of the geometry. These corrections require some knowledge of the local temperature because the CO₂ and H₂O absorption coefficients are temperature dependent and the CO₂ and H₂O number densities are obtained using an assumption of thermal equilibrium in the post-flame gas. Temperature information is also needed to correct for the temperature variation of the NO-LIF signal via the temperature dependence of the laser-excited ground state population, the spectral overlap between the laser-spectral profile and NO absorption spectrum and the fluorescence yield. Thus, NO LIF multi-

line thermometry is to be considered in future work for in-flame temperature measurement.

7.3. Summary

The objective of this chapter was to describe the NO-LIF calibration process in detail. Two different processes were followed to determine the calibration factor at 285.16 and 226.03 nm excitation wavelengths. Online and offline signals were considered separately to determine the calibration factor at 226.03 nm, following the proposal of Thomsen et al. [155]. More widespread and common method from previous studies [314]-[316] was used to determine the calibration factor at 285.16 nm. In this case, the NO LIF images were corrected for background, shot-to-shot laser energy and laser beam energy distribution. Results from this chapter will be used to convert the qualitative data to quantitative NO distribution for future work at GTRC in HPGSB-2.

8. Conclusions

This thesis focused on the development and assessment of chemical reactor models for NO_x predictions, and development and commissioning of optical diagnostics system, namely laser induced fluorescence (LIF) for qualitative NO formation analysis on industrial swirl flames. This study first discussed the source of fuels for GT power generation sectors in the UK and possible emissions from GT operations, focusing on NO_x emissions and subsequently NO_x formation mechanisms were investigated. LIF theory was detailed hereafter, prior to discussing the experimental set-up with different burners for NO-LIF investigations with different excitation wavelengths. The second part of the thesis focused on the development of a chemical reactor model for HPGSB-2 at GTRC to predict exhaust NO_x emissions. The third part of the present research focused on the development and application of 2-D spatially resolved non-intrusive measurement of NO in a Bunsen burner and HPGSB-2 flames. The thesis was concluded by describing NO calibration experiments to quantify qualitative NO distribution data in future. The main findings are summarised below.

8.1. Experimental Set-up and Methodology for NO-LIF

- A methodology was developed for NO-LIF experiments at Cardiff University. Due to the constraints of the laser system, two different NO excitation strategy was employed in this study.
- Experimental facility at GTRC was designed and commissioned to conduct NO-LIF experiments.

8.2. Chemical Reactor Modelling

- Three chemical reactor networks were developed from two existing models in the literature and predictions from these models were compared with experimentally derived data.
- The predictions from the recirculation models matched the experimental values closely compared to the other models.

The simplified model underpredicted NO_x emissions at all conditions considered for validation. However, this model was recommended for further development in the future for its simplicity and low computational cost. The Rizk models were deemed unsuitable for HPGSB-2, mainly due to the 'unmixedness' parameter of these models, and the HPGSB-2 being operated fully premixed.

- The Modified Valera model was selected for NO_x predictions analysis with different fuel-oxidant chemical kinetics mechanisms. The predictions from C1-C4 mechanisms (Aramco 1.3, SanDiego and USII) at 1.1 bara were close to the experimental values across all fuel blends, while GRI-MECH 3.0 mechanism predictions were better matched to the experimental data by the gas analyser at 2.2 and 3.3 bara. The predictions from higher hydrocarbon mechanisms (Ranzi-Paolo and NUIGalway) deviated from the experimental trend at high pressure conditions. This could be due to the smaller presence of higher hydrocarbons in the fuel blends considered for this analysis.

8.3. Qualitative NO Formation Analysis in Unconfined and Confined Flames

- Rich CH_4 flames ($\Phi = 1.28 - 1.4$) were investigated with the unconfined 25 mm Bunsen burner. The flame stabilised closer to the burner exit nozzle with decreasing Φ , as flame speed increased with decreasing premixed gas speed, resulting in higher NO PLIF intensity. Maximum CH and CH_2 mole fraction obtained from numerical calculations were shown to have decreasing trend with increasing Φ and was attributed to decreasing AFT and increasing activation energy requirements. Thus, low NO formation from prompt pathway at high Φ was suggested.

- NO formations in lean to rich conditions ($\Phi = 0.87 - 1.1$) in unconfined HPGSB-2 was investigated thereafter. With increasing Φ , the flame reaction zone retracted axially upstream and radially outward, as the CRZ enveloped more volume due to increased relative fuel content in the flow. NO formation from the PLIF images peaked at $\Phi = 0.94$, whereas NO measured by the gas analyser had the highest value at stoichiometry. This difference in NO formation was attributed to the NO formed downstream from prompt and N_2O pathways. Asymmetry in NO-PLIF images was attributed to the laser energy and fluorescence signal attenuation by UV absorption from CO_2 and H_2O produced in the flame.
- The effect of H_2 addition in the confined HPGSB-2 was analysed and compared with 100% CH_4 flames for same equivalence ratios (0.55 - 0.65). The burning intensity of CH_4 was enhanced by H_2 addition, resulting higher volumetric heat releases from numerical calculations. This increased heat release resulted in higher thermal NO formations visible from NO-PLIF images. This augmented burning intensity also resulted in the flame being stabilised closer to the burner exit nozzle and radial stretch in the heat release, visible from OH^* chemiluminescence images and consequently, elongated NO formation.
- The effect of confinement on flame shape and NO formation was also investigated. Flame was attached to the confinement due to Coanda effect, transforming CRZ from rectangular to circular shape. This change in CRZ shape can also be attributed to the decreasing confinement ratio. Heat release intensity increased in the confined flames due to reduced heat loss compared to the unconfined flames, as was visible in the OH^* chemiluminescence images, resulting in elongated and higher NO formation.

- NO-LIF images were also taken utilising widely used 226.03 nm excitation wavelength to validate the choice of 285.16 nm excitation wavelength. Images from both excitation wavelengths followed the same trends as the flame moved from lean to rich, thus the choice of 285.16 nm excitation wavelength was validated, incorporation with the extensive analysis given on the reasoning behind choosing 285.16 nm NO excitation wavelength in Chapter 3.3.

8.4. NO Calibration towards Quantitative Analysis

- Two calibration curves were obtained at 285.16 and 226.03 nm excitation wavelengths by doping known concentrations of NO in lean CH₄/air flame using 15 mm Bunsen burner. These calibration data would quantify qualitative NO distribution in the flames investigated here.
- Both offline and online points were considered to obtain the calibration curve at 226.03 nm excitation wavelength, as 226.03 nm suffers from O₂ interference.
- Only online signals were taken into account for 285.16 nm excitation wavelength as O₂ interference is negligible at this wavelength.

Recommendations for further Work

Several recommendations for further investigation can be made as a result of the work presented in this thesis:

Further improvements could be made to strengthen the modelling of the modified Valera model. Volume and residence time for CRZ, ERZ and flame zone could be imported from PIV measurements at each point, which will make the model more robust. The simplified model also warrants further investigations due to its low-cost characteristics. Sensitivity analysis for the NO_x formation pathways will make the chemical kinetics mechanisms investigated herein more vigorous.

The work presented here highlighted the importance of the knowledge for in-flame temperature distribution for various corrections in NO-PLIF measurements. Various in-flame temperature measurements techniques like Rayleigh/Raman scattering, two-photon NO-LIF temperature measurement could be investigated along with CFD modelling. By utilising the NO calibration curves discussed in the final chapter of the thesis, incorporation with in-flame temperature distribution, providing opportunities to quantify qualitative NO distribution results presented here.

The NO-PLIF setup commissioned in this study will facilitate further performance of tests at higher values of initial ambient pressure to understand NO formation on industrial scale swirl burner at elevated pressure conditions, such as those experienced in GT combustors. This would also allow for further development and validation of chemical reaction mechanisms.

To address the issues with the increasing variation of natural gas composition at the supply line and its impact on NO_x formation in GTs, further tests could be carried out with the fuel blends (E-mix# 2-4) proposed in this study. Finally, NO_x formations in alternative fuels such as ammonia/hydrogen/methane combinations could be investigated with OH, NH₃ and NH₂ LIF in the future with the current experimental set-up.

References

- [1] T. N. Veziroğlu and S. Şahi'n, '21st Century's energy: Hydrogen energy system', *Energy Convers. Manag.*, vol. 49, no. 7, pp. 1820-1831, Jul. 2008, doi: 10.1016/j.enconman.2007.08.015.
- [2] J. Noailly and R. Smeets, 'Directing technical change from fossil-fuel to renewable energy innovation: An application using firm-level patent data', *J. Environ. Econ. Manag.*, vol. 72, pp. 15-37, Jul. 2015, doi: 10.1016/j.jeem.2015.03.004.
- [3] A. H. Lefebvre, D. R. Ballal, and D. R. Ballal, *Gas Turbine Combustion: Alternative Fuels and Emissions, Third Edition*. CRC Press, 2010. ISBN 1420086049.
- [4] 'Historical CO2 Records from the Law Dome DE08, DE08-2, and DSS Ice Cores'. <https://cdiac.ess-dive.lbl.gov/trends/co2/lawdome.html> (accessed Jan. 23, 2020).
- [5] I. Feygina, J. T. Jost, and R. E. Goldsmith, 'System Justification, the Denial of Global Warming, and the Possibility of "System-Sanctioned Change"', *Pers. Soc. Psychol. Bull.*, vol. 36, no. 3, pp. 326-338, Mar. 2010, doi: 10.1177/0146167209351435.
- [6] J. P. Holdren and P. R. Ehrlich, 'Human Population and the Global Environment: Population growth, rising per capita material consumption, and disruptive technologies have made civilization a global ecological force', *Am. Sci.*, vol. 62, no. 3, pp. 282-292, 1974.
- [7] K. Grove, 'Biopolitics and Adaptation: Governing Socio-Ecological Contingency Through Climate Change and Disaster Studies', *Geogr. Compass*, vol. 8, no. 3, pp. 198-210, 2014, doi: 10.1111/gec3.12118.
- [8] J. P. Evans, 'Resilience, ecology and adaptation in the experimental city', *Trans. Inst. Br. Geogr.*, vol. 36, no. 2, pp. 223-237, Apr. 2011, doi: 10.1111/j.1475-5661.2010.00420.x.
- [9] B. K. Marshall, J. S. Picou, and C. A. Bevc, 'Ecological Disaster as Contextual Transformation: Environmental Values in a Renewable Resource Community', *Environ. Behav.*, vol. 37, no. 5, pp. 706-728, Sep. 2005, doi: 10.1177/0013916505275310.
- [10] D. H. Meadows, J. Randers, and D. L. Meadows, *The Limits to Growth: The 30-year Update*, 1 edition. London: Routledge, 2004. ISBN 1603581553.
- [11] U. N. D. Programme and U. N. D. Programme, *Fighting climate change: Human solidarity in a divided world*. Springer, 2007.
- [12] A. Rechkemmer, A. O'Connor, A. Rai, J. L. Decker Sparks, P. Mudliar, and J. M. Shultz, 'A complex social-ecological disaster: Environmentally induced forced migration', *Disaster Health*, vol. 3, no. 4, pp. 112-120, 2016.
- [13] B. Pease, 'Masculinism, climate change and 'man-made' disasters', *Men Masculinities Disaster*, pp. 21-33, 2016.
- [14] W. N. Adger, T. P. Hughes, C. Folke, S. R. Carpenter, and J. Rockström, 'Social-ecological resilience to coastal disasters', *Science*, vol. 309, no. 5737, pp. 1036-1039, 2005.
- [15] B. Gas, 'Where does UK gas come from?' <https://www.britishgas.co.uk/the-source/our-world-of->

- energy/energys-grand-journey/where-does-uk-gas-come-from (accessed Jan. 23, 2020).
- [16] G. B. D. of E. and C. Change, S. O. (Great Britain), and I. MacLeay, *Digest of United Kingdom energy statistics 2010*. The Stationery Office, 2010.
- [17] K. Harris, 'Digest of United Kingdom energy statistics 2016', 2016.
- [18] M. Qadrdan, M. Chaudry, N. Jenkins, P. Baruah, and N. Eyre, 'Impact of transition to a low carbon power system on the GB gas network', *Appl. Energy*, vol. 151, pp. 1-12, Aug. 2015, doi: 10.1016/j.apenergy.2015.04.056.
- [19] 'Digest of UK Energy Statistics (DUKES) 2019', *GOV.UK*. <https://www.gov.uk/government/statistics/digest-of-uk-energy-statistics-dukes-2019> (accessed Jan. 23, 2020).
- [20] P. E. Dodds and S. Demoullin, 'Conversion of the UK gas system to transport hydrogen', *Int. J. Hydrog. Energy*, vol. 38, no. 18, pp. 7189-7200, Jun. 2013, doi: 10.1016/j.ijhydene.2013.03.070.
- [21] D. J. Abbott and J. P. Bowers, 'THE IMPACT OF NATURAL GAS COMPOSITION VARIATIONS ON THE OPERATION OF GAS TURBINES FOR POWER GENERATION', 2014.
- [22] A. E. E. Khalil and A. K. Gupta, 'Fuel flexible distributed combustion for efficient and clean gas turbine engines', *Appl. Energy*, vol. 109, pp. 267-274, Sep. 2013, doi: 10.1016/j.apenergy.2013.04.052.
- [23] S. Taamallah, K. Vogiatzaki, F. M. Alzahrani, E. M. A. Mokheimer, M. A. Habib, and A. F. Ghoniem, 'Fuel flexibility, stability and emissions in premixed hydrogen-rich gas turbine combustion: Technology, fundamentals, and numerical simulations', *Appl. Energy*, vol. 154, pp. 1020-1047, Sep. 2015, doi: 10.1016/j.apenergy.2015.04.044.
- [24] P. Jansohn, *Modern Gas Turbine Systems: High Efficiency, Low Emission, Fuel Flexible Power Generation*. Elsevier, 2013.
- [25] T. Lieuwen, V. McDonell, E. Petersen, and D. Santavicca, 'Fuel Flexibility Influences on Premixed Combustor Blowout, Flashback, Autoignition, and Stability', *J. Eng. Gas Turbines Power*, vol. 130, no. 1, Jan. 2008, doi: 10.1115/1.2771243.
- [26] P. Nag, M. LaGrow, J. Wu, K. Abou-Jaoude, and J. Engel, 'LNG fuel flexibility in Siemens' land-based gas turbine operations', in *Electric Power Conference*, 2007, pp. 1-3.
- [27] A. Zucca, A. Forte, N. Giannini, C. Romano, and R. Modi, 'Enlarging fuel flexibility for Frame 5 DLN: combustor operability and emissions with high C2+ content', 2015.
- [28] 'Gas Ten Year Statement (GTYS) 2019 | National Grid Gas'. <https://www.nationalgridgas.com/insight-and-innovation/gas-ten-year-statement-gtys> (accessed Jan. 23, 2020).
- [29] 'UK becomes first major economy to pass net zero emissions law', *GOV.UK*. <https://www.gov.uk/government/news/uk-becomes-first-major-economy-to-pass-net-zero-emissions-law> (accessed Jan. 23, 2020).
- [30] 'Green GB'. <https://greengb.campaign.gov.uk/> (accessed Jan. 23, 2020).
- [31] G. Gahleitner, 'Hydrogen from renewable electricity: An international review of power-to-gas pilot plants for stationary

- applications', *Int. J. Hydrog. Energy*, vol. 38, no. 5, pp. 2039-2061, 2013.
- [32] S. B. Walker, U. Mukherjee, M. Fowler, and A. Elkamel, 'Benchmarking and selection of Power-to-Gas utilizing electrolytic hydrogen as an energy storage alternative', *Int. J. Hydrog. Energy*, vol. 41, no. 19, pp. 7717-7731, May 2016, doi: 10.1016/j.ijhydene.2015.09.008.
- [33] M. Qadrdan, M. Abeysekera, M. Chaudry, J. Wu, and N. Jenkins, 'Role of power-to-gas in an integrated gas and electricity system in Great Britain', *Int. J. Hydrog. Energy*, vol. 40, no. 17, pp. 5763-5775, May 2015, doi: 10.1016/j.ijhydene.2015.03.004.
- [34] G. Reiter and J. Lindorfer, 'Global warming potential of hydrogen and methane production from renewable electricity via power-to-gas technology', *Int. J. Life Cycle Assess.*, vol. 20, no. 4, pp. 477-489, Apr. 2015, doi: 10.1007/s11367-015-0848-0.
- [35] 'ETN Hydrogen Gas Turbines report 2020', *ETN*, Jan. 10, 2020. <https://etn.global/news-and-events/news/hydrogen-gas-turbines-report/> (accessed Jan. 23, 2020).
- [36] 'BP Energy Outlook 2019 | Energy economics | Home', *BP global*. <https://www.bp.com/en/global/corporate/energy-economics/energy-outlook.html> (accessed Jan. 23, 2020).
- [37] 'Atmospheric Emissions Calculations'. Department of Energy & Climate Change, Oil & Gas UK, Nov. 11, 2008, [Online]. Available: https://assets.publishing.service.gov.uk/government/uploads/system/uploads/attachment_data/file/136461/atmos-calcs.pdf.
- [38] T. C. Lieuwen and V. Yang, *Gas Turbine Emissions*. Cambridge University Press, 2013.
- [39] Y. Zeldovich, *Oxidation of Nitrogen in Combustion*. Publishing House of the Acad of Sciences of USSR, 1947.
- [40] Y. Levy, V. Sherbaum, and P. Arfi, 'Basic thermodynamics of FLOXCOM, the low-NO_x gas turbines adiabatic combustor', *Appl. Therm. Eng.*, vol. 24, no. 11, pp. 1593-1605, Aug. 2004, doi: 10.1016/j.applthermaleng.2003.11.022.
- [41] W. H. J. Graus and E. Worrell, 'Effects of SO₂ and NO_x control on energy-efficiency power generation', *Energy Policy*, vol. 35, no. 7, pp. 3898-3908, Jul. 2007, doi: 10.1016/j.enpol.2007.01.011.
- [42] O. US EPA, 'Basic Information - RACT/BACT/LAER Clearinghouse'. <https://www3.epa.gov/ttn/catc1/rblc/htm/welcome.html> (accessed Jan. 23, 2020).
- [43] A. Forte, A. Asti, S. Bei, M. Betti, M. D'Ercole, M. Paci, G. Tonno, and J. F. Stewart, 'A Gas Turbine Innovative System for Managing Fuel With Different and Variable-Over-Time Wobbe Indexes', in *ASME Turbo Expo 2008: Power for Land, Sea, and Air*, 2008, pp. 877-885.
- [44] D. J. Abbott, J. Maunand, M. Deneve, and R. Bastiaans, 'The Impact of Natural Gas Quality on Gas Turbine Performance (Position Paper)'. European Turbine Network, Feb. 2009.
- [45] D. Pugh, J. Runyon, P. Bowen, A. Giles, A. Valera-Medina, R. Marsh, B. Gokepte and S. Hewlett, 'An investigation of ammonia primary flame combustor concepts for emissions reduction with OH*, NH₂* and NH* chemiluminescence at elevated conditions', *Proc. Combust. Inst.*, 2020.

- [46] E. C. Okafor, K. Kunkuma, A. Somarathne, R. Ratthanan, A. Hayakawa, T. Kudo, O. Kurata, N. Iki, T. Tsujimura, H. Furutani and H. Kobayashi, 'Control of NO_x and other emissions in micro gas turbine combustors fuelled with mixtures of methane and ammonia', *Combust. Flame*, vol. 211, pp. 406-416, 2020.
- [47] A. Valera-Medina, R. Marsh, J. Runyon, D. Pugh, P. Beasley, T. Hughes and P. Bowen, 'Ammonia-methane combustion in tangential swirl burners for gas turbine power generation', *Appl. Energy*, vol. 185, pp. 1362-1371, Jan. 2017, doi: 10.1016/j.apenergy.2016.02.073.
- [48] 'The first laser'. https://www.press.uchicago.edu/Misc/Chicago/284158_townes.html (accessed Jan. 23, 2020).
- [49] 'Applied Combustion Diagnostics', CRC Press. <https://www.crcpress.com/Applied-Combustion-Diagnostics/KoHse-HoingHaus/p/book/9781560329381> (accessed Jan. 23, 2020).
- [50] A. C. Eckbreth, *Laser diagnostics for combustion temperature and species*. Amsterdam, The Netherlands: Gordon and Breach Publishers, 1996.
- [51] M. V. Heitor and A. L. N. Moreira, 'Thermocouples and sample probes for combustion studies', *Prog. Energy Combust. Sci.*, vol. 19, no. 3, pp. 259-278, 1993.
- [52] E. author, 'FLEX-E-PLANT'. <https://gow.epsrc.ukri.org/NGBOViewGrant.aspx?GrantRef=EP/K021095/1> (accessed Feb. 17, 2020).
- [53] D. Price, R. Birnbaum, R. Batiuk, M. McCullough, and R. Smith, 'Nitrogen oxides: Impacts on public health and the environment', Environmental Protection Agency, Washington, DC (United States). Office of ..., 1997.
- [54] R. J. Blaszczyk, 'Nitrogen Oxides (NO_x): Why and How They Are Controlled; EPA-456/F-99-006R', 1999.
- [55] C. T. Bowman, 'Gas-phase reaction mechanisms for nitrogen oxide formation and removal in combustion', in *Pollutants from Combustion*, Springer, 2000, pp. 123-144.
- [56] C. T. Bowman, 'Control of combustion-generated nitrogen oxide emissions: technology driven by regulation', in *Symposium (International) on Combustion*, 1992, vol. 24, pp. 859-878.
- [57] I. Glassman, R. A. Yetter, and N. G. Glumac, *Combustion*, 5 edition. Waltham, MA: Academic Press, 2014. ISBN 0124115551
- [58] J. Warnatz, U. Maas, and R. W. Dibble, *Combustion: Physical and Chemical Fundamentals, Modeling and Simulation, Experiments, Pollutant Formation*, 4th ed. Berlin Heidelberg: Springer-Verlag, 2006.
- [59] Kenneth K. Kuo, *Principles of Combustion*, 2nd Edition. John Wiley & Sons Inc, 2005. ISBN 9780471046899.
- [60] F. Biagioli and F. Güthe, 'Effect of pressure and fuel-air unmixedness on NO_x emissions from industrial gas turbine burners', *Combust. Flame*, vol. 151, no. 1-2, pp. 274-288, 2007.
- [61] D. L. Baulch, C. T. Bowman, C. J. Cobos, R. A. Cox, T. Just, J. A. Kerr, M. J. Pilling, D. Stocker, J. Troe, W. Tsang, R. W. Walker, J. Warnatz, 'Evaluated kinetic data for combustion modeling:

- supplement II', *J. Phys. Chem. Ref. Data*, vol. 34, no. 3, pp. 757-1397, 2005.
- [62] P. Versailles, G. M. Watson, A. Durocher, G. Bourque, and J. M. Bergthorson, 'Thermochemical Mechanism Optimization for Accurate Predictions of CH Concentrations in Premixed Flames of C1-C3 Alkane Fuels', *J. Eng. Gas Turbines Power*, vol. 140, no. 6, 2018.
- [63] C. P. Fenimore, 'Studies of fuel-nitrogen species in rich flame gases', in *Symposium (International) on Combustion*, 1979, vol. 17, pp. 661-670.
- [64] C. P. Fenimore, 'Formation of nitric oxide in premixed hydrocarbon flames', in *Symposium (International) on Combustion*, 1971, vol. 13, pp. 373-380.
- [65] J. A. Miller and C. T. Bowman, 'Mechanism and modeling of nitrogen chemistry in combustion', *Prog. Energy Combust. Sci.*, vol. 15, no. 4, pp. 287-338, 1989.
- [66] J. Blauwens, B. Smets, and J. Peters, 'Mechanism of 'Prompt' NO formation in hydrogen flames, 16th Symp.(Int'l.) on Combustion', *Combust. Inst.*, 1977.
- [67] J. A. Miller, M. J. Pilling, and J. Troe, 'Unravelling combustion mechanisms through a quantitative understanding of elementary reactions', *Proc. Combust. Inst.*, vol. 30, no. 1, pp. 43-88, 2005.
- [68] S. C. Hill and L. D. Smoot, 'Modeling of nitrogen oxides formation and destruction in combustion systems', *Prog. Energy Combust. Sci.*, vol. 26, no. 4-6, pp. 417-458, 2000.
- [69] A. N. Hayhurst and I. M. Vince, 'The origin and nature of "prompt" nitric oxide in flames', *Combust. Flame*, vol. 50, pp. 41-57, 1983.
- [70] L. V. Moskaleva and M. C. Lin, 'The spin-conserved reaction $\text{CH} + \text{N}_2 \rightarrow \text{H} + \text{NCN}$: A major pathway to prompt NO studied by quantum/statistical theory calculations and kinetic modeling of rate constant', *Proc. Combust. Inst.*, vol. 28, no. 2, pp. 2393-2401, 2000.
- [71] P. Dagaut, P. Glarborg, and M. U. Alzueta, 'The oxidation of hydrogen cyanide and related chemistry', *Prog. Energy Combust. Sci.*, vol. 34, no. 1, pp. 1-46, 2008.
- [72] P. Glarborg, M. U. Alzueta, K. Dam-Johansen, and J. A. Miller, 'Kinetic modeling of hydrocarbon/nitric oxide interactions in a flow reactor', *Combust. Flame*, vol. 115, no. 1-2, pp. 1-27, 1998.
- [73] R. S. Zhu and M. C. Lin, 'Ab initio study on the oxidation of NCN by O (3P): Prediction of the total rate constant and product branching ratios', *J. Phys. Chem. A*, vol. 111, no. 29, pp. 6766-6771, 2007.
- [74] L. B. Harding, S. J. Klippenstein, and J. A. Miller, 'Kinetics of $\text{CH} + \text{N}_2$ revisited with multireference methods', *J. Phys. Chem. A*, vol. 112, no. 3, pp. 522-532, 2008.
- [75] G. P. Smith, 'Evidence of NCN as a flame intermediate for prompt NO', *Chem. Phys. Lett.*, vol. 367, no. 5-6, pp. 541-548, 2003.
- [76] L. Pillier, P. Desgroux, B. Lefort, L. Gasnot, J. F. Pauwels, and I. Da Costa, 'NO prediction in natural gas flames using GDF-Kin® 3.0 mechanism NCN and HCN contribution to prompt-NO formation', *Fuel*, vol. 85, no. 7-8, pp. 896-909, 2006.
- [77] V. Vasudevan, R. K. Hanson, C. T. Bowman, D. M. Golden, and D. F. Davidson, 'Shock tube study of the reaction of CH with N_2 :

- overall rate and branching ratio', *J. Phys. Chem. A*, vol. 111, no. 46, pp. 11818-11830, 2007.
- [78] C. Morley, 'The formation and destruction of hydrogen cyanide from atmospheric and fuel nitrogen in rich atmospheric-pressure flames', *Combust. Flame*, vol. 27, pp. 189-204, 1976.
- [79] D. Stapf and W. Leuckel, 'Flow reactor studies and testing of comprehensive mechanisms for NO_x reburning', in *Symposium (International) on Combustion*, 1996, vol. 26, pp. 2083-2090.
- [80] T. Etzkorn, S. Muris, J. Wolfrum, C. Dembny, H. Bockhorn, P.F. Nelson, A. Attia-Shahin, and J. Warnatz, 'Destruction and formation of NO in low pressure stoichiometric CH₄/O₂ flames', in *Symposium (International) on Combustion*, 1992, vol. 24, pp. 925-932.
- [81] P. Dagaut, F. Lecomte, S. Chevailler, and M. Cathonnet, 'Experimental and detailed kinetic modeling of nitric oxide reduction by a natural gas blend in simulated reburning conditions', *Combust. Sci. Technol.*, vol. 139, no. 1, pp. 329-363, 1998.
- [82] L. Prada and J. A. Miller, 'Reburning using several hydrocarbon fuels: a kinetic modeling study', *Combust. Sci. Technol.*, vol. 132, no. 1-6, pp. 225-250, 1998.
- [83] K. G. Unfried, G. P. Glass, and R. F. Curl, 'Infrared flash kinetic spectroscopy of the ketyenyl radical', *Chem. Phys. Lett.*, vol. 177, no. 1, pp. 33-38, 1991.
- [84] J. A. Miller, M. C. Branch, W. J. Mclean, D. W. Chandler, M. D. Smooke, and R. J. Kee, 'The conversion of HCN to NO and N₂ in H₂- O₂- HCN- Ar flames at low pressure', in *Symposium (International) on Combustion*, 1985, vol. 20, pp. 673-684.
- [85] R. W. Coutant, E. L. Merryman, and A. Levy, 'Formation of NO₂ in range-top burners', *Environ. Int.*, vol. 8, no. 1-6, pp. 185-192, 1982.
- [86] C. P. Fenimore, 'The ratio NO₂NO in fuel-lean flames', *Combust. Flame*, vol. 25, pp. 85-90, 1975.
- [87] G. M. Johnson and M. Y. Smith, 'Emissions of nitrogen dioxide from a large gas-turbine power station', *Combust. Sci. Technol.*, vol. 19, no. 1-2, pp. 67-70, 1978.
- [88] S. M. Correa, 'A review of NO_x formation under gas-turbine combustion conditions', *Combust. Sci. Technol.*, vol. 87, no. 1-6, pp. 329-362, 1993.
- [89] J. A. Miller, M. Branch, and R. J. Kee, 'A chemical kinetic model for the selective reduction of nitric oxide by ammonia', *Combust. Flame*, vol. 43, pp. 81-98, 1981.
- [90] J. A. Miller and P. Glarborg, 'Modelling the formation of N₂O and NO₂ in the thermal De-NO_x process', in *Gas phase chemical reaction systems*, Springer, 1996, pp. 318-333.
- [91] P. Glarborg, K. Dam-Johansen, and J. A. Miller, 'The reaction of ammonia with nitrogen dioxide in a flow reactor: Implications for the NH₂+ NO₂ reaction', *Int. J. Chem. Kinet.*, vol. 27, no. 12, pp. 1207-1220, 1995.
- [92] C. C. Schmidt and C. T. Bowman, 'Flow reactor study of the effect of pressure on the thermal de-NO_x process', *Combust. Flame*, vol. 127, no. 1-2, pp. 1958-1970, 2001.

- [93] J. A. Miller, 'Theory and modeling in combustion chemistry', Sandia National Labs., Albuquerque, NM (United States), 1996.
- [94] J. W. Bozzelli and A. M. Dean, 'O+ NNH: A possible new route for NO_x formation in flames', *Int. J. Chem. Kinet.*, vol. 27, no. 11, pp. 1097-1109, 1995.
- [95] J. E. Harrington, G. P. Smith, P. A. Berg, A. R. Noble, J. B. Jeffries, and D. R. Crosley, 'Evidence for a new NO production mechanism in flames', in *Symposium (international) on combustion*, 1996, vol. 26, pp. 2133-2138.
- [96] S. J. Klippenstein, L. B. Harding, P. Glarborg, and J. A. Miller, 'The role of NNH in NO formation and control', *Combust. Flame*, vol. 158, no. 4, pp. 774-789, 2011.
- [97] R. Günther, 'Flames - Their Structure, Radiation and Temperature. Von A. G. Gaydon und H. G. Wolfhard. Chapman and Hall Ltd., London 1979 4. Aulf., XIII, 449 S., zahlr. Abb. u. Tab., Ln., £ 18.00', *Chem. Ing. Tech.*, vol. 51, no. 7, pp. 765-765, 1979, doi: 10.1002/cite.330510724.
- [98] H. P. Broida and A. G. Gaydon, 'The mechanism of formation of OH, CH and HCO in flame spectra, using deuterium as tracer', *Proc. R. Soc. Lond. Ser. Math. Phys. Sci.*, vol. 218, no. 1132, pp. 60-69, 1953.
- [99] C. S. Panoutsos, Y. Hardalupas, and A. Taylor, 'Numerical evaluation of equivalence ratio measurement using OH* and CH* chemiluminescence in premixed and non-premixed methane-air flames', *Combust. Flame*, vol. 156, no. 2, pp. 273-291, 2009.
- [100] V. Nori and J. Seitzman, 'Evaluation of chemiluminescence as a combustion diagnostic under varying operating conditions', in *46th AIAA Aerospace Sciences Meeting and Exhibit*, 2008, p. 953.
- [101] A. Lantz, R. Collin, M. Aldén, A. Lindholm, J. Larfeldt, and D. Lörstäd, 'Investigation of hydrogen enriched natural gas flames in a SGT-700/800 burner using OH PLIF and chemiluminescence imaging', *J. Eng. Gas Turbines Power*, vol. 137, no. 3, 2015.
- [102] D. Guyot, F. Guethe, B. Schuermans, A. Lacarelle, and C. O. Paschereit, 'CH*/OH* chemiluminescence response of an atmospheric premixed flame under varying operating conditions', in *ASME Turbo Expo 2010: Power for Land, Sea, and Air*, 2010, pp. 933-944.
- [103] F. Guethe, D. Guyot, G. Singla, N. Noiray, and B. Schuermans, 'Chemiluminescence as diagnostic tool in the development of gas turbines', *Appl. Phys. B*, vol. 107, no. 3, pp. 619-636, 2012.
- [104] M. Lauer and T. Sattelmayer, 'Heat release calculation in a turbulent swirl flame from laser and chemiluminescence measurements', in *14th International Symposium on Applications of Laser Techniques to Fluid Mechanics*, 2008, pp. 7-10.
- [105] L. C. Haber, U. Vandsburger, W. R. Saunders, and V. K. Khanna, 'An experimental examination of the relationship between chemiluminescent light emissions and heat-release rate under non-adiabatic conditions', VIRGINIA POLYTECHNIC INST AND STATE UNIV BLACKSBURG DEPT OF MECHANICAL ..., 2001.
- [106] P. Kutne, I. Boxx, M. Stöhr, and W. Meier, 'Experimental analysis of the combustion behaviour of low calorific syngas mixtures in a

- gas turbine model combustor', in *Proceedings of the 3rd European Combustion Meeting*, 2007, pp. 11-13.
- [107] G. Cabot, D. Vauchelles, B. Taupin, and A. Boukhalfa, 'Experimental study of lean premixed turbulent combustion in a scale gas turbine chamber', *Exp. Therm. Fluid Sci.*, vol. 28, no. 7, pp. 683-690, 2004.
- [108] K. T. Walsh, 'Experimental and Computational Study fo CH, CH*, and OH* in an Axisymmetric Laminar Diffusion Flame', 1998.
- [109] J. W. Daily, 'Laser induced fluorescence spectroscopy in flames', *Prog. Energy Combust. Sci.*, vol. 23, no. 2, pp. 133-199, Jan. 1997, doi: 10.1016/S0360-1285(97)00008-7.
- [110] D. R. CROSLEY, 'Laser Probes for Combustion Chemistry', *Am. Chem. Soc. Symp. Ser.*, vol. 134, p. 271, 1980.
- [111] K. Kohse-Höinghaus, 'Laser techniques for the quantitative detection of reactive intermediates in combustion systems', *Prog. Energy Combust. Sci.*, vol. 20, no. 3, pp. 203-279, Jan. 1994, doi: 10.1016/0360-1285(94)90015-9.
- [112] W. Demtröder, *Laser Spectroscopy: Vol. 1: Basic Principles*, 4th ed. Berlin Heidelberg: Springer-Verlag, 2008.
- [113] C. N. Banwell, E. M. McCash, and H. K. Choudhury, 'Fundamentals of Molecular Spectroscopy, 5th ed.', p. 2.
- [114] W. P. Partridge and N. M. Laurendeau, 'Formulation of a dimensionless overlap fraction to account for spectrally distributed interactions in fluorescence studies', *Appl. Opt.*, vol. 34, no. 15, pp. 2645-2647, May 1995, doi: 10.1364/AO.34.002645.
- [115] Geo. Glockler, 'Molecular Spectra and Molecule Structure. I. Diatomic Molecules. By Gerhard Herzberg.', *J. Phys. Chem.*, vol. 44, no. 5, pp. 682-682, May 1940, doi: 10.1021/j150401a019.
- [116] A. Yariv, 'Quantum Electronics, 3rd Edition | Wiley, 2007. ISBN 0471971766.
- [117] W. G. Vincenti and C. H. Kruger, *Introduction to physical gas dynamics*. New York: Wiley, 1965.
- [118] M. D. Di Rosa and R. K. Hanson, 'Collision broadening and shift of NO γ (0, 0) absorption lines by O₂ and H₂O at high temperatures', *J. Quant. Spectrosc. Radiat. Transf.*, vol. 52, no. 5, pp. 515-529, 1994.
- [119] M. D. Dirosa and R. K. Hanson, 'Collision-Broadening and -Shift of NO γ (0,0) Absorption Lines by H₂O, O₂, and NO at 295K', *J. Mol. Spectrosc.*, vol. 164, no. 1, pp. 97-117, Mar. 1994, doi: 10.1006/jmsp.1994.1059.
- [120] A. Y. Chang, M. D. DiRosa, and R. K. Hanson, 'Temperature dependence of collision broadening and shift in the NO A \leftarrow X (0, 0) band in the presence of argon and nitrogen', *J. Quant. Spectrosc. Radiat. Transf.*, vol. 47, no. 5, pp. 375-390, May 1992, doi: 10.1016/0022-4073(92)90039-7.
- [121] A. O. Vyrodov, J. Heinze, and U. E. Meier, 'Collisional broadening of spectral lines in the A-X (0-0) system of NO by N₂, Ar, and He at elevated pressures measured by laser-induced fluorescence', *J. Quant. Spectrosc. Radiat. Transf.*, vol. 53, no. 3, pp. 277-287, Mar. 1995, doi: 10.1016/0022-4073(95)90060-8.

- [122] B. H. Armstrong, 'Spectrum line profiles: The Voigt function', *J. Quant. Spectrosc. Radiat. Transf.*, vol. 7, no. 1, pp. 61-88, Jan. 1967, doi: 10.1016/0022-4073(67)90057-X.
- [123] J. W. Daily, 'Saturation effects in laser induced fluorescence spectroscopy', *Appl. Opt.*, vol. 16, no. 3, pp. 568-571, Mar. 1977, doi: 10.1364/AO.16.000568.
- [124] J. W. Daily, W. G. Bessler, C. Schulz, V. Sick, and T. B. Settersten, 'Nonstationary Collisional Dynamics in Determining Nitric Oxide Laser-Induced Fluorescence Spectra', *AIAA J.*, vol. 43, no. 3, pp. 458-464, 2005, doi: 10.2514/1.8783.
- [125] T. B. ettersten, 'Population Cycling in Laser-Induced Fluorescence Detection of NO', *4th Jt. Meet. US Sect. Combust. Inst. 2005 Combust. Inst. Phila.*, 2005.
- [126] N. M. Laurendeau, 'Temperature measurements by light-scattering methods', 1988.
- [127] J. Luque and D. R. Crosley, 'LIFbase: Database and Spectral Simulation', 1999.
- [128] M. D. D. ROSA, K. G. KLAVUHN, and R. K. HANSON, 'LIF Spectroscopy of NO and O2 in High-Pressure Flames', *Combust. Sci. Technol.*, vol. 118, no. 4-6, pp. 257-283, Oct. 1996, doi: 10.1080/00102209608951981.
- [129] W. G. Bessler, C. Schulz, V. Sick, and J. W. Daily, 'A versatile modeling tool for nitric oxide LIF spectra', in *Proceedings of the Third Joint Meeting of the US sections of the Combustion Institute*, 2003, vol. 3.
- [130] W. G. Bessler, T. Lee, C. Schulz, J. B. Jeffries, and R. K. Hanson, 'Strategies for quantitative NO-concentration and temperature measurements by NO LIF in high pressure flames', in *3rd Joint Meeting of the US Sections of the Combustion Institute*, 2003, p. D33.
- [131] W. H. Press, S. A. Teukolsky, B. P. Flannery, and W. T. Vetterling, *Numerical Recipes in FORTRAN 77: Volume 1, Volume 1 of Fortran Numerical Recipes: The Art of Scientific Computing*. Cambridge University Press, 1992.
- [132] D. R. Grieser and R. H. Barnes, 'Nitric oxide measurements in a flame by laser fluorescence', *Appl. Opt.*, vol. 19, no. 5, pp. 741-743, 1980.
- [133] R. L. McKenzie and K. P. Gross, 'Two-photon excitation of nitric oxide fluorescence as a temperature indicator in unsteady gasdynamic processes', *Appl. Opt.*, vol. 20, no. 12, pp. 2153-2165, 1981.
- [134] G. Kychakoff, R. D. Howe, and R. K. Hanson, 'Quantitative flow visualization technique for measurements in combustion gases', *Appl. Opt.*, vol. 23, no. 5, pp. 704-712, 1984.
- [135] J. M. Seitzman, G. Kychakoff, and R. K. Hanson, 'Instantaneous temperature field measurements using planar laser-induced fluorescence', *Opt. Lett.*, vol. 10, no. 9, pp. 439-441, 1985.
- [136] P. PAUL and R. HANSON, 'Applications of planar laser-induced fluorescence imaging diagnostics to reacting flows', in *26th Joint Propulsion Conference*, 1990, p. 1848.
- [137] J. E. Dec and R. E. Canaan, 'PLIF imaging of NO formation in a DI diesel engine', *SAE Trans.*, pp. 176-204, 1998.

- [138] P. Jamette, V. Ricordeau, B. Deschamps, and P. Desgroux, 'Laser induced fluorescence detection of NO in the combustion chamber of an optical GDI engine with AX (0, 1) excitation', SAE technical paper, 2001.
- [139] W. G. Bessler, C. Schulz, T. Lee, J. B. Jeffries, and R. K. Hanson, 'Strategies for laser-induced fluorescence detection of nitric oxide in high-pressure flames. III. Comparison of A-X excitation schemes', *Appl. Opt.*, vol. 42, no. 24, pp. 4922-4936, 2003.
- [140] W. G. Bessler, C. Schulz, T. Lee, J. B. Jeffries, and R. K. Hanson, 'Strategies for laser-induced fluorescence detection of nitric oxide in high-pressure flames. II. A-X (0, 1) excitation', *Appl. Opt.*, vol. 42, no. 12, pp. 2031-2042, 2003.
- [141] P. Andresen, G. Meijer, H. Schluter, H. Voges, A. Koch, W. Hentschel, W. Oppermann, and E. Rothe, 'Fluorescence imaging inside an internal combustion engine using tunable excimer lasers', *Appl. Opt.*, vol. 29, no. 16, pp. 2392-2404, 1990.
- [142] T. Lee, J. B. Jeffries, and R. K. Hanson, 'Experimental evaluation of strategies for quantitative laser-induced-fluorescence imaging of nitric oxide in high-pressure flames (1-60 bar)', *Proc. Combust. Inst.*, vol. 31, no. 1, pp. 757-764, 2007.
- [143] B. K. McMillin, J. L. Palmer, and R. K. Hanson, 'Temporally resolved, two-line fluorescence imaging of NO temperature in a transverse jet in a supersonic cross flow', *Appl. Opt.*, vol. 32, no. 36, pp. 7532-7545, 1993.
- [144] J. L. Palmer and R. K. Hanson, 'Shock tunnel flow visualization using planar laser-induced fluorescence imaging of NO and OH', *Shock Waves*, vol. 4, no. 6, pp. 313-323, 1995.
- [145] D. D. Thomsen, F. F. Kuligowski, and N. M. Laurendeau, 'Modeling of NO formation in premixed, high-pressure methane flames', *Combust. Flame*, vol. 119, no. 3, pp. 307-318, 1999.
- [146] M. C. Drake, J. W. Ratcliffe, R. J. Blint, C. D. Carter, and N. M. Laurendeau, 'Measurements and modeling of flamefront NO formation and superequilibrium radical concentrations in laminar high-pressure premixed flames', in *Symposium (International) on Combustion*, 1991, vol. 23, pp. 387-395.
- [147] J. R. Reisel and N. M. Laurendeau, 'Laser-induced fluorescence measurements and modeling of nitric oxide formation in high-pressure flames', *Combust. Sci. Technol.*, vol. 98, no. 1-3, pp. 137-160, 1994.
- [148] J. R. Reisel, C. D. Carter, and N. M. Laurendeau, 'Laser-induced fluorescence measurements of nitric oxide in laminar C [sub 2] H [sub 6]/O [sub 2]/N [sub 2] flames at high pressure', *Combust. Flame United States*, vol. 92, no. 4, 1993.
- [149] J. R. Reisel and N. M. Laurendeau, 'Quantitative LIF measurements of nitric oxide in laminar high-temperature flames', *Energy Fuels*, vol. 8, no. 5, pp. 1115-1122, 1994.
- [150] J. R. Reisel and N. M. Laurendeau, 'Quantitative LIF measurements and modeling of nitric oxide in high-pressure C₂H₄/O₂/N₂ flames', *Combust. Flame*, vol. 101, no. 1-2, pp. 141-152, 1995.
- [151] C. S. Cooper and N. M. Laurendeau, 'Parametric study of NO production via quantitative laser-induced fluorescence in high-

- pressure, swirl-stabilized spray flames', *Proc. Combust. Inst.*, vol. 28, no. 1, pp. 287-293, 2000.
- [152] C. S. Cooper and N. M. Laurendeau, 'Comparison of laser-induced and planar laser-induced fluorescence measurements of nitric oxide in a high-pressure, swirl-stabilized, spray flame', *Appl. Phys. B*, vol. 70, no. 6, pp. 903-910, 2000.
- [153] C. S. Cooper and N. M. Laurendeau, 'Quantitative measurements of nitric oxide in high-pressure (2-5 atm), swirl-stabilized spray flames via laser-induced fluorescence', *Combust. Flame*, vol. 123, no. 1-2, pp. 175-188, 2000.
- [154] D. Charlston-Goch, B. L. Chadwick, R. J. S. Morrison, A. Campisi, D. D. Thomsen, and N. M. Laurendeau, 'Laser-Induced fluorescence measurements and modeling of nitric oxide in premixed flames of CO+ H₂+ CH₄ and air at high pressures: I. Nitrogen fixation', *Combust. Flame*, vol. 125, no. 1-2, pp. 729-743, 2001.
- [155] D. D. Thomsen, F. F. Kuligowski, and N. M. Laurendeau, 'Background corrections for laser-induced-fluorescence measurements of nitric oxide in lean, high-pressure, premixed methane flames', *Appl. Opt.*, vol. 36, no. 15, pp. 3244-3252, 1997.
- [156] J. R. Reisel, W. P. Partridge Jr, and N. M. Laurendeau, 'Transportability of a laser-induced fluorescence calibration for no at high pressure', *J. Quant. Spectrosc. Radiat. Transf.*, vol. 53, no. 2, pp. 165-178, 1995.
- [157] A. O. Vyrodov, J. Heinze, M. Dillmann, U. E. Meier, and W. Stricker, 'Laser-induced fluorescence thermometry and concentration measurements on NOA-X (0-0) transitions in the exhaust gas of high pressure CH₄/air flames', *Appl. Phys. B*, vol. 61, no. 5, pp. 409-414, 1995.
- [158] C. Schulz, J. B. Jeffries, D. F. Davidson, J. D. Koch, J. Wolfrum, and R. K. Hanson, 'Impact of UV absorption by CO₂ and H₂O on no lif in high-pressure combustion applications', *Proc. Combust. Inst.*, vol. 29, no. 2, pp. 2735-2742, 2002.
- [159] C. Schulz, J. D. Koch, D. F. Davidson, J. B. Jeffries, and R. K. Hanson, 'Ultraviolet absorption spectra of shock-heated carbon dioxide and water between 900 and 3050 K', *Chem. Phys. Lett.*, vol. 355, no. 1-2, pp. 82-88, 2002.
- [160] S. Böckle, J. Kazenwadel, T. Kunzelmann, and C. Schulz, 'Laser-diagnostic multi-species imaging in strongly swirling natural gas flames', *Appl. Phys. B*, vol. 71, no. 5, pp. 741-746, 2000.
- [161] A. B. Sahu and R. V. Ravikrishna, 'Quantitative LIF measurements and kinetics assessment of NO formation in H₂/CO syngas-air counterflow diffusion flames', *Combust. Flame*, vol. 173, pp. 208-228, 2016.
- [162] G. M. Watson, P. Versailles, and J. M. Bergthorson, 'NO formation in rich premixed flames of C₁-C₄ alkanes and alcohols', *Proc. Combust. Inst.*, vol. 36, no. 1, pp. 627-635, 2017.
- [163] G. M. Watson, J. D. Munzar, and J. M. Bergthorson, 'Diagnostics and modeling of stagnation flames for the validation of thermochemical combustion models for NO_x predictions', *Energy Fuels*, vol. 27, no. 11, pp. 7031-7043, 2013.

- [164] G. M. Watson, P. Versailles, and J. M. Bergthorson, 'NO formation in premixed flames of C1-C3 alkanes and alcohols', *Combust. Flame*, vol. 169, pp. 242-260, 2016.
- [165] B. Alataş, J. A. Pinson, T. A. Litzinger, and D. A. Santavicca, 'A study of NO and soot evolution in a DI diesel engine via planar imaging', *SAE Trans.*, pp. 1463-1473, 1993.
- [166] A. Bräumer, V. Sick, J. Wolfrum, V. Drewes, M. Zahn, and R. Maly, 'Quantitative two-dimensional measurements of nitric oxide and temperature distributions in a transparent square piston SI engine', SAE Technical Paper, 1995.
- [167] B. E. Battles and R. K. Hanson, 'Laser-induced fluorescence measurements of NO and OH mole fraction in fuel-lean, high-pressure (1-10 atm) methane flames: fluorescence modeling and experimental validation', *J. Quant. Spectrosc. Radiat. Transf.*, vol. 54, no. 3, pp. 521-537, 1995.
- [168] H. Nakagawa, H. Endo, Y. Deguchi, M. Noda, H. Oikawa, and T. Shimada, 'NO measurement in Diesel spray flame using laser induced fluorescence', *SAE Trans.*, pp. 1349-1358, 1997.
- [169] P. A. Berg, G. P. Smith, J. B. Jeffries, and D. R. Crosley, 'Nitric oxide formation and reburn in low-pressure methane flames', in *Symposium (International) on Combustion*, 1998, vol. 27, pp. 1377-1384.
- [170] L. Pillier, C. Moreau, X. Mercier, J. F. Pauwels, and P. Desgroux, 'Quantification of stable minor species in confined flames by cavity ring-down spectroscopy: application to NO', *Appl. Phys. B*, vol. 74, no. 4-5, pp. 427-434, 2002.
- [171] M.-S. Chou, A. M. Dean, and D. Stern, 'Laser induced fluorescence and absorption measurements of NO in NH₃/O₂ and CH₄/air flames', *J. Chem. Phys.*, vol. 78, no. 10, pp. 5962-5970, 1983.
- [172] C. Schulz, B. Yip, V. Sick, and J. Wolfrum, 'A laser-induced fluorescence scheme for imaging nitric oxide in engines', *Chem. Phys. Lett.*, vol. 242, no. 3, pp. 259-264, 1995.
- [173] F. Hildenbrand, C. Schulz, V. Sick, H. Jander, and H. G. Wagner, 'Applicability of KrF excimer laser induced fluorescence in sooting high-pressure flames', *VDI BERICHTE*, vol. 1492, pp. 269-274, 1999.
- [174] C. Schulz, V. Sick, J. Wolfrum, V. Drewes, and R. Maly, 'Quantitative 2D single-shot imaging of NO concentrations and temperatures in a transparent SI engine', in *Symposium (International) on Combustion*, 1996, vol. 26, pp. 2597-2604.
- [175] F. Hildenbrand, C. Schulz, V. Sick, G. Josefsson, I. Magnusson, O. Andersson, and M. Alden, 'Laser Spectroscopic Investigation of Flow Fields and NO-Formation in a Realistic SI Engine', *SAE Trans.*, vol. 107, pp. 205-214, 1998.
- [176] F. Hildenbrand, C. Schulz, M. Hartmann, F. Puchner, and G. Wawrschin, 'In-Cylinder NO-LIF Imaging in a Realistic GDI Engine Using KrF Excimer Laser Excitation', *SAE Trans.*, vol. 108, pp. 1683-1693, 1999.
- [177] W. G. Bessler, C. Schulz, M. Hartmann, and M. Schenk, 'Quantitative In-Cylinder NO-LIF Imaging in a Direct-Injected Gasoline Engine with Exhaust Gas Recirculation', *SAE Trans.*, vol. 110, pp. 1837-1846, 2001.

- [178] F. Hildenbrand, C. Schulz, J. Wolfrum, F. Keller, and E. Wagner, 'Laser diagnostic analysis of no formation in a direct injection diesel engine with pump-line-nozzle and common rail injection systems', *Proc. Combust. Inst.*, vol. 28, no. 1, pp. 1137-1143, Jan. 2000, doi: 10.1016/S0082-0784(00)80323-9.
- [179] F. Hildenbrand, C. Schulz, F. Keller, G. König, and E. Wagner, 'Quantitative Laser Diagnostic Studies of the NO Distribution in a DI Diesel Engine with PLN and CR Injection Systems', *SAE Trans.*, vol. 110, pp. 1608-1618, 2001.
- [180] M. Knapp, A. Luczak, H. Schlüter, V. Beushausen, W. Hentschel, and P. Andresen, 'Crank-angle-resolved laser-induced fluorescence imaging of NO in a spark-ignition engine at 248 nm and correlations to flame front propagation and pressure release', *Appl. Opt.*, vol. 35, no. 21, pp. 4009-4017, Jul. 1996, doi: 10.1364/AO.35.004009.
- [181] V. Beushausen, M. Knapp, A. Luczak, S. Eisenberg, and P. Andersen, 'Application of laser-induced fluorescence and spontaneous Raman scattering to technically applied combustion systems: four cylinder spark ignition engine and oil burning furnace'. OSA Technical Digest Series (Optical Society of America, Washington DC), 1996.
- [182] M. Knapp, A. Luczak, V. Beushausen, W. Hentschel, P. Manz, and P. Andresen, 'Quantitative In-Cylinder NO LIF Measurements with a KrF Excimer Laser Applied to a Mass-Production SI Engine Fueled with Isooctane and Regular Gasoline', *SAE Trans.*, vol. 106, pp. 1128-1139, 1997.
- [183] K. Akihama, T. Fujikawa, and Y. Hattori, 'Laser-Induced Fluorescence Imaging of NO in a Port-Fuel-Injected Stratified-Charge SI Engine - Correlations Between NO Formation Region and Stratified Fuel Distribution', *SAE Trans.*, vol. 107, pp. 711-721, 1998.
- [184] W. G. Bessler, M. Hofmann, F. Zimmermann, G. Suck, J. Jakobs, S. Nicklitzsch, T. Le, J. Wolfrum, and C. Schulz, 'Quantitative in-cylinder NO-LIF imaging in a realistic gasoline engine with spray-guided direct injection', *Proc. Combust. Inst.*, vol. 30, no. 2, pp. 2667-2674, Jan. 2005, doi: 10.1016/j.proci.2004.08.123.
- [185] A. M. Wodtke, L. Huwel, H. Schluter, G. Meijer, P. Andersen, and H. Voges, 'High-sensitivity detection of NO in a flame using a tunable ArF laser', *Opt. Lett.*, vol. 13, no. 10, pp. 910-912, Oct. 1988, doi: 10.1364/OL.13.000910.
- [186] M. Versluis, M. Ebben, M. Drabbels, and J. J. ter Meulen, 'Frequency calibration in the ArF excimer laser-tuning range using laser-induced fluorescence of NO', *Appl. Opt.*, vol. 30, no. 36, pp. 5229-5234, Dec. 1991, doi: 10.1364/AO.30.005229.
- [187] M. P. Lee and R. K. Hanson, 'Calculations of O₂ absorption and fluorescence at elevated temperatures for a broadband argon-fluoride laser source at 193 nm', *J. Quant. Spectrosc. Radiat. Transf.*, vol. 36, no. 5, pp. 425-440, Nov. 1986, doi: 10.1016/0022-4073(86)90098-1.
- [188] N. Dam, W. Meerts, and J. J. ter Meulen, 'Laser Diagnostics of Nitric Oxide Inside a Two-Stroke DI Diesel Engine', in *Laser Techniques Applied to Fluid Mechanics*, Berlin, Heidelberg, 2000, pp. 473-486, doi: 10.1007/978-3-642-56963-0_31.

- [189] T. M. Brugman, G. G. M. Stoffels, N. Dam, W. L. Meerts, and J. J. ter Meulen, 'Imaging and post-processing of laser-induced fluorescence from NO in a diesel engine', *Appl. Phys. B*, vol. 64, no. 6, pp. 717-724, Jun. 1997, doi: 10.1007/s003400050239.
- [190] G. G. M. Stoffels, E. J. Boom, C. M. I. Spaanjaars, N. Dam, W. L. Meerts, J. J. Meulen, J. L. C. Duff, and D. J. Rickeard, 'In-Cylinder Measurements of NO Formation in a Diesel Engine', *SAE Trans.*, vol. 108, pp. 920-935, 1999.
- [191] T. Tanaka, M. Fujimoto, and M. Tabata, 'Planar Measurements of NO in an S.I. Engine Based on Laser Induced Fluorescence', *SAE Trans.*, vol. 106, pp. 1359-1368, 1997.
- [192] Th. M. Brugman, R. Klein-Douwel, G. Huigen, E. van Walwijk, and J. J. ter Meulen, 'Laser-induced-fluorescence imaging of NO in an n-heptane- and diesel-fuel-driven diesel engine', *Appl. Phys. B*, vol. 57, no. 6, pp. 405-410, Dec. 1993, doi: 10.1007/BF00357383.
- [193] A. Arnold, F. Dinkelacker, T. Heitzmann, P. Monkhouse, M. Schafer, V. Sick, J. Wolfrum, W. Hentschel, and K. P. Schindler, 'Di diesel engine combustion visualized by combined laser techniques', *Symp. Int. Combust.*, vol. 24, no. 1, pp. 1605-1612, Jan. 1992, doi: 10.1016/S0082-0784(06)80187-6.
- [194] C. K. Law, *Combustion Physics*. Cambridge: Cambridge University Press, 2010.
- [195] D. Bradley, P. H. Gaskell, and X. J. Gu, 'Burning velocities, Markstein lengths, and flame quenching for spherical methane-air flames: a computational study', *Combust. Flame*, vol. 104, no. 1-2, pp. 176-198, 1996.
- [196] C. J. Rallis and A. M. Garforth, 'The determination of laminar burning velocity', *Prog. Energy Combust. Sci.*, vol. 6, no. 4, pp. 303-329, 1980.
- [197] M. Metghalchi and J. C. Keck, 'Laminar burning velocity of propane-air mixtures at high temperature and pressure', *Combust. Flame*, vol. 38, pp. 143-154, 1980.
- [198] T. W. Ryan III and S. S. Lestz, 'The laminar burning velocity of isooctane, n-heptane, methanol, methane, and propane at elevated temperature and pressures in the presence of a diluent', *SAE Trans.*, pp. 652-664, 1980.
- [199] J. P. J. Van Lipzig, E. J. K. Nilsson, L. P. H. De Goey, and A. A. Konnov, 'Laminar burning velocities of n-heptane, iso-octane, ethanol and their binary and tertiary mixtures', *Fuel*, vol. 90, no. 8, pp. 2773-2781, 2011.
- [200] P. Dirrenberger, P. A. Glaude, R. Bounaceur, H. L. Gall, A. P. Cruz, A. A. Konnov, and F. Battin-Leclerc, 'Laminar burning velocity of gasolines with addition of ethanol', *Fuel*, vol. 115, pp. 162-169, 2014.
- [201] L. Sileghem, V. A. Alekseev, J. Vancoillie, K. M. Van Geem, E. J. K. Nilsson, S. Verhelst, and A. A. Konnov, 'Laminar burning velocity of gasoline and the gasoline surrogate components iso-octane, n-heptane and toluene', *Fuel*, vol. 112, pp. 355-365, 2013.
- [202] R. G. Abdel-Gayed, D. Bradley, M. Lawes, and F. K. K. Lung, 'Premixed Turbulent Burning during Ex-plosions, 21st Symp.(Int.) on Combustion', *Combust. Inst.*, 1986.

- [203] K. W. Ragland and K. M. Bryden, *Combustion Engineering*. Boca Raton: CRC Press, 2011.
- [204] R. D. Matthews, M. J. Hall, W. Dai, W. Dai, and G. C. Davis, 'Combustion modeling in SI engines with a peninsula-fractal combustion model', *SAE Trans.*, pp. 180-195, 1996.
- [205] C. Casci, Ed., *Recent Advances in the Aerospace Sciences: In Honor of Luigi Crocco on His Seventy-fifth Birthday*. Springer US, 1985.
- [206] N. Peters, 'Laminar flamelet concepts in turbulent combustion', in *Symposium (International) on Combustion*, 1988, vol. 21, no. 1, pp. 1231-1250.
- [207] T. Poinso, D. Veynante, and S. Candel, 'Diagrams of premixed turbulent combustion based on direct simulation', in *Symposium (international) on Combustion*, 1991, vol. 23, no. 1, pp. 613-619.
- [208] S. Turns, *An Introduction to Combustion: Concepts and Applications*. New York: McGraw-Hill Education, 2011.
- [209] N. Syred and J. M. Beér, 'Combustion in swirling flows: A review', *Combust. Flame*, vol. 23, no. 2, pp. 143-201, Oct. 1974, doi: 10.1016/0010-2180(74)90057-1.
- [210] N. Syred, 'A review of oscillation mechanisms and the role of the precessing vortex core (PVC) in swirl combustion systems', *Prog. Energy Combust. Sci.*, vol. 32, no. 2, pp. 93-161, 2006.
- [211] T. C. Claypole and N. Syred, *The effect of swirl burner aerodynamics on NOx formation. Symp Combust 18: 81-89*. 1981.
- [212] W. B. Jensen, 'The Origin of the Bunsen Burner', *J Chem Educ*, vol. 82, no. 4, p. 518, Apr. 2005, doi: <https://doi.org/10.1021/ed082p518>.
- [213] P. Flecken and N. Abildgaard, 'Mass flow meter operating by the Coriolis principle', US4768384A, Sep. 06, 1988.
- [214] J. K. Simonsen and H. J. Moos, 'Mass flow meter on the coriolis principle', US4680974A, Jul. 21, 1987.
- [215] 'Coriolis mass flow measuring principle', *Bronkhorst*. <https://bronkhorst.com/int/service-support/technologies/coriolis-mass-flow-measuring-principle/> (accessed Feb. 08, 2020).
- [216] Y. A. Sevcenco, M. G. Mojarrad, R. Marsh, S. Morris, P. J. Bowen, and N. Syred, 'Integrating Hypersonics into a Combustion Test Facility with 3D Viewing Capability', in *20th AIAA International Space Planes and Hypersonic Systems and Technologies Conference*, American Institute of Aeronautics and Astronautics.
- [217] J. Lewis, R. Marsh, A. Valera-Medina, S. Morris, and H. Baej, 'The Use of CO₂ to Improve Stability and Emissions of an IGCC Combustor', presented at the ASME Turbo Expo 2014: Turbine Technical Conference and Exposition, Sep. 2014, doi: 10.1115/GT2014-25446.
- [218] N. Syred, S. M. Morris, P. J. Bowen, A. Valera-Medina, and R. Marsh, 'Preliminary Results from a High Pressure Optical gas Turbine Combustor Model with 3D Viewing Capability', in *53rd AIAA Aerospace Sciences Meeting*, American Institute of Aeronautics and Astronautics.
- [219] A. Bagdanavicius, P. J. Bowen, D. Bradley, M. Lawes, and M. S. Mansour, 'Stretch rate effects and flame surface densities in premixed turbulent combustion up to 1.25 MPa', *Combust. Flame*,

- vol. 162, no. 11, pp. 4158-4166, Nov. 2015, doi: 10.1016/j.combustflame.2015.08.007.
- [220] A. Bagdanavicius, P. Bowen, N. Syred, and A. Crayford, 'Turbulent Flame Structure of Methane-Hydrogen Mixtures at Elevated Temperature and Pressure', *Combust. Sci. Technol.*, vol. 185, no. 2, pp. 350-361, Feb. 2013, doi: 10.1080/00102202.2012.718005.
- [221] J. Runyon, 'Gas turbine fuel flexibility: pressurized swirl flame stability, thermoacoustics, and emissions', phd, Cardiff University, 2017.
- [222] M. Buffi, A. Valera-Medina, J. Runyon, D. Pugh, A. Giles, R. Marsh, and D. Chiaramonti, 'Evaluation of combustion behavior of renewable jet fuel in a combustor rig: influence of HEFA and its blends on flame stability and emissions compared to aviation kerosene', presented at the 24th European Biomass Conference, Amsterdam, The Netherlands, 2016, Accessed: Feb. 08, 2020. [Online]. Available: <http://orca.cf.ac.uk/90686/>.
- [223] J. Runyon, R. Marsh, A. Valera-Medina, A. Giles, S. Morris, D. Pugh, Y. Sevcenco, and P. Bowen, 'Methane-Oxygen Flame Stability in a Generic Premixed Gas Turbine Swirl Combustor at Varying Thermal Power and Pressure', presented at the ASME Turbo Expo 2015: Turbine Technical Conference and Exposition, Aug. 2015, doi: 10.1115/GT2015-43588.
- [224] J. Runyon, R. Marsh, Y. A. Sevcenco, D. Pugh, and S. Morris, 'Development and commissioning of a chemiluminescence imaging system for an optically-accessible high-pressure generic swirl burner', in *EMC 2015: 7th European Combustion Meeting, March 30 - April 2, 2015, Budapest, Hungary*, Budapest, Hungary, 2015, pp. 1-6, Accessed: Feb. 08, 2020. [Online]. Available: <http://www.ecm2015.hu/papers/P3-29.pdf>.
- [225] R. Marsh, J. Runyon, A. Giles, S. Morris, D. Pugh, A. Valera-Medina, and P. Bowen, 'Premixed methane oxycombustion in nitrogen and carbon dioxide atmospheres: measurement of operating limits, flame location and emissions. Proceedings of the Combustion Institute', *Proc. Combust. Inst.*, vol. 36, no. 3, pp. 3949-3958, Jan. 2017, doi: 10.1016/j.proci.2016.06.057.
- [226] H. Kurji, A. Valera-Medina, J. Runyon, A. Giles, D. Pugh, R. Marsh, N. Cerone, F. Zimbardi, and V. Valerio, 'Combustion characteristics of biodiesel saturated with pyrolysis oil for power generation in gas turbines', *Renew. Energy*, vol. 99, pp. 443-451, Dec. 2016, doi: 10.1016/j.renene.2016.07.036.
- [227] J. Runyon, R. Marsh, D. Pugh, P. Bowen, A. Giles, S. Morris, and A. Valera-Medina, 'Experimental Analysis of Confinement and Swirl Effects on Premixed CH₄-H₂ Flame Behavior in a Pressurized Generic Swirl Burner', presented at the ASME Turbo Expo 2017: Turbomachinery Technical Conference and Exposition, Aug. 2017, doi: 10.1115/GT2017-64794.
- [228] 'Quantel TDL-90 Datasheet', Feb. 08, 2020. Quantel TDL-90 Datasheet.
- [229] A. E. Siegman, *Lasers*, 1990 edition. Mill Valley, California: University Science Books, 1990. ISBN 0935702113.
- [230] O. Svelto, *Principles of Lasers*, 5th ed. edition. New York: Springer US, 2010. ISBN 0306457482.

- [231] C. C. Davis, *Lasers and Electro-optics: Fundamentals and Engineering*. Cambridge University Press, 1996.
- [232] 'Heraeus Transmission Calculator'. https://www.heraeus.com/en/hca/fused_silica_quartz_knowledge_base_1/t_calc_1/transmission_calculator_hca.html?selection=spectrosil_2000&chart=0&rangeX=120,5000&rangeY=0,100 (accessed Feb. 09, 2020).
- [233] B. Higgins, M. Q. McQuay, F. Lacas, J. C. Rolon, N. Darabiha, and S. Candel, 'Systematic measurements of OH chemiluminescence for fuel-lean, high-pressure, premixed, laminar flames', *Fuel*, vol. 80, no. 1, pp. 67-74, Jan. 2001, doi: 10.1016/S0016-2361(00)00069-7.
- [234] U. Stopper, M. Aigner, W. Meier, R. Sadanandan, M. Stöhr, and I. S. Kim, 'Flow Field and Combustion Characterization of Premixed Gas Turbine Flames by Planar Laser Techniques', *J. Eng. Gas Turbines Power*, vol. 131, no. 2, Mar. 2009, doi: 10.1115/1.2969093.
- [235] M. Lauer, M. Zellhuber, T. Sattelmayer, and C. J. Aul, 'Determination of the Heat Release Distribution in Turbulent Flames by a Model Based Correction of OH* Chemiluminescence', *J. Eng. Gas Turbines Power*, vol. 133, no. 12, Dec. 2011, doi: 10.1115/1.4004124.
- [236] R. V. Ravikrishna and N. M. Laurendeau, 'Laser-induced fluorescence measurements and modeling of nitric oxide in methane-air and ethane-air counterflow diffusion flames', *Combust. Flame*, vol. 120, no. 3, pp. 372-382, Feb. 2000, doi: 10.1016/S0010-2180(99)00101-7.
- [237] R. V. Ravikrishna and N. M. Laurendeau, 'Laser-induced fluorescence measurements and modeling of nitric oxide in counterflow partially premixed flames', *Combust. Flame*, vol. 122, no. 4, pp. 474-482, Sep. 2000, doi: 10.1016/S0010-2180(00)00136-X.
- [238] R. V. Ravikrishna, C. S. Cooper, and N. M. Laurendeau, 'Comparison of saturated and linear laser-induced fluorescence measurements of nitric oxide in counterflow diffusion flames', *Combust. Flame*, vol. 117, no. 4, pp. 810-820, Jun. 1999, doi: 10.1016/S0010-2180(98)00123-0.
- [239] R. V. RAVIKRISHNA, D. D. THOMSEN, and N. M. LAURENDEAU, 'Laser-Induced Fluorescence Measurements and Modeling of Nitric Oxide in High-Pressure Counterflow Diffusion Flames', *Combust. Sci. Technol.*, vol. 157, no. 1, pp. 243-261, Aug. 2000, doi: 10.1080/00102200008947318.
- [240] S. V. Naik and N. M. Laurendeau, 'Laser-saturated and linear laser-induced fluorescence measurements of nitric oxide in counterflow diffusion flames under non-sooting oxygen-enriched conditions', *Combust. Sci. Technol.*, vol. 174, no. 2, pp. 1-21, Feb. 2002, doi: 10.1080/714922744.
- [241] S. V. Naik and N. M. Laurendeau, 'LIF measurements and chemical kinetic analysis of methylidyne formation in high-pressure counterflow partially premixed and non-premixed flames', *Appl. Phys. B*, vol. 79, no. 7, pp. 891-905, Nov. 2004, doi: 10.1007/s00340-004-1630-3.
- [242] D. G. Pugh, P. J. Bowen, R. Marsh, A. P. Crayford, J. Runyon, S. Morris, A. Valera-Medina, and A. Giles, 'Dissociative influence of

- H₂O vapour/spray on lean blowoff and NO_x reduction for heavily carbonaceous syngas swirling flames', *Combust. Flame*, vol. 177, pp. 37-48, Mar. 2017, doi: 10.1016/j.combustflame.2016.11.010.
- [243] A. Valera Medina, S. Morris, J. Runyon, D. G. Pugh, R. Marsh, P. Beasley, and T. Hughes, 'Ammonia, methane and hydrogen for gas turbines', *Energy Procedia*, vol. 75, pp. 118-123, Aug. 2015, doi: 10.1016/j.egypro.2015.07.205.
- [244] R. Marsh, A. Giles, J. Runyon, D. Pugh, P. Bowen, S. Morris, A. Valera-Medina, T. Best, K. Finney, M. Pourkashanian, 'SELECTIVE EXHAUST GAS RECYCLING FOR CARBON CAPTURE APPLICATIONS: COMBUSTION AND OPERABILITY MEASUREMENT', The Future of Gas Turbine Technology, 8th International Gas Turbine Conference, 12-13 October 2016, Brussels, Belgium.
- [245] D. Pugh, P. Bowen, A. Crayford, R. Marsh, J. Runyon, S. Morris, and A. Giles, 'Catalytic Influence of Water Vapor on Lean Blowoff and NO_x Reduction for Pressurised Swirling Syngas Flames', presented at the ASME Turbo Expo 2017: Turbomachinery Technical Conference and Exposition, Aug. 2017, doi: 10.1115/GT2017-64609.
- [246] K. Altfeld and D. Pinchbeck, 'Admissible hydrogen concentrations in natural gas systems', *Gas Energy*, vol. 2103, no. 03, pp. 1-2, 2013.
- [247] T. Isaac, 'HyDeploy: The UK's First Hydrogen Blending Deployment Project', *Clean Energy*, vol. 3, no. 2, pp. 114-125, May 2019, doi: 10.1093/ce/zkz006.
- [248] D. Burnes and A. Camou, 'Impact of Fuel Composition on Gas Turbine Engine Performance', *J. Eng. Gas Turbines Power*, vol. 141, no. 10, Oct. 2019, doi: 10.1115/1.4044238.
- [249] R. M. Flores, V. G. McDonell, and G. S. Samuelsen, 'Impact of Ethane and Propane Variation in Natural Gas on the Performance of a Model Gas Turbine Combustor', *J. Eng. Gas Turbines Power*, vol. 125, no. 3, pp. 701-708, Jul. 2003, doi: 10.1115/1.1584480.
- [250] D. Straub, D. Ferguson, K. Casleton, and G. Richards, 'Effects of Propane/Natural Gas Blended Fuels on Gas Turbine Pollutant Emissions', p. 13.
- [251] 'Guidebook to Gas Interchangeability and Gas Quality. International Gas Union'. BP, 2011, [Online]. Available: https://www.igu.org/sites/default/files/node-page-field_file/Guidebook%20to%20Gas%20Interchangeability%20and%20Gas%20Quality%2C%20August%202011.pdf.
- [252] R. J. Kee, F. M. Rupley, J. A. Miller, M. E. Coltrin, J. F. Gircar, E. Meeks, H. K. Moffat, A. E. Lutz, G. Dixon-Lewis, C. Wang, and O. Adigun, *CHEMKIN PRO, Reaction Design, San Diego, CA*.
- [253] H. Xiao and A. Valera-Medina, 'Chemical Kinetic Mechanism Study on Premixed Combustion of Ammonia/Hydrogen Fuels for Gas Turbine Use', *J. Eng. Gas Turbines Power*, vol. 139, no. 8, Aug. 2017, doi: 10.1115/1.4035911.
- [254] E. C. Okafor, Y. Naito, S. Colson, A. Ichikawa, T. Kudo, A. Hayakawa, and H. Kobayashi, 'Experimental and numerical study of the laminar burning velocity of CH₄-NH₃-air premixed flames', *Combust. Flame*, vol. 187, pp. 185-198, 2018.

- [255] N. Bouvet, 'Experimental and Numerical Studies of the Fundamental Flame Speeds of Methane/Air and Syngas (H₂/CO)/Air Mixtures', Université d'Orléans, 2009.
- [256] 'CHEMKIN - A software package for the analysis of gas-phase chemical and plasma kinetics - Manual'. Reaction Design, 2000.
- [257] G.-N. Dixon-Lewis, 'Flame structure and flame reaction kinetics II. Transport phenomena in multicomponent systems', *Proc. R. Soc. Lond. Ser. Math. Phys. Sci.*, vol. 307, no. 1488, pp. 111-135, 1968.
- [258] S. Gordon and B. J. McBride, 'Computer Program for Calculation of Complex Chemical Equilibrium Compositions, Rocket Performance, Incident and Reflected Shocks, and Chapman-Jouguet Detonations. Interim Revision, March 1976', 1976.
- [259] R. J. Kee, J. F. Grcar, M. D. Smooke, J. A. Miller, and E. Meeks, 'PREMIX: a Fortran program for modeling steady laminar one-dimensional premixed flames', *Sandia Natl. Lab. Rep.*, no. SAND85-8249, 1985.
- [260] 'GRI-Mech 3.0'. <http://combustion.berkeley.edu/gri-mech/version30/text30.html> (accessed Feb. 11, 2020).
- [261] F. Halter, C. Chauveau, N. Djebaili-Chaumeix, and I. Gökalp, 'Characterization of the effects of pressure and hydrogen concentration on laminar burning velocities of methane-hydrogen-air mixtures', *Proc. Combust. Inst.*, vol. 30, no. 1, pp. 201-208, 2005.
- [262] J. M. Smith, *Chemical Engineering Kinetics*, 3rd edition. New York: McGraw-Hill Education, 1981. ISBN 0070857377.
- [263] 'Transport Properties Calculator'. <http://navier.engr.colostate.edu/code/code-2/index.html> (accessed Feb. 11, 2020).
- [264] C. K. Law, A. Makino, and T. F. Lu, 'On the off-stoichiometric peaking of adiabatic flame temperature', *Combust. Flame*, vol. 145, no. 4, pp. 808-819, 2006.
- [265] G. Jomaas, C. K. Law, and J. K. Bechtold, 'On transition to cellularity in expanding spherical flames', *J. Fluid Mech.*, vol. 583, pp. 1-26, Jul. 2007, doi: 10.1017/S0022112007005885.
- [266] W. K. Metcalfe, S. M. Burke, S. S. Ahmed, and H. J. Curran, 'A Hierarchical and Comparative Kinetic Modeling Study of C₁ - C₂ Hydrocarbon and Oxygenated Fuels', *Int. J. Chem. Kinet.*, vol. 45, no. 10, pp. 638-675, 2013, doi: 10.1002/kin.20802.
- [267] E. Ranzi, C. Cavallotti, A. Cuoci, A. Frassoldati, M. Pelucchi, and T. Faravelli, 'New reaction classes in the kinetic modeling of low temperature oxidation of n-alkanes', *Combust. Flame*, vol. 162, no. 5, pp. 1679-1691, May 2015, doi: 10.1016/j.combustflame.2014.11.030.
- [268] 'Chemical Mechanism: Combustion Research Group at UC San Diego'. <https://web.eng.ucsd.edu/mae/groups/combustion/mechanism.html> (accessed Feb. 11, 2020).
- [269] H. Wang, X. You, A. V. Joshi, S. G. Davis, A. Laskin, F. Egolfopoulos, C. K. Law, 'USC Mech Version II. High-temperature combustion reaction model of H₂/CO/C₁-C₄ compounds', *Combust. Kinet. Lab. Univ. South. Calif. Los Angel. CA* Accessed Aug, vol. 21, p. 2017, 2007.

- [270] P. Berta, S. K. Aggarwal, and I. K. Puri, 'An experimental and numerical investigation of n-heptane/air counterflow partially premixed flames and emission of NO_x and PAH species', *Combust. Flame*, vol. 145, no. 4, pp. 740-764, 2006.
- [271] G. Bourque, D. Healy, H. Curran, C. Zinner, D. Kalitan, J. Vries, C. Aul, E. Petersen, 'Ignition and flame speed kinetics of two natural gas blends with high levels of heavier hydrocarbons', *J. Eng. Gas Turbines Power*, vol. 132, no. 2, 2010.
- [272] N. K. Rizk, J. S. Chin, A. W. Marshall, and M. K. Razdan, 'Predictions of NO_x formation under combined droplet and partially premixed reaction of diffusion flame combustors', 1999.
- [273] G. J. Sturgess, J. Zelina, D. T. Shouse, and W. M. Roquemore, 'Emissions reduction technologies for military gas turbine engines', *J. Propuls. Power*, vol. 21, no. 2, pp. 193-217, 2005.
- [274] A. Valera-Medina, A. Giles, D. Pugh, S. Morris, M. Pohl, and A. Ortwein, 'Investigation of combustion of emulated biogas in a gas turbine test rig', *J. Therm. Sci.*, vol. 27, no. 4, pp. 331-340, 2018.
- [275] A. Alsaegh, 'Computational Fluid Dynamics Analysis for Fuel Flexible Gas Turbines (in progress)'.
- [276] S.-E. Zitouni, 'Influence of alternative fuel composition and thermal-diffusive effect on premixed flame propagation', 2020.
- [277] D. F. Swinehart, 'The beer-lambert law', *J. Chem. Educ.*, vol. 39, no. 7, p. 333, 1962.
- [278] J. Li, Z. Zhao, A. Kazakov, and F. L. Dryer, 'An updated comprehensive kinetic model of hydrogen combustion', *Int. J. Chem. Kinet.*, vol. 36, no. 10, pp. 566-575, 2004, doi: 10.1002/kin.20026.
- [279] J. Li, Z. Zhao, A. Kazakov, M. Chaos, F. L. Dryer, and J. J. Scire, 'A comprehensive kinetic mechanism for CO, CH₂O, and CH₃OH combustion', *Int. J. Chem. Kinet.*, vol. 39, no. 3, pp. 109-136, 2007, doi: 10.1002/kin.20218.
- [280] C. K. Westbrook and F. L. Dryer, 'Chemical kinetic modeling of hydrocarbon combustion', *Prog. Energy Combust. Sci.*, vol. 10, no. 1, pp. 1-57, 1984.
- [281] M. K. el_Hossaini, 'Review of the New Combustion Technologies in Modern Gas Turbines', *Prog. Gas Turbine Perform.*, Jun. 2013, doi: 10.5772/54403.
- [282] H. Shaw, 'The effects of water, pressure, and equivalence ratio on nitric oxide production in gas turbines', 1974.
- [283] A. Bhargava, D. W. Kendrick, M. B. Colket, W. A. Sowa, K. H. Casleton, and D. J. Maloney, 'Pressure effect on NO_x and CO emissions in industrial gas turbines', 2000.
- [284] D. S. Smith, R. F. Sawyer, and E. S. Starkman, 'Oxides of nitrogen from gas turbines', *J. Air Pollut. Control Assoc.*, vol. 18, no. 1, pp. 30-35, 1968.
- [285] D. Dunn-Rankin, *Lean combustion: technology and control*. Academic Press, 2011.
- [286] A. A. Quader, 'Lean combustion and the misfire limit in spark ignition engines', *SAE Trans.*, pp. 3274-3296, 1974.
- [287] M. M. Noor, A. P. Wandel, and T. Yusaf, 'MILD combustion: the future for lean and clean combustion technology', *Int. Rev. Mech. Eng.*, vol. 8, no. 1, pp. 251-257, 2014.

- [288] G. J. Germane, C. G. Wood, and C. C. Hess, 'Lean combustion in spark-ignited internal combustion engines-a review', SAE Technical Paper, 1983.
- [289] U. Mukherjee, M. Elsholkami, S. Walker, M. Fowler, A. Elkamel, and A. Hajimiragha, 'Optimal sizing of an electrolytic hydrogen production system using an existing natural gas infrastructure', *Int. J. Hydrog. Energy*, vol. 40, no. 31, pp. 9760-9772, 2015.
- [290] I. G. Wilson, A. J. Rennie, and P. J. Hall, 'Great Britain's energy vectors and transmission level energy storage', *Energy Procedia*, vol. 62, pp. 619-628, 2014.
- [291] S. Yolcular, 'Hydrogen production for energy use in European Union countries and Turkey', *Energy Sources Part A*, vol. 31, no. 15, pp. 1329-1337, 2009.
- [292] I. A. Gondal, 'Hydrogen integration in power-to-gas networks', *Int. J. Hydrog. Energy*, vol. 44, no. 3, pp. 1803-1815, 2019.
- [293] F. Ma, Y. Wang, H. Liu, Y. Li, J. Wang, and S. Ding, 'Effects of hydrogen addition on cycle-by-cycle variations in a lean burn natural gas spark-ignition engine', *Int. J. Hydrog. Energy*, vol. 33, no. 2, pp. 823-831, 2008.
- [294] E. Hu, Z. Huang, B. Liu, J. Zheng, and X. Gu, 'Experimental study on combustion characteristics of a spark-ignition engine fueled with natural gas-hydrogen blends combining with EGR', *Int. J. Hydrog. Energy*, vol. 34, no. 2, pp. 1035-1044, 2009.
- [295] F. Ma, Y. Wang, H. Liu, Y. Li, J. Wang, and S. Zhao, 'Experimental study on thermal efficiency and emission characteristics of a lean burn hydrogen enriched natural gas engine', *Int. J. Hydrog. Energy*, vol. 32, no. 18, pp. 5067-5075, 2007.
- [296] C. G. Bauer and T. W. Forest, 'Effect of hydrogen addition on the performance of methane-fueled vehicles. Part I: effect on SI engine performance', *Int. J. Hydrog. Energy*, vol. 26, no. 1, pp. 55-70, 2001.
- [297] H. Kido, M. Nakahara, J. Hashimoto, and D. Barat, 'Turbulent burning velocities of two-component fuel mixtures of methane, propane and hydrogen', *JSME Int. J. Ser. B Fluids Therm. Eng.*, vol. 45, no. 2, pp. 355-362, 2002.
- [298] Z. Han and S. Hochgreb, 'The response of stratified swirling flames to acoustic forcing: Experiments and comparison to model', *Proc. Combust. Inst.*, vol. 35, no. 3, pp. 3309-3315, 2015.
- [299] E. J. Nilsson, A. van Sprang, J. Larfeldt, and A. A. Konnov, 'The comparative and combined effects of hydrogen addition on the laminar burning velocities of methane and its blends with ethane and propane', *Fuel*, vol. 189, pp. 369-376, 2017.
- [300] E. Hu, Z. Huang, J. He, and H. Miao, 'Experimental and numerical study on laminar burning velocities and flame instabilities of hydrogen-air mixtures at elevated pressures and temperatures', *Int. J. Hydrog. Energy*, vol. 34, no. 20, pp. 8741-8755, Oct. 2009, doi: 10.1016/j.ijhydene.2009.08.044.
- [301] Y. Zhang, Z. Huang, L. Wei, J. Zhang, and C. K. Law, 'Experimental and modeling study on ignition delays of lean mixtures of methane, hydrogen, oxygen, and argon at elevated pressures', *Combust. Flame*, vol. 159, no. 3, pp. 918-931, 2012.

- [302] J. K. Bechtold and M. Matalon, 'The dependence of the Markstein length on stoichiometry', *Combust. Flame*, vol. 127, no. 1-2, pp. 1906-1913, Oct. 2001, doi: 10.1016/S0010-2180(01)00297-8.
- [303] T. Watanabe, S. Keskin, S. Nair, and D. S. Sholl, 'Computational identification of a metal organic framework for high selectivity membrane-based CO₂/CH₄ separations: Cu(hfipbb)(H₂hfipbb)0.5', *Phys. Chem. Chem. Phys.*, vol. 11, no. 48, pp. 11389-11394, 2009.
- [304] A. K. Gupta, D. G. Lilley, and N. Syred, 'Swirl flows', *Tunbridge Wells Kent Engl. Abacus Press 1984 488 P*, 1984.
- [305] N. Syred and K. R. Dahman, 'Effect of high levels of confinement upon the aerodynamics of swirl burners', *J. Energy*, vol. 2, no. 1, pp. 8-15, 1978.
- [306] N. Syred, C. Wong, V. Rodriguez-Martinez, J. Dawson, and R. Kelso, 'Characterisation of the occurrence of the precessing vortex core in partially premixed and non-premixed swirling flow', 2004.
- [307] I. Reba, 'APPLICATIONS OF THE COANDA EFFECT', *Sci. Am.*, vol. 214, no. 6, pp. 84-93, 1966.
- [308] F. J. Duarte and L. W. Hillman, *Dye Laser Principles*. Elsevier, 1990.
- [309] R. K. Hanson and S. Salimian, 'Survey of rate constants in the N/H/O system', in *Combustion chemistry*, Springer, 1984, pp. 361-421.
- [310] J. Wolfrum, 'Lasers in combustion: from basic theory to practical devices', in *Symposium (International) on Combustion*, 1998, vol. 27, pp. 1-41.
- [311] C. Schulz, V. Sick, U. E. Meier, J. Heinze, and W. Stricker, 'Quantification of NO A-X (0, 2) laser-induced fluorescence: investigation of calibration and collisional influences in high-pressure flames', *Appl. Opt.*, vol. 38, no. 9, pp. 1434-1443, 1999.
- [312] R. J. Cattolica, J. A. Cavolowsky, and T. G. Mataga, 'Laser-fluorescence measurements of nitric oxide in low-pressure H₂/O₂/NO flames', in *Symposium (International) on Combustion*, 1989, vol. 22, pp. 1165-1173.
- [313] T. B. Settersten, B. D. Patterson, and J. A. Gray, 'Temperature- and species-dependent quenching of NO A Σ^+ 2 ($v'=0$) probed by two-photon laser-induced fluorescence using a picosecond laser', *J. Chem. Phys.*, vol. 124, no. 23, p. 234308, 2006.
- [314] J. R. Reisel, C. D. Carter, N. M. Laurendeau, and M. C. Drake, 'Laser-saturated fluorescence measurements of nitric oxide in laminar, flat, C₂H₆/O₂/N₂ flames at atmospheric pressure', *Combust. Sci. Technol.*, vol. 91, no. 4-6, pp. 271-295, 1993.
- [315] J. R. Reisel, C. D. Carter, and N. M. Laurendeau, 'Measurements and modeling of OH and NO in premixed C₂H₆/O₂/N₂ flames at atmospheric pressure', *Energy Fuels*, vol. 11, no. 5, pp. 1092-1100, 1997.
- [316] W. P. Partridge Jr, J. R. Reisel, and N. M. Laurendeau, 'Laser-saturated fluorescence measurements of nitric oxide in an inverse diffusion flame', *Combust. Flame*, vol. 116, no. 1-2, pp. 282-290, 1999.
- [317] M. D. Bohon, 'Experimental and Kinetic Investigation of the Influence of OH Groups on NO_x Formation', 2016.

- [318] R. V. Ravikrishna, S. V. Naik, C. S. Cooper, and N. M. Laurendeau, 'Quantitative laser-induced fluorescence measurements and modeling of nitric oxide in high-pressure (6-15 atm) counterflow diffusion flames', *Combust. Sci. Technol.*, vol. 176, no. 1, pp. 1-21, 2004.

APPENDIX A - NO and O₂ Excitation Spectra at the 'doubling range' of Dye Laser

Appendix A.1 - NO Excitation Spectra - 1780 K

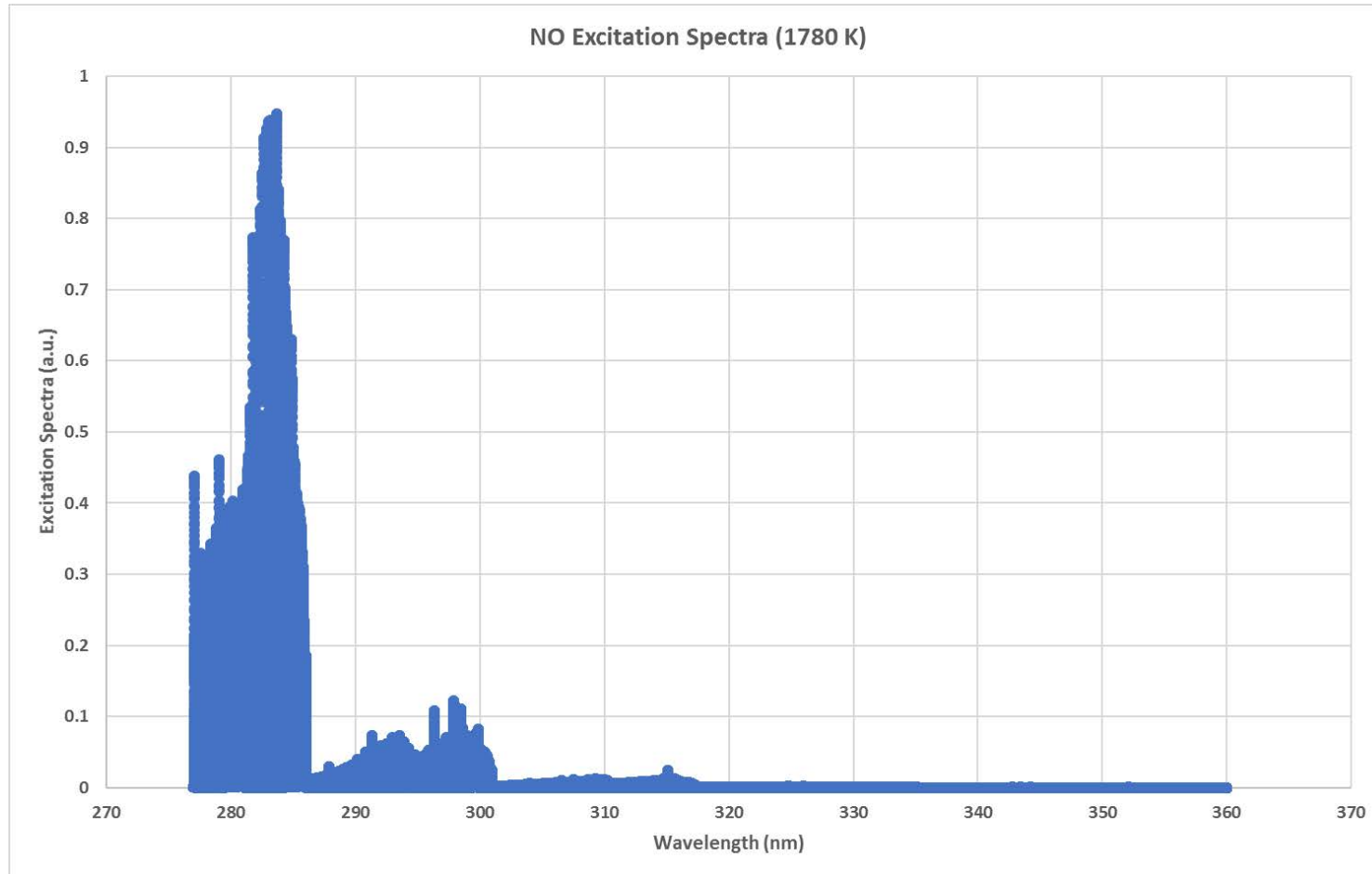
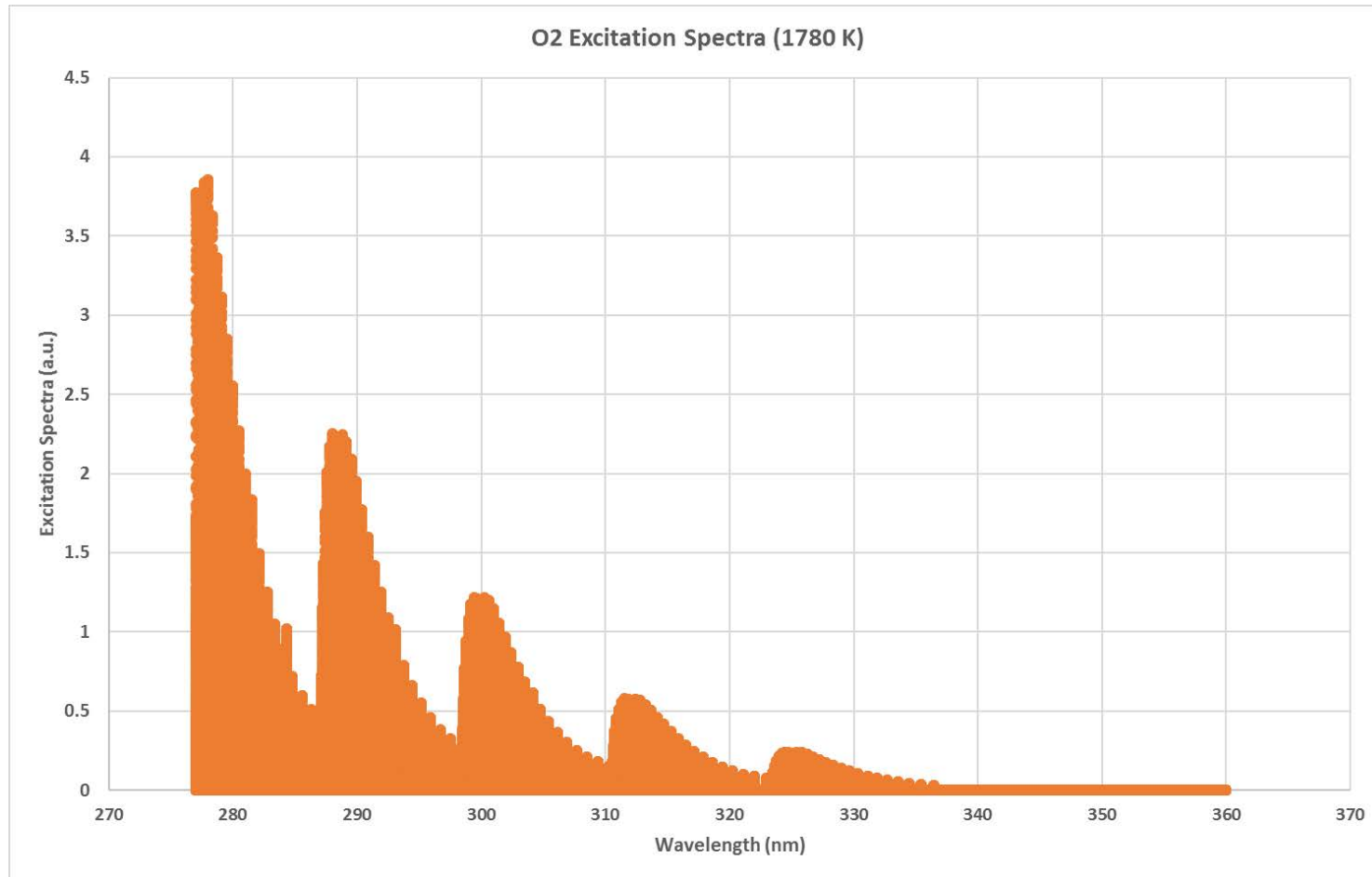


Figure A-0-1: NO Excitation Spectra at minimum AFT

Appendix A.2 - O₂ Excitation Spectra - 1780 KFigure A-0-2: O₂ Excitation Spectra at minimum AFT

Appendix A.3 - NO Excitation Spectra - 2210 K

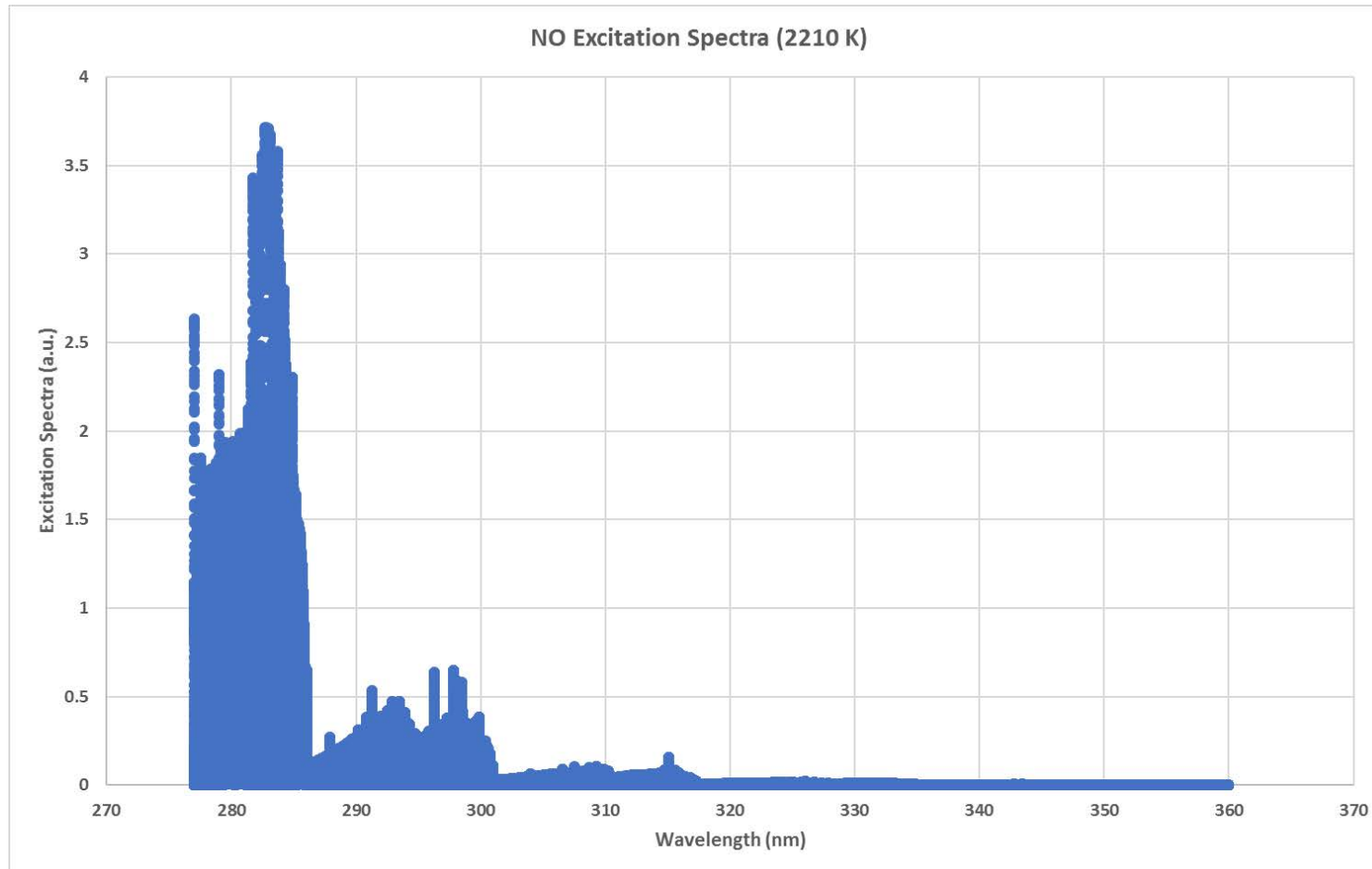
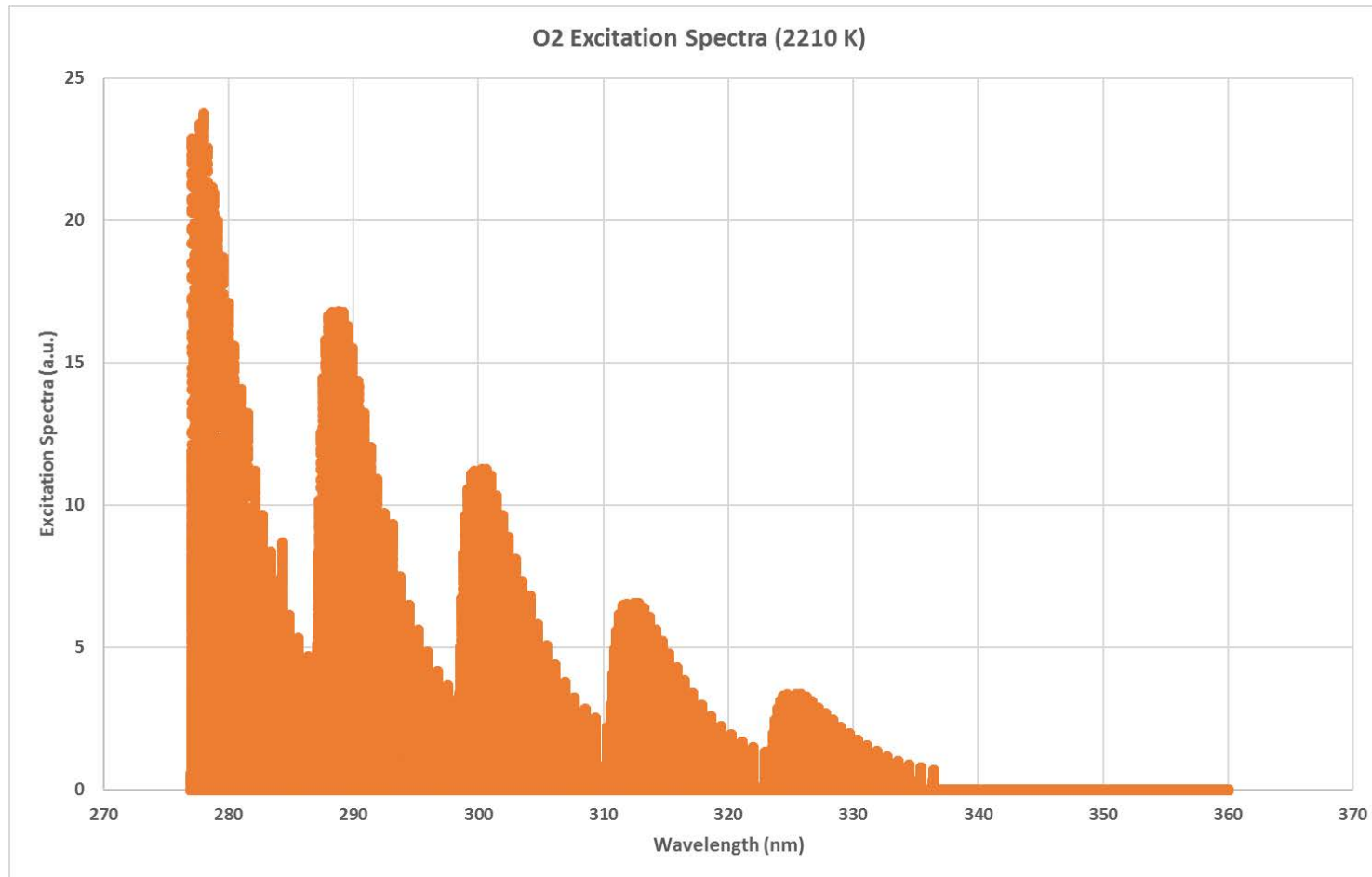
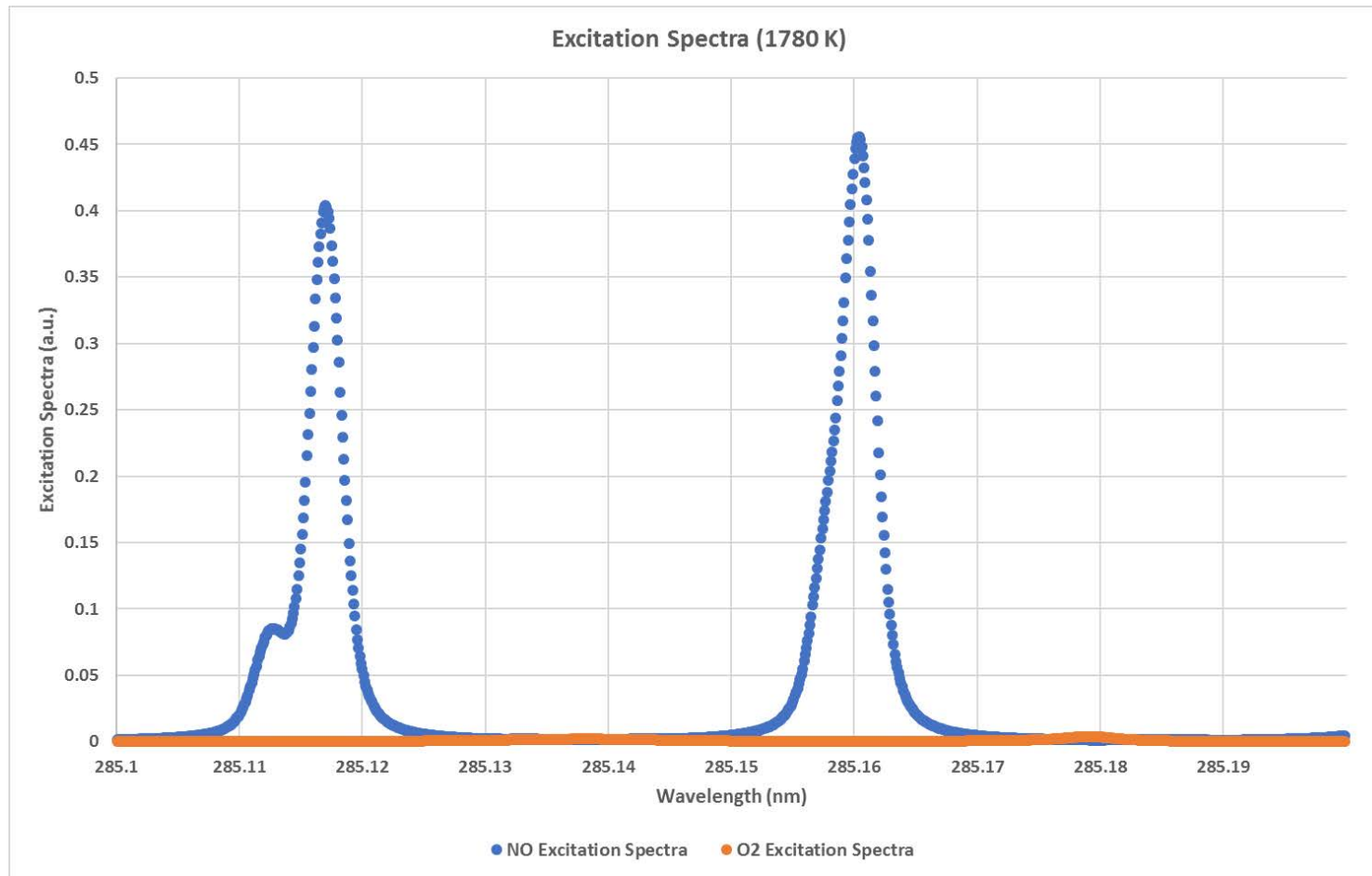
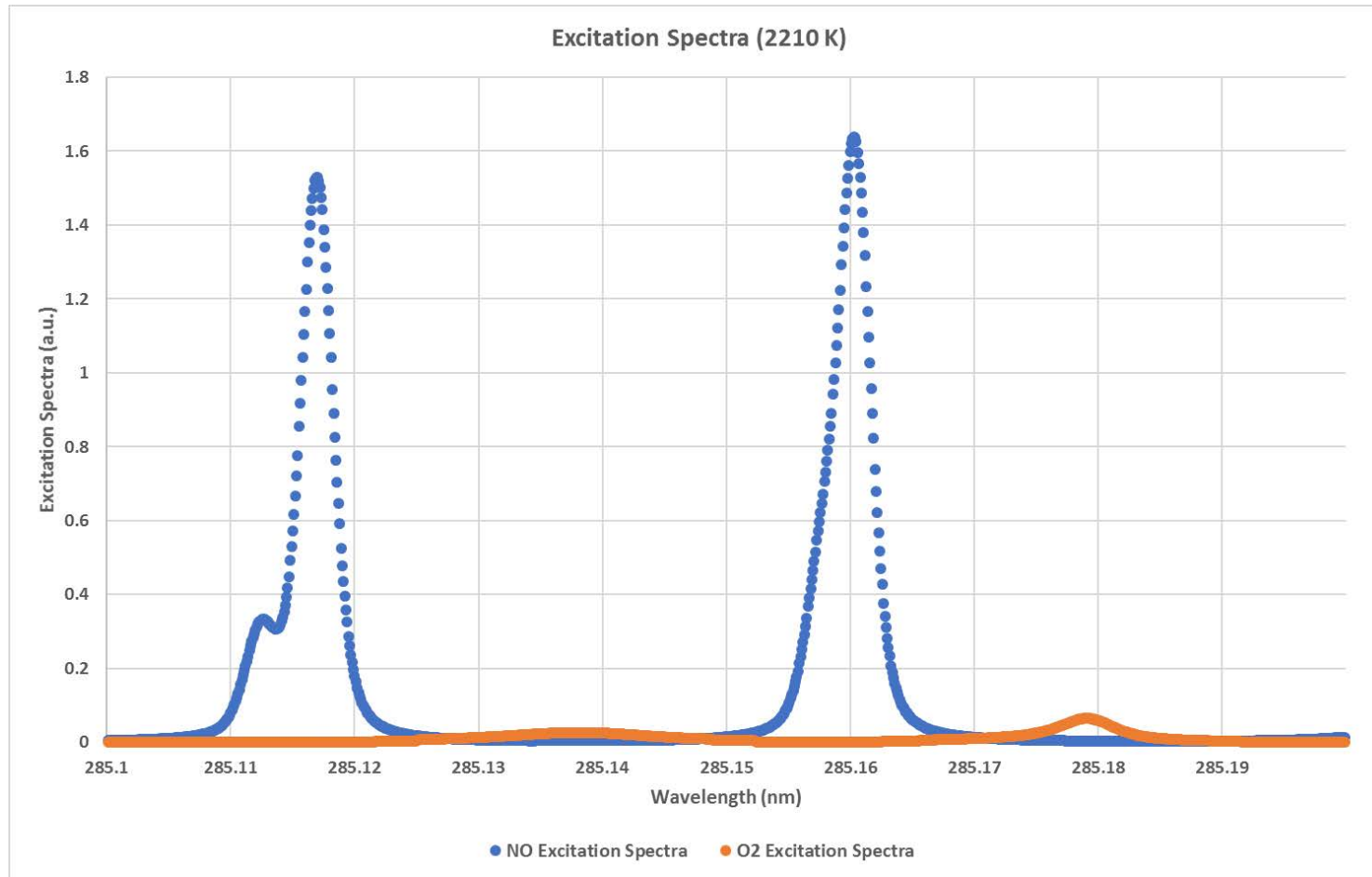


Figure A-0-3: NO Excitation Spectra at maximum AFT

Appendix A.4 - O₂ Excitation Spectra - 2210 KFigure A-0-4: O₂ Excitation Spectra at maximum AFT

Appendix A.5 - NO and O₂ Excitation Spectra (285.1 - 285.2 nm) - 1780 KFigure A-0-5: NO and O₂ excitation spectra (285.1 - 285.2 nm) at minimum AFT

Appendix A.6 - NO and O₂ Excitation Spectra (285.1 - 285.2 nm) - 2210 KFigure A-0-6: NO and O₂ excitation spectra (285.1 - 285.2 nm) at maximum AFT

APPENDIX B - MATLAB Routines

Appendix B.1 - MATLAB code for normalising shot-to-shot laser energy to the maximum laser energy

This code calls for the .CSV file where laser energy is saved and normalises the laser energies to the maximum laser energy of the test campaign for data comparison between different experimental results.

```
%Open dialogue box for user to select recorded shot-to-shot laser
energy file
[listOfFiles, folder] = uigetfile ('*.csv', 'Select acoustic
data');
fullFileName = fullfile(folder, listOfFiles);
%Reads the .CSV file from B9 to B999000
A = xlsread(fullFileName, 1, 'B9:B999000');
%Normalises the laser energy to the maximum energy
Anorm = (A/7.30e-4);
%Opens the intended directory
cd 'C:\NO PLIF\NO PLIF - Quartz Off';
%Creates a new text file
filename=sprintf('TP4_Offline.txt');
%Saves the normalised laser energies in a text file with the given
name and
%to the given directory
dlmwrite(filename,Anorm);
```

Appendix B.2 - MATLAB code for temporally averaging baseline images

the 'BL_AVG.m' function calculates temporal average of 200 instantaneous baseline images. Baseline images were taken at every experimental point without laser firing at the flame.

```
function [BL_AVGout, BL_AVGout_zero, BL_cmap, Img_IntenINSTAN,
Img_IntenAVG] = BL_AVG(NumImages)
%Open dialogue box for user to select .TIF image files
[listOfFiles, folder] = uigetfile ('*.tif', 'Select your
image','MultiSelect', 'on');
fullFileName = fullfile(folder, listOfFiles{1});
[I cmap] = imread(fullFileName);
[rows columns] = size(I);
%Initialize output matrix and vector variables
BL_AVGout_zero = zeros(rows,columns);
Img_IntenINSTAN = zeros(1, NumImages);
MaxValue = zeros(1, NumImages);
%Check number of images selected matches number input by user
if NumImages ~= length(listOfFiles)
    msg = 'Error Occured - Image Number Mismatch';
    error(msg);
else
    for j=1:length(listOfFiles)
        fullFileName = fullfile(folder, listOfFiles{j});
        I2 = imread(fullFileName);
        %Convert .TIF image to double precision
        I2_double = double(I2);
        %Filter the image with a 3x3 median filter
        I2_double_filt = medfilt2(I2_double, 'symmetric');
        %Add each image to the proceeding image
        BL_AVGout_zero = BL_AVGout_zero + I2_double_filt;
        %Calculate and store the instantaneous image integral intensity
        Img_IntenINSTAN(1,j) = sum(I2_double_filt(:));
        MaxValue(1,j) = max(max(I2_double_filt(:)));
    end
end
%Calculate the temporal average image
BL_AVGout = BL_AVGout_zero ./ NumImages;
BL_cmap = cmap;
%Calculate the integral intensity of the temporal average image
%after correction
Img_IntenAVG = sum(BL_AVGout(:));
%Opens the intended directory
cd 'F:\NO PLIF data\20 Feb 2018 - Qualitative comparison';
%Saves the time averaged file
saveastiff(BL_AVGout,'Target.tif');
%Calculate the integral intensity of the temporal average image
%after correction
Img_IntenAVG = sum(BL_AVGout(:))/(rows*columns);
%Chirping sound notification upon completion
load chirp;
sound(y,Fs);
```

Appendix B.3: MATLAB code for correcting online and offline images for baseline and normalised shot-to-shot laser energy variation

The 'Laser_Energy_Correction.m' code corrects raw online and offline images for respective baseline and normalised laser energy. The code outputs the corrected images in a directory defined by the user.

```
function LASER_ENERGY_CORRECTION(NumImages, BASELINE)
%Open dialogue box for user to select .TIF image files
[listOfFiles, folder] = uigetfile (*.tif', 'Select your image',
'MultiSelect', 'on');
fullFileName = fullfile(folder, listOfFiles{1});
[I,cmap] = imread(fullFileName);
[rows, columns] = size(I);
%Converts BASELINE image into double precision
BASELINE_double = double(BASELINE);
%Defines rows, columns and number of images in a 3D space
image3d = zeros(rows, columns, NumImages);
%Check number of images selected matches number input by user
if NumImages ~= length(listOfFiles)
    msg = 'Error Occured - Image Number Mismatch';
    error(msg);
else
%Reads raw images before converting them to double precision and
subtract
%BASELINE image
    for k = 1 : length(listOfFiles)
        fullFileName = fullfile(folder, listOfFiles{k});
        I2 = imread(fullFileName);
        I2_double = double(I2);
        I2_NO_BG = I2_double - BASELINE_double;
        image3d(:,:,k) = I2_NO_BG;
    end
%Loads the intended directory
cd 'C:\NO PLIF\NO PLIF - Quartz Off';
%loads and reads the .txt file containing normalised laser energy
load 'TP5_Online.txt';
A=textread('TP5_Online.txt');
%Loads the intended directory for saving corrected images
cd 'C:\NO PLIF\NO PLIF - Quartz Off\Corrected\TP5\Online';
%Corrects images with the corresponding normalised laser energy
and saves the corrected images
    for k=1:length(listOfFiles)
        filename=sprintf('image%d.tif',k);
        filename1=image3d(:,:,k)./A(k);
        saveastiff(filename1,filename);
    end
end
%Chirping sound notification upon completion
load chirp;
sound(y,Fs);
end
```

Appendix B.4: MATLAB code for time averaging NO-PLIF images at 285.16 nm excitation and laser sheet distribution correction

The 'PLIF_AVG_SHEETNORM.m' code temporally average the online images at first and then applies the precalculated gaussian distribution of the laser sheet. The code also calculate average and maximum intensity of PLIF image as well as pixel location of the maximum intensity.

```
function [m, Z, row, col, PLIF_AVGout, PLIF_cmap, Img_IntenAVG] =
    PLIF_AVG_SHEETNORM(NumImages)
% Open dialog box to prompt for .TIF NO PLIF file selection
[listOfFiles, folder] = uigetfile ('*.tif', 'Select your image',
    'MultiSelect', 'on');
fullFileName = fullfile(folder, listOfFiles{1});
[I cmap] = imread(fullFileName);
[rows columns] = size(I);
PLIF_AVGout_zero = zeros(rows,columns);
PLIF_Sheet_Norm_zero = zeros(rows,columns);
%Error check if the number of selected images is equal NumImages
if NumImages ~= length(listOfFiles)
    msg = 'Error Occured - Image Number Mismatch';
    error(msg);
else
    for j=1:length(listOfFiles)
        fullFileName = fullfile(folder, listOfFiles{j});
        % Read in first instantaneous NO PLIF image
        I2 = imread(fullFileName);
        % Convert the image to double precision
        I2_double = im2double(I2);
        % Apply 3x3 pixel median filter to reduce noise
        I2_double_filt = medfilt2(I2_double, 'symmetric');
        % Apply laser sheet intensity distribution correction
        for i = 1:rows
            % Find the maximum NO PLIF intensity value in each row
            [RowMax Loc] = max(I2_double_filt(i,:));
            % Convert the row pixel location to "mm" distance
            LocMM = Loc/16.9;
            LocNorm = LocMM / (LocMM / 1.0407e+5);
            GaussInten = (0.8416*exp(-((LocNorm-116900)/34270)^2)) +
                (0.5878*exp(-((LocNorm-(61230))/38900)^2));
            % Normalize the maximum NO PLIF intensity value
            IntenNorm = RowMax/GaussInten;
            PLIF_Sheet_Norm_zero(i,:) = I2_double_NoBG(i,:);
            PLIF_Sheet_Norm_zero(i, Loc) = IntenNorm;
            % Apply the Gaussian normalization in upstream direction from
            % the maximum NO PLIF intensity location
            for l = 1:187
                if (Loc - l) == 0
                    break
                end
                LocNormL = 1.0407e+5-((Loc-(Loc-l))*(7486.865/16.9));
                GaussIntenL = (0.8416*exp(-((LocNormL-116900)/34270)^2)) +
                    (0.5878*exp(-((LocNormL-(61230))/38900)^2));
                IntenNormL = I2_double_NoBG(i, (Loc-l))/GaussIntenL;
                PLIF_Sheet_Norm_zero(i, (Loc-l)) = IntenNormL;
            end
        end
    end
end
```

APPENDIX B - MATLAB Routines

```
% Apply the Gaussian normalization in the downstream % direction
from the maximum NO PLIF intensity location
for k = 1:111
if (Loc + k) > 1344
break
end
LocNormK = 1.0407e+5+(((Loc+k)-Loc)*(-9828.59/16.9));
GaussIntenK = (0.8416*exp(-((LocNormK-116900)/34270)^2)) +
(0.5878*exp(-((LocNormK-(61230))/38900)^2));
IntenNormK = I2_double_NoBG(i, (Loc+k))/GaussIntenK;
PLIF_Sheet_Norm_zero(i, (Loc+k)) = IntenNormK;
end
end
PLIF_AVGout_zero = PLIF_AVGout_zero + PLIF_Sheet_Norm_zero;
end
end
%Calculate the temporal average NO PLIF image
PLIF_AVGout = PLIF_AVGout_zero ./ NumImages;
%Output the .TIF file colormap for easier image plotting
PLIF_cmap = cmap;
%Crops the ouput image into area of interest
Z=imcrop(PLIF_AVGout, [1 1 650 1023]);
[rowz columnz] = size(Z);
%Calculates average intensity
Img_IntenAVG = sum(Z(:))/(rowz*columnz);
%Finds maximum intensity
m=max(max(Z));
%Loads the intended directory
cd 'C:\NO PLIF\NO PLIF - Quartz Off\Corrected\TP5';
%Saves the image
saveastiff(PLIF_AVGout, 'TP5_Online6.tif');
%Finds the location of maximum intensity
[row, col] = find(ismember(Z, max(Z(:))));
%Chirping sound notification upon completion
load chirp;
sound(y,1/2*Fs);
end
```

Appendix B.5: MATLAB code for time-averaging offline images

This code was used to time-average offline images prior to beam intensity correction at 225.94 nm excitation wavelength.

```
function [m, Z, row, col, LIF_AVGout, LIF_cmap, Img_IntenAVG] =
LIF_AVG_BEAMNORM_OFFLINE(NumImages)
% Open dialog box to prompt for .TIF LIF file selection
[listOfFiles, folder] = uigetfile ('*.tif', 'Select your image',
'MultiSelect', 'on');
fullFileName = fullfile(folder, listOfFiles{1});
[I cmap] = imread(fullFileName);
[rows columns] = size(I);
LIF_AVGout_zero = zeros(rows,columns);
LIF_Beam_Norm_zero = zeros(rows,columns);
%Error check if the number of selected images is equal NumImages
if NumImages ~= length(listOfFiles)
msg = 'Error Occured - Image Number Mismatch';
error(msg);
else
for j=1:length(listOfFiles)
fullFileName = fullfile(folder, listOfFiles{j});
% Read in first instantaneous LIF image
I2 = imread(fullFileName);
% Convert the image to double precision
I2_double = im2double(I2);
% Apply 3x3 pixel median filter to reduce noise
I2_double_filt = medfilt2(I2_double, 'symmetric');
% Apply laser sheet intensity distribution correction
for i = 1:rows
% Find the maximum NO LIF intensity value in each row
[RowMax Loc] = max(I2_double_filt(i,:));
% Convert the row pixel location to "mm" distance
LocMM = Loc/17.7;
LocNorm = LocMM / (LocMM / 1.215e+5);
GaussInten = 0.7802*exp(-((LocNorm-1.215e+5)/1.564e+5)^2);
% Normalize the maximum LIF intensity value
IntenNorm = RowMax/GaussInten;
LIF_Beam_Norm_zero(i,:) = I2_double_filt(i,:);
LIF_Beam_Norm_zero(i, Loc) = IntenNorm;
% Apply the Gaussian normalization in upstream direction from
% the maximum LIF intensity location
for l = 1:44
if (Loc - l) == 0
break
end
LocNormL = 1.215e+5-((Loc-(Loc-l))*(1/17.7));
GaussIntenL = 0.7802*exp(-((LocNormL-1.215e+5)/1.564e+5)^2);
IntenNormL = I2_double_filt(i, (Loc-l))/GaussIntenL;
LIF_Beam_Norm_zero(i, (Loc-l)) = IntenNormL;
end
% Apply the Gaussian normalization in the downstream % direction
from the maximum LIF intensity location
for k = 1:44
if (Loc + k) > 1024
break
end
LocNormK = 1.215e+5+(((Loc+k)-Loc)*(1/17.7));
GaussIntenK = 0.7802*exp(-((LocNormK-1.215e+5)/1.564e+5)^2);
IntenNormK = I2_double_filt((Loc+k), i)/GaussIntenK;
LIF_Beam_Norm_zero((Loc+k), i) = IntenNormK;
end
end
end
```

```
end
LIF_AVGout_zero = LIF_AVGout_zero + LIF_Beam_Norm_zero;
end
end
%Calculate the temporal average LIF image
LIF_AVGout = LIF_AVGout_zero ./ NumImages;
%Output the .TIF file colormap for easier image plotting
LIF_cmap = cmap;
%Crops the output image into area of interest
Z=imcrop(LIF_AVGout, [318 199 702 301]);
[rowz columnz] = size(Z);
%Calculates average intensity
Img_IntenAVG = sum(Z(:))/(rowz*columnz);
%Finds maximum intensity
m=max(max(Z));
%Loads the intended directory
cd 'C:\NO PLIF\Calibration - NO LIF\Corrected\1000ppm';
%Saves the image
saveas(LIF_AVGout, '1000ppm_Offline.tif');
%Finds the location of maximum intensity
[row, col] = find(ismember(Z, max(Z(:))));
%Chirping sound notification upon completion
load chirp;
sound(y,1/2*Fs);
end
```

Appendix B.6: MATLAB code for time averaging offline corrected NO-LIF images at 226.03 nm excitation and laser beam distribution correction

The 'LIF_AVG_BEAMNORM.m' code subtracts the temporally-averaged offline image from online images and then average the online images. Laser beam distribution then applied from the maximum pixel to the either sides of image.

```
function [m, Z, row, col, LIF_AVGout, LIF_cmap, Img_IntenAVG] =
LIF_AVG_BEAMNORM(NumImages, LIF_OFFLINE)
% Open dialog box to prompt for .TIF NO LIF file selection
[listOfFiles, folder] = uigetfile ('*.tif', 'Select your image',
'MultiSelect', 'on');
fullFileName = fullfile(folder, listOfFiles{1});
[I cmap] = imread(fullFileName);
[rows columns] = size(I);
LIF_AVGout_zero = zeros(rows,columns);
LIF_Beam_Norm_zero = zeros(rows,columns);
LIF_BG_double = im2double(LIF_OFFLINE);
%Error check if the number of selected images is equal NumImages
if NumImages ~= length(listOfFiles)
msg = 'Error Occured - Image Number Mismatch';
error(msg);
else
for j=1:length(listOfFiles)
fullFileName = fullfile(folder, listOfFiles{j});
% Read in first instantaneous NO LIF image
I2 = imread(fullFileName);
% Convert the image to double precision
I2_double = im2double(I2);
% Apply 3x3 pixel median filter to reduce noise
I2_double_filt = medfilt2(I2_double, 'symmetric');
% Correct the instaneous NO LIF image for the input background
% image
I2_double_NoBG = I2_double_filt - LIF_BG_double;
% Apply laser beam intensity distribution correction
for i = 1:rows
% Find the maximum NO LIF intensity value in each row
[RowMax Loc] = max(I2_double_NoBG(i,:));
% Convert the row pixel location to "mm" distance
LocMM = Loc/16.9;
LocNorm = LocMM / (LocMM / 1.215e+5);
GaussInten = 0.7802*exp(-((LocNorm-1.215e+5)/1.564e+5)^2);
% Normalizes the maximum NO LIF intensity value
IntenNorm = RowMax/GaussInten;
LIF_Beam_Norm_zero(i,:) = I2_double_NoBG(i,:);
LIF_Beam_Norm_zero(i, Loc) = IntenNorm;
% Apply the Gaussian normalization in upstream direction from
% the maximum NO LIF intensity location
for l = 1:187
if (Loc - l) == 0
break
end
LocNormL = 1.215e+5-((Loc-(Loc-l))*(1/16.9));
GaussIntenL = 0.7802*exp(-((LocNormL-1.215e+5)/1.564e+5)^2);
IntenNormL = I2_double_NoBG(i, (Loc-l))/GaussIntenL;
LIF_Beam_Norm_zero(i, (Loc-l)) = IntenNormL;
end
end
end
```

```

end
% Apply the Gaussian normalization in the downstream % direction
from the maximum NO LIF intensity location
for k = 1:111
if (Loc + k) > 1344
break
end
end
LocNormK = 1.215e+5+(((Loc+k)-Loc)*(1/16.9));
GaussIntenK = 0.7802*exp(-((LocNormK-1.215e+5)/1.564e+5)^2);
IntenNormK = I2_double_NoBG(i, (Loc+k))/GaussIntenK;
LIF_Beam_Norm_zero(i, (Loc+k)) = IntenNormK;
end
end
LIF_AVGout_zero = LIF_AVGout_zero + LIF_Beam_Norm_zero;
end
end
%Calculate the temporal average NO LIF image
LIF_AVGout = LIF_AVGout_zero ./ NumImages;
%Output the .TIF file colormap for easier image plotting
LIF_cmap = cmap;
%Crops the ouput image into area of interest
Z=imcrop(LIF_AVGout, [1 1 220 1023]);
[rowz columnz] = size(Z);
%Calculates average intensity
Img_IntenAVG = sum(Z(:))/(rowz*columnz);
%Finds maximum intensity
m=max(max(Z));
%Loads the intended directory
cd 'C:\NO PLIF\Calibration - NO LIF\Corrected\0ppm';
%Saves the image
saveastiff(LIF_AVGout, '0ppm_Online_beam.tif');
%Finds the location of maximum intensity
[row, col] = find(ismember(Z, max(Z(:))));
%Chirping sound notification upon completion
load chirp;
sound(y,1/2*Fs);
end

```

Appendix B.7: MATLAB code for temporally averaging OH* chemiluminescence images

This code was adapted from a previous study at Cardiff University [221]. The code temporally averages the raw chemiluminescence images.

```
function [CHEMI_AVGout, CHEMI_cmap, Img_IntenINSTAN, Img_IntenAVG]
= CHEMI_AVG(NumImages)
%Open dialogue box for user to select .TIF image files
[listOfFiles, folder] = uigetfile (*.tif', 'Select your image',
'MultiSelect', 'on');
fullFileName = fullfile(folder, listOfFiles{1});
[I cmap] = imread(fullFileName);
[rows columns] = size(I);
%Initialize output matrix and vector variables
CHEMI_AVGout_zero = zeros(rows,columns);
Img_IntenINSTAN = zeros(1, NumImages);
%Check number of images selected matches number input by user
if NumImages ~= length(listOfFiles)
msg = 'Error Occured - Image Number Mismatch';
error(msg);
else
for j=1:length(listOfFiles)
fullFileName = fullfile(folder, listOfFiles{j});
I2 = imread(fullFileName);
%Convert .TIF image to double precision
I2_double = im2double(I2);
%Filter the image with a 3x3 median filter
I2_double_filt = medfilt2(I2_double, 'symmetric');
%Add each image to the proceeding image
CHEMI_AVGout_zero = CHEMI_AVGout_zero + I2_double_filt;
%Calculate and store the instantaneous image integral intensity
Img_IntenINSTAN(1,j) = sum(I2_double_filt(:));
end
end
%Calculate the temporal average image
CHEMI_AVG_1 = CHEMI_AVGout_zero ./ NumImages;
CHEMI_AVG_mode = mode(CHEMI_AVG_1(:));
%Background correction using the statistical mode of the temporal
average
CHEMI_AVGout = CHEMI_AVG_1 - CHEMI_AVG_mode;
%Minimum value correction
CHEMI_AVGout = CHEMI_AVGout - min(CHEMI_AVGout(:));
CHEMI_cmap = cmap;
%Calculate the integral intensity of the temporal average image
after
%correction
Img_IntenAVG = sum(CHEMI_AVGout(:));
```

Appendix B.8: MATLAB code for Abel Conversion of time-averaged OH* chemiluminescence image

This code was also adapted from the same previous study. This code works in conjunction with 'abel_inversion.m', 'compute_expansion.m' and 'solve_isq.m' codes from literature. The code requires the user to define central pixel column location as well as the half of the image to be processed.

```
function [ImAbel] = HalfAbel(Image, R, CentXPix, WhichWay)
[i j] = size (Image);
n = (j/2) + 1;
if WhichWay == 1
NewEdge = (2*(j-CentXPix));
%Initialize output image matrix
ImAbel = zeros(i, NewEdge);
k = (NewEdge/2) - 1;
%For loop cycles through each row of the input image
for z = 1:i
%Extract single image row
A = Image(z, CentXPix:j);
%Convert image row to double precision
A2 = im2double(A, 'indexed');
%Calls the Abel inversion function one row at a time with an
%input of 5 cosinus expansions in the Fourier-series-like
%expansion
[f_rec , X] = abel_inversion(A2,R,5);
%Add the Abel deconvoluted row to the output matrix
ImAbel(z, (NewEdge/2):NewEdge) = f_rec(:,1);
%Rotate the Abel deconvoluted row about the central axis
f_rec = flipud(f_rec);
ImAbel(z, 1:k) = f_rec(2:(NewEdge/2),1);
end
end
if WhichWay == 2
NewEdge = (2*CentXPix);
ImAbel = zeros(i, NewEdge);
k = (NewEdge/2) - 1;
%For loop cycles through each row in the input image
for z = 1:i
%Extract single image row
A = Image(z, 1:(CentXPix+1));
A = fliplr(A);
%Convert image row to double precision
A2 = im2double(A, 'indexed');
%Calls the Abel inversion function one row at a time with an input
%of 5 cosinus expansions in the Fourier-series-like expansion
[f_rec , X] = abel_inversion(A2,R,5);
%Add the Abel deconvoluted row to the output matrix
ImAbel(z, (NewEdge/2):NewEdge) = f_rec(:,1);
%Rotate the Abel deconvoluted row about the central axis
f_rec = flipud(f_rec);
ImAbel(z, 1:k) = f_rec(2:(NewEdge/2),1);
end
end
end
```

Appendix B.9: MATLAB code for calculating flame thickness from Abel Deconvoluted OH* chemiluminescence image

This code was also adapted from a previous study with minor changes to work with Abel Deconvoluted OH* chemiluminescence image rather than OH PLIF image.

```
function [FlameMax, FlameSurf, FlameThk, FlameArea,
I_CHEMI_MAX_LOCS, LFT_EDGE_LOCS, RHT_EDGE_LOCS, ROW_FLM_THK] =
CHEMI_FLAME_MAX(CHEMI_AVG, CenterLinePixel, PixScale, ProgVar)
[rows columns] = size(CHEMI_AVG);
X = 1:CenterLinePixel;
X = X.';
% Select half of the average OH chemi image to evaluate
CHEMI_AVG_Half = imcrop(CHEMI_AVG, [0 0 CenterLinePixel rows]);
% Find the maximum OH chemi intensity value in the selected half
image
I_CHEMI_MAX_Crop = max(CHEMI_AVG_Half(:));
FlameMax = zeros(rows, CenterLinePixel);
FlameSurf = zeros(rows, CenterLinePixel);
I_CHEMI_MAX_LOCS = zeros(rows,1);
LFT_EDGE_LOCS = zeros(rows,1);
RHT_EDGE_LOCS = zeros(rows,1);
ROW_FLM_THK = zeros(rows,1);
% Calculate the pixel area (mm^2) from the input pixel scale
(pixel/mm)
PixelArea = (1/PixScale)^2;
for k = 1:rows
% Find the maximum OH chemi intensity value in each row
[I_CHEMI_MAX I_CHEMI_MAX_LOC] = max(CHEMI_AVG_Half(k,:));
% If the maximum value is less that 50% of the overall image
% maximum chemi intensity, move to the next row
if I_CHEMI_MAX/I_CHEMI_MAX_Crop < 0.5
continue
end
FlameMax(k, I_CHEMI_MAX_LOC) = 1;
I_CHEMI_MAX_LOCS(k) = ((CenterLinePixel/PixScale)-
(I_CHEMI_MAX_LOC/PixScale));
% Extract the entire row distribution of OH chemi intensity values
I_CHEMI_ROW = CHEMI_AVG_Half(k,:);
I_CHEMI_ROW = I_CHEMI_ROW.';
% Fit a 9th order polynomial to the row OH chemi intensity
% distribution
[P,~,MU] = polyfit(X,I_CHEMI_ROW, 9);
F = polyval(P,X,[],MU);
% Calculate the 1st derivative of the row OH chemi intensity
distribution
Fx = gradient(F);
% Extract OH chemi intensity values from the left edge of the row
% to the maximum location
Fx_LR = flipud(Fx(1:I_CHEMI_MAX_LOC-1));
% Error checking
FX_LR_EMPCHK = isempty(Fx_LR);
if FX_LR_EMPCHK == 1 || numel(Fx_LR) < 3
continue
end
% Find the locations of the peaks in the 1st derivative
% distribution from the left edge to the maximum location
[Fx_LR_PK, Fx_LR_LOC] = findpeaks(Fx_LR);
% If no peaks are found, take 2nd derivative and find
```

```

%Locations closest to 0
if numel(Fx_LR_LOC)==0
Fx2 = gradient(Fx);
[P2,~,MU2] = polyfit(X,Fx2, 9);
F2 = polyval(P2,X,[],MU2);
Fx2_LR = flipud(Fx2(1:I_CHEMI_MAX_LOC-1));
Fx_LR_LOC = find(abs(Fx2_LR-0)==min(abs(Fx2_LR-0)));
end
% Calculate the left edge location
LFT_EDGE_LOC = (I_CHEMI_MAX_LOC - ceil(2*ProgVar*Fx_LR_LOC(1)));
if LFT_EDGE_LOC < 0
continue
end
% Convert the left edge location to mm
LFT_EDGE_LOCS(k) = ((CenterLinePixel/PixScale)-
(LFT_EDGE_LOC/PixScale));
% Extract OH chemi intensity values from the maximum location to
% the right edge of the row
Fx_RL = Fx((I_CHEMI_MAX_LOC+1):CenterLinePixel);
% Error checking
FX_RL_EMPCHK = isempty(Fx_RL);
if FX_RL_EMPCHK == 1 || numel(Fx_RL) < 3
continue
end
% Find the locations of the peaks in the 1st derivative
% distribution from the maximum location to the right edge
[Fx_RL_PK, Fx_RL_LOC] = findpeaks(-Fx_RL);
% If no peaks are found, take 2nd derivative and find
% Location closest to 0
if numel(Fx_RL_LOC)==0
Fx3 = gradient(Fx);
[P3,~,MU3] = polyfit(X,Fx3, 9);
F3 = polyval(P3,X,[],MU3);
Fx3_RL = Fx3((I_CHEMI_MAX_LOC+1):CenterLinePixel);
Fx_RL_LOC = find(abs(Fx3_RL-0)==min(abs(Fx3_RL-0)));
end
% Calculate the right edge location
RHT_EDGE_LOC = (I_CHEMI_MAX_LOC + ceil(2*ProgVar*Fx_RL_LOC(1)));
if RHT_EDGE_LOC > CenterLinePixel
continue
end
% Convert the right edge location to mm
RHT_EDGE_LOCS(k) = ((CenterLinePixel/PixScale)-
(RHT_EDGE_LOC/PixScale));
% Binarizing the flame surface from left to right in the row
FlameSurf(k,LFT_EDGE_LOC:RHT_EDGE_LOC) = 1;
% Calculating the individual row flame thickness (mm)
ROW_FLM_THK(k) = 0.5*(LFT_EDGE_LOCS(k)-RHT_EDGE_LOCS(k));
end
% Calculate the mean flame thickness (mm)from the row thicknesses
FlameThk = mean(nonzeros(ROW_FLM_THK));
% Calculate the mean flame area (mm^2) from the binary flame
surface
FlameArea = (bwarea(FlameSurf))/PixelArea;
end

```


Appendix C.2: CFD Result used for CRZ, ERZ and Flame Zone Volume
Calculation

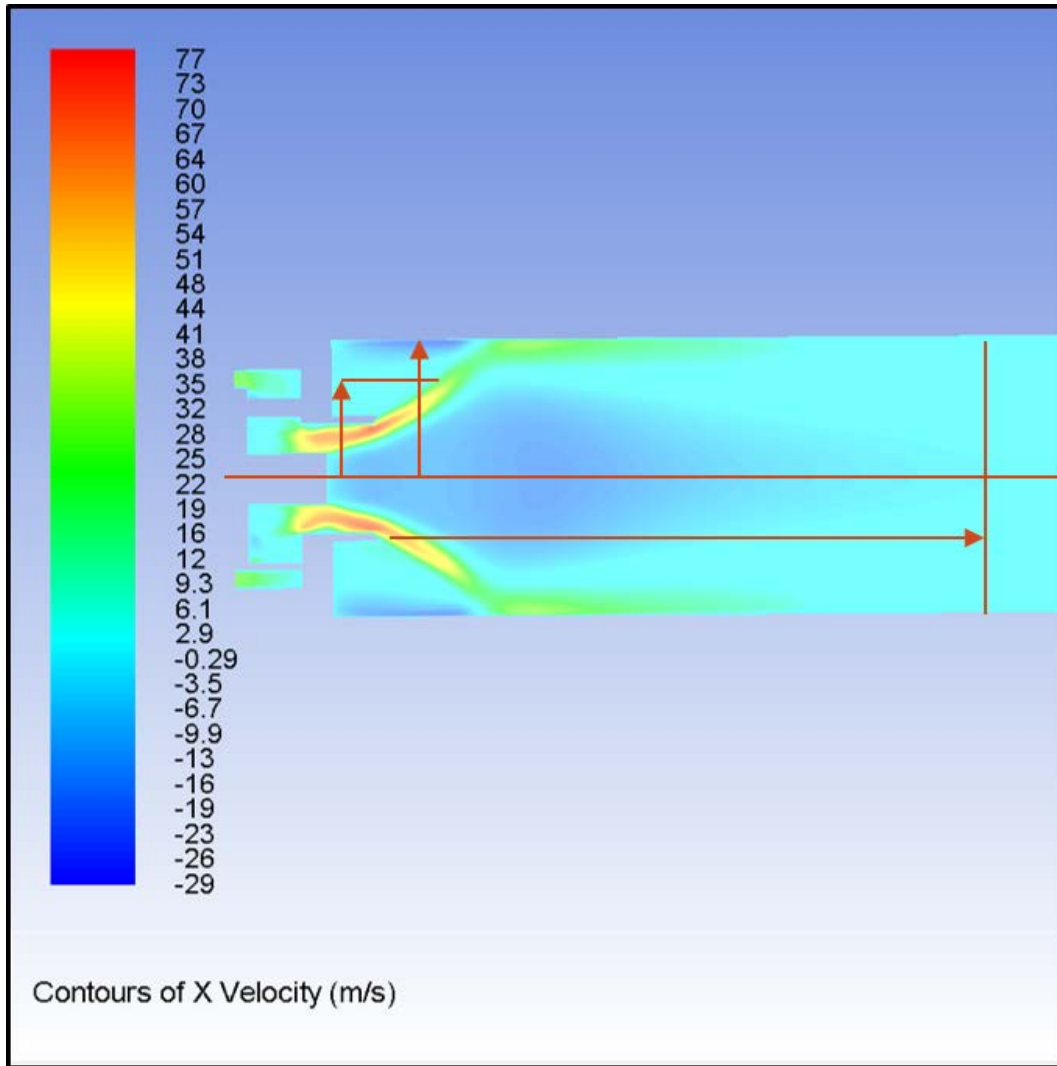


Figure C-0-2: CFD result used for CRZ, ERZ and flame zone volume calculation.
Reproduced from [275].

APPENDIX D - Photographs of HPOC and Bunsen Burner Setup

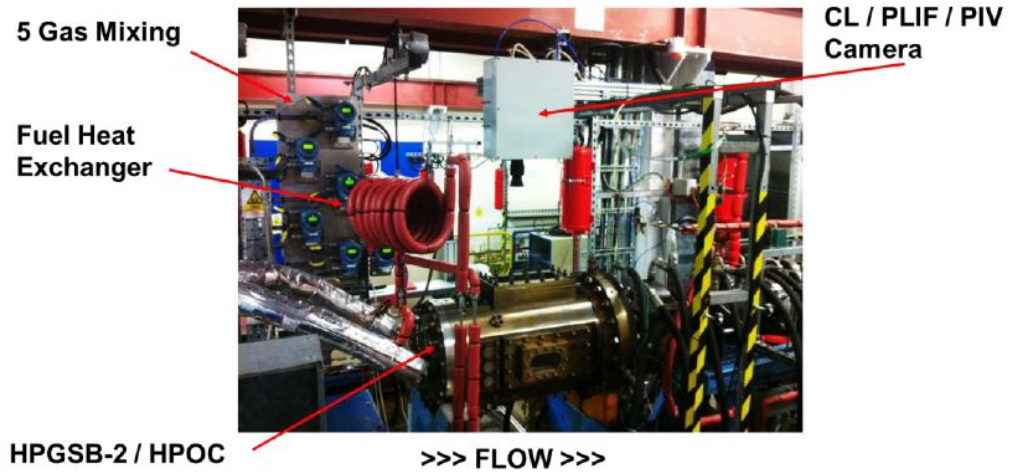


Figure D-0-1: Photograph of HPCR setup with HPGSB-2

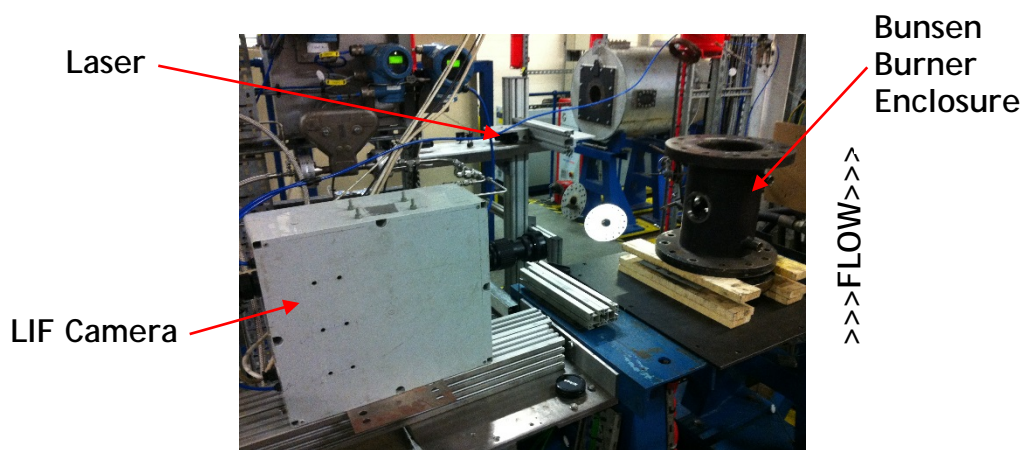


Figure D-0-2: Photograph of Bunsen burner setup

APPENDIX E - Updated Chemical Kinetics

**Mechanisms with NO_x Formation Pathways and
Required Inputs for the Models**

Appendix E.1 - NO_x pathways for Aramco 1.3 Mechanism

Gas-phase kinetics for NO_x pathways

N+NO<=>N2+O	2.700E+13	.000	355.00
N+O2<=>NO+O	9.000E+09	1.000	6500.00
N+OH<=>NO+H	3.360E+13	.000	385.00
N2O+O<=>N2+O2	1.400E+12	.000	10810.00
N2O+O<=>2NO	2.900E+13	.000	23150.00
N2O+H<=>N2+OH	3.870E+14	.000	18880.00
N2O+OH<=>N2+HO2	2.000E+12	.000	21060.00
N2O(+M)<=>N2+O(+M)	7.910E+10	.000	56020.00
LOW / 6.370E+14	.000	56640.00/	
H2/2.00/ H2O/6.00/ CH4/2.00/ CO/1.50/ CO2/2.00/ C2H6/3.00/ AR/ .625/			
HO2+NO<=>NO2+OH	2.110E+12	.000	-480.00
NO+O+M<=>NO2+M	1.060E+20	-1.410	.00
H2/2.00/ H2O/6.00/ CH4/2.00/ CO/1.50/ CO2/2.00/ C2H6/3.00/ AR/ .70/			
NO2+O<=>NO+O2	3.900E+12	.000	-240.00
NO2+H<=>NO+OH	1.320E+14	.000	360.00
NH+O<=>NO+H	4.000E+13	.000	.00
NH+H<=>N+H2	3.200E+13	.000	330.00
NH+OH<=>HNO+H	2.000E+13	.000	.00
NH+OH<=>N+H2O	2.000E+09	1.200	.00
NH+O2<=>HNO+O	4.610E+05	2.000	6500.00
NH+O2<=>NO+OH	1.280E+06	1.500	100.00
NH+N<=>N2+H	1.500E+13	.000	.00
NH+H2O<=>HNO+H2	2.000E+13	.000	13850.00
NH+NO<=>N2+OH	2.160E+13	-.230	.00
NH+NO<=>N2O+H	3.650E+14	-.450	.00
NH2+O<=>OH+NH	3.000E+12	.000	.00
NH2+O<=>H+HNO	3.900E+13	.000	.00
NH2+H<=>NH+H2	4.000E+13	.000	3650.00
NH2+OH<=>NH+H2O	9.000E+07	1.500	-460.00
NNH<=>N2+H	3.300E+08	.000	.00
NNH+M<=>N2+H+M	1.300E+14	-.110	4980.00
H2/2.00/ H2O/6.00/ CH4/2.00/ CO/1.50/ CO2/2.00/ C2H6/3.00/ AR/ .70/			
NNH+O2<=>HO2+N2	5.000E+12	.000	.00
NNH+O<=>OH+N2	2.500E+13	.000	.00

NNH+O<=>NH+NO	7.000E+13	.000	.00
NNH+H<=>H2+N2	5.000E+13	.000	.00
NNH+OH<=>H2O+N2	2.000E+13	.000	.00
NNH+CH3<=>CH4+N2	2.500E+13	.000	.00
H+NO+M<=>HNO+M	4.480E+19	-1.320	740.00
H2/2.00/ H2O/6.00/ CH4/2.00/ CO/1.50/ CO2/2.00/ C2H6/3.00/ AR/ .70/			
HNO+O<=>NO+OH	2.500E+13	.000	.00
HNO+H<=>H2+NO	9.000E+11	.720	660.00
HNO+OH<=>NO+H2O	1.300E+07	1.900	-950.00
HNO+O2<=>HO2+NO	1.000E+13	.000	13000.00
CN+O<=>CO+N	7.700E+13	.000	.00
CN+OH<=>NCO+H	4.000E+13	.000	.00
CN+H2O<=>HCN+OH	8.000E+12	.000	7460.00
CN+O2<=>NCO+O	6.140E+12	.000	-440.00
CN+H2<=>HCN+H	2.950E+05	2.450	2240.00
NCO+O<=>NO+CO	2.350E+13	.000	.00
NCO+H<=>NH+CO	5.400E+13	.000	.00
NCO+OH<=>NO+H+CO	0.250E+13	.000	.00
NCO+N<=>N2+CO	2.000E+13	.000	.00
NCO+O2<=>NO+CO2	2.000E+12	.000	20000.00
NCO+M<=>N+CO+M	3.100E+14	.000	54050.00
H2/2.00/ H2O/6.00/ CH4/2.00/ CO/1.50/ CO2/2.00/ C2H6/3.00/ AR/ .70/			
NCO+NO<=>N2O+CO	1.900E+17	-1.520	740.00
NCO+NO<=>N2+CO2	3.800E+18	-2.000	800.00
HCN+M<=>H+CN+M	1.040E+29	-3.300	126600.00
H2/2.00/ H2O/6.00/ CH4/2.00/ CO/1.50/ CO2/2.00/ C2H6/3.00/ AR/ .70/			
HCN+O<=>NCO+H	2.030E+04	2.640	4980.00
HCN+O<=>NH+CO	5.070E+03	2.640	4980.00
HCN+O<=>CN+OH	3.910E+09	1.580	26600.00
HCN+OH<=>HOCN+H	1.100E+06	2.030	13370.00
HCN+OH<=>HNCO+H	4.400E+03	2.260	6400.00
HCN+OH<=>NH2+CO	1.600E+02	2.560	9000.00
H+HCN(+M)<=>H2CN(+M)	3.300E+13	.000	.00
LOW /	1.400E+26	-3.400	1900.00/
H2/2.00/ H2O/6.00/ CH4/2.00/ CO/1.50/ CO2/2.00/ C2H6/3.00/ AR/ .70/			
H2CN+N<=>N2+CH2	6.000E+13	.000	400.00
C+N2<=>CN+N	6.300E+13	.000	46020.00
CH+N2<=>HCN+N	3.120E+09	0.880	20130.00
CH+N2(+M)<=>HCNN(+M)	3.100E+12	.150	.00
LOW /	1.300E+25	-3.160	740.00/
TROE/	.6670	235.00	2117.00 4536.00 /
H2/2.00/ H2O/6.00/ CH4/2.00/ CO/1.50/ CO2/2.00/ C2H6/3.00/ AR/ 1.0/			

**APPENDIX E - Updated Chemical Kinetics Mechanisms with NOX
Formation Pathways and Required Inputs for the Models**

CH2+N2<=>HCN+NH	1.000E+13	.000	74000.00
CH2(S)+N2<=>NH+HCN	1.000E+11	.000	65000.00
C+NO<=>CN+O	1.900E+13	.000	.00
C+NO<=>CO+N	2.900E+13	.000	.00
CH+NO<=>HCN+O	4.100E+13	.000	.00
CH+NO<=>H+NCO	1.620E+13	.000	.00
CH+NO<=>N+HCO	2.460E+13	.000	.00
CH2+NO<=>H+HNCO	3.100E+17	-1.380	1270.00
CH2+NO<=>OH+HCN	2.900E+14	-.690	760.00
CH2+NO<=>H+HCNO	3.800E+13	-.360	580.00
CH2(S)+NO<=>H+HNCO	3.100E+17	-1.380	1270.00
CH2(S)+NO<=>OH+HCN	2.900E+14	-.690	760.00
CH2(S)+NO<=>H+HCNO	3.800E+13	-.360	580.00
CH3+NO<=>HCN+H2O	9.600E+13	.000	28800.00
CH3+NO<=>H2CN+OH	1.000E+12	.000	21750.00
HCNN+O<=>CO+H+N2	2.200E+13	.000	.00
HCNN+O<=>HCN+NO	2.000E+12	.000	.00
HCNN+O2<=>O+HCO+N2	1.200E+13	.000	.00
HCNN+OH<=>H+HCO+N2	1.200E+13	.000	.00
HCNN+H<=>CH2+N2	1.000E+14	.000	.00
HNCO+O<=>NH+CO2	9.800E+07	1.410	8500.00
HNCO+O<=>HNO+CO	1.500E+08	1.570	44000.00
HNCO+O<=>NCO+OH	2.200E+06	2.110	11400.00
HNCO+H<=>NH2+CO	2.250E+07	1.700	3800.00
HNCO+H<=>H2+NCO	1.050E+05	2.500	13300.00
HNCO+OH<=>NCO+H2O	3.300E+07	1.500	3600.00
HNCO+OH<=>NH2+CO2	3.300E+06	1.500	3600.00
HNCO+M<=>NH+CO+M	1.180E+16	.000	84720.00
H2/2.00/ H2O/6.00/ CH4/2.00/ CO/1.50/ CO2/2.00/ C2H6/3.00/ AR/ .70/			
HCNO+H<=>H+HNCO	2.100E+15	-.690	2850.00
HCNO+H<=>OH+HCN	2.700E+11	.180	2120.00
HCNO+H<=>NH2+CO	1.700E+14	-.750	2890.00
HOCN+H<=>H+HNCO	2.000E+07	2.000	2000.00
HCCO+NO<=>HCNO+CO	0.900E+13	.000	.00
CH3+N<=>H2CN+H	6.100E+14	-.310	290.00
CH3+N<=>HCN+H2	3.700E+12	.150	-90.00
NH3+H<=>NH2+H2	5.400E+05	2.400	9915.00
NH3+OH<=>NH2+H2O	5.000E+07	1.600	955.00
NH3+O<=>NH2+OH	9.400E+06	1.940	6460.00
NH+CO2<=>HNO+CO	1.000E+13	.000	14350.00
CN+NO2<=>NCO+NO	6.160E+15	-0.752	345.00
NCO+NO2<=>N2O+CO2	3.250E+12	.000	-705.00

```

N+CO2<=>NO+CO          3.000E+12  .000  11300.00
O+CH3=>H+H2+CO         3.370E+13  .000    .00
CH+H2(+M)<=>CH3(+M)     1.970E+12  .430  -370.00
  LOW/ 4.820E+25 -2.80 590.0 /
  TROE/ .578 122.0 2535.0 9365.0 /
H2/2.00/ H2O/6.00/ CH4/2.00/ CO/1.50/ CO2/2.00/ C2H6/3.00/ AR/ .70/
END
    
```

Thermodynamics data for NO_x pathway

THERMO

```

N2          G 8/02N  2  0  0  OG  200.000  6000.00  1000.00  1
  2.95257637E+00  1.39690040E-03-4.92631603E-07  7.86010195E-11-4.60755204E-15  2
 -9.23948688E+02  5.87188762E+00  3.53100528E+00-1.23660988E-04-5.02999433E-07  3
  2.43530612E-09-1.40881235E-12-1.04697628E+03  2.96747038E+00  0.00000000E+00  4
HCN         L 7/88H  1C  1N  1  OG  200.000  6000.000  1000.  1
  0.38022392E+01  0.31464227E-02-0.10632185E-05  0.16619757E-09-0.97997567E-14  2
  0.14910512E+05  0.15754601E+01  0.22589885E+01  0.10051170E-01-0.13351763E-04  3
  0.10092349E-07-0.30089029E-11  0.15215853E+05  0.89164418E+01  0.16236675E+05  4
N           120186N  1          G  0300.00  5000.00  1000.00  1
  0.02450268E+02  0.10661458E-03-0.07465337E-06  0.01879652E-09-0.10259839E-14  2
  0.05611604E+06  0.04448758E+02  0.02503071E+02-0.02180018E-03  0.05420529E-06  3
 -0.05647560E-09  0.02099904E-12  0.05609890E+06  0.04167566E+02  4
NNH        T07/93N  2H  1          G  200.000  6000.000  1000.000  1
  0.37667544E+01  0.28915082E-02-0.10416620E-05  0.16842594E-09-0.10091896E-13  2
  0.28650697E+05  0.44705067E+01  0.43446927E+01-0.48497072E-02  0.20059459E-04  3
 -0.21726464E-07  0.79469539E-11  0.28791973E+05  0.29779410E+01  4
NCO        EA 93 N  1C  1O  1  G  200.000  6000.000  1000.000  1
  0.51521845E+01  0.23051761E-02-0.88033153E-06  0.14789098E-09-0.90977996E-14  2
  0.14004123E+05-0.25442660E+01  0.28269308E+01  0.88051688E-02-0.83866134E-05  3
  0.48016964E-08-0.13313595E-11  0.14682477E+05  0.95504646E+01  4
HNCO       T 6/94H  1N  1C  1O  1G  200.000  6000.000  1000.  1
  0.52936894E+01  0.40307770E-02-0.14130589E-05  0.22445562E-09-0.13287683E-13  2
 -0.15973489E+05-0.30864710E+01  0.22432188E+01  0.14491349E-01-0.15236174E-04  3
  0.83345851E-08-0.17104033E-11-0.15233708E+05  0.12157321E+02-0.14039745E+05  4
NH         L11/89N  1H  1  0  OG  200.000  6000.000  1000.  1
  0.27836929E+01  0.13298429E-02-0.42478047E-06  0.78348504E-10-0.55044470E-14  2
  0.42134514E+05  0.57407798E+01  0.34929084E+01  0.31179197E-03-0.14890484E-05  3
  0.24816442E-08-0.10356967E-11  0.41894294E+05  0.18483277E+01  0.42940822E+05  4
    
```

APPENDIX E - Updated Chemical Kinetics Mechanisms with NOX Formation Pathways and Required Inputs for the Models

NH2	L12/89N	1H	2	0	OG	200.000	6000.000	1000.	1	
										2
										3
										4
CN	T 6/94C	1N	1	0	OG	200.000	6000.000	1000.	1	
										2
										3
										4
HCN	L 7/88H	1C	1N	1	OG	200.000	6000.000	1000.	1	
										2
										3
										4
HCNN	SRI/94C	1N	2H	1	G	300.000	5000.000	1000.000	1	
										2
										3
										4
H2CN	41687H	2C	1N	1	G	300.00	4000.000	1000.000	1	
										2
										3
										4
N2O	L 7/88N	2O	1	0	OG	200.000	6000.000	1000.	1	
										2
										3
										4
HNO	L12/89H	1N	1O	1	OG	200.000	3500.000	1000.	1	
										2
										3
										4
NH3 AMONIA	RUS 89N	1H	3	0	OG	200.000	6000.000	1000.	1	
										2
										3
										4
NO2	L 7/88N	1O	2	0	OG	200.000	6000.000	1000.	1	
										2
										3
										4
N2H	T07/93N	2H	1	0	OG	200.000	6000.000	1000.	1	
										2
										3
										4

NO	RUS 89N	1O	1	0	OG	200.000	6000.000	1000.	1
	3.26071234E+00	1.19101135E-03	-4.29122646E-07	6.94481463E-11	-4.03295681E-15				2
	9.92143132E+03	6.36900518E+00	4.21859896E+00	-4.63988124E-03	1.10443049E-05				3
	-9.34055507E-09	2.80554874E-12	9.84509964E+03	2.28061001E+00	1.09770882E+04				4
HCNO	BDEA94H	1N	1C	1O	1G	300.000	5000.000	1382.000	1
	6.59860456E+00	3.02778626E-03	-1.07704346E-06	1.71666528E-10	-1.01439391E-14				2
	1.79661339E+04	-1.03306599E+01	2.64727989E+00	1.27505342E-02	-1.04794236E-05				3
	4.41432836E-09	-7.57521466E-13	1.92990252E+04	1.07332972E+01					4
HOCN	BDEA94H	1N	1C	1O	1G	300.000	5000.000	1368.000	1
	5.89784885E+00	3.16789393E-03	-1.11801064E-06	1.77243144E-10	-1.04339177E-14				2
	-3.70653331E+03	-6.18167825E+00	3.78604952E+00	6.88667922E-03	-3.21487864E-06				3
	5.17195767E-10	1.19360788E-14	-2.82698400E+03	5.63292162E+00					4

APPENDIX E - Updated Chemical Kinetics Mechanisms with NO_x
Formation Pathways and Required Inputs for the Models

Appendix E.2 - NO_x pathways for USII Mechanism

Gas-phase kinetics for NO_x pathway

NH3+M=NH2+H+M	.2200E+17	.000	93470.0
NH2+H=NH+H2	.4000E+14	.000	3650.0
NH2+O=HNO+H	.6600E+15	-.500	.0
NH2+O=NH+OH	.6800E+13	.000	.0
NH2+O=NO+H2	.1300E+09	1.025	-627.0
NH2+O2=HNO+OH	.4500E+13	.000	25000.0
NH2+OH=NH+H2O	.4000E+07	2.000	1000.0
NH2+HO2=H2NO+OH	.5000E+14	.000	.0
H2NO+O=NH2+O2	.2000E+15	.000	.0
NH2+N=N2+H+H	.7000E+14	.000	.0
NH2+NH=N2H2+H	.5000E+14	.000	.0
NH2+NH2=N2H2+H2	.8500E+12	.000	.0
NH2+NH2=NH3+NH	.5000E+14	.000	10000.0
NH2+NH2(+M)=N2H4(+M)	.1500E+14	.000	.0
LOW/	.1000E+19	.000	.0/
N2/	2.50/H2O/	5.00/NH3/	10.00/
NH2+NO=NNH+OH	.8900E+13	-.350	.0
NH2+NO=N2+H2O	.1720E+20	-2.294	1058.0
NH2+NO2=N2O+H2O	.3200E+19	-2.200	.0
NH2+NO2=H2NO+NO	.3500E+13	.000	.0
NH+H=N+H2	.3000E+14	.000	.0
NH+O=NO+H	.9200E+14	.000	.0
NH+OH=HNO+H	.2000E+14	.000	.0
NH+OH=N+H2O	.5000E+12	.500	2000.0
NH+OH=NO+H2	.2000E+14	.000	.0
NH+O2=HNO+O	.4600E+06	2.000	6500.0
NH+O2=NO+OH	.1300E+07	1.500	100.0
NH+NH=N2+H+H	.2500E+14	.000	.0
NH+N=N2+H	.3000E+14	.000	.0
NH+NO=N2+OH	.2200E+14	-.230	.0
NH+NO2=N2O+OH	.1000E+14	.000	.0
N+OH=NO+H	.3800E+14	.000	.0
N+O2=NO+O	.6400E+10	1.000	6280.0
N+NO=O+N2	.3300E+13	.300	.0
N2H4+H=N2H3+H2	.1300E+14	.000	2500.0
N2H4+O=N2H2+H2O	.8500E+14	.000	1200.0
N2H4+OH=N2H3+H2O	.4000E+14	.000	.0
N2H4+NH2=N2H3+NH3	.3900E+13	.000	1500.0

N2H3+M=N2H2+H+M	.3500E+17	.000	46000.0
N2H3+H=NH2+NH2	.1600E+13	.000	.0
N2H3+O=N2H2+OH	.5000E+13	.000	5000.0
N2H3+O=NH2+HNO	.1000E+14	.000	.0
N2H3+OH=N2H2+H2O	.1000E+14	.000	1000.0
N2H3+OH=NH3+HNO	.1000E+13	.000	15000.0
N2H3+NH=N2H2+NH2	.2000E+14	.000	.0
N2H2+M=NNH+H+M	.5000E+17	.000	50000.0
N2/ 2.00/H2/ 2.00/O2/ 2.00/H2O/ 15.00/			
N2H2+H=NNH+H2	.5000E+14	.000	1000.0
N2H2+O=NH2+NO	.1000E+14	.000	1000.0
N2H2+O=NNH+OH	.2000E+14	.000	1000.0
N2H2+OH=NNH+H2O	.1000E+14	.000	1000.0
N2H2+NO=N2O+NH2	.4000E+13	.000	11922.0
N2H2+NH=NNH+NH2	.1000E+14	.000	1000.0
N2H2+NH2=NNH+NH3	.1000E+14	.000	1000.0
NNH=N2+H	.1000E+08	.000	.0
NNH+H=N2+H2	.1000E+15	.000	.0
NNH+O=N2O+H	.1000E+15	.000	.0
NNH+O=NH+NO	.5000E+14	.000	.0
NNH+OH=N2+H2O	.5000E+14	.000	.0
NNH+O2=N2+HO2	.6670E+14	.000	.0
NNH+O2=N2+H+O2	.5000E+14	.000	.0
NNH+NH=N2+NH2	.5000E+14	.000	.0
NNH+NH2=N2+NH3	.5000E+14	.000	.0
NNH+NO=N2+HNO	.5000E+14	.000	.0
HNNO+M=N2O+H+M	.2200E+16	.000	21600.0
HNNO+M=N2+OH+M	.1000E+16	.000	25600.0
HNNO+H=N2O+H2	.2000E+14	.000	.0
HNNO+H=NNH+OH	.1000E+14	.000	.0
HNNO+O=N2O+OH	.2000E+14	.000	.0
HNNO+O=NNH+O2	.1000E+14	.000	.0
HNNO+OH=N2O+H2O	.2000E+14	.000	.0
HNNO+OH=NNH+HO2	.1000E+14	.000	.0
HNNO+NO=N2O+HNO	.1000E+13	.000	.0
HNNO+NO=NNH+NO2	.3200E+13	.000	270.0
HNNO+NO2=NNH+NO3	.1000E+14	.000	.0
HNNO+NO2=N2O+HONO	.1000E+13	.000	.0
NO+HO2=NO2+OH	.2100E+13	.000	-480.0
NO+O+M=NO2+M	.7500E+20	-1.410	.0
N2/ 1.70/O2/ 1.50/H2O/ 10.00/			
NO+OH(+M)=HONO(+M)	.2000E+14	.000	.0

**APPENDIX E - Updated Chemical Kinetics Mechanisms with NOX
Formation Pathways and Required Inputs for the Models**

LOW/	.2330E+24	-2.400	.0/		
HCO+NO=CO+HNO	.7200E+13	.000	.0		
H+NO+M=HNO+M	.4000E+21	-1.750	.0		
N2/	1.00/H2O/	4.10/H2/	1.25/		
HNO+H=NO+H2	.4400E+12	.720	650.0		
HNO+O=NO+OH	.1000E+14	.000	.0		
HNO+OH=NO+H2O	.3600E+14	.000	.0		
HNO+O2=NO+HO2	.1000E+14	.000	25000.0		
HNO+NH2=NO+NH3	.2000E+14	.000	1000.0		
HNO+NO=N2O+OH	.2000E+13	.000	26000.0		
HNO+NO2=HONO+NO	.6000E+12	.000	2000.0		
HNO+HNO=N2O+H2O	.9000E+09	.000	3100.0		
NO2+H2=HONO+H	.3000E+14	.000	29000.0		
HONO+O=NO2+OH	.1200E+14	.000	6000.0		
HONO+OH=NO2+H2O	.4000E+13	.000	.0		
HONO+NH=NH2+NO2	.1000E+14	.000	.0		
HONO+NH2=NH3+NO2	.5000E+13	.000	.0		
HONO+HONO=NO+NO2+H2O	.1020E+14	.000	8540.0		
H2NO+M=HNO+H+M	.1000E+17	.000	50000.0		
H2NO+H=HNO+H2	.3000E+08	2.000	2000.0		
H2NO+H=NH2+OH	.5000E+14	.000	.0		
H2NO+O=HNO+OH	.3000E+08	2.000	2000.0		
H2NO+OH=HNO+H2O	.2000E+08	2.000	1000.0		
H2NO+NO=HNO+HNO	.2000E+05	2.000	13000.0		
H2NO+NH2=HNO+NH3	.3000E+13	.000	1000.0		
H2NO+NO2=HONO+HNO	.6000E+12	.000	2000.0		
NO3+H=NO2+OH	.6000E+14	.000	.0		
NO3+O=NO2+O2	.1000E+14	.000	.0		
NO3+OH=NO2+HO2	.1400E+14	.000	.0		
NO3+HO2=NO2+O2+OH	.1500E+13	.000	.0		
NO3+NO2=NO+NO2+O2	.5000E+11	.000	2940.0		
NO3=NO+O2	.2500E+07	.000	12000.0		
NO3+NO3=NO2+NO2+O2	.5100E+12	.000	6750.0		
HCO+NO2=H+CO2+NO	.8400E+16	-.750	1930.0		
NO2+H=NO+OH	.1320E+15	.000	360.0		
NO2+O=NO+O2	.3900E+13	.000	-238.0		
NO2+O+M=NO3+M	.2940E+22	-2.000	.0		
NO2+HO2=HONO+O2	.6310E+09	1.250	5000.0		
NO2+NO2=NO+NO+O2	.1600E+13	.000	26123.0		
NO2+NO2=NO3+NO	.9600E+10	.730	20923.0		
DUPLICATE					
NO2+NO2=NO3+NO	.1600E+13	.000	26123.0		

DUPLICATE			
CO+NO2=CO2+NO	.9040E+14	.000	33800.0
HCO+NO2=CO+HONO	.1200E+24	-3.290	2355.0
CN+H2=HCN+H	.3000E+06	2.450	2245.0
HCN+O=NCO+H	.1400E+05	2.640	4980.0
HCN+O=NH+CO	.3500E+04	2.640	4980.0
HCN+O=CN+OH	.2700E+10	1.580	29200.0
HCN+OH=CN+H2O	.3900E+07	1.830	10300.0
HCN+OH=HOCN+H	.5900E+05	2.400	12500.0
HCN+OH=HNCO+H	.2000E-02	4.000	1000.0
HCN+OH=NH2+CO	.7800E-03	4.000	4000.0
CN+O=CO+N	.7700E+14	.000	.0
CN+OH=NCO+H	.4000E+14	.000	.0
CN+O2=NCO+O	.7500E+13	.000	-389.0
NCO+M=N+CO+M	.3100E+17	-.500	48000.0
N2/ 1.50/			
NCO+H=NH+CO	.5000E+14	.000	.0
NCO+O=NO+CO	.4700E+14	.000	.0
NCO+N=N2+CO	.2000E+14	.000	.0
N2O+CO=N2+CO2	.2700E+12	.000	20237.0
NCO+O2=NO+CO2	.2000E+13	.000	20000.0
NCO+OH=HCO+NO	.5000E+13	.000	15000.0
NCO+HCO=HNCO+CO	.3600E+14	.000	.0
NCO+CH2O=HNCO+HCO	.6000E+13	.000	.0
NCO+NO2=CO+NO+NO	.1300E+14	.000	.0
NCO+NO2=CO2+N2O	.5400E+13	.000	.0
NCO+HNO=HNCO+NO	.1800E+14	.000	.0
NCO+HONO=HNCO+NO2	.3600E+13	.000	.0
NCO+NCO=CO+CO+N2	.1800E+14	.000	.0
HCNO+H=HCN+OH	.1100E+14	.000	.0
HOCN+H=HNCO+H	.2000E+08	2.000	2000.0
HOCN+OH=NCO+H2O	.6400E+06	2.000	2560.0
HOCN+O=NCO+OH	.1500E+05	2.640	4000.0
HCNO+O=HCO+NO	.6300E+14	.000	.0
HCNO+O=NCO+OH	.7000E+13	.000	.0
HCNO+OH=CH2O+NO	.1000E+13	.000	.0
HCNO+OH=NO+CO+H2	.6500E+13	.000	.0
HCNO+OH=NCO+H+OH	.4500E+13	.000	.0
HCNO+OH=NCO+H2O	.3500E+13	.000	.0
HCNO+OH=HCO+HNO	.3500E+13	.000	.0
HNCO+M=CO+NH+M	.1100E+17	.000	86000.0
N2/ 1.50/			

**APPENDIX E - Updated Chemical Kinetics Mechanisms with NOX
Formation Pathways and Required Inputs for the Models**

HNCO+H=NH2+CO	.2250E+08	1.700	3800.0
HNCO+O=NCO+OH	.2200E+07	2.110	11430.0
HNCO+O=NH+CO2	.9600E+08	1.410	8520.0
HNCO+O=HNO+CO	.1500E+09	1.570	44012.0
HNCO+HO2=NCO+H2O2	.3000E+12	.000	22000.0
HNCO+O2=HNO+CO2	.1000E+13	.000	35000.0
HNCO+NH2=NH3+NCO	.5000E+13	.000	6200.0
HNCO+NH=NH2+NCO	.3000E+14	.000	23700.0
HNCO+NO2=HNNO+CO2	.2500E+13	.000	26200.0
HNCO+CN=NCO+HCN	.1500E+14	.000	.0
NCO+H2=HNCO+H	.7600E+03	3.000	4000.0
HNCO+OH=NCO+H2O	.6400E+06	2.000	2560.0
NCO+NO=N2+CO2	.7800E+18	-1.730	763.0
NCO+NO=N2O+CO	.6200E+18	-1.730	763.0
H2CN+M=HCN+H+M	.3000E+15	.000	21860.0
CO2+N=NO+CO	.1900E+12	.000	3400.0
CO2+CN=NCO+CO	.3670E+07	2.160	26887.0
CH3+N=H2CN+H	.7100E+14	.000	.0
CH3+NO=HCN+H2O	.1500E+00	3.523	3950.0
CH3+NO=H2CN+OH	.1500E+00	3.523	3950.0
CH2+N=HCN+H	.5000E+14	.000	.0
CH2+N2=HCN+NH	.1000E+14	.000	73520.0
CH+N=CN+H	.1300E+14	.000	.0
CH+N2=HCN+N	.4000E+13	.000	21900.0
CH+N2O=HCN+NO	.9600E+13	.000	-993.0
C+N2=CN+N	.6300E+14	.000	46000.0
C+NO=CN+O	.1900E+14	.000	.0
C+NO=N+CO	.2900E+14	.000	.0
CH+NO=HCN+O	.1100E+15	.000	.0
CH+NO=H+NCO	.2000E+14	.000	.0
CH+NO=N+HCO	.3000E+14	.000	.0
CH2+NO=NCO+H2	.3500E+13	.000	-378.0
CH2*+NO=NCO+H2	.3500E+13	.000	-378.0
CH2+NO=HCN+OH	.3900E+12	.000	-378.0
CH2*+NO=HCN+OH	.2000E+14	.000	.0
CH2+NO=H+HNCO	.1300E+13	.000	-378.0
CH2*+NO=H+HNCO	.3100E+18	-1.380	1270.0
CH2+NO=HCNO+H	.3100E+13	.000	-378.0
CH2*+NO=H+HCNO	.3800E+14	-.360	580.0
HCNO+H=H+HNCO	.5000E+11	.000	.0
C2H6+CN=C2H5+HCN	.1200E+06	2.770	-1790.0
C2H6+NCO=C2H5+HNCO	.1500E-08	6.890	-2910.0

C2H4+CN=C2H3+HCN	.5900E+15	-.240	.0
C2H3+NO=C2H2+HNO	.1000E+13	.000	1000.0
C2H2+NCO=HCCO+HCN	.1400E+13	.000	1815.0
CH2CO+CN=HCCO+HCN	.2000E+14	.000	.0
CH4+CN=HCN+CH3	.6200E+05	2.640	-437.0
CH2CN+O=CH2O+CN	.1000E+15	.000	.0
CH2OH+CN=CH2CN+OH	.5000E+14	.000	.0
CH3+CN=CH2CN+H	.1000E+15	.000	.0
C2H3+N=HCN+CH2	.2000E+14	.000	.0
HCCO+N=HCN+CO	.5000E+14	.000	.0
HCCO+NO2=HCNO+CO2	.1600E+14	.000	.0
HCCO+NO=HCNO+CO	.5500E+14	.000	436.0
HCCO+NO=HCN+CO2	.1400E+14	.000	1674.0
C2H+NO=HCN+CO	.2100E+14	.000	.0
C3H3+N=HCN+C2H2	.1000E+15	.000	.0
N2O+M=N2+O+M	.4000E+15	.000	56100.0
N2/ 1.70/O2/ 1.40/H2O/ 12.00/CO/ 1.50/CO2/ 3.00/			
N2O+H=N2+OH	.3300E+11	.000	4729.0
DUPLICATE			
N2O+H=N2+OH	.4400E+15	.000	19254.0
DUPLICATE			
NH+NO=N2O+H	.3190E+15	-.455	.0
N2O+O=NO+NO	.2900E+14	.000	23150.0
N2O+O=N2+O2	.1400E+13	.000	10800.0
N2O+OH=N2+HO2	.2000E+13	.000	40000.0
HCN+O2=CN+HO2	.5000E+13	.000	72500.0
CH3+NO2=CH3O+NO	.1500E+14	.000	.0
C2H5+NO2=>CH3+CH2O+NO	.1000E+14	.000	.0
NO+CH4=HNO+CH3	.5000E+12	.000	50000.0
NO+C2H6=HNO+C2H5	.7000E+12	.000	48000.0
CH3NO2(+M)=CH3+NO2(+M)	.1780E+17	.000	58500.0
LOW/ .1260E+18 .000 42000.0/			
TROE/ .1830 .1000E-29 .1000E+31 /			
HNO2+H=NO2+H2	.2400E+09	1.500	5087.0
HNO2+O=NO2+OH	.1700E+09	1.500	3020.0
HNO2+OH=NO2+H2O	.1200E+07	2.000	-596.0
HNO2+CH3=NO2+CH4	.8100E+06	1.870	4838.0
HNO2=HONO	.1300E+30	-5.470	52814.0
HONO+CH3=NO2+CH4	.8100E+06	1.870	5504.0
OH+NO2(+M)=HONO2(+M)	.2400E+14	.000	.0
LOW/ .6420E+33 -5.490 2351.0/			
TROE/ .5250 .1000E-14 .1000E-14 .1000E+16/			

**APPENDIX E - Updated Chemical Kinetics Mechanisms with NOX
Formation Pathways and Required Inputs for the Models**

```

H2O/ 5.00/
HONO2+OH=NO3+H2O          .1030E+11  .000 -1240.0
CH3O+NO(+M)=CH3ONO(+M)    .1210E+14  .000 -322.0
LOW/ .2700E+25 -3.500  .0/
CH3O+NO=CH2O+HNO          .6000E+14  -.600  .0
CH3+NO(+M)=CH3NO(+M)      .2170E+12  .600  .0
LOW/ .2060E+28 -3.500  .0/
CH3O+NO2(+M)=CH3ONO2(+M)  .1200E+14  .000  .0
LOW/ .1400E+31 -4.500  .0/
CH3O+NO2=CH2O+HONO        .4000E+13  .000 2285.0
NO2  +CH2CO=>HONO  +HCCO .2562E+07 2.0 19137.67
NH2  +CH2CO=>NH3  +HCCO .3377E+05 2.0 -218.01
NH2  +H2=>NH3    +H    .1576E+06 2.0 3954.86
NH2  +CH4=>NH3    +CH3 .7880E+05 2.0 6420.66
NO2  +C2H2=>HONO  +C2H .1708E+07 2.0 30041.75
NH2  +C2H2=>NH3  +C2H .2251E+05 2.0 7178.43
CN   +C2H2=>HCN  +C2H .6799E+07 2.0 1228.43
NO2  +C2H4=>HONO  +C2H3 .6831E+07 2.0 30041.75
NH2  +C2H4=>NH3  +C2H3 .9005E+05 2.0 6668.39
NH2  +C2H6=>NH3  +C2H5 .1013E+06 2.0 3863.80
NO2  +C3H8=>HONO  +NC3H7 .6831E+07 2.0 24525.57
NH2  +C3H8=>NH3  +NC3H7 .9005E+05 2.0 3603.31
CN   +C3H8=>HCN  +NC3H7 .2720E+08 2.0 -1307.69
! ABSTRACTION REACTION N. 10
! R+C3H8>RH+IC3H7
! NUMBER OF H ABSTRACTED: 2.0
! TYPE OF H ABSTRACTED: 1
NO2  +C3H8=>HONO  +IC3H7 .1708E+07 2.0 20933.63
NH2  +C3H8=>NH3  +IC3H7 .2251E+05 2.0 1777.23
CN   +C3H8=>HCN  +IC3H7 .6799E+07 2.0 -2457.22
! ABSTRACTION REACTION N. 11
! R+C4H4>RH+C4H3
! NUMBER OF H ABSTRACTED: 8.0
! TYPE OF H ABSTRACTED: 4
O2   +C4H4=>HO2  +C4H3 .2385E+08 2.0 51172.82
NO2  +C4H4=>HONO  +C4H3 .1195E+08 2.0 29656.90
NH2  +C4H4=>NH3  +C4H3 .1576E+06 2.0 6553.39
CN   +C4H4=>HCN  +C4H3 .4759E+08 2.0 675.88
! ABSTRACTION REACTION N. 12
! R+C4H6>RH+C4H5
! NUMBER OF H ABSTRACTED: 12.0
! TYPE OF H ABSTRACTED: 7

```

O2 +C4H6=>HO2 +C4H5 .4089E+08 2.0 51633.86
NO2 +C4H6=>HONO +C4H5 .2049E+08 2.0 30041.75
NH2 +C4H6=>NH3 +C4H5 .2702E+06 2.0 6586.90
CN +C4H6=>HCN +C4H5 .8159E+08 2.0 636.90
! ABSTRACTION REACTION N. 14
! R+NC4H8>RH+CH2C3H5
! NUMBER OF H ABSTRACTED: 3.0
! TYPE OF H ABSTRACTED: 0
O2 +NC4H8=>HO2 +CH2C3H5 .5111E+07 2.0 45025.57
NO2 +NC4H8=>HONO +CH2C3H5 .2562E+07 2.0 24525.57
NH2 +NC4H8=>NH3 +CH2C3H5 .3377E+05 2.0 3627.57
CN +NC4H8=>HCN +CH2C3H5 .1020E+08 2.0 -1283.43
! ABSTRACTION REACTION N. 15
! R+iC4H8>RH+iC4H7
! NUMBER OF H ABSTRACTED: 6.0
! TYPE OF H ABSTRACTED: 1
NO2 +iC4H8=>HONO +iC4H7 .5123E+07 2.0 20933.63
NH2 +iC4H8=>NH3 +iC4H7 .6754E+05 2.0 3143.17
CN +iC4H8=>HCN +iC4H7 .2040E+08 2.0 -1091.27
NH2 +H2O=>NH3 +OH .1126E+06 2.0 8169.13
! ABSTRACTION REACTION N. 17
! R+H2O2>RH+HO2
! NUMBER OF H ABSTRACTED: 2.0
! TYPE OF H ABSTRACTED: 6
NO2 +H2O2=>HONO +HO2 .6831E+06 2.0 14711.89
NH2 +H2O2=>NH3 +HO2 .9005E+04 2.0 -1507.20
CN +H2O2=>HCN +HO2 .2720E+07 2.0 -4569.75
! ABSTRACTION REACTION N. 18
! R+CH3OH>RH+CH3O
! NUMBER OF H ABSTRACTED: 1.0
! TYPE OF H ABSTRACTED: 9
NO2 +CH3OH=>HONO +CH3O .4270E+06 2.0 23242.74
NH2 +CH3OH=>NH3 +CH3O .5628E+04 2.0 1198.83
CN +CH3OH=>HCN +CH3O .1700E+07 2.0 -3470.54
! ABSTRACTION REACTION N. 19
! R+CH3OH>RH+CH2OH
! NUMBER OF H ABSTRACTED: 3.0
! TYPE OF H ABSTRACTED: 0
NO2 +CH3OH=>HONO +CH2OH .2562E+07 2.0 24525.57
NH2 +CH3OH=>NH3 +CH2OH .3377E+05 2.0 4513.05
CN +CH3OH=>HCN +CH2OH .1020E+08 2.0 -397.95
! ABSTRACTION REACTION N. 20

APPENDIX E - Updated Chemical Kinetics Mechanisms with NOX Formation Pathways and Required Inputs for the Models

! R+CH2O>RH+HCO
! NUMBER OF H ABSTRACTED: 2.0
! TYPE OF H ABSTRACTED: 8
NO2 +CH2O=>HONO +HCO .6831E+07 2.0 18752.82
NH2 +CH2O=>NH3 +HCO .9005E+05 2.0 1189.51
CN +CH2O=>HCN +HCO .2720E+08 2.0 -2634.16
! ABSTRACTION REACTION N. 21
! R+CH3CHO>RH+CH3CO
! NUMBER OF H ABSTRACTED: 1.5
! TYPE OF H ABSTRACTED: 8
NO2 +CH3CHO=>HONO +CH3CO .5123E+07 2.0 18752.82
NH2 +CH3CHO=>NH3 +CH3CO .6754E+05 2.0 1520.39
CN +CH3CHO=>HCN +CH3CO .2040E+08 2.0 -2303.28
! ABSTRACTION REACTION N. 22
! R+CH3CHO>RH+CH2CHO
! NUMBER OF H ABSTRACTED: 3.0
! TYPE OF H ABSTRACTED: 0
NO2 +CH3CHO=>HONO +CH2CHO .2562E+07 2.0 24525.57
NH2 +CH3CHO=>NH3 +CH2CHO .3377E+05 2.0 4712.83
CN +CH3CHO=>HCN +CH2CHO .1020E+08 2.0 -198.17
! ABSTRACTION REACTION N. 23
! R+PC3H4>RH+C3H3
! NUMBER OF H ABSTRACTED: 30.0
! TYPE OF H ABSTRACTED: 7
O2 +PC3H4=>HO2 +C3H3 .1022E+09 2.0 51633.86
NO2 +PC3H4=>HONO +C3H3 .5123E+08 2.0 30041.75
NH2 +PC3H4=>NH3 +C3H3 .6754E+06 2.0 8910.90
CN +PC3H4=>HCN +C3H3 .2040E+09 2.0 2960.90
! ABSTRACTION REACTION N. 24
! R+AC3H4>RH+C3H3
! NUMBER OF H ABSTRACTED: 30.0
! TYPE OF H ABSTRACTED: 7
O2 +AC3H4=>HO2 +C3H3 .1022E+09 2.0 51633.86
NO2 +AC3H4=>HONO +C3H3 .5123E+08 2.0 30041.75
NH2 +AC3H4=>NH3 +C3H3 .6754E+06 2.0 8910.90
CN +AC3H4=>HCN +C3H3 .2040E+09 2.0 2960.90
! ABSTRACTION REACTION N. 25
! R+C5H4O>RH+C4H3+CO
! NUMBER OF H ABSTRACTED: 8.0
! TYPE OF H ABSTRACTED: 4
O2 +MCPTD=>HO2 +C6H6+H .1704E+08 2.0 38570.96
NO2 +MCPTD=>HONO +C6H6+H .8539E+07 2.0 19137.67

```

NH2  +MCPTD=>NH3  +C6H6+H .1126E+06 2.0 159.29
CN   +MCPTD=>HCN   +C6H6+H .3399E+08 2.0 -3736.87
! ABSTRACTION REACTION N. 28
! R+C6H6>RH+C6H5
! NUMBER OF H ABSTRACTED: 8.0
! TYPE OF H ABSTRACTED: 7
NO2  +C6H6=>HONO  +C6H5 .1366E+08 2.0 30041.75
NH2  +C6H6=>NH3   +C6H5 .1801E+06 2.0 4857.23
CN   +C6H6=>HCN   +C6H5 .5439E+08 2.0 -1092.77
! ABSTRACTION REACTION N. 29
! R+CH3OOH>RH+CH3OO
! NUMBER OF H ABSTRACTED: 2.0
! TYPE OF H ABSTRACTED: 1
CN   +NH3=>HCN   +NH2 .1020E+09 2.0 2733.92
! ABSTRACTION REACTION N. 44
! R+HCN>RH+CN
! NUMBER OF H ABSTRACTED: .3
! TYPE OF H ABSTRACTED: 5
NO2  +HCN=>HONO  +CN .1281E+07 2.0 37097.34
NH2  +HCN=>NH3   +CN .1689E+05 2.0 7644.92
! ABSTRACTION REACTION N. 45
! R+CH3NO2>RH+NO+CH2O
! NUMBER OF H ABSTRACTED: 3.0
! TYPE OF H ABSTRACTED: 1
O2   +CH3NO2=>HO2  +NO+CH2O .5111E+07 2.0 40722.49
NO2  +CH3NO2=>HONO  +NO+CH2O .2562E+07 2.0 20933.63
NH2  +CH3NO2=>NH3   +NO+CH2O .3377E+05 2.0 1315.38
CN   +CH3NO2=>HCN   +NO+CH2O .1020E+08 2.0 -2919.06
END
!=====

```

Thermodynamics data for NO_x pathway

```

THERMO
298.000 1000.000 5000.000
N2      121286N 2      G 0300.00 5000.00 1000.00 1
0.02926640E+02 0.14879768E-02 0.05684760E-05 0.10097038E-09 0.06753351E-13 2
-0.09227977E+04 0.05980528E+02 0.03298677E+02 0.14082404E-02 0.03963222E-04 3
0.05641515E-07 0.02444854E-10 0.10208999E+04 0.03950372E+02 4
CH3NO      C 1H 3O 1N 1G 300.00 3500.00 860.00 1
1.73828229e+00 1.65479495e-02 8.69271695e-06 2.17002760e-09 2.08463444e-13 2
8.36473513e+03 1.74966005e+01 2.23451684e+00 1.42398818e-02 4.66701756e-06 3
-9.50669597e-10 6.98715974e-13 8.27938279e+03 1.51773992e+01 4
CH3NO2     C 1H 3O 2N 1G 300.00 3500.00 1620.00 1

```

APPENDIX E - Updated Chemical Kinetics Mechanisms with NOX Formation Pathways and Required Inputs for the Models

5.94771391e+00	1.22319078e-02	4.98716389e-06	9.73177561e-10	7.54873508e-14	2
-1.14691242e+04	-2.73415041e+00	-2.05952276e-01	2.74261453e-02	-1.90559023e-05	3
6.76278185e-09	9.68944802e-13	-9.47533640e+03	2.99224212e+01		4
CH3ONO	C	1H 3O 2N 1G	300.00 3500.00 1800.00		1
8.58034518e+00	8.90954082e-03	-3.35922089e-06	6.18588139e-10	-4.68096982e-14	2
-1.15569624e+04	-1.97194056e+01	1.99249583e+00	2.35492060e-02	-1.55589419e-05	3
5.13700333e-09	-6.74367363e-13	-9.18533663e+03	1.59354094e+01		4
CH3ONO2	C	1H 3O 3N 1G	300.00 3500.00 1800.00		1
1.07457798e+01	1.03362024e-02	-4.39539782e-06	8.95959797e-10	-7.26862027e-14	2
-1.81031090e+04	-3.08875015e+01	1.35155390e+00	3.12122600e-02	-2.17921125e-05	3
7.33918744e-09	-9.67578931e-13	-1.47211877e+04	1.99560088e+01		4
CN	C	1N 1 G	300.00 3500.00 810.00		1
2.73859606e+00	2.23580966e-03	-1.33797023e-06	4.34996429e-10	-5.05222621e-14	2
5.14568835e+04	8.20480076e+00	4.08532688e+00	-4.41471288e-03	1.09778123e-05	3
-9.70145006e-09	3.07801060e-12	5.12387131e+04	1.99138758e+00		4
H2CN	C	1H 2N 1 G	300.00 3500.00 1800.00		1
5.22111320e+00	3.42647499e-03	-8.36137799e-07	4.74833030e-11	4.28153350e-15	2
2.75312364e+04	-4.80262216e+00	1.81354567e+00	1.09988473e-02	-7.14644805e-06	3
2.38463525e-09	-3.20322903e-13	2.87579607e+04	1.36398442e+01		4
H2NO	H	2O 1N 1 G	300.00 3500.00 1200.00		1
1.43405821e+00	9.01333883e-03	-3.38828321e-06	4.28655869e-10	-2.36936075e-15	2
7.27341661e+03	1.79341864e+01	2.78935895e+00	4.49566971e-03	2.25880318e-06	3
-2.70861435e-09	6.51228601e-13	6.94814443e+03	1.11485432e+01		4
HCN	C	1H 1N 1 G	300.00 3500.00 850.00		1
3.48152100e+00	3.81748410e-03	-1.53642929e-06	3.02291150e-10	-2.35861473e-14	2
1.50427831e+04	3.30702298e+00	2.53139665e+00	8.28865751e-03	-9.42673531e-06	3
6.49076646e-09	-1.84372594e-12	1.52043042e+04	7.73641055e+00		4
HCNO	C	1H 1O 1N 1G	300.00 3500.00 1350.00		1
7.12423974e+00	1.61853378e-03	2.31339437e-07	-2.53211924e-10	3.63453797e-14	2
1.67567928e+04	-1.48886865e+01	2.20954024e+00	1.61806064e-02	-1.59487412e-05	3
7.73695136e-09	-1.44331449e-12	1.80837616e+04	1.02968215e+01		4
HNCO	C	1H 1O 1N 1G	300.00 3500.00 1660.00		1
7.29502452e+00	4.88032844e-04	8.74568316e-07	-4.09105701e-10	5.01959355e-14	2
-1.52722297e+04	-1.41696888e+01	2.99127956e+00	1.08585026e-02	-8.49633812e-06	3
3.35431054e-09	-5.16583618e-13	-1.38433864e+04	8.77460657e+00		4
HNNO	H	1O 1N 2 G	300.00 3500.00 1360.00		1
4.88500308e+00	5.60936901e-03	-2.60717829e-06	5.93839036e-10	-5.41495114e-14	2
2.58926738e+04	6.01980007e-01	2.29344827e+00	1.32315890e-02	-1.10140386e-05	3
4.71484900e-09	-8.11688108e-13	2.65975767e+04	1.39015974e+01		4
HNO	H	1O 1N 1 G	300.00 3500.00 900.00		1
2.72673666e+00	5.06770488e-03	-2.61122761e-06	6.38493559e-10	-6.01581004e-14	2
1.09769405e+04	9.63912842e+00	3.40204752e+00	2.06632330e-03	2.39107502e-06	3

-3.06691580e-09	9.69122277e-13	1.08553846e+04	6.45229501e+00	4	
HNO2	H 1O 2N 1	G 300.00	3500.00 1800.00	1	
3.30359406e+00	7.74006618e-03	3.91474332e-06	9.47112178e-10	8.88494507e-14	2
-8.65702544e+03	7.10072496e+00	1.68890715e+00	1.13282593e-02	6.90490427e-06	3
2.05457920e-09	2.42664314e-13	8.07573815e+03	1.58397474e+01	4	
HOCN	C 1H 1O 1N 1G	300.00	3500.00 1760.00	1	
6.92286755e+00	1.77083687e-04	1.06417841e-06	4.55819441e-10	5.43563991e-14	2
-3.77375638e+03	1.08544042e+01	3.05788784e+00	8.96112848e-03	6.42222341e-06	3
2.37993882e-09	3.48450172e-13	2.41328352e+03	9.97681509e+00	4	
HONO	H 1O 2N 1	G 300.00	3500.00 1420.00	1	
5.88742112e+00	3.49329101e-03	1.17730803e-06	1.65569378e-10	6.87715202e-15	2
-1.14386309e+04	5.23866548e+00	2.37883184e+00	1.33766411e-02	1.16174666e-05	3
5.06705227e-09	8.69814280e-13	1.04421916e+04	1.29185606e+01	4	
HONO2	H 1O 3N 1	G 300.00	3500.00 1310.00	1	
5.20949091e+00	9.97123440e-03	5.50725421e-06	1.39250696e-09	1.33157469e-13	2
-1.74464288e+04	1.35430787e+00	8.85706040e-01	2.31736309e-02	2.06245022e-05	3
9.08576291e-09	1.60133609e-12	1.63135971e+04	2.06729940e+01	4	
NH	H 1N 1	G 300.00	3500.00 1550.00	1	
2.53691464e+00	1.74532708e-03	6.66818142e-07	1.34160653e-10	1.04190033e-14	2
4.21821879e+04	7.12732805e+00	3.75007687e+00	1.38541418e-03	2.36293147e-06	3
-1.16895746e-09	1.99761337e-13	4.18061076e+04	7.42847188e-01	4	
NH2	H 2N 1	G 300.00	3500.00 1120.00	1	
2.67687765e+00	3.48484078e-03	1.28570820e-06	2.72091630e-10	2.36034281e-14	2
2.20303372e+04	7.34730162e+00	4.18313061e+00	1.89463407e-03	5.91894562e-06	3
-4.01639279e-09	9.33647558e-13	2.16929365e+04	9.01998745e-02	4	
NH3	H 3N 1	G 300.00	3500.00 1210.00	1	
2.21117984e+00	6.52182453e-03	2.30931532e-06	3.98907128e-10	2.80385645e-14	2
-6.39009604e+03	8.86905603e+00	3.21689186e+00	3.19715670e-03	1.81217371e-06	3
-1.87188573e-09	4.41133513e-13	6.63347835e+03	3.82536772e+00	4	
NNH	H 1N 2	G 300.00	3500.00 720.00	1	
2.67540125e+00	5.35668680e-03	2.94990450e-06	7.78541240e-10	7.91413867e-14	2
2.84746064e+04	1.03028707e+01	3.96823590e+00	1.82572793e-03	1.20134595e-05	3
-1.30764254e-08	4.73161093e-12	2.82884383e+04	4.49039228e+00	4	
NO	O 1N 1	G 300.00	3500.00 970.00	1	
2.69775018e+00	2.39887133e-03	1.31644700e-06	3.38235813e-10	3.29394890e-14	2
9.99854348e+03	9.40230813e+00	3.91290193e+00	2.61206371e-03	6.43242163e-06	3
-4.98744709e-09	1.33965920e-12	9.76280404e+03	3.57691592e+00	4	
NO2	O 2N 1	G 300.00	3500.00 1800.00	1	
5.25673685e+00	1.64343307e-03	6.24197948e-07	1.07065150e-10	6.88584753e-15	2
1.95363563e+03	2.35827568e+00	2.61409592e+00	7.51596848e-03	5.51797745e-06	3
1.91957608e-09	2.58623476e-13	2.90498637e+03	1.19442483e+01	4	
NO3	O 3N 1	G 300.00	3500.00 1330.00	1	

APPENDIX E - Updated Chemical Kinetics Mechanisms with NOX Formation Pathways and Required Inputs for the Models

```

7.66391925e+00 2.28165967e-03 8.16241554e-07 1.11367864e-10 3.38429715e-15 2
5.62975022e+03 -1.51899442e+01 4.06541943e-01 2.41083583e-02 -2.54328190e-05 3
1.24505044e-08 -2.32277087e-12 7.56021258e+03 2.18923574e+01 4
N2O          O 1N 2      G 300.00 3500.00 1650.00 1
5.52129143e+00 1.46645965e-03 -3.04694075e-07 -1.87106858e-11 8.50389041e-15 2
7.81312268e+03 -6.17451657e+00 2.68521969e+00 8.34178508e-03 -6.55498992e-06 3
2.50666137e-09 -3.74128239e-13 8.74902635e+03 8.92812480e+00 4
N2H2         H 2N 2      G 300.00 3500.00 930.00 1
1.94872574e+00 9.02206572e-03 -4.48167913e-06 1.07159624e-09 -9.96387287e-14 2
2.46850174e+04 1.27074554e+01 2.44745784e+00 6.87698140e-03 -1.02186571e-06 3
-1.40855675e-09 5.67069064e-13 2.45922533e+04 1.03375547e+01 4
N2H3         H 3N 2      G 300.00 3500.00 1610.00 1
5.06961797e+00 6.18061831e-03 -1.87909018e-06 2.33273638e-10 -8.03110073e-15 2
1.63477734e+04 -4.00218491e+00 1.71415249e+00 1.45171785e-02 -9.64607174e-06 3
3.44941507e-09 -5.07431944e-13 1.74282333e+04 1.37839838e+01 4
N2H4         H 4N 2      G 300.00 3500.00 1160.00 1
4.91914378e+00 9.71187969e-03 -3.62925367e-06 6.36530934e-10 -4.28508947e-14 2
9.36304606e+03 -2.64395648e+00 3.60425651e-01 2.54315974e-02 -2.39564748e-05 3
1.23188419e-08 -2.56059034e-12 1.04206687e+04 2.00258283e+01 4
NCO          C 1O 1N 1      G 300.00 3500.00 1700.00 1
5.80612871e+00 1.29457396e-03 -2.96387145e-07 -4.45669057e-12 6.00806513e-15 2
1.70053704e+04 -6.33800183e+00 2.87969597e+00 8.18029805e-03 -6.37202605e-06 3
2.37814680e-09 -3.44374801e-13 1.80003575e+04 9.33319238e+00 4
CH3ONO       C 1H 3O 2N 1G 300.00 3500.00 1800.00 1
8.58034518e+00 8.90954082e-03 -3.35922089e-06 6.18588139e-10 -4.68096982e-14 2
-1.15569624e+04 -1.97194056e+01 1.99249583e+00 2.35492060e-02 -1.55589419e-05 3
5.13700333e-09 -6.74367363e-13 -9.18533663e+03 1.59354094e+01 4
CH3ONO2      C 1H 3O 3N 1G 300.00 3500.00 1800.00 1
1.07457798e+01 1.03362024e-02 -4.39539782e-06 8.95959797e-10 -7.26862027e-14 2
-1.81031090e+04 -3.08875015e+01 1.35155390e+00 3.12122600e-02 -2.17921125e-05 3
7.33918744e-09 -9.67578931e-13 -1.47211877e+04 1.99560088e+01 4
CH2CN        C 2H 2N 1      G 300.00 3500.00 980.00 1
4.41880974e+00 9.83430327e-03 -4.98991807e-06 1.22319871e-09 -1.17396557e-13 2
2.92390343e+04 2.02769260e+00 2.71162977e+00 1.68023848e-02 -1.56553489e-05 3
8.47859386e-09 -1.96826267e-12 2.95736416e+04 1.02293594e+01 4
ENDOFDATA

```

Appendix E.3 - NO_x pathways for NUIGalway Mechanism

Gas-phase kinetics for NO_x pathway

n+no<=>n2+o	2.700E+13	.000	355.00
n+o2<=>no+o	9.000E+09	1.000	6500.00
n+oh<=>no+h	3.360E+13	.000	385.00
n2o+o<=>n2+o2	1.400E+12	.000	10810.00
n2o+o<=>2no	2.900E+13	.000	23150.00
n2o+h<=>n2+oh	3.870E+14	.000	18880.00
n2o+oh<=>n2+ho2	2.000E+12	.000	21060.00
n2o(+M)<=>n2+o(+M)	7.910E+10	.000	56020.00
LoW / 6.370E+14	.000	56640.00/	
h2/2.00/ h2o/6.00/ ch4/2.00/ co/1.50/ co2/2.00/ c2h6/3.00/ ar/ .625/			
ho2+n<=>no2+oh	2.110E+12	.000	-480.00
no+o+M<=>no2+M	1.060E+20	-1.410	.00
h2/2.00/ h2o/6.00/ ch4/2.00/ co/1.50/ co2/2.00/ c2h6/3.00/ ar/ .70/			
no2+o<=>no+o2	3.900E+12	.000	-240.00
no2+h<=>no+oh	1.320E+14	.000	360.00
nh+o<=>no+h	4.000E+13	.000	.00
nh+h<=>n+h2	3.200E+13	.000	330.00
nh+oh<=>hno+h	2.000E+13	.000	.00
nh+oh<=>n+h2o	2.000E+09	1.200	.00
nh+o2<=>hno+o	4.610E+05	2.000	6500.00
nh+o2<=>no+oh	1.280E+06	1.500	100.00
nh+n<=>n2+h	1.500E+13	.000	.00
nh+h2o<=>hno+h2	2.000E+13	.000	13850.00
nh+no<=>n2+oh	2.160E+13	-.230	.00
nh+no<=>n2o+h	3.650E+14	-.450	.00
nh2+o<=>oh+nh	3.000E+12	.000	.00
nh2+o<=>h+hno	3.900E+13	.000	.00
nh2+h<=>nh+h2	4.000E+13	.000	3650.00
nh2+oh<=>nh+h2o	9.000E+07	1.500	-460.00
nnh<=>n2+h	3.300E+08	.000	.00
nnh+M<=>n2+h+M	1.300E+14	-.110	4980.00
h2/2.00/ h2o/6.00/ ch4/2.00/ co/1.50/ co2/2.00/ c2h6/3.00/ ar/ .70/			
nnh+o2<=>ho2+n2	5.000E+12	.000	.00
nnh+o<=>oh+n2	2.500E+13	.000	.00
nnh+o<=>nh+no	7.000E+13	.000	.00
nnh+h<=>h2+n2	5.000E+13	.000	.00
nnh+oh<=>h2o+n2	2.000E+13	.000	.00
nnh+ch3<=>ch4+n2	2.500E+13	.000	.00
h+no+M<=>hno+M	4.480E+19	-1.320	740.00

**APPENDIX E - Updated Chemical Kinetics Mechanisms with NOX
Formation Pathways and Required Inputs for the Models**

h2/2.00/ h2o/6.00/ ch4/2.00/ co/1.50/ co2/2.00/ c2h6/3.00/ ar/ .70/

hno+o<=>no+oh	2.500E+13	.000	.00
hno+h<=>h2+no	9.000E+11	.720	660.00
hno+oh<=>no+h2o	1.300E+07	1.900	-950.00
hno+o2<=>ho2+no	1.000E+13	.000	13000.00
cn+o<=>co+n	7.700E+13	.000	.00
cn+oh<=>nco+h	4.000E+13	.000	.00
cn+h2o<=>hcn+oh	8.000E+12	.000	7460.00
cn+o2<=>nco+o	6.140E+12	.000	-440.00
cn+h2<=>hcn+h	2.950E+05	2.450	2240.00
nco+o<=>no+co	2.350E+13	.000	.00
nco+h<=>nh+co	5.400E+13	.000	.00
nco+oh<=>no+h+co	0.250E+13	.000	.00
nco+n<=>n2+co	2.000E+13	.000	.00
nco+o2<=>no+co2	2.000E+12	.000	20000.00
nco+M<=>n+co+M	3.100E+14	.000	54050.00

h2/2.00/ h2o/6.00/ ch4/2.00/ co/1.50/ co2/2.00/ c2h6/3.00/ ar/ .70/

nco+no<=>n2o+co	1.900E+17	-1.520	740.00
nco+no<=>n2+co2	3.800E+18	-2.000	800.00
hcn+M<=>h+cn+M	1.040E+29	-3.300	126600.00

h2/2.00/ h2o/6.00/ ch4/2.00/ co/1.50/ co2/2.00/ c2h6/3.00/ ar/ .70/

hcn+o<=>nco+h	2.030E+04	2.640	4980.00
hcn+o<=>nh+co	5.070E+03	2.640	4980.00
hcn+o<=>cn+oh	3.910E+09	1.580	26600.00
hcn+oh<=>hocn+h	1.100E+06	2.030	13370.00
hcn+oh<=>hnco+h	4.400E+03	2.260	6400.00
hcn+oh<=>nh2+co	1.600E+02	2.560	9000.00
h+hcn(+M)<=>h2cn(+M)	3.300E+13	.000	.00

LoW / 1.400E+26 -3.400 1900.00/

h2/2.00/ h2o/6.00/ ch4/2.00/ co/1.50/ co2/2.00/ c2h6/3.00/ ar/ .70/

h2cn+n<=>n2+ch2	6.000E+13	.000	400.00
c+n2<=>cn+n	6.300E+13	.000	46020.00
ch+n2<=>hcn+n	3.120E+09	0.880	20130.00
ch+n2(+M)<=>hcnn(+M)	3.100E+12	.150	.00

LoW / 1.300E+25 -3.160 740.00/

TRoE/ .6670 235.00 2117.00 4536.00 /

h2/2.00/ h2o/6.00/ ch4/2.00/ co/1.50/ co2/2.00/ c2h6/3.00/ ar/ 1.0/

ch2+n2<=>hcn+nh	1.000E+13	.000	74000.00
ch2(s)+n2<=>nh+hcn	1.000E+11	.000	65000.00
c+no<=>cn+o	1.900E+13	.000	.00
c+no<=>co+n	2.900E+13	.000	.00
ch+no<=>hcn+o	4.100E+13	.000	.00

ch+no<=>h+nco	1.620E+13	.000	.00
ch+no<=>n+hco	2.460E+13	.000	.00
ch2+no<=>h+hnco	3.100E+17	-1.380	1270.00
ch2+no<=>oh+hcn	2.900E+14	-.690	760.00
ch2+no<=>h+hcno	3.800E+13	-.360	580.00
ch2(s)+no<=>h+hnco	3.100E+17	-1.380	1270.00
ch2(s)+no<=>oh+hcn	2.900E+14	-.690	760.00
ch2(s)+no<=>h+hcno	3.800E+13	-.360	580.00
ch3+no<=>hcn+h2o	9.600E+13	.000	28800.00
ch3+no<=>h2cn+oh	1.000E+12	.000	21750.00
hcnn+o<=>co+h+n2	2.200E+13	.000	.00
hcnn+o<=>hcn+no	2.000E+12	.000	.00
hcnn+o2<=>o+hco+n2	1.200E+13	.000	.00
hcnn+oh<=>h+hco+n2	1.200E+13	.000	.00
hcnn+h<=>ch2+n2	1.000E+14	.000	.00
hnco+o<=>nh+co2	9.800E+07	1.410	8500.00
hnco+o<=>hno+co	1.500E+08	1.570	44000.00
hnco+o<=>nco+oh	2.200E+06	2.110	11400.00
hnco+h<=>nh2+co	2.250E+07	1.700	3800.00
hnco+h<=>h2+nco	1.050E+05	2.500	13300.00
hnco+oh<=>nco+h2o	3.300E+07	1.500	3600.00
hnco+oh<=>nh2+co2	3.300E+06	1.500	3600.00
hnco+M<=>nh+co+M	1.180E+16	.000	84720.00
h2/2.00/ h2o/6.00/ ch4/2.00/ co/1.50/ co2/2.00/ c2h6/3.00/ ar/ .70/			
hcno+h<=>h+hnco	2.100E+15	-.690	2850.00
hcno+h<=>oh+hcn	2.700E+11	.180	2120.00
hcno+h<=>nh2+co	1.700E+14	-.750	2890.00
hocn+h<=>h+hnco	2.000E+07	2.000	2000.00
hcco+no<=>hcno+co	0.900E+13	.000	.00
ch3+n<=>h2cn+h	6.100E+14	-.310	290.00
ch3+n<=>hcn+h2	3.700E+12	.150	-90.00
nh3+h<=>nh2+h2	5.400E+05	2.400	9915.00
nh3+oh<=>nh2+h2o	5.000E+07	1.600	955.00
nh3+o<=>nh2+oh	9.400E+06	1.940	6460.00
nh+co2<=>hno+co	1.000E+13	.000	14350.00
cn+no2<=>nco+no	6.160E+15	-0.752	345.00
nco+no2<=>n2o+co2	3.250E+12	.000	-705.00
n+co2<=>no+co	3.000E+12	.000	11300.00
end			

**APPENDIX E - Updated Chemical Kinetics Mechanisms with NOX
Formation Pathways and Required Inputs for the Models**

Thermodynamics data for NO_x pathway

thermo

```

300.000 1000.000 5000.000
h2cn      41687h 2c 1n 1 G 300.00 4000.000 1000.000 1
0.52097030E+01 0.29692911E-02-0.28555891E-06-0.16355500E-09 0.30432589E-13 2
0.27677109E+05-0.44444780E+01 0.28516610E+01 0.56952331E-02 0.10711400E-05 3
-0.16226120E-08-0.23511081E-12 0.28637820E+05 0.89927511E+01 4
hcn       GRI/98h 1c 1n 1 G 200.000 6000.000 1000.000 1
0.38022392E+01 0.31464228E-02-0.10632185E-05 0.16619757E-09-0.97997570E-14 2
0.14407292E+05 0.15754601E+01 0.22589886E+01 0.10051170E-01-0.13351763E-04 3
0.10092349E-07-0.30089028E-11 0.14712633E+05 0.89164419E+01 4
hno       And93 h 1n 1o 1 G 200.000 6000.000 1000.000 1
0.29792509E+01 0.34944059E-02-0.78549778E-06 0.57479594E-10-0.19335916E-15 2
0.11750582E+05 0.86063728E+01 0.45334916E+01-0.56696171E-02 0.18473207E-04 3
-0.17137094E-07 0.55454573E-11 0.11548297E+05 0.17498417E+01 4
n         L 6/88n 1 G 200.000 6000.000 1000.000 1
0.24159429E+01 0.17489065E-03-0.11902369E-06 0.30226245E-10-0.20360982E-14 2
0.56133773E+05 0.46496096E+01 0.25000000E+01 0.00000000E+00 0.00000000E+00 3
0.00000000E+00 0.00000000E+00 0.56104637E+05 0.41939087E+01 4
nhh       T07/93n 2h 1 G 200.000 6000.000 1000.000 1
0.37667544E+01 0.28915082E-02-0.10416620E-05 0.16842594E-09-0.10091896E-13 2
0.28650697E+05 0.44705067E+01 0.43446927E+01-0.48497072E-02 0.20059459E-04 3
-0.21726464E-07 0.79469539E-11 0.28791973E+05 0.29779410E+01 4
n2o       L 7/88n 2o 1 G 200.000 6000.000 1000.000 1
0.48230729E+01 0.26270251E-02-0.95850874E-06 0.16000712E-09-0.97752303E-14 2
0.80734048E+04-0.22017207E+01 0.22571502E+01 0.11304728E-01-0.13671319E-04 3
0.96819806E-08-0.29307182E-11 0.87417744E+04 0.10757992E+02 4
nh        And94 n 1h 1 G 200.000 6000.000 1000.000 1
0.27836928E+01 0.13298430E-02-0.42478047E-06 0.78348501E-10-0.55044470E-14 2
0.42120848E+05 0.57407799E+01 0.34929085E+01 0.31179198E-03-0.14890484E-05 3
0.24816442E-08-0.10356967E-11 0.41880629E+05 0.18483278E+01 4
nh2       And89 n 1h 2 G 200.000 6000.000 1000.000 1
0.28347421E+01 0.32073082E-02-0.93390804E-06 0.13702953E-09-0.79206144E-14 2
0.22171957E+05 0.65204163E+01 0.42040029E+01-0.21061385E-02 0.71068348E-05 3
-0.56115197E-08 0.16440717E-11 0.21885910E+05-0.14184248E+00 4
nh3       J 6/77n 1h 3 G 200.000 6000.000 1000.000 1
0.26344521E+01 0.56662560E-02-0.17278676E-05 0.23867161E-09-0.12578786E-13 2
-0.65446958E+04 0.65662928E+01 0.42860274E+01-0.46605230E-02 0.21718513E-04 3
-0.22808887E-07 0.82638046E-11-0.67417285E+04-0.62537277E+00 4
no        RUS 78n 1o 1 G 200.000 6000.000 1000.000 1
0.32606056E+01 0.11911043E-02-0.42917048E-06 0.69457669E-10-0.40336099E-14 2

```

```

0.99209746E+04 0.63693027E+01 0.42184763E+01-0.46389760E-02 0.11041022E-04 3
-0.93361354E-08 0.28035770E-11 0.98446230E+04 0.22808464E+01 4
no2      L 7/88n 1o 2      G 200.000 6000.000 1000.000 1
0.48847542E+01 0.21723956E-02-0.82806906E-06 0.15747510E-09-0.10510895E-13 2
0.23164983E+04-0.11741695E+00 0.39440312E+01-0.15854290E-02 0.16657812E-04 3
-0.20475426E-07 0.78350564E-11 0.28966179E+04 0.63119917E+01 4
hcno     BDEA94h 1n 1c 1o 1G 300.000 5000.000 1382.000 1
6.59860456E+00 3.02778626E-03-1.07704346E-06 1.71666528E-10-1.01439391E-14 2
1.79661339E+04-1.03306599E+01 2.64727989E+00 1.27505342E-02-1.04794236E-05 3
4.41432836E-09-7.57521466E-13 1.92990252E+04 1.07332972E+01 4
hocn     BDEA94h 1n 1c 1o 1G 300.000 5000.000 1368.000 1
5.89784885E+00 3.16789393E-03-1.11801064E-06 1.77243144E-10-1.04339177E-14 2
-3.70653331E+03-6.18167825E+00 3.78604952E+00 6.88667922E-03-3.21487864E-06 3
5.17195767E-10 1.19360788E-14-2.82698400E+03 5.63292162E+00 4
hnco     BDEA94h 1n 1c 1o 1G 300.000 5000.000 1478.000 1
6.22395134E+00 3.17864004E-03-1.09378755E-06 1.70735163E-10-9.95021955E-15 2
-1.66599344E+04-8.38224741E+00 3.63096317E+00 7.30282357E-03-2.28050003E-06 3
-6.61271298E-10 3.62235752E-13-1.55873636E+04 6.19457727E+00 4
nco      EA 93 n 1c 1o 1 G 200.000 6000.000 1000.000 1
0.51521845E+01 0.23051761E-02-0.88033153E-06 0.14789098E-09-0.90977996E-14 2
0.14004123E+05-0.25442660E+01 0.28269308E+01 0.88051688E-02-0.83866134E-05 3
0.48016964E-08-0.13313595E-11 0.14682477E+05 0.95504646E+01 4
cn       hBh92 c 1n 1      G 200.000 6000.000 1000.000 1
0.37459805E+01 0.43450775E-04 0.29705984E-06-0.68651806E-10 0.44134173E-14 2
0.51536188E+05 0.27867601E+01 0.36129351E+01-0.95551327E-03 0.21442977E-05 3
-0.31516323E-09-0.46430356E-12 0.51708340E+05 0.39804995E+01 4
hcnn     SRI/94c 1n 2h 1 G 300.000 5000.000 1000.000 1
0.58946362E+01 0.39895959E-02-0.15982380E-05 0.29249395E-09-0.20094686E-13 2
0.53452941E+05-0.51030502E+01 0.25243194E+01 0.15960619E-01-0.18816354E-04 3
0.12125540E-07-0.32357378E-11 0.54261984E+05 0.11675870E+02 4
n2       121286n 2      G 300.000 5000.000 1000.000 1
0.02926640E+02 0.14879768E-02-0.05684760E-05 0.10097038E-09-0.06753351E-13 2
-0.09227977E+04 0.05980528E+02 0.03298677E+02 0.14082404E-02-0.03963222E-04 3
0.05641515E-07-0.02444854E-10-0.10208999E+04 0.03950372E+02 4
end

```

**APPENDIX E - Updated Chemical Kinetics Mechanisms with NOX
Formation Pathways and Required Inputs for the Models**

Appendix E.4: Inputs required for the Rizk chemical reactor Network

Variable	Definition
FZ_ChemKinInputs.Inlet_Phi (distribution)	Equivalence ratios for each FZ reactor
FZ_ChemKinInputs.Inlet_mdot (distribution)	Mass flow for each FZ reactor
FZ_ChemKinInputs.Inlet_T (distribution)	Temperature for each FZ reactor
FZ_ChemKinInputs.Inlet_Fuel (distribution)	Fuel flow for each FZ reactor
FZ_ChemKinInputs.Mixer_P (distribution)	Pressure for each FZ mixer
FZ_ChemKinInputs.Mixer_Vol (distribution)	Volume for each FZ mixer
FZ_ChemKinInputs.Inlet_P (distribution)	Pressure for each FZ reactor
FZ_ChemKinInputs.Inlet_Vol (distribution)	Volume for each FZ reactor
PFZ_Volume	Post-flame zone volume
PFZ_Total_Pressure	Post-flame zone pressure

Appendix E.5: Inputs required for the Valera chemical reactor network

Variable	Definition
MZ_ChemKinputs.Inlet_Phi	Equivalence ratios for mixing zone reactor
MZ_ChemKinputs.Inlet_mdot	Mass flow for mixing zone reactor
MZ_ChemKinputs.Inlet_T	Temperature for mixing zone reactor
MZ_ChemKinputs.Inlet_Fuel	Fuel flow for mixing zone reactor
MZ_ChemKinputs.Inlet_P	Pressure for mixing zone reactor
MZ_ChemKinputs.Inlet_Vol	Volume for mixing zone reactor
FZ_Volume	Flame zone volume
FZ_Total_Pressure	Flame zone total pressure
RZ_Volume	Recirculation zone volume
RZ_Total_Pressure	Recirculation zone total pressure
PFZ_Volume	Post-flame zone volume
PFZ_total_pressure	Post-flame zone pressure

APPENDIX E - Updated Chemical Kinetics Mechanisms with NOX
 Formation Pathways and Required Inputs for the Models
 Appendix E.6: Inputs required for the modified Rizk chemical reactor
 network

Variable	Definition
FZ_ChemKininputs.Inlet_Phi	Equivalence ratios for FZ reactor
FZ_ChemKininputs.Inlet_mdots	Mass flow for FZ reactor
FZ_ChemKininputs.Inlet_T	Temperature for FZ reactor
FZ_ChemKininputs.Inlet_Fuel	Fuel flow for FZ reactor
FZ_ChemKininputs.Mixer_P	Pressure for FZ mixer
FZ_ChemKininputs.Mixer_Vol	Volume for FZ mixer
FZ_ChemKininputs.Inlet_P	Pressure for FZ reactor
FZ_ChemKininputs.Inlet_Vol	Volume for FZ reactor
PFZ_Volume	Post-flame zone volume
PFZ_Total_Pressure	Post-flame zone pressure

Appendix E.7: Inputs required for the modified Valera chemical reactor network

Variable	Definition
MZ_ChemKinputs.Inlet_Air	Air flow for mixing zone reactor
MZ_ChemKinputs.Inlet_T	Temperature for mixing zone reactor
MZ_ChemKinputs.Inlet_Fuel	Fuel flow for mixing zone reactor
MZ_ChemKinputs.Inlet_P	Pressure for mixing zone reactor
MZ_Volume	Volume for mixing zone reactor
MZ_Heat_Loss_Rate	Heat loss rate for mixing zone reactor
MZ_Residence_Time	Residence time for mixing zone reactor
FZ_Volume	Flame zone volume
FZ_Total_Pressure	Flame zone total pressure
FZ_Heat_Loss_Rate	Heat loss rate for flame zone reactor
FZ_Residence_Time	Residence time for flame zone reactor
CRZ_Volume	Central recirculation zone volume
CRZ_Total_Pressure	Central recirculation zone total pressure
CRZ_Heat_Loss_Rate	Heat loss rate for central recirculation zone reactor
CRZ_Residence_Time	Residence time for central recirculation zone reactor
ERZ_Volume	Edge recirculation zone volume
ERZ_Total_Pressure	Edge recirculation zone total pressure
ERZ_Heat_Loss_Rate	Heat loss rate for edge recirculation zone reactor
ERZ_Residence_Time	Residence time for edge recirculation zone reactor
PFZ_Volume	Post-flame zone volume
PFZ_total_pressure	Post-flame zone pressure

**APPENDIX E - Updated Chemical Kinetics Mechanisms with NOX
Formation Pathways and Required Inputs for the Models**

**Appendix E.8: Inputs required for the simplified chemical reactor
network**

Variable	Definition
MZ_ChemKinputs.Inlet_Phi	Equivalence ratios for mixing zone reactor
MZ_ChemKinputs.Inlet_mdot	Mass flow for mixing zone reactor
MZ_ChemKinputs.Inlet_T	Temperature for mixing zone reactor
MZ_ChemKinputs.Inlet_Fuel	Fuel flow for mixing zone reactor
MZ_ChemKinputs.Inlet_P	Pressure for mixing zone reactor
MZ_ChemKinputs.Inlet_Vol	Volume for mixing zone reactor
FZ_Volume	Flame zone volume
FZ_Total_Pressure	Flame zone pressure
PFZ_Volume	Post-flame zone volume
PFZ_Total_Pressure	Post-flame zone pressure

Appendix E.9: Inputs required for the unconfined HPGSB-2 chemical reactor network

Variable	Definition
MZ_ChemKininputs.Inlet_Air	Air flow for mixing zone reactor
MZ_ChemKininputs.Inlet_T	Temperature for mixing zone reactor
MZ_ChemKininputs.Inlet_Fuel	Fuel flow for mixing zone reactor
MZ_ChemKininputs.Inlet_P	Pressure for mixing zone reactor
MZ_Volume	Volume for mixing zone reactor
MZ_Heat_Loss_Rate	Heat loss rate for mixing zone reactor
MZ_Residence_Time	Residence time for mixing zone reactor
FZ_Volume	Flame zone volume
FZ_Total_Pressure	Flame zone total pressure
FZ_Heat_Loss_Rate	Heat loss rate for flame zone reactor
FZ_Residence_Time	Residence time for flame zone reactor
CRZ_Volume	Central recirculation zone volume
CRZ_Total_Pressure	Central recirculation zone total pressure
CRZ_Heat_Loss_Rate	Heat loss rate for central recirculation zone reactor
CRZ_Residence_Time	Residence time for central recirculation zone reactor
ERZ_Volume	Edge recirculation zone volume
ERZ_Total_Pressure	Edge recirculation zone total pressure
ERZ_Heat_Loss_Rate	Heat loss rate for edge recirculation zone reactor
ERZ_Residence_Time	Residence time for edge recirculation zone reactor
PFZ_Volume	Post-flame zone volume
PFZ_total_pressure	Post-flame zone pressure

**APPENDIX E - Updated Chemical Kinetics Mechanisms with NOX
Formation Pathways and Required Inputs for the Models**

**Appendix E.10: Inputs required for the confined HPGSB-2 chemical
reactor network**

Variable	Definition
MZ_ChemKininputs.Inlet_Air	Air flow for mixing zone reactor
MZ_ChemKininputs.Inlet_T	Temperature for mixing zone reactor
MZ_ChemKininputs.Inlet_Fuel	Fuel flow for mixing zone reactor
MZ_ChemKininputs.Inlet_P	Pressure for mixing zone reactor
MZ_Volume	Volume for mixing zone reactor
MZ_Heat_Loss_Rate	Heat loss rate for mixing zone reactor
MZ_Residence_Time	Residence time for mixing zone reactor
FZ_Volume	Flame zone volume
FZ_Total_Pressure	Flame zone total pressure
FZ_Heat_Loss_Rate	Heat loss rate for flame zone reactor
FZ_Residence_Time	Residence time for flame zone reactor
CRZ_Volume	Central recirculation zone volume
CRZ_Total_Pressure	Central recirculation zone total pressure
CRZ_Heat_Loss_Rate	Heat loss rate for central recirculation zone reactor
CRZ_Residence_Time	Residence time for central recirculation zone reactor
ERZ_Volume	Edge recirculation zone volume
ERZ_Total_Pressure	Edge recirculation zone total pressure
ERZ_Heat_Loss_Rate	Heat loss rate for edge recirculation zone reactor
ERZ_Residence_Time	Residence time for edge recirculation zone reactor
PFZ_Volume	Post-flame zone volume
PFZ_total_pressure	Post-flame zone pressure